COASTAL FLOODING: MODELING, MONITORING, AND PROTECTION SYSTEMS

EDITED BY: Valentina Prigiobbe, Clint Dawson, Yao Hu, Hatim O. Sharif and Navid Tahvildari

PUBLISHED IN: Frontiers in Climate and Frontiers in Water

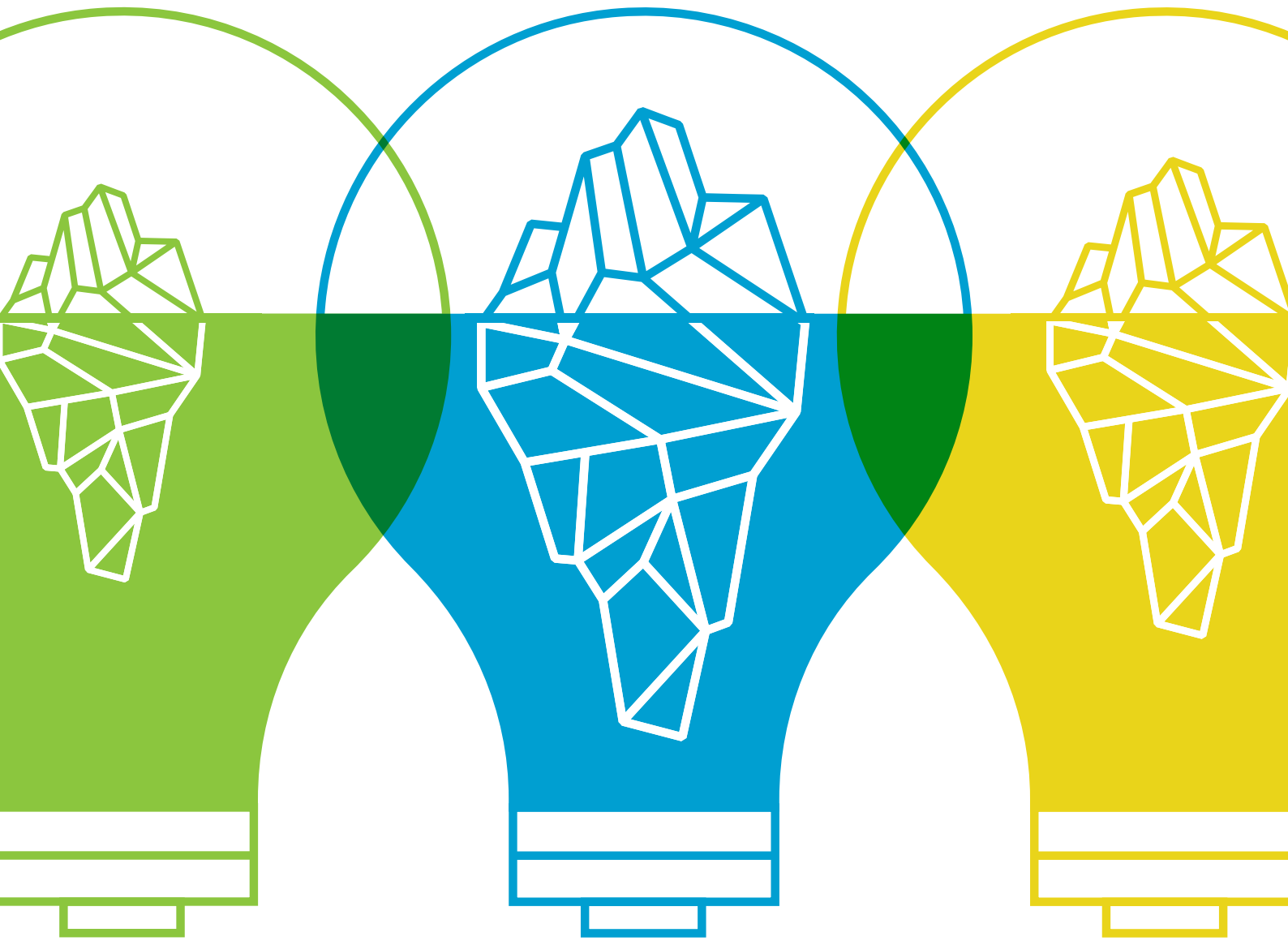

frontiers Research Topics

ISSN 1664-8714
ISBN 978-2-88974-455-8
DOI 10.3389/978-2-88974-455-8

About Frontiers

Frontiers is more than just an open-access publisher of scholarly articles: it is a pioneering approach to the world of academia, radically improving the way scholarly research is managed. The grand vision of Frontiers is a world where all people have an equal opportunity to seek, share and generate knowledge. Frontiers provides immediate and permanent online open access to all its publications, but this alone is not enough to realize our grand goals.

Frontiers Journal Series

The Frontiers Journal Series is a multi-tier and interdisciplinary set of open-access, online journals, promising a paradigm shift from the current review, selection and dissemination processes in academic publishing. All Frontiers journals are driven by researchers for researchers; therefore, they constitute a service to the scholarly community. At the same time, the Frontiers Journal Series operates on a revolutionary invention, the tiered publishing system, initially addressing specific communities of scholars, and gradually climbing up to broader public understanding, thus serving the interests of the lay society, too.

Dedication to Quality

Each Frontiers article is a landmark of the highest quality, thanks to genuinely collaborative interactions between authors and review editors, who include some of the world's best academicians. Research must be certified by peers before entering a stream of knowledge that may eventually reach the public - and shape society; therefore, Frontiers only applies the most rigorous and unbiased reviews.
Frontiers revolutionizes research publishing by freely delivering the most outstanding research, evaluated with no bias from both the academic and social point of view. By applying the most advanced information technologies, Frontiers is catapulting scholarly publishing into a new generation.

What are Frontiers Research Topics?

Frontiers Research Topics are very popular trademarks of the Frontiers Journals Series: they are collections of at least ten articles, all centered on a particular subject. With their unique mix of varied contributions from Original Research to Review Articles, Frontiers Research Topics unify the most influential researchers, the latest key findings and historical advances in a hot research area! Find out more on how to host your own Frontiers Research Topic or contribute to one as an author by contacting the Frontiers Editorial Office: frontiersin.org/about/contact

COASTAL FLOODING: MODELING, MONITORING, AND PROTECTION SYSTEMS

Topic Editors:
Valentina Prigiobbe, Stevens Institute of Technology, United States
Clint Dawson, University of Texas at Austin, United States
Yao Hu, University of Delaware, United States
Hatim O. Sharif, University of Texas at San Antonio, United States
Navid Tahvildari, Old Dominion University, United States

Citation: Prigiobbe, V., Dawson, C., Hu, Y., Sharif, H. O., Tahvildari, N., eds. (2022). Coastal Flooding: Modeling, Monitoring, and Protection Systems. Lausanne: Frontiers Media SA. doi: 10.3389/978-2-88974-455-8

Table of Contents

04 ***Editorial: Coastal Flooding: Modeling, Monitoring, and Protection Systems***
Valentina Prigiobbe, Clint Dawson, Yao Hu, Hatim O. Sharif and Navid Tahvildari

06 ***Estuarine and Coastal Ecosystems as Defense Against Flood Damages: An Economic Perspective***
Edward B. Barbier

18 ***Developing a Modeling Framework to Simulate Compound Flooding: When Storm Surge Interacts With Riverine Flow***
Mark Loveland, Amin Kiaghadi, Clint N. Dawson, Hanadi S. Rifai, Shubhra Misra, Helena Mosser and Alessandro Parola

31 ***Enhancing Flood Hazard Assessments in Coastal Louisiana Through Coupled Hydrologic and Surge Processes***
Matthew V. Bilskie, Haihong Zhao, Don Resio, John Atkinson, Zachary Cobell and Scott C. Hagen

50 ***Hurricane Scenario Generation for Uncertainty Modeling of Coastal and Inland Flooding***
Kyoung Yoon Kim, Wen-Ying Wu, Erhan Kutanoglu, John J. Hasenbein and Zong-Liang Yang

65 ***Assessment of Riverine Dredging Impact on Flooding in Low-Gradient Coastal Rivers Using a Hybrid 1D/2D Hydrodynamic Model***
Haitham A. Saad and Emad H. Habib

85 ***Optimization of Coastal Protections in the Presence of Climate Change***
Yuki Miura, Philip C. Dinenis, Kyle T. Mandli, George Deodatis and Daniel Bienstock

99 ***Hurricane Irma Simulation at South Florida Using the Parallel CEST Model***
Yuepeng Li, Qiang Chen, Dave M. Kelly and Keqi Zhang

111 ***Assessing Damages to Built and Natural Environments: Linking Hydrodynamic and Geospatial Enviro-Economical Models***
Hanadi S. Rifai, Amin Kiaghadi and Daniel W. Burleson

128 ***Skew Surge and Storm Tides of Tropical Cyclones in the Delaware and Chesapeake Bays for 1980–2019***
John A. Callahan, Daniel J. Leathers and Christina L. Callahan

147 ***Estimation of Return Levels for Extreme Skew Surge Coastal Flooding Events in the Delaware and Chesapeake Bays for 1980–2019***
John A. Callahan and Daniel J. Leathers

frontiers in Climate

EDITORIAL
published: 14 January 2022
doi: 10.3389/fclim.2021.830946

Editorial: Coastal Flooding: Modeling, Monitoring, and Protection Systems

Valentina Prigiobbe[1]*, *Clint Dawson*[2], *Yao Hu*[3], *Hatim O. Sharif*[4] and *Navid Tahvildari*[5]

[1] Department of Civil, Environmental and Ocean Engineering, Stevens Institute of Technology, Hoboken, NJ, United States, [2] Department of Aerospace Engineering and Engineering Mechanics, The University of Texas at Austin, Austin, TX, United States, [3] Department of Geography and Spatial Sciences, Civil and Environmental Engineering, University of Delaware, Newark, DE, United States, [4] Department of Civil and Environmental Engineering, The University of Texas at San Antonio, San Antonio, TX, United States, [5] Department of Civil and Environmental Engineering, Old Dominion University, Norfolk, VA, United States

Keywords: coastal flooding, flooding prediction, extreme weather events, climate change, sea level rise, protection systems, coastal ecosystems and management, coastal urban areas

Editorial on the Research Topic

Coastal Flooding: Modeling, Monitoring, and Protection Systems

Coastal flooding has received significant attention in recent years due to future sea-level rise (SLR) projections and intensification of precipitation, which will exacerbate frequent flooding, coastal erosion, and eventually create permanently inundated low-elevation land. Coastal governments will be forced to implement measures to manage risk on the population and infrastructure and build protection systems to mitigate or adapt to the negative impacts of flooding. Research in this area is required to establish holistic frameworks for timely and accurate flooding forecast and design of protection systems.

In this Research Topic, a combination of Original Research Articles on monitoring and modeling of coastal flooding, design of protection systems, and economic perspective of coastal damage provides up-to-date information on diverse aspects of the risk and impact of coastal flooding and how it can be predicted and mitigated. The next paragraphs describe each of the published articles within the themes covered by the special issue.

The improvement of storm surge forecasting is necessary to implement strategies to minimize the damage of coastal flooding. The works by Callahan and Leathers and Callahan et al. study the impact of hurricanes in the Mid-Atlantic along one of the most developed and commercially active regions in the USA, the Delaware and Chesapeake Bays. The analysis of the spatial variability of the detrended and normalized skew surge combined with regional storm rankings and storm tracks allow to identify the surge impact of past TC on nearby coastal communities and set the approach to predict future risk damage (Callahan and Leathers). They evaluate two traditional approaches [namely, Block Maxima fit to General Extreme Value distribution (BM/GEV) and Points-Over-Threshold fit to Generalized Pareto distribution (POT/GP)] to determine the return sea levels for extreme skew surge (Callahan et al.). They conclude that POT/GP is more consistent with the data and has a narrower uncertainty band. The increased reliability of projections of extreme water levels using POT/GP will help plan more effective mitigation and adaptation strategies.

In addition to being reasonably accurate, storm surge forecasts must also be timely and be made available to users well before the onset of the event. The work by Li et al. focuses on the improved efficiency of the Coastal and Estuarine Storm Tide (CEST) model developed to simulate the storm surge due to the combined action of (anti)cylonic winds and astronomical tides. The new model version includes an upgraded advection algorithm and a simpler parallelization. As a proof-of-concept, they consider the impact of hurricane Irma in South Florida that lasted 4 days

OPEN ACCESS

Edited and reviewed by:
Maria Carmen Lemos, University of Michigan, United States

***Correspondence:**
Valentina Prigiobbe
valentina.prigiobbe@stevens.edu

Specialty section:
This article was submitted to Climate Risk Management, a section of the journal Frontiers in Climate

Received: *07 December 2021*
Accepted: *22 December 2021*
Published: *14 January 2022*

Citation:
Prigiobbe V, Dawson C, Hu Y, Sharif HO and Tahvildari N (2022) Editorial: Coastal Flooding: Modeling, Monitoring, and Protection Systems. Front. Clim. 3:830946. doi: 10.3389/fclim.2021.830946

and the improved CEST model was able to run it in just 22 min. Coastal flooding is not only attributed to storm surge, the work by Loveland et al. analyzes the combination of storm surge and river discharge as a specific case of compound flooding related to hurricane. The authors present a coupled modeling approach to simulate and forecast compound flooding using the Advanced Circulation (ADCIRC) model as the primary model to simulate the compounding effects of fluvial flooding and storm surge at regional scale. They stress the need to account for river discharge to accurately predict flood patterns, water surface elevations, and duration of drainage. However, in order to capture the complexity of compound flooding at the large regional or even global scale, it is envisaged to develop new holistic and numerically integrated models for compound flooding description.

Damage of flooding upon storm surge can go beyond the coast and affect inland regions. In their work, Kim et al. propose a probabilistic scenario generation approach to forecast coastal and inland flooding coupling coastal and fluvial models and incorporating uncertainty of hurricane landfall locations and inland precipitation intensity. In the simulation scenarios, the authors consider the case of Hurricane Harvey that devastated coastal areas of Texas and Louisiana (USA) in August 2017. A probabilistic scenario generation approach provides better tools to decision makers for mitigation strategies and preparedness decisions.

Flood-prone inland areas are also subject to the consequence of erroneous modifications of natural drainage systems. The work by Saad and Habib investigates the effect of large-scale channel modifications via riverine dredging. The article analyzes the case of Vermilion River in south Louisiana (USA) and shows that dredging can increase the hydraulic conveyance of the river system but also the runoff volumes delivered by the urbanized tributaries which can outweigh the larger in-channel storage. Moreover, as the work by Bilskie et al. shows, antecedent rainfall has an important effect on the flooding of south Louisiana. The results show that antecedent and TC-driven rainfall increase simulated peak water levels within the watershed. The work highlights the need to extend both the spatial and temporal boundaries of flooding prediction in coastal regions. This is particularly important in those areas with complex hydrological features. There it is recommended to undertake a watershed-centered approach instead of a riverine-centered approach combined with earlier storm events to plan flood mitigation strategies.

Damage to coastal areas due to flooding can be significant but it could also be challenging to assess, especially in environmentally vulnerable regions. The paper by Rifai et al. presents a holistic approach for damage assessment caused by severe hydrologic events. The approach combines a water quality model, Environmental Fluid Dynamic Code-Storm Surge model (EFDC-SS), and Facility Economic Damage and Environmental Release Planning (FEDERAP). The framework allows to determine the impact of spills from waste storage and contaminated sites at regional scale and estimate the cost of remediation.

Finally, the works by Miura et al. and Barbier focus on the optimization of protection systems. Miura et al. report a methodology that aims at minimizing the overall expected losses within a prescribed budget. They consider human-made protective systems such as seawalls, barriers, artificial dunes, raising individual buildings, sealing parts of the infrastructure, strategic retreat, and insurance that could be activated over time and built throughout the sensitive area. The effectiveness of each solution and their spatio-temporal combination was evaluated under different SLR scenarios using the storm surge computational model GeoClawflood. The authors apply a proof-of-concept of the method to the urban area of Lower Manhattan in New York City (NY). Barbier analyzes the economics of protective systems based on natural estuarine and coastal ecosystems (ECE) such as marsh, mangroves, coral reefs, and sea grass meadow. He observes that ECEs do not only provide flood mitigation but also have environmental benefits related to long-term coastal restoration and protection, which should considered. Alone, or in combination with human-made structures, ECEs can significantly reduce the vulnerability of the coastal areas while providing critical habitats of the land-sea interface.

With this Research Topic we provide a platform for scientists and engineers that are interested in modeling and monitoring coastal flooding, the design of protection systems, and the human and environmental impact of coastal flooding. The excellent contributions to this Research Topic are a demonstration of a highly active research community in coastal science and engineering focused on assessment of coastal flooding impacts. Together they provide a detailed overview of the state-of-the-art of the subject and future research needs.

AUTHOR CONTRIBUTIONS

VP is the lead author on this manuscript. All authors have contributed to the writing of this editorial and approved it for publication.

ACKNOWLEDGMENTS

The authors thank the Frontiers team for their professional help with this Research Topic.

Conflict of Interest: The authors declare that the research was conducted in the absence of any commercial or financial relationships that could be construed as a potential conflict of interest.

Publisher's Note: All claims expressed in this article are solely those of the authors and do not necessarily represent those of their affiliated organizations, or those of the publisher, the editors and the reviewers. Any product that may be evaluated in this article, or claim that may be made by its manufacturer, is not guaranteed or endorsed by the publisher.

frontiers in Climate

REVIEW
published: 18 December 2020
doi: 10.3389/fclim.2020.594254

Estuarine and Coastal Ecosystems as Defense Against Flood Damages: An Economic Perspective

*Edward B. Barbier**

Department of Economics, Colorado State University, Fort Collins, CO, United States

The rapid loss of estuarine and coastal ecosystems (ECEs) in recent years has raised concerns over their role in protecting coastal communities from storms that damage property, cause deaths, and inflict injuries. This paper reviews valuation studies of the protective service of ECEs in terms of reducing flood damages. Although the number of studies have grown significantly, there is still a need for a greater range of studies in more locations and for a wider variety of ecosystems. This review also examines, from an economic perspective, the issues and challenges surrounding estimating the protective benefits of ECEs, as exemplified by some of the recent valuation studies. Recent developments in valuation methods are summarized and critically reviewed. Important challenges remain in valuing coastal ecosystems as a defense against flood damages. The review discusses two of them, such as how protective benefits are subject to spatial variability and dependent on connectivity across "seascapes." These challenges, along with analyzing the multiple benefits of estuarine and coastal ecosystems, are important areas of future research priority.

Keywords: estuarine and coastal ecosystems, marsh, mangroves, storm protection service, economic valuation, wave attenuation

OPEN ACCESS

Edited by:
Valentina Prigiobbe, Stevens Institute of Technology, United States

Reviewed by:
José Maria Cardoso Da Silva, University of Miami, United States
Meri Davlasheridze, Texas A&M University at Galveston, United States
Denise Reed, University of New Orleans, United States

***Correspondence:**
Edward B. Barbier
Edward.barbier@colostate.edu

Specialty section:
This article was submitted to Climate Risk Management, a section of the journal Frontiers in Climate

Received: *12 August 2020*
Accepted: *24 November 2020*
Published: *18 December 2020*

Citation:
Barbier EB (2020) Estuarine and Coastal Ecosystems as Defense Against Flood Damages: An Economic Perspective. Front. Clim. 2:594254. doi: 10.3389/fclim.2020.594254

INTRODUCTION

The rapid loss of estuarine and coastal ecosystems (ECEs) globally has focused attention on their role in protecting coastal communities from storms that damage property and cause deaths and injury. It is now well-documented that many of these habitats provide such protection (Koch et al., 2009; Loder et al., 2009; Wamsley et al., 2010; Gedan et al., 2011; Paul et al., 2012; Armitage et al., 2019). These include specific studies of marshes (Shepard et al., 2011; Rupprecht et al., 2017), mangroves (Cochard et al., 2008; Zhang et al., 2012; Dasgupta et al., 2019; Montgomery et al., 2019), near-shore coral reefs (Ferrario et al., 2014; Reguero et al., 2018) and seagrass beds (Paul et al., 2012; Christianen et al., 2013; Ondiviela et al., 2014). This protective value of ECEs is increasingly used to justify coastal conservation and restoration efforts worldwide (Temmerman et al., 2012; Arkema et al., 2013; Duarte et al., 2013; Barbier, 2014; Elliott et al., 2016; Narayan et al., 2016; Ruckelshaus et al., 2016; Hochard et al., 2019; Menéndez et al., 2020; Newton et al., 2020).

Given that ECE conservation and restoration are increasingly advocated for protecting coastal communities from flooding hazards that damage property and cause deaths and injury, there is growing interest in quantifying and valuing such benefits. But despite the importance of this coastal protection service, there are still not many economic studies that have estimated a value for it and geographic coverage is still thin. In addition, questions have been raised about some of the methods used, and whether they are sufficiently robust to serve as a guide for policy

(Barbier, 2007; Kousky, 2010; Arnold, 2013). However, more reliable economic estimates of the protective value of mangrove and marsh systems are emerging. The purpose of this review is to examine, from an economic perspective, the issues and challenges surrounding measuring the protective benefits from ecosystem restoration, as exemplified by some of the recent valuation studies.

The paper begins with an overview of selective economic studies globally that have valued the protection benefit provided by ECEs. The paper then briefly summarizes recent developments in valuation methods that have been employed to estimate coastal protection. It is also important to recognize that ECEs provide other valuable benefits in addition to protection service. Nevertheless, important challenges remain in valuing coastal ecosystems as a defense against flood damages. The paper identifies two of them, such as how protective benefits are subject to spatial variability and dependent on connectivity across "seascapes." The final section of this paper concludes by discussing how further research can address these challenges in valuing the protective service of estuarine and coastal ecosystems.

VALUATION STUDIES AND METHODS

Review of Valuation Studies

Table 1 lists 41 studies, selected from peer-reviewed academic journals, which value the storm protection service of estuarine and coastal ecosystems (ECEs). This value is estimated for the ability of various ECEs to reduce the flood damage to property and other economic assets, and in some instances the risk of loss of life or injury, from coastal storms. The studies are grouped by type of ECE and geographical location.

The key ecological function that allows ECEs to provide a protection service is their ability to attenuate, or reduce the height, of the storm surges and waves as they approach shorelines, or to buffer winds (see **Table 1**). Both wave attenuation and wind buffering are directly related to the vegetation contained in some ECEs, such as marsh, seagrass beds and mangroves. However, the effects may vary for types and characteristics of hazardous events, the presence of emergent vs. submerged vegetation, and tidal and other seasonal conditions (Koch et al., 2009). For example, studies of wave attenuation by marsh wetlands consistently demonstrate significant wave height reductions per unit distance across marsh vegetation, although most of this wave attenuation effect was measured only for small to moderate waves (Shepard et al., 2011). Montgomery et al. (2019) note that numerous studies have found that mangroves provide effective coastal protection from storm waves, but their research in New Zealand and Florida show that mangroves can also reduce storm surge, which is the temporary increase in water level resulting from the combination of high winds and low atmospheric pressure during a weather event. Their study also shows that the effectiveness of mangroves in reducing surges depends not only on storm characteristics but also the density of the vegetation and the extent and depth of the mangroves along shorelines. Seagrass meadows on their own may provide only limited coastal protection in shallow waters and low wave energy environments, with the most effective protection provided by large, long-living and slow-growing seagrass species (Ondiviela et al., 2014). In contrast, the coastal protection from near-shore coral reefs can be significant, as it is their reticulated structure that provides a natural barrier to storm waves (Koch et al., 2009; Ferrario et al., 2014; Reguero et al., 2018).

Bathymetric effects, such as from sediment trapping and sedimentation that cause shorelines to become higher, are additionally important factors for the wave attenuation function of marshes (Koch et al., 2009; Loder et al., 2009; Wamsley et al., 2010; Rupprecht et al., 2017; Armitage et al., 2019). Sea-to-land shoreline elevation also contributes to the wave attenuation function provided by coastal landscapes populated by mangroves (Alongi, 2008; Cochard, 2011; Laso-Bayas et al., 2011; Armitage et al., 2019). For example, Alongi (2008) suggests that the extent to which mangroves offer protection against catastrophic natural disasters, such as tsunamis, may depend on a range of structural features and conditions within the mangrove ecosystem, such as width of forest, slope of forest floor, forest density, tree diameter and height, proportion of above-ground biomass in the roots, soil texture and forest location (open coast vs. lagoon).

In recent years, there have been a growing number of economic studies estimating the protective value of ECEs, especially for marsh and mangroves (see **Table 1**). Of the 41 studies listed, 31 have been published since 2010. In addition, estimates for coral reefs are starting to emerge. In contrast, few studies have valued the coastal protection benefits of seagrass meadows, which are more effective in shoreline stabilization than attenuation of large waves (Paul et al., 2012; Christianen et al., 2013; Ondiviela et al., 2014). Many additional studies for ECEs exist other than those listed in **Table 1**; however, especially for some of the earlier efforts, there have been problems in the reliability of the valuation methods employed (Barbier, 2007; Kousky, 2010; Arnold, 2013; Chaikumbung et al., 2016; Vedogbeton and Johnston, 2020).

Geographical coverage is also limited, with most valuation studies occurring in the United States and tropical Asia. This is not surprising, given that since Hurricanes Katrina, Rita, Sandy, and Harvey in the United States, the Indian Ocean tsunami in South and Southeast Asia, and Typhoon Haiyan in the Philippines, there has been increasing alarm that the loss ECEs in these regions has made their coastal areas and communities more vulnerable. But as the concern about damaging and life-threatening storms in all low-lying coastal areas grows, there are likely to be more studies in other parts of the world. For example, in Europe, the recognition that tidal marshes and other habitats provide protection against coastal flooding has led to increased studies of the potential wave attenuating function of these ECEs (Liquete et al., 2013; Guisado-Pintado et al., 2016; Schoutens et al., 2019).

Finally, because of the growing interest in the storm protection service provided by estuarine and coastal ecosystems, global analyses of this benefit are beginning to emerge. **Table 1** lists one example for coral reefs (Beck et al., 2018) and two for mangroves (Hochard et al., 2019; Menéndez et al., 2020). For example, Beck et al. (2018) estimate that the absence of the protective benefit of coral reefs would double the annual expected damages from flooding globally and triple the costs from frequent

TABLE 1 | Examples of studies that estimate the protective value of estuarine and coastal ecosystems.

Ecosystem structure and function	Ecosystem service	Valuation examples (chronologically by location)
Attenuates and/or dissipates waves, buffers wind	Protection of coastal communities against property damage, loss of life and/or injuries, risk.	(Badola and Hussain, 2005; Das and Vincent, 2009; Das and Crépin, 2013, mangroves, India) (Sathirathai and Barbier, 2001; Barbier, 2007, 2012; Barbier et al., 2008; Barbier and Lee, 2014, mangroves, Thailand) (Farber, 1987, 1996; Landry et al., 2011; Petrolia and Kim, 2011; Barbier et al., 2013; Kim and Petrolia, 2013; Barbier and Enchelmeyer, 2014; Petrolia et al., 2014; Boutwell and Westra, 2016, marsh and coastal wetlands, Louisiana, United States) (Rezaie et al., 2020, marsh, New Jersey, United States) (Highfield et al., 2018; Atoba et al., 2020, coastal wetlands, Texas, United States) (Boutwell and Westra, 2015, coastal wetlands, US Gulf Coast) (Narayan et al., 2017, marsh, northeastern United States) (Costanza et al., 2008, marsh, US Atlantic and Gulf Coasts) (Vázquez-González et al., 2019, coastal wetlands, Mexico) (King and Lester, 1995; Mangi et al., 2011, marsh, United Kingdom) (Liu et al., 2019, coastal wetlands, China) (Ouyang et al., 2018, coastal wetlands, China and Australia) (Huxham et al., 2015, mangroves, Kenya) (Menéndez et al., 2018, mangroves, Philippines) (Mahmud and Barbier, 2016, mangroves, Bangladesh) (Laso-Bayas et al., 2011), mangroves, Aceh, Indonesia) (del Valle et al., 2020), mangroves, Central America) (van Zanten et al., 2014, coral reefs, U.S. Virgin Islands) (Wilkinson et al., 1999, coral reefs, Indian Ocean) (Pascal et al., 2016, coral reefs, Caribbean and Pacific) (Beck et al., 2018, coral reefs, global) (Hochard et al., 2019; Menéndez et al., 2020, mangroves, global) (Rao et al., 2015; Narayan et al., 2016, estuarine and coastal ecosystems, global)

The 41 studies selected are from peer-reviewed academic journals only, and are grouped by type of estuarine and coastal ecosystem and its location.

storms. Improved reef management would especially benefit Indonesia, Philippines, Malaysia, Mexico, and Cuba, with each country reducing annual flood damages by at least $400 million. Hochard et al. (2019) analyze the impact of mangrove extent in protecting economic activity in coastal regions from cyclones over 2000 to 2012 for nearly 2,000 tropical and sub-tropical communities globally. For a community with an average cover of 6.3 m of mangroves extending inland from the seaward edge, direct cyclone exposure can reduce economic activity permanently by 5.4–6.7 months, whereas for a community with 25.6 m of mangroves extending inland from the shoreline, the loss in activity is 2.6–5.5 months. Menéndez et al. (2020) value the global flood protection benefits of mangroves at over $US 65 billion per year, and estimate that the loss of all mangroves would mean that 15 million more people worldwide would be susceptible to annual flooding. The countries benefiting the most include the United States, China, India, Mexico, Vietnam, and Bangladesh.

Economic Valuation Methods

As can be seen from the valuation studies in **Table 1**, as the number of studies valuing the protective value of ECEs has increased, important developments have occurred in the methods used to estimate the protective value of estuarine and coastal ecosystems (ECEs). Many of the early studies employed the replacement cost method to value the storm prevention and flood mitigation services, which involves estimating the costs of constructing physical barriers to perform the same services provided for free by ECEs (King and Lester, 1995; Sathirathai and Barbier, 2001; Mangi et al., 2011; Huxham et al., 2015; Narayan et al., 2016). However, as a valuation method, there are two overall limitations to this replacement cost approach. First, it estimates a benefit (e.g., storm protection) by a cost (e.g., the expenses incurred for constructing seawalls, breakwaters, dykes, groins and other physical structures), and second, human-built structures are not always cost-effective as an alternative to ECEs in providing the same level of coastal protection benefit (Barbier, 2007; Freeman et al., 2014; World Bank, 2016; Kousky and Light, 2019).

The limitations of employing the replacement cost method to value the protective benefit of an ECE are illustrated in **Figure 1**. Assume that the initial landscape area of a marsh or mangrove is S_0. Because the ecosystem provides this service for "free," there is no cost, and thus it corresponds to the horizontal axis $0S_0$. However, suppose conversion causes some of the ECE area to decrease to S_1. The replacement cost method would value any subsequent loss in protection benefit by the additional cost of "replacing" it with seawalls, breakwaters, levies and other human-built structures to reduce storm surge and waves. However, the additional—or marginal cost—of building more and more structures to provide coastal protection is likely to rise as the level of protection increases. In **Figure 1**, the marginal cost of building such a physical storm barrier is MC_H. Thus, the "replacement cost" of using the human built barrier to provide the same storm protection service as the S_0S_1 amount of wetlands lost is measured by the difference between the two cost curves, or

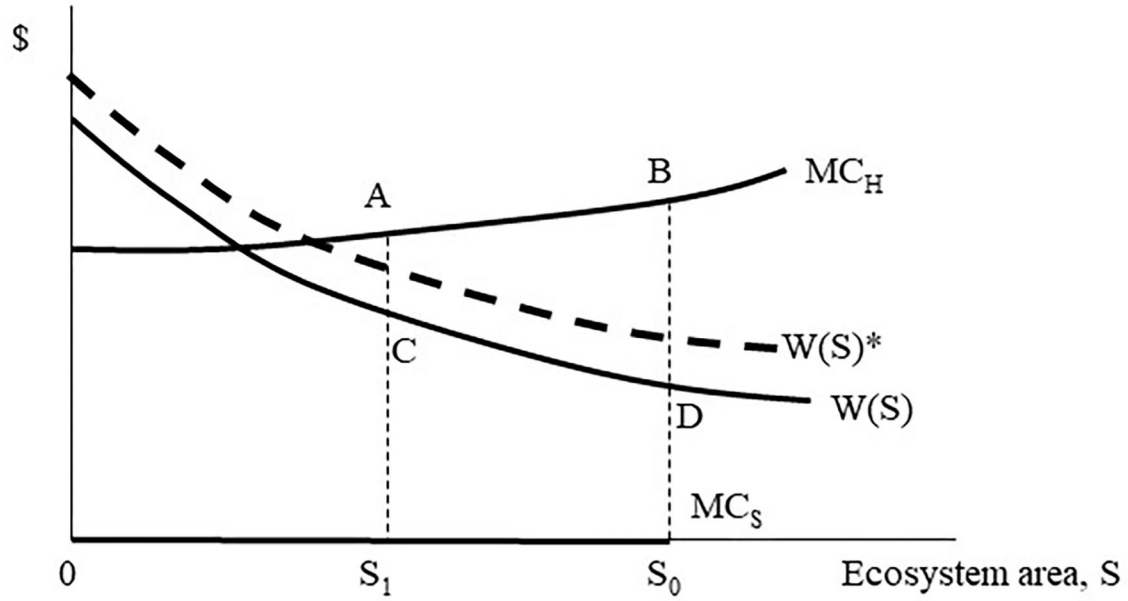

FIGURE 1 | The net benefits of the storm protection service provided by an estuarine and coastal ecosystem of area S_0. The cost of the storm protection service provided by the ecosystem is "free" and is thus $0S_0$. However, if the ecosystem area declines to S_1, then there is a loss in net benefits from protection service represented by area S_0CDS_1. If the cost of replacing the loss in service by a human-built barrier is used to estimate the net benefits, this "replacement cost" estimate would be area S_0ABS_1. This method over-estimates the net benefits of the storm protection service by area ABCD. Note that, if the willingness to pay for protection service also includes not just protection of property and other assets from storms [curve W(S)] but also reducing the risk of injury, illness, or death and the disutility of risk exposure [curve W(S)*], the net benefits of storm protection service will be greater than area S_0CDS_1. However, as shown in the figure, the replacement cost method still over-estimates these net benefits. MCs, Marginal cost of the "free" protective service provided by the coastal wetland; MCH, Marginal cost of building a storm barrier "replace" the protective service provided by the coastal wetland; W(S), Demand, or marginal willingness to pay, for protection service provided by wetlands of area S; W(S)*, Demand, or marginal willingness to pay, for protection service provided by ECE of area S, including reducing the risk of injury, illness or death and the disutility of risk exposure.

area S_0ABS_1. However, this cost difference is not measuring the benefit of having the wetlands provide the storm protection service. Instead, this benefit is represented by the demand curve, which indicates how much extra individuals are willing to pay for the additional protection provided by having more wetlands. This demand curve is represented by $W(S)$ in **Figure 1**. Consequently, if S_0S_1 amount of wetlands is converted, the loss in net benefit is the difference in the demand for protection that would have been met by that amount of wetlands, less the costs of the wetlands providing this service (which as noted previously is "free"). In **Figure 1**, this net benefit corresponds to area S_0CDS_1. Thus, the replacement cost method overestimates the net benefits of the storm protection service by area ABCD.

More recently, some valuation studies of the protective value of estuarine and coastal ecosystems (ECEs) have developed the expected damage function approach as an alternative to the replacement cost method (Barbier, 2007; Barbier and Enchelmeyer, 2014; World Bank, 2016; Beck et al., 2018; Highfield et al., 2018; Menéndez et al., 2020; Rezaie et al., 2020). This method assumes that an ECE provides a non-marketed service, such as "protection" of economic activity, property and even human lives, which benefits individuals through limiting damages. Consequently, the expected damage function adopts the production function methodology of valuing the environment as an input into the production of a final benefit, which is the protection of human lives, property or economic activity (Barbier, 2007). Utilizing this approach requires modeling how an ECE provides the "production" of this protection service, and then estimating its value of this environmental input or service in terms of the expected damages avoided to property, lives or activity. For example, suppose in **Figure 1**, the benefits of marsh or mangrove are from reducing flood damage to coastal property, and the loss of the wetland will increase the willingness to pay to avoid these damages as represented by the demand curve in the figure. When applied correctly, the expected damage method will yield the true net benefit of this service in terms of protecting coastal property and other assets from flood damages, which in **Figure 1** is denoted by area S_0CDS_1.

Barbier (2007) estimates the welfare impacts of a loss of the storm protection service due to mangrove deforestation in Thailand by both the expected damage function approach and the replacement cost method, and finds that the benefits estimated by the latter method are eight times more than those of the expected damage function approach. Similarly, Narayan et al. (2016) compare the cost of building submerged breakwater compared to natural-based defense provided by mangrove restoration projects. They estimate that the costs of building

artificial breakwaters is on average five time more expensive (ranging from 3.1 to 6.9 times expensive across the sample) in providing the same level of storm protection as restored mangroves. Increasingly, it is recognized that in remote and inaccessible sheltered bays where mangroves are normally found, artificial barriers, breakwaters, and seawalls are not the least-cost options for providing storm protection benefits, especially when compared to conserving existing mangrove forests or restoring them.

However, with respect to mangrove restoration for coastal protection, other considerations are also important. For example, there have been problems with the restoration success of mangrove replanting schemes, especially for the large-scale programs in the Philippines, Thailand, and elsewhere throughout South East Asia that have been instigated in response to major storm events in the regions (Primavera et al., 2016; Thompson, 2018; Lee et al., 2019). These issues include poor long-term survival rates of afforested or reforested mangroves, the over-reliance on area-based planting targets over long-term ecosystem restoration, and planting at sites that are unsuitable for mangroves. As a study in Central Philippines reveals, the result is that mangrove plantations and reforested areas are significantly less reliable in providing coastal protection compared to natural forests (Primavera et al., 2016).

As **Table 1** indicates, the expected damage function method is increasingly used in many studies that value coastal protection provided by ECEs. However, under certain conditions, this approach may under-estimate this benefit. When households living in coastal areas are risk averse, the expected damage function may not necessarily capture the entire *ex ante* willingness to pay to reduce or avoid the risk from storm damages from ECE protection (Barbier, 2016). Instead, the reduction in expected storm damages to, say, coastal property may be only one component of the marginal willingness-to-pay (WTP) associated with greater protection against storms. This *ex ante* WTP will also depend on avoiding or lowering the risks associated with the storm, such as the threat of death, illness or injury or the general dislike of violent storms, which may be substantial for risk-averse households. Nevertheless, despite its limitations, the expected damage function is a direct compensation surplus measure for estimating an important component of the protective value of ECEs, and thus can be considered a lower-bound estimate of this benefit. This is illustrated in **Figure 1**, where the demand, or marginal willingness to pay, for protection service provided by ECE of area S, is now the dashed $W(S)^*$ curve, as it includes reducing the risk of injury, illness or death, and lowering the disutility of risk exposure.

Very few studies are able to estimate this entire marginal willingness to pay for the protective benefit of ECEs. The studies that do estimate *ex ante* willingness to pay often employ survey-based methods, and have difficulty distinguishing the various components that comprise this storm protection value (Barbier, 2016). Some willingness to pay estimates for an ECE intervention that might reduce future storm event risks may include other values as well. For example, Landry et al. (2011) estimate that the average U.S. household is willing to pay $103 to reduce future flood risk in New Orleans through coastal restoration, but this value may also reflect concern by these households over the past devastation caused by the 2005 Hurricane Katrina to New Orleans.

Some studies have documented the role of ECEs, notably mangroves, in reducing storm-related deaths after major events. For example, one estimate indicates that, during the 1999 cyclone in Orissa, India, there would have been 1.72 additional deaths per village within 10 km of the coast if mangroves had not been present (Das and Vincent, 2009). Similarly, during the 2004 Indian Ocean tsunami, mangroves, forests and plantations may have decreased loss of life by 3 to 8% in Acheh, Indonesia (Laso-Bayas et al., 2011). In the Philippines, an analysis of 384 coastal villages impacted by flooding from the 2013 Typhoon Haiyan found that the presence of mangroves was significantly correlated with both lower deaths and less structural damage (Seriño et al., 2017).

Other studies have employed survey methods to estimate the entire marginal willingness to pay for storm protection benefits, as represented by the dashed $W(S)^*$ curve in **Figure 1**. For example, by employing a choice experiment survey for different coastal wetland restoration programs in southeast Louisiana, Petrolia et al. (2014) are able to determine how much a typical U.S. household is willing to pay for different levels of protection as the amount of restored wetland area increases. The average U.S. household is willing to pay $149 for an intermediate increase in storm surge protection through coastal wetland restoration, but will pay only $2 more for a further increase to high levels of protection. In a follow-up study of Louisiana households, Petrolia and Kim (2011) find that each household is willing to pay $111 to prevent future coastal wetland losses. However, households citing storm protection benefits as a top priority were 48% more likely to pay for preventing coastal wetland loss, which allowed the authors to estimate the overall storm protection benefits as $53 per household.

Finally, it should be pointed out that ECEs and artificial protection may also be complementary at the early stages of restoration efforts, and fully restored ECEs may also reinforce the effectiveness of artificial storm barriers, such as dykes and seawalls. For example, when mangrove tree seeds or seedlings are artificially reintroduced or naturally propagated, both frequent storms and the high energy of tides in coastal zones can prevent the establishment of young mangrove trees in bare sediments (Bosire et al., 2003; Moreno-Mateos et al., 2015). In Vietnam, this problem was solved by establishing bamboo T-fences to reduce coastal erosion and protect the sediment balance necessary for natural regeneration of mangroves (Albers and Schmitt, 2015). At US$50–60 per meter (m), such low-cost and temporary fencing (they last on average 5–7 years) is a relatively inexpensive way to improve the success of mangrove restoration at its crucial early stages of tree establishment. After successful restoration of sites suitable for mangrove growth, natural regeneration of mangroves will occur and the forest area expand. If artificial dykes are constructed inshore from the restored mangroves, then protection of coastal populations and property from sea level rise and the increasing frequency and intensity of storms is further enhanced.

This is especially important in developing countries such as Vietnam, as the construction of dykes is expensive (US$ 2,270 per m for a 3.5 m high concrete dyke), and the possibility of increasing dyke height is limited due to the load-bearing capacity of the soil (Albers and Schmitt, 2015). Similarly, in China, a comparison of constructing marsh and other coastal wetlands as an alternative of seawalls for storm protection, led the authors to conclude that "wetlands are a less costly alternative for storm protection" and should be incorporated with seawalls in national coastal defense strategies (Liu et al., 2019). A study for the United Kingdom showed that fronting protective structures with coastal wetlands significantly lowered seawall requirements and resulted in subsequent savings in construction costs (Mangi et al., 2011). Such a combination of "green" and "gray" infrastructure may be the most effective way of protecting vulnerable coasts from the variability of sea level rise, increased frequency and intensity of storms, and the risks of climate change (Mangi et al., 2011; Arkema et al., 2013; Barbier, 2014; Sandilyan and Kathiresan, 2015; World Bank, 2016; Dasgupta et al., 2019; Liu et al., 2019).

OTHER BENEFITS

Storm protection is only one of the many benefits of conserved or restored ECEs. For example, as noted previously, Petrolia et al. (2014) estimate that the average U.S. household is willing to pay $149 for increased storm surge protection through coastal wetland restoration in southeast Louisiana, but is willing to pay $973 per household for restoration when the additional ecosystem benefits of supporting wildlife habitat and commercial fisheries are also included.

The additional ecosystem services of mangroves, which include income and subsistence benefits from collecting products from the mangroves, nursery, and breeding habitats for offshore fisheries, and carbon sequestration, might be smaller compared to storm protection benefits but important to the overall decision as to whether or not to conserve mangroves or invest in their restoration (Barbier, 2007). In addition, products collected directly from the mangroves and also the artisanal fisheries supported by them may also be important in terms of food security and subsistence needs of local coastal communities (Sarntisart and Sathirathai, 2004; Andrew et al., 2007; Walters et al., 2008; Nfotabong et al., 2009; Béné et al., 2010).

For example, Barbier (2007) estimates that local coastal communities in Thailand gain net present value in income from collecting mangrove products worth $484 to $584 per hectare (ha), and an additional $708 to $987 per ha in net present value from support provided to coastal fisheries provided by mangroves as breeding and nursery habitat. Such benefits are considerable when compared to the average incomes of coastal households in Thailand. For example, surveys of mangrove-dependent communities reveal that the average household annual income ranges from $2,606 to $6,623, and the overall incidence of poverty (corresponding to an annual income of US$180 or lower) in three out of four villages surveyed exceeded the average incidence rate of 8% in rural Thailand (Sarntisart and Sathirathai, 2004). If the income to households from collecting mangrove forest products is excluded, then the incidence of poverty would rise to 55.3 and 48.1% in two of the villages, and to 20.7 and 13.64% in the other two communities.

Similar evidence exists of the importance of income from mangroves and other ECEs to support the livelihoods and subsistence of poor households across many low and middle-income countries (Bandaranayake, 1998; Naylor and Drew, 1998; Badola and Hussain, 2005; Walton et al., 2006; Rönnbäck et al., 2007; Walters et al., 2008; Nfotabong et al., 2009; Mukherjee et al., 2014; Hassan and Crafford, 2015; Huxham et al., 2015). In addition, coastal people often associate important cultural values with local ECE habitats that goes beyond their support for economic livelihoods. For example, a study of mangrove-dependent coastal communities in Micronesia has shown that the communities "place some value on the existence and ecosystem functions of mangroves over and above the value of mangroves' marketable products" (Naylor and Drew, 1998, p. 488). An extensive survey of coastal communities in Papua New Guinea found that people ascribed most importance to ECE services that directly contributed to their livelihoods, especially through food, income and shelter, such as fishing, collecting forest and reef materials, and habitats that support these services (Lau et al., 2019). But the survey also found that communities often placed great importance on local traditions, environmental knowledge and importance for future generations of their stewardship of the environment and ECE services.

DISCUSSION

Despite the considerable progress in valuing the protective service of ECEs and the growing number of empirical studies, important challenges remain. Here, we discuss two of them: how protective benefits are subject to spatial variability and are dependent on connectivity across "seascapes."

Spatial Variability

Increasingly, field studies and experiments indicate that the wave attenuation function of marsh, mangroves and other ECEs, which is critical to their protective value, varies spatially across the extent of these habitats (Madin and Connolly, 2006; Koch et al., 2009; Loder et al., 2009; Wamsley et al., 2010; Gedan et al., 2011; Shepard et al., 2011; Zhang et al., 2012; Rupprecht et al., 2017; Schoutens et al., 2019). This implies that, as storm waves travel across the extent of ECE landscape, the force and magnitude of the waves are increasingly dissipated. Equally, the strength and duration of the storm, and the presence of high or low tides, can impact wave attenuation by ECEs significantly (Koch et al., 2009; Loder et al., 2009; Wamsley et al., 2010; Barbier et al., 2011). Only recently are valuation studies taking into account spatial and temporal variability of wave attenuation by ECEs in estimating their potential protective value (Barbier et al., 2008; Barbier, 2012; Dasgupta et al., 2019; Hochard et al., 2019).

For example, storm surge modeling for the US Gulf Coast of southeastern Louisiana indicates how the attenuation of surge by wetlands is affected by the bottom friction caused by

vegetation, the surrounding coastal landscape, and the strength and duration of the storm forcing (Wamsley et al., 2010). Early studies of the protective value of Gulf Coast wetlands in reducing flood damages do not incorporate such factors (Farber, 1996; Costanza et al., 2008). However, more recent studies of this storm protection benefit do incorporate simulations from storm surge modeling that account for the hydrodynamic properties of surges and the influences of varying wetland landscape and vegetation conditions (Barbier et al., 2013; Barbier and Enchelmeyer, 2014).

Similarly, assessments of how well-mangroves and other coastal forests offered protection against the damages and casualties caused by the 2004 Indian Ocean tsunami found that important landscape and spatial characteristics, such as the variations in coastal topography, shoreline slope, distance of villages to shore and other coastal features, were important factors influences on protection (Cochard, 2011). For example, Laso-Bayas et al. (2011) found that the presence of coastal vegetation significantly reduced the casualties caused by the tsunami in Acheh, Indonesia, and the most important factor in determining casualties and infrastructure damage was the distance of villages from the coast.

Connectivity

Because estuarine and coastal ecosystems occur at the interface between the coast, land, and watersheds, there is a high degree of "interconnectedness" or "connectivity" in the land-sea interface across these systems. The term *seascape* is now widely used to refer to spatial mosaics of interconnected coastal and near-shore marine habitat types, such as mangroves, saltmarsh, seagrasses and coral reefs, as the *connectivity* between and among these coastal and near-shore marine habitats is the most pronounced (Moberg and Rönnbäck, 2003; Harborne et al., 2006; Boström et al., 2011; Pittman et al., 2011; Olds et al., 2016; Pittman, 2017). This connectivity, in turn, reinforces and augments the storm protection service provided by each of these ECEs individually.

For example, Alongi (2008) has pointed out that the storm protection provided by mangroves will be enhanced further by the presence of foreshore habitats, such as coral reefs, seagrass beds, and dunes. Koch et al. (2009) also note similar cumulative effects occur for attenuating waves that cross seascapes containing coral reefs, seagrasses, and marshes. Modeling simulations based on a Caribbean reef-seagrass-mangrove seascape illustrate that the storm protection service provided by the entire seascape is greater than for either of the three ECE habitats on their own (Sanchirico and Springborn, 2012). Mumby and Hastings (2008) also find that mangroves and coral in the Caribbean not only combine to protect coastlines from storms, but in addition, the mangroves help coral reef fish populations recover from the severe disturbances caused by hurricanes and other extreme events. The cumulative effect of storm protection can sometimes be revealed if an important ECE is absent from the seascape. For instance, Sheppard et al. (2005) document how rising coral reef mortality and deterioration in the Seychelles have increased significantly the wave energy reaching shores, whereas health reefs would normally protect coastlines from storm surges.

To provide further insight into the management implications of valuing the storm protection service across a seascape, Barbier and Lee (2014) develop a model of a two-habitat marine system. The model illustrates how the connectivity of two habitats (a near-shore coral reef and a mangrove habitat) comprising the seascape influences protection against coastal flood damages. That is, the presence of coral reefs in the near-shore marine environment attenuates waves thus enhancing the storm protection service of the coastal mangrove habitat. The model also accounts for spatial variation in wave attenuation across the seascape by allow for the storm protection service provided by mangroves to be greater for their seaward as supposed to the inland boundaries. The model was applied to a representative mangrove-coral reef system, in which the mangroves faced irreversible conversion to commercial shrimp farms. The outcome for this development decision when seascape connectivity was taken into account was compared to the outcome when the storm protection service of the mangroves was considered in isolation from the rest of the seascape (i.e., the coral reef).

Figure 2 illustrates how mangrove-coral reef connectivity across the seascape affects the development decision. As shrimp ponds can be located in any part of the mangroves with little loss of productivity, it is assumed that the returns to shrimp farming is constant across the landscape at a net present value (NPV) of $1,220 per ha (red line in **Figure 2**). Without considering any connectivity between coral reef and mangrove storm protection, the NPV per ha of this service provided by the mangroves begins at nearly $16,000 per ha at the seaward edge and declines to $108 per ha 1 km inland (green line in **Figure 2**). However, taking into account seascape connectivity, the storm protection value is over $20,000 per ha at the seaward edge and declines to almost $140 per ha at the inland boundary (blue line in **Figure 2**). Thus, without taking into account coral reef connectivity, it is optimal to conserve the first 515 meters (m) from the seaward edge, and convert the rest to shrimp farms. However, if the enhancement of mangrove storm protection by coral reefs is taken into account, then conservation of mangroves should extend further to 563 m inland.

CONCLUSION

Due to increasing concerns about sea level rise, climate change and the frequency of coastal storms, there is more interest than ever in the protective value of estuarine and coastal ecosystems (ECEs). As a result, there are a growing number of studies that attempt to estimate this value, for more ECEs around the world. However, as this review has shown, the geographical coverage of these studies is still limited. In addition, valuation has focused mainly on marsh and mangroves. Coral reefs have received more attention in recent years, but there is still a lack of valuation studies of the protective role of sea grass meadows in reducing coastal flood damages, which appear to be more effective in shoreline stabilization than attenuation of large waves (Paul et al., 2012; Christianen et al., 2013; Ondiviela et al., 2014). There is clearly a need for a greater range of studies for different

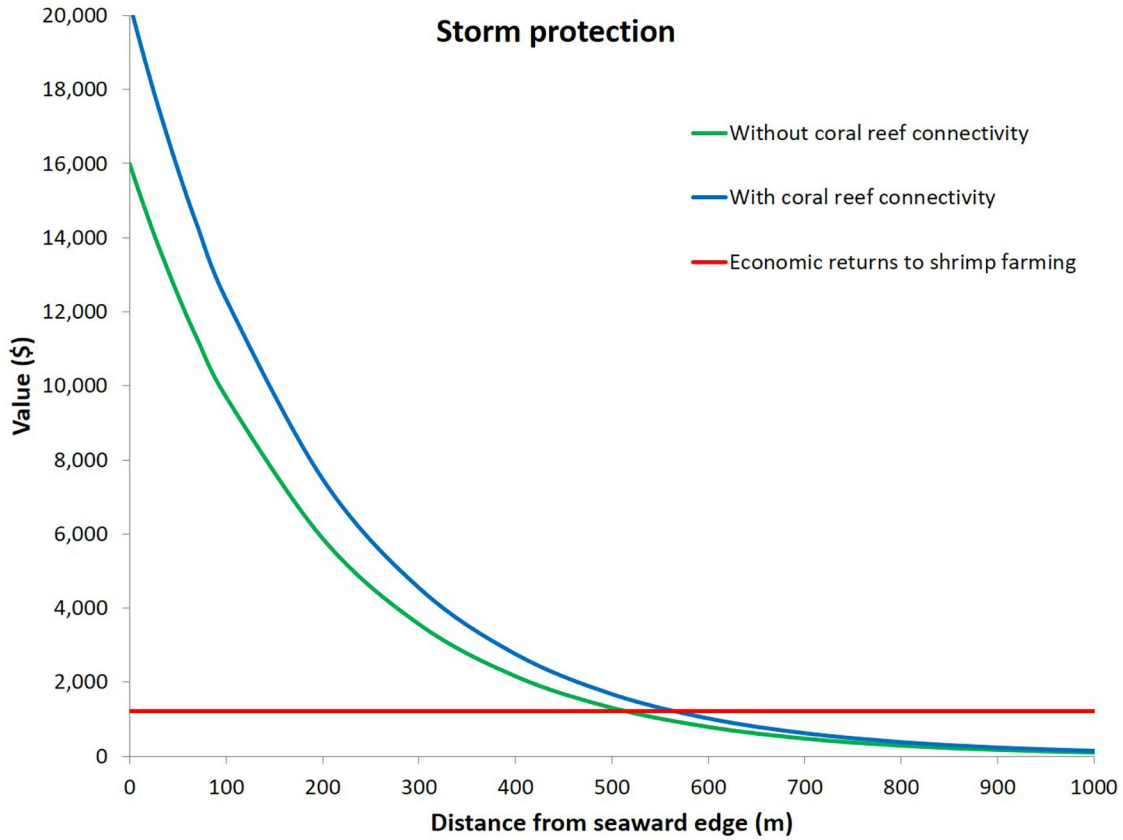

FIGURE 2 | Storm protection service and seascape connectivity between mangroves and coral reefs. The net benefits of storm protection of mangroves, with and without support from a near-shore coral reef, are compared to the economic returns of converting the mangrove landscape to shrimp aquaculture (red line). Without taking into account coral reef connectivity (green line), only the first 515 meters (m) of mangroves from the seaward edge should be conserved. However, if reef connectivity is included (blue line), then conservation of mangroves should extend further to 563 m inland. Based on Barbier and Lee (2014).

locations and a wider variety of ecosystems. As Newton et al. (2020) point out, the continuing loss and degradation of coastal wetlands globally are causing ongoing declines in a wide range of ecosystem services, of which the protection service of ECEs is most prominent.

There have been considerable improvements in the valuation methods used to estimate the benefits of ECEs in reducing coastal flood damages. However, there is still too much reliance on the use of less reliable approaches, such as the replacement cost method, which is likely to lead to inflated estimates. Increasingly, studies are valuing the protective service of ECEs more directly, in terms of reducing the expected damages to property and other assets. This value may be an under-estimate of the full benefit of this service, which should also include reducing the risk of injury, illness or death and lowering the disutility of risk exposure.

Improving the reliability and overall methods of valuing the protective role of ECEs is important, given concerns over estimates of such benefits are sufficiently robust to serve as a guide for policy (Barbier, 2007; Kousky, 2010; Arnold, 2013). Overcoming such concerns through better valuation of the protective benefits of ECEs is especially important for meeting the management challenge of convincing policy makers and other local stakeholders that such "natural defenses" have a role in coastal zones (Kousky, 2010). In addition, valuing the benefits of ECEs in reducing coastal flood damages can aid in the development of more innovative policies to promote the conservation and restoration of these coastal habitats, such as using insurance to protect ECEs and including their protective value to guide buyouts of flood-damaged property (Kousky and Light, 2019; Atoba et al., 2020).

In addition, the storm protection benefit of ECEs may be just one of many important benefits provided by these systems. Nevertheless, many studies confirm that the protective value of ECEs are one of the more significant benefits sacrificed when these habitats are lost or degraded. Global assessments for both coral reefs and mangroves are also illustrating the economic significance of this protective benefit (Beck et al., 2018; Hochard et al., 2019; Menéndez et al., 2020).

Better understanding of how various ECEs attenuate waves and buffer winds has helped in the development of methods for assessing the protective benefits of these

ecosystems. For example, for marsh and mangroves, an important contribution has been to distinguish between the role of vegetation and other ECE attributes in storm protection compared to coastal topography and near-shore bathymetry. Improved hydrodynamic modeling of the storm surge and wind characteristics of various storm events and their interaction with ECE landscape characteristics has also been insightful. An interesting challenge for future research is to account for the connectivity across ECE habitats, such as mangroves, saltmarsh, seagrasses and coral reefs, to assess their cumulative influence on the wave attenuation and wind buffering functions underlying the protection of coastlines against storms and floods. Only recently have valuation studies begun to model this connectivity and assess how it impacts the protective service provided by an entire seascape of ECEs.

Finally, although this paper has focused mainly on the storm and flood protection benefit of ECEs, one should not forget the multiple benefits provided by these natural systems. This array of benefits are what give ECEs an important advantage compared to human-made structures that are built solely to protect coastlines. Consequently, decisions as to whether or not to invest in ECE restoration either in combination with or as an alternative to human-made structures should not be based solely on their storm protection service alone but should take into account all the economic benefits provided by ECEs as well. Such considerations are important to long-term coastal restoration and protection and restorations. A good example is the Master Plan for the Louisiana Coast, which combines human-built coastal defenses and creating or maintaining over 2,000 km^2 of marsh and other coastal land over the next 50 years to provide storm protection and other ecosystem benefits [(Coastal Protection and Restoration Authority of Louisiana (LCPRA), 2012, 2017; Barbier, 2014)]. Even when the focus is exclusively on storm protection benefits, it is clear that ECE protection and restoration have an important role. For example, Arkema et al. (2013) have shown that substantial ECE restoration along the U.S. coast could reduce significantly the vulnerability of populations and property to future natural disasters as well as to sea-level rise. As the studies reviewed here suggest, many important coastal management decisions over the coming years will depend on improving the valuation of the protective service of ECEs, as well as assessing other significant benefits provided by these critical habitats of the land-sea interface.

AUTHOR CONTRIBUTIONS

EB designed the review, wrote the manuscript, and approved the submitted version.

ACKNOWLEDGMENTS

This review is based on a presentation by the author, Coastal Ecosystems as a Defense against Flood Damages: An Economic Perspective at the 2018 Ecological Society of America Annual Meeting, New Orleans, LA, 5–10 August 2018. The author is grateful to Mick Hanley and Tjeerd Bouma for comments and suggestions on an earlier version of this paper, and to Valentina Prigiobbe and three referees.

REFERENCES

Albers, T., and Schmitt, K. (2015). Dyke design, floodplain restoration and mangrove co-management as parts of an area coastal protection strategy for the mud coasts of the Mekong Delta, Vietnam. *Wetlands Ecol. Manag.* 23, 991–1004. doi: 10.1007/s11273-015-9441-3

Alongi, D. (2008). Mangrove forests: resilience, protection from tsunamis and responses to global climate change. *Estuar. Coast. Shelf Sci.* 76, 1–13. doi: 10.1016/j.ecss.2007.08.024

Andrew, N. L., Béné, C., Hall, S. J., Allison, E. H., Heck, S., and Ratner, B. D. (2007). Diagnosis and management of small-scale fisheries in developing countries. *Fish Fish.* 8, 227–240. doi: 10.1111/j.1467-2679.2007.00252.x

Arkema, K. K., Guannel, G., Verutes, G., Wood, S. A., Guerry, A., Ruckelshaus, M., et al. (2013). Coastal habitats shield people and proprery from sea-level rise and storms. *Nat. Clim. Change* 3, 913–918. doi: 10.1038/nclimate1944

Armitage, A. R., Weaver, C. A., Kominoski, J. S., and Pennings, S. C. (2019). Resistance to hurricane effects varies among wetland vegetation types in the marsh–mangrove ecotone. *Estuaries Coasts* 43, 960–970. doi: 10.1007/s12237-019-00577-3

Arnold, G. (2013). Use of monetary wetland value estimates by EPA clean water act section 404 regulators. *Wetlands Ecol. Manag.* 21, 117–129. doi: 10.1007/s11273-013-9283-9

Atoba, K. O., Brody, S. D., Highfield, W. E., Shepard, C. C., and Verdone, L. N. (2020). Strategic property buyouts to enhance flood resilience: a multi-criteria spatial approach for incorporating ecological values into the selection process. *Environ. Hazards*. doi: 10.1080/17477891.2020.1771251

Badola, R., and Hussain, S. A. (2005). Valuing ecosystems functions: an empirical study on the storm protection function of bhitarkanika mangrove ecosystem, India. *Environ. Conserv.* 32, 85–92. doi: 10.1017/S0376892905001967

Bandaranayake, W. M. (1998). Traditional and medicinal uses of mangroves. *Mangroves Salt Marsh.* 2, 133–148. doi: 10.1023/A:1009988607044

Barbier, E. B. (2007). Valuing ecosystems as productive inputs. *Econ. Policy* 22, 177–229. doi: 10.1111/j.1468-0327.2007.00174.x

Barbier, E. B. (2012). A spatial model of coastal ecosystem services. *Ecol. Econ.* 78, 70–79. doi: 10.1016/j.ecolecon.2012.03.015

Barbier, E. B. (2014). A global strategy for protecting vulnerable coastal populations. *Science* 345, 1250–1251. doi: 10.1126/science.1254629

Barbier, E. B. (2016). The protective value of estuarine and coastal ecosystem services in a wealth accounting framework. *Environ. Resour. Econ.* 64, 37–58. doi: 10.1007/s10640-015-9931-z

Barbier, E. B., and Enchelmeyer, B. (2014). Valuing the storm surge protection service of US Gulf Coast wetlands. *J. Environ. Econ. Policy* 3, 167–185. doi: 10.1080/21606544.2013.876370

Barbier, E. B., Georgiou, I. Y., Enchelmeyer, B., and Reed, D. J. (2013).The value of wetlands in protecting southeast Louisiana from hurricane storm surges. *PLoS ONE* 8:e58715. doi: 10.1371/journal.pone.0058715

Barbier, E. B., Hacker, S. D., Kennedy, C., Koch, E. M., Stier, A. C., and Silliman, B. R. (2011). The value of estuarine and coastal ecosystem services. *Ecol. Monogr.* 81, 169–183. doi: 10.1890/10-1510.1

Barbier, E. B., Koch, E. M., Silliman, B. R., Hacker, S. D., Wolanski, E., Primavera, J., et al. (2008). Coastal ecosystem-based management with nonlinear ecological functions and values. *Science* 319, 321–323. doi: 10.1126/science.1150349

Barbier, E. B., and Lee, K. D. (2014). Economics of the marine seascape. *Int. Rev. Environ. Resour. Econ.* 7, 35–65. doi: 10.1561/101.00000056

Beck, M. W., Losada, I. J., Menédez, P., Raguero, B. G., Díaz-Simal, P., and Fernández, F. (2018). The global flood protection savings provided by coral reefs. *Nat. Commun.* 9:2186. doi: 10.1038/s41467-018-04568-z

Béné, C., Hersoug, B., and Allison, E. H. (2010). Not by rent alone: analysing the pro-poor functions of small-scale fisheries in developing countries. *Dev. Policy Rev.* 28, 325–358. doi: 10.1111/j.1467-7679.2010.00486.x

Bosire, J. O., Dahdouh-Guebas, F., Kairo, J. G., and Koedam, N. (2003). Colonization of non-planted mangrove species into restored mangrove stands in Gazi Bay, Kenya. *Aquat. Bot.* 76, 267–279. doi: 10.1016/S0304-3770(03)00054-8

Boström, C., Pittman, S. J., Simenstad, C., and Kneib, R. T. (2011). Seascape ecology of coastal biogenic habitats: advances, gaps and challenges. *Mar. Ecol. Prog. Ser.* 427:101–217 doi: 10.3354/meps09051

Boutwell, J. L., and Westra, J. V. (2015). Evidence of diminishing marginal product of wetlands for damage mitigation. *Nat. Resour.* 6, 48–55. doi: 10.4236/nr.2015.61006

Boutwell, J. L., and Westra, J. V. (2016). The role of wetlands for mitigating economic damage from hurricanes. *J. Am. Water Resour. Assoc.* 52,1472–1481. doi: 10.1111/1752-1688.12473

Chaikumbung, M., Doucouliagos, H., and Scarborough, H. (2016). The economic value of wetlands in developing countries: a meta-regression analysis. *Ecol. Econ.* 124, 164–174. doi: 10.1016/j.ecolecon.2016.01.022

Christianen, M. J. A., van Belzen, J., Herman, P. M. J., van Katwijk, M. M., Lamers, L. P., van Leent, P. J., et al. (2013). Low-canopy seagrass beds still provide important coastal protection services. *PLoS ONE* 8:e62413. doi: 10.1371/journal.pone.0062413

Coastal Protection and Restoration Authority of Louisiana (LCPRA) (2017). *Louisiana's Comprehensive Master Plan for a Sustainable Coast 2017*. Baton Rouge, LA: Office of Coastal Protection and Restoration.

Coastal Protection and Restoration Authority of Louisiana (LCPRA) (2012). *Louisiana's Comprehensive Master Plan for a Sustainable Coast*. Baton Rouge, LA: Office of Coastal Protection and Restoration.

Cochard, R. (2011). On the strengths and drawbacks of tsunami-buffer forests. *Proc. Natl. Acad. Sci. U.S.A.* 108, 18571–18572. doi: 10.1073/pnas.1116156108

Cochard, R., Ranamukhaarachchi, S. L., Shivakotib, G. P., Shipin, O. V., Edwards, P. J., and Seeland, K. T. (2008). The 2004 tsunami in Aceh and Southern Thailand: a review on coastal ecosystems, wave hazards and vulnerability. perspectives in plant ecology. *Evol. Syst.* 10, 3–40. doi: 10.1016/j.ppees.2007.11.001

Costanza, R., Pérez-Maqueo, O., Martinez, M. L., Sutton, P., Anderson, S. J., and Mulder,. K. (2008). The value of coastal wetlands for hurricane protection. *Ambio* 37, 241–248. doi: 10.1579/0044-7447(2008)37[241:TVOCWF]2.0.CO;2

Das, S., and Crépin, A.-S. (2013). Mangroves can provide against wind damage during storms. *Estuar. Coast. Shelf Sci.* 134, 98–107. doi: 10.1016/j.ecss.2013.09.021

Das, S., and Vincent, J. R. (2009). Mangroves protected villages and reduced death toll during Indian super cyclone. *Proc. Natl. Acad. Sci. U.S.A.* 106, 7357–7360. doi: 10.1073/pnas.0810440106

Dasgupta, S., Islam, M. S., Huq, M., Huque Khan, Z., and Hasib, M. R. (2019). Quantifying the protective capacity of mangroves from storm surges in coastal Bangladesh. *PLoS ONE* 14:e0214079. doi: 10.1371/journal.pone.0214079

del Valle, A., Eriksson, M., Ishizawa, O. A., and Miranda, J. J. (2020). Mangroves protect coastal economic activity from hurricanes. *Proc. Natl. Acad. Sci. U.S.A.* 117, 265–270. doi: 10.1073/pnas.1911617116

Duarte, C. M., Losado, I. J., Hendriks, I. E., Mazarrasa, I., and Marba, N. (2013). The role of coastal plant communities for climate change mitigation and adaption. *Nat. Clim. Chang.* 3, 961–968. doi: 10.1038/nclimate1970

Elliott, M., Mander, L., Mazik, K., Simenstad, C., Valesini, F., Whitfield, A., et al. (2016). Ecoengineering with ecohydrology: successes and failures in estuarine restoration. *Estuar. Coast. Shelf Sci.* 176, 12–36. doi: 10.1016/j.ecss.2016.04.003

Farber, S. (1987). The value of coastal wetlands for protection of property against hurricane wind damage. *J. Environ. Econ. Manag.* 14, 143–151. doi: 10.1016/0095-0696(87)90012-X

Farber, S. (1996). Welfare loss of wetlands disintegration: a Louisiana study. *Contemp. Econ. Policy* 14, 92–106. doi: 10.1111/j.1465-7287.1996.tb00606.x

Ferrario, F., Beck, M. W., Storlazzi, C. D., Micheli, F., Shepard, C. C., and Airoldi, L. (2014). The effectiveness of coral reefs for coastal hazard risk reduction and adaptation. *Nat. Commun.* 5:3794. doi: 10.1038/ncomms4794

Freeman, I. I. I., A. M., Herriges, J. A., and Kling, C. L. (2014). *The Measurement of Environmental and Resource Values: Theory and Methods*. London: Routledge.

Gedan, K. B., Kirwan, M. L., Wolanski,. E., Barbier, E. B., and Silliman, B. R. (2011). The present and future role of coastal wetland vegetation in protecting shorelines: answering recent challenges to the paradigm. *Clim. Change* 106, 7–29. doi: 10.1007/s10584-010-0003-7

Guisado-Pintado, E., Navas, F., and Malvárez, G. (2016). Ecosystem services and their benefits in coastal protection in highly urbanized environments. *J. Coast. Res.* 75,1097–1101. doi: 10.2112/SI75-220.1

Harborne, A. R., Mumby, P. J., Micheli, F., Perry, C. T., Dahlgren, C. P., Holmes, K. E., et al. (2006). The functional value of Caribbean coral reef, seagrass and mangrove habitats to ecosystem processes. *Adv. Mar. Biol.* 50, 57–189. doi: 10.1016/S0065-2881(05)50002-6

Hassan, R. M., and Crafford, J. G. (2015). Measuring the contribution of ecological composition and functional services to the dynamics of KwaZulu-Natal coast fisheries. *Ecol. Econ.* 119, 306–313. doi: 10.1016/j.ecolecon.2015.09.014

Highfield, W. E., Brody, S. D., and Shepard, C. C. (2018). The effects of estuarine wetlands on flood losses associated with storm surge. *Ocean Coast. Manag.* 157, 50–55. doi: 10.1016/j.ocecoaman.2018.02.017

Hochard, J. P., Hamilton, S., and Barbier, E. B. (2019). Mangroves shelter coastal economic activity from cyclones. *Proc. Natl. Acad. Sci. U.S.A.* 116,12232–12237. doi: 10.1073/pnas.1820067116

Huxham, M., Emerton, L., Kairo, J., Munyi, F., Abdirizak, H., Muriuiki, T., et al. (2015). Applying climate compatible development and economic valuation to coastal management: a case study of Kenya's mangrove forests. *J. Environ. Manage* 157, 168–181. doi: 10.1016/j.jenvman.2015.04.018

Kim, T.-G., and Petrolia, D. R. (2013). Public perceptions of wetland restoration benefits in Louisiana. *ICES J. Marine Sci.* 70, 1045–1054. doi: 10.1093/icesjms/fst026

King, S. E., and Lester, J. N. (1995). The value of salt marsh as a sea defence. *Mar. Pollut. Bull.* 30,180–189. doi: 10.1016/0025-326X(94)00173-7

Koch, E. W., Barbier, E. B., Silliman, B. R., Reed, D. J., Perillo, G. M., Hacker, S. D., et al. (2009). Non-linearity in ecosystem services: temporal and spatial variability in coastal protection. *Front. Ecol. Environ.* 72, 9–37. doi: 10.1890/080126

Kousky, C. (2010). Using natural capital to reduce disaster risk. *J. Nat. Resour. Policy Res.* 2, 343–356. doi: 10.1080/19390459.2010.511451

Kousky, C., and Light, S. E. (2019). Insuring nature. *Duke Law J.* 69, 323–376. Available online at: https://scholarship.law.duke.edu/dlj/vol69/iss2/2

Landry, C. E., Hindsley, P., Bin, O., Kruse, J. B., Whitehead, J. C., and Wilson, K. (2011). Weathering the storm: measuring household willingness-to-pay for risk-reduction in post-Katrina New Orleans. *South. Econ. J.* 77, 991–1013. doi: 10.4284/0038-4038-77.4.991

Laso-Bayas, J. C., Marohn, C., Dercon, G., Dewi, S., Piepho, H. P., Joshi, L., et al. (2011). Influence of coastal vegetation on the 2004 tsunami wave impact Aceh. *Proc. Natl. Acad. Sci. U.S.A.* 108, 18612–18617. doi: 10.1073/pnas.1013516108

Lau, J. D., Hicks, C. C., Gurney, G. G., and Cinner, J. E. (2019). "What matters to whom and why? understanding the importance of coastal ecosystem services in developing coastal communities. *Ecosyst. Serv.* 35, 219–230. doi: 10.1016/j.ecoser.2018.12.012

Lee, S. Y., Hamilton, S., Barbier, E. B., and Primavera, J. (2019). Better restoration policies are needed to conserve mangrove ecosystems. *Nat. Ecol. Evol.* 3, 870–872. doi: 10.1038/s41559-019-0861-y

Liquete, C., Zulian, G., Delgado, I., Stips, A., and Maes, J. (2013). Assessment of coastal protection as an ecosystem service in Europe. *Ecol. Indic* 30, 205–2017. doi: 10.1016/j.ecolind.2013.02.013

Liu, X., Wang, Y., Costanza, R., Kubiszeewski, I., Xu, N., and Yuan, M. (2019). The value of China's coastal wetlands and seawalls for storm protection. *Ecosyst. Serv.* 36:100905. doi: 10.1016/j.ecoser.2019.100905

Loder, N. M., Irish, J. L., Cialone, M. A., and Wamsley, M. V. (2009). Sensitivity of hurricane surge to morphological parameters of coastal wetlands. *Estuarine Coast. Shelf Sci.* 84, 625–636. doi: 10.1016/j.ecss.2009.07.036

Madin, J. S., and Connolly, S. R. (2006). Ecological consequences of major hydrodynamic disturbances on coral reefs. *Nature* 444, 477–480. doi: 10.1038/nature05328

Mahmud, S., and Barbier, E. B. (2016). Are private defensive expenditures against storm damages affected by public programs and natural barriers? *evidence from the coastal areas of Bangladesh. Environ. Dev. Econ.* 21, 767–788. doi: 10.1017/S1355770X16000164

Mangi, S. C., Davis, C. E., Payne, L. A., Austen, M. C., Simmonds, D., Beaumont, N. J., et al. (2011). Valuing the regulatory services provided by marine ecosystems. *Environmetrics* 22, 686–698. doi: 10.1002/env.1095

Menéndez, P., Losada, I. J., Beck, M. W., Torres-Ortega, S., Espejo, A., Narayan, S., et al. (2018). Valuing the protection services of mangroves at national scale: the Philippines. *Ecosyst. Serv.* 34, 24–36. doi: 10.1016/j.ecoser.2018.09.005

Menéndez, P., Losada, I. J., Torres-Ortega, S., Narayan, S., and Beck, M. W. (2020). The global flood protection benefits of mangroves. *Sci. Rep*. 10:4404. doi: 10.1038/s41598-020-61136-6

Moberg, F., and Rönnbäck, P. (2003). Ecosystem services of the tropical seascape: interactions, substitutions and restoration. *Ocean Coast. Manag.* 46, 27–46. doi: 10.1016/S0964-5691(02)00119-9

Montgomery, J. M., Bryan, K. R., Mullarney, J. C., and Hortsman, E. M. (2019). Attenuation of storm surges by coastal mangroves. *Geophys. Res. Lett.* 46, 2680–2689. doi: 10.1029/2018GL081636

Moreno-Mateos, D., Meli, P., Vara-Rodríguez, M. I., and Aronson, J. (2015). Ecosystem response to interventions: lessons from restored and created wetland ecosystems. *J. Appl. Ecol.* 52, 1528–1537. doi: 10.1111/1365-2664.12518

Mukherjee, N., Sutherland, W. J., Dicks, L., Hugé, J., Koedam, N., and Dahdouh-Buebas, F. (2014). Ecosystem service valuations of mangrove ecosystems to inform decision making and future valuation exercises. *PLoS ONE* 9:e107706. doi: 10.1371/journal.pone.0107706

Mumby, P. J., and Hastings, A. (2008). The impact of ecosystem connectivity on coral reef resilience. *J. Appl. Ecol.* 45, 854–862. doi: 10.1111/j.1365-2664.2008.01459.x

Narayan, S., Beck, M. W., Reguero, B. G., Losada, I. J., Van Wesenbeeck, B., Pontee, N., et al. (2016). The effectiveness, costs and coastal protection benefits of natural and nature-based defences. *PLoS ONE* 11:e0154735. doi: 10.1371/journal.pone.0154735

Narayan, S., Beck, M. W., Wilson, P., Thomas, C. J., Guerrero, A., Shepard, C. C., et al. (2017). The value of coastal wetlands for flood damage reduction in the northeastern USA. *Sci. Rep*. 7:9463. doi: 10.1038/s41598-017-09269-z

Naylor, R., and Drew, M. (1998). Valuing mangrove resources in Kosrae, Micronesia. *Environ. Dev. Econ.* 3, 471–490. doi: 10.1017/S1355770X98000242

Newton, A., Icely, J., Cristina, S., Perillo, G. M., Turner, R. E., Ashan, D., et al. (2020). Anthropogenic, direct pressures on coastal wetlands. *Front. Ecol. Evol.* 8:144. doi: 10.3389/fevo.2020.00144

Nfotabong, A., Din, N., Longonje, S. N., Koedam, N., and Dahdouh-Guebas, F. (2009). Commercial activities and subsistence utilization of mangrove forests around the wouri estuary and the douala-edea reserve (*Cameroon*). *J. Ethnobiol. Ethnomed.* 5, 35–49. doi: 10.1186/1746-4269-5-35

Olds, A. D., Connolly, R. M., Pitt, K. A., Pittman, S. J., Maxwell, P. S., Huijbers, C. M., et al. (2016). Quantifying the conservation value of seascape connectivity: a global synthesis. *Glob. Ecol. Biogeogr.* 25, 3–15. doi: 10.1111/geb.12388

Ondiviela, B., Losada, I. J., Lara, J. L., Maza, M., Galván, Bouma, T. J., and van Belzen, J. (2014). The role of seagrasses in a coastal protection in a changing climate. *Coast. Eng.* 87, 138–158. doi: 10.1016/j.coastaleng.2013.11.005

Ouyang, X., Lee, S. Y., Connolly, R. M., and Kainz, M. J. (2018). Spatially-explicit valuation of coastal wetlands for cyclone mitigation in Australia and China. *Sci. Rep*. 8:3035. doi: 10.1038/s41598-018-21217-z

Pascal, N., Allenbach, M., Brathwaite, A., Burke, L., Le Port, G., and Clua, E. (2016). Economic valuation of coral reef ecosystem service of coastal protection: a pragmatic approach. *Ecosyst. Serv.* 21, 72–80. doi: 10.1016/j.ecoser.2016.07.005

Paul, M., Bouma, T. J., and Amos, C. L. (2012). Wave attenuation by submerged vegetation: Combining the effect of organism traits and tidal current. *Mar. Ecol. Prog. Ser.* 444, 31–41. doi: 10.3354/meps09489

Petrolia, D. R., Interis, M. G., and Hwang, J. (2014). America's wetland? a national survey of willingness to pay for restoration of Louisiana's coastal wetlands. *Marine Resour. Econ.* 29, 17–37. doi: 10.1086/676289

Petrolia, D. R., and Kim, T.-G. (2011). Preventing land loss in coastal Louisiana: estimates of WTP and WTA. *J. Environ. Manag.* 92, 859–865. doi: 10.1016/j.jenvman.2010.10.040

Pittman, S. J., Kneib, R. T., and Simenstad, C. A. (2011). Practicing coastal seascape ecology. *Mar. Ecol. Prog. Ser.* 427, 197–190. doi: 10.3354/meps09139

Pittman, S. J (ed). (2017). *Seascape Ecology*. New York, NY: Wiley-Blackwell.

Primavera, J. H., dela Cruz, M., Montilijao, C., Consunji, H., dela Paz, M., Rollon, R. N., et al. (2016). Preliminary assessment of post-haiyan mangrove damage and short-term recovery in Eastern Samar, central Philippines. *Mar. Pollut. Bull.* 109, 744–750. doi: 10.1016/j.marpolbul.2016.05.050

Rao, N. S., Ghermandi, A., Portela, R., and Wang, X. (2015). Global values of coastal ecosystem services: a spatial economic analysis of shoreline protection values. *Ecosyst. Serv.* 11, 95–105. doi: 10.1016/j.ecoser.2014.11.011

Reguero, B. G., Beck, M. W., Agostini, V. N., Kramer, P., and Hancock, B. (2018). Coral reefs for coastal protection: a new methodological approach and engineering case study in Grenada. *J. Environ. Manage.* 210, 146–161. doi: 10.1016/j.jenvman.2018.01.024

Rezaie, A. M., Loerzel, J., and Ferreira, C. M. (2020). Valuing natural habitats for enhancing coastal resilience: wetlands reduce property damage from storm surge and sea level rise. *PLoS ONE* 15:e0226275. doi: 10.1371/journal.pone.0226275

Rönnbäck, P., Crona, B., and Ingwall, L. (2007). The return of ecosystem goods and services in replanted mangrove forests – perspectives from local communities in Gazi Bay, Kenya. *Environ. Conserv.* 34, 313–324. doi: 10.1017/S0376892907004225

Ruckelshaus, M. H., Guannel, G., Arkema,. K., Verutes, G., Griffin, R., Guerry, A., et al. (2016). Evaluating the benefits of green infrastructure for coastal areas: location, location, location. *Coast. Manag.* 44, 504–516. doi: 10.1080/08920753.2016.1208882

Rupprecht, F., Möller, I., Paul, M., Kudella, M., Spencer, T., Van Wesenbeeck, B. K., et al. (2017). Vegetation-wave interactions in salt marshes under storm surge conditions. *Ecol. Eng.* 100, 301–315. doi: 10.1016/j.ecoleng.2016.12.030

Sanchirico, J. N., and Springborn, M. (2012). How to get there from here: ecological and economic dynamics of ecosystem service provision. *Environ. Resour. Econ.* 48, 243–267. doi: 10.1007/s10640-010-9410-5

Sandilyan, S., and Kathiresan, K. (2015). Mangroves as bioshields: an undisputed fact. *Ocean Coast. Manag.* 103, 94–96. doi: 10.1016/j.ocecoaman.2014.11.011

Sarntisart, I., and Sathirathai, S. (2004). "Mangrove Dependency, Income Distribution and Conservation." In *Chapter 6 in Shrimp Farming and Mangrove Loss in Thailand*, eds E.B. Barbier and S. Sathirathai (Cheltenham: Edward Elgar), 96–114.

Sathirathai, S., and Barbier, E. B. (2001). Valuing mangrove conservation in southern Thailand. *Contemp. Econ. Policy* 19, 109–122. doi: 10.1111/j.1465-7287.2001.tb00054.x

Schoutens, K., Heuner, M., Minden, V., Schulte Ostermann, T., Silinski, A., Belliard, J. P., et al. (2019). How effective are tidal marshes as nature-based shoreline protection throughout seasons?. *Limnol. Oceanogr.* 64, 1750–1762. doi: 10.1002/lno.11149

Seriño, M. N., Ureta, J. C., Baldesco, J., Galvez, K. J., Predo, C., and Seriño, E. K. (2017). *Valuing the Protection Service Provided by Mangroves in Typhoon-Hit Areas in the Philippines. EEPSEA Research Report No. 2017-RR19*. Economy and Environment Program for Southeast Asia, Laguna, Philippines. Available online at: http://www.eepseapartners.org/wp-content/uploads/publication/2017-RR19Serino_web.pdf (accessed November 11, 2020).

Shepard, C. C., Crain, C. M., and Beck, M. W. (2011). The protective role of coastal marshes: a systematic review and meta-analysis. *PLoS ONE* 6:e27374. doi: 10.1371/journal.pone.0027374

Sheppard, C., Dixon, D.J., Gourlay, M., Sheppard, A., and Payet, R. (2005). Coral mortality increases wave energy reaching shores protected by reef flats: examples from the Seychelles. *Estuarine Coast. Shelf Sci.* 64, 223–234. doi: 10.1016/j.ecss.2005.02.016

Temmerman, S., Meire, P., Bouma, T. J., Herman, P. M. J., Ysebaert, T., and De Vriend, H. J. (2012). Ecosystem-based coastal defence in the face of global change. *Nature* 504, 79–82. doi: 10.1038/nature12859

Thompson, B. S. (2018). The political ecology of mangrove forest restoration in Thailand: institutional arrangements and power dynamics. *Land Use Policy* 78, 503–514. doi: 10.1016/j.landusepol.2018.07.016

van Zanten, B. T., van Beukering, P. J. H., and Wagtendonk, A. J. (2014). Coastal protection by coral reefs: a framework for spatial assessment and economic valuation. *Ocean Coast. Manag.* 96, 94–103. doi: 10.1016/j.ocecoaman.2014.05.001

Vázquez-González, C., Moreno-Casasolo, P., Peralta Peláez, L. A., Monroy, P., and Espejel, I. (2019). The value of coastal flood protection lost to urbanization on the coastal plain of the Gulf of Mexico: an analysis of flood damage by hurricane

impacts. *Int. J. Disaster Risk Reduct.* 37:101180. doi: 10.1016/j.ijdrr.2019.101180

Vedogbeton, H., and Johnston, R. J. (2020). Commodity-consistent meta-analysis of wetland valuation: an illustration for coastal marsh habitat. *Environ. Resour. Econ.* 75, 835–865. doi: 10.1007/s10640-020-00409-0

Walters, B. B., Rönnbäck, P., Kovacs, J. M., Crona, B., Hussain, S. A., Badola, R., et al. (2008). Ethnobiology, socio-economics and management of mangrove forests: a review. *Aquat. Bot.* 89, 220–236. doi: 10.1016/j.aquabot.2008.02.009

Walton, M. E., Giselle, M., Samonte-Tan, P. B., Primavera, J. H., Edwards-Jones, G., and Le Vay,. L. (2006). Are mangroves worth replanting? the direct economic benefits of a community-based reforestation project. *Environ. Conserv.* 33, 335–343. doi: 10.1017/S0376892906003341

Wamsley, T. V., Cialone, M. A., Smith, J. M., Atkinson, J. H., and Rosati, J. D. (2010). The potential of wetlands in reducing storm surge. *Ocean Eng.* 37, 59–68. doi: 10.1016/j.oceaneng.2009.07.018

Wilkinson, C., Linden, O., Cesar, H., Hodgson, G., Rubens, J., and Strong,. A. E. (1999). Ecological and socioeconomic impacts of 1998 coral mortality in the Indian Ocean: an ENSO impact and a warning of future change? *Ambio* 28, 188–196.

World Bank (2016). "Managing coasts with natural solutions: guidelines for measuring and valuing the coastal protection services of mangroves and coral reefs," in *Wealth Accounting and the Valuation of Ecosystem Services Partnership(WAVES),* eds. M. W. Beck and G-M. Lange (Washington, DC: World Bank).

Zhang, K., Liu, H., Liu, Y., Li, Y., Shen, J., Rhome, J., et al. (2012). The role of mangroves in attenuating storm surges. *Estuar. Coast. Shelf Sci.* 102–103, 11–23. doi: 10.1016/j.ecss.2012.02.021

Conflict of Interest: The author declares that the research was conducted in the absence of any commercial or financial relationships that could be construed as a potential conflict of interest.

frontiers in Climate

ORIGINAL RESEARCH
published: 04 February 2021
doi: 10.3389/fclim.2020.609610

Developing a Modeling Framework to Simulate Compound Flooding: When Storm Surge Interacts With Riverine Flow

Mark Loveland[1], *Amin Kiaghadi*[1,2]*, *Clint N. Dawson*[1], *Hanadi S. Rifai*[2], *Shubhra Misra*[3], *Helena Mosser*[4] *and Alessandro Parola*[4]

[1] Computational Hydraulics Group, Oden Institute, University of Texas at Austin, Austin, TX, United States, [2] Civil and Environmental Engineering, University of Houston, Houston, TX, United States, [3] Hurricane Flood Risk Reduction Design Branch, U.S. Army Corps of Engineers Galveston District, Galveston, TX, United States, [4] Water Resource Branch, U.S. Army Corps of Engineers Fort Worth District, Fort Worth, TX, United States

Compound flooding is a physical phenomenon that has become more destructive in recent years. Moreover, compound flooding is a broad term that envelops many different physical processes that can range from preconditioned, to multivariate, to temporally compounding, or spatially compounding. This research aims to analyze a specific case of compound flooding related to tropical cyclones where the compounding effect is on coastal flooding due to a combination of storm surge and river discharge. In recent years, such compound flood events have increased in frequency and magnitude, due to a number of factors such as sea-level rise from warming oceans. Therefore, the ability to model such events is of increasing urgency. At present, there is no holistic, integrated modeling system capable of simulating or forecasting compound flooding on a large regional or global scale, leading to the need to couple various existing models. More specifically, two more challenges in such a modeling effort are determining the primary model and accounting for the effect of adjacent watersheds that discharge to the same receiving water body in amplifying the impact of compound flooding from riverine discharge with storm surge when the scale of the model includes an entire coastal line. In this study, we investigated the possibility of using the Advanced Circulation (ADCIRC) model as the primary model to simulate the compounding effects of fluvial flooding and storm surge *via* loose one-way coupling with gage data through internal time-dependent flux boundary conditions. The performance of the ADCIRC model was compared with the Hydrologic Engineering Center- River Analysis System (HEC-RAS) model both at the watershed and global scales. Furthermore, the importance of including riverine discharges and the interactions among adjacent watersheds were quantified. Results showed that the ADCIRC model could reliably be used to model compound flooding on both a watershed scale and a regional scale. Moreover, accounting for the interaction of river discharge from multiple watersheds is critical in accurately predicting flood patterns when high amounts of riverine flow occur in conjunction with storm surge. Particularly, with storms such as Hurricane Harvey (2017), where river flows were near record levels, inundation patterns and water surface elevations were highly dependent on

OPEN ACCESS

Edited by:
Navid Tahvildari, Old Dominion University, United States

Reviewed by:
Hamed Moftakhari, University of Alabama, United States
Antonia Sebastian, University of North Carolina at Chapel Hill, United States

***Correspondence:**
Amin Kiaghadi
amin.kiaghadi2013@gmail.com

Specialty section:
This article was submitted to Climate Risk Management, a section of the journal Frontiers in Climate

Received: *23 September 2020*
Accepted: *21 December 2020*
Published: *04 February 2021*

Citation:
Loveland M, Kiaghadi A, Dawson CN, Rifai HS, Misra S, Mosser H and Parola A (2021) Developing a Modeling Framework to Simulate Compound Flooding: When Storm Surge Interacts With Riverine Flow. Front. Clim. 2:609610. doi: 10.3389/fclim.2020.609610

the incorporation of the discharge input from multiple watersheds. Such an effect caused extra and longer inundations in some areas during Hurricane Harvey. Comparisons with real gauge data show that adding internal flow boundary conditions into ADCIRC to account for river discharge from multiple watersheds significantly improves accuracy in predictions of water surface elevations during coastal flooding events.

Keywords: ADCIRC, HEC-RAS, numerical modeling, hurricanes, inundation

INTRODUCTION

The observed increasing trend in the destructiveness of coastal storms over the past decades (Emanuel, 1987, 2005; Demaria and Kaplan, 1994; Jongman et al., 2012; Hinkel et al., 2014) has been attributed to the changing climate (Levitus et al., 2000); a trend that does not appear to be slowing down. Part of the increase in damage of more recent storms can be attributed to the higher levels of flooding due to combined effects from riverine flows and storm surge (Bakhtyar et al., 2020a). While oceanic processes such as tides and storm surge impact flooding in low lying coastal areas, meteorological and hydrological mechanisms influence flooding due to rainfall. When these processes interact, they can cause much higher flooding levels than if they were to occur separately. A compound event can be defined as a combination of simultaneous or sequential processes leading to a more significant event (Couasnon et al., 2020). Applying this definition to coastal flooding, a compound flooding event is flooding due to the interaction of the open ocean, meteorological behavior, and hydrological factors (Zscheischler et al., 2018).

The increase in damage to coastal areas from hurricanes in recent years present the need to model the compounding effects from storm surge and riverine discharge more accurately so that reliable flood-risk assessments, including forecasts can be made. Compounding processes pose a challenge to current coastal models because there are a vast amount of physical processes such as tides, storm surge, sea level rise, wind, and river discharge that all interact with each other to significantly impact flooding in coastal areas (Bilskie et al., 2016; Moftakhari et al., 2017, 2019; Saleh et al., 2017; Bilskie and Hagen, 2018; Muñoz et al., 2020; Ye et al., 2020). While there are many physics-based coastal, hydrodynamic, hydraulic, and hydrologic models, most have typically been applied to account for one or more limited processes involved in compound flooding and not the entire set of forcing parameters. For instance, there are many well-validated models for storm surge such as the Sea, Lake and Overland Surges from Hurricanes (SLOSH) model (Jelesnianski et al., 1992), the Semi-implicit Cross-scale Hydroscience Integrated System Model (SHCISM) (Zhang and Baptista, 2008; Zhang et al., 2016), DELFT3D (Veeramony et al., 2016), and the Advanced Circulation (ADCIRC) model (Fleming et al., 2008). There are also many well-validated hydrological and hydraulic models that model rainfall-runoff processes such as the Gridded Surface Subsurface Hydrological Analysis Model (GSSHA) (Downer et al., 2004), the Hydrologic Engineering Center River Analysis System (HEC-RAS) (Brunner, 2002; Hicks and Peacock, 2005), and the Watershed Systems of 1-D Stream-River Network, 2-D Overland Regime, and 3-D Subsurface Media (WASH123D). Some of these models are capable of modeling streamflow, surface-runoff flow, and subsurface flow represented using a common set of governing equations (Yeh et al., 2005). Though models such as WASH123D, GSSHA, and HEC-RAS excel at modeling a diverse array of physics in coastal environments, these models typically cover a single watershed and therefore do not model wind-driven storm surge coming in the open ocean which is important in order to perform forecasts (Santiago-Collazo et al., 2019).

To simulate compound flooding and more specifically the compounding effects of storm surge and riverine discharge on coastal flooding, there have been many recent efforts that could be categorized into the following approaches: (1) a single model that contains all of the size, detail, and physics needed to capture compound flooding from wind-driven storm surge from the open ocean and riverine discharge from inland, (2) loose coupling of a storm surge model with a hydrological/hydraulic model (for river discharge) through boundary conditions (one or two ways), and (3) dynamic coupling by passing back and forth boundary conditions at each synched time-step (Santiago-Collazo et al., 2019). Among these approaches, the loose coupling of the hydrological model with the storm surge model *via* boundary conditions, and making a single integrated, holistic modeling framework are the most common and most challenging methods, respectively. To date, to the best knowledge of the authors, there is no single modeling system that could address all aspects of compound flooding. However, many studies have coupled two or more models, loosely or dynamically, to simulate different compounding effects such as the compounding effect of storm surge and riverine discharge which this research focuses on. Kumbier et al. (2018) investigated the compounding effects of riverine discharge and storm surge off the coast of Australia by incorporating upstream river discharge boundary conditions from gauge data into the Delft3D model and found that neglecting riverine discharge resulted in an underprediction of flood levels by 30% (Kumbier et al., 2018). Zhang et al. (2019) utilized the hydrological model National Water Model (NWM) to account for the compounding effect from riverine discharge as input into the SCHISM ocean dynamics model *via* exterior boundary conditions in order to model Hurricane Irene's impact on Delaware Bay (Zhang et al., 2019). It was found that the inclusion of riverine discharge into the SCHSIM model resulted in elevated water surface levels for more than 2 weeks after Hurricane Irene hit that area. Bakhtyar et al. (2020b) executed a loose one-way coupling between the NWM and ADCIRC/WAVEWATCH III using the D-Flow FM hydraulic

model to assess compound flooding impacts for tropical cyclones in the Delaware river basin and it was shown that water level predictions depend on a detailed representation of riverine discharge and elevated sea levels as well as detailed pressure and wind forcing (Bakhtyar et al., 2020b). Gori et al. (2020) investigated the contribution of flooding due to river discharge along the North Carolina coast by loosely coupling the storm surge model ADCIRC, and the hydraulic model HEC-RAS by using ADCIRC output as downstream boundary conditions into the 1-D/2-D HEC-RAS hydraulic model in order to account for the effects of storm surge (Gori et al., 2020). It was found that riverine contributions increased peak storm tide by up to 0.36 m. Environmental Fluid Dynamics Code (EFDC) (Hamrick, 1992) was coupled with ADCIRC to examine the concurrent impact of hurricane surge and floods due to significant rainfall with different return periods (Alarcon et al., 2014a,b), and to simulate the fate and transport of spills during compound events (Kiaghadi et al., 2018). Results showed increases in land inundated with longer inundation times along with up to 2 m higher water depth in areas with a higher number of discharging bayous. Additionally, it was found the velocities were significantly higher during the receding surge when riverine flows were included. In these loosely coupled modeling frameworks, there is a "primary" model which simulates the dominant physical processes in the area of interest, with the "secondary" model providing boundary conditions to the primary model.

While the idea of using two or more models in a coupled framework is common in simulating compound flooding, choosing the primary model is challenging. Selecting the right primary model is a function of various factors including but not limited to the purpose and scale of modeling, reliability of the model, computational time, and ease of use. When simulating compound flooding scenarios (or real-time modeling) where both riverine discharge and storm surge are occurring, determining the downstream boundary condition is challenging. For instance, in a loosely coupled framework with a small domain model as the primary one, the discharge upstream could be directly affected by the downstream water surface elevation (WSE) modeled by a separate large domain model that does not take the discharge flux into account. This compound effect on the WSE can also be influenced by contributions from adjacent watersheds that discharge to the same receiving water body (e.g., lake or bay). Thus, the application of using some of the existing hydrodynamic models such as EFDC or HEC-RAS as the primary model to simulate a compound flooding event, would be limited to a small domain for a hindcast scenario. These limitations are mainly due to not being fully parallelized [not using a high-performance computational (HPC) platform] that leads to a need for a downstream boundary condition that is not far away from the affected zone by the storm surge, upstream discharges, and any adjacent watersheds. Furthermore, some of the hydrodynamic models do not have the capability to simulate wind-driven flows from the open ocean. Hence, within the context of compound flood modeling related to tropical cyclones, it is essential to evaluate the ability of a storm surge model that is capable of simulating wind-driven surges and riverine flows that could be run on an HPC platform. In other words, the primary model should have the capability of simulating the maximum possible components of compound flooding individually with the minimum requirement of boundary data being provided by the secondary model.

In this study, ADCIRC was chosen as the primary model because it is a well-validated model and is maintained by a large community of users (Dietrich et al., 2011a, 2012; Hagen, 2011; Bhaskaran et al., 2013; Hope et al., 2013; Technology Riverside Inc., and AECOM, 2015). Since it has an unstructured mesh design (Luettich and Westerink, 2004), it allows for a large domain where ocean dynamics far from the coast (wind-driven hurricanes) can be modeled with enough detail to capture critical features in coastal areas such as rivers and weirs, which will allow for incorporating compound flooding effects. Furthermore, ADCIRC has been written in parallel with Message Passing Interface (MPI), so it is capable of evaluating large domains that contain millions of nodes in a short period of time (Dietrich et al., 2011b). For this study, the approach to model compound flooding is by loosely one-way coupling internal flux boundary conditions into the ADCIRC model to account for river discharge.

HEC-RAS 2-D was chosen as the secondary model since it is a well-documented model with many validated test cases that excels at modeling hydraulics on a single watershed with high accuracy when calibrated (Hicks and Peacock, 2005; Brunner, 2016; Quirogaa et al., 2016; Balbhadra et al., 2020). The 2-D version of HEC-RAS was specifically chosen so that comparisons with ADCIRC, which is a 2-D model as well, can be made in order to evaluate ADCIRC's validity as a model for combined riverine discharge and storm surge on the scale of a watershed.

The main objectives of this study are (i) evaluating ADCIRC's validity in modeling river discharge. This will be accomplished by simulating compound floods around a single river and comparing the results with the observed data and a validated hydraulic model (HEC-RAS 2-D) as benchmarks, (ii) evaluating ADCIRC's validity in modeling a storm system from the open ocean with river discharge included, this riverine discharge will be interpolated from the flux input from the validated HEC-RAS 2-D model. This will be accomplished by running ADCIRC in a larger domain that includes multiple rivers as well as the coast and greater ocean. The results will then be compared with the aforementioned benchmarks, and (iii) including discharges from multiple adjacent watersheds to evaluate the codependency between WSE and riverine discharge and how a large domain model could capture this effect. For the first objective, a fixed downstream boundary condition will be used to mimic the storm surge effect within the domain, while for the second and third ones, a wind field will be used to generate the storm surge far away from the watershed of interest.

METHODS

Model Theory

As noted earlier, the main objective of this research is to evaluate the reliability of ADCIRC as the primary model in simulating compound flooding and comparing its performance with the HEC-RAS model. The two models utilize different physics

equations to model WSE; HEC-RAS solves the 2-D Shallow Water Equations while ADCIRC solves the Generalized Wave Continuity Equations (GWCE) (Luettich and Westerink, 2004; Dietrich et al., 2012). The GWCE in spherical coordinates is a differential form of the continuity and momentum conservation equations specifically for shallow water (where the horizontal length scale is much larger than the depth length scale) systems (see the **Supplementary Materials** section for more details).

It is important to recall that ADCIRC's numerical approximation to the GWCE utilizes a finite element approximation on an unstructured triangular mesh. This contrasts with HEC-RAS, which uses a finite volume method on a structured rectangular mesh. It is important here to see that the GWCE from ADCIRC was first designed for modeling the open ocean and wind-driven storm surge and so ADCIRC contains many more forcing terms than the HEC-RAS equations. The HEC-RAS model was created for evaluating river floodplains, and so processes that occur in the open ocean, such as wind-driven surge and tides are not accounted for in the governing equations but are instead included as external boundary conditions when needed. However, as an advantage for HEC-RAS 2D, it has the capability of modeling direct rainfall excess onto the grid which ADCIRC cannot currently handle. Since HEC-RAS requires a uniform grid and is parallelized using a shared-memory approach, it is not as scalable as ADCIRC. As a result, ADCIRC is capable of modeling much larger coastal systems than HEC-RAS. However, HEC-RAS has the advantage in that it is typically run in small but very highly detailed domains and can account for rainfall effects.

Study Area, Model Domains, and Inputs

The focus of this study is on the lower Neches River from the Salt Water Barrier to Sabine Lake, located in southeast Texas, very close to its border with Louisiana. **Figure 1** shows the location of the lower Neches River as well as the Sabine River, which also discharges into Sabine Lake (3 miles east of Neches outflow). In this study, an existing calibrated and validated HEC-RAS model developed by the USACE for the study areas was used. The HEC-RAS 2-D domain developed by the U.S. Army Corps of Engineers (USACE), Fort Worth District, which includes ∼26,000 rectangular computational cells (121.9 m by 121.9 m), is also shown in **Figure 1** (Mosser et al., 2019). The domain covers ∼28 miles of the Lower Neches River and includes the conveyance of the Neches River floodplain. Manning's roughness coefficients for the model were determined based on USGS developed land use raster file titled National Land Cover Database 2011 Land Cover (Homer et al., 2015) and areas of open water were overwritten with a value of 0.035. The bathymetry was specified by two sources; all area above normal water surface was determined by 1-m Light Detection and Ranging (LiDAR) data surveyed from 2017 to 2018 by the Texas Natural Resources Information System (TNRIS) while all area beneath the normal water surface level was determined from bathymetric data from the Sabine-to-Galveston ADCIRC model (Melby et al., 2019). An approximate trapezoidal channel along the Neches River was burned into the terrain below the water surface whenever the Sabine-to-Galveston ADCIRC bathymetric data was not refined enough. The HEC-RAS 2-D model has two boundary conditions: (1) upstream boundary (flow hydrograph) based on the available observed discharge values from the United States Geological Survey (USGS) streamflow gage at the Salt Water Barrier shown in **Figure 1**, and (2) downstream boundary (stage hydrograph) based on the WSE collected at National Oceanic and Atmospheric Administration (NOAA) 8770475 Port Arthur, TX gage. For the upstream boundary when gage data is not available, there is a calibrated HEC-HMS model created by the USACE that covers the 25534 square kilometers of the Neches River watershed just upstream of the upstream boundary condition in the HEC-RAS domain that will provide the flow rates. For the downstream boundary condition, in the absence of data from the NOAA gauge, WSE from ADCIRC or other models could be fed into HEC-RAS, however in this case the NOAA gauge was sufficient.

For ADCIRC, two meshes, one small (**Figure 2B**) and one large (**Figure 2A**) were used. The small mesh was used for evaluating ADCIRC's ability to model riverine discharge (objective 1), and the larger mesh was used to evaluate ADCIRC's ability to model a storm coming from the open ocean in combination with riverine discharge (objectives 2 and 3). A highly detailed and fine resolution mesh, provided by the USACE, with a total of 9,182,080 unstructured triangular elements (**Figure 2A**), was used as the large mesh. The large ADCIRC mesh includes the entire Gulf of Mexico as well as the Atlantic coast. A MATLAB tool (could be accessed through https://github.com/kiaghadi/Codes/blob/master/Extracting_XYZ_Manning_From_ADCIRC.m) was developed to extract the bathymetry and manning coefficients within the large ADCIRC mesh that coincide with the HEC-RAS 2D model (the full domain is shown in **Figure 1** and part of the HEC-RAS mesh is shown in **Figure 2C**). The selected nodes were then exported to ArcMap where the "Extract Values to Point" was used to assign the bathymetry, land elevation, and manning values to the ADCIRC nodes from the HEC-RAS input rasters. Another MATLAB tool (https://github.com/kiaghadi/Codes/blob/master/Cutting_ADCIRC_Mesh.m) was developed to custom cut the large mesh to the size of the HEC-RAS domain and export the updated nodes, cells, boundary conditions, bathymetry, land elevation, and node attributes in order to create the small ADCIRC mesh. The output was the small ADCRIC mesh with a total of 122,839 unstructured triangular elements (part of the small mesh is shown in **Figure 2B**). The effects of river discharge were added into the small and large ADCIRC models *via* internal time-dependent flux boundary conditions across a string of seven nodes. A sensitivity analysis, using the small mesh, was performed in order to determine the location of the internal time-dependent flux boundary conditions. The sensitivity analysis resulted in the boundary conditions being added into the ADCIRC meshes (both small and large) in an area that is as far upstream in the Neches River as possible but where there is still high enough mesh refinement to describe the river feature. In addition to the Neches River flow boundary condition that was added to both small and large mesh, an additional boundary condition was implemented on the large mesh to represent discharges from the Sabine River. After the meshes

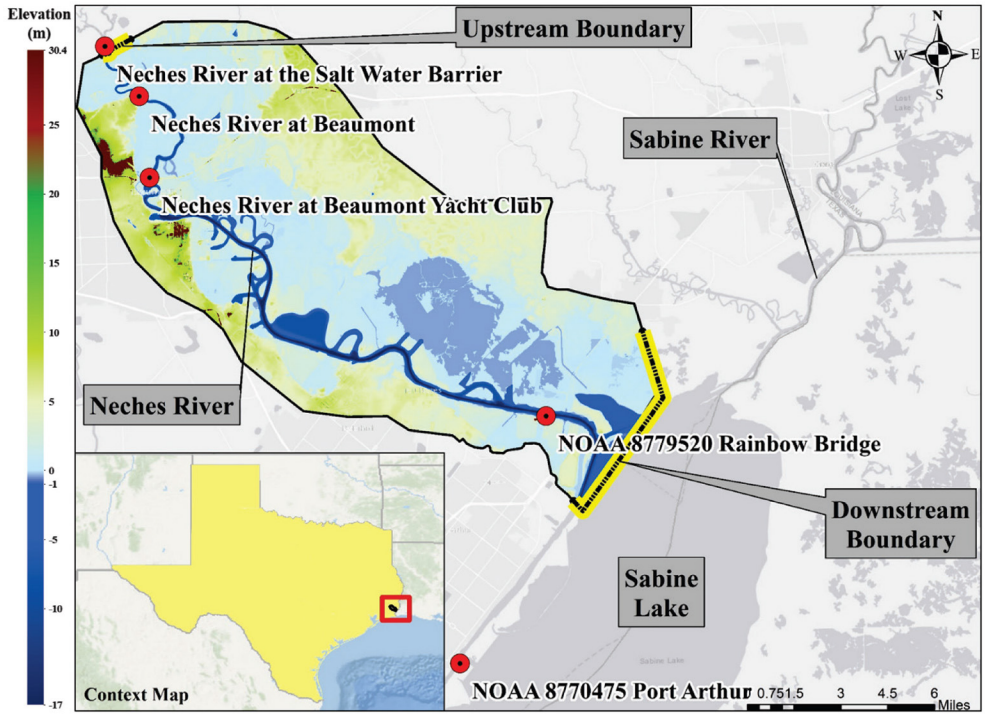

FIGURE 1 | Lower Neches River watershed and Sabine River and Sabine Lake locations. The color-coded figure shows the bathymetry and land elevation. The HEC-RAS domain is outlined in black. Location of gages demarcated by red dots.

were created, a Python code (https://github.com/Markloveland/Writefort20) was developed to automate the process of reading the time-dependent flux boundary data by interpolating the same boundary data that was used for the upstream boundary conditions in HEC-RAS, which was derived from nearby USGS gage data, onto the ADCIRC meshes. The code distributes the flux among boundary nodes and delivers flux at each node for the time periods of the simulations. ADCIRC treats flow as flux; thus, the flow data (usually given in cms or cfs) was converted to m^2/s using the width between the flow boundary nodes.

For the ADCIRC small domain, the downstream boundary condition was defined as a non-periodic, time-varying elevation boundary condition. To determine the values for downstream boundary condition in ADCIRC, WSE was extracted from the HEC-RAS 2D model input, which was derived from data from the closest NOAA gage, and then interpolated into ADCIRC model input. For the ADCIRC large domain, instead of having a downstream boundary condition the exterior boundaries were tidal boundary conditions in the North Atlantic Ocean. The tidal boundary conditions were determined using OceanMesh2D software (Pringle, 2018) which interpolates output from the Oregon State University TPXO9 tidal model (Egbert and Erofeeva, 2002) into external elevation specified boundary conditions. In the large domain, winds were incorporated as inputs in order to account for storm surge. Official hindcast winds and pressure data were obtained from the USACE Research & Development Center Coastal & Hydraulics Laboratory in the Oceanweather Inc. (OWI) format and used as the forcing input for ADCIRC. The OWI winds and pressures were given over three uniform grids with three levels of refinement at time intervals of 15 min. The coarsest grid extended over most of the Gulf of Mexico and Atlantic coast with latitudes from 5 degrees North up to 42 degrees North and longitudes from 99 degrees West to 55 degrees West with refinement of 0.2 degrees in both directions. The next level of refinement has a grid from 18 degrees North to 31 degrees North and 98 degrees West to 80 degrees West with refinement of 0.08 degrees in both directions. The level of highest refinement was from 26.5 degrees North to 29.5 degrees North and from 98.5 degrees West to 95.4 degrees West with a refinement of 0.02 degrees in both directions. ADCIRC automatically interpolates both temporally and spatially these winds and pressures from the uniform OWI grids onto each node of the ADCIRC mesh by taking the winds and pressures from the grid with the highest refinement at the location of a given node.

Scenarios

After constructing the meshes, Hurricane Harvey (2017) was simulated in each model and model results were compared to measured data from USGS and NOAA gages. Although peak storm surge caused by Hurricane Harvey was observed in Corpus Christi, the hurricane produced moderate surge levels in the study area. Furthermore, Hurricane Harvey caused historical precipitation in the study area leading to unprecedented flow rates in the Neches River, making it a good case study for compound flooding.

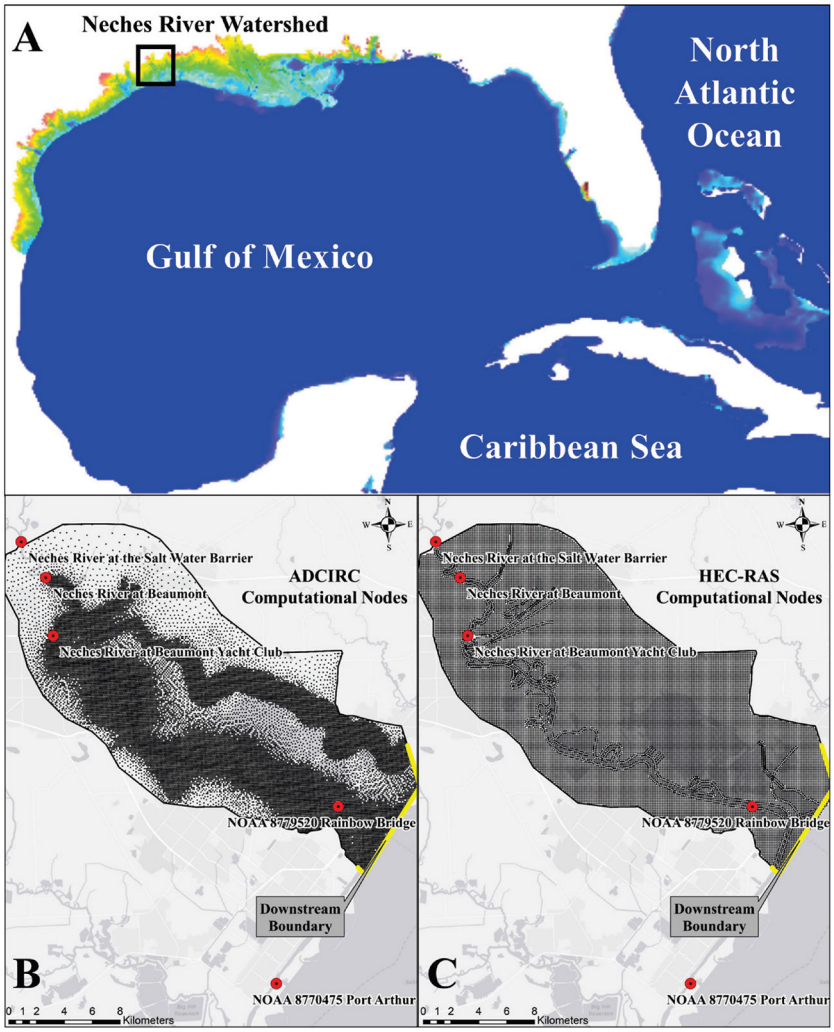

FIGURE 2 | (A) Location of the Neches River watershed within the large ADCIRC mesh that include the Gulf of Mexico and part of the north Atlantic Ocean, **(B)** ADCIRC small mesh structure, each black dot indicates a computational node, and **(C)** HEC-RAS mesh structure, the black lines separate each of the finite volume elements.

To evaluate the capability of the ADCIRC model in simulating compound flooding, we ran the ADCIRC model with the Hurricane Harvey test case for 12 days using the small mesh (with the same domain size as HEC-RAS) with the boundary conditions set to the same as the HEC-RAS model (USGS gage data in upstream boundary and NOAA gage data for the downstream boundary condition) just interpolated onto the small ADCIRC mesh. We then compared the ADCIRC results with the validated HEC-RAS model, which ran for the same 12 days (by USACE), and gage data. Next, we ran the ADCIRC model with the large mesh for five different scenarios: (i) Hurricane Harvey with both Neches and Sabine Rivers, and storm surge (wind and pressure driven) inputs, (ii) Hurricane Harvey with no flow input (surge effect), (iii) Hurricane Harvey with flow input only from Neches River, (iv) Hurricane Harvey with flow input but with no wind field, and (v) Hurricane Harvey with no flow and no wind output (just tides). The first scenario was developed to evaluate the performance of the ADCIRC model as the primary model in simulating compound flooding and compare its performance in its full capacity (e.g., by including the wind field) with HEC-RAS. The second scenario was chosen to evaluate the effect of having riverine flows not only within the watershed but also farther downstream. The third scenario was tested to assess the effect of flow discharging from the adjacent watersheds (Sabine River) when evaluating the compound flooding within a watershed (Neches River). Finally, the last two scenarios were tested to see the effect of storm surge and examine to see if compound flooding from storm surge and river discharge played a significant role during Hurricane Harvey. It should be noted that the WSEs in the Sabine Lake, where both rivers discharging into, are a function of tides, storm surge (wind driven), and discharges from both rivers. Although

the HEC-RAS model developed for the Neches River watershed does not include the discharge rates from Sabine river, using the actual WSEs observed during a hydrologic event (i.e., Hurricane Harvey) will incorporate the effect of the aforementioned variables into the model. In other words, the effect of Sabine River discharge on Neches River inundation pattern is dictated to the model through the downstream boundary condition that is based on observed data. This dependency to the downstream boundary condition could be problematic when the model is being used to test scenarios instead of hindcast studies. In this case, a significant error in the model results could be introduced by not considering the effect of adjacent watersheds or not including them in the coupled models (e.g., ADCIRC).

Comparison Metrics

In order to analyze the differences in WSE output of the HEC-RAS and ADCIRC models, it is essential to quantitatively evaluate the differences in the models as well as the difference between each model and real data collected during the hydrologic event. As seen in **Figure 1**, there are four locations within the HEC-RAS and corresponding ADCIRC domains that have USGS or NOAA gauge data. These locations are the Neches River at the Saltwater Barrier, the Neches River at Beaumont, the Neches River at Beaumont Yacht Club, and Rainbow Bridge (see **Figure 1**). Among these four locations, the Neches River at the Saltwater Barrier (USGS gage) is located upstream of the flow boundary in the ADCIRC domain and very close to the HEC-RAS upstream boundary condition. Furthermore, there is a hydraulic structure located at that location that is not included in the ADCIRC mesh. Thus, in this study, data from the other three gauges were used for comparisons with model results. In the subsequent section, the resulting output from ADCIRC and HEC-RAS models will be compared with each other and the gauge data at these three locations. In order to evaluate the magnitude of error between the models and the real data quantitatively, the root means square error (RMSE) is computed for each comparison. RMSE is described by the following:

$$RMSE = \sqrt{\frac{\sum_{t=1}^{T} \left(\hat{y}_t - y_t\right)^2}{T}} \tag{1}$$

Where t is the time step, $\hat{y}_t$ is the observed WSE at time step t, y_t is the model output at time step t, and T is the total number of time steps. In addition to RMSE, the coefficient of determination (R^2) is computed for each of the comparisons in order to evaluate how well the models are replicating measured data. R^2 is described by the following:

$$R^2 = 1 - \frac{\sum_{t=1}^{T} \left(\hat{y}_t - y_t\right)^2}{\sum_{t=1}^{T} \left(\bar{y} - y_t\right)^2} \tag{2}$$

Here $\bar{y}$ denotes the mean of the observed data. While RMSE provides information on the accuracy of the model in predicting the magnitude, R^2 evaluates how close the model fits the data. A value of $R^2$of 1 means that the model fits the data exactly. In addition to evaluating the accuracy, the bias and mean absolute error (MAE) will also be calculated in order to see if the models have an underlying tendency in undershooting or overshooting measurements and to evaluate the aggregate of error between the models and data time series. MAE and bias are calculated using the following formulas:

$$MAE = \frac{1}{T} \sum_{t=1}^{T} \frac{\left|\hat{y}_t - y_t\right|}{\hat{y}_t} \tag{3}$$

$$bias = \bar{y} - \left(\sum_{t=1}^{T} \frac{y_t}{T}\right) \tag{4}$$

It should be noted that instead of relying on real observational data from the hindcast that the small mesh uses, the large ADCIRC mesh relies on wind driven storm surge and the harmonic tide from the open ocean. As a result, less accurate results are anticipated from the large mesh simulations; however, the general trends and periodicity of the rise in WSE is expected to remain similar to the HEC-RAS and ADCIRC small mesh.

RESULTS AND DISCUSSION

Comparing ADCIRC and HEC-RAS

The small ADCIRC mesh, large ADCIRC mesh (with both Neches and Sabine Rivers), and HEC-RAS models were run for the Hurricane Harvey case and resulted in the following WSE time-series (**Figure 3**) at the Neches River at Beaumont, Neches River at Beaumont Yacht Club, Rainbow Bridge stations, and HEC-RAS downstream boundary location (see **Figure 1** for the locations). The comparison metrics for all simulations are shown in **Table 1**. The small ADCIRC mesh showed a very similar pattern in predicting WSE when compared to HEC-RAS ($0.76 < R^2 < 0.88$). It is apparent that, in general, the ADCIRC small mesh simulation underpredicted WSEs (**Figure 3**) with an RMSE between 0.13 and 0.59 m and bias between −0.01 and 0.50 m compared to the HEC-RAS model. The small mesh ADCIRC results at Rainbow Bridge, the most downstream observational gauge, compared well with the HEC-RAS results as shown in **Figure 3**. At this station, there was an RMSE of only 0.13 m with an R^2 of 0.88, MAE of ∼11.7% and a small bias of −0.01 m, which corresponds to an overprediction.

The large ADCIRC mesh performed somewhat similar to the small ADCIRC mesh; the large mesh results were slightly less accurate (compared to observational data) and underestimated the WSE even more than the small mesh. The RMSEs in comparison to the HEC-RAS output and real-time observations were between 0.21–0.62 m and 0.12–0.84 m, respectively. The observed data, in Rainbow Bridge and Neches River at Beaumont stations, as seen in **Figure 3**, was too sparse, so the evaluation metrics presented in **Table 1** should be treated with care for these two stations. However, qualitatively, the observed data followed very close to the HEC-RAS output.

Based on the results depicted in **Figure 3** and **Table 1**, it appears that the ADCIRC model is capable of computing changes in WSE due to riverine flooding though with underprediction of WSEs in some areas. As discussed in the methods section, HEC-RAS and ADCIRC models have different equations as well

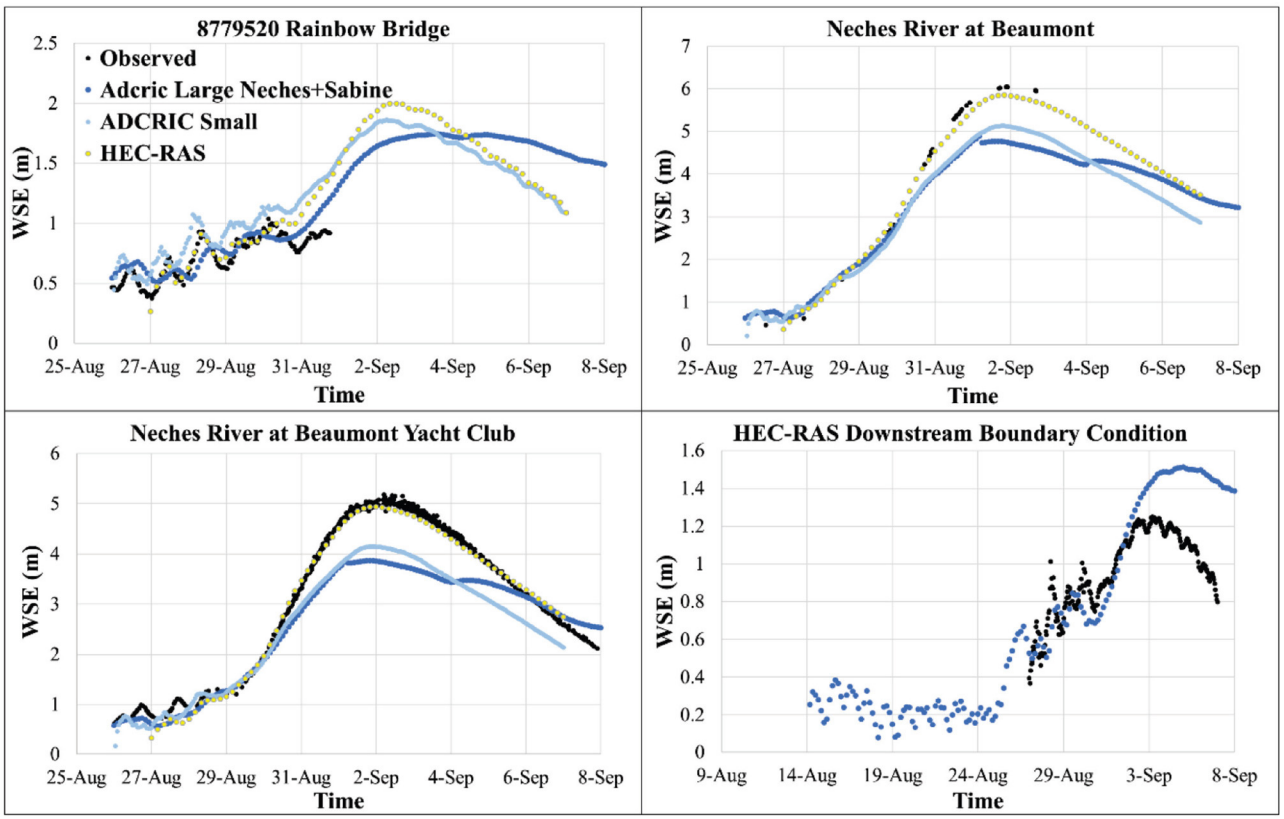

FIGURE 3 | Results of various ADCIRC simulation scenarios for water surface elevations (WSEs) at different locations (see **Figure 1** for the locations).

as various numerical schemes. However, another reason that could account for the underprediction of the first two stations is the fidelity of the ADCIRC mesh. The small ADCIRC mesh simulation was very accurate in modeling the WSE at Rainbow Bridge; the domain in the small model has a much heavier refinement in its mesh. The two stations where model results from ADCIRC underpredicted the WSE were in locations where the ADCIRC mesh was less detailed than the HEC-RAS mesh (as seen in **Figures 2B,C**). It has been shown that increasing the density of nodes in an ADCIRC mesh, especially near geographic features such as channels or lakes where there are steep variations in elevation, can drastically improve accuracy (Pringle et al., 2020). Finally, it should be noted that the HEC-RAS model was intensively calibrated for the Hurricane Harvey event while the ADCIRC model was not calibrated explicitly for this event. While the ADCIRC meshes were tuned to match the HEC-RAS model, tuning parameters and nodal attributes could also increase the accuracy as have be seen in multiple validations and sensitivity analyses using ADCIRC (Blain, 1998; Dietrich et al., 2011a, 2012; Bhaskaran et al., 2013; Hope et al., 2013).

Impact From Storm Surge

Since Hurricane Harvey was characterized by exceptionally high riverine discharge that heavily impacted water surface elevations in the Neches river watershed and Sabine Lake areas, it remains to be seen what influence storm surge had in compounding with the riverine discharge. As shown in **Figure 4A** even with all the flow emanating from Sabine and Neches Rivers, the WSE in the mouth of the Gulf of Mexico (GOM) did not change significantly without the presence of a wind field (storm surge). However, once the wind was considered an increase of almost 0.6 m (2 ft) was observed around August 25 when Hurricane Harvey hit the study area. Such an increase in WSE in the downstream of the study area accompanied by the flow from upstream could be considered a compound flooding event. The effect of flow on WSE at this location was observed several days after the passage of the strongest wind field when the riverine flow had continued to drain the runoff from the upper watersheds to GOM. The compounding effect of the wind and riverine flow in locations further upstream of the GOM mount (i.e., at the confluence of Neches River and Sabine Lake) is shown in **Figure 4B**. The simulations with the wind field showed higher level of WSE at the beginning of Harvey but once the high volume of runoff was introduced to the system and the wind field passed the study area, the scenarios with and without wind that considered flow showed almost identical results.

Effect of Riverine Flow

In this section, the results of the effects of including riverine flow on the large ADCIRC mesh are presented. The ADCIRC large mesh was run for the same Hurricane Harvey test case, once with

TABLE 1 | Evaluation metrics for different simulation scenarios.

Metric*	Comparison Scenarios**				
	HEC—small	HEC—large	HEC—Obs	Small—Obs	Large—Obs
Rainbow bridge* **					
RMSE	0.13	0.21	0.16	0.25	0.12
R^2	0.88	0.78	0.72	0.31	0.58
MAE	11.77%	14.86%	14.03%	29.80%	13.57%
Bias	−0.01	0.02	0.08	0.22	0.03
Neches river at Beaumont Yacht club					
RMSE	0.59	0.61	0.16	0.62	0.68
R^2	0.76	0.73	0.98	0.79	0.66
MAE	17.12%	13.64%	6.48%	15.70%	14.43%
Bias	0.46	0.43	−0.04	0.46	−0.49
Neches river at Beaumont* **					
RMSE	0.58	0.62	0.21	0.71	0.84
R^2	0.84	0.79	0.98	0.80	0.71
MAE	13.90%	11.98%	7.30%	15.47%	15.18%
Bias	0.50	0.46	−0.10	−0.55	−0.64

RMSE, Root mean square error; R2, Coefficient of determination; MAE, Mean absolute error. Units are in meters unless otherwise specified.

***HEC, HEC-RAS; Small, Small ADCIRC mesh; Large, Large ADCIRC mesh; Obs, Observation.*

****Observed data was available only for a part of simulation time (see **Figure 3**).*

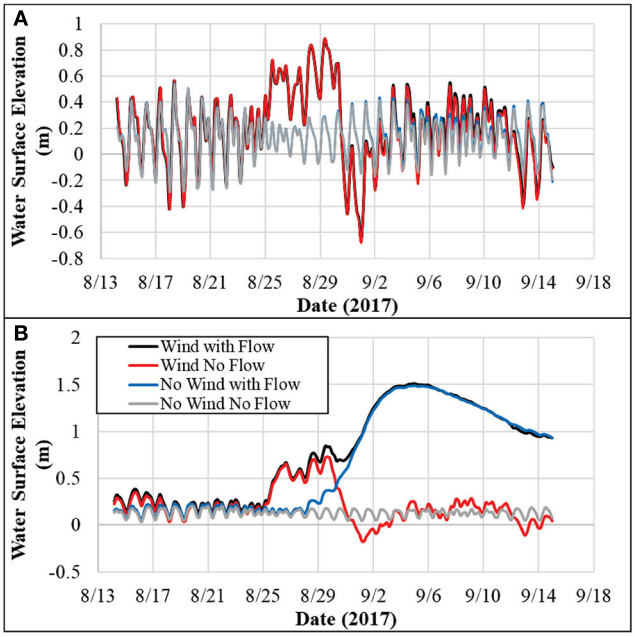

FIGURE 4 | Water surface elevations from ADCIRC with various forcing conditions turned on/off **(A)** just downstream of the Sabine Lake at its confluence with Gulf of Mexico, and **(B)** at the confluence of Neches River and Sabine Lake (HEC-RAS and ADCIRC small mesh downstream boundaries).

riverine discharge included from both Sabine and Neches rivers, and once with no riverine flow.

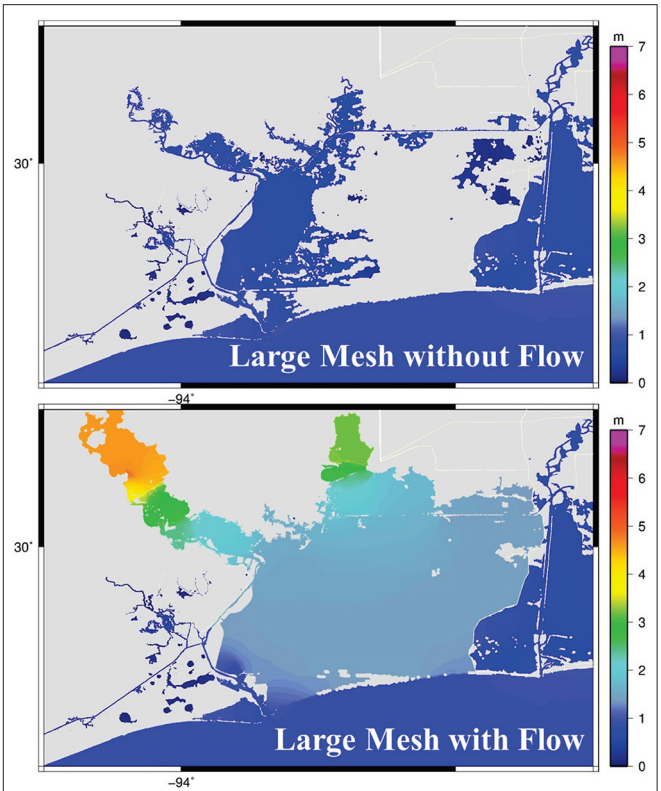

FIGURE 5 | Maximum elevation in the computational elements over the period of simulation for the large ADCIRC mesh with and without riverine flow inputs.

Figure 5 shows the maximum WSE at each model node over the course of the entire simulation (also known as maxele) for the large ADCIRC mesh with and without riverine flow inputs. The maximum elevation plots are not representative of any singular point in time, but instead, the maximum elevation reached at each point in space over the course of the whole simulation. Such plots are useful in evaluating the overall differences between the two simulations. It is apparent in **Figure 5** that there is a large discrepancy in the WSE patterns between the two simulations (with and without riverine flows).

In addition to having much larger areas of inundation, the simulation with riverine flow had much higher peak WSEs, which indicates that there is indeed a compound flooding effect. The riverine flow compounds with the incoming storm surge, resulting in higher WSE than with either riverine flow or surge considered separately. In order to analyze these results in more detail, the same three stations as in the previous section were used for comparisons. Additionally, one location near the downstream boundary of the HEC-RAS domain, one location in the middle of the Sabine Lake, as well as one location at the mouth of the Gulf of Mexico were used (see **Figure 6**).

There are quite large differences in WSEs between the simulations that include and neglect the riverine discharges. Such a large difference indicates that flooding in an estuarine system is a function of both storm surge and riverine discharge; without including the riverine flow in the simulation, many of

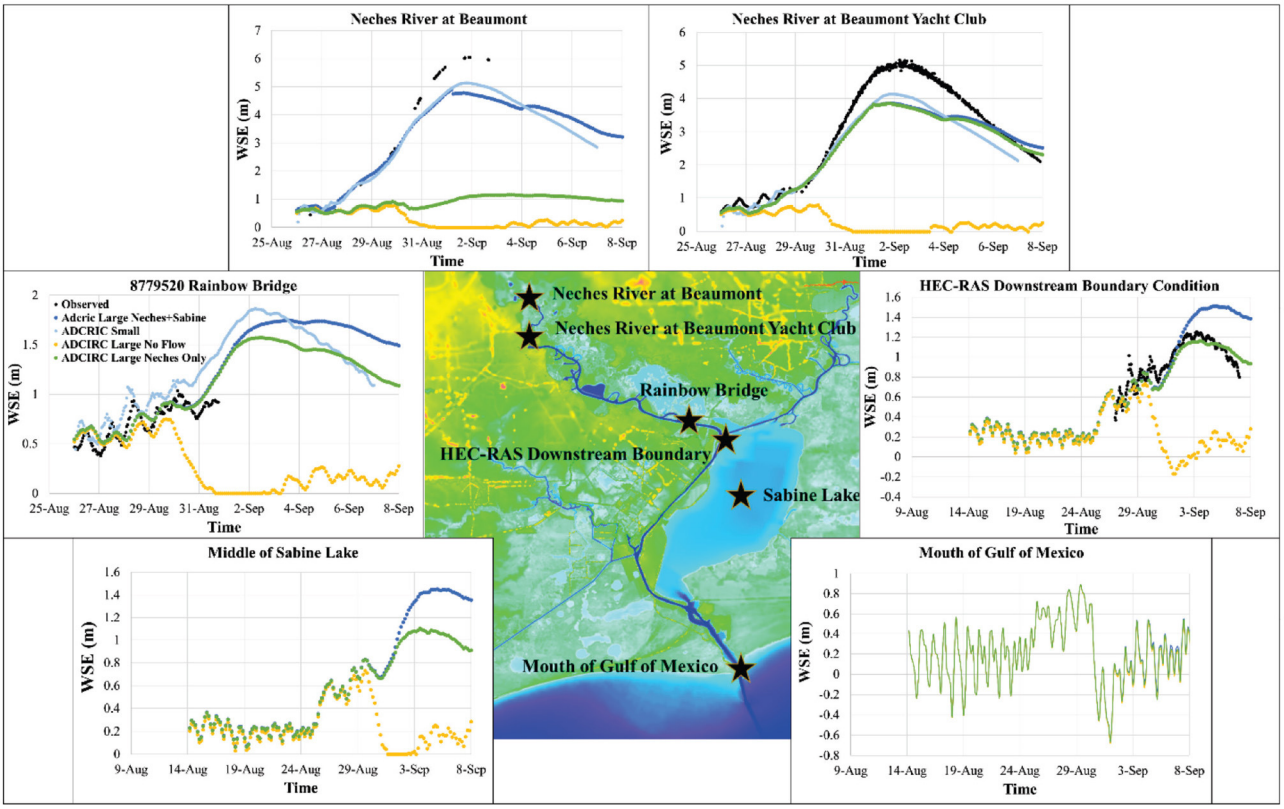

FIGURE 6 | ADCIRC output for different scenarios at the location of all comparison stations shown in the center colored panel.

the computational elements did not even become inundated for the bulk of the simulation (**Figure 5**). Including riverine flow in the simulation results in a dramatic increase in accuracy. For instance, as shown in **Table 1**, for the large mesh (with the flow), the RMSE at Neches River at Beaumont was 0.62 and 0.84 m when compared to HEC-RAS and observed data, respectively. This RMSE is much smaller than the RMSEs of >4.00 m for the ADCIRC large mesh without flow. Similarly, the Neches River at Beaumont Yacht Club and Rainbow Bridge (**Figure 6**) show that running the ADCIRC simulation with riverine flow taken into account dramatically increases accuracy when compared to the real data and the validated HEC-RAS model.

The inclusion of riverine flow influences WSE further downstream, outside of where the small mesh ADCIRC and HEC-RAS domains end. **Figure 6** shows the difference in WSEs due to including flow in the central part of Sabine Lake, where it was heavily flooded during Hurricane Harvey. The differences in WSEs were as large as 1.3 m. In this location, up to August 28th, the WSEs are relatively similar, indicating that the changes in the mild rise in WSE over this period are a result of tides and storm surge. However, after this time, the two WSE time-series diverge. This divergence agrees with the timing of the increasing flow input in the upstream. The results at the mouth of the Gulf revealed that the riverine discharge does not affect the WSEs beyond the estuarine system. As shown in **Figure 6**, the scenario with both Neches and Sabine River (with flow) resulted in a minor increase (0–5 cm) in the WSE at the mouth of the Gulf where the Sabine Lake discharges into the Gulf of Mexico. During an event such as Hurricane Harvey where the spatial extent of the rainfall-induced flows from the event was an extremely large area including many watersheds, not considering the riverine flows and their compound effect in determining WSEs could lead to significant underpredictions of inundation and flood risk. Thus, when evaluating storms where river discharge is large, it is critical to incorporate river flow in order to obtain accurate WSEs. This comes as no surprise especially when modeling a storm with such high riverine discharge as Hurricane Harvey. These results are also not limited to just this test case as ADCIRC has been shown to increase in accuracy when incorporating the effects of riverine discharge through boundary conditions (Bunya et al., 2010).

Interaction Among Watersheds

The previous sections demonstrate conclusively that adding riverine flow into the ADCIRC model can allow for much higher accuracy in modeling storms with compound flooding. In this section, the codependences of two watersheds are analyzed. In the previous simulations, when the ADCIRC large mesh with the riverine flow was used, the discharges from both the Neches and Sabine watersheds were included since they are in close proximity, and both feed into the Sabine Lake. **Figure 7** shows the significance of incorporating both watershed discharges as opposed to just from the Neches. Including the Sabine River

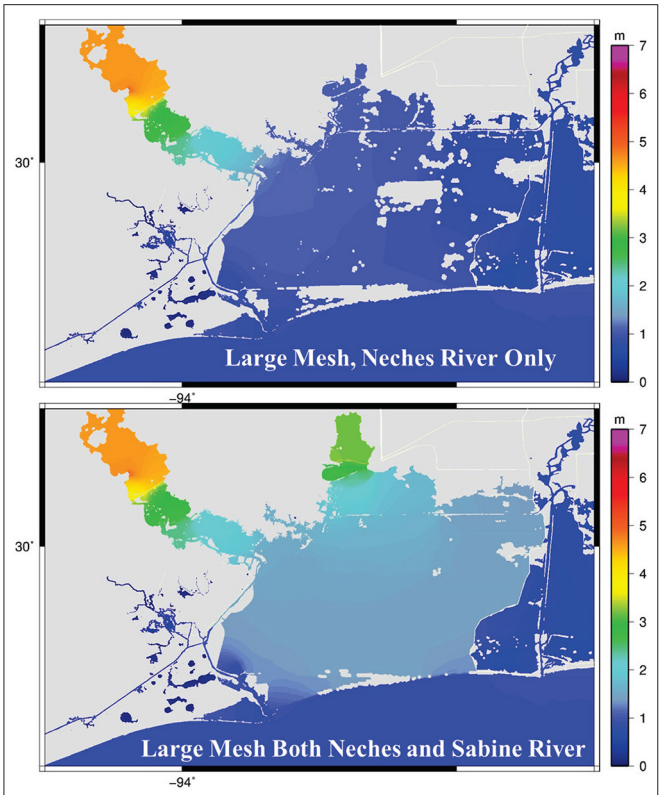

FIGURE 7 | Maximum elevation in the computational elements over the period of simulation for the large ADCIRC mesh with only Neches River and both Neches and Sabine River flows. These plots are not representative of any singular point in time, but instead, the maximum elevation reached at each point in space over the course of the whole simulation.

caused higher and more intense inundations in the system. In addition to areas located in the downstream of both Neches and Sabine River, adding the Sabine River discharge caused changes in the WSEs and flooding pattern of areas within the Neches River (**Figure 6**).

Incorporating the two watersheds as opposed to just Neches had the highest effect on the WSE at the Neches River at Beaumont, followed by Rainbow Bridge and then Beaumont Yacht Club (see **Figures 1**, **6** for locations). Neches River at Beaumont showed the highest impact from the Sabine River, while it is the farthest from the confluence of Neches and Sabine Rivers. This high impact might be due to the fact that the presence of Sabine River discharge in the system caused some water to flow back into the Neches River which resulted in more inundation in the Neches River upstream. Without the addition of the Sabine watershed, the accuracy of the Neches River at Beaumont would be marginally better than not including any flow at all. It is also interesting that the Neches only simulation at Rainbow Bridge station remains quite similar to the simulation with both watersheds up until around September 2nd when the overflow from the Sabine watershed starts increasing WSE in the Neches. Such an increase in the WSEs far away from the watershed outlets emphasizes the importance of considering interactions among watersheds when modeling compound flooding.

In addition to the areas upstream of the confluence of the two rivers, including the discharges from Sabine River, could potentially affect the downstream water bodies and floodplains as well. As shown in **Figure 6**, right at the downstream boundary condition of HEC-RAS and small ADCIRC model (see **Figure 1**) the effect of extra flow is substantial. This finding is particularly important when ADCIRC is being used for real-time simulation or coupling with other hydrodynamic models (e.g., HEC-RAS). A coupled system that only focuses on a single watershed without considering the interactions among adjacent watersheds could result in inaccurate WSEs. The discharge from Sabine River also caused a 0.5 m increase in WSE in the Sabine lake (**Figure 6**) which caused more inundation in the adjacent lands (**Figure 7**). Similar to the previous section, the effect of adding more discharge on WSEs of the Gulf was minimal.

CONCLUSIONS

This research demonstrated ADCIRC's ability to model compounding effects from storm surge and riverine discharge *via* loose one-way coupling with gage data through internal time-dependent flux boundary conditions in a single watershed by comparing ADCIRC with a validated 2-D hydraulic model in HEC-RAS. As presented in this study, accounting for adjacent watersheds through the incorporation of internal time dependent flux boundary conditions in ADCIRC could have significant impact on the accuracy of the WSEs during a tropical cyclone. Furthermore, the results suggest that adjacent watersheds can significantly impact the WSEs (as high as 4 m observed) of their neighboring watersheds at times of high riverine discharge and should be considered when modeling compound flooding events that affect more than one watershed in the same geographic region. Some limitations in this study that can be improved upon in the future are that short range waves and pluvial flooding were neglected. A common way of addressing short range waves in ADCIRC has been coupling ADCIRC with a wave model such as WAVEWATCH III or the Simulating Waves Nearshore model (SWAN). The contribution to compound flooding by pluvial flooding in ADCIRC has not yet been addressed and is currently an open area of research. Further improvements can be made such as mesh refinement in the upstream locations in the ADCIRC mesh as well as parameter calibration in order to increase accuracy in the WSE when compared to gage data. Additionally, including more watersheds across the Gulf of Mexico, attempting to use this modeling framework to hindcast more historical storms other than Hurricane Harvey, as well as using this framework in a forecasting setting is a future goal.

DATA AVAILABILITY STATEMENT

The raw data supporting the conclusions of this article will be made available by the authors, without undue reservation.

AUTHOR CONTRIBUTIONS

ML and AK developed the idea and completed the majority of the modeling, analysis, and writings. CD helped with running

the ADCIRC model as well as developing the research idea and overall project management in coordination with SM. HM, SM, and AP helped with the HEC-RAS model as well as data acquisition. HR helped with developing the methodology. CD, HR, SM, and AP helped with data analysis and review of writing. All authors contributed to the article and approved the submitted version.

FUNDING

This research was based upon work supported by, or in part by, the Department of Defense High Performance Computing Modernization Program (HPCMP) under User Productivity Enhancement, Technology Transfer, and Training (PETTT) contract # GS04T09DBC0017. Support was also provided from the National Science Foundation grant # 1934192 and the Hurricane Resilience Research Institute at the University of Houston. Additional support was provided by National Science Foundation grant #1854986.

SUPPLEMENTARY MATERIAL

The Supplementary Material for this article can be found online at: https://www.frontiersin.org/articles/10.3389/fclim.2020.609610/full#supplementary-material

REFERENCES

Alarcon, V. J., Johnson, D., Mcanally, W. H., van der Zwaag, J., Irby, D., and Cartwright, J. (2014a). "Design and deployment of a dynamic-coupling tool for EFDC BT," in *Computational Science and Its Applications – ICCSA 2014*, eds B. Murgante, S. Misra, A. M. A. C. Rocha, C. Torre, J. G. Rocha, M. I. Falcão, et al. (Cham: Springer International Publishing), 615–624.

Alarcon, V. J., Johnson, D., McAnally, W. H., van der Zwaag, J., Irby, D., and Cartwright, J. (2014b). Nested hydrodynamic modeling of a coastal river applying dynamic-coupling. *Water Resour. Manag.* 28, 3227–3240. doi: 10.1007/s11269-014-0671-6

Bakhtyar, R., Maitaria, K., Velissariou, P., Trimble, B., Flowers, T., Moghimi, S., et al. (2020a). *Characterizing Compound Coastal-Riverine Behavior along the U.S. East Coast using a Coupled Hydrologic-Hydrodynamic Model*. Available online at: https://agu.confex.com/agu/osm20/meetingapp.cgi/Paper/646141 (accessed September 19, 2020).

Bakhtyar, R., Maitaria, K., Velissariou, P., Trimble, B., Mashriqui, H., Moghimi, S., et al. (2020b). A new 1D/2D coupled modeling approach for a riverine-estuarine system under storm events: application to Delaware River Basin. *J. Geophys. Res. Ocean* 125:e2019JC015822. doi: 10.1029/2019JC015822

Balbhadra, T., Ranjan, P., Ajay, K., Sajjad, A., and Ritu, G. (2020). Coupling HEC-RAS and HEC-HMS in precipitation runoff modelling and evaluating flood plain inundation map. *World Environ. Water Resour. Congr*. 2017, 240–251. doi: 10.1061/9780784480625.022

Bhaskaran, P. K., Nayak, S., Bonthu, S. R., Murty, P. L. N., and Sen, D. (2013). Performance and validation of a coupled parallel ADCIRC-SWAN model for THANE cyclone in the Bay of Bengal. *Environ. Fluid Mech.* 13, 601–623. doi: 10.1007/s10652-013-9284-5

Bilskie, M. V., and Hagen, S. C. (2018). Defining flood zone transitions in low-gradient coastal regions. *Geophys. Res. Lett.* 45, 2761–2770. doi: 10.1002/2018GL077524

Bilskie, M. V., Hagen, S. C., Alizad, K., Medeiros, S. C., Passeri, D. L., Needham, H. F., et al. (2016). Dynamic simulation and numerical analysis of hurricane storm surge under sea level rise with geomorphologic changes along the northern Gulf of Mexico. *Earth's Futur.* 4, 177–193. doi: 10.1002/2015EF000347

Blain, C. A. (1998). *Coastal Tide Prediction Using the ADCIRC-2DDI Hydrodynamic Finite Element Method: Model Validation and Sensitivity Analyses in the Southern North Sea/English Channel*. Available online at: https://apps.dtic.mil/dtic/tr/fulltext/u2/a358752.pdf

Brunner, G. (2002). *Hec-ras (River Analysis System)*. North American Water and Environment Congress. Available online at: https://cedb.asce.org/CEDBsearch/record.jsp?dockey=0100264 (accessed August 19, 2020).

Brunner, G. (2016). *HEC-RAS River Analysis System Hydraulic Reference Manual*. Available online at: www.hec.usace.army.mil (accessed August 13, 2020).

Bunya, S., Dietrich, J. C., Westerink, J. J., Ebersole, B. A., Smith, J. M., Atkinson, J. H., et al. (2010). A high-resolution coupled riverine flow, tide, wind, wind wave, and storm surge model for Southern Louisiana and Mississippi. Part I: model development and validation. *Mon. Weather Rev.* 138, 345–377. doi: 10.1175/2009MWR2906.1

Couasnon, A., Eilander, D., Muis, S., Veldkamp, T. I. E., Haigh, I. D., Wahl, T., et al. (2020). Measuring compound flood potential from river discharge and storm surge extremes at the global scale. *Hazards Earth Syst. Sci.* 20, 489–504. doi: 10.5194/nhess-20-489-2020

Demaria, M., and Kaplan, J. (1994). Sea surface temperature and the maximum intensity of atlantic tropical cyclones. *J. Clim.* 7, 1324–1334. doi: 10.1175/1520-0442(1994)007<1324:SSTATM>2.0.CO;2

Dietrich, J. C., Tanaka, S., Westerink, J. J., Dawson, C. N., Luettich, R. A., Zijlema, M., et al. (2012). Performance of the unstructured-mesh, SWAN+ ADCIRC model in computing hurricane waves and surge. *J. Sci. Comput.* 52, 468–497. doi: 10.1007/s10915-011-9555-6

Dietrich, J. C., Westerink, J. J., Kennedy, A. B., Smith, J. M., Jensen, R. E., Zijlema, M., et al. (2011a). Hurricane gustav (2008) waves and storm surge: hindcast, synoptic analysis, and validation in southern Louisiana. *Mon. Weather Rev.* 139, 2488–2522. doi: 10.1175/2011MWR3611.1

Dietrich, J. C., Zijlema, M., Westerink, J. J., Holthuijsen, L. H., Dawson, C., Luettich, R. A., et al. (2011b). Modeling hurricane waves and storm surge using integrally-coupled, scalable computations. *Coast. Eng.* 58, 45–65. doi: 10.1016/j.coastaleng.2010.08.001

Downer, C. W., Asce, M., and Ogden, F. L. (2004). GSSHA: model to simulate diverse stream flow producing processes. *Artic. J. Hydrol. Eng.* 9, 161–174. doi: 10.1061/(ASCE)1084-0699(2004)9:3(161)

Egbert, G. D., and Erofeeva, S. Y. (2002). Efficient inverse modeling of barotropic ocean tides. *J. Atmos. Ocean. Technol.* 19, 183–204. doi: 10.1175/1520-0426(2002)019<0183:EIMOBO>2.0.CO;2

Emanuel, K. (2005). Increasing destructiveness of tropical cyclones over the past 30 years. *Nature* 436, 686–688. doi: 10.1038/nature03906

Emanuel, K. A. (1987). The dependence of hurricane intensity on climate. *Nature* 326, 483–485. doi: 10.1038/326483a0

Fleming, J. G., Fulcher, C. W., Luettich, R. A., Estrade, B. D., Allen, G. D., and Winer, H. S. (2008). "A real time storm surge forecasting system using ADCIRC," in *Estuarine and Coastal Modeling*, ed M. L. Spaulding (Reston, VA: American Society of Civil Engineers), 893–912. Available online at: https://ascelibrary.org/doi/book/10.1061/9780784409909

Gori, A., Lin, N., and Smith, J. (2020). Assessing compound flooding from landfalling tropical cyclones on the North Carolina Coast. *Water Resour. Res.* 56. doi: 10.1029/2019WR026788

Hagen, S. (2011). Hydrodynamics of the 2004 Florida Hurricanes. *J. Coast. Res.* 28:1121. doi: 10.2112/JCOASTRES-D-10-00170.1

Hamrick, J. M. (1992). *A Three-Dimensional Environmental Fluid Dynamics Computer Code: Theoretical and Computational Aspects*. Special report in applied marine science and ocean engineering. Virginia Institute of Marine Science, William & Mary. Available online at: https://doi.org/10.21220/V5TT6C

Hicks, F. E., and Peacock, T. (2005). Suitability of HEC-RAS for flood forecasting. *Can. Water Resour. J.* 30, 159–174. doi: 10.4296/cwrj3002159

Hinkel, J., Lincke, D., Vafeidis, A. T., Perrette, M., Nicholls, R. J., Tol, R. S. J., et al. (2014). Coastal flood damage and adaptation costs under 21st century sea-level rise. *Proc. Natl. Acad. Sci. U.S.A.* 111, 3292–3297. doi: 10.1073/pnas.1222469111

Homer, C. G., Dewitz, J., Yang, L., Jin, S., Danielson, P., Xian, G. Z., et al. (2015). Completion of the 2011 National Land Cover Database for the conterminous United States – representing a decade of land cover change information. *Photogramm. Eng. Remote Sens.* 81, 345–354. doi: 10.14358/PERS.81.5.345

Hope, M. E., Westerink, J. J., Kennedy, A. B., Kerr, P. C., Dietrich, J. C., Dawson, C., et al. (2013). Hindcast and validation of Hurricane Ike (2008) waves, forerunner, and storm surge. *J. Geophys. Res. Ocean*. 118, 4424–4460. doi: 10.1002/jgrc.20314

Jelesnianski, C. P., Chen, J., and Shaffer, W. A. (1992). *SLOSH: Sea, Lake, and Overland Surges from Hurricanes.* NOAA Technical Report NWS 48, National Oceanic and Atmospheric Administration, U. S. Department of Commerce, 71. Scanning courtesy of NOAA's NOS's Coastal Service's Center.

Jongman, B., Ward, P. J., and Aerts, J. C. J. H. (2012). Global exposure to river and coastal flooding: long term trends and changes. *Glob. Environ. Chang.* 22, 823–835. doi: 10.1016/j.gloenvcha.2012.07.004

Kiaghadi, A., Rifai, H. S., Kiaghadi, A., and Rifai, H. S. (2018). *The Effect of Local Runoff from Concurrent Rainfall Events with Storm Surge on Hydrodynamics and Land Inundation*. AGUFM 2018, NH23A-01. Available online at: https://ui.adsabs.harvard.edu/abs/2018AGUFMNH23A..01K/abstract (accessed August 21, 2020).

Kumbier, K., Carvalho, R. C., Vafeidis, A. T., Woodroffe, C. D., and Carvalho, R. C. (2018). Investigating compound flooding in an estuary using hydrodynamic modelling: a case study from the Shoalhaven River, Australia. *Hazards Earth Syst. Sci.* 18, 463–477. doi: 10.5194/nhess-18-463-2018

Levitus, S., Antonov, J. I., Boyer, T. P., and Stephens, C. (2000). Warming of the world ocean. *Science* 287, 2225–2229. doi: 10.1126/science.287.5461.2225

Luettich, R. A., and Westerink, J. J. (2004). *Formulation and Numerical Implementation of the 2D/3D ADCIRC Finite Element Model Version 44.XX*, Morehead City, NC. Available online at: https://www.worldcat.org/title/formulation-and-numerical-implementation-of-the-2d3d-adcirc-finite-element-model-version-44-xx/oclc/57466266

Melby, J. A., Barrett, A. L., Massey, T. C., Nadal-Caraballo, N. C., Misra, S., and Gonzalez, V. (2019). *Sabine to Galveston Pre-Construction, Engineering and Design*. PED: Coastal Storm Surge and Wave Hazard Assessment. Port Arthur - Contract 1. ERDC/CHL Technical Report.

Moftakhari, H., Schubert, J. E., AghaKouchak, A., Matthew, R. A., and Sanders, B. F. (2019). Linking statistical and hydrodynamic modeling for compound flood hazard assessment in tidal channels and estuaries. *Adv. Water Resour*. 128, 28–38. doi: 10.1016/j.advwatres.2019.04.009

Moftakhari, H. R., Salvadori, G., AghaKouchak, A., Sanders, B. F., and Matthew, R. A. (2017). Compounding effects of sea level rise and fluvial flooding. *Proc. Natl. Acad. Sci. U.S.A.* 114, 9785–9790. doi: 10.1073/pnas.1620325114

Mosser, H., Ghanuni, H., and DiGesu, J. (2019). *Sabine Pass to Galveston Bay Orange County, Port Arthur & Freeport Hurricane Flood Protection System Preconstruction, Engineering and Design: Lower Neches Riverine Flooding Analyses.* U. S. Army Corps of Engineers, Fort Worth District, Technical Report.

Muñoz, D. F., Moftakhari, H., and Moradkhani, H. (2020). Compound effects of flood drivers and wetland elevation correction on coastal flood hazard assessment. *Water Resour. Res.* 56. doi: 10.1029/2020WR027544

Pringle, W. (2018). *(PDF) OceanMesh2D: User Guide - Precise Distance-Based Two-Dimensional Automated Mesh Generation Toolbox Intended for Coastal Ocean/Shallow Water*. Available online at: https://www.researchgate.net/publication/326327226_OceanMesh2D_User_guide_-_Precise_distance-based_two-dimensional_automated_mesh_generation_toolbox_intended_for_coastal_oceanshallow_water (accessed August 25, 2020).

Pringle, W. J., Wirasaet, D., Roberts, K. J., and Westerink, J. (2020). Global storm tide modeling with ADCIRC v55: unstructured mesh design and performance. *Geosci. Model Dev. Discuss.* 1, 1–40. doi: 10.5194/gmd-2020-123

Quirogaa, V. M., Kurea, S., Udoa, K., and Manoa, A. (2016). Application of 2D numerical simulation for the analysis of the February 2014 Bolivian Amazonia flood: application of the new HEC-RAS version 5. *Ribagua* 3, 25–33. doi: 10.1016/j.riba.2015.12.001

Riverside Technology, Inc, and Aecom (2015). *Mesh Development, Tidal Validation, and Hindcast Skill Assessment of an Adcirc Model for the Hurricane Storm Surge Operational Forecast System on the Us Gulf-Atlantic Coast.* doi: 10.17615/4z19-y130

Saleh, F., Ramaswamy, V., Wang, Y., Georgas, N., Blumberg, A., and Pullen, J. (2017). A multi-scale ensemble-based framework for forecasting compound coastal-riverine flooding: the Hackensack-Passaic watershed and Newark Bay. *Adv. Water Resour*. 110, 371–386. doi: 10.1016/j.advwatres.2017.10.026

Santiago-Collazo, F. L., Bilskie, M. V., and Hagen, S. C. (2019). A comprehensive review of compound inundation models in low-gradient coastal watersheds. *Environ. Model. Softw*. 119, 166–181. doi: 10.1016/j.envsoft.2019.06.002

Veeramony, J., Condon, A., Linzell, R., and Watson, K. (2016). *Validation of Delft3D as a Coastal Surge and Inundation Prediction System*. Available online at: https://apps.dtic.mil/sti/citations/ADA631769 (accessed August 19, 2020).

Ye, F., Zhang, Y. J., Yu, H., Sun, W., Moghimi, S., Myers, E., et al. (2020). Simulating storm surge and compound flooding events with a creek-to-ocean model: importance of baroclinic effects. *Ocean Model.* 145:101526. doi: 10.1016/j.ocemod.2019.101526

Yeh, G.-T., Huang, G., Zhang, F., Cheng, H.-P., and Lin, H.-C. (2005). *WASH123D: A Numerical Model of Flow, Thermal Transport, and Salinity, Sediment, and Water Quality Transport in WAterSHed Systems of 1-D Stream-River Network, 2-D Overland Regime, and 3-D Subsurface Media Acknowledgments and Disclaimers.* Available online at: https://www.researchgate.net/profile/Gour-Tsyh_Yeh/publication/236975269_WASH123D_All/links/0deec51a94e0aebb5a000000/WASH123D-All.pdf (accessed August 21, 2020).

Zhang, Y., and Baptista, A. M. (2008). SELFE: A semi-implicit Eulerian-Lagrangian finite-element model for cross-scale ocean circulation. *Ocean Model*. 21, 71–96. doi: 10.1016/j.ocemod.2007.11.005

Zhang, Y. J., Ye, F., Stanev, E. V., and Grashorn, S. (2016). Seamless cross-scale modeling with SCHISM. *Ocean Model.* 102, 64–81. doi: 10.1016/j.ocemod.2016.05.002

Zhang, Y. J., Ye, F., Yu, H., Sun, W., Moghimi, S., Myers, and, E., et al. (2019). Simulating compound flooding events in a hurricane. *Ocean Dyn*. 70, 621–640. doi: 10.1007/s10236-020-01351-x

Zscheischler, J., Westra, S., van den Hurk, B. J. J. M., Seneviratne, S. I., Ward, P. J., Pitman, A., et al. (2018) Future climate risk from compound events. *Nat. Clim Change* 8, 469–477. doi: 10.1038/s41558-018-0156-3

Conflict of Interest: The authors declare that the research was conducted in the absence of any commercial or financial relationships that could be construed as a potential conflict of interest.

The handling editor is currently organizing a Research Topic with one of the authors CD.

frontiers in Water

ORIGINAL RESEARCH
published: 05 February 2021
doi: 10.3389/frwa.2021.609231

Enhancing Flood Hazard Assessments in Coastal Louisiana Through Coupled Hydrologic and Surge Processes

Matthew V. Bilskie[1], Haihong Zhao[2], Don Resio[3], John Atkinson[4], Zachary Cobell[5] and Scott C. Hagen[6,7]*

[1] School of Environmental, Civil, Agricultural, and Mechanical Engineering, University of Georgia, Athens, GA, United States, [2] Arcadis International, Roseville, CA, United States, [3] College of Computing, Engineering, and Construction, University of North Florida, Jacksonville, FL, United States, [4] Arcadis International, Wexford, PA, United States, [5] The Water Institute of the Gulf, Baton Rouge, LA, United States, [6] Department of Civil and Environmental Engineering, Louisiana State University, Baton Rouge, LA, United States, [7] Center for Coastal Resiliency, Louisiana State University, Baton Rouge, LA, United States

Traditional coastal flood hazard studies do not typically account for rainfall-runoff processes in quantifying flood hazard and related cascading risks. This study addresses the potential impacts of antecedent rainfall-runoff, tropical cyclone (TC)-driven rainfall, and TC-driven surge on total water levels and its influence in delineating a coastal flood transition zone for two distinct coastal basins in southeastern Louisiana (Barataria and Lake Maurepas watersheds). Rainfall-runoff from antecedent and TC-driven rainfall along with storm surge was simulated using a new rain-on-mesh module incorporated into the ADCIRC code. Antecedent rainfall conditions were obtained for 21 landfalling TC events spanning 1948–2008 *via* rain stations. A parametric, TC-driven, rainfall model was used for precipitation associated with the TC. Twelve synthetic storms of varying meteorological intensity (low, medium, and high) and total rainfall were utilized for each watershed and provided model forcing for coastal inundation simulations. First, it was found that antecedent rainfall (pre-TC landfall) is influential up to 3 days pre-landfall. Second, results show that antecedent and TC-driven rainfall increase simulated peak water levels within each basin, with antecedent rainfall dominating inundation across the basin's upper portions. Third, the delineated flood zones of coastal, transition, and hydrologic show stark differences between the two basins.

Keywords: compound flooding, coastal inundation, rainfall runoff, Louisiana, coastal flood transition zone

OPEN ACCESS

Edited by:
Navid Tahvildari, Old Dominion University, United States

Reviewed by:
Dongmei Feng, University of Massachusetts Amherst, United States
Ramin Familkhalili, Old Dominion University, United States

****Correspondence:***
Matthew V. Bilskie
mbilskie@uga.edu

Specialty section:
This article was submitted to Water and Built Environment, a section of the journal Frontiers in Water

Received: *22 September 2020*
Accepted: *12 January 2021*
Published: *05 February 2021*

Citation:
Bilskie MV, Zhao H, Resio D, Atkinson J, Cobell Z and Hagen SC (2021) Enhancing Flood Hazard Assessments in Coastal Louisiana Through Coupled Hydrologic and Surge Processes. Front. Water 3:609231. doi: 10.3389/frwa.2021.609231

INTRODUCTION

The great Louisiana flood of 2016 resulted in immediate and lingering flooding impacts that exemplify a need to understand better the interplay between hydrologic, tide, and surge processes. More than a week after the extreme rainfall event, the overland and riverine flows resulted in unsuspected complications. Flooding at or near a confluence of two rivers produced dangerous backwater flooding that led to inundation in dense urban regions. Areas in the lower portions of the watershed are also vulnerable to hurricane storm surges, which warrants consideration of the contribution from both overland and coastal flows to flood hazards and ultimately flood risk (Leonard et al., 2014; Wahl et al., 2015; Wu et al., 2018).

Historically, similar events have occurred, resulting in complex interactions between rainfall- and coastal-induced flooding: Hurricane Rita followed Katrina <4 weeks later. The devastation of Hurricane Ike was exacerbated by having Gustav hit Louisiana 12 days sooner. Hurricane Harvey (2017) caused record rainfalls (1,539 mm) in Texas along with 3 m coastal storm surge (Blake and Zelinksy, 2018; Valle-Levinson et al., 2020). Similarly, Hurricane Florence (2018) caused 3 m surges along the North Carolina coast, with over 900 mm of rainfall (Erdman, 2018; Gori et al., 2020). Just a few weeks before the time of this writing (August 2020), Hurricanes Marco and Laura were forecast to make landfall across the Louisiana coast hours apart. Hurricane Sally (September 2020) is currently causing widespread flooding due to storm surge and prolonged rainfall along the Alabama and Florida panhandle. To better prepare for such outcomes, hurricane storm surge models must incorporate a representation of overland flooding from rainfall-runoff (including antecedent conditions) and tropical cyclone (TC) induced storm tides. Especially under uncertain future climates (Silva-Araya et al., 2018; Zscheischler et al., 2018; Paerl et al., 2019; Santiago-Collazo et al., 2019).

A shortcoming of most coastal flood studies (both return period and risk analyses) assumes that coastal and fluvial floods are mutually exclusive events (Zscheischler et al., 2018; Santiago-Collazo et al., 2019). Damage caused by recent TC and unnamed storm events (e.g., 2016 Baton Rouge flood) that resulted in compound floods has pushed the research community to develop improved representations of combined hydrologic and surge processes into the quantification of flood hazards and risk. Furthermore, science-based information on flood hazards and risk are needed for policy-makers and emergency managers (White et al., 2010; Thaler and Levin-Keitel, 2016; Stephens et al., 2017; DeLorme et al., 2020). Early efforts to solve this problem have included simplistic model integration of hydrologic and coastal ocean models using linking and one-way coupling approaches. However, there is a need to refine and develop holistic modeling frameworks to simulate the compound effects of rainfall-runoff and storm surge flooding. Tightly-coupled approaches that account for the complex and nonlinear interactions across the coastal land margin are ideal (Bilskie and Hagen, 2018; Santiago-Collazo et al., 2019; Shen et al., 2019).

There is a new recognition that flood risk at the coastal land margin is influenced by hydrologic and tidal/surge processes, especially in deltaic floodplains. This realization has led to the awareness that there exists a transitional flood hazard zone (i.e., flood transition zone) flanked by regions dominated by hydrologic- and surge-only flooding mechanisms as defined by Bilskie and Hagen (2018) and later examined by Shen et al. (2019). The location and spatial extent of the flood transition zone are event-dependent and a function of individual forcings (e.g., rainfall and tropical cyclone characteristics) and regional landscape characteristics (Bilskie and Hagen, 2018). Evaluating the coupled hydrologic and surge influence on coastal flood hazards will define coastal flood hazard transition zones that span from hydrologic to coastal surge dominance. We aim to address the fundamental issues of compound flooding and the delineation of coastal flood zones by defining regions where both rainfall that produces antecedent (i.e., with respect to the storm surge) runoff and rainfall within the TC-driven storm surge overlap *via* the development of a coupled hydrologic and hydrodynamic model to enable more comprehensive enhanced flood zone assessments.

Here, we present a novel approach for defining the coastal flood transition zone using a series of synthetic TC events. The computational model simulates water levels and currents driven by antecedent rainfall, TC-driven rainfall, and hurricane storm surge, all within the ADCIRC model framework. Water levels resulting from rainfall-runoff was simulated using a new rain-on-mesh module within ADCIRC. Rainfall accumulation for antecedent conditions was obtained from observed rainfall from historic hurricane events, and a parametric rainfall model was used for TC-driven precipitation. We focus our modeling efforts and flood zone delineation for two distinct coastal basins in southeastern Louisiana—the Barataria and Lake Maurepas watersheds.

MATERIALS AND METHODS

Study Area

We focus on two distinct hydrologic basins located in southeastern Louisiana, the Lake Maurepas and Barataria watersheds (**Figure 1**). These basins are hydrologically separated by the Mississippi River and its extensive levee system and have the following distinguishing characteristics.

Barataria Watershed

The Barataria watershed (Hydrologic Unit Code - HUC6 080903) experiences flood hazards dominated by coastal surges (including tropical and winter storms) and intense rainfall. The 7,000 km^2 watershed is roughly funnel-shaped and extends from Donaldsonville to the Gulf of Mexico, about 110 km long and 50 km wide (**Figure 1A**). The watershed has been closed off from river flows since the 1930–40's with the Mississippi River's leveeing and the closure of Bayou Lafourche-Mississippi River connection in 1902. Minimal sedimentation is present in the watershed. With a combination of subsidence and shoreline erosion, the series of bays, lakes, and bayous have enlarged, forming a network of hydraulically connected water bodies within the basin (Morgan, 1967; Conner and Day, 1987). Bathymetric depths within the basin are between 2 and 3 m NAVD88 and topographic elevations for most of the watershed are <2 m NAVD88, and most of the area is <1 m NAVD88 (**Figure 1B**). The landscape consists of emergent estuarine wetland to the south, a palustrine emergent wetland in the central, and palustrine forested wetland in the upper portions of the basin outlines by developed and cultivated land with the outer levee system.

Lake Maurepas Watershed

The Lake Maurepas watershed (HUC6 080702) presents alternative characteristics to Barataria (**Figure 1A**). Hydrologic processes dominate the majority of the Lake Maurepas watershed flood hazard zone. It likely has never been exposed to surge flooding except for the area surrounding Lake Maurepas. The

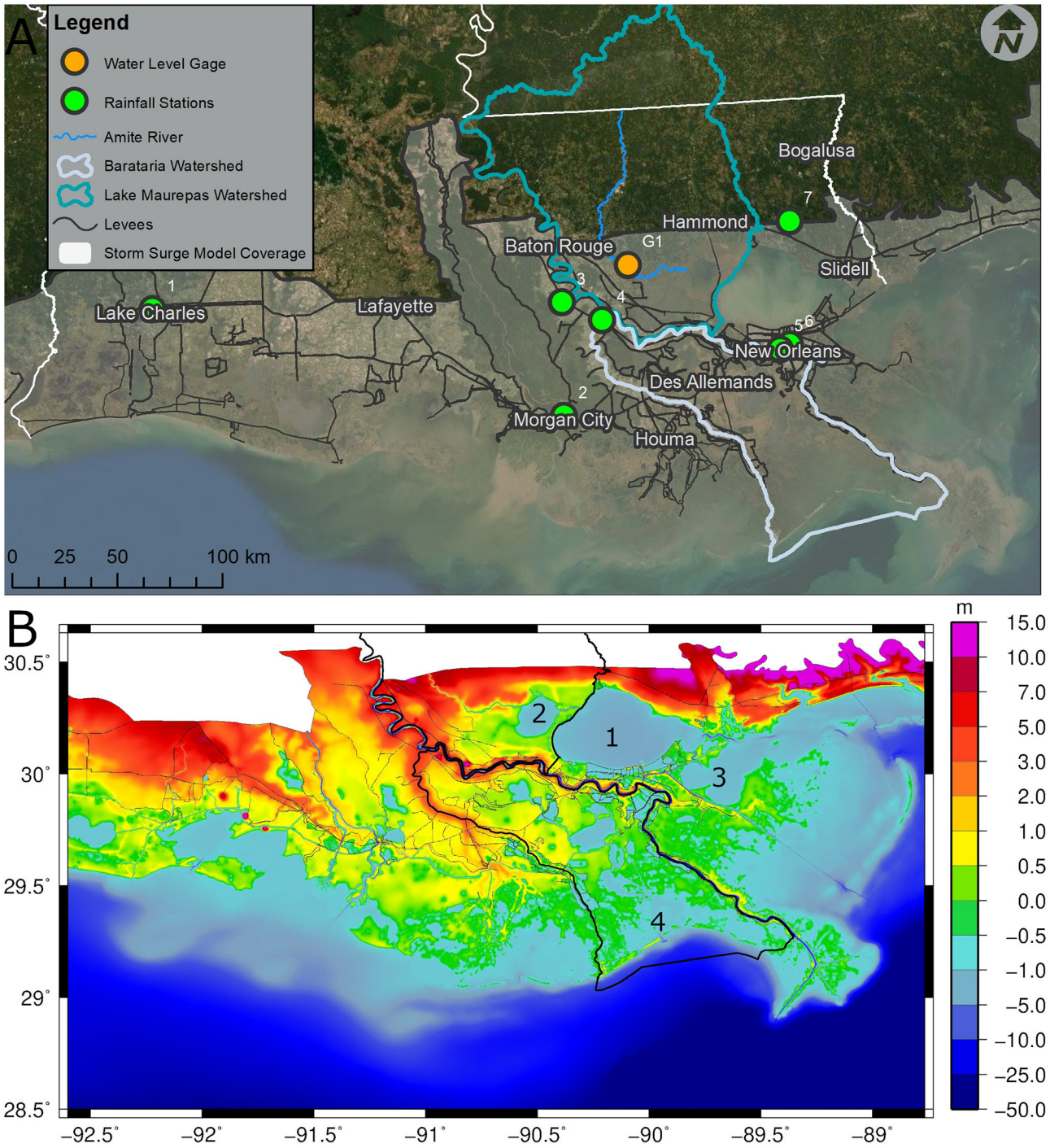

FIGURE 1 | (A) Overall region of study in southeastern Louisiana. The ADCIRC storm surge model boundary is shown as a transparent background that extends across the coastal floodplain in naturally dry regions. Barataria and Lake Maurepas Watersheds are enveloped by bold off-white and aqua lines. USGS gage 07380120 is shown in orange (G1). Rainfall stations are labeled as follows: (1) Lake Charles, (2) Morgan City, (3) Baton Rouge, (4) Donaldsonville, (5) New Orleans Audubon Park, (6) New Orleans International Airport, and (6) Abita Springs. Thin white lines delineate the state boundaries. Service Layer Credits: Source: Esri, Maxar, GeoEye, Earthstart Geographics, CNES/Airbus DS, USDA, USGS, AeroGRID, IGN, and the GIS User Community. **(B)** Topographic and bathymetric elevations (m, NAVD88) of the ADCIRC unstructured mesh of coastal Louisiana. The Lake Maurepas and Barataria watersheds are outlined in black. Label (1) is Lake Pontchartrain, (2) is Lake Maurepas, (3) is Lake Borgne, and (4) is Barataria Bay.

basin is the principal drainage system of Baton Rouge through the Comite and Amite Rivers into Lake Maurepas and then Lake Pontchartrain. The watershed area is 12,445 km^2 with elevations ranging from over 100 m NAVD88 in southwestern Mississippi to under 1 m in the wetlands around Lake Maurepas (**Figure 1B**). The landscape is made up of Estuarine and Palustrine Emergent Wetlands near the outlet and Palustrine Forested Wetlands adjacent to Lake Maurepas and the Amite River. The majority of the watershed's middle and upper portions are collections of grasslands, forests, and developed regions. Herein, when referencing the Lake Maurepas watershed, we focus on the portion south of Interstate 10, the shaded region south of Baton Rouge and Hammond, shown in **Figure 1A**. This southern portion of the watershed area is 3,364 km^2 (27% of the total watershed area).

Hydrodynamic Model Setup

ADCIRC

Computations are performed using ADCIRC (ADvanced CIRCulation), which is a set of computer codes that solves the nonlinear form of the depth-integrated shallow water equations (specifically the generalized wave community equation) for water surface elevation and currents across an unstructured finite element mesh (Kinnmark, 1985; Kolar et al., 1994; Luettich and Westerink, 2004; Westerink et al., 2008). In this work, the implicit solver was employed with a 1-s time-step (Courant-limited). Wetting and drying are activated (threshold of 5 cm), baroclinic and advection terms are neglected, and a spatially-constant horizontal eddy viscosity for the momentum equations was set to 50 m^2/s. Surface roughness parameters are based on the Coastal Change Analysis Program (C-CAP), including Manning's n coefficient for bottom roughness and vegetation canopy (Dietrich et al., 2011; Cobell et al., 2013). Vegetation canopy reduces marine-based wind speed over land based on upwind conditions (Atkinson et al., 2011). Wind drag across the water surface employed the storm sector-based Powell formulation with a wind drag of 0.002 (Powell, 2006; Black et al., 2007; Dietrich et al., 2011).

Coastal Louisiana Unstructured Mesh

The unstructured mesh used in this study originates from the 2017 Louisiana Coastal Master Plan ADCIRC model mesh (Roberts and Cobell, 2017), but with updates bringing the model to represent present-day (**Figure 1B**). The mesh contains 1,454,454 vertices and 2,831,106 elements. The mesh spans the western north Atlantic Ocean (westward from 60° longitude), the Caribbean Sea, and the Gulf of Mexico with high resolution across coastal Louisiana. Mesh resolution in the Gulf of Mexico ranges from 14 km in the central portion of the basin to 2 km along the continental shelf and variable resolution of 15–500 m across the Louisiana coastal floodplain. The Amite River from Lake Maurepas to Interstate-10 (which is the northern mesh boundary) was inserted into the mesh with a local resolution of ∼40 m and depths of 4 m NAVD88. This mesh has undergone extensive validation for astronomic tides, wind-waves, and hurricane storm surge [see Roberts and Cobell (2017) for validation results]. This model is currently deployed for real-time surge forecasts to support the state of Louisiana.

Bathymetric and topographic elevations of the mesh were obtained *via* the USGS topographic elevation model of the northern Gulf of Mexico (US Geological Survey, 2020), United States Army Corps of Engineers (USACE) channel surveys, levee surveys, and recent bathymetric surveys provided by the state of Louisiana. This mesh (and its precursors) has been validated for astronomic tides, and numerous hurricanes, including Katrina and Rita (2005), Ike and Gustav (2008), and Isaac (2012) (Bunya et al., 2010; Dietrich et al., 2011, 2012; Cobell et al., 2013; Roberts and Cobell, 2017) and has been used for projects such as the Louisiana Coastal Master Plan, FEMA flood insurance studies, levee recertification, and real-time storm surge forecasting (Dietrich et al., 2013).

Antecedent Rainfall

A general investigation into the probability of antecedent rainfall amounts before hurricane landfalls examined available precipitation data sources along the Louisiana coast. Since a reliable record of hurricane landfalls exists well into the 1800's, the limiting factor was any limitation in the available precipitation data. In developing a plan to optimize the information content in rain-field probabilities in advance of hurricane landfall, two factors were considered: spatial resolution and length of record. An initial effort examined the application of HRAP (Hydrological Rainfall Analysis Projection) data, with grid cells that cover an area on a polar stereographic grid. The Limited Fine-Mesh grid version for data available from 2002 to 2019 at the time of this project was conducted utilized a mapping routine to convert to grid cells that were ∼4-km by 4-km. Unfortunately, the 2002 data could not be retrieved in a usable form, and only post-2003 data was available for this study. Thus, this data contained an insufficient range of hurricane parameters needed to establish a reliable representation of long-term rainfall probabilities occurring before landfall despite the high spatial resolution.

Since additional samples were required, the only choice available was to use rainfall from meteorological station data available from the National Climatic Data Center (NCDC). Due to size limits in downloads, this data was downloaded over a period of about a month. Much of the data in volunteer stations were missing during some hurricane events but were available for others. Therefore, all of the obtained data was filtered to selected rainfall records within the 10-days before landfall. The stations used in the final analysis are shown in **Figure 1A**. All stations used reported hourly rainfall except for the Abita Springs location, which reports daily rainfall totals. Abita Springs was included due to its proximity to the study area and its relatively complete record. Days 1–3 before the day of landfall were included for this daily data. Storms with central pressures higher than 990 mb were excluded since these would be primarily rain events inland, leaving a total of 21 storms during the period from 1948 to 2019 as the storms considered in this analysis. In chronological order, these are as follows: 1948, Barbara (1953), Bertha (1957), Ethel (1960), Camille (1969), Danny (1985), Elena (1985), Juan (1985), Bonnie (1986), Florence (1988), Chantal

(1989), Andrew (1992), Danny (1997), Isadore (2002), Lili (2002), Bill (2003), Matthew (2004), Cindy (2005), Edouard (2008), Gustav (2008), and Ike (2008). The final antecedent rainfall pattern contains the mean total rainfall (at available rainfall gage stations—see **Figure 1A**) from each of the 21 hurricane events. The result is a 0.5 × 1.0 deg grid that spans the coastal region. Additionally, the rainfall grid is adjusted laterally to account for a given storm's landfall location.

Parametric Tropical Cyclone Rainfall Model

Rainfall intensities associated with tropical cyclones (TC) were taken from Lonfat et al. (2004) and the US Army Corps of Engineers (2006) Interagency Performance Evaluation Task Force (IPET) study for southeast Louisiana. Rainfall intensity associated with tropical cyclones (TC) varies as a function of distance from the TC center (r) and azimuth relative to the TC forward motion (β). The mean rainfall intensity field (m_I), as a function of r and β, spatially varies with the central pressure deficit (ΔP), radius to maximum winds (R_{max}), and vertical wind shear (S). Spatially-varying rainfall intensity for a TC is given by:

$$m_I(r) = \begin{cases} 1.14 + 0.12\Delta P, & for\ r \le R_{\max} \\ (1.14 + 0.12\Delta P)\, e^{-0.3\left(\frac{r - R_{\max}}{R_{\max}}\right)}, & for\ r > R_{\max} \end{cases} \quad (1)$$

Where rainfall intensity is in mm/hr and the central pressure deficit is in mb. Since rainfall intensity varies with azimuth about the TC center, an asymmetric factor of 1.5 is applied to the rainfall intensity on the TC track's right-hand side. **Figure 4D** shows an example of the total rainfall accumulation for synthetic storm 145.

Rain-On-Mesh

A rain-on-mesh module was developed and applied to the ADCIRC source code. During run time, rain is applied to individual mesh nodes and elements and is based on the current wet/dry status. Wet nodes receive rainfall by totaling the incremental rainfall for the current time-step to the water surface elevation:

$$\eta_i = \eta_{i,t-1} + R_t \quad (2)$$

Where η is the water surface elevation at node i and R is the rainfall at time t. The rainfall applied for the current time-step, R, is rainfall intensity multiplied by the model time-step. This rainfall is marked as accounted rainfall as it directly translates into a change in surface water elevation.

Rainfall is also applied at dry nodes under specific constraints to avoid wetting elements with small inundation depths. If the total rainfall accumulation is less than a specified threshold for a mesh node, then the node remains dry. This rainfall is considered unaccounted rainfall as it does not directly translate to surface water elevations during the current time step. Once the total rainfall is equal to or exceeds the specified threshold, the node is ready to change to a wet state. When the total rainfall for all three nodes for a given element exceeds the minimum rainfall accumulation threshold, then the element and its nodes are marked as wet. The nodes and elements are then activated and participate in the computations, and rainfall is received discussed with **Equation (2)**, and the rainfall is marked as accounted rainfall. Herein, the rainfall accumulation threshold to wet (activate) dry (currently inactive) nodes was set to 50 mm. A rainfall accumulation threshold of 100 mm was tested. However, 100 mm was too large of a threshold to determine when rainfall-runoff was allowed to begin. Once the node is activated, mesh nodes are set to an initial water depth of 0.10 m above the land surface. A value of 0.10 m is a depth of similar magnitude to typical values used for a minimum wetting depth threshold in coastal surge models that employ wetting and drying (Dietrich et al., 2006; Medeiros and Hagen, 2012). This value was selected to allow for sufficient wetting to occur while limiting numerical artifacts due to wetting/drying. Rainfall was not applied to areas enclosed by a levee system below mean sea level as there is no natural outlet for water to flow. In coastal Louisiana, rainfall is routed to outfall canals *via* complex pump systems.

Rainfall intensity can be applied to a simulation in three ways. The first is *via* a gridded rainfall intensity field (refer to Section antecedent rainfall). The second is rainfall intensity associated with a TC that is internally computed within ADCIRC (refer to Section parametric tropical cyclone rainfall model). The third method involves joining the gridded rain with TC-driven rain. Application of rainfall into the model was accomplished by considering the maximum rainfall intensity value at each point in the model domain at each time-step between the gridded and TC-driven rain:

$$r_{i,t} = \max\left(r_{i,t}^{G}, r_{i,t}^{TC}\right) \quad (3)$$

Where $r_{i,t}$ is the rainfall intensity at node i and time t, r^G is the rainfall intensity from the gridded data, and r^{TC} is the rainfall associated with the TC. In this work, the antecedent condition is applied using a gridded rainfall intensity field.

Synthetic Storm Selection and Simulations Set

The magnitude of the surge generated by a TC is an essential factor in determining coastal flooding's contribution to total combined flood levels. For scenarios where storm surge is large relative to antecedent and rainfall magnitudes, the area of combined flooding dominated by coastal dynamics will increase, and the transition zone will extend further. For scenarios where storm surge is small relative to the contribution of antecedent conditions and rainfall, combined flood levels are less influenced by coastal processes, and the transition zone will extend further toward the coast. For this study, surge magnitude is represented by the return period (i.e., annual exceedance probability) of flooding generated by a TC in the areas of interest.

To investigate how flooding dynamics are influenced by the combination of coastal storm surge and rainfall-runoff, a small set of synthetic TC (also called synthetic storms) were selected from the total FEMA storm suite (FEMA USACE, 2008). Two separate storms sets were established: one for the Barataria basin and one

TABLE 1 | Return period stillwater elevations (m, NAVD88) for the points of interest.

Study basin	Point of interest	Return period (m, NAVD88)		
		10-years	50-years	100-years
Upper Barataria Basin	B1	0.94	1.37	1.55
	B2	1.04	1.49	1.71
	B3	1.19	1.71	1.95
	B4	1.22	1.74	1.98
Target Barataria Basin Flood Elevation		1.16	1.65	1.89
Lake Maurepas	M1	1.83	2.56	2.87
	M2	1.80	2.47	2.77
	M3	1.80	2.50	2.83
	M4	1.89	2.83	3.23
	M5	1.92	2.93	3.38
	M6	1.31	1.83	2.10
Target Lake Maurepas Basin Flood Elevation		1.86	2.65	3.02

The target basin flood elevation was determined from a combination of the return period stillwater elevation values (m, NAVD88) for each point of interest and their respective location in the basin. The target values were used for synthetic storm selection.

for the Lake Maurepas watershed. Synthetic storms were selected based upon the peak water level generated at locations within the study watershed areas. Published FEMA flood elevations for the 10-, 50-, and 100-years return periods were defined as target flood elevations within each basin (see **Table 1**). For each return period, storms were selected from the FEMA synthetic storm suite that most closely generated the target flood elevation at the sampling points. Storm characteristics were also considered to reduce the number of storms to a set of four storms for each return period. From the subset of storms that matched the target surge elevations, storms were prioritized that made landfall with proximity to the area of interest to attain impactful rainfall intensity. Storms that track and make landfall far from the area of interest generate rainfall with little to no flooding impacts. Efforts were also made to include a range of track headings, forward speeds, and radius of maximum wind within the final storm suite.

The target flood elevations are based on the return still water levels at sampling locations within each basin (**Figure 2**). For the Lake Maurepas basin, six points were laid out to characterize the flood elevations, where the points to the west experience higher flood elevations. For the upper portion of the Barataria basin, four points were laid out to characterize the flood elevations. It is noted that point B1 lies in an area sheltered by levees, thus not influencing the selection of representative TCs. The target stillwater elevations are summarized in **Table 1**.

A preliminary set of 7–10 storms was selected that generate peak water levels similar to a set of target return period flood elevations. Of the initial set of 7–10 tropical cyclones, four were selected according to the following procedure:

1. Sort the candidate storms in ascending order of the differences between the peak storm surge of an individual storm and the target flood elevation.
2. Eliminate the storms that are far away from the area of interest, e.g., twice the radius of maximum wind away.
3. Prioritize the storm with different parameters, such as forward speed, headings, and radius of maximum wind.

After screening, four storms were selected for each basin's return period, as shown in **Figure 3** described in **Table 2**. These storms are used in the model simulations to represent the TC-driven coastal flooding scenarios.

Rather than refer to the synthetic storms as the storm that represent a given return period stillwater elevation, we will simplify and use the following terminology: low) selected synthetic storms that generated a 10-year return period water level; medium) synthetic storms that caused a 50-year return period water level; and high) synthetic storms that generated a 100-year return period water level (**Table 2**).

Simulation Set

A total of 12 simulation sets were performed for using the synthetic TCs identified in section synthetic storm selection and simulations set for each watershed. Astronomic tide forcing was not included in any of the simulations. Each simulation set formed four individual runs: (1) storm surge only, (2) storm surge and rainfall-runoff from TC-driven rain, (3) rainfall-runoff from antecedent rainfall only (no storm surge), and (4) rainfall-runoff from antecedent and TC-driven rain and storm surge in the same simulation. These scenarios result in 48 simulations for each watershed and 96 overall simulations.

The simulations that included storm surge were forced by wind speed and pressure for the synthetic storms outlined in Section synthetic storm selection and simulations set. The storm surge and TC-driven rainfall-runoff include the same forcing as in (1) and rainfall-runoff associated with the TC using the rain-on-mesh module introduced in section rain-on-mesh and rainfall accumulation defined by the parametric rainfall model described in section parametric tropical cyclone rainfall model. The simulation of antecedent rainfall employed the rain-on-mesh module with rainfall accumulation from antecedent conditions prescribed in Section antecedent rainfall and no meteorological forcing. Finally, the forcings from the synthetic TC, antecedent rain, and TC-driven rainfall were included in a single model simulation.

Flood Zone Delineation

The delineation of the hydrologic, coastal, and coastal flood transition zones is similar to that proposed in Bilskie and Hagen (2018). The following notation is used: ζ_R is the peak water level from the antecedent rainfall only simulation, ζ_S is the peak water level from storm surge only (no rainfall) simulation, and ζ_{RS} is the peak water level resulting from the combined rainfall-runoff, TC-driven rain, and surge simulation. Therefore, the we define the hydrologic zone as the region where $\zeta_R \cong \zeta_{RS}$ (area covered wetted only by rainfall), the coastal flood transition zone is defined as the region where $\zeta_R > \zeta_S$ and $\zeta_{RS} > \zeta_R$, and the coastal zone is defined as the region where $\zeta_S > \zeta_R$. It is likely that peak water levels in the coastal zone will be greater for ζ_{RS} than ζ_S, but this region is dominated by storm surge, hence $\zeta_S > \zeta_R$.

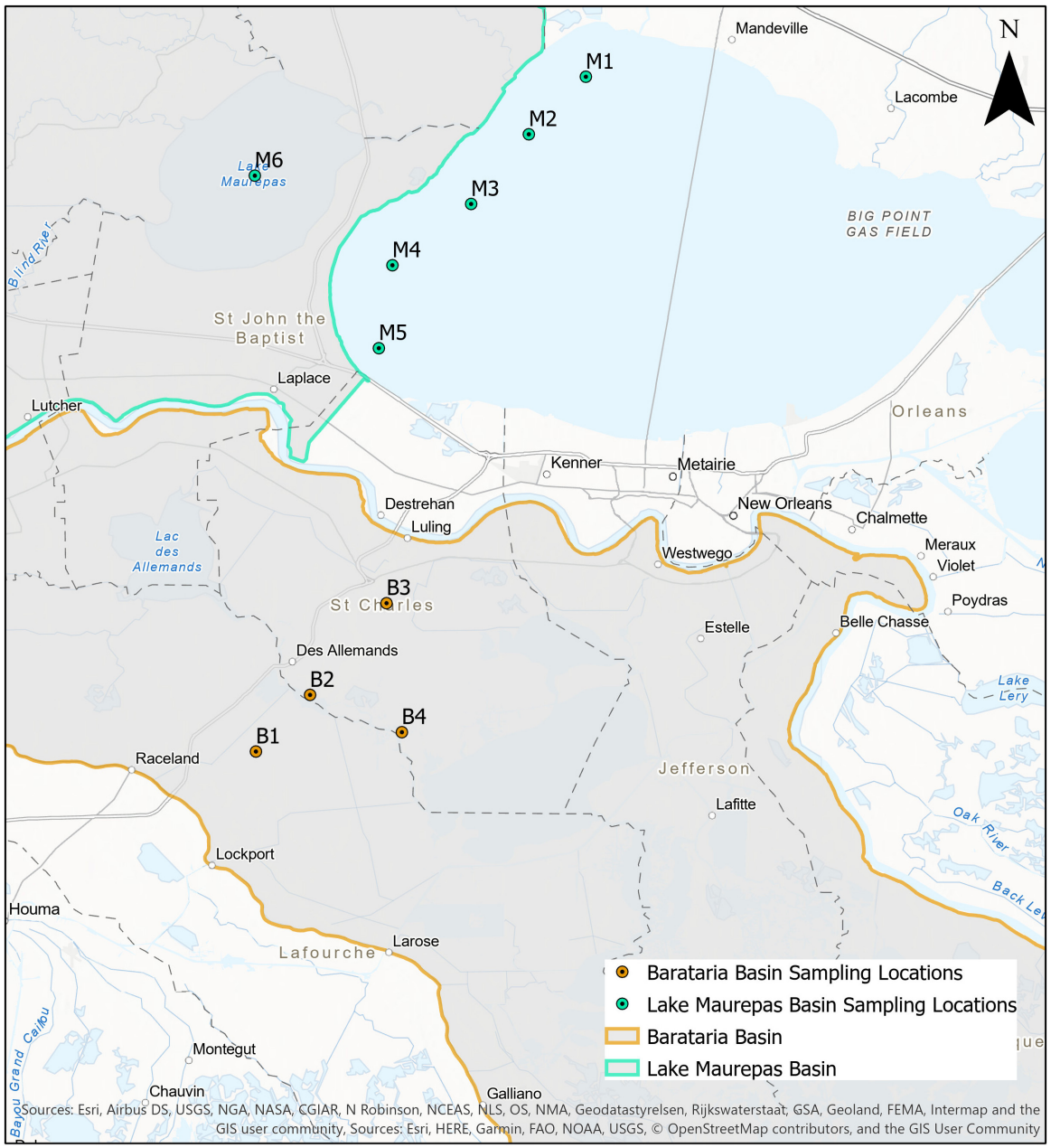

FIGURE 2 | Sampling locations for the synthetic storm selection in the Barataria watershed (B, orange circles) and Lake Maurepas (M, green circle) watersheds.

The classification of the three possible flood zones was performed for each mesh node within the two respective basins for each set of simulations. Based on the flood zone classification, each mesh node was assigned either a value of 100 for the coastal zone, 200 for the coastal flood transition zone, or 300 representing the hydrologic zone. The unstructured mesh with these values was then transformed into a structured grid (IMG format) with a horizontal resolution of 20 m and imported into ESRI ArcMap. Within ArcMap, the raster was converted to a series of polygons where each polygon represented one of the three flood zone types.

In addition, the flood zones were generalized based on the low-, medium-, and high-intensity storm sets. All four flood zone maps were combined for each return period. The coastal flood transition zone was defined as any region within the watershed that was classified as a flood transition zone for any of the four event-driven flood zone classifications. The hydrologic zone was the region where all four individual

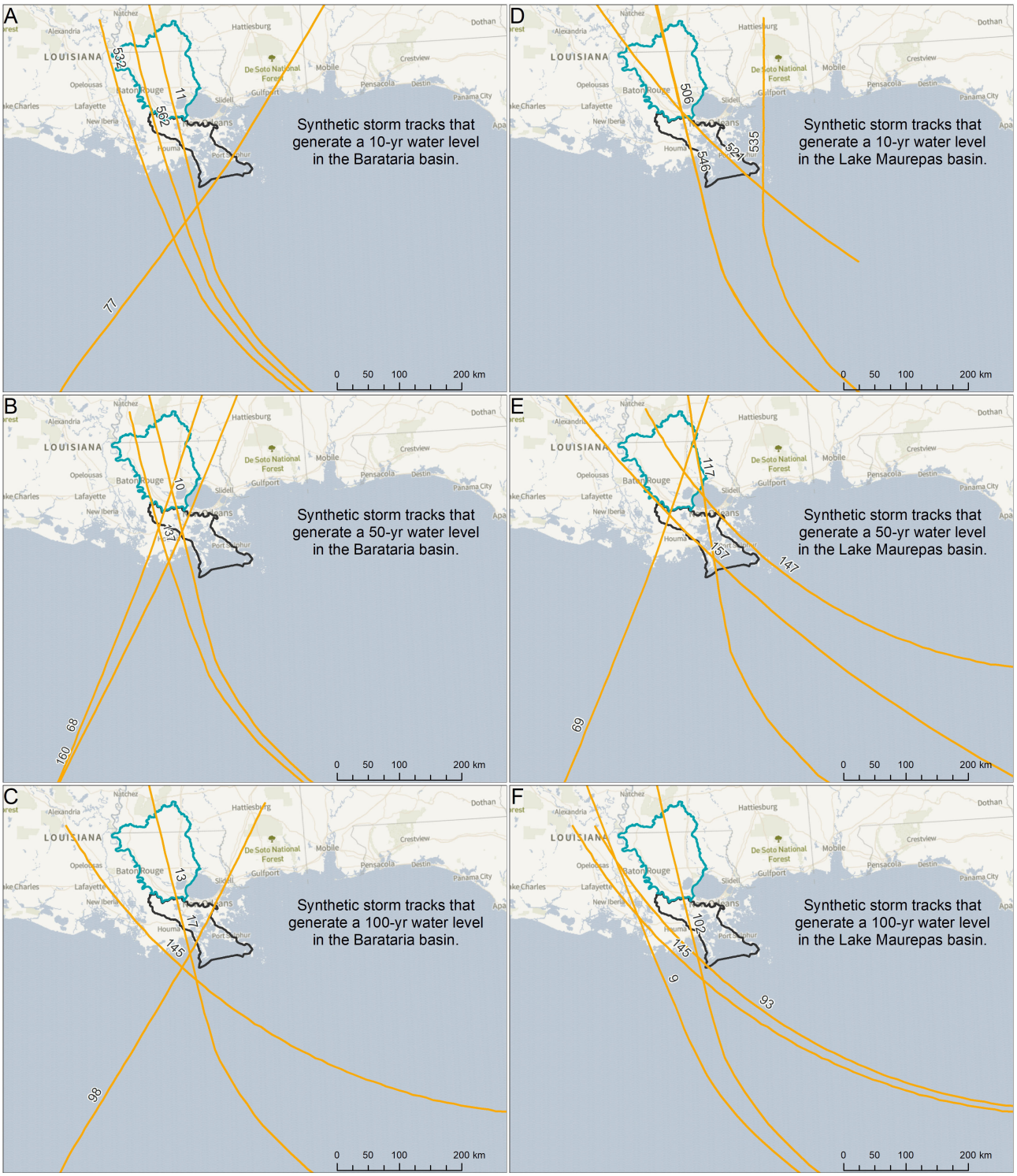

FIGURE 3 | Synthetic storm tracks for the Barataria **(A–C)** and Lake Maurepas **(D–F)** watersheds. **(A,D)** are the storms that cause the 10-year stillwater surge (low), **(B,E)** the 50-year (medium), and **(C,F)** the 100-year (high). Storms 506 and 546 in **(B)** are the same track, but have different storm parameters. Storm parameters are shown in **Table 2**. Basemap courtesy of Mapbox.

TABLE 2 | Synthetic storm parameters.

Basin	Storm set	Synthetic storm ID	Central pressure (mb)	Forward speed (m s^{-1})	Radius (km)	Wind speed (m s^{-1})	Peak surge at B4/M4 (m)
Barataria Basin	10-years storms (Low)	532	975	3.09	28.97	–	1.19
		562	975	3.09	28.97	–	1.22
		11	960	5.66	33.80	32	1.22
		77	900	5.66	28.97	46	1.19
	50-years storms (Medium)	10	960	5.66	17.70	44	1.65
		68	900	5.66	19.31	56	1.71
		137	960	3.09	27.36	30	1.65
		160	930	8.75	27.36	44	1.68
	100-years storms (High)	13	930	5.66	12.87	51	1.92
		17	900	5.66	22.53	49	1.92
		98	930	3.09	27.36	37	1.89
		145	930	3.09	27.36	26	1.83
Lake Maurepas Basin	10-years storms (Low)	506	975	5.66	57.94	–	1.86
		521	975	5.66	40.23	–	1.86
		535	975	3.09	28.97	–	1.43
		546	975	8.75	28.97	–	1.98
	50-years storms (Medium)	69	900	5.66	28.97	46	2.83
		117	960	5.66	27.36	33	2.77
		147	930	3.09	27.36	26	3.05
		157	930	8.75	27.36	34	3.23
	100-years storms (High)	9	900	5.66	33.80	47	3.02
		93	930	3.09	27.36	26	3.20
		102	930	8.75	27.36	45	3.54
		145	930	3.09	27.36	26	3.17

Values of central pressure (mb), forward speed (m s^{-1}), radius to maximum winds (km), and wind speed (m s^{-1}) are taken at landfall. Blank wind speed values (–) indicate storms are of tropical storm intensity.

simulations resulted in a hydrologic zone, and the coastal zone was classified similarly.

RESULTS

Validation

Herein, we perform a model validation based on an extreme rainfall event across the Lake Maurepas watershed in August 2016 (Wang et al., 2016; van der Wiel et al., 2017). The validation period was from Aug. 1 to Aug. 31, 2016. No astronomic tides or wind/pressure forcing was employed as we wanted to examine model results within the Amite River away from tidal influence. Two model simulations were setup using details provided in Section hydrodynamic model setup and included a 5-days ramping function to initialize the stage in the Amite River (Aug. 1–5). The first model run included time-varying inflow for the simulation's duration into the Amite River prescribed by USGS gage 07380120 located in Denham Springs (near Interstate 10) (**Figure 1A**). The second model run included the time-varying inflow and was forced with rainfall from Aug. 11–15. The spatiotemporal rainfall pattern was obtained from the National Oceanic and Atmospheric Administration (NOAA) National Centers for Environmental Information (NCEP) Rapid Refresh (RAP) numerical weather model. The RAP model includes surface precipitation rate in mm/sec on a 13-km grid. Rainfall rates were converted to mm/hr and included in the ADCIRC simulation using the rain-on-mesh module (Section rain-on-mesh).

The results of the two model simulations are shown in **Supplementary Figure 1** for the USGS gage 07380120. Both models well-represent the rising limb, peak, and falling limb of the river stage hydrograph and the peak stage timing. The model run without rainfall; however, it under-predicts the peak water level by 0.3 m. The simulation with rainfall included a better prediction of the peak stage with an under-prediction of 0.04 m. This gage is the only available gage with reasonable water levels for this event. There is a USGS gage (ID 07380200) downstream of Port Vincent, near French Settlement; however, the gage location is located slightly downstream of the Amite Diversion Canal. The diversion of flow between the Amite River and diversion canal and the diversion canal's bathymetric representation is not well-known.

Rainfall Accumulation

Rainfall accumulation was included for TC-driven rainfall, antecedent conditions, and their joint combination. An example of the total rainfall accumulation is shown for storm 145 (high

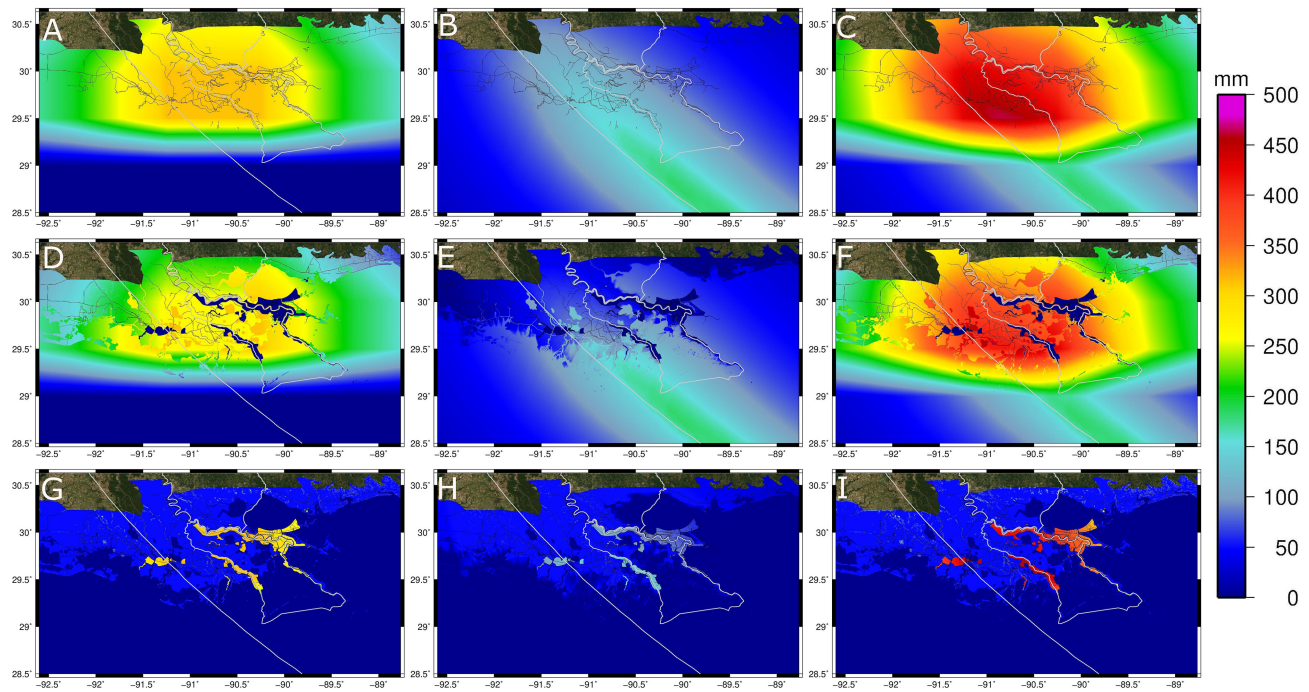

FIGURE 4 | Rainfall totals (mm) based on storm 145 for antecedent conditions **(A)**, tropical cyclone-driven rain **(B)**, and combined rainfall (antecedent and TC-driven rain) **(C)**. The top row **(A–C)** represents the total rainfall amount, the middle row **(D–F)** is the portion of rainfall amount applied to the model simulation, and the bottom row **(G–I)** is the unaccounted portion of the total rainfall. The Barataria and Lake Maurepas watersheds are outlined in gray. The storm track is also shown in gray.

TC – see **Figures 3C,F** for the track and **Table 2** for storm parameters) in **Figure 4**. The total antecedent rainfall (mm) is shown in **Figure 4A**, TC-driven total rainfall in **Figure 4B**, and their joint combination in **Figure 4C** [refer to **Equation (3)**—the joint combination is not the sum of the two rainfall products, but the maximum at each time-step]. The largest rainfall amount for the antecedent conditions was 310 mm and focused on the storm track's northeast region. Total rainfall along the storm track was found on the storm's eastern edge with a maximum value of 183 mm; however, the largest values are generally offshore. The joint antecedent and TC-driven rainfall amounts were the largest east of the track near the landfall location, with a maximum value of 460 mm.

A cumulative hyetograph from rainfall associated with storm 145 within the (A) Barataria (B3 in **Figure 2**) and (B) Lake Maurepas (M6 in **Figure 2**) watersheds are shown in **Figure 4**. Rainfall associated with antecedent conditions produces the highest rainfall at both locations until 24-h before landfall (vertical dashed line in the plots). Rainfall from the TC is zero until just over 24-h pre-landfall when the storm's outer portion comes onshore in Barataria and 10 h pre-landfall for Lake Maurepas. The total rainfall included in the joint rainfall ADCIRC simulation is shown in **Figure 5** as the dashed gray curve. Barataria's location is on dry ground, and therefore a portion of the total rainfall is not included as this location starts as dry. Rainfall is not accounted for until the total rainfall exceeds 50 mm (refer to Section rain-on-mesh). On the other hand, the Lake Maurepas location, shown in **Figure 4B**, is in the middle of the Lake as it is always wet. Therefore, the cumulative accounted rainfall is equal to the joint rainfall.

Simulated Inundation

Time-series water levels for a location in Barataria (B3 in **Figure 2**) and Lake Maurepas (M3 in **Figure 2**) are shown in **Figures 5B,C** for synthetic storm 145. Barataria's location is on the landscape (naturally dry ground), and the location of Lake Maurepas is in the lake (always wet). With antecedent rainfall-runoff only (black line), the Barataria location wets a few hours into the simulation to a water level just over 0.50 m NAVD88. It gradually increases to 0.72 m NAVD88 before slowly reducing. Water levels are zero before the storm's landfall and drives water levels up to a peak near 1.62 m NAVD88 for the surge and TC-driven rain simulation (black dashed line). The combined simulation (black dash-dotted line) that accounts for antecedent rainfall-runoff, TC-rain, and storm surge follows the antecedent rainfall only simulation. It then gradually increases until the surge begins at hour 90 up to a peak of 1.84 m NAVD88. The superposition of the individual simulations (gray dashed line) over-estimate Barataria's surge level by 0.41 m. Similar trends were observed for Lake Maurepas. However, the water level overprediction was not as substantial as the Maurepas location (superposition over-estimates by 0.05 m). This is caused by the Lake Maurepas location being in open water. Therefore, a linear addition (or superposition) of individual surface water runoff and coastal surge will tend to over-predict the coastal flood hazard, especially in normally dry areas.

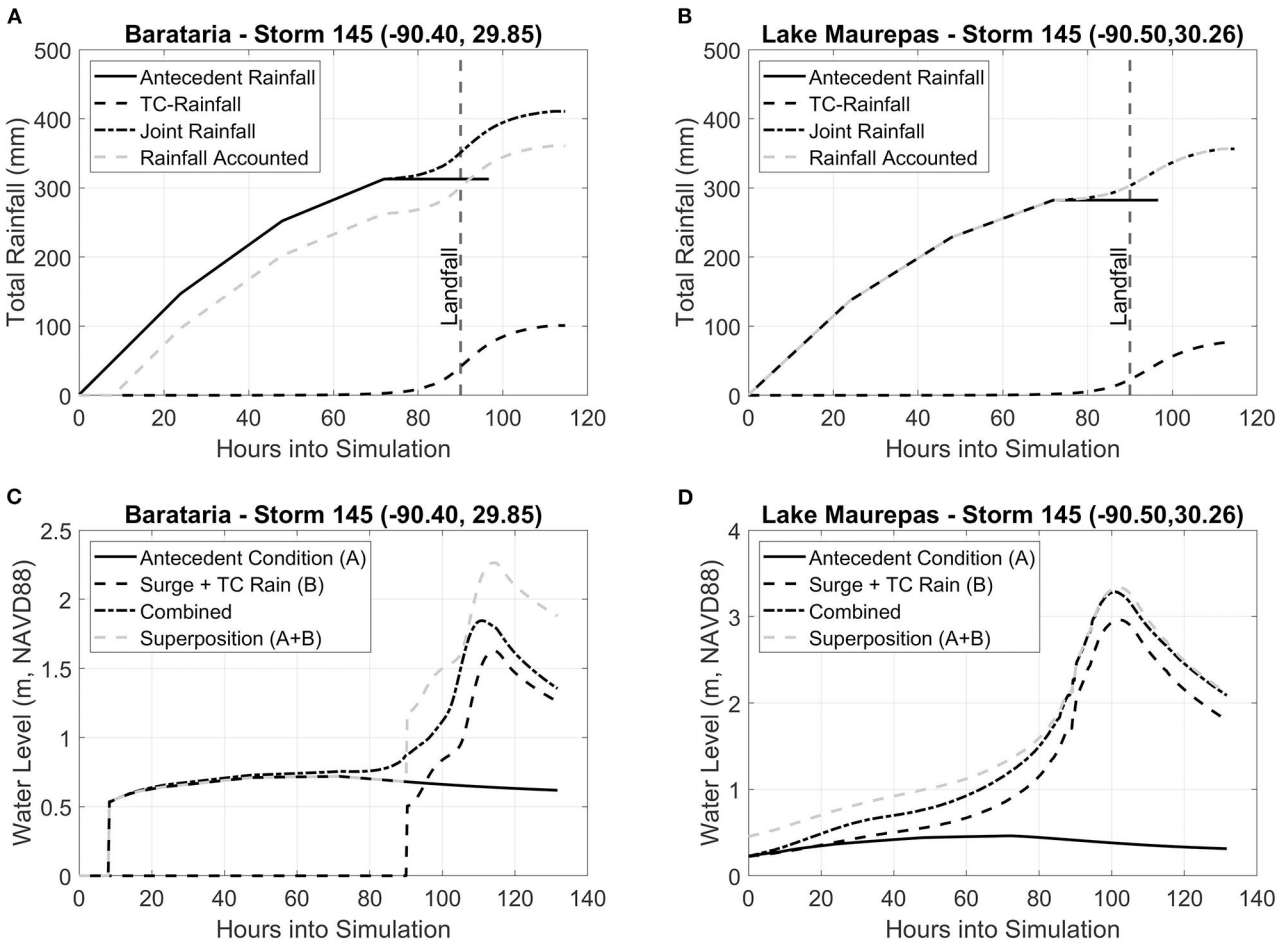

FIGURE 5 | Total rainfall accumulation hyetograph for synthetic storm 145 within the **(A)** Barataria watershed and **(B)** Lake Maurepas. Locations are shown in **Figure 2** (B3 and M6). Storm 145 makes landfall at 90 h (vertical dashed line). Water surface elevation (m, NAVD88) for synthetic storm 145 within the **(C)** Barataria watershed and **(D)** Lake Maurepas. Water levels from antecedent rainfall only (no surge) is shown as the solid black line. Water levels for storm surge and TC-driven rain (no antecedent rain) is shown as the dashed black line. Water levels for a combined storm surge, TC-driven rain, and antecedent rain is shown as the dash-dot black line. A superposition of the individual curves from the antecedent and surge with TC-rain is shown as the gray dashed line.

Peak water levels from each intensity level of storms (low, medium, and high) were combined to generate a set of maximum of maximums (MOM) water level across the study watersheds. For example, the maximum simulated water level among the four low intensity storms for Barataria (storms 11, 77, 532, and 562 in **Table 2**) were combined by taking the maximum value at each computational point in the mesh. This was done for the surge only (**Figure 6A**), surge plus TC-driven rainfall (**Figure 6B**), antecedent conditions only (no storm surge) (**Figure 6C**), and the combined storm surge, TC-driven rain, and antecedent rainfall simulation (**Figure 6D**).

For the low set of synthetic storms in Barataria, the MOM water levels are relatively low (<2 m) for simulations with storm surge only (no rainfall); however, the majority of the basin is inundated (**Figure 6A**). Including TC-driven rainfall causes a small increase in the basin's inundated area (**Figure 6B**). On the other hand, the antecedent rainfall MOM water levels span the basin's entirety outside the flood protection system, albeit naturally dry regions experience a small inundated depth above ground (**Figure 6C**). The MOM water levels from the simulations containing antecedent and TC-driven rainfall and storm surge show increased water levels in the lower Barataria basin compared to the storm surge only MOM water levels (**Figure 6D**). Similar trends in water levels were found as storm intensities increased (medium and high) (**Figures 7**, **8**). However, with increasing intensity, the coastal water levels are higher and raise water levels further into the Barataria watershed. For example, water levels as high as 3 m NAVD88 are found in the middle portion of Barataria Bay under the simulated compound flood event (**Figures 7D**, **8D**).

Simulated water levels in Lakes Pontchartrain and Maurepas show substantial increases when rainfall is included in the storm surge simulation, particularly the antecedent conditions (**Figures 9–11**). For the low and medium intensity TCs, water levels increase by nearly 0.3 m (or 15–20%) (**Figures 9B**, **10B**) when antecedent rainfall is incorporated (**Figures 9D**, **10D**).

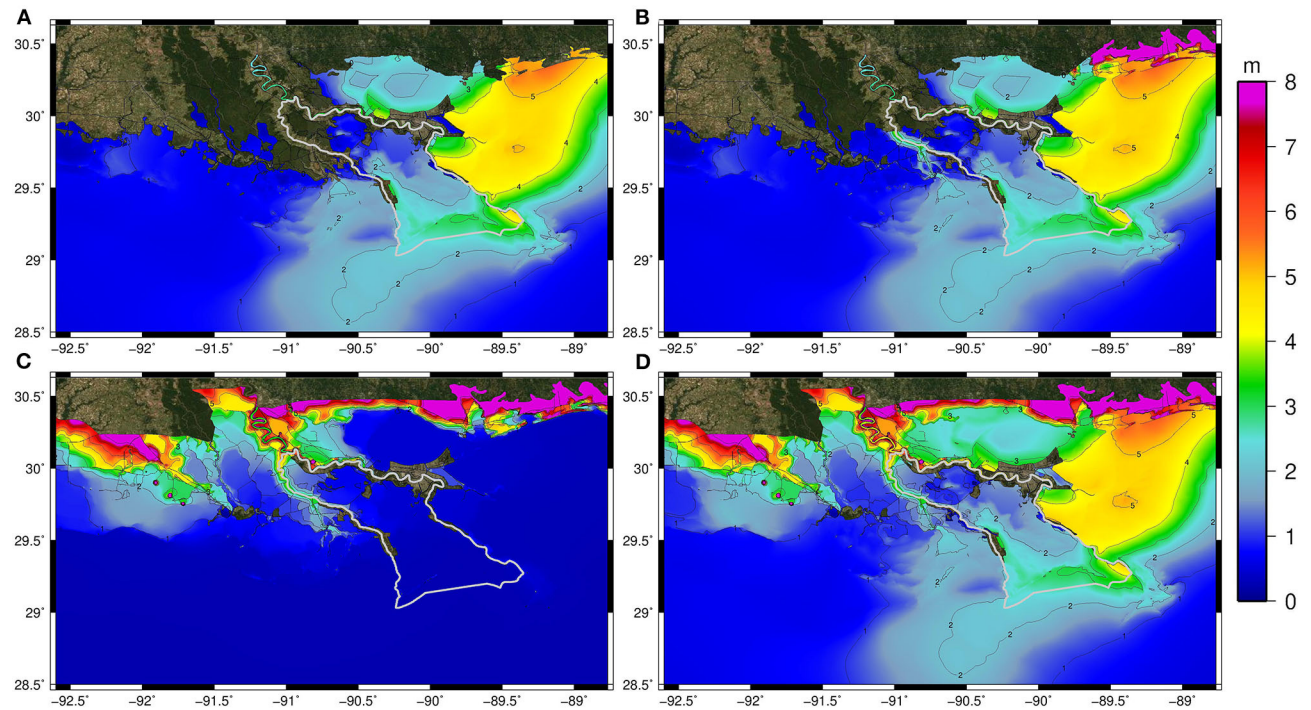

FIGURE 6 | Maximum of maximums (MOM) simulated peak water levels (m, NAVD88) for the Barataria watershed low event synthetic storms for **(A)** storm surge only (no rainfall), **(B)** storm surge and TC-driven rain, **(C)** antecedent rainfall only (no storm surge), and **(D)** antecedent rainfall, TC-driven rainfall, and storm surge in a single simulation.

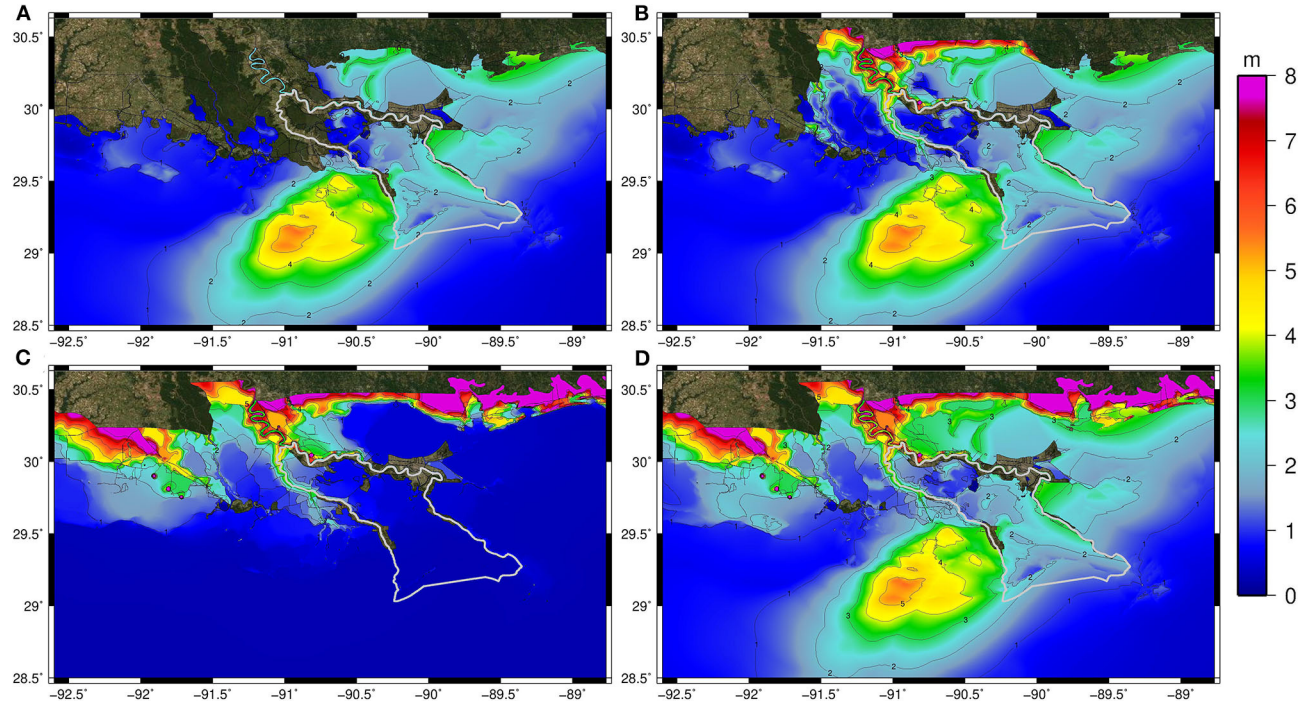

FIGURE 7 | Maximum of maximums (MOM) simulated peak water levels (m, NAVD88) for the Barataria watershed medium event synthetic storms for **(A)** storm surge only (no rainfall), **(B)** storm surge and TC-driven rain, **(C)** antecedent rainfall only (no storm surge), and **(D)** antecedent rainfall, TC-driven rainfall, and storm surge in a single simulation.

For the high-intensity TC, peak water levels increased by 40 cm within the Lakes Pontchartrain and Maurepas (10–15%) when antecedent conditions were included in the storm surge model simulation and TC-driven rainfall (**Figure 11**). The higher TC events caused larger surges in Lake Maurepas than Lake Pontchartrain, even when rain was not accounted for (the peak water levels are larger in Lake Pontchartrain than Maurepas for medium and low TCs). Although peak water levels moderately increased in the tidal lakes, results demonstrated an increase near 1 m (33% of the total water level) across portions of the [normally dry] floodplain adjacent to Lake Maurepas. These results begin to indicate how the surge penetration is altered when incorporating runoff from antecedent rainfall. This will be further evaluated with the definition of the flood zones, particularly the coastal flood transition zone.

Flood Zones

The spatial extent of each coastal, hydrologic, and flood transition zone is dependent on the rainfall, TC, and landscape characteristics (**Figure 12**). In Barataria, the coastal flood zone makes up 66% of the basin's total area (**Table 3**) and horizontally extends ∼100 km from the Gulf of Mexico to Des Allemands (**Figures 12A–C**). The transition zone spans ∼20 km for the lesser TC events to near 60 km toward the basin's northern boundary, bounded by levees, for the more extreme TC events. For all TC events simulated for the Barataria watershed, the coastal zone is nearly identical, with small variations near Des Allemands Lake, south of LaPlace. The little variation results from the low-lying topography, the funnel-shape of the basin, and its outer boundaries of naturally raised features and levee structures. Surge can penetrate 100 km inland. It is only in the upper portions of the watershed that rainfall has a substantial impact.

The coastal zone across the Lake Maurepas watershed extends along the eastern edge of the basin and encompasses Lake Maurepas in its entirety. The coastal zone ranges from 7 to 9% of total basins area (27–34% of the basin south of Interstate 10) for the 10-year and 100-year TC events, respectively. The coastal flood transition zone and the hydrologic zone vary substantially between the varying events. For the 10-year TC event, the transition zone is 377 km^2 (11% of the watershed area) and increases to 1,254 km^2 (37% of the watershed area) for the 100-year TC event. The increase in the coastal flood transition zone within the Lake Maurepas basin reduces the hydrologic zone from 2,057 km^2 (61%W of the area) to 959 km^2 (29% of the area). The transition and hydrologic zones are 1,329 km^2 and 1,000 km^2 for the 50-year TC event, respectively.

In the Lake Maurepas watershed, the transition zone for all return period events spans the 2 m elevation contour (NAVD88) from the Louisiana/Mississippi border to the Amite River. The flood transition zone is also generally locked along the western edge of Lake Maurepas for return period TC events; however, this edge does not follow a general contour line. The difference in the expanse of the transition and hydrologic flood zones is dominated along the western edge of the basin, including flood protection infrastructure and levees along the eastern bank of the Mississippi River. Furthermore, the flood transition zone extends into portions of East Baton Rouge Parish with higher return period TC events.

DISCUSSION AND CONCLUSION

This research address the simulation of compound coastal flood events and the delineation of a coastal flood transition zone (Bilskie and Hagen, 2018) for two distinct coastal basins in southeastern Louisiana. Rainfall-runoff from antecedent and TC-driven rainfall along with storm surge was simulated using a new rain-on-mesh module incorporated into the ADCIRC code. Antecedent rainfall conditions were obtained for seven rainfall stations with reliable data records for 21 landfalling TC events spanning 1948-2008. A parametric, TC-driven rainfall model was used for precipitation associated with the TC (Lonfat et al., 2004; US Army Corps of Engineers, 2006). Twelve synthetic storms of varying meteorological intensity (low, medium, and high) and total rainfall were utilized for each watershed (Barataria and Lake Maurepas) and provided model forcing for simulations of coastal inundation.

First, it was found that antecedent rainfall (pre-TC landfall) is influential up to 3 days pre-landfall. Rain gages along southeastern LA that measured total rainfall for 21 storm events showed little rainfall accumulation beyond 3 days before TC landfall. Second, results show that antecedent and TC-driven rainfall increase simulated peak water levels within each basin, with antecedent rainfall dominating inundation across the basin's upper portions. This increase is nonlinear. The superposition of water levels resulting from antecedent rainfall alone and water levels from storm surge (and TC-driven rain) does not equal the peak water levels generated from the simulation, including antecedent and TC-driven rain along with storm surge. The non-linear interaction is caused by the variation in the rainfall runoff's timing with the storm surge flooding along with interactions with the topography, friction, and the forcing. This nonlinearity underscores the need for further development of numerical models that tightly couple hydrologic and coastal surge processes into a single model framework (Santiago-Collazo et al., 2019) as well as the need to define the transition of flood zone hazards and risk (Bilskie and Hagen, 2018; Wu et al., 2018). Additionally, work should focus on examining the reasons for the nonlinear interaction.

Third, the delineated flood zones of coastal, transition, and hydrologic show stark differences between the two basins (**Figure 12** and **Table 3**). The coastal zone makes up most of the Barataria basin under all scenarios (over 65% of the basin area), followed by the transition (over 13%) and hydrologic. Under the medium and high-intensity TCs, the hydrologic zone is 2% or less of the entire basin, indicating that rainfall, from both antecedent conditions and TCs, influences the basin

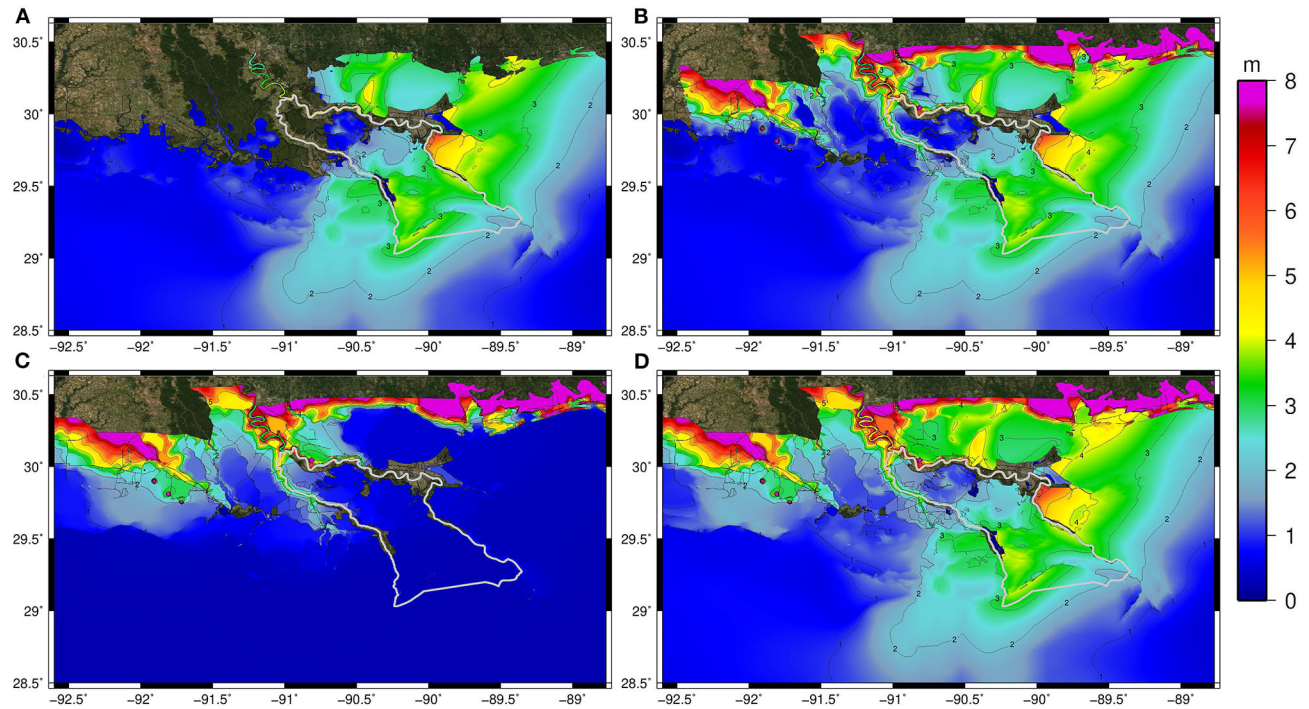

FIGURE 8 | Maximum of maximums (MOM) simulated peak water levels (m, NAVD88) for the Barataria watershed high event synthetic storms for **(A)** storm surge only (no rainfall), **(B)** storm surge and TC-driven rain, **(C)** antecedent rainfall only (no storm surge), and **(D)** antecedent rainfall, TC-driven rainfall, and storm surge in a single simulation.

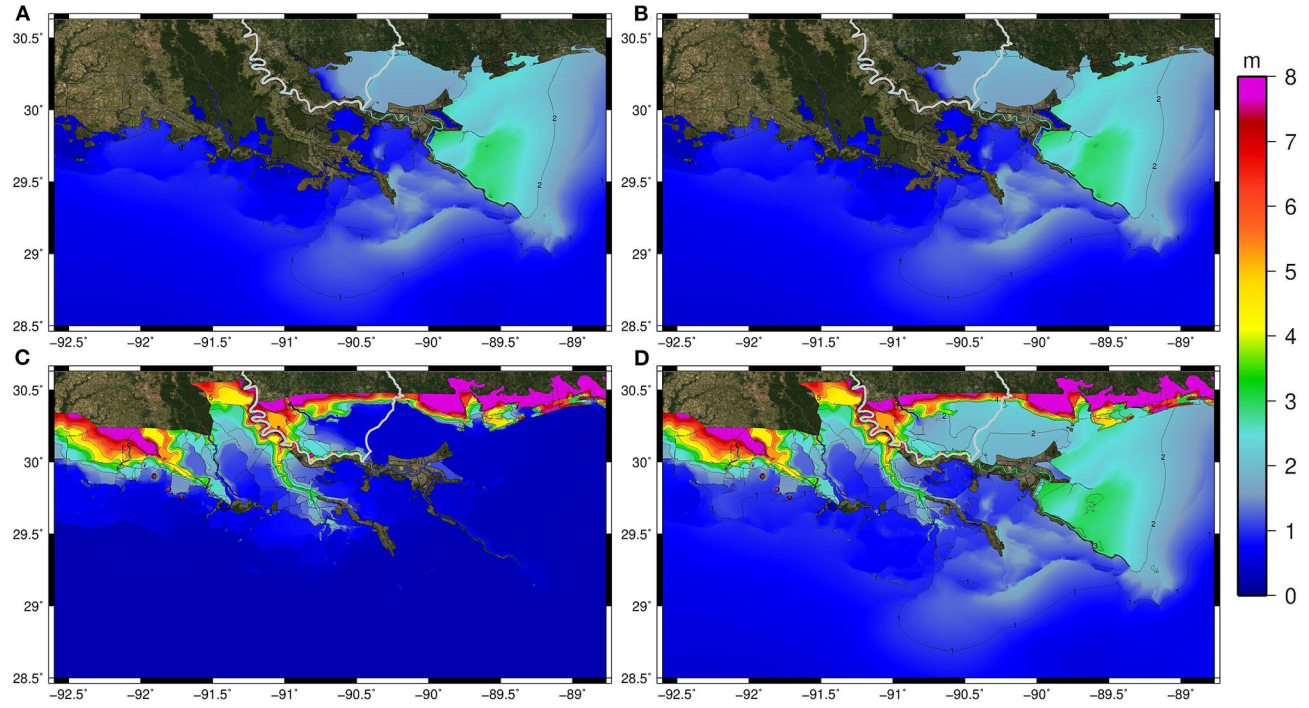

FIGURE 9 | Maximum of maximums (MOM) simulated peak water levels (m, NAVD88) for the Lake Maurepas 10-year TC events from **(A)** storm surge only (no rainfall), **(B)** storm surge and TC-driven rain, **(C)** antecedent rainfall only (no storm surge), and **(D)** antecedent rainfall, TC-driven rainfall, and storm surge in a single simulation.

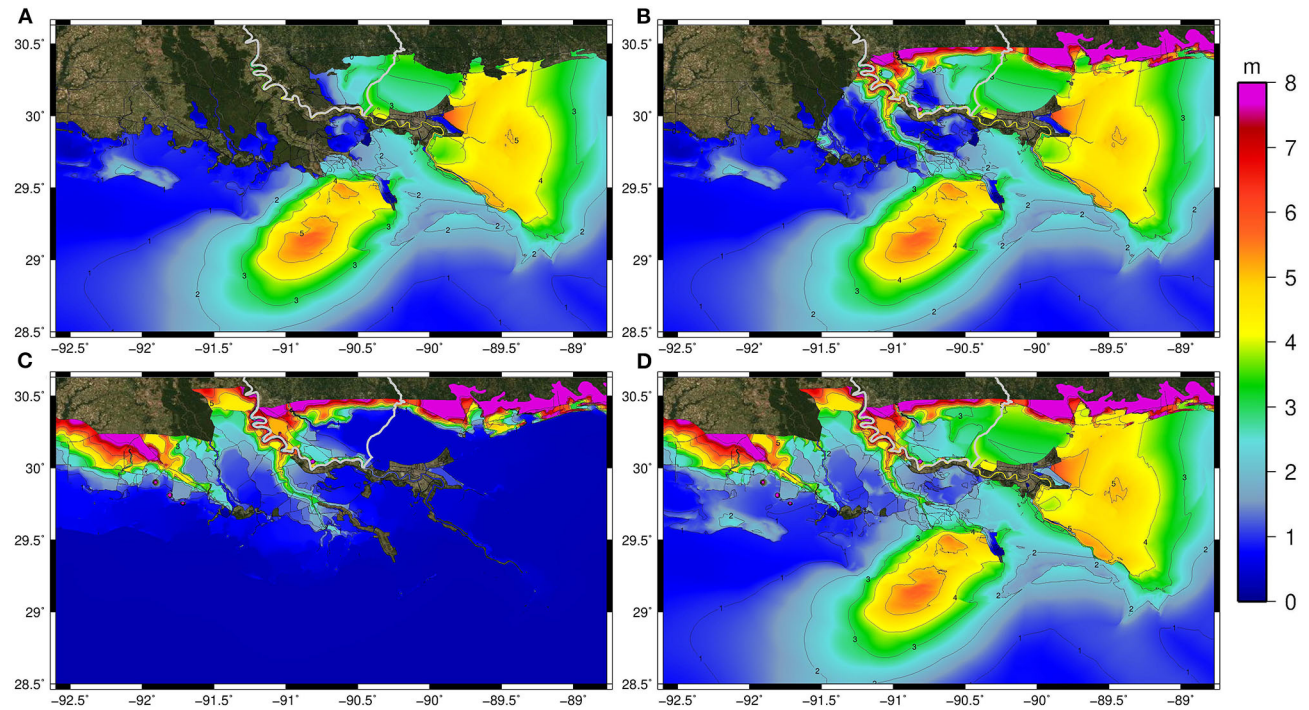

FIGURE 10 | Maximum of maximums (MOM) simulated peak water levels (m, NAVD88) for the Lake Maurepas 50-year TC events from **(A)** storm surge only (no rainfall), **(B)** storm surge and TC-driven rain, **(C)** antecedent rainfall only (no storm surge), and **(D)** antecedent rainfall, TC-driven rainfall, and storm surge in a single simulation.

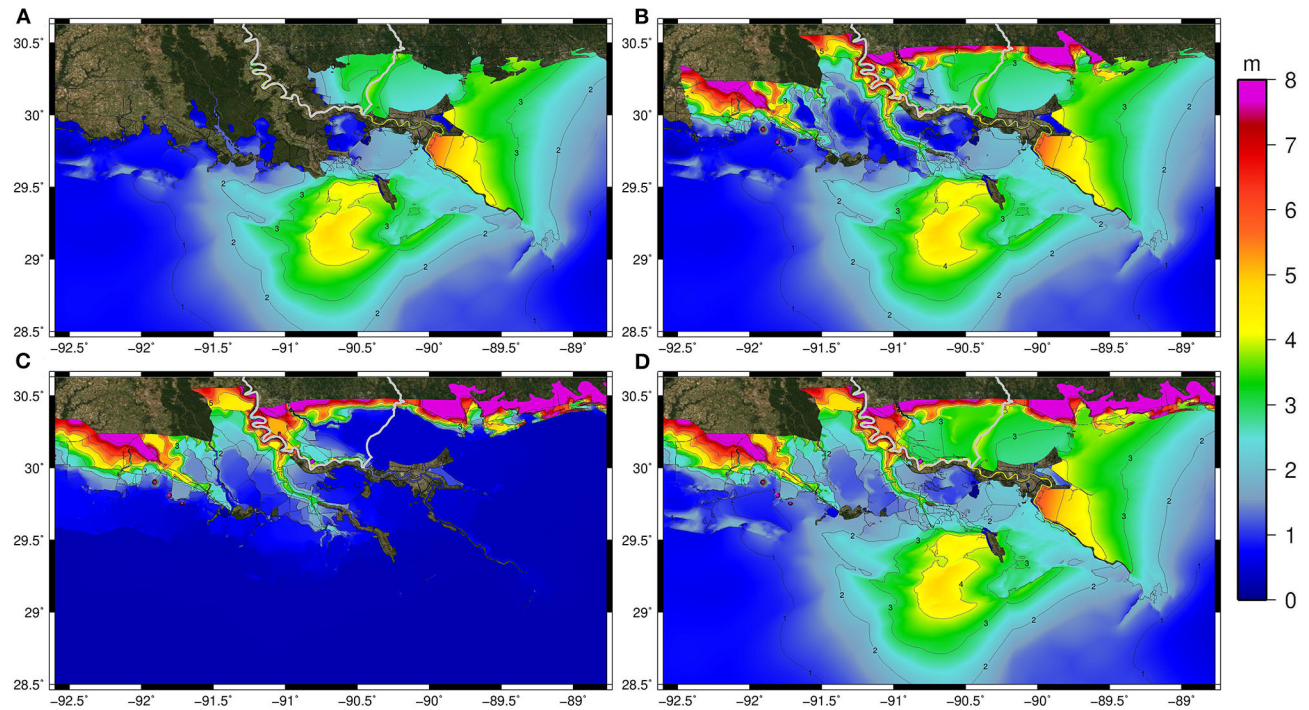

FIGURE 11 | Maximum of maximums (MOM) simulated peak water levels (m, NAVD88) for the Lake Maurepas 100-year TC events from **(A)** storm surge only (no rainfall), **(B)** storm surge and TC-driven rain, **(C)** antecedent rainfall only (no storm surge), and **(D)** antecedent rainfall, TC-driven rainfall, and storm surge in a single simulation.

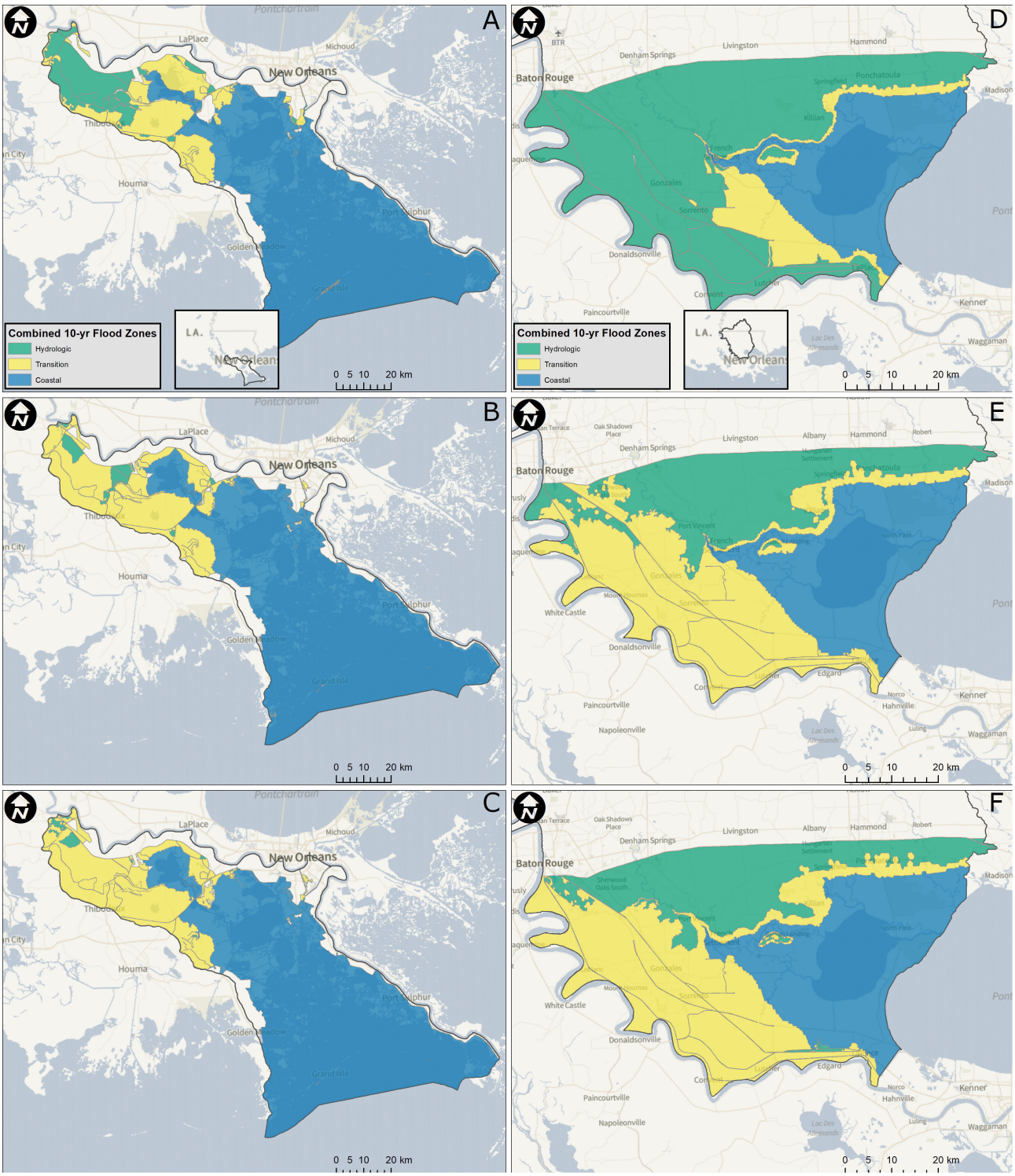

FIGURE 12 | Flood zone delineation for **(A–C)** Barataria watershed and **(D–F)** Lake Maurepas watershed for the **(A,D)** 10-year, **(B,E)** 50-year, and **(C,F)** 100-year return period storm surge stillwater elevation. Basemap courtesy of Mapbox.

and should be considered flood hazard and risk assessments. However, in Lake Maurepas, the coastal zone makes up 28–34% of the basins area (basin area south of Interstate-10). The transition zone is held constant for the medium and high-intensity events at 40% of the area, but only 11% for the low-intensity events. The hydrologic zone is large (61% of the area) for

TABLE 3 | Percent of watershed made up of each flood zone type (coastal, transition, and hydrologic).

Basin	Return period	Percent of watershed		
		Coastal	Transition	Hydrologic
Barataria	10	66%	13%	8%
	50	68%	18%	2%
	100	69%	18%	1%
Lake Maurepas	10	28%	11%	61%
	50	31%	40%	29%
	100	34%	40%	26%

The percentage for the Lake Maurepas watershed is based on a total watershed area south of Interstate 10 (3,364 km^2).

the low events but increase to 26–29% for the medium and high, respectively. The transition zone extends along the southwestern portion of the Lake Maurepas basin along the Mississippi River's east bank and into southern areas of greater Baton Rouge. The transition zone's extent indicates the vulnerability of compound flood events for a large area in the lower half of the watershed. As with Barataria, rainfall (for both hydrologic and surge processes) should be included in coastal flood hazard and risk studies.

This research has a variety of implications. Most important is the further refinement of capturing the spatial variation of the three flood zones (coastal, transition, and hydrologic), and in particular, the coastal flood transition zone (**Figure 12**). The coastal flood transition zone extends into the middle and upper portions of coastal watersheds, even coastal watersheds adjacent to tidal lakes removed from open ocean conditions (e.g., Lake Maurepas watershed). Antecedent rainfall conditions, as well as rainfall associated with TC, should be integrated into coastal flood hazard studies. The framework developed in this research to incorporate rain in a coastal inundation model and define the coastal flood transition zone is not specific to the two watersheds studied herein. The methods outlined can be extended to other coastal watersheds that are prone to compound flood events. For example, Shen et al. (2019) found similar flood transition zone results in Norfolk, VA, as did Bilskie and Hagen (2018) using different numerical models and techniques to include rainfall-runoff for different intensities and scenarios. There is a need to understand compound flooding fundamentals as it is a complex, nonlinear process. Finally, combining total water levels from individual model simulations of rainfall-runoff driven models and coastal inundation models are not sufficient for rigorous flood hazard studies. This basic approach is likely to overestimate the actual hazard. We must gain a fuller appreciation of the actual risks and recognize the integrated natural and human system that exists at the coastal land-margin.

Although this effort builds upon contemporary research of compound flood modeling, it has limitations that should be considered and based on future endeavors. First, our rain-on-mesh module does not include soil moisture, infiltration, or evapotranspiration. These mechanisms will reduce the amount of available rainfall excess, leading to changes in the available volume of water for surface runoff (Brocca et al., 2008; Bedient et al., 2018). Second, currently employed wetting/drying schemes are not well-suited for rainfall-driven runoff (Medeiros and Hagen, 2012). Further developments in wetting/drying algorithms for surface water routing should be emphasized in future efforts. Finally, our study employed a minimal number of synthetic storms, and a more comprehensive range of storm intensities and tracks is desirable. Such future efforts, among others, can enable a probabilistic understanding of the coastal flood transition zone and with the comprehension of consequence a more complete appreciation of flood risk at the coastal land-margin.

DATA AVAILABILITY STATEMENT

The datasets presented in this study can be found in online repositories. The names of the repository/repositories and accession number(s) can be found at: http://doi.org/10.17605/OSF.IO/G7DFJ.

AUTHOR CONTRIBUTIONS

MB contributed to the research ideas, developed the rain-on-mesh module, performed ADCIRC simulations, analyzed results including the flood zone delineation, led this article's writing, and was previously at the Louisiana State University Center for Coastal Resiliency, where he carried out most of his research contributions to this article, but has since been at the University of Georgia as of August 1, 2020. HZ provided guidance on developing the rain-on-mesh module, conducted simulations, post-processing of results for the Barataria watershed, and contributed to the writing of this article. DR led the antecedent rainfall analysis and contributed text to this article. JA provided guidance on the rain-on-mesh module, led the synthetic storm selection, and contributed text to this article. ZC wrote/tested computer code for TC-driven and gridded rainfall. SH is the PI and conceived the original research ideas, provided guidance during the development of the rain-on-mesh module, assisted in analyzing results, and aided in writing/reviewing this article. All authors contributed to the article and approved the submitted version.

FUNDING

This project was paid for with federal funding from the Department of the Treasury through the Louisiana Coastal Protection and Restoration Authority's Center of Excellence Research Grants Program under the Resources and Ecosystems Sustainability, Tourist Opportunities, and Revived Economies of the Gulf Coast States Act of 2012 (RESTORE Act) (Award No. CPRA-2015-COE-MB). This project was also paid in part by the Gulf Research Program (GRP) of the National Academies of Sciences, Engineering, and Medicine (Award No. 200000829), Robert Wood Johnson Foundation

(RWJF) (Award No. 200000829), and the Louisiana Sea Grant Laborde Chair.

ACKNOWLEDGMENTS

The statements, findings, conclusions, and recommendations are those of the authors and do not necessarily reflect the views of the Department of the Treasury, GRP, RWJF, or the Louisiana Sea Grant College Program.

SUPPLEMENTARY MATERIAL

The Supplementary Material for this article can be found online at: https://www.frontiersin.org/articles/10.3389/frwa.2021.609231/full#supplementary-material

REFERENCES

Atkinson, J. H., Roberts, H. J., Hagen, S. C., Zou, S., Bacopoulos, P., Medeiros, S. C., et al. (2011). Deriving frictional parameters and performing historical validation for an ADCIRC storm surge model of the Florida Gulf Coast, Florida. *Watershed J.* 4, 22–27. Available online at: https://bluetoad.com/publication/?m=12306&i=69376&p=20

Bedient, P. B., Huber, W. C., and Vieux, B. E. (2018). *Hydrology and Floodplain Analysis*. 6th ed. (Pearson), 832.

Bilskie, M. V., and Hagen, S. C. (2018), Defining flood zone transitions in low-gradient coastal regions. *Geophys. Res. Lett.* 45, 2761–2770. doi: 10.1002/2018GL077524

Black, P. G., D'Asaro, E. A., Sanford, T. B., Drennan, W. M., Zhang, J. A., French, J. R., et al. (2007). Air–sea exchange in hurricanes: synthesis of observations from the coupled boundary layer air–sea transfer experiment. *Bullet. Am. Meteorol. Soc.* 88, 357–374. doi: 10.1175/BAMS-88-3-357

Blake, E. S., and Zelinksy, D. A. (2018). *National Hurricane Center Tropical Cyclone Report: Hurricane HarveyRep.*

Brocca, L., Melone, F., and Moramarco, T. (2008). On the estimation of antecedent wetness conditions in rainfall–runoff modelling. *Hydrol. Process.* 22, 629–642. doi: 10.1002/hyp.6629

Bunya, S., Dietrich, J. C., Westerink, J. J., Ebersole, B. A., Smith, J. M., Atkinson, J. H., et al. (2010). A high-resolution coupled riverine flow, tide, wind, wind wave, and storm surge model for southeastern Louisiana and Mississippi. Part I: Model development and validation. *Monthly Weather Rev.* 128, 345–377. doi: 10.1175/2009MWR2906.1

Cobell, Z., Zhao, H., Roberts, H. J., Clark, F. R., and Zou, S. (2013). Surge and wave modeling for the Louisiana 2012 coastal master plan. *J. Coastal Res.* 7, 88–108. doi: 10.2112/SI_67_7

Conner, W. H., and Day, J. W. (1987). *The Ecology of Barataria Basin, Louisiana: An Estuarine ProfileRep.* (US Fish and Wildlife Service), 165.

DeLorme, D. E., Stephens, S. H., Bilskie, M. V., and Hagen, S. C. (2020). Coastal decision-makers' perspectives on updating storm surge guidance tools. *J. Contingencies Crisis Manag.* 28, 158–168. doi: 10.1111/1468-5973.12291

Dietrich, J. C., Dawson, C. N., Proft, J. M., Howard, M. T., Wells, G., Fleming, J. G., et al. (2013). "Real-time forecasting and visualization of hurricane waves and storm surge using SWAN+ADCIRC and FigureGen," in *Computational Challenges in the Geosciences*, eds C. Dawson and M. Gerritsen (New York, NY: Springer), 49–70. doi: 10.1007/978-1-4614-7434-0_3

Dietrich, J. C., Kolar, R. L., and Westerink, J. J. (2006). Refinements in continous galerkin wetting and drying algorithms. in *Ninth International Conference on Estuarine and Coastal Modeling*, (Charleston, SC) 637–656. doi: 10.1061/40876(209)37

Dietrich, J. C., Tanaka, S., Westerink, J. J., Dawson, C. N., Luettich, R. A., Zijlema, M., et al. (2012). Performance of the unstructured-mesh, SWAN+ADCIRC model in computing hurricane waves and surge. *J. Sci. Comput.* 52, 468–497. doi: 10.1007/s10915-011-9555-6

Dietrich, J. C., Westerink, J. J., Kennedy, A. B., Smith, J. M., Jensen, R. E., Zijlema, M., et al. (2011). Hurricane Gustav (2008) waves and storm surge: hindcast, synoptic analysis, and validation in Southern Louisiana. *Monthly Weather Rev.* 139, 2488–2522. doi: 10.1175/2011MWR3611.1

Erdman, J. (2018). *Florence Sets Preliminary North Carolina and South Carolina Tropical Cyclone Rain Records; Third, Fourth States to Do So in 12 Months*. Weather Channel.

FEMA and USACE (2008). *Flood Insurance Study: Southeastern Parishes, Louisiana, Intermediate Submission 2: Offshore Water Levels and WavesRep. FEMA Region 6 and USACE New Orleans District*.

Gori, A., Lin, N., and Smith, J. (2020). Assessing compound flooding from landfalling tropical cyclones on the North Carolina Coast. *Water Resourc. Res.* 56:e2019WR026788. doi: 10.1029/2019WR026788

Kinnmark, I. (1985). "The shallow water wave equations: formulation, analysis, and application," in *Lecture Notes in Engineering*. New York, NY: Springer-Verlag. doi: 10.1007/978-3-642-82646-7

Kolar, R. L., Gray, W. G., Westerink, J. J., Cantekin, M. E., and Blain, C. A. (1994). Aspects of nonlinear simulations using shallow-water models based on the wave continuity equation. *Comput. Fluids* 23, 523–538. doi: 10.1016/0045-7930(94)90017-5

Leonard, M., Westra, S., Phatak, A., Lambert, M., van den Hurk, B., McInnes, K., et al. (2014). A compound event framework for understanding extreme impacts. *Wiley Interdiscipl. Rev. Climate Change* 5, 113–128. doi: 10.1002/wcc.252

Lonfat, M., Marks, F. D., Jr., and Chen, S. S. (2004). Precipitation distribution in tropical cyclones using the tropical rainfall measuring mission (TRMM) microwave imager: a global perspective. *Monthly Weather Rev.* 132, 1645–1660. doi: 10.1175/1520-0493(2004)132<1645:PDITCU>2.0.CO;2

Luettich, R. A., and Westerink, J. J. (2004). *Formulation and numerical implementations of the 2D/3D ADCIRC finite element model version 44.XXRep., 12/08/2004*. Available online at: http://citeseerx.ist.psu.edu/viewdoc/download?doi=10.1.1.675.3043&rep=rep1&type=pdf

Medeiros, S., and Hagen, S. C. (2012). Review of wetting and drying algorithms for numerical tidal flow models. *Int. J. Numerical Methods Fluids* 71, 473–487. doi: 10.1002/fld.3668

Morgan, J. P. (1967). "Ephemeral estuaries of the deltaic environment," in *Estuaries: AAAS Monograph*, ed G. H. Lauff, 115–120.

Paerl, H. W., Hall, N. S., Hounshell, A. G., Luettich, R. A., Rossignol, K. L., Osburn, C. L., et al. (2019). Recent increase in catastrophic tropical cyclone flooding in coastal North Carolina, USA: long-term observations suggest a regime shift. *Sci. Rep.* 9:10620. doi: 10.1038/s41598-019-46928-9

Powell, M. D. (2006). *National Oceanic and Atmospheric Administration (NOAA) Joint Hurricane Testbed (JHT) Program*. Final Report. Silver Spring, MD: National Oceanic and Atmospheric Administration.

Roberts, H., and Cobell, Z. (2017). *2017 Coastal Master Plan: Attachment C3-25.1: Storm SurgeRep.* (Louisiana: Coastal Protection and Restoration Authority, Baton Rouge, LA), 1–110.

Santiago-Collazo, F. L., Bilskie, M. V., and Hagen, S. C. (2019). A comprehensive review of compound inundation models in low-gradient coastal watersheds. *Environ. Model. Softw.* 119, 166–181. doi: 10.1016/j.envsoft.2019.06.002

Shen, Y., Morsy, M. M., Huxley, C., Tahvildari, N., and Goodall, J. L. (2019). Flood risk assessment and increased resilience for coastal urban watersheds under the combined impact of storm tide and heavy rainfall. *J. Hydrol.* 579:124159. doi: 10.1016/j.jhydrol.2019.124159

Silva-Araya, W., Santiago-Collazo, F., Gonzalez-Lopez, J., and Maldonado-Maldonado, J. (2018). Dynamic modeling of surface runoff and storm surge during hurricane and tropical storm events. *Hydrology* 5:13. doi: 10.3390/hydrology5010013

Stephens, S., DeLorme, D., and Hagen, S. (2017). Evaluation of the design features of interactive sea-level rise viewers for risk communication. *Environ. Commun.* 11, 248–262. doi: 10.1080/17524032.2016.1167758

Thaler, T., and Levin-Keitel, M. (2016). Multi-level stakeholder engagement in flood risk management—a question of roles and power: lessons from England. *Environ. Sci. Policy* 55, 292–301. doi: 10.1016/j.envsci.2015.04.007

US Army Corps of Engineers (2006). *Performance Evaluation of the New Orleans and Southeast Louisiana Hurricane Protection SystemRep.* Final Report of the Interagency Performance Evaluation Task Force.

US Geological Survey (2020). *Coastal National Elevation Database (CoNED) Project - Topobathymetric Digital Elevation Model (TBDEM).*

Valle-Levinson, A., Olabarrieta, M., and Heilman, L. (2020). Compound flooding in Houston-Galveston Bay during Hurricane Harvey. *Sci. Total Environ.* 747:141272. doi: 10.1016/j.scitotenv.2020.141272

van der Wiel, K., Kapnick, S. B., van Oldenborgh, G. J., Whan, K., Sjoukje, P., Vecchi, G. A., et al. (2017). Rapid attribution of the August 2016 flood-inducing extreme precipitation in south Louisiana to climate change. *Hydrol. Earth System Sci.* 21, 897–921. doi: 10.5194/hess-21-897-2017

Wahl, T., Jain, S., Bender, J., Meyers, S. D., and Luther, M. E. (2015). Increasing risk of compound flooding from storm surge and rainfall for major US cities. *Nat. Climate Change* 5:1093. doi: 10.1038/nclimate2736

Wang, S. Y. S., Zhao, L., and Gillies, R. R. (2016). Synoptic and quantitative attributions of the extreme precipitation leading to the August 2016 Louisiana flood. *Geophys. Res. Lett.* 43, 11805–811814. doi: 10.1002/2016GL071460

Westerink, J. J., Luettich, R. A., Feyen, J. C., Atkinson, J. H., Dawson, C., Roberts, H. J., et al. (2008). A basin- to channel-scale unstructured grid hurricane storm surge model applied to Southern Lousiana. *Monthly Weather Rev.* 136, 833–864. doi: 10.1175/2007MWR1946.1

White, I., Kingston, R., and Barker, A. (2010). Participatory geographic information systems and public engagement within flood risk management. *J. Flood Risk Manag.* 3, 337–346. doi: 10.1111/j.1753-318X.2010.01083.x

Wu, W., McInnes, K., O'Grady, J., Hoeke, R., Leonard, M., and Westra, S. (2018). Mapping dependence between extreme rainfall and storm surge. *J. Geophys. Res. Oceans* 123, 2461–2474. doi: 10.1002/2017JC013472

Zscheischler, J., Westra, S., van den Hurk, B. J. J. M., Seneviratne, S. I., Ward, P. J., Pitman, A., et al. (2018). Future climate risk from compound events. *Nat. Climate Change* 8, 469–477. doi: 10.1038/s41558-018-0156-3

Conflict of Interest: The authors declare that the research was conducted in the absence of any commercial or financial relationships that could be construed as a potential conflict of interest.

frontiers in Climate

ORIGINAL RESEARCH
published: 15 March 2021
doi: 10.3389/fclim.2021.610680

Hurricane Scenario Generation for Uncertainty Modeling of Coastal and Inland Flooding

Kyoung Yoon Kim[1]*, *Wen-Ying Wu*[2], *Erhan Kutanoglu*[1], *John J. Hasenbein*[1] and *Zong-Liang Yang*[2]

[1] Operations Research and Industrial Engineering, The University of Texas at Austin, Austin, TX, United States, [2] Jackson School of Geosciences, The University of Texas at Austin, Austin, TX, United States

Hurricanes often induce catastrophic flooding due to both storm surge near the coast, and pluvial and fluvial flooding further inland. In an effort to contribute to uncertainty quantification of impending flood events, we propose a probabilistic scenario generation scheme for hurricane flooding using state-of-art hydrological models to forecast both inland and coastal flooding. The hurricane scenario generation scheme incorporates locational uncertainty in hurricane landfall locations. For an impending hurricane, we develop a method to generate multiple scenarios by the predicated landfall location and adjusting corresponding meteorological characteristics such as precipitation. By combining inland and coastal flooding models, we seek to provide a comprehensive understanding of potential flood scenarios for an impending hurricane. To demonstrate the modeling approach, we use real-world data from the Southeast Texas region in our case study.

Keywords: flooding, scenario generation, Inland flooding, coastal flooding, storm surge, high water mark, validation, hospital and nursing home evacuation

OPEN ACCESS

Edited by:
Yao Hu,
University of Delaware, United States

Reviewed by:
Brian Blanton,
University of North Carolina at Chapel Hill, United States
Yi Hong,
University of Michigan, United States

***Correspondence:**
Kyoung Yoon Kim
erickim@utexas.edu

Specialty section:
This article was submitted to Climate Risk Management, a section of the journal Frontiers in Climate

Received: *26 September 2020*
Accepted: *17 February 2021*
Published: *15 March 2021*

Citation:
Kim KY, Wu W-Y, Kutanoglu E, Hasenbein JJ and Yang Z-L (2021) Hurricane Scenario Generation for Uncertainty Modeling of Coastal and Inland Flooding. Front. Clim. 3:610680. doi: 10.3389/fclim.2021.610680

1. INTRODUCTION

Since 1980, the U.S. has sustained 263 weather and climate disasters where the overall damage costs reached or exceeded $1 billion, and the total cost of these 263 events exceeds $1,774 billion. Among the 263 billion-dollar disasters in the last 40 years, the years of 2017, 2018, and 2019 have produced 44 events with a total cost of $460 billion (NOAA National Centers for Environmental Information, 2020). Hurricane Harvey in 2017, which was the most significant tropical cyclone rainfall event in U.S. history, caused catastrophic flooding in Harris and Galveston counties in Texas (Blake and Zelinsky, 2018), and was one major motivation for developing the methodology in this paper.

In preparing for future hurricanes and other disasters, federal, state, and local agencies engage in joint efforts. Especially for decisions like mobilizing resources and prepositioning supplies for rescue missions, which take place before an imminent but forecasted disaster such as a hurricane, the agencies have utilized flood prediction tools that were developed in support of decision making. A review of the relevant literature indicates that these models do not function as an event- and location-specific tool for impending emergencies but rather as a general guideline for preparing for potential floods. Moreover, in predicting floods due to hurricanes, to the best of our knowledge, inland and coastal floods are modeled separately. For agencies that must allocate evacuation resources, coordinate patient evacuation from multiple affected hospitals and nursing homes to multiple receiving facilities, comprehensive flood mapping of both inland and coastal area are important.

In this paper, we propose a rigorous modeling and methodological effort that integrates statistical implementation of models in predicting inland and coastal flooding. The main goal is to help decision makers immediately before a hurricane or potential flood event, for decisions that are made 48–72 h before landfall. The remainder of the paper is organized as follows. In section 2, we review flood forecasting tools that are used in government agencies. We further investigate different approaches in coastal flood forecasting. In section 3, we introduce a framework for hurricane scenario generation by combining outputs of inland and coastal models. A modified stratified sampling technique is used to simulate hurricane landfall locations. For each simulated landfall location, two models predict inundation in the southeast Texas region, generating a potential flood map, and the predicted inundation is validated in section 4. In section 5, we demonstrate our scenario generation method on the hospital and nursing home evacuation problem for Hurricane Harvey. In section 6, we outline future research directions: alternative ways of perturbing hurricane scenarios to generate flood scenarios and methods for improving the model accuracy.

2. LITERATURE REVIEW

About half of the deaths due to flooding caused by tropical cyclones happened inland (National Oceanic and Atmospheric Administration, 2018). However, it has been challenging to model event-specific and real-time inland flood inundation. The Federal Emergency Management Agency (FEMA) provides a 100-year floodplain publicly, which is used as a standard for flood insurance. However, 100-year flood maps are not informative in preparing for a specific incoming hurricane, since they reflect estimates that are aggregated over many flood events. Furthermore, such flood maps provide no information about the spatial correlation in flooding for specific events. In contrast, the methodology in this paper is tailored to enhance decision making for a specific hurricane. It also specifically incorporates the spatial correlation of flooding induced by an event.

The primary source of coastal flooding is the storm surge, an abnormal rise of water generated by a storm. The studies in coastal flooding begin with modeling the atmospheric part of the storm. As presented by Contento et al. (2018), many researchers have explored ways to evaluate storm surge with storm characteristics such as wind velocity and intensity. Two well-known storm surge models, the Advanced Circulation Model (ADCIRC) (Westerink et al., 1994) and Sea, Lake, and Overland Surges from Hurricanes (SLOSH) (Jelesnianski, 1992), couple storm characteristics with hydraulic characteristics of impact regions to predict storm surges. While the advantage of ADCIRC is in its use of an unstructured grid for capturing the complex spatial variability of the surge phenomenon (Dietrich et al., 2011), it requires high-performance computing resources in order to compute ensemble forecasts without degradation of its resolution benefits (Mandli and Dawson, 2014). Originally developed for real-time forecasting of storm surges, SLOSH is an efficient model that can generate multiple ensemble of forecasts for forthcoming hurricanes. However, its accuracy when compared to high water marks (HWMs) and tide gauges measured after storms is within 20% (National Hurricane Center, n.d.b). For Hurricane Katrina, this accuracy reduces to 5% when the surge forecast is compared to HWMs marked as "excellent" quality (National Hurricane Center, n.d.b). Mandli and Dawson introduce an alternative computationally efficient model, GeoClaw, using an adaptive mesh refinement (AMR) algorithm bridging the gap between the current state-of-art storm surge models (Mandli and Dawson, 2014). The AMR-based model significantly reduces the computational cost of simulation. When compared to Hurricane Ike gauge data, the GeoClaw simulation compares favorably with the ADCIRC simulation.

To build probabilistic storm surge scenarios for an impending hurricane, instead of using a computationally burdensome model like ADCIRC, researchers have developed metamodels. Such models estimate storm surge heights as functions of storm characteristics and are calibrated with ADCIRC simulations. To draw relationships between surge height and storm characteristics, researchers apply different techniques such as kriging metamodel (Jia and Taflanidis, 2013) and artificial neural networks (Kim et al., 2015). However, the metamodels cannot include historical records in the calibration data and do not extrapolate to regions different from those for which they have been calibrated (Contento et al., 2018).

To the best of our knowledge, no studies have considered providing both comprehensive inland and coastal flood maps for an impending hurricane. We further distinguish our work by utilizing weather forecasts in generating hurricane scenarios to provide a more pragmatic solution to the problem. Next, we discuss in more detail how we integrate the inland and coastal models to forecast potential flooding events for impending hurricanes.

3. METHODOLOGY

In this section, we explain our method for generating flood scenarios. During hurricanes, coastal regions suffer from flooding primarily due to storm surge, while inland locations are subjected to flooding from water overflowing from streams. As described in the sequel, we combine models for inland and coastal regions to predict the overall impact of flooding via scenario generation. The overall process of generating flood scenarios is summarized in **Figure 1**. While the methodology is general, we use Hurricane Harvey as a descriptive example, as it is also used in our case study.

3.1. Data Input to Forecasting Models

Inland flood forecasting is driven by the weather forecast, which are output variables from numerical weather models. The meteorological inputs used in this study include precipitation, wind speed, temperature, humidity, and radiation (see **Supplementary Table 1**) which are the outputs from the Global Forecast System (GFS). The original 13 km output data from GFS was processed to 1 km data by statistical interpolation for the 1-km Weather Research and Forecasting model-Hydrological modeling system (WRF-Hydro) simulation. This regridding was

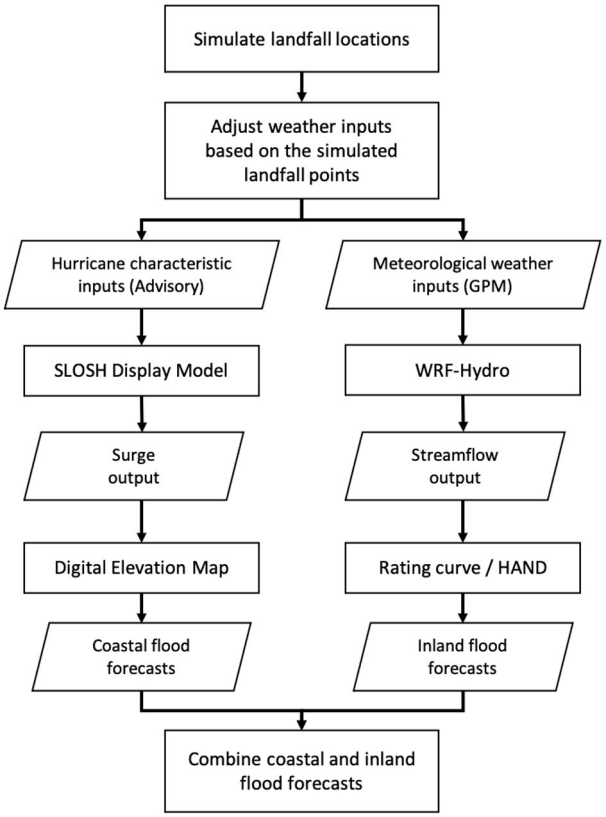

FIGURE 1 | The flow diagram summarizes the overall flood scenario generation methodology which combines both inland and coastal flooding.

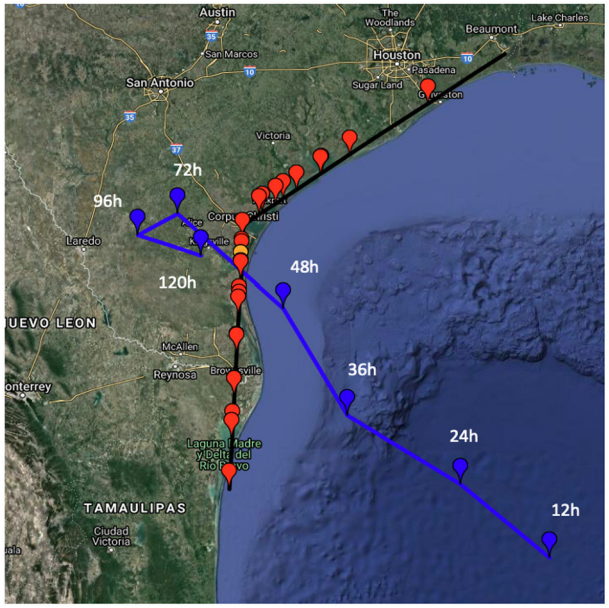

FIGURE 2 | Twenty-five simulated landfall locations for Hurricane Harvey.

done by NOAA, and we downloaded the 1 km data directly from them. These inputs are then used in the inland flood forecasting model, WRF-Hydro (Gochis et al., 2015, 2018, 2020), which we ran on a local supercomputer. The dynamic input data (atmospheric forcing) were downloaded from the NOAA archive at Renaissance Computing Institute (Alcantara et al., 2017). It should be noted that WRF-Hydro incorporates weather forecasts that are not limited to the characteristics of tropical cyclones.

A center of Tropical Cyclone (TC) is usually defined by the location of the minimum wind field or pressure. We use one of the GFS forecasts which are produced four times per day to define the TC track. We estimate the hourly TC center based on the location of minimum surface wind field. In order to choose one from the multiple GFS forecasts, we need to take the decision-making period (T) into consideration. To provide potential flooding scenarios for impending hurricanes to the decision makers, we utilize the most up-to-date hurricane information by choosing a reference GFS forecast issued T hours before landfall.

When the potential TC might be hazardous, the National Hurricane Center (NHC) issues TC advisories which contain storm information such as position of storm, maximum sustained winds, and potential track. Usually, the advisories are issued in every 6 h. Among the advisories, we choose one advisory as our reference and use the storm information in the advisory as inputs to the storm surge forecasting model, SLOSH Display Program (SDP). We explain the method of choosing a reference advisory in section 3.2. After selecting the reference advisory, among the information contained in the advisory, we collect Saffir-Simpson hurricane intensity and hurricane forward speed as our inputs to the storm surge forecasting model. Two other inputs, the hurricane direction and tide level, are necessary to run SDP. The method for obtaining the inputs from the reference advisory is discussed in section 3.3.

3.2. Scenario Generation Method

We propose a method for scenario generation that considers track error. The tropical cyclone track dominates the distribution of rainfall (Elsberry, 2002; Marchok et al., 2007), which leads to flooding. To create scenarios, we assume that the hurricane landfall location is modeled by a normal random variable, distributed along the Texas coastline, with the mean located at the crossing point between the forecasted hurricane track and the coastline.

In this study, we approximate the Texas coastline with a piecewise linear function with two segments (**Figure 2**). The first segment is defined by connecting two cities, Port Arthur and Corpus Christi, Texas with a line. The second segment is defined by connecting Corpus Christi and Brownsville, Texas. The GPS coordinates of the three cities are listed in **Supplementary Table 3**. Note that the distribution is not bounded by the two cities, Brownsville and Port Arthur. The piecewise linear model of the Texas coast described above can be succinctly expressed as follows:

$$f(x) = \begin{cases} -17.273x + 1709.991 & x \geq 97.39^\circ W \\ -0.603x + 86.516 & x < 97.39^\circ W, \end{cases} \quad (1)$$

where x is the longitude and $f(x)$ is the corresponding latitude. The longitude of Corpus Christi, which is 97.39° W, is used as the center-point dividing the domain into two intervals. Then, we define the intersection of the hurricane track drawn from the reference GFS forecast and the Texas coastline as the "mean" landfall location.

The mean landfall location is the reference point for generating inputs for multiple scenarios. Our assumption is that potential landfall locations are normally distributed along the piecewise linear model, with the mean as just described. The standard deviation of the normal distribution can be inferred from the cone of uncertainty. The cone corresponds to the probable track of the TC center. The sizes of cones represent the forecast position errors over the previous 5-year period. The radii of the cone circles in 2017 for the Atlantic basin that are used for the Harvey case study later are given in **Supplementary Table 2** (National Hurricane Center, n.d.a).

Since the estimated landfall hour does not perfectly match with one of the forecast periods in **Supplementary Table 2**, we perform a simple linear interpolation. By calculating the ratio, we compute the corresponding radius of two-thirds cone of uncertainty circle, $r = 89$ nautical miles. Using the standard normal distribution, we find the standard deviation, σ, of the landfall distribution by using

$$\sigma = \frac{r}{z_{5/6}} \tag{2}$$

where $z_{5/6}$ is the critical point from a standard normal. Let L be a random variable representing distance from a landfall location to the mean landfall point. Clearly, $L = 0$ at the mean, and $L < 0$ for the landfall locations on the left (west) side of the mean location.

Having created a distribution of potential landfall locations, we now describe the stratified sampling method. First, we divide the coastal model into m equiprobable segments. Within each segment, we sample N landfall locations according to the conditional normal distribution on that segment. As mentioned above, once sampled, the resulting mN locations are viewed as being equally likely in later calculations, each occurring with probability of $1/(mN)$.

For $m = 5$ and $N = 5$, the segment boundaries are defined by four quantiles (m_1 to m_4) along the coastline. For example, $P(L \leq m_1) = 1/5$. Then, for the first segment we sample five quantiles (p_1 to p_5) from a Uniform (0, 1/5). For the remaining four segments, we also sample quantiles for each segment from a Uniform $((k-1)/5, k/5)$, for $k = 2, \ldots, 5$. Overall, we have 25 quantiles which are next translated to landfall locations.

In order to find the physical location of the landfall points, we find z-scores of the sampled quantiles using the standard normal distribution. From the standard normal table, we calculate z_{p_n}, where $n = 1, ..., mN$, and use

$$l_n = \sigma z_{p_n} \tag{3}$$

to calculate the distance l_n from the mean crossing point in the coastline model, for the corresponding quantile. Finally, the GPS coordinates corresponding to l_n are found by solving for x_n and y_n in the following system:

$$cos(\theta) = \frac{|x_R - x_n|}{l_n} \tag{4}$$

$$sin(\theta) = \frac{|y_R - y_n|}{l_n} \tag{5}$$

$$\theta = \arctan(a_c) \tag{6}$$

where a_c is the slope of the coastline that contains the mean location. Here, x_R and y_R are the longitude and latitude of the mean landfall location.

The orange dot in **Figure 2** is the mean predicted landfall location for Harvey. Red dots show 25 simulated landfall locations and blue dots indicate the TC center at 12, 24, 36, 48, 72, 96, and 120 h obtained from the reference GFS forecast. Once we have the potential landfall locations, we then run WRF-Hydro to obtain streamflow simulations.

The meteorological conditions at a given time step (hourly here) are used to force the WRF-Hydro model. The atmospheric inputs provided at a 1 × 1 km resolution from the weather models are obtained from the NOAA archive (see **Supplementary Figure 1**). For each sampled landfall location, we compute the spatial shift, a vector, by using the landfall reference point (the orange point in **Figure 2**) and the sampled location. Then, for each scenario we shift the atmospheric inputs according to the corresponding vector. To generate comprehensive flood scenarios from hurricanes, we need to combine the inland flooding computations with a coastal flooding model. In our model, we directly combine each inland flooding scenario with a coastal flooding scenario by matching the direction of a hurricane. The detailed steps of aligning the two models are discussed in section 3.3.

3.3. Flood Prediction Methods

3.3.1. Inland Flood Model

We first review our inland flood prediction method. As mentioned at the beginning of section 3.1, we downloaded WRF-Hydro and the corresponding input data from NOAA. Secondly, for scenario generation, we processed the input data to generate 25 sets of input data (as described in section 3.2). Thirdly, the streamflow ouputs from WRF-Hydro were used with HAND datasets to generate inland flood mapping. The details of this third step are described in this section.

WRF-Hydro is an integrated hydrological framework connecting several modules, including the Noah-Multiparameterization Land Surface Model (Noah-MP), a terrain routing module, and a river routing module. The framework enables different models to work with different spatial coordinates. WRF-Hydro simulates typical hydrological processes. The one-dimensional and coarse-resolution land surface model (Noah-MP) is coupled with a two-dimensional and finer resolution terrain routing module, which simulates the hillslope feature for the gravitational redistribution of water.

Finally, the river routing module simulates the water flows from upstream to downstream.

The spatial resolution is 1 km for the land surface model and 250 m for the terrain routing module. The river routing module uses a vector-based channel network from the National Hydrography Dataset Plus (NHDPlus) version 2. To estimate the flood level, we apply the Height Above Nearest Drainage (HAND) flood mapping methodology (Liu et al., 2018, 2020; Zheng et al., 2018b). The HAND methodology is a computationally efficient and terrain-based inundation mapping. The HAND is defined as the height of a given location with respect to the nearest stream it drains to. The HAND value of a location is the difference between its elevation and the minimum channel elevation. The resolution of the HAND product is 10 m based on the USGS Digital Elevation Model (DEM) data.

Real-time, street-level inundation mapping is time-consuming. Instead, we process the studied locations in the GIS tool to obtain the corresponding catchment ID and HAND values. This is a one-time approach. Once the WRF-Hydro forecast is produced, we are able to use the pre-processed catchment ID and HAND values to calculate the flood levels.

First, we convert the streamflow to a stage height using a rating curve. The rating curve is a flow-depth relationship that depends on the hydraulic characteristics of the stream channel. Here we use the rating curves included in the HAND product[1]. The product provides a table look-up rating curve with a series of 1-foot incremental water levels. We apply linear interpolation to convert streamflow to stage height.

Second, the water level at any given location is calculated from the stage height minus the HAND value if the result is greater than zero. Otherwise, the water level is set to zero if the stage height is smaller than the HAND value. We repeat these steps for each scenario and each location to obtain maximum water levels in 10-day forecast period (from August 24 to September 2, 2017, for Harvey).

3.3.2. Coastal Flood Prediction

We turn our attention to the hydrological model used to predict flooding in the coastal region. When a hurricane makes landfall, the storm brings seawater to the shore, and this phenomenon is called storm surge. To predict the flooding due to the storm surge, we need to know the elevation of the addresses and the storm surge height due to the hurricane. For a particular location, we find the relative surge level above ground by subtracting the elevation from the surge height.

One of the USGS National Geospatial Program products is the 3D Elevation Program (3DEP)[2]. Standard DEMs represent the topographic surface of the earth and contain flattened water surfaces. Each DEM data set is identified by its horizontal resolution and is produced to a consistent set of specifications (United States Geospatial Services, n.d.). We use the standard DEM with the resolution of 1/3 arc-second which is approximately 10 m, and the elevation is referenced to the North American Vertical Datum of 1988 (NAVD88).

There are several storm surge simulation models available to the public. One of the tools that NHC uses to predict storm surges is the SLOSH model. The SLOSH model is a computerized numerical model developed by the NWS to estimate storm surge heights resulting from historical, hypothetical, or predicted hurricanes by taking into account the atmospheric pressure, size, forward speed, and track data (Jelesnianski, 1992). Prior to hurricane landfalls, SLOSH is widely used as a support tool for decision makers in emergency management agencies. To enhance decision making, multiple surge-related products provided by NHC are available.

Using SLOSH, the NHC developed the SDP that supports emergency managers in visualizing storm surge vulnerabilities. The SDP outputs the predicted storm surge levels for fan-shaped basins covering the coastal regions by taking four attributes of a hurricane as input: Saffir-Simpson storm category, storm direction, forward speed, and tide level. A basin is divided into smaller grids and the SDP model predicts the surge height above the sea level for each grid. The model outputs storm surge heights for a particular area in feet above the reference sea level NAVD88. To interpret the surge level, users need to subtract the elevation from the surge heights as discussed earlier.

For our surge forecasting tool, we use the SDP. For a particular region, a user can input the four attributes of the hurricane to obtain the Maximum Envelope of Water (MEOW)[3] which provides a worst-case basin snapshot of surge levels for a particular storm category, forward speed, hurricane direction, and tide level. Since the MEOW highlights the worst case of an expected hurricane, it is a time-independent concept, unlike the WRF-Hydro stage height output. The downside of using the time-independent measure is that the duration of high waters is ignored. The SDP output does not indicate how long the storm surge covers the impacted areas. Nonetheless, the MEOW is "robust" from the view point of optimization because it based on the worst-case outcome for a particular storm, instead of, for example, the average outcome or a probability distribution over multiple outcomes.

Before generating storm surge scenarios, we need to study the input parameters of the SDP in more detail. As mentioned earlier, there are four input parameters for the MEOW product: storm direction, intensity, tide level, and forward speed. The available surge outputs in SDP depend on each basin. For the Galveston basin, which we use for our case study, there are nine cardinal trajectory directions available from west-southwest to east-northeast (WSW, W, WNW, NW, NNW, N, NNE, NE, and ENE). We assume that a storm may come in one of nine directions with a fixed storm intensity, tide level, and forward speed. To determine the incoming storm's characteristics other than direction, we study the reference hurricane advisory provided by the NHC. The forecast advisory issued by the NHC provides present movement speed, direction, hurricane track, and maximum wind speed in time series.

To choose the storm intensity represented by the Saffir-Simpson hurricane wind scale, we look at the expected maximum wind speed within the 5-day hurricane forecast

[1]https://cfim.ornl.gov/data/

[2]https://viewer.nationalmap.gov/basic/

[3]https://www.nhc.noaa.gov/surge/meowOverview.php

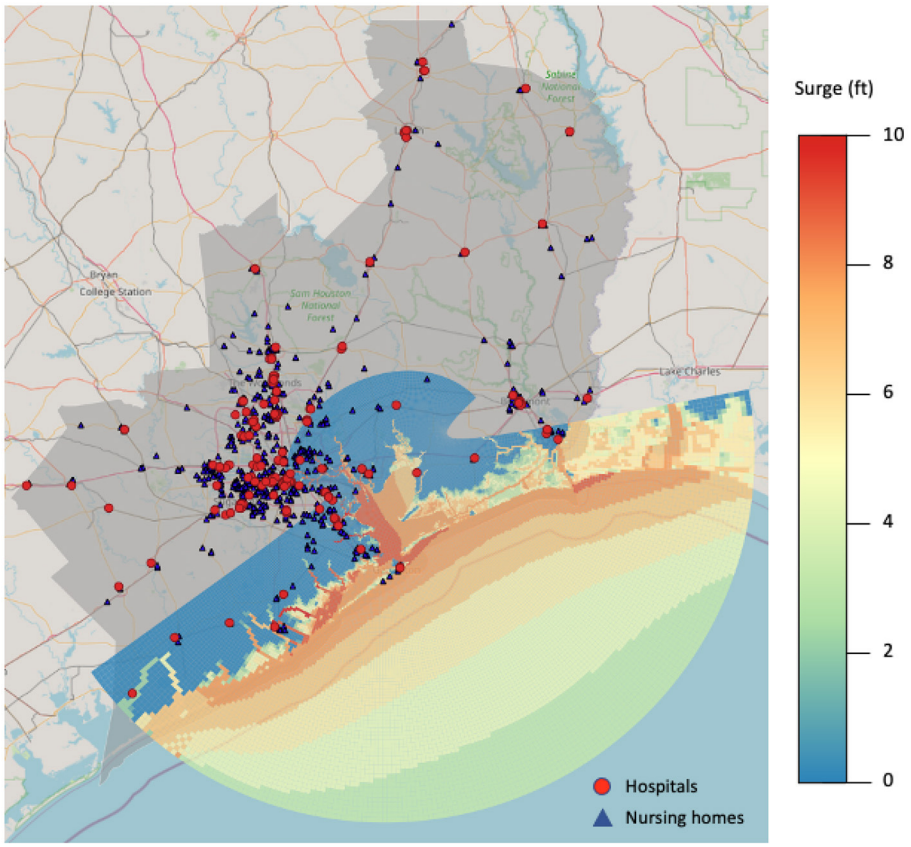

FIGURE 3 | Storm surge output from SDP generated with a Category 2 storm traveling in north direction with forward speed of 5 mph at high tide shows impact on the hospitals (red dots) and nursing homes (blue triangles) in our region of interest.

by the NHC. According to the 5-day Forecast Track and Watch/Warning Graphic of the reference advisory, Advisory 14 (see **Supplementary Figure 1**), the maximum sustained wind speed is listed as 74–110 mph, which can be easily converted to Category 2 of Saffir-Simpson category scale. In the SDP, there are two tide levels available: mean and high tide. Since the tide hours vary by location and SDP does not generate the time-specific output, we assume that the storm makes landfall at the high-tide level. There are three forward speed categories: 5, 10, 15 mph. The forward speed from the advisory is 2 mph. We choose the closest forward speed category, 5 mph, among the three options.

Figure 3 shows a SDP output generated from a Category 2 storm traveling in north direction with forward speed of 5 mph at high tide. Within the study region colored in gray, the hospital and nursing home locations are indicated by red dots and blue triangles, respectively. The elliptical shaped mesh grids are used to output surge levels, and the resolution of each cell ranges from tens to hundreds of meters to a kilometer or more. A darker color indicates a higher surge level.

To cover the hospital locations in our interest region, we collect one-degree blocks of DEM spanning from 29 to 32° N and 94 to 97° W. We use a GIS software, QGIS 3.8, to extract the elevation of hospital locations.

3.3.3. Combined Flood Prediction

Now, we are able to combine each inland flooding scenario with a coastal flooding scenario by matching the direction of a hurricane. For each hurricane scenario, we are able to define the hurricane direction by connecting the sampled landfall location and a reference hurricane center point which is defined as the *current* hurricane location (note that this is different from the earlier reference point, the mean predicted landfall location). To find the current hurricane location we use the GFS forecast generated at 00:00 UTC on August 24th. Once we have the hurricane direction for an inland flooding hurricane scenario, we determine the closest storm direction in the coastal flooding model. This allows us to produce a set of inundated locations due to storm surge. To produce the set of all flooded locations for a particular scenario we then take the union of the set of locations flooded according to the inland model and the set of locations flooded according to the coastal (storm surge) models. Note that our methodology does not take into account combined inland and coastal flooding effects. This is an important direction for future research.

For example, in **Figure 2**, the southern-most landfall location in the simulated inland flooding model is at (24.50° N, 97.58° W). The closest storm direction in SDP to the direction generated

TABLE 1 | Landfall locations and matching storm surge directions.

Scenario name	Latitude (° N)	Longitude (° W)	Landfall location	Direction
L1	24.50	97.58	p1	w
L2	25.14	97.54	p2	wnw
L3	25.46	97.53	p3	wnw
L4	25.67	97.51	p4	wnw
L5	25.68	97.51	p5	wnw
L6	26.21	97.48	p6	wnw
L7	26.22	97.48	p7	wnw
L8	26.68	97.46	p8	wnw
L9	26.74	97.45	p9	nw
L10	26.81	97.45	p10	nw
L11	27.12	97.43	p11	nw
L12	27.13	97.43	p12	nw
L13	27.23	97.42	p13	nw
L14	27.37	97.42	p14	nw
L15	27.40	97.41	p15	nw
L16	27.63	97.40	p16	nw
L17	27.93	97.18	p17	nw
L18	27.95	97.14	p18	nw
L19	28.05	96.97	p19	nw
L20	28.11	96.87	p20	nw
L21	28.22	96.69	p21	nw
L22	28.41	96.37	p22	nnw
L23	28.42	96.36	p23	nnw
L24	28.64	95.99	p24	nnw
L25	29.27	94.95	p25	nnw

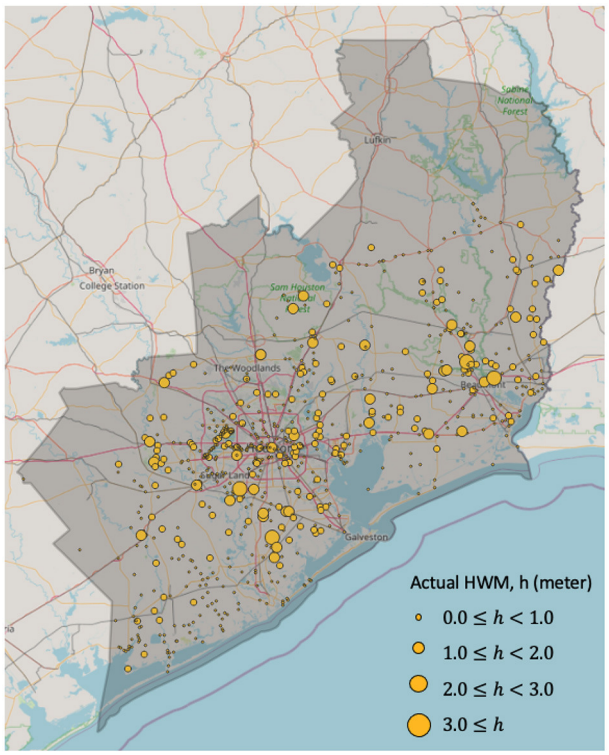

FIGURE 4 | The circles represent the actual HWMs of the 750 sites within the CMOC region.

by connecting the reference hurricane center point at 12 h and the southern-most landfall location is the west direction. The 25 landfall locations and their matching directions are shown in **Table 1**.

4. VALIDATION

Our model validation is performed using the High Water Marks (HWMs) collected by the USGS after Hurricane Harvey[4]. We remove HWM locations outside the region of interest or in catchments of lakes and reservoirs, in which the current WRF-Hydro-HAND methodology cannot provide flooding information. The measurements we used were the maximum HWM reading at each site having an excellent, good, or fair reading. **Figure 4** displays 750 unique HWM sites within our study region. We observe that many HWM sites are concentrated near the center of the figure, close to central Houston.

We evaluate the accuracy of our methodology in flood prediction in capturing using the following rates:

$$\text{Hit Rate (HR)} = P(M_1|H_1) = \frac{P(M_1 \cap H_1)}{P(H_1)} \tag{7}$$

$$\text{False Positive Rate (FPR)} = P(M_1|H_0) = \frac{P(M_1 \cap H_0)}{P(H_0)}. \tag{8}$$

From a statistical viewpoint, we interpret M_0 as the event that the model predicted a site to be dry (0) and M_1 as the event that the model predicted a site to be wet (1) (i.e., flooded). Similarly, H_0 and H_1 indicate events that the site is actually dry (0) and wet (1) by the HWM. Thus, $P(H_1)$ is the number of flooded sites with HWM value greater than threshold level divided by the total number of sites. The threshold is set as 0 m. Unlike the false alarm ratio used in Wing et al. (2017), we use the false positive rate which directly represents the probability of Type 1 error. If the flood predictions are used in evacuation decisions, then it is likely that the false negative rate is more critical than the false positive rate since the consequences of not evacuating a location that floods are usually worse than unnecessarily evacuating. The false negative rate can be easily obtained by subtracting the hit rate from one.

Column (a) in **Table 2** shows the hit rates and false positive rates by computing over all 750 HWM sites. The hit rate and false negative rate improve in the middle scenarios (around L11–L16, around L13) and tend to decrease for landfall locations farther from the mean path (farthest ones are L1 and L25). The false positive rates are higher in the middle scenarios, suggesting that the model tends to overestimate flooding in scenarios where the

[4]https://stn.wim.usgs.gov/FEV/

landfall location is close to the mean path. Note that both rainfall and storm surge are expected to be most severe in the region of interest, in the middle scenarios. In turn, this induces an increase in both the hit rate and an overestimation of flooding in more HWM sites.

In order to assess the effect of catchment size on accuracy, we divide the HWM sites by the area of encompassing catchments. We find the median catchment area and evaluate the model under both metrics for sites within catchments smaller than the median. We perform the same calculation for the remaining sites within larger catchments. Among the 750 sites, there are 318 sites within a catchment area smaller than the median area of 9.26 km^2. The remaining 432 sites are within the larger catchments. In Columns (b) and (c) of **Table 2**, we compare the two metrics obtained from the two types of sites. A similar trend in hit rates and false positive rates is observed. In both cases, the hit rates improve in the middle scenario whereas the false positive rates are worse. Comparing the overall metrics of (a), (b), and (c), the hit rate is the best in the sites in smaller catchments whereas the false positive rate is worse. This suggests that the sensitivity of the flood prediction model is greater for smaller catchments.

In order to provide some graphical intuition for the results of the HWM evaluation, we compare our WRF-Hydro-HAND model results with USGS-FEMA flood-inundation maps (Watson et al., 2018), which are created using HWMs and Lidar elevation data. The modeled results are created with the maximum streamflow in the predicted period. **Figure 5** shows an underestimated case at Reach 1520007 on the East Fork San Jacinto River and its corresponding NHDPlus catchment in the black boundary. The inundation extent in L13 and L25 are similar but smaller than the inundation as estimated from USGS-FEMA. Furthermore, the results from L13 and L25 are very similar to one generated with the National Water Model reanalysis product, which is driven by observed precipitation (results not shown). In contrast, the inundation extent in L1 is small because the precipitation in this scenario is the smallest in our studied region due to the simulated landfall location.

TABLE 2 | The comparison of hit rates (HR) and false positive rates (FPR) for 25 hurricane scenarios.

Scenario	(a) All catchments		(b) Less than median area		(c) Greater than median area	
	HR	FPR	HR	FPR	HR	FPR
L1	0.15	0.15	0.18	0.23	0.13	0.09
L2	0.17	0.19	0.20	0.29	0.14	0.12
L3	0.20	0.22	0.24	0.31	0.16	0.15
L4	0.23	0.22	0.28	0.32	0.19	0.15
L5	0.24	0.22	0.28	0.32	0.20	0.15
L6	0.34	0.31	0.41	0.45	0.28	0.21
L7	0.34	0.31	0.41	0.45	0.28	0.21
L8	0.39	0.40	0.48	0.53	0.32	0.30
L9	0.40	0.40	0.49	0.53	0.33	0.32
L10	0.41	0.42	0.50	0.55	0.35	0.32
L11	0.47	0.47	0.56	0.60	0.39	0.38
L12	0.47	0.46	0.57	0.60	0.39	0.36
L13	0.48	0.52	0.57	0.59	0.41	0.47
L14	0.48	0.56	0.57	0.59	0.42	0.54
L15	0.48	0.55	0.56	0.58	0.42	0.53
L16	0.48	0.54	0.55	0.55	0.43	0.54
L17	0.43	0.41	0.50	0.50	0.38	0.35
L18	0.44	0.39	0.51	0.50	0.38	0.32
L19	0.41	0.33	0.47	0.45	0.36	0.24
L20	0.38	0.31	0.46	0.41	0.33	0.24
L21	0.38	0.29	0.46	0.39	0.32	0.22
L22	0.36	0.31	0.42	0.41	0.31	0.24
L23	0.35	0.31	0.42	0.41	0.31	0.24
L24	0.34	0.35	0.39	0.41	0.30	0.30
L25	0.28	0.22	0.34	0.30	0.24	0.16

5. CASE STUDY

5.1. Study Region and Locations

In our case study, we focus on hospitals and nursing homes in the southeast Texas region. SETRAC, the Southeast Texas Regional Advisory Council, is responsible for coordinating patient evacuation in 25-county service region in and around Houston. For example, during Hurricane Harvey in 2017, SETRAC coordinated 773 patient movement missions that evacuated 1,544 patients from 24 hospitals. As such, SETRAC provided important guidance in formulating the case study described here. To choose hospitals and nursing homes from the greater Houston region, we utilize the datasets from the Homeland Infrastructure Foundation-Level Data (HIFLD)[5]. We choose the facilities by filtering the datasets for Texas and the 25 counties, and by selecting locations with status "open." After filtering the datasets, we find 176 hospitals and 716 nursing homes in our region of interest. Among the 176 hospitals, we remove six hospitals and 14 nursing homes that are not in the catchments of rivers (Liu et al., 2018; Zheng et al., 2018a). The remaining 170 hospitals and 702 nursing homes locations are marked in red dots and blue triangles respectively in **Figure 3**.

To provide potential flood scenarios so that SETRAC can plan patient evacuation missions before the hurricane landfall, the 48 h window before landfall is important. When a hurricane is too close to the coast, the road network is expected to be congested because of the evacuating general population. The mobility of emergency medical service vehicles is also restricted by the wind speed. The 48 h window provides assurance that their evacuation operations is minimally affected by the approaching hurricane while providing the most up-to-date information for generating potential flood maps.

5.2. Inland Flooding Analysis

Our modeling domain of WRF-Hydro is the Texas-Gulf region with the watershed boundary of the USGS 2-digit Hydrologic Unit Code (HUC-2 region 12) with approximately 471,000 km^2. The domain consists of 67,294 NHDPlus river reaches

[5]https://hifld-geoplatform.opendata.arcgis.com/datasets/hospitals

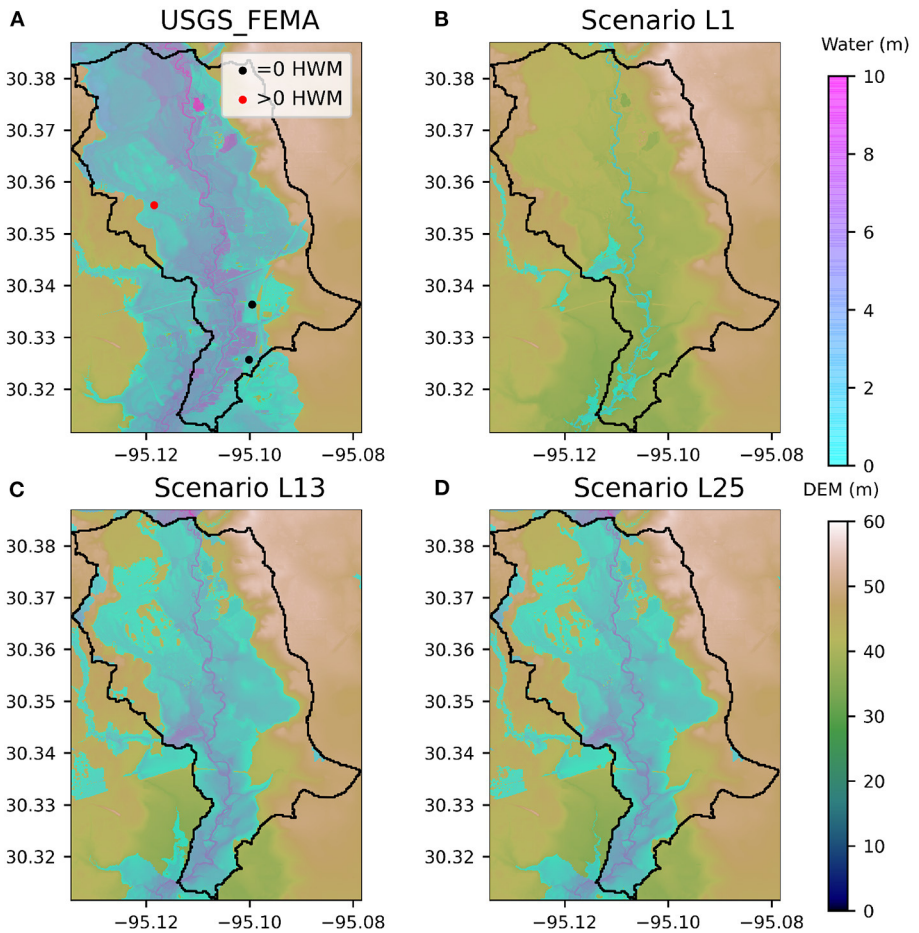

FIGURE 5 | Comparison of inundation maps: **(A)** observed—based on USGS-FEMA, **(B–D)** predicted maximum inundation from scenarios.

and catchments (**Figure 6**). The hospitals and nursing homes in this study are scattered in the area, which is mainly at the lower part of the Colorado River, Brazos River, Trinity River, Neches River, and Sabines River watersheds. Sixty five percent of the studied locations are in the San Jacinto River watershed.

The performance of hydrological simulation is sensitive to the precipitation amount and pattern. **Figure 7** shows the 10-day (from August 24 to September 2, 2017) accumulated precipitation with our studied region highlighted. Here we use the precipitation products from the NASA Global Precipitation Measurement (GPM) (Huffman et al., 2015) as "true" precipitation. Generally, the satellite-based observation shows that most of the precipitation is concentrated in the Houston area. The precipitation forecasts, which are the inputs for WRF-Hydro simulation, are generated on August 24. Compared with GPM, the precipitation forecast predicts that the hurricane would drop heavier rainfall as it makes its first landfall, and the rainfall happens along with the track. It is not surprising that the forecast produced on August 24 is not able to capture the slow movement of the hurricane over eastern Texas. However, among the simulated 25 scenarios, in eleven scenarios, total precipitations in the CMOC region are higher than the precipitation of the mean path scenario (L13). The highest 10-day accumulated precipitation in the CMOC region among all scenarios is 457.26 mm which is experienced in Scenario L21. Total estimated precipitations in all scenarios are lower than the observed precipitation of 549.72 mm.

As part of the Gulf Coastal Plains, the terrain of the majority of the study region is flat, especially for the area close to the coastline (see **Supplementary Figure 3**). The city of Houston is mostly urbanized and flat. Twenty-two hospitals and ten nursing homes are located in one catchment, Brays Bayou (Reach ID 1440385). The HAND values of the address points for hospitals and nursing homes range from 9.45 to 14.40 m, which means that all studied locations are predicted to be flooded when the water level in the channel of Brays Bayou is larger than 14.40 m. Our results suggest that 17 studied locations (13 hospitals and 4 nursing homes in the catchment of Brays Bayou) are estimated to be flooded in a worst-case scenario. These 17 locations have HAND values lower than 11.87 m, which is the maximum predicted stage height.

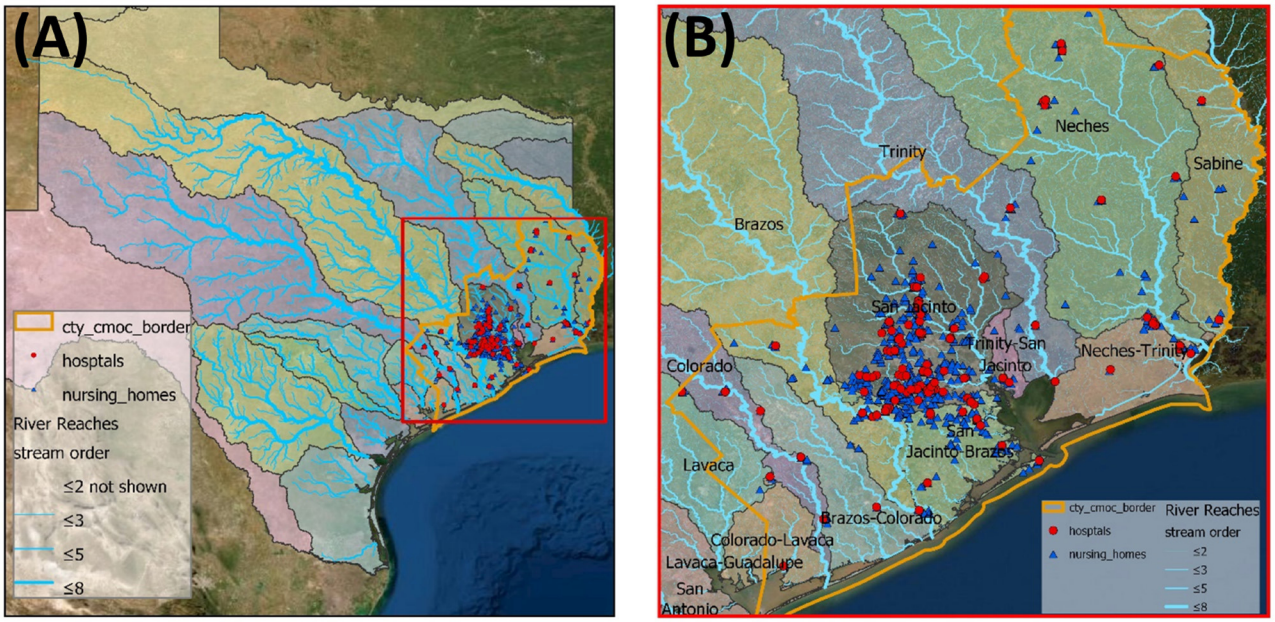

FIGURE 6 | The WRF-Hydro modeling domain within the Texas-Gulf Region. **(A)** Entire modeling domain that consists NHDPlus reaches, **(B)** the region of the hospitals and nursing homes (CMOC).

5.3. Coastal Flooding Analysis

For the 25 flood scenarios, four SDP outputs contribute to the flood mapping. **Table 1** shows that the SDP output generated with the west direction occurs in just one scenario while the west-northwest, northwest and north-northwest directions appear 7, 13, and 4 scenarios, respectively. In the Galveston basin, the maximum surge above the sea level (3.47 m) occurs in the storm surge forecast generated with the northwest direction.

There are nine locations that have mean inundation level greater than the threshold level of 0 m. Among the nine, there are two hospitals (h144, h146) and seven nursing homes (n597, n608, n610, n612, n615, n640, n662). Two nursing homes (n640, n662) are located near Port Arthur, TX, while the rest of the locations are in the Galveston area. **Supplementary Table 4** summarizes storm surge statistics, elevation above sea level (NAV88) and the inundation level of the nine hospitals. There are seven locations (h33, n298, n574, n603, n607, n622, n623) in which the elevation is greater than forecasted surge levels in every scenario resulting the mean inundation level as 0.

5.4. Combined Flooding Analysis

Recall that there are 25 flood sets that are formed by taking the union of the inland and coastal flooding sets. With a threshold level of 0 m, the minimum number of flooded locations (21 locations) is realized in Scenario L1. The number of flooded location is maximum (153 locations) in Scenario L15. The mean number of flooded locations from the 25 scenarios is approximately 92. When the landfall location is expected to be at the southern-most location, the number of flooded hospitals is minimal. When the hurricane landfall location is toward the center of the distribution, the model generates the maximum number of flooded hospitals.

In total, there are 215 locations that experience flooding in at least one of the 25 scenarios. **Figure 8A** shows the mean flood levels (measured above ground level) of the 215 flooded facilities. The darker color indicates a higher mean flood level. Examining the locations of the flooded facilities in the figure, we are able to see that majority of the flooded locations are located in inland. **Figure 8B** shows the locations and their probability of flooding (indicating a positive flood level). Darker colors indicate higher probability of flood level being >0. Comparing the two figures, we highlight that locations with higher flood level are likely to have higher probability of flooding.

There are two locations (n640, n662) that are both impacted by streamflow and storm surge. In our analysis, we assume no interaction between streamflow and storm surge, and define their flood level with higher flood level obtained from either streamflow or storm surge. In both locations, flooding due to streamflow generates higher water level above ground. The mean flood levels of the two locations (n640, n662) from storm surge are (0.555, 0.623 m) while the flood levels from streamflow are (2.923, 2.947 m), respectively.

Table 3 shows how the number of flooded locations changes with increasing the flood threshold level. The mean number of flooded locations due to coastal flooding approaches 0 when the threshold is increased from 0 to 1 m. The maximum number of flooded locations for threshold levels 0.0 and 1.0 m occurs in Scenario L15. When the threshold level is 0.5 m, the number of flooded locations is maximum in Scenario L14. For all threshold levels, the number of flooded locations is minimized in Scenario L1.

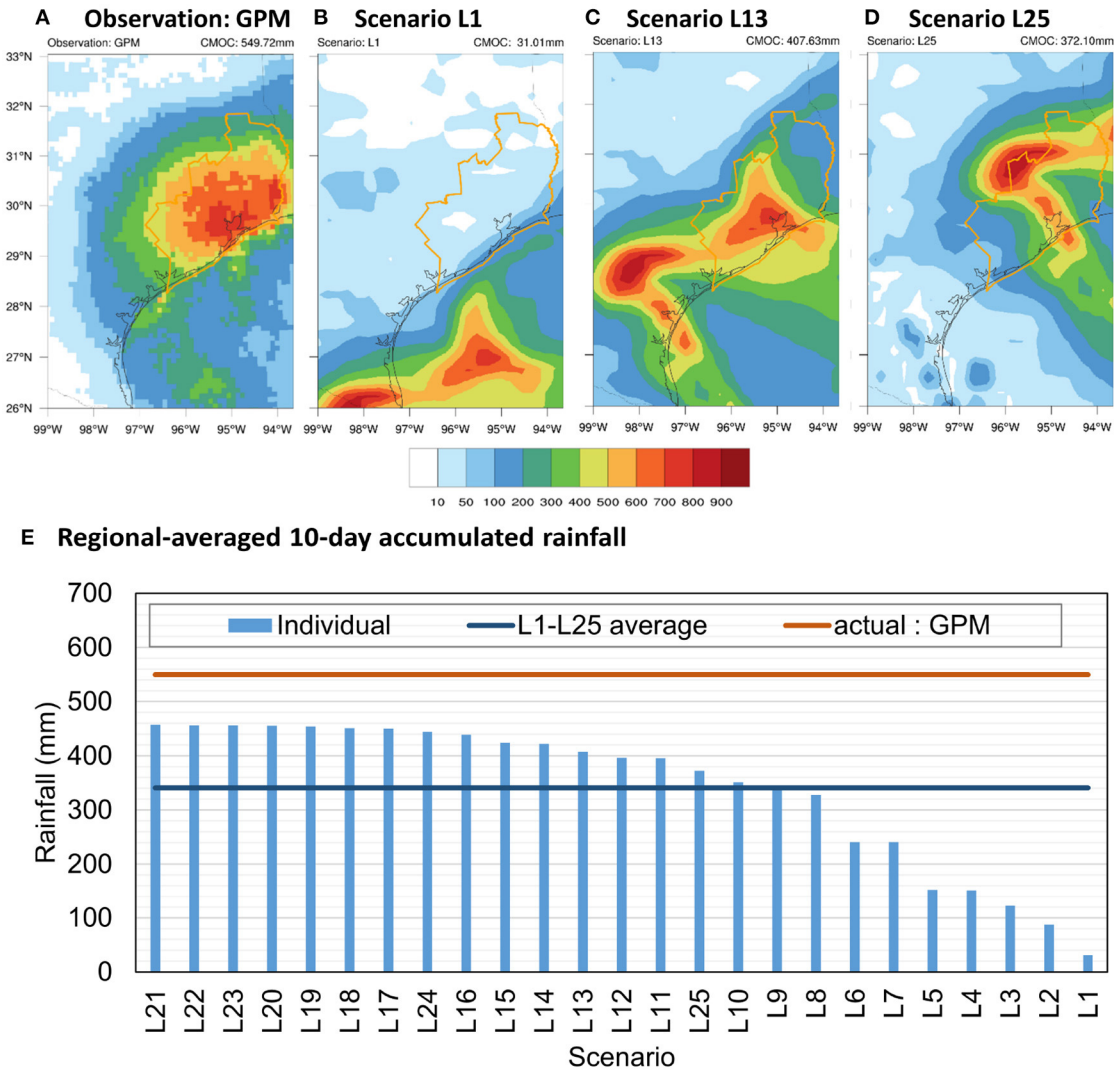

FIGURE 7 | Comparison of 10-day accumulated rainfall in the CMOC region between 25 scenarios (model) and GPM (observation). **(A)** Spatial pattern of GPM, **(B)** results from scenario L1, **(C)** results from L13, **(D)** results from L25, **(E)** CMOC regional-averaged rainfall from scenarios using weather predictions and from satellite-based observations from GPM from August 24 to September 2, 2017.

Now, instead of looking both hospital and nursing home locations, we only look at a subset, the hospitals in the region, to provide more detailed results a decision maker can use with an access to our probabilistic scenario-based analysis. For example, decision makers who plan for mitigation actions for hospital flooding should consider not only the flood probability but also the various statistics of flood levels because the capability of each hospital to withstand flooding is different. As a sampling of such analysis, **Table 4** shows 45 hospital locations subjected to flooding in the 25 scenarios. It shows flooding probabilities of hospital locations and their minimum, maximum, and average flood height. According to the analysis, Hospitals h72 and h151 are expected to suffer from the most severe flooding. Three hospitals (h144, h150, h151) are expected to be flooded in every scenario. The flood probability of Hospital h150 is 1, but the average and maximum flood levels are 0.28 and 0.84 m. Contrast that to Hospital h35, with the average and maximum flood levels at 2.21 and 5.90 m, respectively, and with 0.72 probability of flooding. Although Hospital h150 is expected to be flooded in every scenario, the degree of flooding in this location may not be severe enough to plan for an evacuation. In comparison, due to the magnitude of the expected flood level, it might be a good idea to prepare for flooding (say evacuate) for Hospital h35.

In flood level forecasting, it is useful for evacuation decision makers to ask how often the flood level is above a particular level. **Table 5** shows the complementary cumulative distributions, $P_s(H > h)$, of flood level random variable, H, of 45 flooded hospitals (s). In the table, the flood level values (h), from 0 to 4 m with an increment of 0.5, are chosen to describe the distributions. The probability of Hospital h45 to have flood level >0 is 0.40, and it does not expect a flood level above 0.5 m. This indicates, in any scenario, the maximum flood level at h45 does not exceed

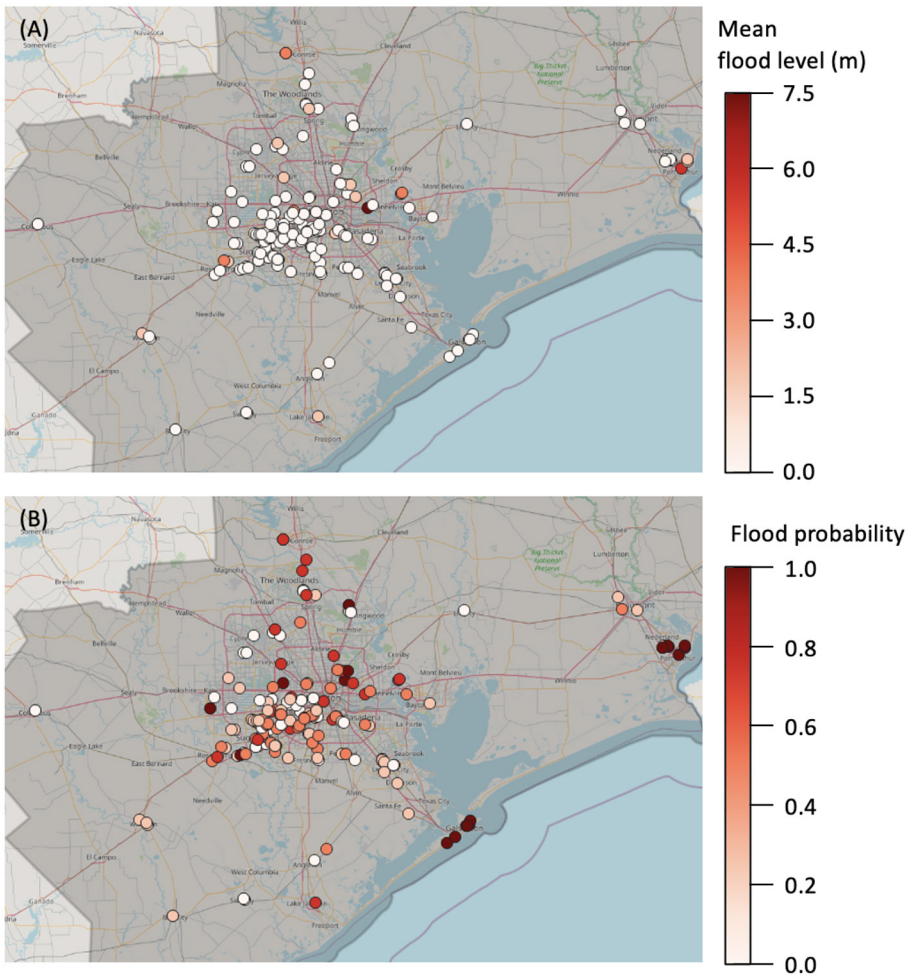

FIGURE 8 | (A) Mean flood levels (calculated from 25 scenarios)—darker colors indicate higher mean flood levels. **(B)** Flood probabilities—darker colors indicate higher probabilities of flooding (i.e., flood level being positive).

TABLE 3 | Number of flooded locations in different threshold levels (ξ).

		$\xi = 0.0$ m			$\xi = 0.5$ m			$\xi = 1.0$ m		
		Min.	**Max.**	**Avg.**	**Min.**	**Max.**	**Avg.**	**Min.**	**Max.**	**Avg.**
Coast	Hospital	1	2	1.96	0	0	0	0	0	0
	Nursing home	7	7	7	3	5	4.64	0	0	0.28
	Total	8	9	8.96	3	5	4.64	0	0	0.28
Inland	Hospital	2	33	17.24	1	23	11.16	1	15	7.64
	Nursing home	13	123	67.76	3	89	44	0	55	26.24
	Total	15	156	85	4	112	55.16	1	70	33.88
	Grand total	21	163	91.96	7	115	58.16	1	70	34.16

0.5 m. On the other hand, the probabilities that Hospital h72 to have flood level >2 and 4 m are 0.68 and 0.60, respectively. From the table, we can also make inferences on the forecasted flood level distribution. For Hospitals h48 and h96, we see that the forecasted flood levels lie in the intervals (0, 0.5m] and (1.5, 2m]. When dealing with a bimodal flood level distribution, such analyses are more useful than looking at the mean and standard deviation of flood levels, as in **Table 4**.

Depending on the flood prevention structures in each hospital, one may be comfortable with certain levels of flood level during flooding events. Another factor in an evacuation decision is the risk preference of the decision maker. The hospital

TABLE 4 | Flood statistics (in meters) and probability of flood level (H) greater than zero for hospitals in the region of interest.

Hospital	Mean	Std.	Min.	Max.	P (H>0)	Hospital	Mean	Std.	Min.	Max.	P (H>0)
h7	0.41	0.45	–	1.04	0.52	h66	0.98	1.13	–	2.43	0.44
h8	–	0.02	–	0.12	0.04	h72	6.14	4.83	–	11.83	0.76
h9	0.03	0.07	–	0.29	0.20	h76	0.09	0.14	–	0.35	0.36
h11	0.18	0.20	–	0.50	0.44	h78	0.01	0.03	–	0.10	0.32
h12	0.43	0.51	–	1.26	0.44	h86	0.77	0.88	–	2.01	0.52
h13	0.01	0.02	–	0.07	0.28	h94	0.01	0.03	–	0.09	0.20
h15	0.30	0.28	–	0.70	0.72	h96	0.67	0.80	–	1.73	0.44
h16	–	–	–	0.02	0.12	h97	–	0.02	–	0.12	0.04
h17	–	0.02	–	0.08	0.08	h98	1.35	1.22	–	2.96	0.64
h20	0.59	0.71	–	1.55	0.44	h101	0.10	0.20	–	0.57	0.32
h24	0.07	0.12	–	0.36	0.32	h107	0.08	0.16	–	0.48	0.24
h28	0.38	0.57	–	1.45	0.32	h110	0.04	0.06	–	0.17	0.32
h30	0.31	0.38	–	0.86	0.40	h116	1.39	1.24	–	3.02	0.64
h35	2.21	1.93	–	5.90	0.72	h123	0.62	0.53	–	1.42	0.72
h43	0.80	0.93	–	2.02	0.44	h130	0.34	0.63	–	1.86	0.28
h45	0.07	0.09	–	0.26	0.40	h138	0.51	0.59	–	1.43	0.52
h47	0.22	0.28	–	0.64	0.40	h139	0.01	0.05	–	0.27	0.04
h48	0.72	0.85	–	1.85	0.44	h144	0.44	0.04	0.30	0.46	1.00
h49	0.20	0.25	–	0.59	0.40	h146	0.14	0.04	–	0.16	0.96
h55	0.36	0.44	–	0.99	0.40	h150	0.28	0.25	0.10	0.84	1.00
h56	–	0.01	–	0.03	0.12	h151	4.86	4.49	1.33	12.43	1.00
h63	0.92	1.07	–	2.30	0.44	h154	0.15	0.40	–	1.50	0.24
h65	0.04	0.13	–	0.58	0.12						

evacuation decision is a unique decision making process because the decision maker is expected to make balanced decisions between financial and medical losses caused by evacuating and unfortunate consequences from not evacuating.

The number of flooded hospitals induced by the mean path scenario (L13) is 39 while the mean number of flooded hospital over all scenarios is 19.2. We generate flood level distribution of each hospital from 25 scenarios. **Supplementary Figure 3** Shows the positions of flood level from mean path (marked as "x") at each hospital's flood level distribution. There are nine hospitals at which the flood level from mean path is at or below the median. Similarly, when the flood levels from mean path are compared to the average of each hospital's flood level (in dots), there are nine hospitals whose average flood levels from the scenarios are greater than the mean path flood levels. There are 39 hospitals whose average flood levels from the scenarios are greater than the median flood levels suggesting distributions to be right-skewed.

6. FUTURE WORK

In preparing for future hurricanes, government agencies continue to rely on flood models that are not designed for specific forthcoming hurricanes, and the comprehensive flood mapping for both inland and coastal area is still in need. In this paper, we have developed a probabilistic scenario generation scheme for hurricane flooding. By sampling landfall locations of an impending hurricane, we simulate inland flooding scenarios and align each of them with a coastal flooding scenario based on the hurricane directions. Considering Hurricane Harvey as our instance, by using the data obtained two days before the hurricane, the uncertainty in hurricane-induced flooding is quantified. We have shown how the probabilistic flood scenarios can support disaster response decisions such as hospital evacuation planning. For this study, we have attempted to replicate flooding scenarios for Hurricane Harvey. We plan to apply our flood scenario generation to multiple hurricane events and compare our predictions with the high-water marks and perform calibration. In the model validation steps, it is suggested that the hit rate of flooding improves when the model is applied to smaller catchments. Incorporating the higher resolution water routing model and enhancing the land surface model in runoff routing due to precipitation will improve the accuracy of the overall methodology.

We plan to reinforce technical aspects of scenario generation. The current method involves locational shifting of meteorological inputs such as precipitation based on the possible hurricane landfall location. We believe that our methodology can take advantage of the improvements in ensemble meteorological forecasting and high performance computing, to achieve an ensemble-based flood forecasting taking advantage of potential cross-disciplinary approaches. We also intend to improve the current technique of data assimilation by calibrating hydrological model outputs with high water mark observations. Moreover, to improve the storm surge-side of the forecasting in flood prediction, we plan to enhance the methods for accounting for more sources of uncertainty. Finally, the scenario generation

TABLE 5 | Complementary cumulative distribution functions of flood level (m) at hospitals.

Hospital	P (H>0.0)	P (H>0.5)	P (H>1.0)	P (H>1.5)	P (H>2.0)	P (H>2.5)	P (H>3.0)	P (H>3.5)	P (H>4.0)
h7	0.52	0.40	0.08	–	–	–	–	–	–
h8	0.04	–	–	–	–	–	–	–	–
h9	0.20	–	–	–	–	–	–	–	–
h11	0.44	0.04	–	–	–	–	–	–	–
h12	0.44	0.40	0.20	–	–	–	–	–	–
h13	0.28	–	–	–	–	–	–	–	–
h15	0.72	0.40	–	–	–	–	–	–	–
h16	0.12	–	–	–	–	–	–	–	–
h17	0.08	–	–	–	–	–	–	–	–
h20	0.44	0.40	0.40	0.12	–	–	–	–	–
h24	0.32	–	–	–	–	–	–	–	–
h28	0.32	0.32	0.24	–	–	–	–	–	–
h30	0.40	0.40	–	–	–	–	–	–	–
h35	0.72	0.68	0.64	0.56	0.52	0.44	0.36	0.32	0.20
h43	0.44	0.44	0.40	0.40	0.04	–	–	–	–
h45	0.40	–	–	–	–	–	–	–	–
h47	0.40	0.32	–	–	–	–	–	–	–
h48	0.44	0.40	0.40	0.40	–	–	–	–	–
h49	0.40	0.24	–	–	–	–	–	–	–
h55	0.40	0.40	–	–	–	–	–	–	–
h56	0.12	–	–	–	–	–	–	–	–
h63	0.44	0.44	0.40	0.40	0.40	–	–	–	–
h65	0.12	0.04	-	–	–	–	–	–	–
h66	0.44	0.44	0.44	0.40	0.40	–	–	–	–
h72	0.76	0.76	0.72	0.68	0.68	0.68	0.68	0.64	0.60
h76	0.36	–	–	–	–	–	–	–	–
h78	0.32	–	–	–	–	–	–	–	–
h86	0.52	0.40	0.40	0.36	0.04	–	–	–	–
h94	0.20	–	–	–	–	–	–	–	–
h96	0.44	0.40	0.40	0.40	–	–	–	–	–
h97	0.04	–	–	–	–	–	–	–	–
h98	0.64	0.60	0.52	0.44	0.44	0.36	–	–	–
h101	0.32	0.12	–	–	–	–	–	–	–
h107	0.24	–	–	–	–	–	–	–	–
h110	0.32	–	–	–	–	–	–	–	–
h116	0.64	0.60	0.52	0.48	0.44	0.36	0.04	–	–
h123	0.72	0.52	0.32	–	–	–	–	–	–
h130	0.28	0.24	0.16	0.16	–	–	–	–	–
h138	0.52	0.44	0.32	–	–	–	–	–	–
h139	0.04	–	–	–	–	–	–	–	–
h144	1.00	–	–	–	–	–	–	–	–
h146	0.96	–	–	–	–	–	–	–	–
h150	1.00	0.24	–	–	–	–	–	–	–
h151	1.00	1.00	1.00	0.64	0.40	0.36	0.36	0.36	0.36
h154	0.24	0.08	0.08	–	–	–	–	–	–

approach can be integrated more directly with the decision making and resource allocation models, giving the involved decision makers better tools to quantify uncertainty and to make more informed mitigation and preparedness decisions.

DATA AVAILABILITY STATEMENT

The raw data supporting the conclusions of this article will be made available by the authors, without undue reservation.

AUTHOR CONTRIBUTIONS

All authors listed have made a substantial, direct and intellectual contribution to the work, and approved it for publication.

FUNDING

NSF grant: CoPe EAGER: Addressing Human-Centric Decision-Making Challenges from Coastal Hazards via Integrated Geosciences Modeling and Stochastic Optimization supported the publication fee along with the support for all the authors. This research was also funded by a grant from the Planet Texas 2050 program at the University of Texas at Austin.

SUPPLEMENTARY MATERIAL

The Supplementary Material for this article can be found online at: https://www.frontiersin.org/articles/10.3389/fclim.2021.610680/full#supplementary-material

REFERENCES

Alcantara, M. A. S., Crawley, S., Stealey, M. J., Nelson, E. J., Ames, D. P., and Jones, N. L. (2017). Open water data solutions for accessing the National Water Model. *Open Water J*. 4:3.

Blake, E. S., and Zelinsky, D. A. (2018). *National Hurricane Center Tropical Cyclone Report: Hurricane Harvey*. Technical report, National Hurricane Center.

Contento, A., Xu, H., and Gardoni, P. (2018). "A physics-based transportable probabilistic model for climate change dependent storm surge," in *Routledge Handbook of Sustainable and Resilient Infrastructure*. 1st Edn, ed P. Gardoni (New York, NY: Routledge), 662–682. doi: 10.4324/9781315142074-34

Dietrich, J., Zijlema, M., Westerink, J., Holthuijsen, L., Dawson, C., Luettich, R. Jr, et al. (2011). Modeling hurricane waves and storm surge using integrally-coupled, scalable computations. *Coast. Eng.* 58, 45–65. doi: 10.1016/j.coastaleng.2010.08.001

Elsberry, R. L. (2002). Predicting hurricane landfall precipitation: optimistic and pessimistic views from the symposium on precipitation extremes. *Bull. Am. Meteorol. Soc.* 83, 1333–1339. doi: 10.1175/1520-0477(2002)083<1333:PHLPOA>2.3.CO;2

Gochis, D., Barlage, M., Cabell, R., Casali, M., Dugger, A., FitzGerald, K., et al. (2020). *The WRF-Hydro®Modeling System Technical Description (Version 5.1.1)*. doi: 10.5281/zenodo.3625238

Gochis, D., Barlage, M., Dugger, A., FitzGerald, K., Karsten, L., McAllister, M., et al. (2018). *The WRF-Hydro Modeling System Technical Description (Version 5.0)*. doi: 10.5065/D6J38RBJ

Gochis, D., Yu, W., and Yates, D. (2015). *The WRF-Hydro Model Technical Description and User's Guide, Version 3.0*. doi: 10.5065/D6DN43TQ

Huffman, G., Stocker, E., Bolvin, D., Nelkin, E., and Tan, J. (2015). *GPM IMERG Final Precipitation L3 1 Day 0.1 Degree x 0.1 Degree V06*. Greenbelt, MD.

Jelesnianski, C. P. (1992). *SLOSH: Sea, Lake, and Overland Surges from Hurricanes, Vol. 48*. U.S. Department of Commerce, National Oceanic and Atmospheric Administration, National Weather Service.

Jia, G., and Taflanidis, A. A. (2013). Kriging metamodeling for approximation of high-dimensional wave and surge responses in real-time storm/hurricane risk assessment. *Comput. Methods Appl. Mech. Eng.* 261, 24–38. doi: 10.1016/j.cma.2013.03.012

Kim, S., Melby, J. A., Nadal-Caraballo, N. C., and Ratcliff, J. (2015). A time-dependent surrogate model for storm surge prediction based on an artificial neural network using high-fidelity synthetic hurricane modeling. *Nat. Hazards* 76, 565–585. doi: 10.1007/s11069-014-1508-6

Liu, Y. Y., Maidment, D. R., Tarboton, D. G., Zheng, X., and Wang, S. (2018). A CyberGIS integration and computation framework for high-resolution continental-scale flood inundation mapping. *JAWRA J. Am. Water Resour. Assoc.* 54, 770–784. doi: 10.1111/1752-1688.12660

Liu, Y. Y., Tarboton, D. G., and Maidment, D. R. (2020). *Height Above Nearest Drainage (HAND) and Hydraulic Property Table for CONUS - Version 0.2.1. (20200601)*. Oak Ridge Leadership Computing Facility.

Mandli, K. T., and Dawson, C. N. (2014). Adaptive mesh refinement for storm surge. *Ocean Model.* 75, 36–50. doi: 10.1016/j.ocemod.2014.01.002

Marchok, T., Rogers, R., and Tuleya, R. (2007). Validation schemes for tropical cyclone quantitative precipitation forecasts: evaluation of operational models for U.S. landfalling cases. *Weath. Forecast.* 22, 726–746. doi: 10.1175/WAF1024.1

National Hurricane Center (n.d.a). *NHC GIS Archive - Tropical Cyclone Advisory Forecast*. Available online at: https://www.nhc.noaa.gov/gis/archive_forecast_results.php?id=al09&year=2017&name=Hurricane%20HARVEY

National Hurricane Center (n.d.b). *Sea Lake and Overland Surge from Hurricanes (SLOSH)*. Available online at: https://slosh.nws.noaa.gov/slosh/index.php?L=7#intro

National Oceanic and Atmospheric Administration (2018). *Inland Flooding: A Hidden Danger of Tropical Cyclone*. Available online at: https://www.noaa.gov/stories/inland-flooding-hidden-danger-of-tropical-cyclones

NOAA National Centers for Environmental Information (NCEI) (2020). *U.S. Billion-Dollar Weather and Climate Disasters*. Available online at: https://www.ncdc.noaa.gov/billions/

United States Geospatial Services (n.d.). *About 3DEP Products & Services*. Available online at: https://www.usgs.gov/core-science-systems/ngp/3dep/about-3dep-products-services

Watson, K., Welborn, T., Stengel, V., Wallace, D., and McDowell, J. (2018). *Data Used to Characterize Peak Streamflows and Flood Inundation Resulting From Hurricane Harvey of Selected Areas in Southeastern Texas and Southwestern Louisiana, August-September 2017: U.S. Geological Survey Data Release*. doi: 10.3133/sir20185070

Westerink, J. J., Luettich R. Jr., Blain, C., and Scheffner, N. W. (1994). *ADCIRC: An Advanced Three-Dimensional Circulation Model for Shelves, Coasts, and Estuaries. Report 2. User's Manual for ADCIRC-2DDI*. Technical report, ARMY Engineer Waterways Experiment Station, Vicksburg, MS.

Wing, O. E., Bates, P. D., Sampson, C. C., Smith, A. M., Johnson, K. A., and Erickson, T. A. (2017). Validation of a 30 m resolution flood hazard model of the conterminous United States. *Water Resour. Res.* 53, 7968–7986. doi: 10.1002/2017WR020917

Zheng, X., Maidment, D. R., Tarboton, D. G., Liu, Y. Y., and Passalacqua, P. (2018a). GeoFlood: Large-scale flood inundation mapping based on high-resolution terrain analysis. *Water Resour. Res.* 54, 10–13. doi: 10.1029/2018WR023457

Zheng, X., Tarboton, D. G., Maidment, D. R., Liu, Y. Y., and Passalacqua, P. (2018b). River channel geometry and rating curve estimation using height above the nearest drainage. *JAWRA J. Am. Water Resour. Assoc.* 54, 785–806. doi: 10.1111/1752-1688.12661

Conflict of Interest: The authors declare that the research was conducted in the absence of any commercial or financial relationships that could be construed as a potential conflict of interest.

frontiers in Water

ORIGINAL RESEARCH
published: 15 March 2021
doi: 10.3389/frwa.2021.628829

Assessment of Riverine Dredging Impact on Flooding in Low-Gradient Coastal Rivers Using a Hybrid 1D/2D Hydrodynamic Model

*Haitham A. Saad and Emad H. Habib**

Department of Civil Engineering, Louisiana Watershed Flood Center, University of Louisiana at Lafayette, Lafayette, LA, United States

The current study investigates the effect of large-scale channel modifications via riverine dredging on flood dynamics in low-gradient river systems located in inland-coastal flood transition zones. The study site is the Vermilion River in south Louisiana, US, which is characterized by complex flow regimes, reversal and bi-directional flows, presence of large swamps with significant river-swamp interactions, and large volumes of runoff contributions from lateral tributaries. The study aims to understand the interplay of these factors and how they modulate and get affected by different dredging approaches that vary in spatial extent and the modifications introduced to the channel. The study deploys a hybrid, one-/two-dimensional (1D/2D), hydrodynamic model that simulates flow and stage dynamics in the main river and its major tributaries, as well as the flow exchanges with the interconnected swamp system. Overall, the results show that the dredging activities can significantly alter the flow regime in the watershed and affect flow exchanges between the river and the swamp system. In terms of flooding impact, only dredging approaches that are extensive in spatial extent and modifications to channel longitudinal slope can result in sizeable reductions in flood stages. However, these benefits come at the expense of significant increases in the amplitude and inland propagation of the Gulf tidal wave. On the other hand, less-extensive dredging can still provide moderate and spatially limited flood mitigation; however, they further expose downstream communities to increased levels of flooding, especially during more frequent events. The results reveal that while dredging can increase the hydraulic conveyance of the river system, the large runoff volumes delivered by the urbanized tributaries seem to outweigh the added improvement in the in-channel storage, thus reducing the anticipated flood relief. The results suggest that a watershed-centered approach, instead of a riverine-centered approach is needed for flood management in these systems so that the relative benefits and tradeoffs of different mitigation alternatives can be examined.

Keywords: riverine dredging, channel modification, tidal propagation, swamps, floods, reverse flows

OPEN ACCESS

Edited by:
Valentina Prigiobbe, Stevens Institute of Technology, United States

Reviewed by:
Hong Xuan Do, Ho Chi Minh City University of Agriculture and Forestry, Vietnam
Hatim O. Sharif, University of Texas at San Antonio, United States

****Correspondence:***
Emad H. Habib
emad.habib@louisiana.edu

Specialty section:
This article was submitted to Water and Built Environment, a section of the journal Frontiers in Water

Received: *13 November 2020*
Accepted: *15 February 2021*
Published: *15 March 2021*

Citation:
Saad HA and Habib EH (2021) Assessment of Riverine Dredging Impact on Flooding in Low-Gradient Coastal Rivers Using a Hybrid 1D/2D Hydrodynamic Model. Front. Water 3:628829. doi: 10.3389/frwa.2021.628829

INTRODUCTION

Watersheds that are located in inland-coastal transition zones (Bilskie and Hagen, 2018) are increasingly subject to extreme flooding due to both man-made alterations and natural processes. Examples of such processes include compound inland and coastal storms, accelerated relative sea-level rise, and increased population and urbanization (Crossett et al., 2013; NCEI, 2020). Flooding in these areas is further exacerbated by the typical low gradients that characterize the main rivers and their tributaries. Flow regimes under low-gradient conditions typically lead to channel sedimentation and reduction of the channel conveyance capacity, and thus an increase in fluvial flooding during moderate and extreme storms.

Flood mitigation measures are often sought in these regions to alleviate the impact of riverine-induced flooding. One of the traditional and most common flood mitigation practices in coastal watersheds is watercourse dredging or channelization (Liao et al., 2019). Dredging refers to activities that include any combination of removing instream and riparian sediment and vegetation, modifying channel width, depth, and gradient, and straightening the river (Hooke, 1990). By structurally altering one or more of the hydraulic variables that govern channel flow and its conveyance capacity (e.g., slope, depth, width, roughness), the water stages are typically decreased, which can reduce the spatial extent of the flood inundation and the associated flood risk.

Early studies on watercourse dredging provided empirical and theoretical evidence that channelization, if appropriately designed to prevent the bank erosion and channel silting, can be quite effective as a flood mitigation measure (Nunnally, 1978; Shankman and Pugh, 1992). However, recent feasibility studies examined potential dredging scenarios for tidally-dominated sections of coastal rivers in southwest UK and demonstrated that dredging did not lower the peak flood levels significantly during winter storms (Webster et al., 2014). The study showed that the shape of the river cross-section and the heights of the riverbanks played a significant role in determining the actual flood level reduction. Other studies showed that dredging can have unintended consequences in other parts of the watershed, especially in the downstream communities. For example, Prestegaard et al. (1994) reported that areas downstream of a modified section of the Raccoon River in Iowa had experienced higher-magnitude floods compared to sections from rivers that have upstream similarly-sized drainage areas. Rose and Peters (2001) showed that channel cross-section enlargement increases the flood wave velocity, thereby speeding the arrival time of flood peaks downstream.

Other studies have focused primarily on the adverse effects of channelization on water quality (Schoof, 1980), ecological alterations of the stream and the riparian corridor (Juan et al., 2020), and stream degradation (Pierce and King, 2013). Another potential aspect of river dredging activities is the effect on tidal propagation. Cai et al. (2012) applied an analytical model to show that a reduction in river discharge and degradation of the riverbed both lead to a significant reduction in the travel time of the tidal wave. The study also highlighted that the amplification of the tidal amplitude, as a result of dredging, could facilitate the penetration of storm surges into the estuary. Likewise, Ralston et al. (2019) studied the effect of dredging on New York Harbor and the tidal Hudson River and found that such modification doubled the tidal amplitude and increased the landward conveyance of coastal storm surge.

While dredging can increase the hydraulic efficiency of river channels and potentially reduce overbank flooding, the impact on flow hydrodynamics and the overall flooding regime needs to be better understood, especially in watersheds that are located within inland-coastal transition zones. In such regions, river systems are typically characterized with complex flow dynamics due to factors, such as flow reversals and bi-directional flows (e.g., Burton and Demas, 2016; Watson et al., 2017), dynamic connectivity and flow exchanges with large natural storage areas, such as swamps and wetlands (Saad et al., 2020); tidal influences, and the large volumes of synchronized tributary flows from urbanized sub-watersheds (e.g., Pattison et al., 2014; Wang et al., 2019). The complexity of flow regimes in these regions has implications for flood mitigation; therefore, it is imperative to develop a comprehensive understanding of the impacts of riverine dredging that emerge as a possible mitigation strategy in response to decreased channel capacities and increased flood risk. This study deploys a hydrodynamic model to investigate the various impacts of channel dredging and their implications for flood mitigation and how it may alter the overall flow regime. The study site is in the Vermilion River in southern Louisiana, US, a representative of low-gradient tidally-influenced river systems that are located in flood transition zones. The study focuses on understanding the effect on flow regime and reduction in water surface elevations under a suite of dredging approaches that represent varying degrees of channel cross-sectional modifications, changes to the riverbed slope, and the spatial extent of the dredging along the river. The analysis will be performed for different storm conditions (e.g., 10-year and >100-year return periods) to assess the dependence on the storm magnitude and the amount of runoff generated in the watershed. A special attention is given to how dredging may also alter the river-swamp interactions. Swamps, which are a common feature in low-gradient coastal watersheds, play a significant role in flood mitigation and provide flood relief in large river basins (Wu et al., 2020). The scientific literature shows a need for understanding the impact of riverine dredging on flow exchanges with swamp areas and their ecosystem viability. Given the direct connection with the Gulf of Mexico, the analysis will also examine the effects of the spatial location and extent of the dredging on the amplitude and propagation of the tidal wave along the river. Besides the main river, it is also of importance to assess the propagation of any potential flood mitigation benefits into the tributaries that are connected to the river. Unlike most previous studies that depended on 1-dimensional (1D) hydraulic modeling in simulating pre- and post-dredging conditions, the current study utilizes a hybrid 1D/2D approach that allows for more accurate representation of the flow dynamics in low-gradient complex river systems (Saad et al., 2020).

METHODS

Study Area

The Vermilion River is a tidally-influenced river located in south central Louisiana, US, and has a watershed that covers an area of about 1,560 km^2 (**Figure 1**). The Vermilion River basin, a representative of other low-gradient inland-coastal transitional basins (Bilskie and Hagen, 2018), has a long history of severe flooding since the major flood that occurred in August 1940 until the most recent in August 2016 (USACE, 1995; Watson et al., 2017). The river starts at the confluence of Bayou Bourbeux and Bayou Fusilier, after which it travels ∼115 km until it intersects with the Gulf Intracoastal Waterway (GIWW). The river eventually drains into the Gulf of Mexico through the Vermilion Bay. The river functions as a major artery that collects runoff from many intersecting lateral tributaries, locally referred to as coulees (Kim et al., 2012). The Vermilion River receives flow diversions from another river in the east, Bayou Teche, through Bayou Fusilier and Ruth Canal (**Figure 1**). Flow diversions are regulated through a concrete weir and a manually-operated gate that permits about 25% the flow of Bayou Teche to be diverted during non-flood conditions (Baker, 1988).

A major feature that adds complexity to flood dynamics in the basin is a series of inter-connected swamps and lakes, locally known as the Bayou Tortue Swamp and Lake Martin (**Figure 1**) that occupy a large area of the watershed (∼35.2 km^2). These swamps function as a natural storage area by accepting reverse flows (i.e., flow traveling upstream) from the Vermilion River. During low and normal river stages, the river collects inflows from its tributaries and travels downstream (south) toward the bay. However, during extreme flooding events, the river becomes bidirectional and shows a reverse flow toward the north where it drains into the Bayou Tortue swamps. The division point between downstream flows (toward the Vermilion Bay) and upstream flows (toward the Bayou Tortue swamps) depends on the severity of the flooding event. During high-frequency events, the bidirectional flow often initiates where one of the main tributaries, Coulee Mine, enters the river (**Figure 1**). If the storm event is extreme enough, a further downstream change in bidirectional flow division may occur where two other major tributaries, Coulee Ile des Cannes and Isaac Verot Coulee, enter the river. In both cases, extensive flooding occurs along many reaches of the river and its tributaries, and especially over the urbanized areas of the City of Lafayette and its surrounding communities. Examples of reverse flows are shown in **Figure 2**. The hydrographs also show excessively slow recession of flood peaks, which are driven by outflows from the swamp after the river stage has started to recede. Observations on river stage and streamflow are available at four locations within the domain of interest to the current study (**Figure 1**). Stage measurements are available at three road crossings over the Vermilion river, namely Surrey, HWY733, and Perry, while the fourth location is just upstream the inlet control gates of Ruth canal (**Figure 1**). Streamflow (flow rate) data are available only at Surrey and Perry gauges. More details about the streamflow observations are available in the **Supplementary Material**.

The historically navigable reach of the Vermilion River extends between the City of Lafayette (river kilometer of 76, measured from the river mouth at the Vermilion bay) and the GIWW (river kilometer 5), and has periodically been subject to channel dredging for maintenance purposes. However, due to the declining navigation activities and other logistical reasons, the river has not been dredged for the last two decades. This has resulted in riverbed shoaling and reduction in the conveyance capacity of the river, especially in the central reaches that pass through the urbanized sub-watersheds in Lafayette.

Simulation Periods

The dredging analysis of this study was conducted for two multi-storm simulation periods, August 1st−30th, 2016 and May 15th–June 5th, 2014 (**Figure 2**), that capture different storm magnitudes and flooding impacts. The two simulation periods were associated with widespread flooding in different parts of the watershed. The stage and streamflow hydrographs observed during both periods clearly illustrate the reverse flows that happen within the Vermilion River, as well as the extremely slow recession that continue for several days after the end of the rainfall storm.

The August 2016 storms generated devastating flooding within the basin and across many areas of the state (van der Wiel et al., 2017; Watson et al., 2017). Based on a rainfall duration-depth analysis, the August 2016 storm can be classified as a 100–200-year storm. A total of 762 mm of rainfall was recorded during the August 2016 period, with hourly rainfall intensities exceeding 90 mm/h. Rainfall events during the 2014 simulation period can be classified as a 2–10-year storm, depending on the duration considered. During the May–June 2014 period, a total rainfall depth of 250 mm was recorded, with hourly rainfall intensities reaching 37 mm/h, causing significant flooding where lateral coulees meet the Vermilion River (Advanced Hydrologic Prediction Service, 2018).

Hydrodynamic Model

In this study, an unsteady hybrid 1D/2D hydrodynamic model for the Vermilion River and its main tributaries was used to simulate the existing conditions and the proposed dredging scenarios. The model is an expansion of an earlier version (Saad et al., 2020) that was developed using the Hydrologic Engineering Center's River Analysis System (HEC-RAS) version 5.0.7. The HEC-RAS system allows for 1D and 2D unsteady flow simulations using either dynamic or diffusive wave approximations of the shallow water equations. For the purposes of this study, the HEC-RAS 1D solver was used in the case of 1D simulations (e.g., the main channel of the river) to solve the full 1D St. Venant equations for unsteady open channel flow. These equations are discretized using the finite difference method and solved using a four point implicit method (USACE, 2016). For 2D simulations, this study opted to use the diffusive wave approximation of the shallow water equations since similar results were obtained when the full dynamic solver was used. While performing the 2D computations, the HEC-RAS uses an implicit finite difference scheme to discretize time derivatives and a combination of finite difference

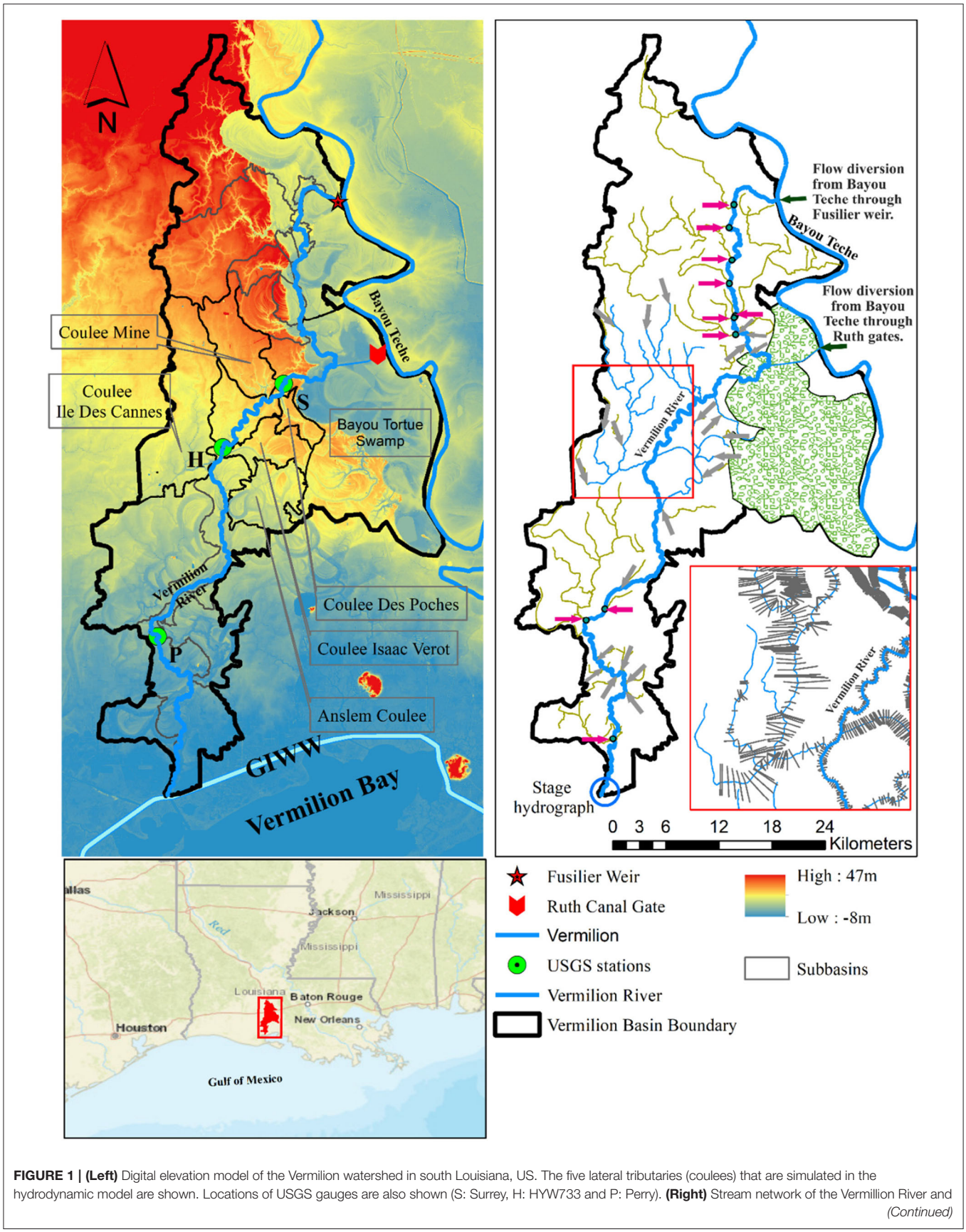

FIGURE 1 | (Left) Digital elevation model of the Vermilion watershed in south Louisiana, US. The five lateral tributaries (coulees) that are simulated in the hydrodynamic model are shown. Locations of USGS gauges are also shown (S: Surrey, H: HYW733 and P: Perry). **(Right)** Stream network of the Vermillion River and

(Continued)

FIGURE 1 | its 15 tributaries. Streams in blue represent the main river and the five tributaries that are explicitly simulated in the hydrodynamic model as 1D reaches. Gray arrows indicate locations of NWM streamflow hydrographs that feed the upstream ends of the five tributaries. Streams in green represent the other 10 tributaries that were not explicitly simulated in the hydrodynamic model. NWM streamflow hydrographs at the outlets of the 10 tributaries were directly provided into the main river (red arrows). The model is forced by a stage hydrograph at its most downstream boundary and by two upstream streamflow hydrographs that capture flow diversions from Bayou Teche through Ruth Canal gates and Fuselier Weir. The swamp area (hatched) is represented in the model using a 2D setup and is enforced by direct rainfall-over-grid from the Stage IV radar-rainfall product. The inset in the right panel shows an example representation of channel cross sections used in the 1D hydrodynamic simulations.

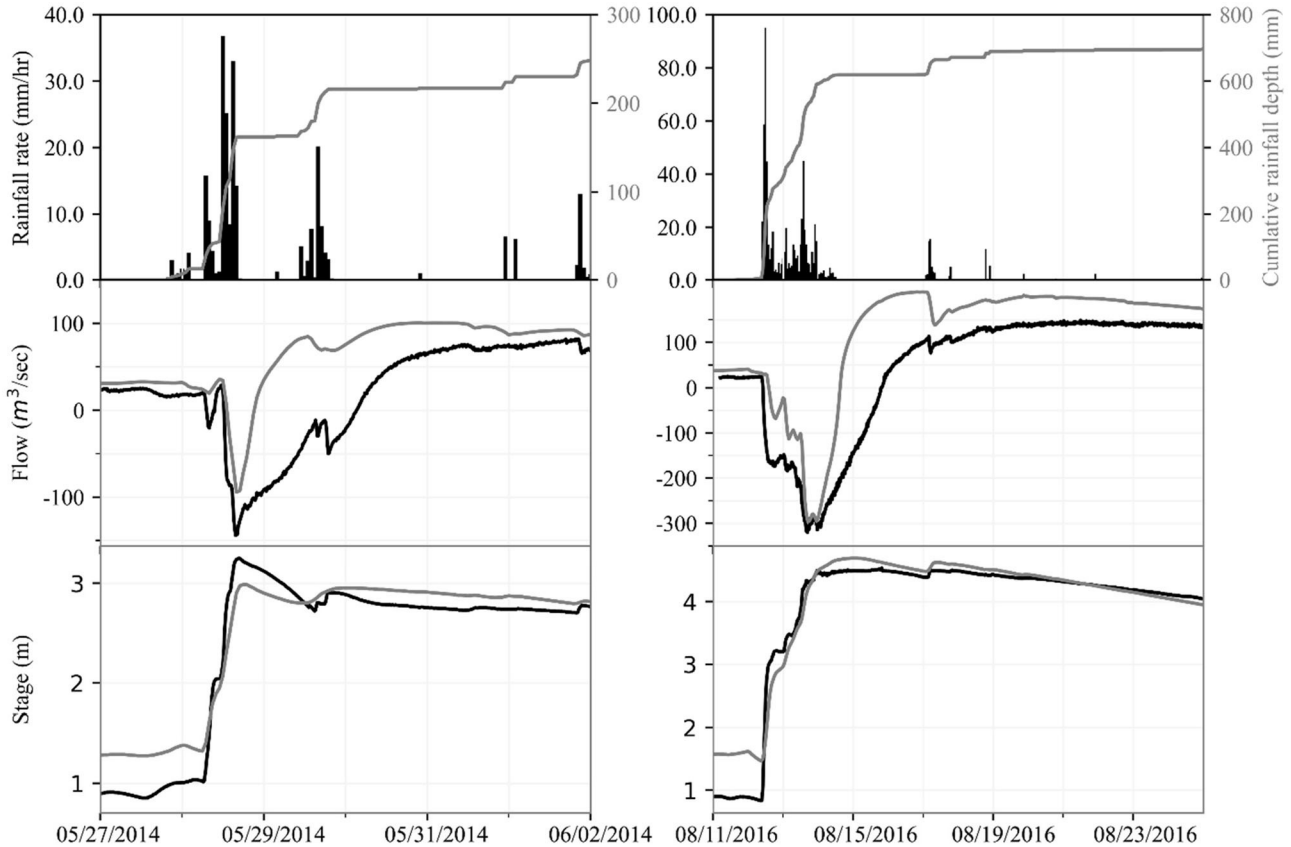

FIGURE 2 | (Top) Hourly rainfall rates (black) and accumulations (gray) extracted from the Stage IV radar product. **(Middle and lower)** Streamflow and stage hydrographs at the USGS Surrey gauge during the 2014 (left) and 2016 (right) simulation periods. Model simulations are in gray and USGS observations are in black.

and finite volume solver (hybrid discretization) to solve for spatial derivatives.

Model 1D/2D Setup

The model encompasses a total of 115 km of the mainstream of the Vermilion River (**Figure 1**), starting at its headwaters, where a flow hydrograph from the Fusilier weir provides an upstream boundary condition. The river also receives flows through the Ruth canal structure that conveys flows from Bayou Teche to Vermilion River. Time-series of flow diversions through the Ruth canal structure and over the Fusilier weir were constructed based on information provided by the Teche-Vermilion Freshwater District responsible for operation of the structures. The model terminates at its intersection with the GIWW, where a stage hydrograph available from a Gulf monitoring station is used as downstream boundary condition.

The hybrid 1D-2D model setup includes the mainstem of the river and five of its major tributaries represented as 1D (**Figure 1**), while the Bayou Tortue swamp system and its surrounding areas were represented as 2D (**Figure 3**). The narrow and steep-sided channel of the Vermilion River (Kinsland and Wildgen, 2006) makes the 1D characterization of the river rather reasonable. Significant flow exchanges occur between the river and the Bayou Tortue swamp system through several tributaries as well as direct bank overflows. To simulate such exchanges, a 2D setup was used to represent the swamp using a total of eight 2D flow areas (**Figure 3**). An unstructured mesh was developed with varying resolutions of 30–90 m. The varying resolution was needed to address model stability and terrain

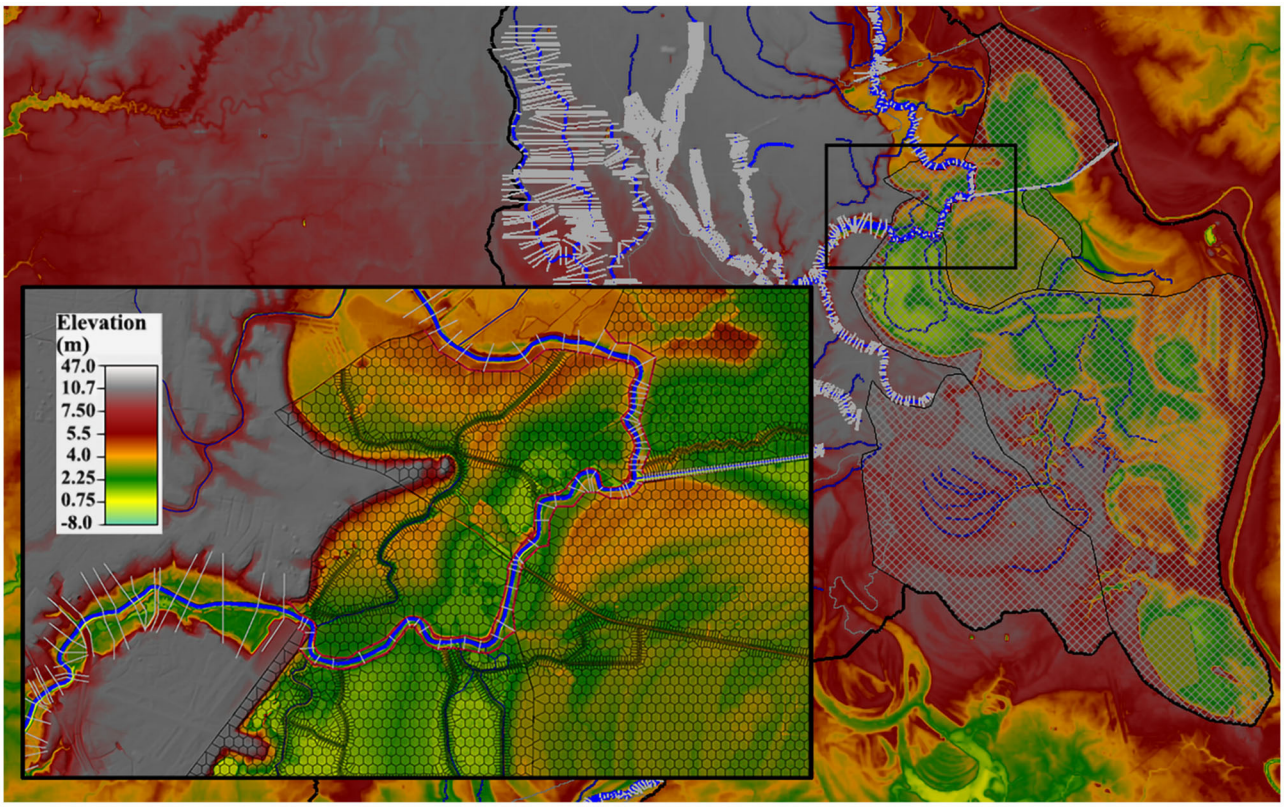

FIGURE 3 | Bayou Tortue swamp system represented using a 2D setup in the hydrodynamic model. The close-up view shows the Vermilion River (modeled as 1D) flowing through the Bayou Tortue swamp. The red lines around the riverbanks represent a set of fictitious lateral structures that were used to simulate the connection between the river and the swamp.

representation. Generally, a fine mesh size was heavily enforced around breaklines and in areas where abrupt changes in the velocity field was encountered. Breaklines were used in the 2D areas to enforce key features of the terrain and ensure that the model reasonably simulates the movement of overland flow. Breaklines were used along channels with concentrated flows and ridgelines that allow flows to spill from one area to another across features, such as road embankments, levees, and natural ridgelines. On the other hand, a coarse mesh resolution was adopted in areas where the 2D flow is relatively uniform. Even in areas with relatively coarse computational grids, a reasonable representation of the swamp hydrodynamics is achieved due to the HEC-RAS implementation of a sub-grid approach that allows for a relatively coarse grid while capturing the finer scale underlying topography (Brunner, 2016). To allow for flow exchanges between the river and the swamp, the 1D (river) and 2D (swamp) parts of the model were coupled through lateral connections represented in the model as fictitious weir structures. During the unsteady flow simulation, the solution algorithm allows for direct feedback at each time step between the 1D and 2D flow elements, which enables an accurate calculation of headwater, tailwater, flow, and any submergence that occurs at the hydraulic structure on a time-step-by-step basis.

Representation of Tributaries and Surface Runoff

Along its main course, the Vermilion River receives runoff contributions from 15 main tributaries and about 23 minor lateral streams. Due to the absence of tributary streamflow observations, the current study depended on readily-available hydrologic simulations from the National Water Model (NWM) Reanalysis to obtain tributary streamflow hydrographs. These tributary hydrographs were then used to drive the hydrodynamic model simulations (red and gray arrows in **Figure 1**). The NWM is a modeling framework that depends on a fully coupled surface/subsurface hydrological model called WRF-Hydro (Gochis et al., 2018). The NWM uses diffusive wave surface routing and saturated subsurface flow routing on a 250-m grid, and channel routing down the NHDPlus stream reaches using the Muskingum-Cunge (MC) method (Shastry et al., 2017). Only five major tributaries (Coulee Des Poches, Coulee Mine, Coulee Isaac Verot, Coulee Ile Des Cannes, and Anslem Coulee), were explicitly simulated in the hydraulic model as 1D reaches (**Figure 1**). These specific tributaries were selected since they play a key role in the river hydrodynamics. Hydrographs were extracted from the NWM dataset at the outlets of the lower-order streams of the five tributaries (gray

arrows in **Figure 1**) and the outlets of the 10 main tributaries that were not fully included in the hydrodynamic model (red arrows in **Figure 1**). These hydrographs were then used to drive the 1D hydrodynamic simulations of the five tributaries and the main river. Examples of NWM hydrographs that were used to enforce the hydrodynamic model are shown in the **Supplementary Material**.

It is also noted that, besides the concentrated streamflow hydrographs, additional overland streamflow hydrographs were extracted from the spatially-distributed NWM outputs. These were then provided as laterally-distributed hydrographs to the 1D reaches of the five tributaries and the main river to capture overland surface runoff that drain directly to the channels (see **Supplementary Material** for more details). Additional surface runoff comes from direct rainfall over the Bayou Tortue swamps. Since the swamps were represented in the model using a 2D setup, a rainfall-on-grid HEC-RAS approach was adopted over the swamps. Rainfall data was available via the hourly, spatially distributed (4×4 km^2) Stage IV radar-rainfall product (Eldardiry et al., 2015). Hourly Stage IV rainfall data were extracted over each of the eight 2D swamp areas and used to drive the 2D hydrodynamic simulations over the swamp domain.

Terrain and Land-Use Representation

A modified terrain model was developed for the Vermilion River basin using a combination of cross sectional surveys, high-resolution LiDAR-based Digital Elevation Models (DEM; Cunningham et al., 2009), and detailed bathymetric surveys for the river (USACE, 2015). To compensate for the inability of the LiDAR technology to "see-through" the water surface (Cook and Merwade, 2009), the LiDAR DEM and the riverine bathymetry were merged to generate an improved terrain model that includes the riverbed survey along the channel reaches and the DEM data elsewhere in the model domain. The merged terrain model was hydrodynamically-corrected following Jarihani et al. (2015). Merging these elevation sources into a single DEM, while keeping the priority for the local surveys and river bathymetry in overlap areas, produces a base DEM that is used in the hydraulic modeling and subsequent analysis of dredging scenarios.

The Vermilion River watershed exhibits a significant heterogeneity in the land-use and land-cover characteristics. To reliably model the flood response of the watershed, the 2011 30-m National Land Cover Database (NLCD) (Homer et al., 2015) was used to develop a lookup table that links each NLCD grid cell with a representative value of the Manning's roughness coefficient. This allowed the model to incorporate a spatially distributed representation for overland and channel roughness characteristics.

Model Calibration

The model was calibrated using the May–June 2014 multi-storm simulation period, while the results were tested under the August 2016 simulation period (**Figure 2**). Due to the lack of adequate flow and stage observations in the basin, only a limited level of model calibration was possible. A visual-based calibration was performed to adjust the model parameters by focusing on key attributes of the river flow regime during flood events (e.g., reverse flows, river-swamp flow exchanges, slow recession of flood waves). The calibration was done primarily by adjusting the Manning's roughness coefficient in the channel reaches that were simulated as 1D and the swamp areas that were simulated as 2D. In channel reaches, the roughness coefficient was adjusted for the main channel as well as for the overbanks. The calibration focused primarily on simulating the magnitudes and timings of flow and stage peaks at the two gauges. In calibrating the model, special attention was given to re-produce the reverse flows that were observed at the Surrey gauge, which is an indication of the model's ability to capture river-to-swamp flow exchanges. Adjustments roughness coefficients were also spatially adjusted over the swamp areas that were simulated using a 2D grid. The adjustments were key in improving the model's ability to simulate the prolonged recession of the receding flood waves, a typical behavior of the river during extreme events that is attributed to swamp-to-river flow exchanges. More details about the model performance and the calibration results are available in Saad et al. (2020).

TABLE 1 | The four dredging scenarios considered for evaluation.

Modifications to river capacity	Spatial extent of modifications	
	Partial	**Full**
Modify channel dimensions	Scenario (A) 27 km; 1.7 mm^3	Scenario (C) 81.1 km; 3.0 mm^3
Modify channel dimensions and bed slope	Scenario (B) 27 km; 2.9 mm^3	Scenario (D) 81.1 km; 7.5 mm^3

The numbers reported for each scenario represent the length of the dredged reach (km) and the volume of bed material that needs to be dredged (million cubic meters, mm^3).

Description of Dredging Scenarios

To investigate the impact of dredging on flow regime within the river, four different scenarios were considered. The scenarios reflect different combinations of spatial extents and changes to the dimensions of the river channel and its longitudinal slope (**Table 1** and **Figure 4**). These combinations also reflect a wide range in the expected volume of the dredged material. Despite the differences between the four dredging scenarios, they all share some common features. All dredging scenarios intend to cut the river cross-section to a 30-m width and side slopes of 2H:1V, while maintaining the river alignment unchanged. These new channel dimensions were based on navigation and flood control criteria set by the Bayou Teche and Vermilion River Operations and Maintenance project (USACE, 1995). In all scenarios, the roughness coefficient was adjusted in the dredged sections to reflect the expected improvement in channel irregularity and bed roughness.

Dredging scenarios A and C focused on changing the channel dimensions only, while scenarios B and D included changes to both of the channel dimensions and the longitudinal bed slope. Modifying the channel dimensions intends to dredge the river bed to a fixed elevation of −3.35 m, based on the North American Vertical Datum of 1988 (NAVD 88), with a width of 30-m and

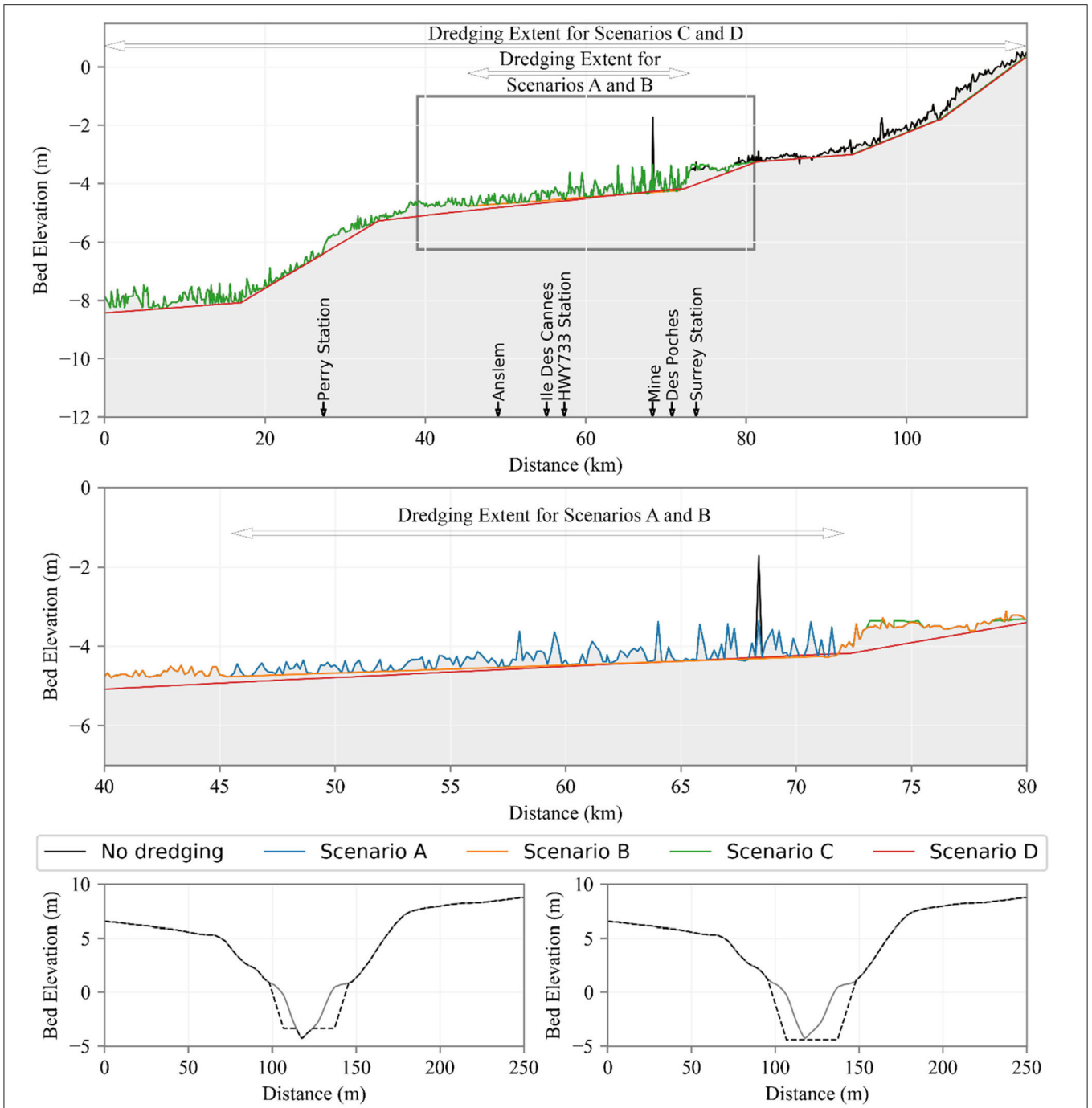

FIGURE 4 | (Top) Bed elevation of the Vermilion River starting from its downstream intersection with the GIWW until its most upstream station. The bed elevation is shown for the existing condition of the river (base scenario, black line in top panel) and the four dredging scenarios, A–D. **(Middle)** Shows a close-up view on the dredging extents of scenarios A and B. A full description of the four dredging scenarios is presented in **Table 1**. Note that the existing bed elevation follows the irregular bed profile and overlaps with some of the scenarios in certain reaches. **(Lower)** Show examples of cross section modified for dredging (solid lines indicate the existing cross section while the dashed lines show the same section after dredging).

side slopes of 2H:1V (**Figure 4**). However, if the existing bed elevation located within the intended dredging reach was already lower than the −3.35-m elevation, which was the case for most of the dredged reaches, the bed elevation is kept unchanged while the new width is carved at the elevation of −3.35 m. In addition to increasing the channel cross-sectional dimensions, scenarios B and D included grading the river bed to achieve a downstream-oriented longitudinal slope (**Figure 4**).

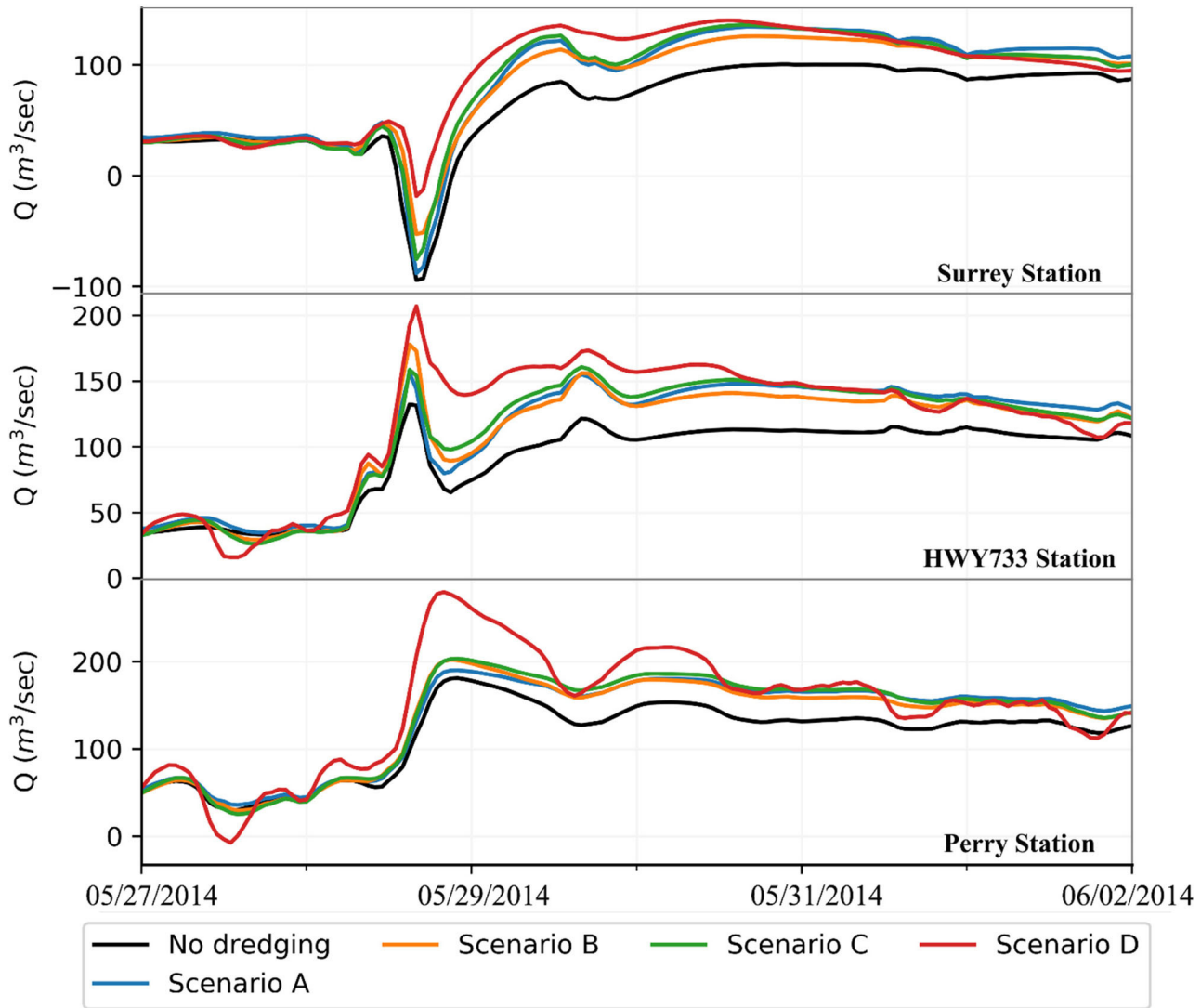

FIGURE 5 | Simulated flow hydrographs at three key stations along the Vermilion River (top: Surrey, middle: HWY733, bottom: Perry; see **Figure 1** for specific locations) during the May–June 2014 simulation period for the no-dredging baseline condition and the four dredging scenarios.

The study also examined two spatial extents of river dredging, a partial dredging extent (scenarios A and B) and a full dredging extent (scenario C and D). The "Full" spatial extent applies dredging for the whole navigation reach of the river, starting from its intersection with the GIWW in the south, and extends north for 81.1 km where the Ruth Canal joins the river. Alternatively, the "Partial" dredging extent covers only 27 km of the river where it passes through the heavily-urbanized areas within the City of Lafayette. The four dredging scenarios capture different degrees of modifications to the channel conveyance capacity and will allow a comprehensive evaluation of impacts on flow regimes and flooding in the river basin. Each dredging scenario will be tested separately using the hydrodynamic numerical model under the 2014 and 2016 simulation periods. The results will then be compared against those of a baseline scenario that represents the existing conditions of the river geometry.

RESULTS AND DISCUSSION

This section presents the results of the hydrodynamic model for the Vermilion River under the existing conditions (baseline scenario) in addition to the four proposed dredging scenarios. To isolate the effects of changing the river bathymetry, the forcing boundary conditions, including the tributary inflow hydrographs and tidal downstream boundary conditions, were all kept the same in all scenarios including the baseline scenario. This approach will allow for inter-scenario comparisons and ensure that reflect only the effect of bathymetric changes due to river dredging.

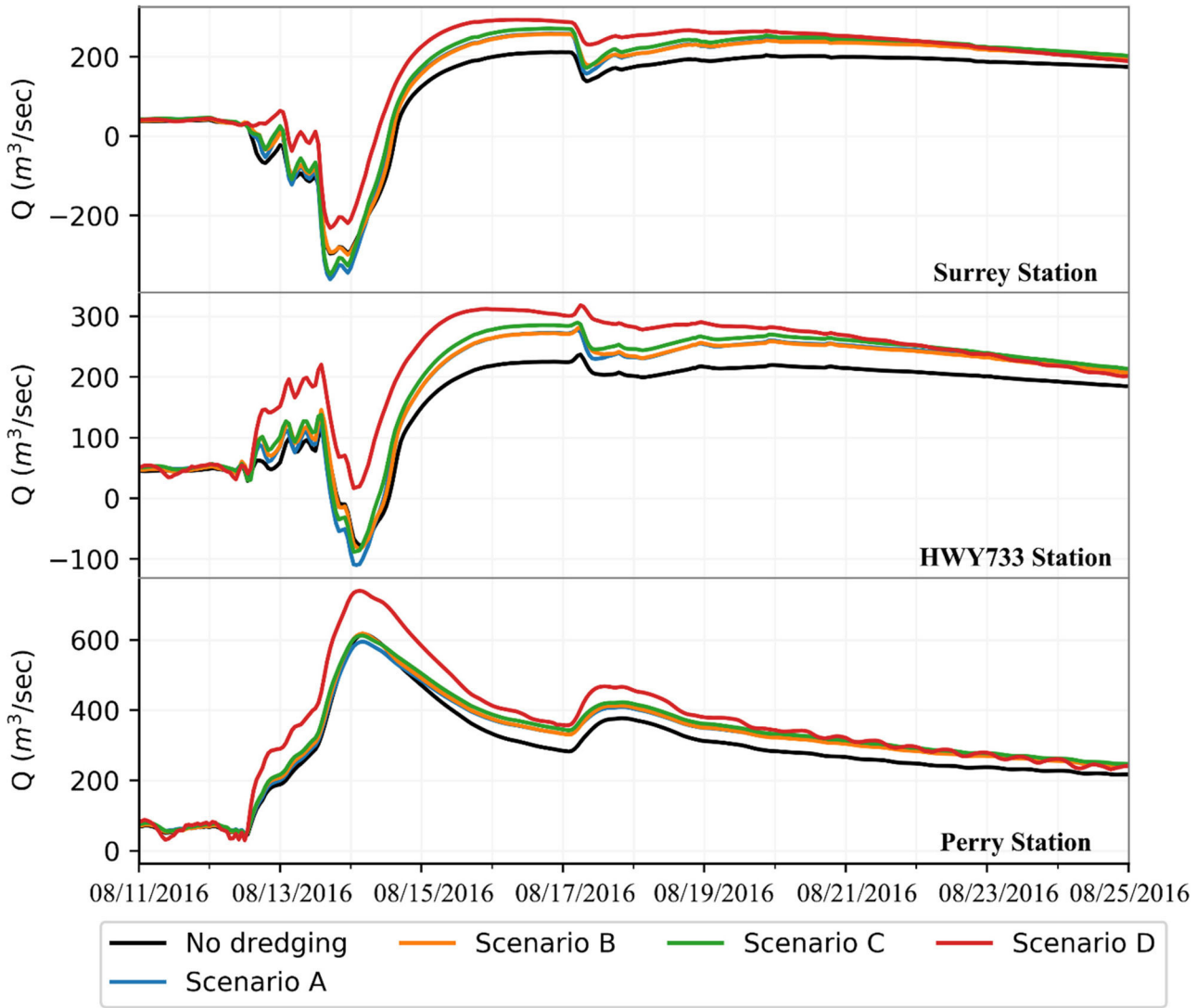

FIGURE 6 | Simulated flow hydrographs at three key stations along the Vermilion River (top: Surrey, middle: HWY733, bottom: Perry; see **Figure 1** for specific locations) during the August 2016 simulation period for the no-dredging baseline case and the four dredging scenarios.

Effect on Flow Regime in the Main River

Figures 5, **6** show the simulated flow hydrographs at three key locations along the Vermilion River for the two simulation periods, May–June 2014, and August 2016. The three locations (Surrey, HWY733, and Perry crossings) are selected in such a way to reflect different flow regimes along the river (e.g., reverse flows, upstream and downstream conditions, water surface gradients). These figures illustrate flow hydrographs from simulating the baseline case (no dredging scenario), and those from the four proposed dredging scenarios (**Table 1**). Prior to discussing the effect of the different dredging scenarios, it is necessary to discuss the flow regime in the river under the existing conditions. The Vermilion River, under its current status, tends to show reverse (negative) flow values at Surrey station (top panels in **Figures 5**, **6**) under moderate and extreme rainfall storm events. These negative values indicate a reverse in flow direction where the river starts to travel north and exchange flows with the Bayou Tortue Swamp, rather than following its normal course south toward the Gulf of Mexico. The specific location where this flow inversion starts mostly depends on the severity of the storm and the spatial distribution of the rainfall over the watershed. This can be seen when comparing the simulated flow hydrographs at HWY733 during May–June 2014 period (moderate 2–10-year events) and August 2016 period (extreme >100-year events). The results suggest that the reach of the river where inversion in flow direction occurred extended much further downstream to reach south of HWY733 during the more extreme August-2016 storm, while it was only limited to shorter reaches during more moderate rainfall events. The degree and spatial extent of the reverse flow are also

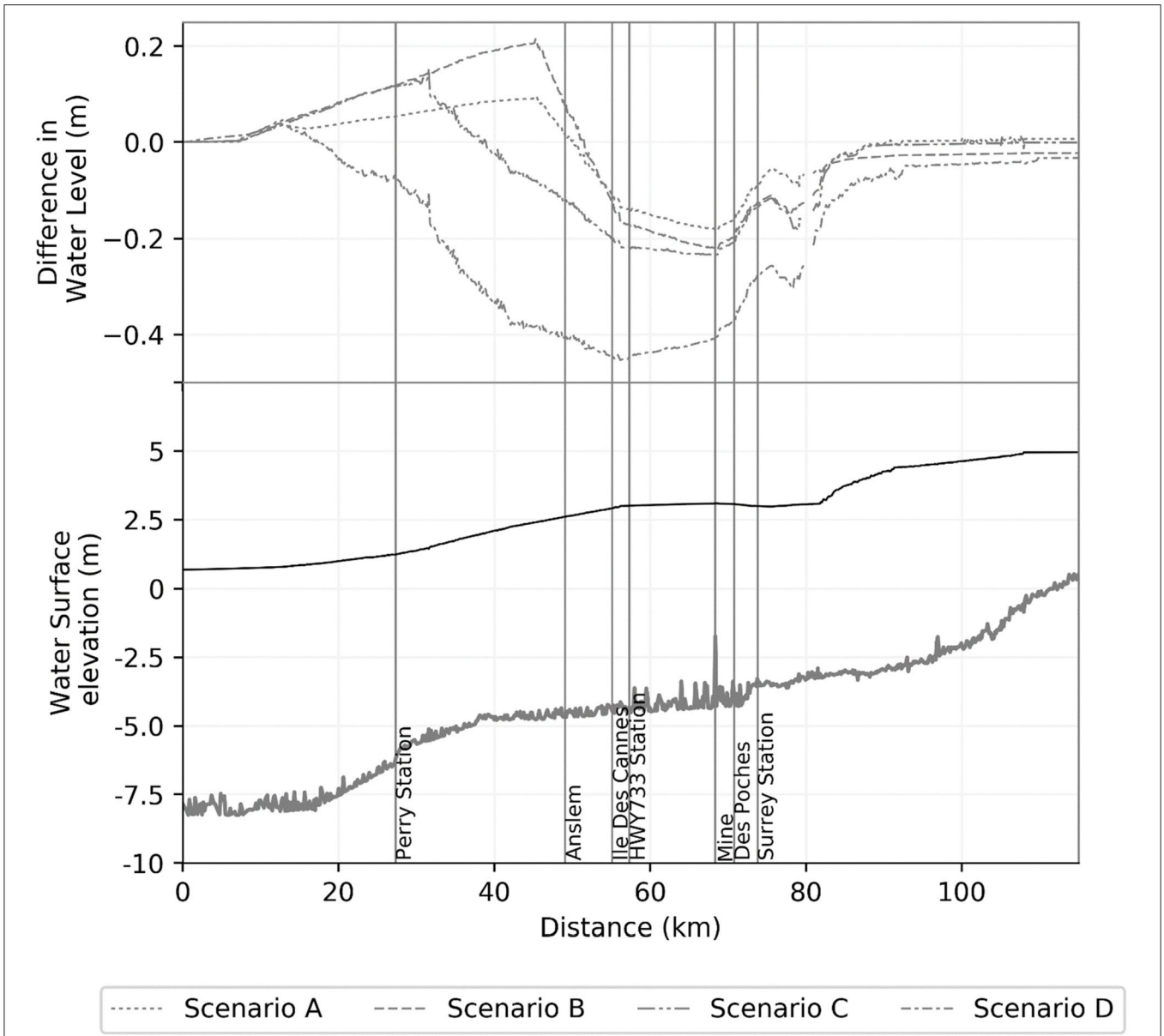

FIGURE 7 | (Lower) Longitudinal profile of maximum water surface elevation (WSE) along the mainstem of the Vermilion River simulated under the baseline case during the May–June 2014 simulation period. The existing river bathymetry is also shown (irregular line). **(Top)** Longitudinal profile of the differences between the maximum WSE simulated under each dredging scenario and the baseline case.

apparent in the longitudinal water surface profiles shown later in **Figures 7**, **8**.

Generally, the different dredging scenarios appear to alter the overall flow regime in the river, especially during moderate storms, such as the May–June 2014 period. All dredging four scenarios tend to reduce the reverse flows during the peak period of the storm while increasing the positive flows during the recession period. Despite differences in the spatial extent and degree of channel modification across the four dredging scenarios, the dredging activities tend to cause the main river to flow in its normal course toward the Gulf of Mexico. This is further evident in the simulated flow hydrographs at HWY733 and Perry locations (**Figure 5**) which experience a general promotion in the positive flow values. Increases in in the magnitudes of downstream flows are also apparent in the slow and elongated recession curve, indicating that the river is now accepting more flows coming from the swamp system and moving into the downstream direction.

The results under a more extreme storm (August 2016) provide other interesting insights on how dredging can significantly alter the flow regime in the river. Note that during this extreme flooding event, the extent of the reverse flow reached much further downstream (top and middle rows in **Figure 6**) than during the 2014 moderate events. During the

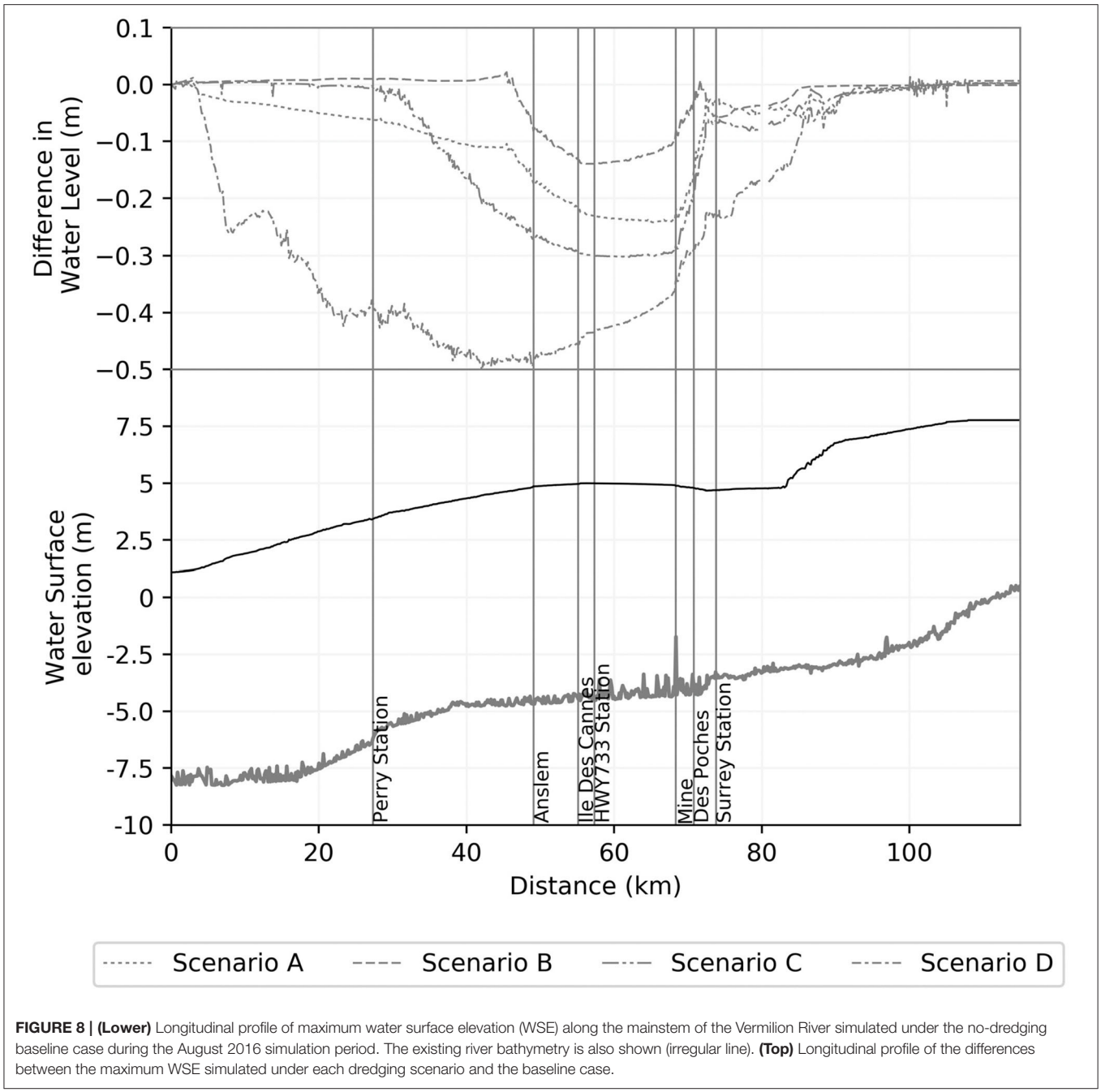

FIGURE 8 | (Lower) Longitudinal profile of maximum water surface elevation (WSE) along the mainstem of the Vermilion River simulated under the no-dredging baseline case during the August 2016 simulation period. The existing river bathymetry is also shown (irregular line). **(Top)** Longitudinal profile of the differences between the maximum WSE simulated under each dredging scenario and the baseline case.

August 2016 period, only the more aggressive Scenarios B and D, which involve implementing downstream-sloped riverbed grading, acted similar to the May–June 2014 period and reduced reverse flows. On the other hand, the less aggressive dredging Scenarios A and C showed an opposite behavior where some increases in the reverse flows were obtained, indicating an increase in the peak flows traveling north toward the Bayou Tortue Swamp. The dredging approach of scenarios A and C involve only enlarging the river cross-sectional dimensions without any grading of the longitudinal bed slope as was done in scenarios B and D. Apparently such approaches lead to an increase in the in-channel storage capacity within the dredged reach of the river without changes the bed slope. During extreme events, such as the August-2016 event, the in-channel storage of the river gets dominated by the amount of rainfall and thus plays a less significant role in controlling the water surface gradient. The runoff delivered to the river through its tributaries overwhelm the river storage capacity and build a hydraulic gradient that makes it easier for the river to travel in the reverse direction toward the Bayou Tortue Swamp system.

The results clearly suggest that the dredging scenarios have an effect on flow exchanges between the river and the swamp

system that provide a valuable flood mitigation service for the entire watershed (Saad et al., 2020). During the peak of the storm, the river flows north into the swamp providing relief for the downstream areas of the watershed. However, after the peak, the large volumes of water that were diverted into the swamp start to drain back into the river resulting in an extremely extended recession of the hydrograph, which leaves the downstream communities under high flood stages for several days. To further examine the impacts of the different dredging scenarios on the river-swamp interactions, hydrographs of flow exchange between the river and the swamp were examined. These hydrographs (not shown) were constructed by tracking the exchange flows through the tributaries and lateral connections that connect the swamp and the river (**Figure 3**). The results confirmed a significant reduction in the volume of river-to-swamp flows by as much as 40–64% under scenario D and an increase in the swamp-to-river outflows into the river by as much as 23%.

Effect on Water Surface Elevations (WSE) in the Main River

Figures 7, **8** show longitudinal profiles of the maximum water surface elevation (WSE) along the river during the two simulation periods for the baseline scenario and the four dredging scenarios. For better clarity, the results for the four dredging scenarios are presented in the form of differences from those of the baseline scenario. In general, the dredging scenarios reduced water surface elevations along some reaches the river, but to various degrees. During the August 2016 period, maximum reductions in water surface elevation were 0.14, 0.22, 0.30, and 0.49 m for dredging scenarios A, B, C, and D, respectively. Smaller reductions (0.19, 0.21, 0.22, and 0.42 m) were obtained during the more-frequent storms of May–June 2014. The reductions are more noticeable over the middle section of the river (∼river km 50 to river km 80). The reduction reached further downstream (∼river km 5–20) under the most aggressive dredging scenario D. Despite the overall reduction in WSE, it is interesting to see that local dredging that doesn't extend downstream enough (e.g., Scenarios A and B), although may reduce water surface elevations within the dredged reach, had actually triggered downstream increases in water surface elevations during the May–June 2014 period where up to a 0.2 m increase was observed in the last third of the river (∼river km 10–45). During more frequent events, spatially-limited increases in the in-channel storage of the river offered localized relief to the water surface profiles but led to a significant backup in water volumes and thus an increase in downstream water surface elevations.

Interestingly, the results obtained from Scenario C, despite being a full dredging scenario that extends for a longer distance down the river, also showed some increase (∼0.15 m) in the water surface elevation in the last reach of the river (up to river km 25). Considering that Scenario C includes increasing the channel dimensions only, the lack of any enhancements to the channel bed slope as it approaches the Gulf didn't allow the river to benefit from the enlargement added to channel size. It is also noted that channel size enlargement implemented in Scenario C were actually much less needed in the last section of the river due it its already existing large channel. The negative consequences of increasing the water surface elevation were not obtained under more extreme storm of 2016. This is simply because the water elevations were already high and the large rainfall volumes created their own gradients regardless of the channel slope or its dimensions.

Effect on the WSE in the Tributaries

In addition to examining the impact of riverine dredging on the main stem of the river, it is also of interest to assess the propagation of such impacts into the tributaries that drain into the river. To allow such examination, five of the main tributaries that drain into the Vermilion River (Coulee Des Poches, Coulee Mine, Coulee Isaac Verot, Coulee Ile des Cannes, and Anslem Coulee) were explicitly modeled as part of the hydrodynamic model. The maximum WSE profiles along two of these tributaries (Coulee Ile des Cannes and Coulee Isaac Verot) are shown in **Figures 9**, **10**. Observations drawn from the profiles of these two tributaries were found consistent for the other tributaries as well.

Compared to the results inside the main river, generally, a lesser reduction in water stage across the tributaries are attained. The Ile des Cannes tributary showed larger drops in water surface elevation, both in magnitude and spatial extent. As expected, the maximum WSE reduction occurred at the outlet of the tributaries, with Scenario D showing the most WSE reduction in both events. Scenario A and Scenario B showed the least WSE reduction, similar to their in the main river. The reduction in WSE propagated upstream into the coulees for relatively limited distances of mostly ∼2 km and no more than 10–13 km. The magnitude and spatial extent of the reduction within each tributary is largely dependent on the longitudinal bed slopes of each tributary and the hydraulic gradient during the flood event. The most downstream reach of Coulee Ile des Cannes is characterized by an average bed slope of 0.037%, while the same reach in Coulee Isaac Verot exhibits a steeper average bed slope of 0.084%. The WSE reduction apparently increases in coulees that have milder slopes. Examining the hydraulic gradient provides some additional insight. During the more frequent storm, May–June 2014, the hydraulic gradient inside the Isaac Verot tributary was estimated as 5.4% for the baseline scenario, resulting in a minimal WSE reduction (0.015 m) that extended for a distance of <2 km under the most extensive dredging scenario (Scenario D). However, the same tributary had a milder hydraulic slope of 3% during the August 2016 extreme event, and thus resulted in a larger reduction in water surface elevation of 0.42 m that extended slightly further upstream under the same dredging Scenario D. Unlike Isaac Verot tributary, the hydraulic gradient in the Ile des Cannes tributary, under the baseline scenario, was 0.004 and 0.005% during the May–June 2014 and August-2016 periods, respectively. As such, these conditions resulted in larger reductions of 0.44 and 0.42 m that extended for longer distances of 13 and 12.1 km, respectively (Scenario D). The very flat bed slope for the Ile des Cannes tributary diminished the effects of differences in the hydraulic gradient between the periods of May–June 2014 and August 2016.

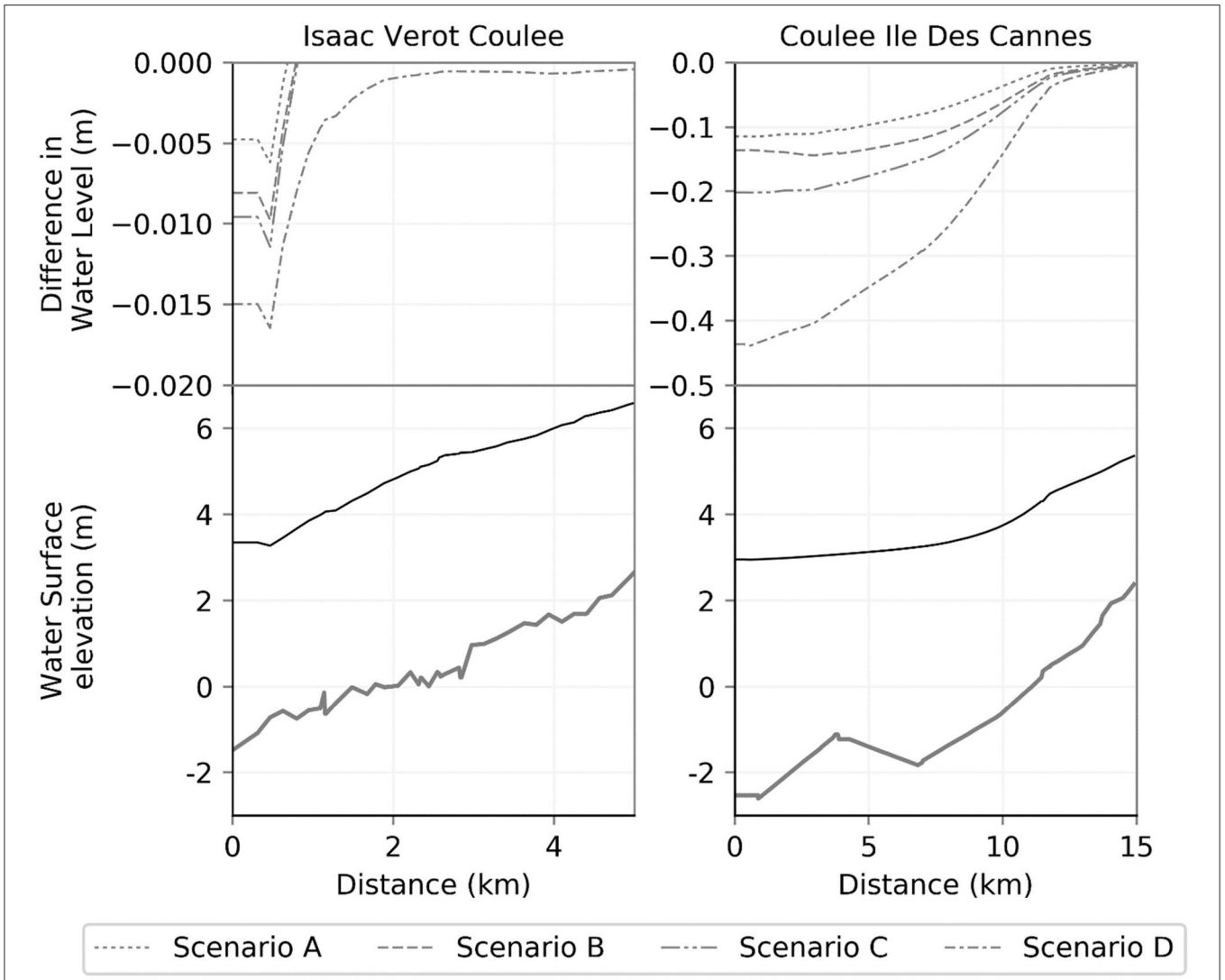

FIGURE 9 | (Lower) Longitudinal profiles of maximum water surface elevation (WSE) for the baseline case during the 2014 simulation period. The existing river bathymetry is shown (irregular line). **(Top)** Longitudinal profile of differences between the maximum WSE of each dredging scenario and that of the baseline case.

Effect on Tidal Propagation

Modifications to the river channel are expected to affect the propagation of tidal wave for rivers, such as the Vermilion River, especially with its connectivity to the Gulf of Mexico through the Vermilion Bay. To assess such potential effects, the model simulations were used to quantify the tidal amplitudes under the different dredging scenarios and compare them to the existing baseline condition. **Figure 12** illustrates the maximum tidal amplitude along the main stem of the river starting from its most downstream intersection with the bay. The amplitudes shown in **Figure 12** were calculated by taking the difference between the maximum and minimum water elevation at each cross section along the river over the temporal span of the simulation period. However, this was performed for the pre-storm period only and without including the water stages during the main storm. The main reason for doing so is to isolate the potential impact of the dredging activities on the tidal hydrodynamics during non-flooding conditions and without including the effects of the inland rainfall storms.

The results (**Figure 12**) obtained under the baseline scenario suggest that the tidal signal in the river is largely diminished around 65–70 km from its outlet to the Gulf. Generally, the results suggest that all dredging scenarios caused a significant alteration in the tidal range along the course of the main river. However, it is clear that dredging Scenario D has the most significant impact in allowing the tidal signal to propagate for longer distances upstream. Scenario D resulted in a drastic increase in the tidal amplitude that extended across the entire river, with an increase of as high as 1.8 times the magnitudes obtained under the baseline scenario. This amplification extended for significant distances upstream and as far as Surrey crossing, ∼73 km landward into the heart of the City of Lafayette. Scenarios A, B, and C resulted in

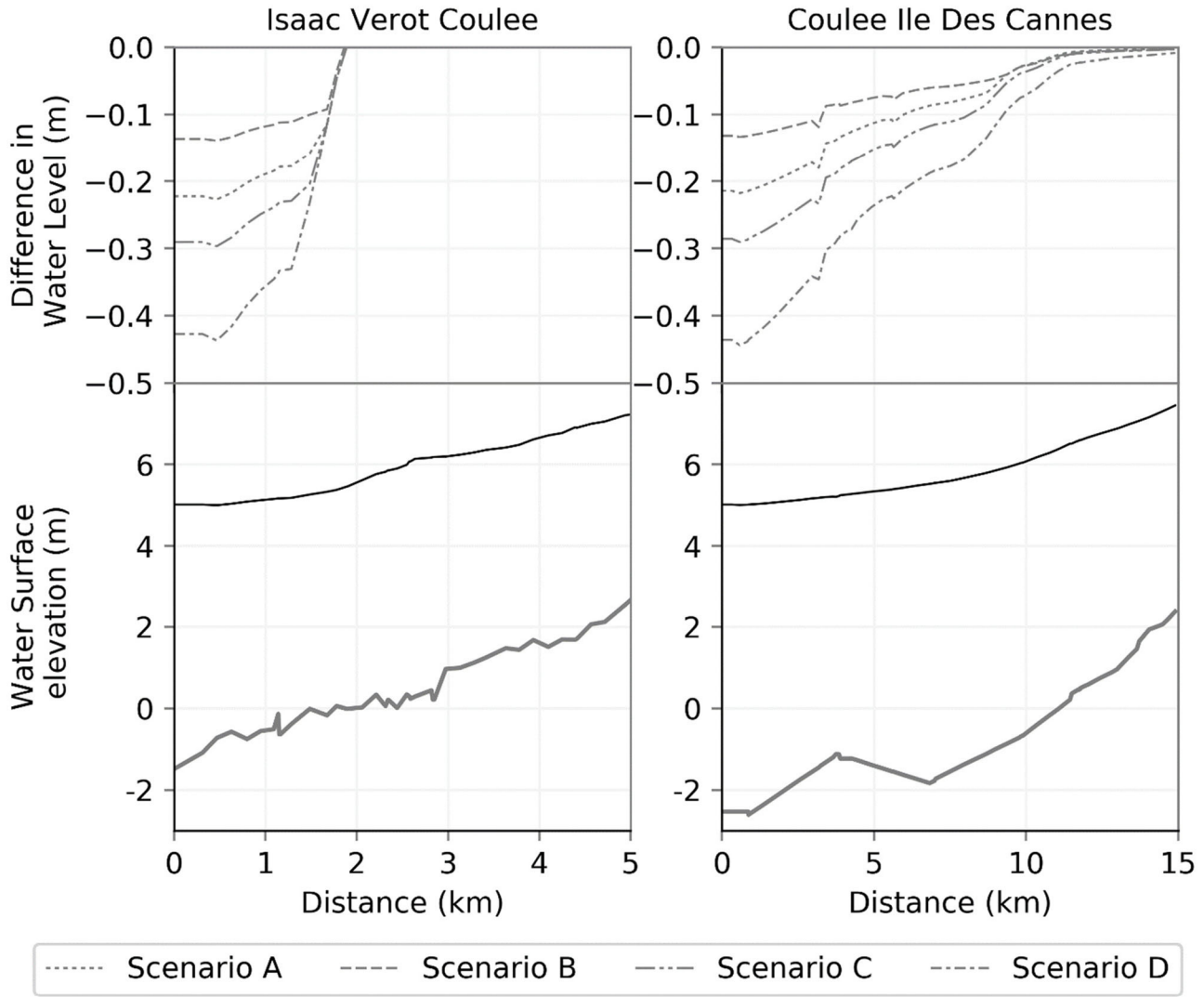

FIGURE 10 | (Lower) Longitudinal profiles of maximum water surface elevation (WSE) for the baseline scenario during the August 2016 simulation period; the existing river bathymetry is shown (irregular line). **(Top)** Longitudinal profile of differences between the maximum WSE of each dredging scenario and the baseline case.

tidal amplitudes similar to the baseline condition, but with some minimal attenuation in the downstream reaches of the river [0–50 km]. Starting at ∼50 km and further north, an inflection in the tidal propagation starts to occur and the reach witnesses a relatively constant tidal amplitude that tends to be higher than the baseline scenario. Such increases are apparently triggered by the channel size enlargement and bed grading involved in this middle reach under scenarios A, B, and C. Also, the results shown in **Figure 11** highlight the value of the Bayou Tortue swamp as a coastal mitigation measure. Along the river reach where it has interconnections with the swamp (73–85 km), the maximum tidal wave height dropped sharply, especially under dredging scenarios B and D, which emphasizes the vital role of the swamp system in attenuating the tidal wave. The swamp storage capacity and its accessibility to the main river seems to have absorbed the effect of the tidal signal and reduced its propagation further upstream.

Effect on Inundation Extent and Duration

The impact of riverine dredging on flooding regime is further examined by assessing the flood inundation along the main river and its major tributaries. The maximum extent of flooded areas that would occur for each dredging scenario and for the baseline case were calculated during both simulation periods. The spatial extent of flood inundation was estimated by comparing the simulated water surface elevations and the LiDAR-based DEM. For the river channel and tributaries that were modeled as 1-D, a water surface model was developed by interpolating the maximum water stages at each cross-section on a grid that has the same spatial extent and resolution of the DEM surface. In areas that were simulated as 2D, the water surface grid is a direct output

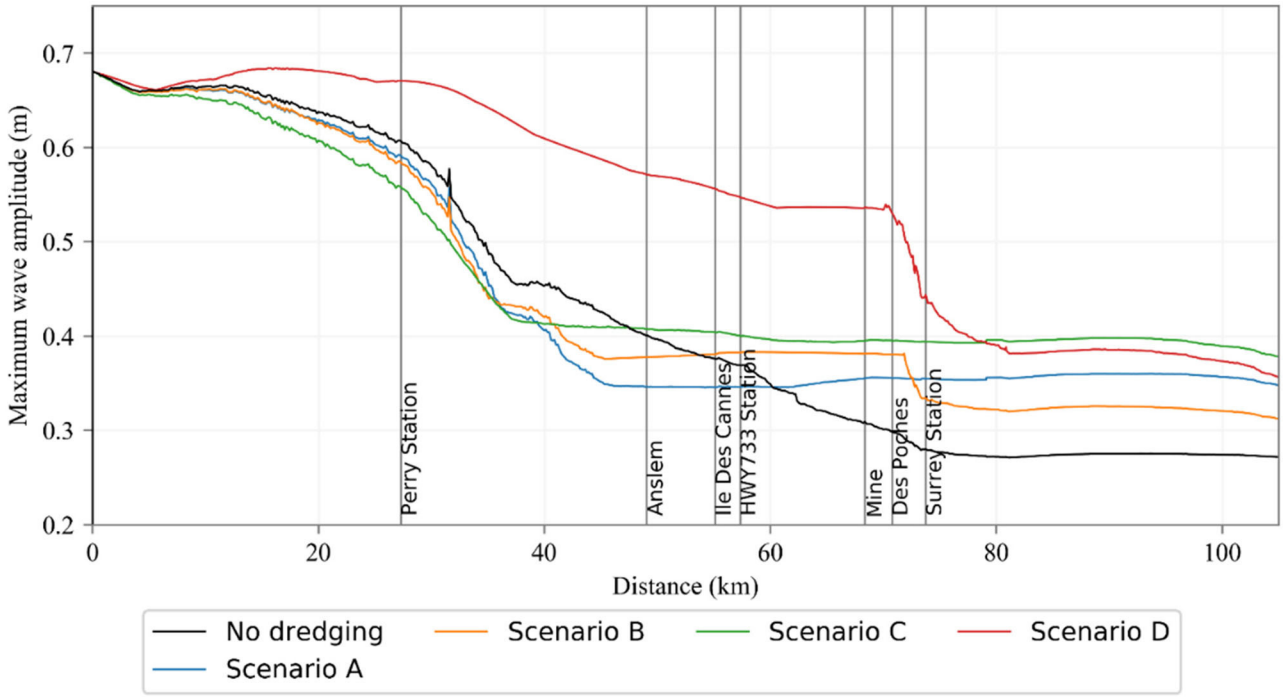

FIGURE 11 | Propagation of tidal amplitude along the Vermilion River under the baseline case and each dredging scenario. Results are based on a non-flood period (07/25/2016 to 08/08/2016) that precedes the August 2016 flood. The vertical gray lines depict the inlet locations of key tributaries along the Vermilion River.

of the hydraulic model and no extra interpolation was required. After mosaicking the water surface grids estimated from 1D and 2D areas, the final water surface grid was overlaid onto the LiDAR grid to calculate differences between the surfaces and delineate the extent of the flood inundation. The results are summarized by calculating the total inundated areas for the entire domain of the river and its tributaries (**Table 2**). As expected, the dredging scenarios resulted in some reductions in the inundated areas; however, such reductions appear rather minimal. The results report reductions in the flooded area in the order of (0.97–6.87 km^2) and (0.48–2.29 km^2) during the August 2016 and May–June 2014 periods, respectively. It is interesting to contrast these rather minimal reductions in inundation spatial extents vs. the more noticeable reductions in the water surface profiles reported earlier (∼0.4–0.5 m reduction; **Figures 7**, **8**). These results indicate that the main river doesn't necessarily fully control the actual extent of inundation on adjacent floodplains, and further suggest that floodwaters of the river are mostly contained within its own main channel. These results are also consistent with the earlier observations on the relatively small propagation of reductions in the water surface elevation from the river into its tributaries (**Figures 9**, **10**).

Besides examining the spatial extent of inundation, it is also of interest to examine the duration of inundation. This becomes particularly relevant given the extreme slow recession of flood waters in low-gradient rivers, such as the Vermilion River (**Figures 5**, **6**). The duration of inundation was quantified by calculating the total number of hours each cell in the composite spatial inundation grid experienced a positive water depth. The number of hours were summed over the full duration of each simulation period. When compiled over the entire domain of the model, scenarios A, B, and C resulted in average reductions of 2–4 days in the inundation duration, while scenario D showed average reductions of 4–6 days. Example of the results are shown in **Figures 12**, **13** for selected areas within the model domain. In these areas and depending on the dredging scenario, the average reduction in inundation duration was in the range of 9.5–28.6 and 6.7–33.3% for the May–June 2014 and the August-2016 periods, respectively. Reductions as high as 6–8 days were obtained, especially with scenario D and in areas around the City of Lafayette and before the river enters connects to the Bayou Tortue Swamp system. Such results reveal that while the dredging activities didn't significantly reduce the spatial extent of inundation, they seem to reduce the duration of such inundations. The reduced inundation durations have implications for communities who are impacted by flooding conditions that last for several days after the peak of the storms.

CONCLUSIONS AND RECOMMENDATIONS

This study investigated how large-scale channel modifications via riverine dredging may alter flood dynamics in the Vermilion River in southern Louisiana, a representative of low-gradient tidally-influenced river systems. With the presence of large

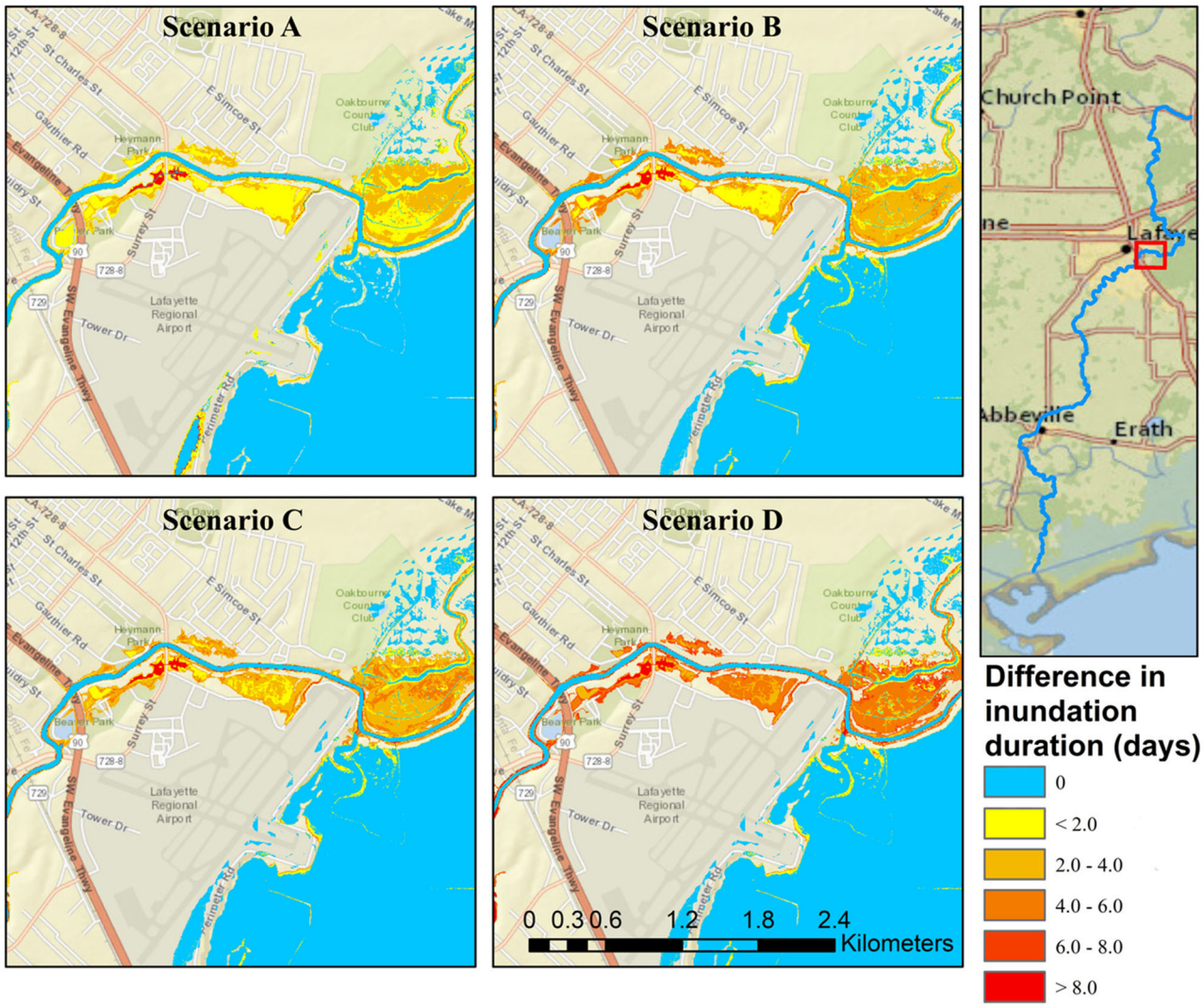

FIGURE 12 | Differences in inundation duration between the baseline case and each dredging scenario during the May–June 2014 simulation period.

TABLE 2 | Inundation areas estimated for each dredging scenario.

Approach	Inundated area (km^2)	
	May–June 2014	August-2016
Baseline	181.26	269.1
Scenario A	180.78	268.1
Scenario B	180.39	267.8
Scenario C	180.09	264.2
Scenario D	178.97	262.2

swamp system within its watershed, the river is characterized by complex flow dynamics where frequent reverse (upstream) flows occur allowing flood waters to travel upstream for temporary storage in the swamps. The study examined the impacts of four different dredging scenarios that represent varying degrees of spatial extent and modifications to the channel cross section and longitudinal bed slope. A hybrid 1D/2D numerical model was used to simulate the impact of dredging activities on the flow hydrodynamics along the main course of the river and five of its major tributaries. The analysis was performed on two flooding periods, May–June 2014 and August 2016, which are classified as <10-year and >100-year storms, respectively. The four different dredging scenarios were assessed by evaluating key characteristics of the flow regime, including changes in flow hydrographs at key locations, reductions in water surface profiles and flood inundation, alterations to river-swamp interactions, and impact on tidal amplitudes and propagation. The results from each dredging scenario were compared against those obtained under the existing no-dredging scenario.

Overall, the results suggest that a watershed-centered approach, instead of a riverine-centered approach is needed

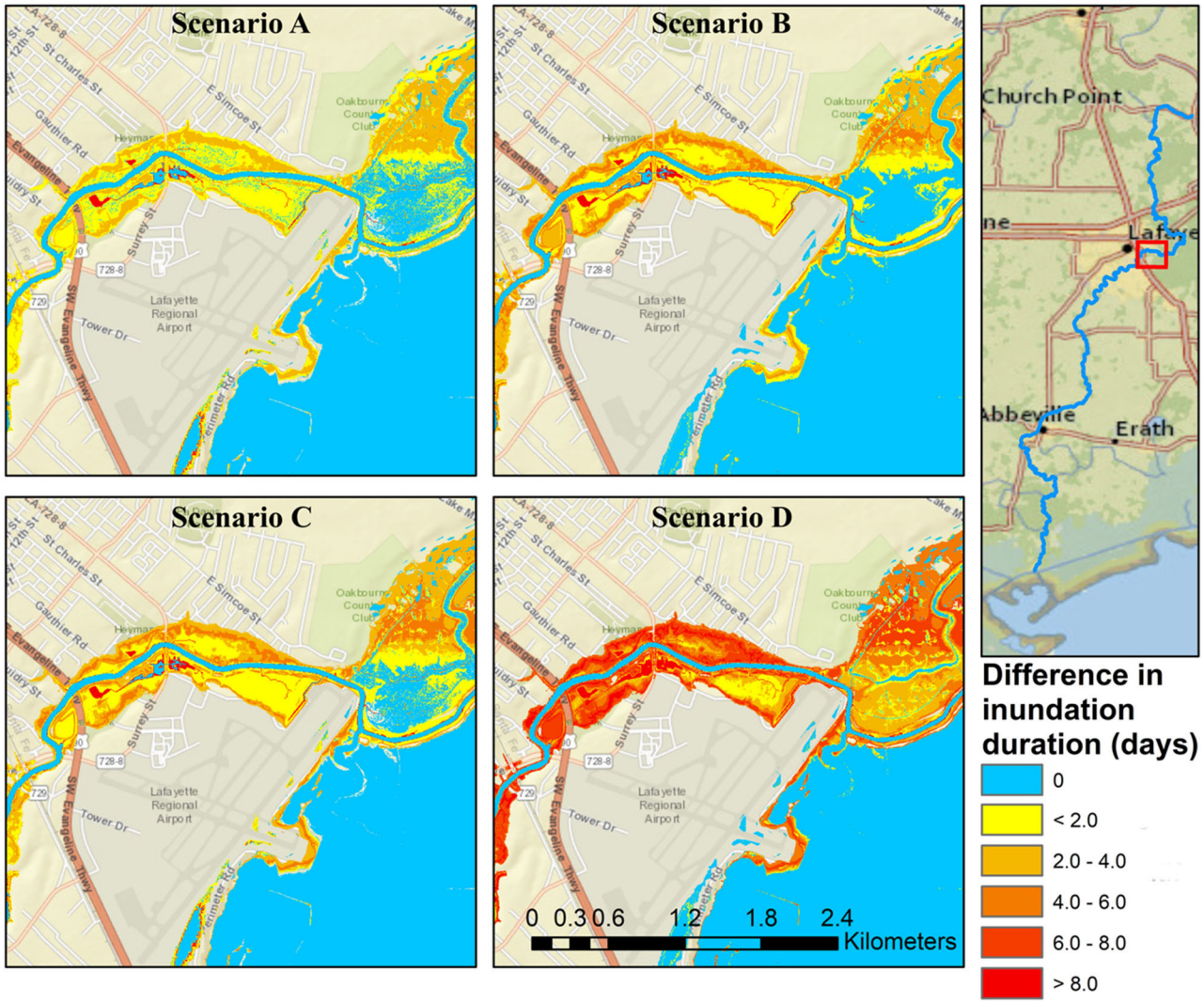

FIGURE 13 | Differences in inundation duration between the baseline condition and each dredging scenario during the August 2016 simulation period.

for assessment of flood mitigation alternatives in such riverine systems. The following conclusions can be formulated based on the findings of the study:

1. The effect of large-scale riverine dredging on the flow regime in the river and the resultant flood conditions is highly controlled and modulated by inter-related and often competing factors, such as extent of the dredging in both volume and spatial coverage, flow exchanges between the river and the inter-connected natural swamps, bed slopes and hydraulic gradients, and the large volumes of runoff contributions from river tributaries and how they compare to induced changes to the river in-channel capacity.
2. Dredging scenarios that modified the river channel modifications and the riverbed slope lead to significant changes to the river flow regime. Overall, reverse river flows that travel to the swamp during the peak period of the storms were reduced. Such impacts have significantly altered the flow exchanges between the river and the swamp and severed the river-to-swamp inflows and increased the swamp outflows. This is expected to affect the hydroperiod of the swamp system and its residence time and may eventually affect its viability as a natural ecosystem.
3. Dredging approaches that were spatially extensive and included modifications to the river slope can result in sizeable reductions in water surface profiles (40–50 cm) along the river during flood conditions. However, such extensive dredging brings significant increase in the amplitude and propagation of the Gulf tidal wave that extended as far as 70 km inland.
4. While less-extensive, spatially-limited dredging approaches can also reduce the water surface profiles to some extent (10–30 cm), they tend to cause an increase in the water surface elevations downstream of the dredged river reaches. Such increases can extend over 20–40 km along the river, exposing

downstream communities to increased flooding especially during more frequent events.
5. The results reveal that while the dredging activities can increase the hydraulic conveyance of the river system and improve its drainage characteristics, the large runoff volumes delivered by the contributing tributaries eventually overwhelm the river and outweigh the added improvement in terms of in-channel storage, thus reducing the anticipated flood relief benefit expected from the dredging.
6. Reductions in water surface profiles in the Vermilion River propagated along the tributaries that drain into the river, but only to limited spatial extents. The degree of reduction inside the tributaries was dependent on the hydraulic gradient and longitudinal bed slopes of each tributary.
7. While there is evidence that dredging can increase channel conveyance and reduce water levels inside the Vermilion River, such reduction was not reflected in a parallel reduction in the spatial extent of flood inundation boundaries under any of the four dredging scenarios. On the other hand, reductions in the duration of inundation were found to be substantial, suggesting that while dredging didn't significantly reduce the maximum extent of inundation, it seems to reduce the duration that flooded areas get inundated.
8. Generally, the results suggest that, regardless of the specific scenario, dredging activities caused a noticeable alteration in the tidal wave range along the river. Extensive dredging scenarios caused a substantial amplification in the tidal signal along the main course of the river, which can facilitate the landward penetration of storm surges into the river.

DATA AVAILABILITY STATEMENT

Publicly available datasets were analyzed in this study. This data can be found at: https://registry.opendata.aws/nwm-archive/; https://data.eol.ucar.edu/dataset/21.093.

AUTHOR CONTRIBUTIONS

HS and EH conceived of the presented idea. HS planned and carried out the numerical simulations, drafted the manuscript, and designed the figures. EH secured the funding for the project, supervised the project, aided in interpreting the results, and worked on reviewing and finalizing the manuscript. Both authors contributed to the article and approved the submitted version.

FUNDING

Model development was supported by institutional resources from the University of Louisiana at Lafayette. Additional support was provided by the United States Army Corps of Engineers New Orleans District to perform the dredging under contract number W912P820P0003.

ACKNOWLEDGMENTS

The authors thank Mr. Donald Sagrera with the Teche Vermilion Freshwater District for providing operational data on the hydraulic structures. The authors also thank Mr. Clyde Barre and Mr. Jeffrey Varisco from the United States Army Corps of Engineers–New Orleans District, for the valuable discussions that informed this study. Insights provided by Dr. Michael Waldon on the complex flow regimes in the river are greatly appreciated.

SUPPLEMENTARY MATERIAL

The Supplementary Material for this article can be found online at: https://www.frontiersin.org/articles/10.3389/frwa.2021.628829/full#supplementary-material

REFERENCES

Advanced Hydrologic Prediction Service (2018). *National Weather Service, 2018*. Lake Charles: Historic Crests at Surrey Station.

Baker, N. T. (1988). *Hydrologic Features and Processes of the Vermilion River, Louisiana*. Baton Rouge: U.S. Geological Survey. doi: 10.3133/wri884019

Bilskie, M. V., and Hagen, S. C. (2018). Defining flood zone transitions in low-gradient coastal regions. *Geophys. Res. Lett.* 45, 2761–2770. doi: 10.1002/2018GL077524

Brunner, G. W. (2016). *HEC-RAS River Analysis System. Hydraulic Reference Manual*. Version 5.0. Davis, CA: Hydrologic Engineering Center.

Burton, J., and Demas, A. (2016). *Backwater Flooding in Baton Rouge*. Reston, VA: USGS.

Cai, H., Savenije, H., Yang, Q., Ou, S., and Lei, Y. (2012). Influence of river discharge and dredging on tidal wave propagation: Modaomen estuary case. *J. Hydraul. Eng.* 138, 885–896. doi: 10.1061/(ASCE)HY.1943-7900.0000594

Cook, A., and Merwade, V. (2009). Effect of topographic data, geometric configuration and modeling approach on flood inundation mapping. *J. Hydrol.* 377, 131–142. doi: 10.1016/j.jhydrol.2009.08.015

Crossett, K., Ache, B., Pacheco, P., and Haber, K. (2013). *National Coastal Population Report, Population Trends From 1970 to 2020*. Washington, DC: NOAA State of the Coast Report Series, US Department of Commerce.

Cunningham, R., Gisclair, D., and Craig, J. (2009). *The Louisiana Statewide LiDAR Project*. Baton Rouge, LA: LSU Department of Geography and Anthropology. Available online at: http://atlas.lsu.edu

Eldardiry, H., Habib, E., Zhang, Y., and Graschel, J. (2015). Artifacts in stage IV NWS real-time multisensor precipitation estimates and impacts on identification of maximum series. *J. Hydrol. Eng.* 22:E4015003. doi: 10.1061/(ASCE)HE.1943-5584.0001291

Gochis, D., Barlage, M., Dugger, A., FitzGerald, K., Karsten, L., McAllister, M., et al. (2018). *The WRF-Hydro Modeling System Technical Description (Version 5.0)*. NCAR Technical Note, 107. Available online at: https://ral.ucar.edu/sites/default/files/public/WRFHydroV511TechnicalDescription.pdf

Homer, C., Dewitz, J., Yang, L., Jin, S., Danielson, P., Xian, G., et al. (2015). Completion of the 2011 National Land Cover Database for the Conterminous United States – Representing a Decade of Land Cover Change. *Information* 81, 346–354. doi: 10.14358/PERS.81.5.345

Hooke, J. M. (1990). Channelized RIVERS: PERSPECTIVES for environmental management, Andrew Brookes, Wiley, Chichester, 1988. No. of pages: 326. *Earth Surf. Process. Landforms* 15, 291–292. doi: 10.1002/esp.3290150312

Jarihani, A. A., Callow, J. N., McVicar, T. R., Van Niel, T. G., and Larsen, J. R. (2015). Satellite-derived digital elevation model (DEM) selection, preparation and correction for hydrodynamic modelling in large, low-gradient and data-sparse catchments. *J. Hydrol.* 524, 489–506. doi: 10.1016/j.jhydrol.2015.02.049

Juan, A., Gori, A., and Sebastian, A. (2020). Comparing floodplain evolution in channelized and unchannelized urban watersheds in Houston, Texas. *J. Flood Risk Manage.* 13:e12604. doi: 10.1111/jfr3.12604

Kim, J., Warnock, A., Ivanov, V. Y., and Katopodes, N. D. (2012). Coupled modeling of hydrologic and hydrodynamic processes including overland and channel flow. *Adv. Water Resour.* 37, 104–126. doi: 10.1016/j.advwatres.2011.11.009

Kinsland, G. L., and Wildgen, J. (2006). "Evolution of the Morphology of the Vermilion River Near Lafayette, Louisiana, USA; Consequent Flooding Problems and a Mitigation Plan; Some Features on the Surface of the Prairie Complex: All Illustrated With LIDAR Imagery", *Gulf Coast Association of Geological Societies Transactions,* Vol. 56, 353–365.

Liao, K. H., Chan, J. K. H., and Huang, Y. L. (2019). Environmental justice and flood prevention: the moral cost of floodwater redistribution. *Landsc. Urban Plan.* 189, 36–45. doi: 10.1016/j.landurbplan.2019.04.012

NCEI (2020). *Billion-Dollar Weather and Climate Disasters*. NOAA National Centers for Environmental Information (NCEI). Available online at: https://www.ncdc.noaa.gov/billions/.

Nunnally, N. R. (1978). Stream renovation: an alternative to channelization. *Environ. Manage.* 2, 403–411. doi: 10.1007/BF01872915

Pattison, I., Lane, S. N., Hardy, R. J., and Reaney, S. M. (2014). The role of tributary relative timing and sequencing in controlling large floods. *Water Resour. Res.* 50, 5444–5458. doi: 10.1002/2013WR014067

Pierce, A. R., and King, S. L. (2013). "12.14 Valley plugs, land use, and phytogeomorphic response," in *Treatise on Geomorphology*, ed J. F. Shroder (San Diego, CA: Academic Press), 221–235. doi: 10.1016/B978-0-12-374739-6.00330-4

Prestegaard, K. L., Matherne, and Katyl, N. (1994). Spatial variations in the magnitude of the 1993 floods, Raccoon River Basin, Iowa. *Geomorphol. Nat. Hazards* 10, 169–182. doi: 10.1016/B978-0-444-82012-9.50016-5

Ralston, D. K., Talke, S., Geyer, W. R., Al-Zubaidi, H. A. M., and Sommerfield, C. K. (2019). Bigger tides, less flooding: effects of dredging on barotropic dynamics in a highly modified estuary. *J. Geophys. Res. Oceans* 124, 196–211. doi: 10.1029/2018JC014313

Rose, S., and Peters, N. E. (2001). Effects of urbanization on streamflow in the Atlanta area (Georgia, USA): a comparative hydrological approach. *Hydrol. Process.* 15, 1441–1457. doi: 10.1002/hyp.218

Saad, H. A., Habib, E. H., and Miller, R. L. (2020). Effect of model setup complexity on flood modeling in low-gradient basins. *J. Am. Water Resour. Assoc.* 1–19. doi: 10.1111/1752-1688.12884

Schoof, R. (1980). Environmental impact of channel modification 1. *J. Am. Water Resour. Assoc.* 16, 697–701. doi: 10.1111/j.1752-1688.1980.tb02451.x

Shankman, D., and Pugh, T. B. (1992). Discharge response to channelization of a coastal plain stream. *Wetlands* 12, 157–162. doi: 10.1007/BF03160604

Shastry, A., Luo, C., Aristizabal, F., and Egbert, R. (2017). *Comparing NWM Inundation Predictions With Hydrodynamic Modeling*. National Water Center Innovators Program Summer Institute Report 2017, 49. Washington, DC: Consortium of Universities for the Advancement of Hydrologic Science, Inc.

USACE (1995). *Lafayette Parish, Louisiana Flood Control: Reconnaissance Report*. New Orleans, LA: US Army Corps of Engineers, New Orleans District.

USACE (2015). *Navigation Condition Surveys*. New Orleans, LA: US Army Corps of Engineers, New Orleans District, Operations Division.

USACE (2016). *HEC-RAS River Analysis System Hydraulic Reference Manual*. Version 5.0. Davis, CA: Institute of Water Resources, Hydrological Engineering Center.

van der Wiel, K., Kapnick, S. B., van Oldenborgh, G. J., Whan, K., Philip, S., Vecchi, G. A., et al. (2017). Rapid attribution of the August 2016 flood-inducing extreme precipitation in south Louisiana to climate change. *Hydrol. Earth Syst. Sci.* 21, 897–921. doi: 10.5194/hess-21-897-2017

Wang, X., Kinsland, G., Poudel, D., and Fenech, A. (2019). Urban flood prediction under heavy precipitation. *J. Hydrol.* 577:123984. doi: 10.1016/j.jhydrol.2019.123984

Watson, K. M., Storm, J. B., Breaker, B. K., and Rose, C. E. (2017). *Characterization of Peak Streamflows and Flood Inundation of Selected Areas in Louisiana from the August 2016 Flood (2017–5005)*. Reston, VA: U.S. Geological Survey. doi: 10.3133/sir20175005

Webster, P., Rangeley-Wilson, C., Juniper, T., and Harrison, P. (2014). *Floods and Dredginga Reality Check*. London: CIWEM.

Wu, Y., Zhang, G., Rousseau, A. N., Xu, Y. J., and Foulon, É. (2020). On how wetlands can provide flood resilience in a large river basin: a case study in Nenjiang river Basin, China. *J. Hydrol.* 587:125012. doi: 10.1016/j.jhydrol.2020.125012

Conflict of Interest: The authors declare that the research was conducted in the absence of any commercial or financial relationships that could be construed as a potential conflict of interest.

frontiers in Climate

ORIGINAL RESEARCH
published: 05 August 2021
doi: 10.3389/fclim.2021.613293

Optimization of Coastal Protections in the Presence of Climate Change

Yuki Miura[1], Philip C. Dinenis[2], Kyle T. Mandli[2], George Deodatis[1] and Daniel Bienstock[3]*

[1] Department of Civil Engineering and Engineering Mechanics, Columbia University, New York, NY, United States, [2] Department of Applied Physics and Applied Mathematics, Columbia University, New York, NY, United States, [3] Department of Industrial Engineering and Operations Research, Columbia University, New York, NY, United States

It is generally acknowledged that interdependent critical infrastructure in coastal urban areas is constantly threatened by storm-induced flooding. Due to changing climate effects, such as sea level rise (SLR), the occurrence of catastrophic events will be more frequent and may trigger an increased likelihood of severe hazards. Planning a protective measure or mitigation strategy is a complex problem given the constraints that it must fit within a prescribed and limited fiscal budget and be beneficial to the community it protects both socially and economically. This article proposes a methodology for optimizing protective measures and mitigation strategies for interdependent infrastructures subjected to storm-induced flooding and climate change impacts such as SLR. Optimality is defined in this methodology as a maximum reduction in overall expected losses within a prescribed budget (compared to the expected losses in the case of doing nothing for protection/mitigation). Protective measures can include seawalls, barriers, artificial dunes, restoration of wetlands, raising individual buildings, sealing parts of the infrastructure, strategic retreat, insurance, and many more. The optimal protective strategy can be a combination of several protective measures implemented over space and time. The optimization process starts with parameterizing the protective measures. Storm-induced flooding and SLR, and their corresponding consequences, are estimated using a GIS-based subdivision-redistribution methodology (GISSR) developed by the authors for finding a rough solution in the first brute-force iterations of the optimization loop. A storm surge computational model called GeoClaw is subsequently used to simulate ensembles of synthetic storms in order to fine-tune and achieve the optimal solution. Damage loss, including economic impacts, is quantified based on calculated flood estimates. The suitability of the potential optimal solution is examined and assessed with input from stakeholders' interviews. It should be mentioned that the results and conclusions provided in this work depend on the assumptions made about future sea level rise (SLR). The authors acknowledge that there are other, more severe predictions for sea level rise (SLR), than the one used in this paper.

Keywords: coastal protection, optimization, sea level rise, storm surge flooding, damage assessment, GeoClaw, mitigation, climate risk

OPEN ACCESS

Edited by:
Valentina Prigiobbe, Stevens Institute of Technology, United States

Reviewed by:
Jose A. Marengo, Centro Nacional de Monitoramento e Alertas de Desastres Naturais (CEMADEN), Brazil
Hatim O. Sharif, University of Texas at San Antonio, United States

***Correspondence:**
Kyle T. Mandli
kyle.mandli@columbia.edu

Specialty section:
This article was submitted to Climate Risk Management, a section of the journal Frontiers in Climate

Received: *01 October 2020*
Accepted: *07 July 2021*
Published: *05 August 2021*

Citation:
Miura Y, Dinenis PC, Mandli KT, Deodatis G and Bienstock D (2021) Optimization of Coastal Protections in the Presence of Climate Change. Front. Clim. 3:613293. doi: 10.3389/fclim.2021.613293

1. INTRODUCTION

Communities in coastal regions are likely to face more severe catastrophic events such as storm-induced flooding in the future due to a changing climate, especially sea level rise (SLR) (Marcos et al., 2015; Marcos and Woodworth, 2017; Marsooli et al., 2019). Rising sea levels will cause smaller storms to become larger threats than would otherwise be expected, leading to possible catastrophic damage to the coastal regions that may not have experienced these types of events as often in the past. Sea level is predicted to rise at least one meter for the worldwide mean by the end of the century (Parris et al., 2012; Stocker et al., 2013). Consequently, the return period of catastrophic storms is expected to shorten. It is observed that there has been a significant increase in nuisance flooding occurrences around the United States because of the steadily increasing sea level (Sweet, 2014). It is also found that the odds of flooding increases exponentially with SLR (Taherkhani et al., 2020). Lin et al. (2012) demonstrated that the present 100-year surge flooding would occur every 20 years or less in New York City, New York, due to the one-meter SLR. Existing and planned coastal defenses will need strengthening or redesigning because of the anticipated SLR in the city (Gornitz et al., 2020). New Orleans, Louisiana, is another vulnerable coastal city due to its low-lying land. The loss from flooding to the city is estimated to be very high (Burkett et al., 2002). Abadie et al. (2020) estimate that the flooding risk will be increased significantly due to SLR in Guangzhou in China and Mumbai in India. Frequent flooding due to SLR will increase the physical and financial damages over the years if there is no action taken to mitigate the risk.

Coastal protection strategies often require a combination of multiple measures. Finding an optimal solution is a particularly complex problem as a large number of uncertain parameters are involved in the decision-making process. A successful protective strategy should account for multiple physical, financial, cultural, and social factors (Adger et al., 2005). For example, the optimal solution will depend on many factors, including the area, scale, economic situation, community, infrastructure interconnectivity, etc. Several models have been developed to assess global flood risk (Hirabayashi et al., 2013; Winsemius et al., 2013) but are limited to the circumstances of an absence of protective strategies. These models also do not account for various factors at the local level, which may be critical in finding the optimal solution. Other methodologies in related areas include the following: Longenecker et al. (2020) introduced a rapid river-gauge-based methodology to support a decision-making process for first responders and communities at the community level in Yerington, Nevada. Although it is a computationally efficient method, it lacks hydrological modeling for higher accuracy. Zwaneveld and Verweij (2014) developed a methodology to optimize the height of a protective dyke in the Netherlands at the country level. However, the model does not account for any other protective measures other than a dyke. Dupuits et al. (2017) introduced a framework for economic optimization of coastal flood defense systems by considering a front protection (e.g., barriers) and a rear protection (e.g., levees). This framework has been applied in the Galveston Bay area near Houston, Texas. While risk assessment tools and techniques have been established in past years (Jonkman et al., 2004), methods to evaluate the efficiency of an investment, or to support decision-making on the investment are lacking (Ward et al., 2015, 2017). A recent study in the Gulf Coast compared the cost-benefit of investments in coastal natural-based, structural, and policy measures using a cost-benefit analysis (Reguero et al., 2018). The methodology can estimate a large scale of losses as it uses a parametric method for widely averaged information of the target area.

Since the loss varies heavily depending on the local economy, interdependency, and building assets, it is crucial to account for the local stakeholders' feedback and the local detailed geographical/economic information for decision-making. Although a number of risk analysis methods have been introduced, finding an optimal solution is still far from a trivial problem.

The proposed optimization methodology incorporates accurate flood estimation models based on hydrological fluid dynamics, detailed building damage assessment, infrastructure inoperability loss analysis, and input from stakeholders' first-hand knowledge. To manage the computation time efficiently, the first iterations of the optimization use a simple flood estimate model based upon Geographical Information Systems (GIS) and Manning's Equation [this is called the GIS-based subdivision-redistribution methodology (GISSR); Miura et al., 2021a]. The GISSR model is a physics-based, extremely efficient, heuristic method using detailed topographical and infrastructure data, Manning's Equation, and Weir's coefficient if there are any protective measures present. After narrowing down the range of potential optimal solutions, the actual optimal solution is determined using the GeoClaw model (Berger et al., 2011), which is highly accurate, though computationally much more expensive than the GISSR model. The damage for every component of the infrastructure (e.g., buildings) is assessed using fragility curves and the estimated height of water at the location. The calculated damage also includes indirect economic losses such as income loss, inventory loss, and loss due to the interconnectivity of different infrastructure sectors. The optimal solution minimizes the expected value of the overall cost (the sum of all types of losses plus the implementation cost of the protective measures) within a prescribed budget and for a prescribed frame.

This article provides some preliminary results for Lower Manhattan in New York City (NYC) using the optimization methodology framework developed in Miura et al. (2021c) and assuming a specific SLR scenario. The main objective of this work is to introduce the methodology and demonstrate the nature of the results/conclusions. It should be noted that different assumptions about the extent of future SLR will lead to different results/conclusions. NYC is selected as a testbed because of its complex infrastructure assets and data availability. In 2012, Hurricane Sandy caused a major power outage and resulted in massive financial losses. Since that event, the city has been planning to enhance its resiliency against similar future hazards. The Big U project (Rebuild By Design, 2015) and the East Side Coastal Resiliency Project (City of New York, 2021) are some of the proposals to increase the city's resiliency. This article is

based on the concept of a similar protective measure like the Big U and the East Side Coastal Resiliency Project. Although the focus of this study is NYC, the methodology is general enough to be applied to different regions when the required data (e.g., topography data, building data, hazard data) is available.

2. METHODOLOGY

The proposed methodology aims at optimizing coastal protective strategies against storm-induced flooding and SLR by integrating physical damage models, economic loss models, and inputs from professional stakeholders with first-hand knowledge of the situation and members of at-risk communities. The methodology framework was introduced in Miura et al. (2021c).

As shown in **Figure 1**, the optimization starts from parameterizing the potential protective measures or strategies in a target area. The protective strategy can consist of multiple protective measures, including seawalls, barriers, artificial dunes, restoration of wetlands, artificial islands and reefs, raising individual buildings, sealing parts of the infrastructure, strategic retreat, insurance, and many more. Once these protective measures are parameterized, inundated areas are analyzed with two types of flooding model tools: a GIS-based subdivision-redistribution methodology (GISSR) (Miura, 2020) and the GeoClaw model (Berger et al., 2011). The GISSR model is a computationally efficient, physics-based heuristic model. It is based on topographical data, infrastructure information, Manning's equations, Weir's coefficient, and ensures mass conservation. The GeoClaw model is based on the finite volume method and solves the shallow water equations to capture flooding more accurately but is computationally more expensive compared to the GISSR model. The GISSR model is used to establish a range of potential optimal strategies during the first iterations of the optimization loop. The GeoClaw model then fine-tunes the optimal solution. Damage and losses are computed using flood height information at each building or component of the infrastructure. The damage cost includes physical damage loss, economic loss, and indirect economic loss. The physical damage percentage is computed first using fragility curves for each building or infrastructure component, and then the actual physical damage value/cost is calculated using the component's available asset value. Based on the physical damage cost, each sector's inoperable dates and restoration period can be computed. The economic loss and indirect economic loss are calculated using these dates and the interdependency ratio of industries or infrastructures. The interdependent critical infrastructures are, for example, transportation systems, the power grid, other utilities, etc. Eventually, with the input from stakeholders and communities with first-hand knowledge of the situation, the overall damage cost, cost of the optimal protection strategy, and suitability and social acceptability of the protective measures are all examined and modified if necessary. The optimization loop then repeats with another protection strategy until the optimal solution meets all objectives and constraints. In the following sections, each step is described in detail.

2.1. Parameterization of Protective Strategy

Each optimization iteration starts with the formulation of a new protective strategy based on the evaluation of the protective strategy in the previous iteration. For the first iteration loop, the comparison is made with the base case of no protective strategy at all. A protective strategy may consist of multiple protective measures implemented at different geographic (spatial) locations and at different times. For example, a protective strategy can consist of building a seawall with a 2 m height in 2020 and then adding an additional meter of height on top of it in 2050. In such a case, an appropriate discount rate has to be considered. Different variables can change for each protective strategy. For example, seawalls or elevating the coastline would need variables such as height, length, location, construction timing, etc. Based on these variables, the implementation cost can be computed. The cost estimate function should account for the local stakeholders' input as such costs may vary significantly locally according to Dols (2019). In the case of a seawall or elevated promenade along the coastline, the topographical data such as the digital elevation model (DEM) is modified by adding the designated wall height or the elevation height of the promenade onto the corresponding DEM cells at the locations where these protective measures are installed.

2.2. Flood Simulation

Two flood simulation models are employed in the optimization iterations: the GISSR model and the GeoClaw model. The first iterations take advantage of the computational efficiency of the GISSR model to identify a rough estimate of the optimal solution. After that, the GeoClaw model takes over to establish the optimal solution with high accuracy.

2.2.1. GIS-Based Subdivision-Redistribution Methodology (GISSR)

As the optimization process requires a large number of iterations, it is necessary to simulate storm-induced flooding with high computational efficiency. The GIS-based subdivision-redistribution methodology (GISSR) (Miura et al., 2021a) is extremely efficient computationally, but it is less accurate than the GeoClaw model. This method is used to get a rough estimate of the optimal solution. The GISSR model requires topographical features (e.g., elevation, surface roughness, slope, etc.), time history data of the water level including surge, tide, and SLR, and a detailed description of the protective strategies as shown in **Figure 2**.

At every point within the area under consideration, the flood height is computed using Manning's Equation and Weir's coefficient. The Manning's equation's coefficient is selected depending on the land type (e.g., urban, wetland) and surface roughness (e.g., the density of buildings) in the area of interest. If a scenario includes a seawall type of protective measure, Weir's coefficient is used to model a protective measure as a weir. The GISSR model first computes the overall flood volume during a hurricane event coming into the area under consideration by dividing the area into a number of smaller-scale "divisions." This overall flood volume is redistributed to adjacent divisions

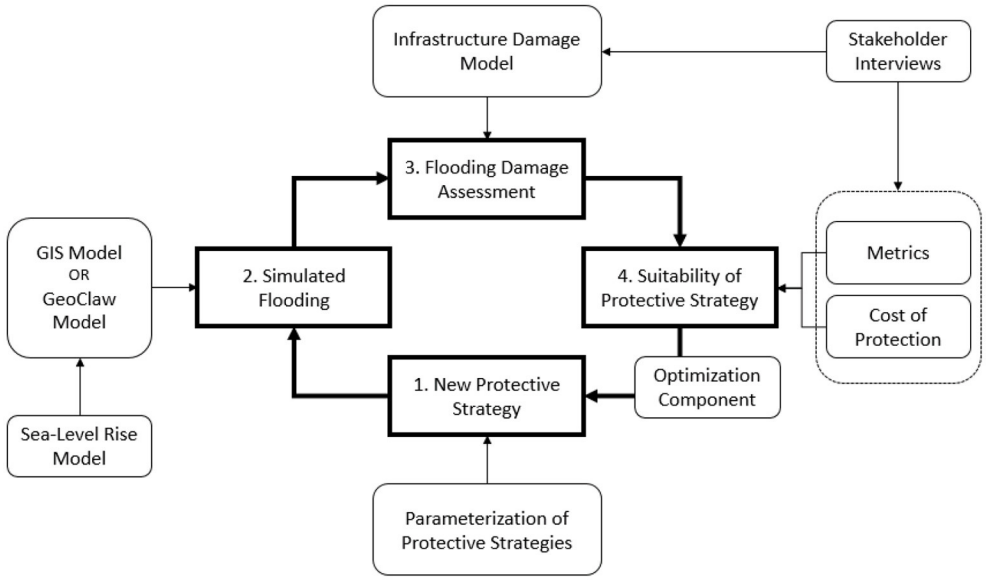

FIGURE 1 | Conceptual layout of the proposed methodological framework (Miura et al., 2021c).

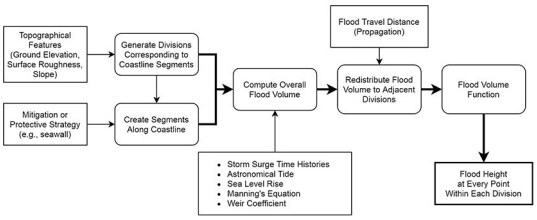

FIGURE 2 | The GISSR flood simulation schematic diagram. Rectangles indicate inputs and rounded rectangles indicate processes.

accounting for water propagation. Once the flood volume in each division is established, it is translated into flood height within each division using a surface volume function (the flood height is uniform in a division).

The maximum surge height for a storm event is modeled by a modified beta distribution (Miura et al., 2021b). The corresponding frequency, duration, and time history are modeled using the method introduced in Lopeman et al. (2015). The simulation eventually establishes the flood height time history at every point within the area under consideration. The computed flood height at every point will be then used as input in the damage assessment model, as described in section 2.3. It should be noted that the GISSR model's accuracy has been validated with Hurricane Sandy's data, and the simulated inundated area and actual inundated area have been found to be almost identical (Miura et al., 2021a).

2.2.2. GeoClaw Model

During the last optimization iterations, flood simulations are carried out using GeoClaw, a numerical solver for 2D shallow water equations over varying topographies as part of Clawpack (Conservation Laws Package) (Berger et al., 2011; Mandli et al., 2016; Clawpack Development Team, 2020). It is important to use this fluid-dynamics model in combination with the GISSR model since this provides a more physically accurate picture of how flood water will redistribute itself.

GeoClaw takes as input a parameterized tropical cyclone (TC) and simulates the resulting storm surge by numerically solving the shallow water equations in the Atlantic basin with forcing terms from the TC. The TC is parameterized according to the model given by Holland (1980). For each time step, the TC has the following parameters: longitude and latitude of the eye of the storm, maximum wind speed, the radius at which maximum wind speed is attained, and central pressure. In the model of Holland (1980), these parameters allow a wind field to be reconstructed, which supplies the forcing terms to the shallow water equations.

For the simulations in this work, an ensemble of such parameterized TCs is run to calculate the expected peak storm surge height. The ensemble of storms is generated from the Columbia Hazard Model (CHAZ), a statistical-dynamical model due to Lee et al. (2018). The CHAZ model takes environmental parameters in a model of the Atlantic basin and stochastically generates TCs. The ensemble is comprised of those TCs that come close to NYC. GeoClaw is also run on a parameterized model of Hurricane Sandy (National Hurricane Center, 2017) with different protective measure scenarios to examine their effectiveness. An example GeoClaw run of Hurricane Sandy's track in the Atlantic Ocean and resulting storm surge on the US east coast is shown in **Figure 3**. A good predictive test of how efficient the protective strategy will be on potential future storms is obtained by carrying out a high-refinement shallow water simulation on storms derived from physical conditions.

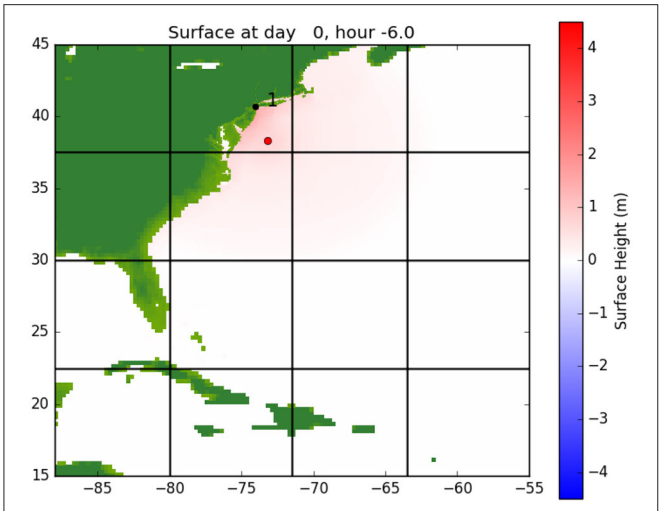

FIGURE 3 | A plot at 6 h before landfall of a GeoClaw simulation of Hurricane Sandy. The red dot indicates the eye of the storm and the black dot (1) indicates Battery Park in Lower Manhattan.

Each GeoClaw storm-surge calculation is significantly more computationally expensive than the GISSR model. As a result, the entire space of protective strategies with GeoClaw simulations is not searched. It is used to test the robustness of a small subset of GISSR suggested optimal solutions over different storms.

2.3. Damage Assessment

Using appropriate fragility functions (e.g., Hazus developed by Department of Homeland Security, Federal Emergency Management, 2018), the damage loss and economic loss for every component of the infrastructure can be quantified (including structural damage, damage to contents, and loss of use). The loss is computed for a given storm with known water height at any location within the geographical area considered (using the GISSR model or the GeoClaw model). The losses are then added for all infrastructure components inside the geographical area considered to establish the overall loss from this specific event, and then for all of the events over the prescribed time frame.

2.3.1. Physical Damage and Economic Damage

For this study, the damage fragility curves provided by Hazus that was developed by the Department of Homeland Security, Federal Emergency Management (2018) are adopted with a slight modification for tall buildings that are prevalent in Lower Manhattan (Miura et al., 2021c). Damage functions are available for a variety of different classes of buildings, including various residential building types, commercial building types, utilities, factories, theaters, hospitals, nursing homes, churches, etc. The total damage/loss C_{dmg} to the built infrastructure in a target area related to physical loss is computed from the expression:

$$C_{\text{dmg}} = \sum_{i}^{N_{\text{b}}} a_i D_i(h_i) \tag{1}$$

where N_{b} is the total number of buildings/infrastructure components in the area, a_i is the total value/asset of building/infrastructure component i, and D_i is the percentage of the total replacement cost associated with flood height h_i observed at the location of building i. The flood height at each location h_i is computed by subtracting the critical elevation of each building from the total flood height computed in section 2.2.

Hazus has also developed functions to compute the economic losses due to suspended business operations during the restoration period. The losses taken into consideration in this article include income losses and inventory losses. If a building has commercial areas and did not collapse (buildings with over 50% damage are considered as collapsed), the damage functions for the total economic losses for each type can be computed as shown in Equations (2) and (3). The total economic losses are the total losses from all the buildings with commercial areas in the area under consideration.

Income loss:

$$C_{\text{inc}} = \sum_{i}^{N_{\text{com}}} (1 - f_i) A_i(h_i) I_i d_i(h_i). \tag{2}$$

Inventory loss:

$$C_{\text{inv}} = \sum_{i}^{N_{\text{inv}}} D_i(h_i) A_i(h_i) G_i B_i. \tag{3}$$

where N_{com} is the total number of buildings with commercial areas, f_i is the income recapture factor for occupancy i, I_i is the income per day for occupancy i, and d_i is the loss of function time for the business in days. N_{inv} is the total number of commercial/industrial buildings dealing with inventories, A_i is the floor area at and below the flood height h_i, G_i denotes the annual gross sales for occupancy i, and B_i is the business inventory which is a percentage of gross annual sales. This applies to retail trade, wholesale trade, and industrial facilities. It should be noted that when a storm destroys more than 50% of a building, the building is considered as collapsed and will be demolished (not repaired) for any types of building/occupancy. It should be pointed out that no building collapsed in Lower Manhattan during Hurricane Sandy. **Figure 4** shows the estimated damage percentage of each building in Lower Manhattan for the Hurricane Sandy scenario, and all the rates are lower than 50%. This result matches what happened in the city during this hurricane event (Miura et al., 2021c).

The total direct damage cost is the summation of the total damage/loss C_{dmg} and the total economic losses (C_{inc} and C_{inv}). For the optimization iterations, the total direct damage cost is computed for all the randomly generated storm events during the prescribed time frame of interest with different batches of storms as inputs for each simulation. **Figure 5** shows an example involving 1,000 simulations of cumulative damage assessment analysis over the next 80 years (2020–2100) in Lower Manhattan in NYC (without the presence of any protective measures). The storms in any year are separated into two seasons: warm season and cold season. The warm season is from June to

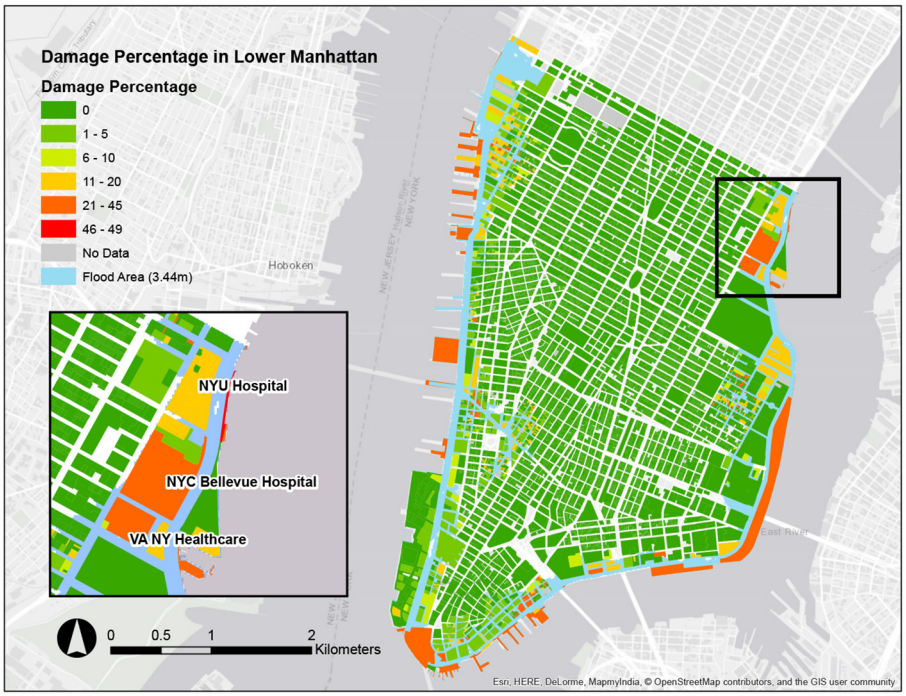

FIGURE 4 | An example of damage percentage calculation for every building/infrastructure component during Hurricane Sandy in Lower Manhattan (Miura et al., 2021c).

November, and the cold season is from December to May. The storm characteristics in each season are physically different. For example, Hurricane Sandy is a warm-season storm, while a Nor'easter is a cold-season storm. The total accumulated damage costs in the year 2100 vary from $2 billion to $4 billion for cold season simulations, and from $1.5 to $9 billion for warm-season simulations, as every batch of storm surge events over the next 80 years is quite different because of the different randomly generated storm events. It should be noted that the storms in the warm season (depicted in red) are relatively less frequent but of larger magnitude. The storms in the cold season (depicted in blue) are vice versa. The different underlying physical mechanisms causing warm-season vs. cold-season storm events cause a larger scatter for warm-season cumulative damages compared to the corresponding cold-season cumulative damages, as can be seen in **Figure 5**. It is observed in **Figure 5** that the damage costs of all the simulations start increasing nonlinearly from around the year 2070 because of the SLR effect.

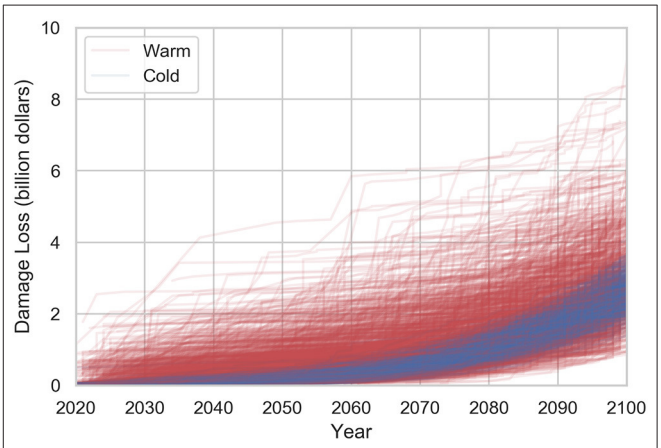

FIGURE 5 | An example of the cumulative direct damage (i.e., the summation of physical damage loss, income loss, inventory loss, and loss from interdependencies) from storm-induced flooding over the next 80 years (2020–2100) resulting from 1,000 different simulations in Lower Manhattan in NYC (without any protective measures present). The total cumulative damage cost/loss over the years varies for each simulation because of the different randomly generated storm events in each one of the 1,000 simulations. Blue lines indicate damage losses from cold-season storms. Red lines indicate damage losses from warm-season storms.

2.3.2. Economic Damage due to Inoperability and Interconnectivity

When an infrastructure component is inoperable due to flooding, the interdependency (interconnectivity) of infrastructure components (infrastructures) may trigger additional financial impacts on other sectors of the infrastructure. This extra economic impact should be accounted for in the damage assessment. During Hurricane Sandy in 2012, there was a major power outage in Lower Manhattan due to an explosion at a flooded utility facility on the Lower East Side. This accident caused not only millions of people to be without electricity, but other infrastructure sectors such as hospitals, fuel distributors, businesses, and many more, to be partially or fully non-functional. Using the Inoperability Input-Output Model (IIM)

(Haimes and Jiang, 2001) based on the I-O model introduced originally by Leontief (1986) and the damage cost computed using the modified Hazus model as described in section 2.3.1, economic loss due to interdependencies of the infrastructures can be calculated using the inoperability ratio. This inoperability ratio is highly dependent on the region of interest as it indicates how much each sector depends on each other financially. For example, a highly urbanized area such as NYC may have higher impacts on industries such as business and commerce.

For NYC, Cimellaro et al. (2019) evaluated Hurricane Sandy induced damages and established the inoperability ratios for the metropolitan area based on IIM. Using the inoperability ratio matrix, this study quantified the losses due to the inoperability of utilities and transportation infrastructures.

2.4. Stakeholders' Feedback Input

A set of interviews with city and state stakeholders who have first-hand knowledge of the NYC area's infrastructures have been planned to check the suitability/acceptability of the optimization model (including flood estimate models, damage assessment models, and information on interdependencies of the infrastructures in the city) and of its results concerning the optimal protective strategy. The first interviews were conducted in the early stages of the project. The stakeholders provided feedback on the models and provided information on the interdependencies of the infrastructures in the target area. The second set of interviews was conducted after reflecting on the first set's inputs, in order to further refine the method and its results. Based on the outcomes of these interviews, the optimization model, including flood simulation models and damage assessment models, will be updated so that the model can generate socially acceptable optimal solutions.

2.5. Optimization

The methodology optimizes coastal protective strategies (this can be a combination of multiple protective measures) given a constraint, here the overall budget for building protection and mitigation measures. For a prescribed budget and a prescribed time horizon of N years (N can be 20, 50, 100 years, or any other number), the optimal solution is the one that minimizes the sum of the total storm-induced losses plus the cost of implementing the protective strategy. The budget can be defined arbitrarily by the user, and different budget levels can be considered to explore different corresponding optimal solutions.

The first step is to calculate the overall expected losses over the N years from all randomly generated storms during this period, without any protective strategy implemented. These losses are denoted by L_{no} (losses are considered in a statistical sense in this section as L_{no} is a random variable computed/realized M times from M different simulations over the period of N years).

Each selected protective strategy at a given iteration of the optimization process is examined using the same set of M simulations of randomly generated storms over N years that was considered for the base case of "no protective strategy/measures." For a selected protective strategy, its total cost (total implementation cost L_{co} of the strategy plus overall losses L_{ps} from all the storms during the period of N years) is computed, again in a statistical sense. This total cost has to be less than L_{no} for the protective strategy to be preferable to the base case of "no protective strategy implemented":

$$L_{\text{co}} + L_{\text{ps}} < L_{\text{no}}. \tag{4}$$

If Equation (4) is not satisfied for a specific protective strategy, then this strategy is unacceptable (since the case of no protective strategy has a lower overall cost).

The total cost is estimated using the damage assessment models (section 2.3) with the estimated flood heights [the outcome of the GISSR model (section 2.2.1) and the GeoClaw model (section 2.2.2)]. As described previously, the GISSR model is used to find a rough estimate of the optimal solution, and the GeoClaw model fine-tunes this rough estimate of the optimal solution. Since the frequency of storms and their magnitude are uncertain over the prescribed period, the methodology uses multiple simulations M over the prescribed N years to find a histogram and a corresponding expected value and standard deviation of the total cost. Each simulation uses a different set of randomly generated storms modeled over the N years.

For a preliminary demonstration of the methodology, this paper uses a brute-force iterative approach for the optimization on a discrete set of protective measures. Each brute-force optimization loop returns a different histogram/probability distribution of the total cost over the N years. If the summation of the implementation cost and overall losses of the protective strategy at iteration (p) is less than that of iteration ($p-1$), then the protective strategy at iteration (p) becomes the temporary optimum solution. Otherwise, the protective strategy at iteration ($p-1$) remains the temporary optimal solution, and a new protective strategy is tested against it. This procedure is expressed as follows:

$$\text{If } (L_{\text{co}} + L_{\text{ps}})_{(p-1)} > (L_{\text{co}} + L_{\text{ps}})_{(p)}, \text{ then } (L_{\text{co}} + L_{\text{ps}})_{(p)} \text{ becomes the new temporary optimal strategy and a new protective strategy is tested against it.} \tag{5a}$$

$$\text{If } (L_{\text{co}} + L_{\text{ps}})_{(p-1)} < (L_{\text{co}} + L_{\text{ps}})_{(p)}, \text{ then } (L_{\text{co}} + L_{\text{ps}})_{(p-1)} \text{ remains as the temporary optimal strategy, } (L_{\text{co}} + L_{\text{ps}})_{(p)} \text{ is discarded, and a new protective strategy is tested against } (L_{\text{co}} + L_{\text{ps}})_{(p-1)}. \tag{5b}$$

The iterations continue until $(L_{\text{co}}+L_{\text{ps}})$ stabilizes, without any substantial further reduction possible in subsequent iterations. It is reminded that as with L_{no}, L_{ps} is considered in a statistical sense.

The optimization variables can change depending on the protective measures considered. For example, in the case of seawalls as protective measures, the variables would be location, height, length, and construction timing.

3. COASTAL PROTECTION OPTIMIZATION IN NEW YORK CITY

Lower Manhattan in NYC is selected as a testbed because of the city's complex infrastructure and data availability. As this is

TABLE 1 | New York City sea level rise projections (the 2000–2004 period is considered as the sea level baseline (Horton et al., 2015; Gornitz et al., 2019).

	Low estimate (10th percentile)	Middle range (25th–75th percentile)	High estimate (90th percentile)
2050s	8 in (0.203 m)	11–21 in (0.279–0.533 m)	30 in (0.762 m)
2080s	13 in (0.330 m)	18–39 in (0.457–0.991 m)	58 in (1.473 m)
2100	15 in (0.381 m)	22–50 in (0.559–1.270 m)	75 in (1.905 m)

the first application of the methodology, the protective measure considered is only a seawall (as there are planned projects called the Big U (Rebuild By Design, 2015) and the East Side Coastal Resiliency Project (City of New York, 2021) involving a seawall in Lower Manhattan).

The optimal solution is narrowed down using the GISSR model (Miura et al., 2021a) and then is validated with the GeoClaw model (Berger et al., 2011). Although the GeoClaw model is in general used to fine-tune the optimal solution established by GISSR, here, it is only used to validate it.

3.1. Future Anticipated Storms and Sea Level Rise

Surge data for storms are generated using the methodology introduced by Lopeman et al. (2015) and a modified beta distribution to model the maximum surge height of a storm. This study accounts for SLR at the Battery, NY, as predicted by Horton et al. (2015) and Gornitz et al. (2019). The projected SLR values are shown in **Table 1**. The projections are estimated with the 2000–2004 period as the reference baseline. For each year examined, the average of the 25th and 75th percentile estimates from **Table 1** is used in this study (which is referred to as the middle estimate). Hence, the middle SLR estimates employed for the 2050s, 2080s, and 2100 are 0.406, 0.724, and 0.9145 m, respectively.

As the number of storms and the corresponding maximum storm surge values are uncertain, M simulations are performed over the N years considered. Each simulation has a different number and magnitude of storms, and these are modeled as random variables. The peak storm surge height is modeled with a modified beta distribution (Miura et al., 2021b). The number of simulations M is set equal to 1,000, and the prescribed number of years N is set equal to 80 (from 2020 to 2100) for this study. **Figure 6** depicts the peak water levels (peak storm surge + SLR + tidal height) for storms randomly generated over the 80-year period from 2020 to 2100, accounting for a middle estimate of SLR. **Figure 6** displays the randomly generated storms from one simulation among the $M = 1,000$ considered. The storms in the warm season (depicted as red dots) are relatively less frequent but larger in magnitude on the average. The storms in the cold season (depicted as blue dots) are the other way around. **Figure 7** displays all the storms from all the $M = 1,000$ simulations considered. Even moderate storms close to the end of this 80-year period can become severe ones in overall water height because of SLR.

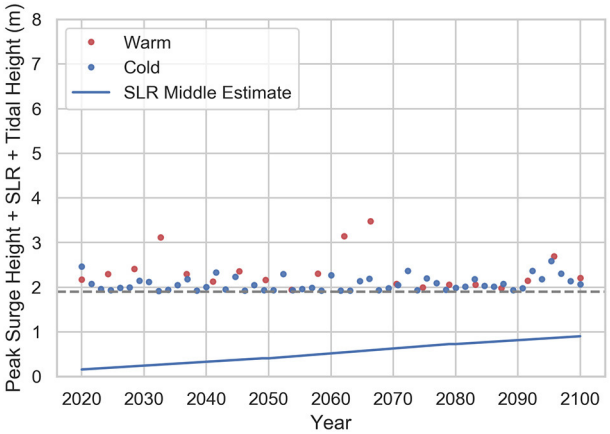

FIGURE 6 | An example of one simulation of randomly generated storms expressed through their corresponding peak water levels (peak storm surge + SLR + tidal height) over the 80-year period considered (2020–2100). The blue dots depict peak storm surges in cold season. The red dots depict peak storm surges in warm season. Middle SLR estimate (Horton et al., 2015; Gornitz et al., 2019) is considered. SLR is denoted by the continuous sloped blue line. The dashed horizontal gray line indicates the 1.9 m threshold, below which there is no flooding observed in Lower Manhattan.

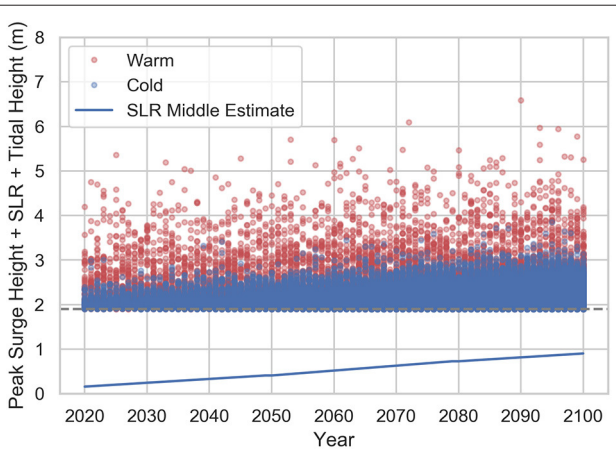

FIGURE 7 | One thousand simulations of randomly generated storms expressed through their corresponding peak water levels (peak storm surge + SLR + tidal height) over the 80-year period considered (2020–2100). The blue dots depict peak storm surges in cold season. The red dots depict peak storm surges in warm season. Middle SLR estimate (Horton et al., 2015; Gornitz et al., 2019) is considered. SLR is denoted by the continuous sloped blue line. The dashed horizontal gray line indicates the 1.9 m threshold, below which there is no flooding observed in Lower Manhattan.

3.2. Potential Protective Measures

Although coastal protective measures can be numerous as mentioned earlier, this article considers only a seawall in Lower Manhattan for demonstration purposes. The seawall configuration is optimized using multiple variables, including its height, length, and specific location as indicated in **Figure 8**.

Based on studies of cost estimates for flood adaptation/mitigation including seawalls (Aerts et al., 2013;

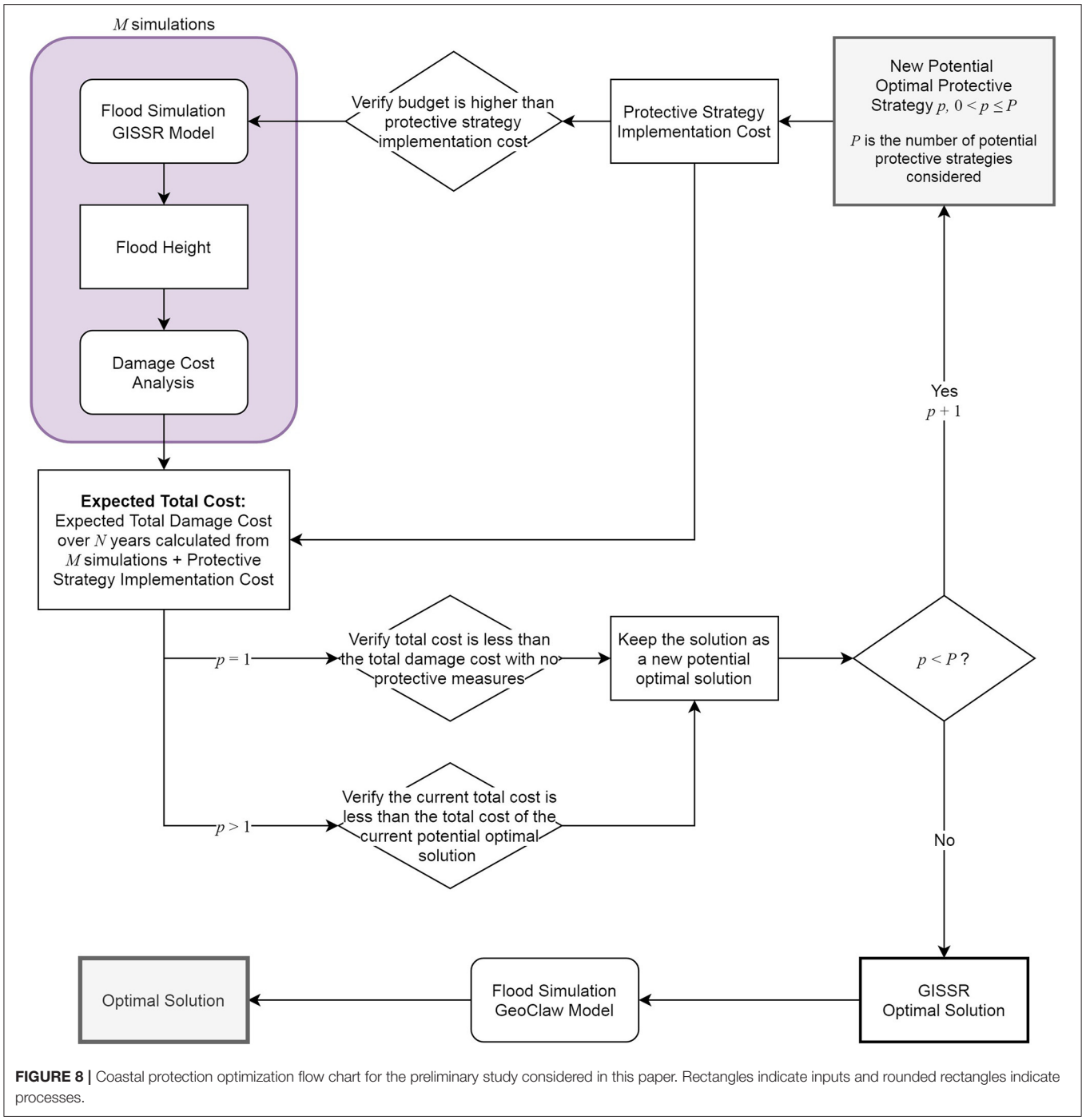

FIGURE 8 | Coastal protection optimization flow chart for the preliminary study considered in this paper. Rectangles indicate inputs and rounded rectangles indicate processes.

Aerts, 2018) and the NY and NJ harbor and tributaries focus area feasibility study (HATS) (Dols, 2019), the construction cost estimate of a seawall in this study is modeled as shown below:

$$L_{\mathrm{co}_{\mathrm{wall}}} = \$49,212\, h_{\mathrm{wall}}\, l_{\mathrm{wall}} \tag{6}$$

where, $L_{\mathrm{co}_{\mathrm{wall}}}$ is the seawall's construction cost in US dollars, h_{wall} is the seawall height in meters, and l_{wall} is the seawall length in meters. In most of its length around Lower Manhattan, the currently considered Big U project is designed as an elevated promenade instead of just a seawall or floodwall. The construction cost of such an elevated promenade is estimated by Dols (2019).

The \$49,212 cost value in Equation (6) corresponds to a wall segment having a length equal to one meter and height also equal to one meter.

3.3. Optimal Solution

The optimal solution in this study is the protective seawall/elevated promenade configuration that minimizes the total expected cost given a prescribed budget. The total expected cost includes the total damage cost (Equations 1–3) and the implementation/building cost of the protective seawall given in Equation (6) (in the following, the elevated promenade/seawall is simply going to be referred as seawall). The damage costs are computed using the dataset provided by the New York City Department of City Planning (2018) for each individual building with property assets data.

The minimum expected cost is found by an exhaustive brute-force search using a discretized set of the protective measure variables ($h_{\text{wall}}, i_{\text{wall}_0}, i_{\text{wall}_f}$).

3.3.1. Objective Function and Constraints

The objective function of the optimization problem is defined as:

$$\min_{\boldsymbol{x}} \left\{ L_{\text{co}}(\boldsymbol{x}) + \mathbb{E}_S \left[\sum_{s \in S_j} f(\boldsymbol{x}; s) \right] \right\} \tag{7}$$

where $f(\boldsymbol{x}; s)$ is the total damage cost (physical damage and economic loss) from each storm event s, S_j is one set of randomly generated storms to hit NYC in the period 2020–2100 considered here, $\mathbb{E}_S$ is the expected value over all $M = 1,000$ simulations considered, and L_{co} is the total implementation/building cost of the protective strategy. The decision variable is:

$$\boldsymbol{x} = (h_{\text{wall}}, i_{\text{wall}_0}, i_{\text{wall}_f}) \tag{8}$$

where, i_{wall_0} and i_{wall_f} represent the start and end locations of the seawall, respectively. The constraints are:

$$\begin{aligned} 0 \leq & h_{\text{wall}} \leq 5\text{m} \\ 0 \leq & i_{\text{wall}_0} \leq i_{\text{wall}_f} \leq i_{\text{wall}_F} \\ & L_{\text{co}} \leq L_{\text{budget}} \end{aligned} \tag{9}$$

As described in Equation (4), the total cost (the summation of the implementation cost L_{co} and overall losses L_{ps}), must be less than the overall losses without any protective measures L_{no}. This is ensured by including the no seawall scenario in the search domain. L_{budget} is the prescribed budget.

In the implementation, an exhaustive search is performed to determine the aforementioned minimum total expected cost over a discretized set of seawalls, specifically $h_{\text{wall}} \in \{0.5, 1.0, 1.5, ..., 5.0\}$ measured in meters, and $i_{\text{wall}_0}, i_{\text{wall}_f} \in \{0, 1, 2, ..., 162\}$ corresponding to 163 locations along the coastline of Lower Manhattan, spaced 100 meters apart. Consequently, the seawall length can be computed:

$$l_{\text{wall}} = 100\text{m}\,(i_{\text{wall}_f} - i_{\text{wall}_0}) \tag{10}$$

1,000 sets of randomly generated storms to hit NYC in the period 2020–2100 are simulated ($M = 1,000$ simulations: $\{S_j\}_{j=1}^{1,000}$).

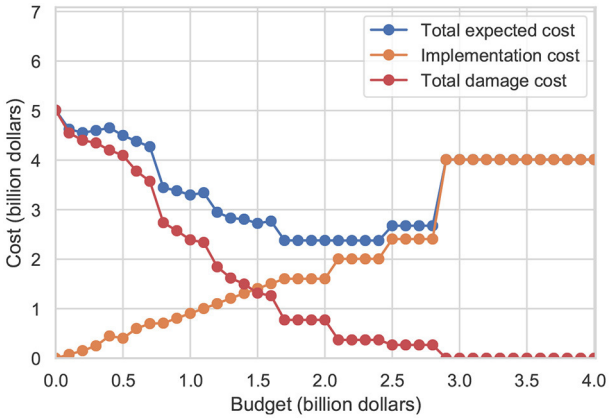

FIGURE 9 | The total expected cost of an optimal solution as a function of the prescribed budget for the Lower Manhattan area. Orange dots represent the implementation cost of the optimal protective strategy, red dots represent the corresponding total damage cost, and blue dots represent the sum of the orange and red dots (total expected cost). The total expected cost of the optimal solution (blue dots) varies significantly as a function of the prescribed budget.

Consequently, the objective function in Equation (7) can be rewritten as:

$$L_{\text{co}}(\boldsymbol{x}) + \frac{1}{1,000} \sum_{j=1}^{1,000} \sum_{s \in S_j} f(\boldsymbol{x}; s) \tag{11}$$

3.3.2. Optimal Solution Using the GISSR model

The optimal solution minimizing the total expected cost (Equations 7, 11) differs significantly as a function of the level of the prescribed budget. **Figure 9** plots the total expected cost of the optimal solution as a function of the prescribed budget (as the total cost is a random variable, its expected value is used here). With zero budget available (no protective measures), the expected value of the total damage cost is around $5 billion. As the level of the prescribed budget increases, the total expected damage cost decreases, as well as the total expected cost. At the $1.7 billion budget level, the total expected cost stabilizes at around $2.4 billion. Further increases of the prescribed budget up to $2.4 billion do not produce any significant variation in the $2.4 billion value of the total expected cost. When the budget becomes larger than $2.4 billion, the total expected cost starts increasing again as seen in **Figure 9**. It should be noted that it is possible to reduce the expected damage cost to zero, but the necessary budget is relatively high (a budget of around $4 billion is necessary to achieve the zero expected damage cost).

Figure 10 displays the actual optimal protective seawall measures for four different levels of the prescribed budget. It is clear that different budget levels lead to different optimal seawall solutions. The $0.5, $1.0, and $1.5 billion budgets produce optimal solutions with seawalls over only a part of the entire coastline. The $2.1 billion budget yields an optimal solution with a 2.5 m high seawall over the entire length of the coastline of Lower Manhattan.

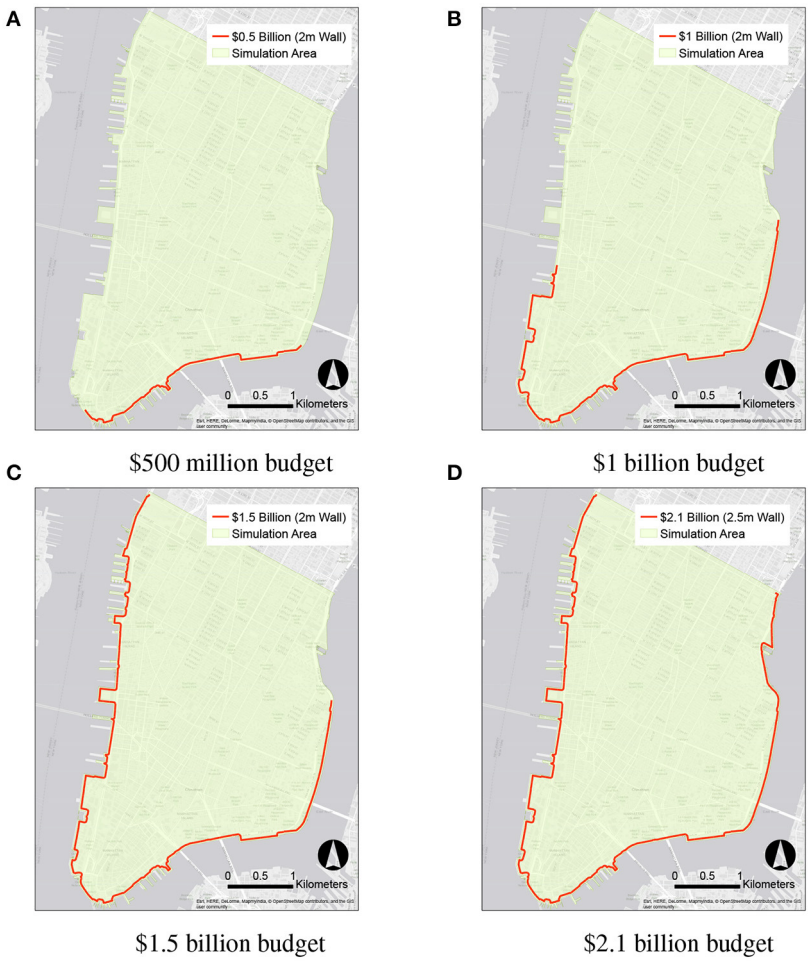

FIGURE 10 | Optimal protective seawall measures corresponding to four different prescribed budget levels. **(A)** $500 million budget, **(B)** $1 billion budget, **(C)** $1.5 billion budget, **(D)** $2.1 billion budget.

3.3.3. Flood Simulations Using the GeoClaw Model

In order to validate and verify the robustness of the optimal solutions found using GISSR, tests are performed against a number of storms modeled in GeoClaw. A representative point at (−74.013, 40.705) is selected in Lower Manhattan, and the peak flood height at this point is calculated using GeoClaw with different storms and different protective seawalls in front of it.

Figure 11 shows results of Hurricane Sandy simulations with different seawalls and no SLR. The images show the flood height and sea surface height at the time of peak flood height. The $1 billion seawall is in front of our point of interest, but because of the high storm surge, water can get over the seawall and around the sides of the wall (see **Figures 10B**, **11C**). As a result, much of Lower Manhattan is inundated, even areas directly behind the wall. The $2.1 billion wall shows some inundation, though much less (see **Figures 10D**, **11D**).

GeoClaw runs of Hurricane Sandy were also performed with SLR corresponding to the middle estimate for the 2020–2100 period. **Figure 12** shows the corresponding peak flood heights at the selected point of interest. **Figure 12** indicates that for Sandy without SLR, the flood protection offered by the 1 billion wall is little to nothing at the selected point of interest, whereas the $2.1 billion wall provides greater protection. With SLR, especially from the year 2080 and onwards, both walls begin to become obsolete, showing only minimal levels of protection.

GeoClaw simulations were also run using an ensemble of 26 TCs that reach land near the NYC area selected from the synthetically generated storms in the Atlantic Ocean in a model of the current climate with no SLR. The mean peak flood heights of the ensemble of 26 storms at the same point of interest depicted in **Figure 11** are plotted in **Figure 13**. The results show that the $1 billion wall provides some protection in comparison to the no wall situation. This difference happens because the storm ensemble contains a number of storms with different induced storm surges, including smaller ones that do not overtop the wall. The $2.1 billion wall provides only a marginal further reduction in the mean peak flood height.

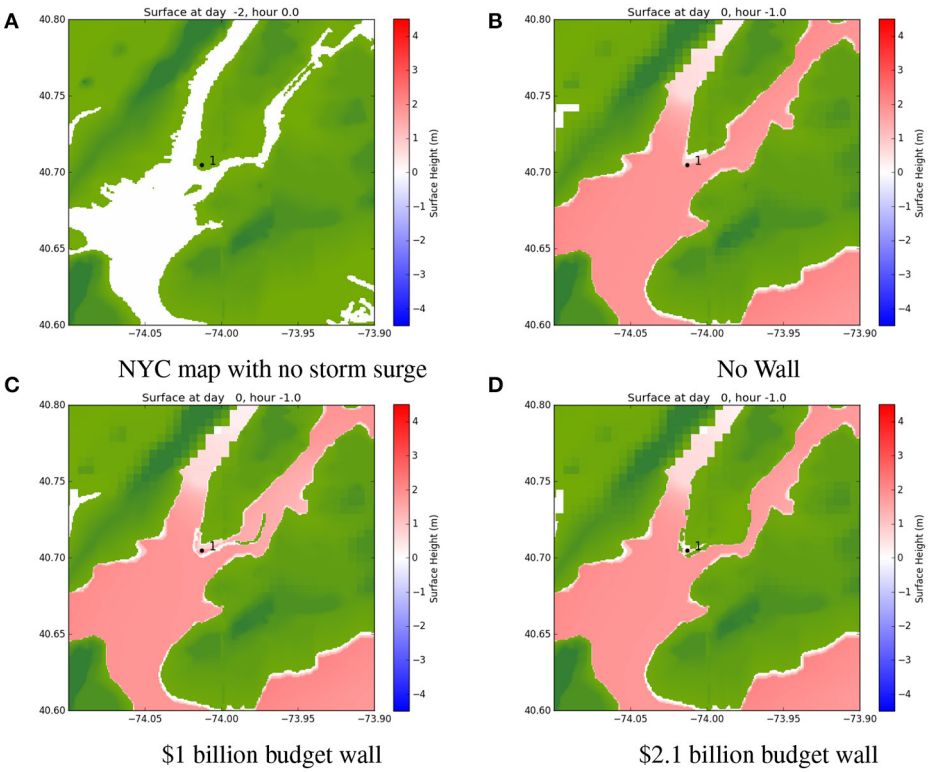

FIGURE 11 | Selected point in Lower Manhattan (denoted by 1) where peak flood heights are calculated for Hurricane Sandy and various different seawalls, using GeoClaw. **(A)** NYC map with no storm surge, **(B)** no wall, **(C)** $1 billion budget wall, **(D)** $2.1 billion budget wall.

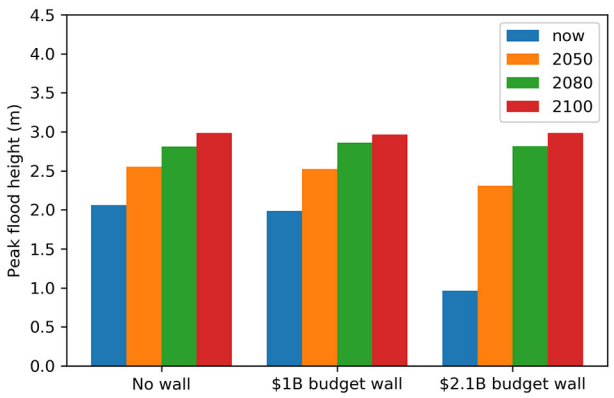

FIGURE 12 | A comparison of peak flood heights at the selected point in Lower Manhattan (identified by 1 in **Figure 11**) for different optimal protective measures and different levels of SLR.

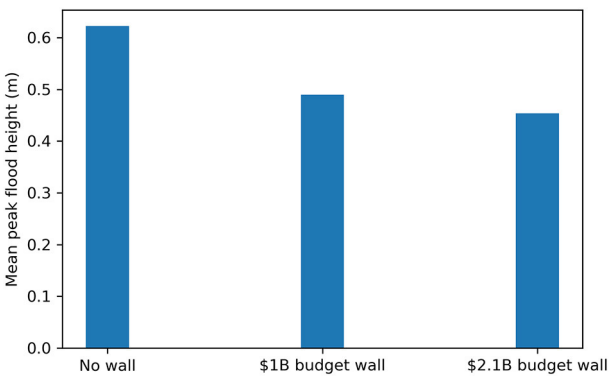

FIGURE 13 | Mean peak flood heights at the point depicted in **Figure 11** resulting from the selected ensemble of 26 TCs.

3.3.4. Comparison of the GISSR Model and the GeoClaw Model

The GeoClaw model is used in section 3.3.3 to validate the protective capability of GISSR-established optimal solutions against Hurricane Sandy and other possible TCs over the 2020–2100 period. As **Figure 12** shows, both walls examined show little protection past 2050, and the $1 billion wall shows little protection even at present against Hurricane Sandy. Against the ensemble of TCs, both walls show some protective capability compared to no wall. This is because the ensemble of storms had on average lower intensity than Hurricane Sandy. The storm inputs to the GeoClaw simulations in this study are all TCs categorized as warm-season storms and are therefore relatively more intense than cold-season storms. For the most

intense storms, the walls lose their protectiveness altogether as the flooding completely overtops them and inundates the area behind them. On the other hand, the GISSR model accounts for both cold and warm season storms. This explains why in the GISSR model, the $2.1 billion wall provides significantly more protection than the $1 billion wall, which in turn provides significantly more protection than no wall at all, even into the year 2100. Together these models show that a large advantage of the walls is their protective capability against frequent smaller storms. When faced with multiple superstorms such as Sandy and SLR, the two different examined seawalls start to diminish in their effectiveness.

4. CONCLUSION AND DISCUSSION

This study provides preliminary results for the optimal protective measures for Lower Manhattan in NYC, given a prescribed budget. The optimal solution is determined to minimize the expected total cost from all the potential storms over the 80-year period from 2020 to 2100, given a prescribed budget. The methodology combines hydrology and physics components, socio-economic factors, and stakeholder feedback to properly model the complex interdependency of the infrastructures. A discrete and exhaustive set of seawalls with different heights, lengths, and locations is examined in this study, and the corresponding expected total costs (i.e., damage cost and implementation/building cost) are computed. The optimal solution varies widely depending on the budget, which can be defined arbitrarily by users. A seawall with a height of 2.5 m along the entire coastline of Lower Manhattan with a budget of $2.1 billion appears to prevent major flooding sufficiently well, as the expected damage cost is decreased significantly. An optimal solution does not necessarily reduce the damage cost to zero since making the damage cost zero would significantly increase the implementation/building cost. The GeoClaw model showed that this seawall might become obsolete past 2050 against an ensemble of major TC storms like Hurricane Sandy and SLR. However, this methodology can help decision-makers evaluate future risks and make optimal decisions.

The results and conclusions provided in this work demonstrate the capability of the proposed methodology in optimizing coastal protective measures given a prescribed budget. This study's main contribution is to introduce the methodology and demonstrate the nature of the results/conclusions. If different SLR projections are used instead of the selected ones in this study (i.e., Horton et al., 2015; Gornitz et al., 2019), the corresponding results and conclusions are expected to be different.

Only the height, length, and location of seawalls were taken into account for this study for the sake of simplicity in demonstrating the capabilities of the methodology. In the future, it is suggested to include other variables such as construction timing, other measures (e.g., structural, nature-based, financial, and political), or a combination of thereof to determine a comprehensive optimal strategy for a target region.

A brute-force optimization approach was employed for simplicity in this study. More sophisticated optimization algorithms should eventually be employed to speed up the search for the optimal solution, such as a derivative-free descent algorithm on the protective measure parameters or a stochastic descent approach.

DATA AVAILABILITY STATEMENT

This study uses the dataset and tool as listed: Berger et al. (2011), Mandli et al. (2016), National Hurricane Center (2017), Department of Information Technology & Telecommunications (2018), New York City Department of City Planning (2018), Clawpack Development Team (2020), Miura (2020).

AUTHOR CONTRIBUTIONS

YM, PD, KM, and GD contributed to conception and design of the study. YM, PD, and KM organized the database. YM and PD performed the analysis. YM wrote the first draft of the manuscript. PD wrote sections of the manuscript. All authors contributed to manuscript revision, read, and approved the submitted version.

ACKNOWLEDGMENTS

The authors gratefully acknowledge support by the National Science Foundation under Grants No. DMS-1720288 and OAC-1735609.

REFERENCES

Abadie, L. M., Jackson, L. P., de Murieta, E. S., Jevrejeva, S., and Galarraga, I. (2020). Comparing urban coastal flood risk in 136 cities under two alternative sea-level projections: RCP 8.5 and an expert opinion-based high-end scenario. *Ocean Coast. Manage.* 193:105249. doi: 10.1016/j.ocecoaman.2020.105249

Adger, W. N., Arnell, N. W., and Tompkins, E. L. (2005). Successful adaptation to climate change across scales. *Global Environ. Change* 15, 77–86. doi: 10.1016/j.gloenvcha.2004.12.005

Aerts, J. C. (2018). A review of cost estimates for flood adaptation. *Water* 10:1646. doi: 10.3390/w10111646

Aerts, J. C., Botzen, W. W., de Moel, H., and Bowman, M. (2013). Cost estimates for flood resilience and protection strategies in New York city. *Ann. N. Y. Acad. Sci.* 1294, 1–104. doi: 10.1111/nyas.12200

Berger, M. J., George, D. L., LeVeque, R. J., and Mandli, K. T. (2011). The GeoClaw software for depth-averaged flows with adaptive refinement. *Adv. Water Res.* 34, 1195–1206. doi: 10.1016/j.advwatres.2011.02.016

Burkett, V. R., Zilkoski, D. B., and Hart, D. A. (2002). "Sea-level rise and subsidence: implications for flooding in New Orleans, Louisiana," in *US Geological Survey Subsidence Interest Group Conference* (Galveston, TX: US Geological Survey), 63–71.

Cimellaro, G. P., Crupi, P., Kim, H. U., and Agrawal, A. (2019). Modeling interdependencies of critical infrastructures after hurricane sandy. *Int. J. Disast. Risk Reduct.* 38:101191. doi: 10.1016/j.ijdrr.2019.101191

City of New York (2021). *The East Side Coastal Resiliency Project*. City of New York.

Clawpack Development Team (2020). *Clawpack Software. Version 5.7.1*. Clawpack Development Team.

Department of Homeland Security, Federal Emergency Management Agency (2018). *Hazus*. Department of Homeland Security, Federal Emergency Management Agency.

Department of Information Technology & Telecommunications (2018). *Building Footprints*. Department of Information Technology & Telecommunications.

Dols, C. (2019). *New York–New Jersey Harbor and Tributaries Coastal Storm Risk Management Feasibility Study Interim Report Cost Appendix*. US Army Corps of Engineers.

Dupuits, E., Schweckendiek, T., and Kok, M. (2017). Economic optimization of coastal flood defense systems. *Reliabil. Eng. Syst. Saf.* 159, 143–152. doi: 10.1016/j.ress.2016.10.027

Gornitz, V., Oppenheimer, M., Kopp, R., Horton, R., Orton, P., Rosenzweig, C., et al. (2020). Enhancing New York city's resilience to sea level rise and increased coastal flooding. *Urban Clim.* 33:100654. doi: 10.1016/j.uclim.2020.100654

Gornitz, V., Oppenheimer, M., Kopp, R., Orton, P., Buchanan, M., Lin, N., et al. (2019). New York city panel on climate change 2019 report chapter 3: Sea level rise. *Ann. N. Y. Acad. Sci.* 1439, 71–94. doi: 10.1111/nyas.14006

Haimes, Y. Y., and Jiang, P. (2001). Leontief-based model of risk in complex interconnected infrastructures. *J. Infrastruct. Syst.* 7, 1–12. doi: 10.1061/(ASCE)1076-0342(2001)7:1(1)

Hirabayashi, Y., Mahendran, R., Koirala, S., Konoshima, L., Yamazaki, D., Watanabe, S., et al. (2013). Global flood risk under climate change. *Nat. Clim. Change* 3, 816–821. doi: 10.1038/nclimate1911

Holland, G. J. (1980). An analytic model of the wind and pressure profiles in hurricanes. *Month. Weath. Rev.* 108, 1212–1218. doi: 10.1175/1520-0493(1980)108<1212:AAMOTW>2.0.CO;2

Horton, R., Little, C., Gornitz, V., Bader, D., and Oppenheimer, M. (2015). New York city panel on climate change 2015 report chapter 2: Sea level rise and coastal storms. *Ann. N. Y. Acad. Sci.* 1336, 36–44. doi: 10.1111/nyas.12593

Jonkman, S., Brinkhuis-Jak, M., and Kok, M. (2004). Cost benefit analysis and flood damage mitigation in the Netherlands. *Heron* 49, 95–111. http://heronjournal.nl/49-1/5.pdf

Lee, C.-Y., Tippett, M. K., Sobel, A. H., and Camargo, S. J. (2018). An environmentally forced tropical cyclone hazard model. *J. Adv. Model. Earth Syst.* 10, 223–241. doi: 10.1002/2017MS001186

Leontief, W. (1986). *Input-Output Economics*. Oxford: Oxford University Press. doi: 10.1057/978-1-349-95121-5_1072-1

Lin, N., Emanuel, K., Oppenheimer, M., and Vanmarcke, E. (2012). Physically based assessment of hurricane surge threat under climate change. *Nat. Clim. Change* 2, 462–467. doi: 10.1038/nclimate1389

Longenecker, H. E., Graeden, E., Kluskiewicz, D., Zuzak, C., Rozelle, J., and Aziz, A. L. (2020). A rapid flood risk assessment method for response operations and nonsubject-matter-expert community planning. *J. Flood Risk Manage.* 13:e12579. doi: 10.1111/jfr3.12579

Lopeman, M., Deodatis, G., and Franco, G. (2015). Extreme storm surge hazard estimation in lower manhattan. *Nat. Hazards* 78, 355–391. doi: 10.1007/s11069-015-1718-6

Mandli, K. T., Ahmadia, A. J., Berger, M., Calhoun, D., George, D. L., Hadjimichael, Y., et al. (2016). Clawpack: building an open source ecosystem for solving hyperbolic PDES. *PeerJ Comput. Sci.* 2:e68. doi: 10.7717/peerj-cs.68

Marcos, M., Calafat, F. M., Berihuete, Á., and Dangendorf, S. (2015). Long-term variations in global sea level extremes. *J. Geophys. Res.* 120, 8115–8134. doi: 10.1002/2015JC011173

Marcos, M., and Woodworth, P. L. (2017). Spatiotemporal changes in extreme sea levels along the coasts of the North Atlantic and the Gulf of Mexico. *J. Geophys. Res.* 122, 7031–7048. doi: 10.1002/2017JC013065

Marsooli, R., Lin, N., Emanuel, K., and Feng, K. (2019). Climate change exacerbates hurricane flood hazards along us Atlantic and gulf coasts in spatially varying patterns. *Nat. Commun.* 10, 1–9. doi: 10.1038/s41467-019-11755-z

Miura, Y. (2020). *High-Speed Gis Flood Simulation*. Available online at: https://github.com/ym2540/GIS_FloodSimulation

Miura, Y., Mandli, K. T., and Deodatis, G. (2021a). High-speed gis-based simulation of storm surge-induced flooding accounting for sea level rise. *Nat. Hazards Rev.* 22:04021018. doi: 10.1061/(ASCE)NH.1527-6996.0000465

Miura, Y., Mandli, K. T., and Deodatis, G. (2021b). Storm surge modeling with modified beta distributions. In Preparation.

Miura, Y., Qureshi, H., Ryoo, C., Dinenis, P. C., Li, J., Mandli, K. T., et al. (2021c). A methodological framework for determining an optimal coastal protection strategy against storm surges and sea level rise. *Nat. Hazards* 107, 1821–1843. doi: 10.1007/s11069-021-04661-5

National Hurricane Center (2017). *Automated Tropical Cyclone Forecast (ATCF) Data Files*/Text Files. National Hurricane Center. Available online at: https://ftp.nhc.noaa.gov/atcf

New York City Department of City Planning (2018). *Mappluto*. New York City, NY: Department of City Planning (accessed August 15, 2020).

Parris, A. S., Bromirski, P., Burkett, V., Cayan, D. R., Culver, M. E., Hall, J., et al. (2012). *Global Sea Level Rise Scenarios for the United States National Climate Assessment*. NOAA technical report, OAR CPO.

Rebuild By Design (2015). *The Big U. Online*, New York. (accessed August 15, 2020).

Reguero, B. G., Beck, M. W., Bresch, D. N., Calil, J., and Meliane, I. (2018). Comparing the cost effectiveness of nature-based and coastal adaptation: a case study from the gulf coast of the United States. *PLoS ONE* 13:e0192132. doi: 10.1371/journal.pone.0192132

Stocker, T. F., Qin, D., Plattner, G.-K., Tignor, M., Allen, S. K., Boschung, J., et al. (2013). *Climate Change 2013: The Physical Science Basis*. Contribution of working group I to the fifth assessment report of the intergovernmental panel on climate change, New York: Cambridge University Press, 1535.

Sweet, W. V. (2014). *Sea Level Rise and Nuisance Flood Frequency Changes Around the United States*. US Department of Commerce, National Oceanic and Atmospheric Administration.

Taherkhani, M., Vitousek, S., Barnard, P. L., Frazer, N., Anderson, T. R., and Fletcher, C. H. (2020). Sea-level rise exponentially increases coastal flood frequency. *Sci. Rep.* 10, 1–17. doi: 10.1038/s41598-020-62188-4

Ward, P. J., Jongman, B., Aerts, J. C., Bates, P. D., Botzen, W. J., Loaiza, A. D., et al. (2017). A global framework for future costs and benefits of river-flood protection in urban areas. *Nat. Clim. Change* 7, 642–646. doi: 10.1038/nclimate3350

Ward, P. J., Jongman, B., Salamon, P., Simpson, A., Bates, P., De Groeve, T., et al. (2015). Usefulness and limitations of global flood risk models. *Nat. Clim. Change* 5, 712–715. doi: 10.1038/nclimate2742

Winsemius, H., Van Beek, L., Jongman, B., Ward, P., and Bouwman, A. (2013). A framework for global river flood risk assessments. *Hydrol. Earth Syst. Sci.* 17, 1871–1892. doi: 10.5194/hess-17-1871-2013

Zwaneveld, P. J., and Verweij, G. (2014). *Safe Dike Heights at Minimal Costs*. The Hague.

Conflict of Interest: The authors declare that the research was conducted in the absence of any commercial or financial relationships that could be construed as a potential conflict of interest.

Publisher's Note: All claims expressed in this article are solely those of the authors and do not necessarily represent those of their affiliated organizations, or those of the publisher, the editors and the reviewers. Any product that may be evaluated in this article, or claim that may be made by its manufacturer, is not guaranteed or endorsed by the publisher.

frontiers in Climate

METHODS
published: 05 August 2021
doi: 10.3389/fclim.2021.609688

Hurricane Irma Simulation at South Florida Using the Parallel CEST Model

Yuepeng Li[1]*, *Qiang Chen*[2], *Dave M. Kelly*[3] and *Keqi Zhang*[1,2]

[1] International Hurricane Research Center, Florida International University, Miami, FL, United States, [2] Department of Earth & Environment, Florida International University, Miami, FL, United States, [3] Centre for Environment, Fisheries and Aquaculture (CEFAS), Lowestoft, United Kingdom

In this study, a parallel extension of the Coastal and Estuarine Storm Tide (CEST) model is developed and applied to simulate the storm surge tide at South Florida induced by hurricane Irma occurred in 2017. An improvement is also made to the existing advection algorithm in CEST. This is achieved through the introduction of high-order, monotone Semi-Lagrangian advection. Distributed memory parallelization is developed via the Message Passing Interface (MPI) library. The parallel CEST model can therefore be run efficiently on machines ranging from multicore laptops to massively High Performance Computing (HPC) system. The principle advantage of being able to run the CEST model on multiple cores is that relatively low run-time is possible for real world storm surge simulations on grids with high resolution, especially in the locality where the hurricane makes landfall. The computational time is critical for storm surge model forecast to finish simulations in 30 min, and results are available to users before the arrival of the next advisory. In this study, simulation of hurricane Irma induced storm surge was approximately 22 min for 4 day simulation, with the results validated by field measurements. Further efficiency analysis reveals that the parallel CEST model can achieve linear speedup when the number of processors is not very large.

Keywords: CEST, hurricane, parallelization, SLOSH, storm surge, advection, open MPI

OPEN ACCESS

Edited by:
Hatim O. Sharif,
University of Texas at San Antonio, United States

Reviewed by:
Muhammad Akbar,
Tennessee State University, United States
Steven Cocke,
Florida State University, United States

***Correspondence:**
Yuepeng Li
yuepli@fiu.edu

Specialty section:
This article was submitted to Climate Risk Management, a section of the journal Frontiers in Climate

Received: *24 September 2021*
Accepted: *02 July 2021*
Published: *05 August 2021*

Citation:
Li Y, Chen Q, Kelly DM and Zhang K (2021) Hurricane Irma Simulation at South Florida Using the Parallel CEST Model. Front. Clim. 3:609688. doi: 10.3389/fclim.2021.609688

1. INTRODUCTION

The Coastal and Estuarine Storm Tide (CEST) numerical model was developed at the International Hurricane Research Center (IHRC), based at Florida International University (FIU) in Miami, around a decade ago. The purpose of the model is to simulate the storm surge due to the combined action of (anti)cylonic winds and astronomical tides. Although the CEST model has both 2D and 3D variants, in this paper we are concerned with the 2D version that is based on the depth–averaged, primitive variable, non–linear shallow water (NLSW) equations expressed on orthogonal curvilinear coordinates. These governing equations are solved via an algorithm that is based on the semi–implicit finite–difference (FD) approach (Casulli, 1990). CEST differs from the approach presented in Casulli (1990) as it employs a straightforward explicit Eulerian advection scheme (Zhang et al., 2008). The CEST model allows for forcing by winds, atmospheric pressure and astronomical tides, and is thus capable of simulating storm tides as well as the wind–driven circulation at estuaries and coasts. As described in Zhang et al. (2008) the CEST model incorporates a novel wetting–drying algorithm that is based on an accumulated water volume approach for dry cells.

Compared to the US operational SLOSH (Sea, Lake, and Overland Surge from Hurricane) model employed by the National Hurricane Center (NHC), CEST has demonstrated favorable results over the hindcast of storm surge induced by Camille (1969), Hugo (1989), Andrew (1992), Wilma (2005), Zhang et al. (2008), and Zhang et al. (2012). The performance and stability of CEST were also examined by conducting simulations for more than 100,000 synthetic hurricanes for nine SLOSH basins covering the Florida coast and Lake Okeechobee (Zhang et al., 2013). It is demonstrated that CEST has the potential to be used for operational forecasts of storm surge.

Recently, NHC has developed several high resolution basins along East Coast and Gulf of Mexico with 100 m grid resolution along the coastal region. South Florida Basin is the one of the basins with about 640,000 computational cells. It takes 1–2 h to finish 4-days simulation by SLOSH or CEST with one CPU. For the storm surge forecast, the P-Surge model is used to compute the ranges of inundation magnitudes and extents (Taylor and Glahn, 2008). Real-time storm surge simulations are required to produce P-Surge products in 20–30 min because the NHC updates the hurricane forecast/advisory every 6 h (Zhang et al., 2013). Therefore, improved algorithm and simple parallelization via the message passing interface (MPI) approach have to be employed to CEST model in order to satisfy the forecast requirement.

In this paper we present a modified version of the CEST model that includes an improved advection algorithm and a simple parallelization via the message passing interface (MPI) library. MPI allows for distributed memory parallelization ensuring that CEST is not limited to the amount of memory on a single machine or the number of processes available on that machine. The new parallel version of CEST can therefore be run on machines ranging from multi-core desktops to massively parallel supercomputers.

The paper is structured as follows in section 2 we detail the governing equations including the transformation to orthogonal curvilinear coordinates. ection 3 gives an overview of the numerical algorithm used to solve the equations with emphasis on improvements and changes made to the original CEST model. This section also includes details on the treatment of wetting–drying fronts and parallelization. A test case result is presented in section 4 which includes a comparison of the CPU time with the original series CEST code. Finally, in section 5, conclusions are drawn.

2. GOVERNING EQUATIONS

The CEST model employs a non–conservation, primitive variable, form of the 2D NLSW equations in orthogonal curvilinear co–ordinates (Zhang et al., 2008). Flow variables are considered to be depth uniform; i.e. the velocities are averaged over the water depth and there is no vertical velocity variation. The curvilinear co–ordinate system used follows that introduced by Blumberg and Herring (1987) and comprises horizontal co–ordinates (ξ, η) and a vertical co–ordinate (z), see **Figure 1**. Metric coefficients, h_1 and h_2, are introduced such that a distance

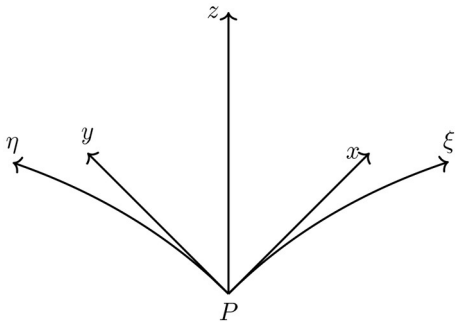

FIGURE 1 | Schematic showing the $\xi - \eta$ orthogonal curvilinear co–ordinate system employed in the IHRC CEST model.

increment satisfies the relation

$$ds^2 = h_1^2 d\xi^2 + h_2^2 d\eta^2 \tag{1}$$

with

$$h_1 = \left\{ \left(\frac{\partial x}{\partial \xi} \right)^2 + \left(\frac{\partial y}{\partial \xi} \right)^2 \right\}^{\frac{1}{2}}, h_2 = \left\{ \left(\frac{\partial x}{\partial \eta} \right)^2 + \left(\frac{\partial y}{\partial \eta} \right)^2 \right\}^{\frac{1}{2}}. \tag{2}$$

The differential arc lengths at point P in **Figure 1** are given by

$$ds_1 = h_1 d\xi, ds_2 = h_2 d\eta. \tag{3}$$

Thus, the u and v components of the depth–averaged velocity are given by

$$u = h_1 \frac{d\xi}{dt}, v = h_2 \frac{d\eta}{dt} \tag{4}$$

With $\zeta = \zeta(\xi, \eta, t)$ denoting the free surface disturbance measured from the undisturbed water level $h = h(\xi, \eta)$. The depth–averaged velocity components are denoted by $u = u(\xi, \eta, t)$ and $v = v(\xi, \eta, t)$ for the ξ and η directions, see **Figure 2**, respectively.

In the orthogonal curvilinear co–ordinate system the continuity equation is then given by

$$\frac{\partial \zeta}{\partial t} + \frac{1}{h_1 h_2} \left[\frac{\partial (H h_2 u)}{\partial \xi} + \frac{\partial (H h_1 v)}{\partial \eta} \right] = 0. \tag{5}$$

The momentum equations are

$$\begin{aligned} &\frac{\partial u}{\partial t} + \frac{1}{h_1 h_2} \left[\frac{\partial (h_2 u^2)}{\partial \xi} + \frac{\partial (h_1 uv)}{\partial \eta} \right] \\ &= fv + \frac{1}{h_1 h_2} \left(v^2 \frac{\partial h_2}{\partial \xi} - uv \frac{\partial h_1}{\partial \eta} \right) \\ &- \frac{g}{h_1} \frac{\partial}{\partial \xi} \left(\zeta + \frac{\Delta P_a}{\rho g} \right) - \frac{\tau_B^{\xi}}{H} + \frac{\tau_W^{\xi}}{H} \\ &+ \frac{1}{h_1 h_2} \frac{A_h}{h_1^2} \frac{\partial^2 u}{\partial \xi^2} + \frac{A_h}{h_2^2} \frac{\partial^2 u}{\partial \eta^2} \end{aligned} \tag{6}$$

and

$$\frac{\partial v}{\partial t} + \frac{1}{h_1 h_2}\left[\frac{\partial (h_2 uv)}{\partial \xi} + \frac{\partial (h_1 v^2)}{\partial \eta}\right] = -fu + \frac{1}{h_1 h_2}\left(u^2 \frac{\partial h_1}{\partial \eta} - uv\frac{\partial h_2}{\partial \xi}\right) - \frac{g}{h_2}\frac{\partial}{\partial \eta}\left(\zeta + \frac{\Delta P_a}{\rho g}\right) - \frac{\tau_B^\eta}{H} + \frac{\tau_W^\eta}{H} + \frac{A_h}{h_1^2}\frac{\partial^2 v}{\partial \xi^2} + \frac{A_h}{h_2^2}\frac{\partial^2 v}{\partial \eta^2}. \quad (7)$$

Here $H(\xi, \eta, t) = h(\xi, \eta, t) + \zeta(\xi, \eta, t)$ is the total water depth. The gravitational acceleration is denoted by g, ρ is the water density, ΔP_a is the air pressure drop and f is the Coriolis parameter. The bottom shear stress is denoted by τ_B and the wind shear stress by τ_W. Closure for the bottom shear stress is obtained using a quadratic law:

$$\frac{\tau_B^\xi}{H} = \Lambda u, \frac{\tau_B^\eta}{H} = \Lambda v, \text{with } \Lambda = \frac{\rho n g}{H^{\frac{4}{3}}}(u^2 + v^2)^{\frac{1}{2}} \quad (8)$$

with n being Manning's coefficient. The wind shear is parametrized using the wind velocities from a wind forcing model coupled to the flow via a drag coefficient based on the Large and Pond (1981) or Garratt (1977) formulation; full details can be found in (Zhang et al., 2012). Importantly, it is noted that, without explicit shock fitting of the type discussed in Pandolfi and Zannetti (1977), these equations are unsuitable for modeling flows that contain or develop discontinuities (shock waves). CEST is capable of using internal parametric wind models such as the Holland model (Holland, 1980) or the Myers and Malkin (1961) that is employed by SLOSH. CEST is also capable of using external wind field time–series generated by the Hurricane Research Division of the US National Oceanic and Atmospheric Administration (NOAA) based on field measurements (H*Wind) (Powell et al., 1998). For Hurricane Irma simulation presented in this paper we use the Myers and Malkin (1961) parametric wind model which parameterizes the wind and atmospheric pressure fields using both the atmospheric pressure drop and radius of maximum wind speed (RMW). Pressure, wind speed, and wind direction are computed assuming a stationary, circularly symmetric, storm. The set up used here for Hurricane Irma is essentially the same as that described in Zhang et al. (2008).

3. METHODS

The numerical solution is effected on a staggered, Arakawa C–type, grid using finite differences. Elevation points are defined at the centers of grid cells, while the u and v velocity components are defined on their respective cell boundaries.

When values of dependent variables are required at non–computation points they are obtained using piecewise linear reconstruction, i.e. $\zeta_{(i+\frac{1}{2},j)} = \frac{1}{2}(\zeta_{(i,j)} + \zeta_{(i+1,j)})$. The model employs the method of fractional steps (Yanenko, 1971) in order to march forward in time. This means that the overall temporal accuracy in CEST is $\mathcal{O}(\Delta t)$.

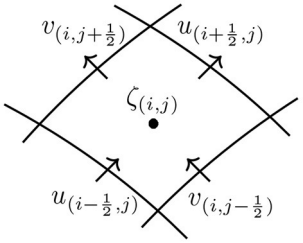

FIGURE 2 | Schematic showing a computational cell on the $\xi - \eta$ orthogonal curvilinear FD grid.

3.1. Modified Advection Algorithm

In its original incarnation CEST (Zhang et al., 2008, 2012) handled advection via a straightforward, fully explicit, Eulerian finite difference scheme. This approach often leads to a prohibitive restriction on the size of the time–step that the original CEST model can employ. This is because, for numerical stability, the time–step used for the entire model must be chosen such that advection satisfies the well-known CFL condition (Courant et al., 1967). Here, in the spirit of Casulli's original approach (Casulli, 1990), we employ a semi–Lagrangian (SL) methodology for the velocity advection. Importantly, however, we extend the approach to high–order accuracy in both space and time by employing second–order Runge Kutta time integration and monotonic cubic spline interpolation in space. In theory, this type of advection is unconditionally stable. When computing the velocity advection, we work purely on the computational (image) grid; working on the curvilinear (physical) grid adds complexity as scales vary arbitrarily between cells and grid curvature is not necessarily constant. In order to effect the interpolation, and limiting, the two–dimensional processes are broken down into a sequence of one–dimensional processes along each co–ordinate axis. This is possible because the computational (image) grid is a regular Cartesian grid. Thus, without loss of generality, when discussing the base point interpolation we need only consider the 1D case. For the spatial interpolation we use Hermite cubic interpolation made monotone by use of the limiter proposed by Nair et al. (1999); from hereonin we shall refer to this as the NCS99 limiter. The NCS99 limiter is applied in each spatial dimensional in turn and works as follows: first find the local maximum and minimum surrounding the particle path base point x_b

$$\begin{aligned} f^+ &= \max[f_{(i)}, f_{(i+1)}] \\ f^- &= \min[f_{(i)}, f_{(i+1)}] \end{aligned} \quad (9)$$

Next, reset the interpolated value (obtained using Hermite cubic interpolation) at the base point $f|_{x=x_b} = f_b$ such that

$$\begin{aligned} f_b &= f^- = \text{if } f_b < f^- \\ f_b &= f^+ = \text{if } f_b > f^+. \end{aligned} \quad (10)$$

Note that this amounts to a simple clamping operation and can lead to the suppression of certain genuine physical waves. For

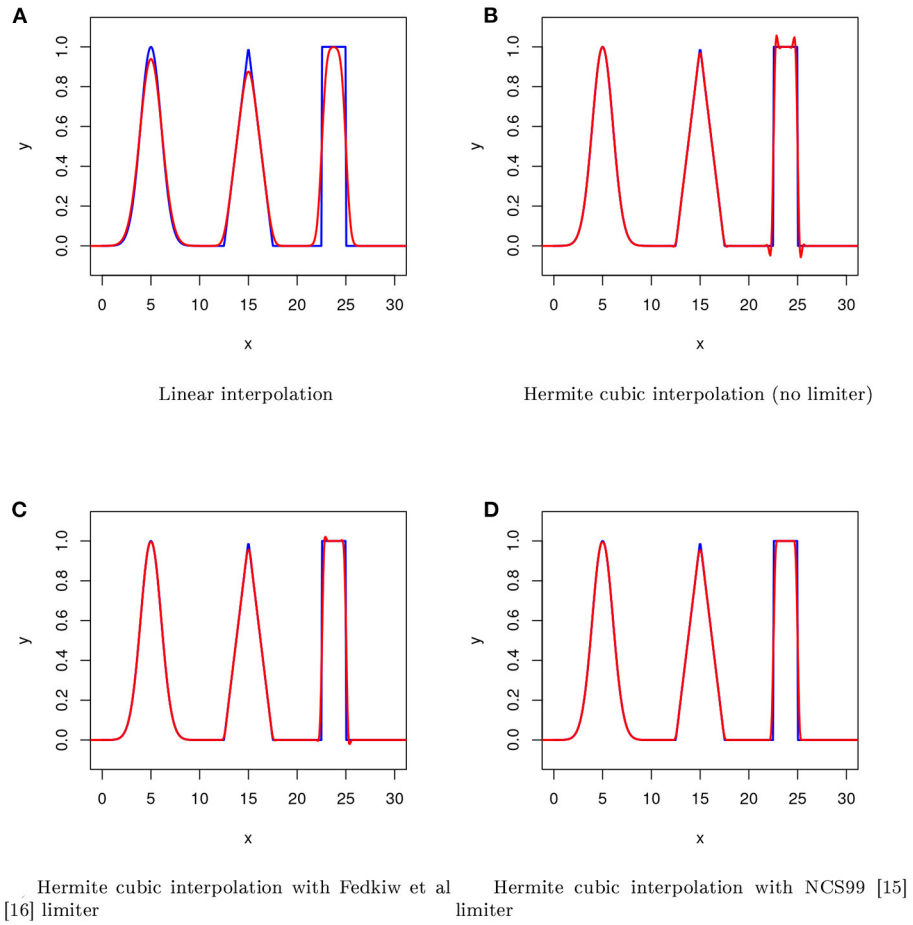

FIGURE 3 | Advection of a complex function in uniform velocity field. The results for **(A)** Linear interpolation, **(B)** Hermite cubic interpolation (no limiter), **(C)** Hermite cubic interpolation with Fedkiew et al. limiter, **(D)** Hermite cubic interpolation with NCS99 limiter, are shown for 500 grid points after 100 time steps. The analytical solution is the blue line and the numerical approximation is the red line.

this reason the NCS99 limiter includes additional checks for monotonicity that must be satisfied before the limiter is applied. First NCS99 introduce the global minimum and global maximum of f denoted by $f_{\min}$ and $f_{\max}$, respectively. Thus, if all of the following four inequalities hold the limiter should not be applied

$$\begin{aligned} f_{\min} \leq f_b \leq f_{\max} \\ (f_{(i-1)} - f_{(i-2)})(f_{(i)} - f_{(i-1)}) > 0, \\ (f_{(i)} - f_{(i-1)})(f_{(i+2)} - f_{(i+1)}) < 0, \\ (f_{(i+2)} - f_{(i+1)})(f_{(i+3)} - f_{(i+2)}) > 0. \end{aligned} \tag{11}$$

This stipulates that the signal contains only one extremum in a five–mesh–length interval (therefore suppressing the Gibbs phenomenon). We have found this limiter to be particularly robust when compared with alternative formulations such as that proposed in Fedkiw et al. (2001). **Figure 3** shows a comparison of SL advection, using a variety of base point interpolation schemes, for the advection of a 1D function with compound waves in a uniform velocity field. The 1D function comprises a combined Gaussian, triangle and square wave. Results are plotted after 100 time–steps for a grid comprising 500 points; clearly Hermite cubic interpolation with the NCS99 limiter gives the best performance in this complex case. Whilst this high–order accurate advection scheme is monotone, it is unsuitable for flows that contain or develop discontinuities as it is not conservative. Moreover, CEST is only suitable for smooth flows as the governing equations are themselves not in a (divergence) form that permits discontinuities. Thus, unless explicit shock fitting is utilized (Moretti, 2002), flow discontinuities cannot be expected to propagate at the correct strength or speed. We mention that, when using SL advection, in wet areas close to dry land, care should be taken to ensure that the particle path is not allowed to project too far back into an area that is completely dry. If this is allowed to happen then the velocity advection can cause a false zeroing of the velocity field in such cells. This issue can be avoided through the use of locally controlled time–stepping.

3.2. Additional Terms and Free Surface Evolution

The physical diffusion terms are treated using a simple forward–in–time centered–in–space (FTCS) scheme (Press et al., 1992). We note that the use of a simple explicit scheme for diffusion

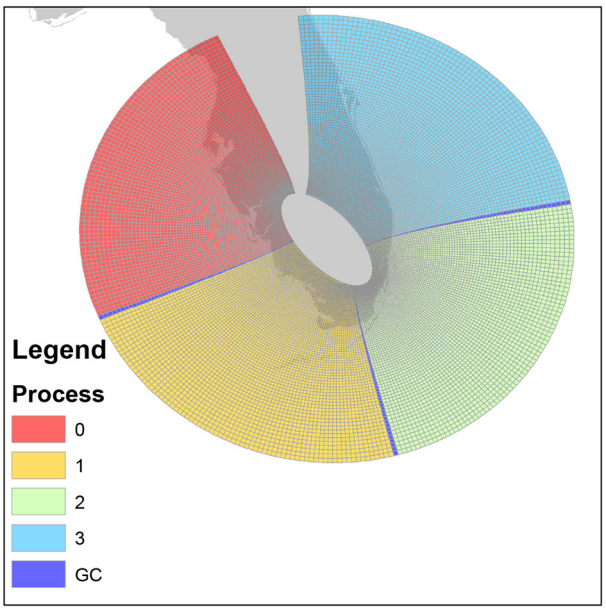

FIGURE 4 | Example of a CEST curvilinear computational grid (shown in physical space) and the strip–type domain decomposition. The shaded strips show the ghost cells (GC) used for inter–process communication. The plot shows the NOAA (NHC) basin used for simulations of hurricane such as Andrew (1992).

introduces its own stability requirements; however, these are far less stringent than those associated with the advective terms. The Coriolis and wind stress terms are updated using first–order explicit Euler time integration and the bottom friction term is treated implicitly in the manner detailed in Kelly et al. (2015). After the velocities have been updated using the method of fractional steps the free surface can be updated. The operator that updates both u and v by SL advection and explicit diffusion, evaluation of curvature terms, pressure drop, wind forcing and finally an implicit bed friction update is denoted by $\mathcal{F}$. Thus, we have

$$u^{n+1}_{i+1/2,j} = \mathcal{F}(u^{n}_{i+1/2,j}, u^{n-1}_{i+1/2,j}), v^{n+1}_{i,j+1/2} = \mathcal{F}(v^{n}_{i,j+1/2}, v^{n-1}_{i,j+1/2}) \tag{12}$$

Evolution of the free surface requires solution of Equation (5). This is achieved using an implicit scheme which results in the following 5–diagonal linear system of equations:

$$\begin{aligned} &-Au_{(i-1,j)}\zeta^{n+1}_{(i-1,j)} - Av_{(i,j-1)}\zeta^{n+1}_{(i,j-1)} \\ &+Az_{(i,j)}\zeta^{n+1}_{(i,j)} - Av_{(i,j)}\zeta^{n+1}_{(i,j+1)} - Au_{(i,j)}\zeta^{n+1}_{(i+1,j)} = b_{(i,j)} \end{aligned} \tag{13}$$

where

$$Au_{(i,j)} = \frac{gh_{2(i+\frac{1}{2},j)}\Delta t^2}{h_{1(i+\frac{1}{2},j)}} \cdot \frac{H^n_{(i+\frac{1}{2},j)}}{1+\Lambda_{(i+\frac{1}{2},j)}\Delta t}, \tag{14}$$

$$Av_{(i,j)} = \frac{gh_{1(i,j+\frac{1}{2})}\Delta t^2}{h_{2(i,j+\frac{1}{2})}} \cdot \frac{H^n_{(i,j+\frac{1}{2})}}{1+\Lambda_{(i,j+\frac{1}{2})}\Delta t} \tag{15}$$

and

$$Az_{(i,j)} = h_{1(i,j)}h_{2(i,j)} + Au_{(i,j)} + Au_{(i-1,j)} + Av_{(i,j)} + Au_{(i,j-1)}. \tag{16}$$

The right hand side of Equation (13) is given by

$$\begin{aligned} b_{(i,j)} \;=\; &\zeta^n_{(i,j)}h_{1(i,j)}h_{2(i,j)} - \Delta t\big(\mathcal{F}u^n_{(i+\frac{1}{2},j)}H^n_{(i+\frac{1}{2},j)}h_{2(i+\frac{1}{2},j)} \\ &-\mathcal{F}u^n_{(i-\frac{1}{2},j)}H^n_{(i-\frac{1}{2},j)}h_{2(i-\frac{1}{2},j)} + \mathcal{F}v^n_{(i,j+\frac{1}{2})}H^n_{(i,j+\frac{1}{2})}h_{1(i,j+\frac{1}{2})} \\ &-\mathcal{F}v^n_{(i,j-\frac{1}{2})}H^n_{(i,j-\frac{1}{2})}h_{1(i,j-\frac{1}{2})}\big). \end{aligned} \tag{17}$$

Finally, after the free surface has been updated, the final velocity update is performed using the pressure gradient. Use is made of the staggered grid to obtain second–order accuracy for the spatial gradient of the free surface in this step.

3.3. Wetting/Drying Fronts

CEST employs a straightforward wetting–drying algorithm that is based on an accumulated water volume (Zhang et al., 2008). Free surface elevation and water depth at both the cell center and its four boundaries are all used to calculate the accumulated water volume. At the beginning of a model timestep, cells are assigned as being either wet or dry based on whether the water depth at the cell center is above or below a threshold depth H_{TOL}. During wetting, if the free surface elevation at the center of a wet cell is higher than that at an adjacent dry cell, and the water depth at the shared boundary between these two cells H_k (obtained by linear interpolation) is greater than a predefined threshold, the water is allowed to flow from the wet cell into the dry cell and accumulate there. The flux of water crosses a maximum of four shared boundaries between a dry cell, and any wet neighbors. The water interchange velocities (u_k, where $k = 1...4$ represents the four cell boundaries) are approximated by solving a simplified 1D momentum equation which ignores the contribution of advection, Coriolis force, air pressure drop and wind shear giving

$$\frac{\partial u_k}{\partial t} + g\frac{\partial \zeta_k}{\partial x_k} + \Lambda u_k = 0, \tag{18}$$

with x_k being the direction of u_k and ζ_k is a linear reconstruction of the free surface elevation at the kth cell interface. The accumulated water volume ΔQ in dry cells is computed as

$$\Delta Q^{n+1}_{(i,j)} = \Delta Q^{n}_{(i,j)} + \sum_k \Delta_k \cdot H_k \cdot u_k \cdot \Delta t, \tag{19}$$

where $\Delta Q^n_{(i,j)}$ is the accumulated volume from the previous time step and Δ_k denotes the cell length (which is $\Delta\xi$ or $\Delta\eta$ depending on the value of k). If the water depth, obtained from the accumulated volume, in a dry cell exceeds H_{TOL} the cell is reflagged as being wet. During drying a cell is set to be dry if the water depth at the cell center falls below H_{TOL}. Note that, if the water depth at a cell boundary is less than H_{TOL}, water will stop flowing across this boundary even before the cell itself is completely dry. Also, if it is the case that the linearly reconstructed water depths at all four boundaries of a cell are less

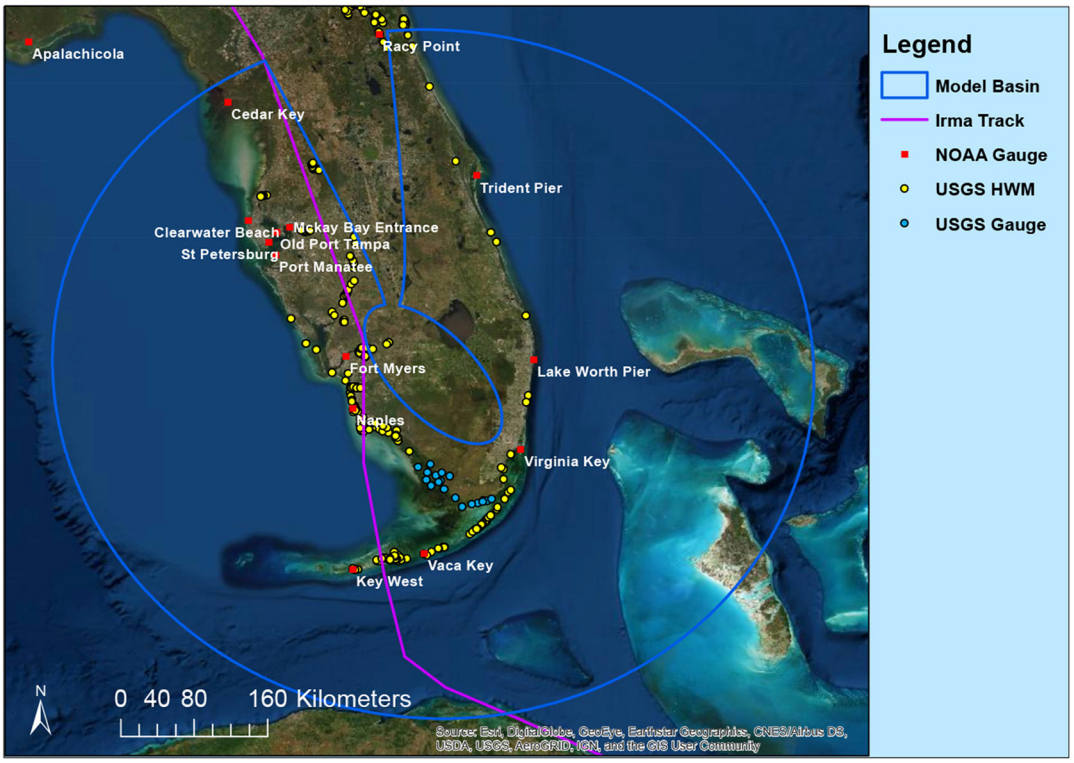

FIGURE 5 | The study area, computational domain, Irma track, and measurement locations.

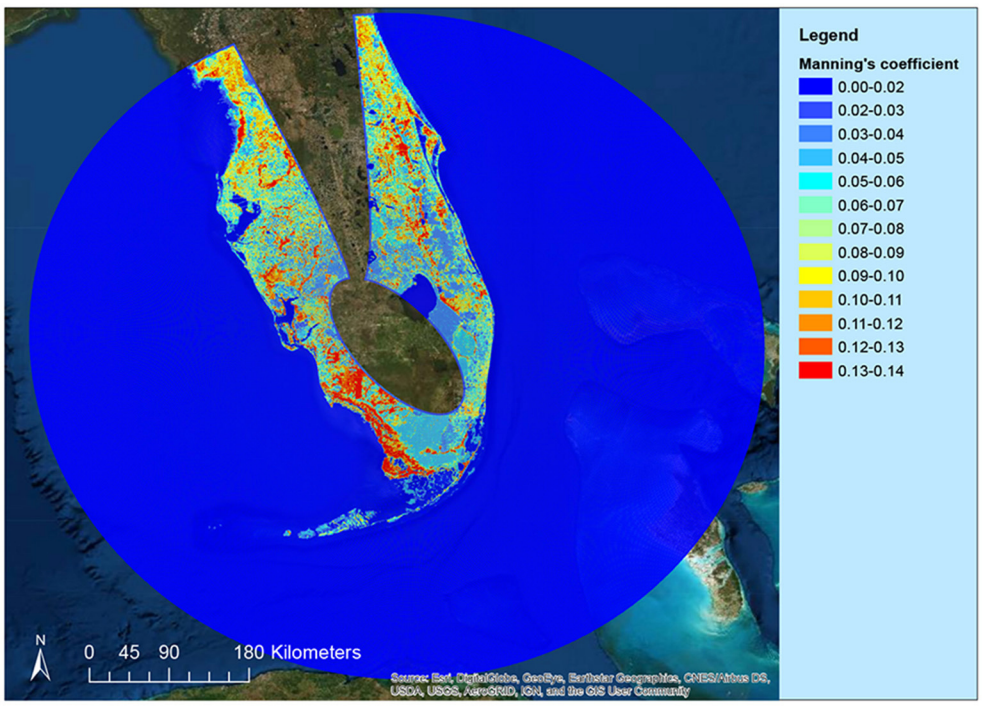

FIGURE 6 | The Manning's coefficient map for the entire computational domain.

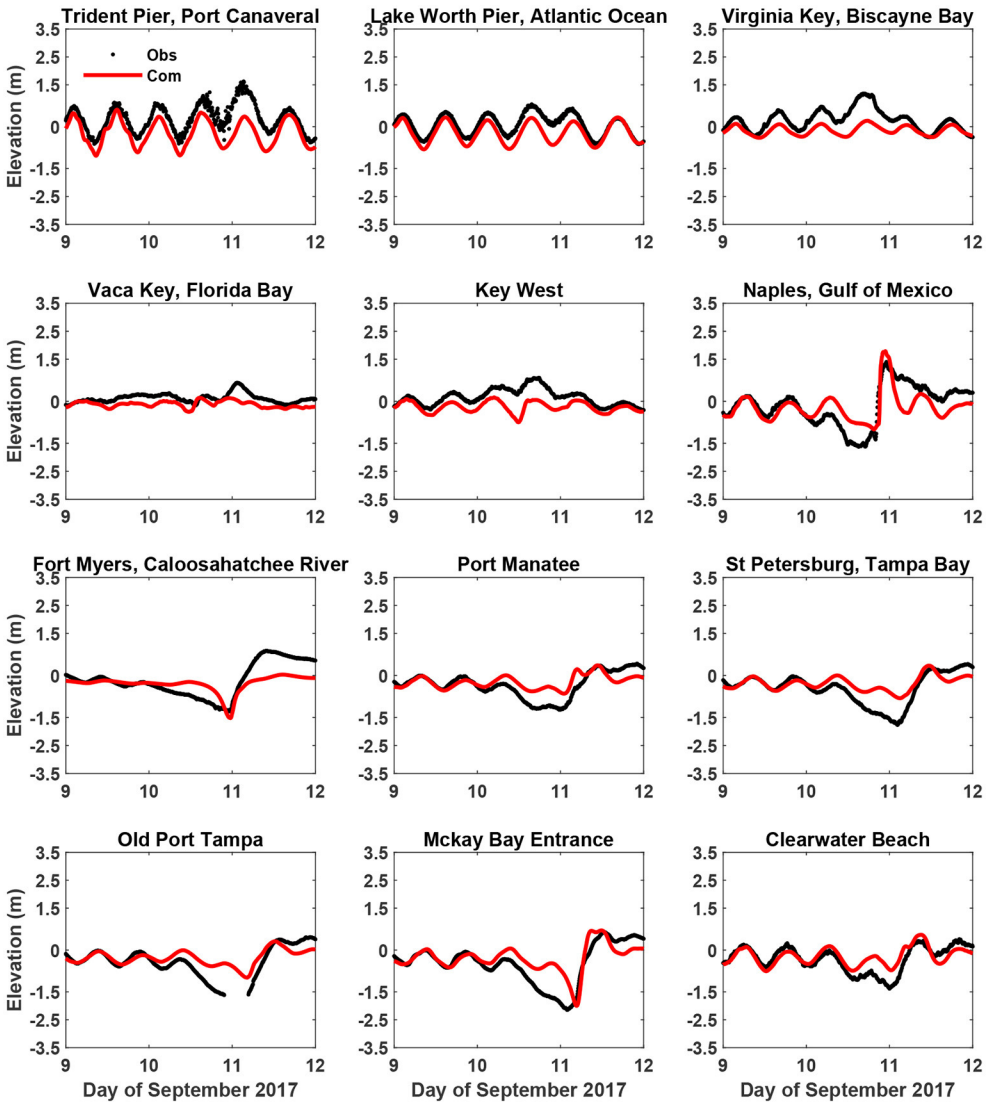

FIGURE 7 | Comparison between the computed and the measured surface elevations at the various NOAA tide gauges.

than H_{TOL} then the cell is set to be dry. This simple algorithm conserves water mass, but not momentum. The approach has proven extremely robust in a huge number of storm surge simulations carried out at the IHRC over the last decade.

3.4. MPI Parallelization and Domain Decomposition

Parallelization of the CEST model is achieved using the Message Passing Interface (MPI) library, see: https://www.open-mpi.org/. To achieve parallelization a horizontal strip–type domain decomposition on the computational (image) grid is employed. The computational domain is split into a number of horizontal strips and strips are allocated to each process on a single strip per process basis. Two layers of halo regions (ghost cells) is employed to transfer information between processes. It should be noted that no load balancing, or process optimization, is currently implemented.

Figure 4 shows a schematic representation of the domain decomposition employed by CEST. Assuming a domain that runs from $\mathtt{y}_{min}$ to $\mathtt{y}_{max}$ and comprises $\mathtt{im} \times \mathtt{jm}$ cells, only J index is split to save on computational time and simplify the domain decomposition. In other words, the computational domain is split vertically among all available processes $\mathtt{np}$, including the root process $\mathtt{p=0}$, according to Algorithm 1. The horizontal direction, I index for each process keeps same.

Whilst the parallelization of the $\mathcal{F}$ operator is straightforwards, solution of the implicit equation for the free surface (Equation 13) is not. To facilitate the paralellization of the code, and avoid the need for multicoloring, the pre–conditioned conjugate gradient (PCCG) method employed to solve the continuity equation for the free surface (Equation 13)

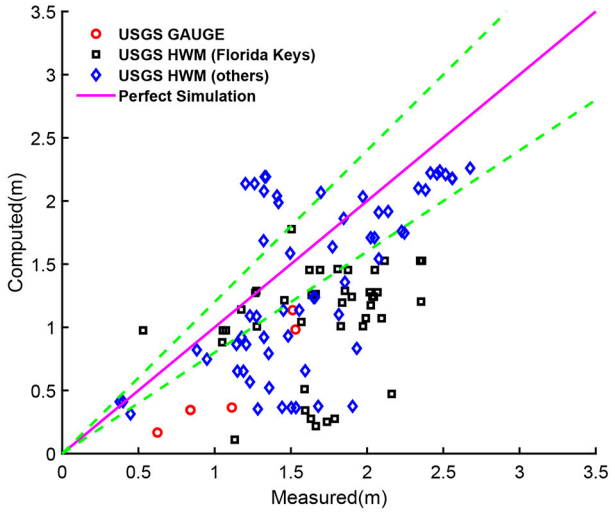

FIGURE 8 | Comparison between the computed and the measured HWMs at the various USGS stations. The green dashed lines represent the perfect simulation×(100 ± 20%). Note that only those measurement stations inundated by the simulated storm surge were used.

Algorithm 1: Strip–Type Domain Decomposition Used in Parallel CEST.

```
procedure StripDecomp
    ϵ = 1 × 10^−4
    dl = (2. ∗ ϵ + jm − 1.)/dble(np)
    for p = 0, np do
        y_min = 1. + dble(p ∗ dl) − ϵ
        y_max = y_min + dl
        for j = 1, jm do
            if y_min ≤ j & j < y_max then
                proc[j] = p
    for p = 0, np do
        for j = 1, jm do
            if proc[j] = p break
        j_min[p] = j
        for j = jm, 1 do
            if proc[j] = p break
        j_max[p] = j
```

in CEST is replaced with simple Jacobi iteration. This allows for a straightforward parallelization of the implicit part of Casulli's algorithm. Whilst this approach leads to slower convergence this is more than offset by the ability to employ multiple processes (and the associated decrease in the linear system size that each process is required to solve).

4. RESULTS

For the verification purpose, a test case with 4-day simulation of Hurricane Irma (2017) is conducted. Following (Zhang et al., 2008) we consider both the storm surge and the tidal component. The simulation starts at 00:00 UTC on 8 September 2017 and ends at 00:00 UTC on 12 September, with a time step of 10 s. In what follows, the detailed setup of the simulation and the results are discussed.

4.1. Model Domain

Figure 5 shows the model domain and the measurement locations for Hurricane Irma (2017), including tide gauges from NOAA, High Water Marks (HWMs) from US Geological Survey (USGS), and river gauges from USGS. We employ a very high–resolution curvilinear grid that comprises approximately 640,000 computational cells. The cell size at the open ocean area is approximately 1,470 × 1,470 m, which gradually reduces to 200 × 200 m at the shoreline areas and further smaller inland. It should be noted that, for display purposes, the grid lines are not shown in **Figure 5**. All model boundaries that lie in water are specified as open; details of the boundary conditions can be found in the section below.

4.2. Topographic and Bathymetric Data and Calculation of Grid Cell Elevation

The bathymetric and topographic data are required for calculating the water depths and elevations of the grid cells in a model basin. The topographic data used in this study mainly come from USGS, and the bathymetric data come from NOAA. Water depths for grid cells at the open ocean were calculated based on the ETOPO1 global relief dataset from NOAA, which has a resolution of 1 arc minute (1.8 km). Water depths for grid cells in coastal areas were interpolated from the U.S. coastal relief dataset from NOAA with a resolution of 3 arc second (90 m) (https://www.ngdc.noaa.gov/mgg/bathymetry/relief.html). The USGS 90, 30, 10, and 3 m digital elevation models (DEM) were used to calculate the elevation of grid cells on the land (http://viewer.nationalmap.gov/viewer/).

4.3. Boundary Conditions

At the open boundaries the model is forced using a nine–component tide comprising the M_2, S_2, K_1, O_1, Q_1, K_2, N_2, M_4, and M_6 components. These constituents were obtained from the ADvanced CIRCulation model (ADCIRC) Tidal Databases East Coast 2015 database of tidal constituents (Szpilka et al., 2016). An inverse pressure adjustment is made to the water surface specification at the tidal boundaries. The inverse pressure approach partially accounts for the meteorological forcing at the boundary by imposing the inverted barometer effect (Blain et al., 1994). Thus, the free surface at the open boundaries is modified by the amount $\Delta\eta(x, y, t) = -\frac{p'_s(x,y,tt)}{\rho_w g}$ where p'_s is an atmospheric pressure change and ρ_w is the sea water density.

4.4. Bottom Friction Coefficient

A spatially varying value of Manning's n is employed. **Figure 6** shows the spatial distribution of the Manning's coefficient used in this paper. This coefficient map was generated based on the national land cover dataset (NLCD) created by USGS in 2001, using the approach proposed in Zhang et al. (2012), where details

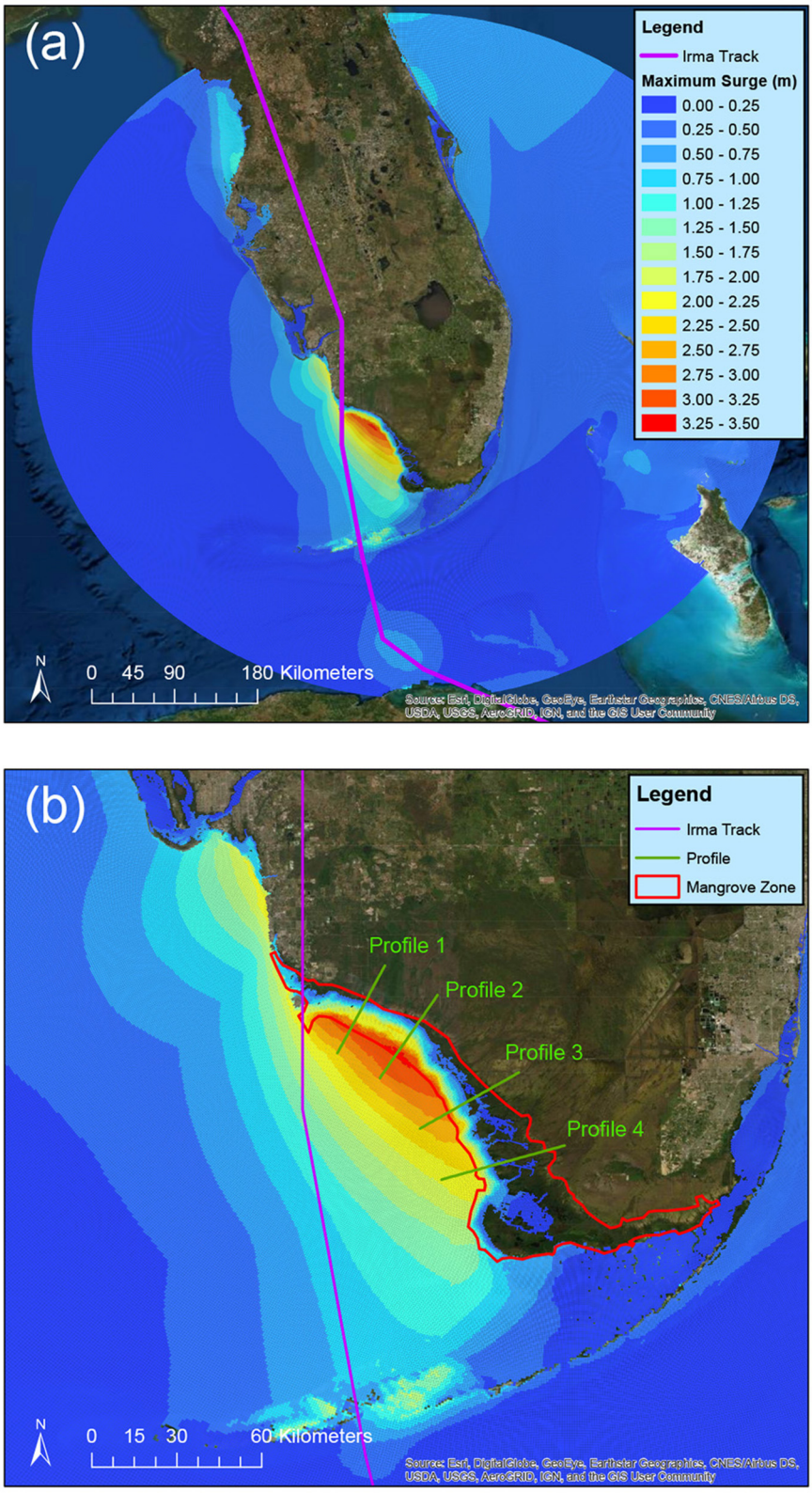

FIGURE 9 | The computed maximum storm surge height in spatial distribution: **(a)** the entire domain, and **(b)** a zoomed-in domain centered at the South Florida mangrove zone. The data are referenced to the NAVD88 vertical datum. The locations of the four profiles for **Figure 10** are also displayed.

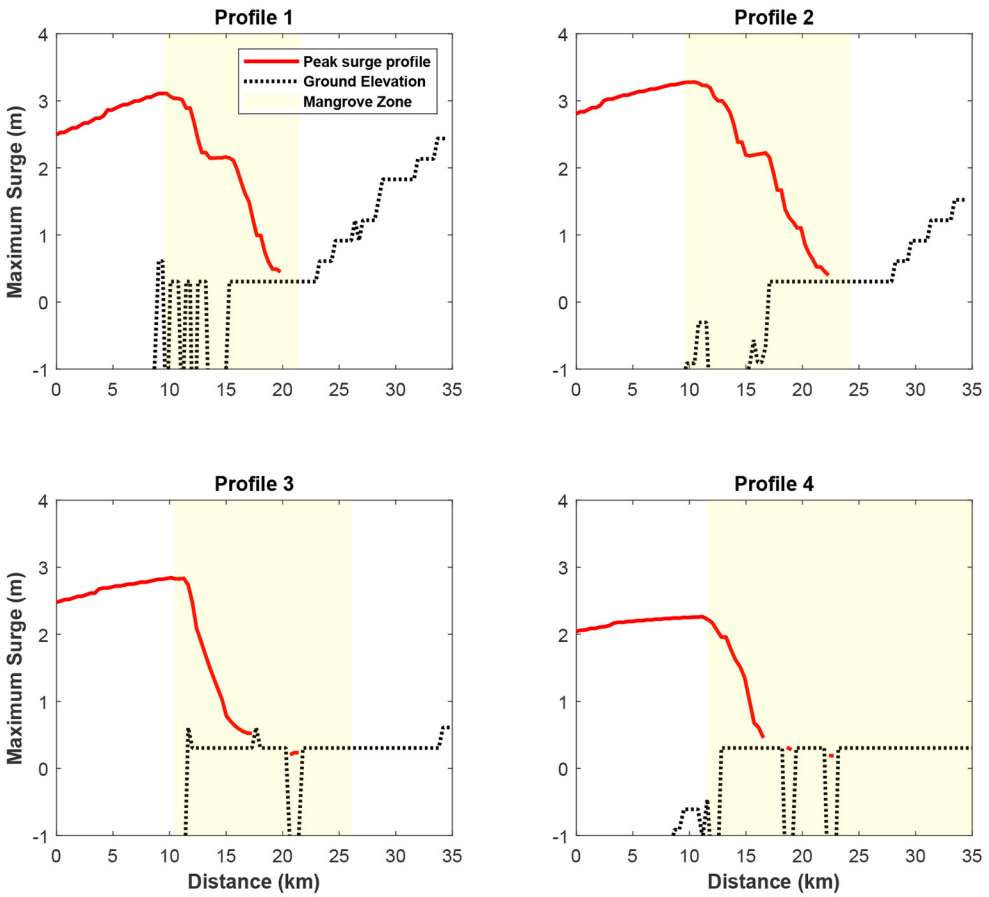

FIGURE 10 | The computed maximum storm surge profiles along the four profile lines depicted in **Figure 9**. The data are referenced to the NAVD88 vertical datum.

can be found. Note that for the open ocean area, a constant coefficient $n = 0.02$ was employed.

4.5. Comparison of Model Predictions and Observations

Figure 7 shows a comparison for the data at the NOAA tide gauges (**Figure 5**). The parallel CEST model in general captures the major trend of the tide and the storm surge induced by Irma (2017). At Naples, Fort Myers, and Mckay Bay Entrance, the surface elevations were relatively well predicted by CEST, while at Virginia Key, St Petersburg, and Old Port Tampa, CEST tends to underestimate the surface elevation variation.

Figure 8 presents the comparison for the HWM data. The CEST predictions have a root mean square error (RMSE) of approximately 0.69 m against the observations. This error is contributed significantly by the underprediction of the HWMs at Florida Keys and the South Florida mangrove zones (where the USGS gauges were marked, see **Figure 5**). A reason for this underprediction may be that these areas are close to the domain boundary, hence there is a limited fetch for wind to push water in.

Figure 9 presents the computed maximum storm surge height across the entire computational domain. It can be seen that the most severe storm surge inundation occurs at the right hand side of the track near the landfall location, where the area is known as the South Florida mangrove zone. The computed maximum storm surge height is over 3 m, but the overall inundation is kept within the mangrove zone due to the resistance of mangrove trees (Zhang et al., 2012). **Figure 10** further shows the computed maximum storm surge profile along the four profiles depicted in **Figure 9b**. The maximum storm surge height gradually reduces as it moves inland. The inundation extents are roughly around 10 km at Profiles 1 and 2, and approximately half of that at Profiles 3 and 4. It should be mentioned however that storm surge could move further upland in the rivers as seen in **Figure 9b**. The overall maximum surge pattern is comparable with ADCIRC model results (Kowaleski et al., 2020).

4.6. Computational Cost and Parallel Efficiency

The parallel performance of CEST on the 4-day simulation of Hurricane Irma (2017) was examined using the parallel efficiency (E_p) and speedup (S_p) coefficients. The coefficients are defined

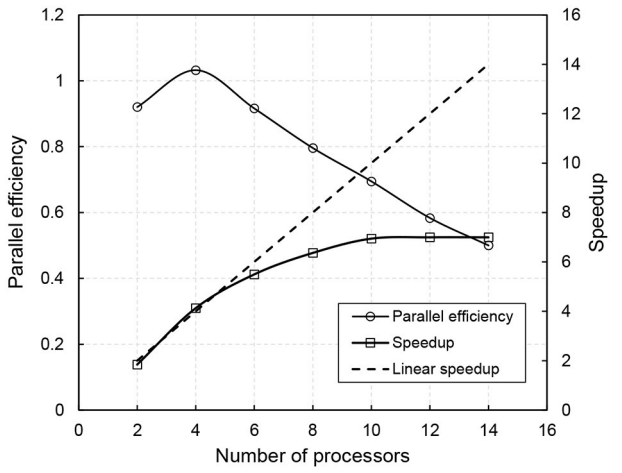

FIGURE 11 | The parallel efficiency and speedup of CEST at different number of processors for the simulation of Hurricane Irma (2017). The dashed line represents the linear speedup and is plotted for comparison purpose.

following Chen et al. (2018):

$$S_p = \frac{T_1}{T_p} \text{ and } E_p = \frac{S_p}{p}, \tag{20}$$

where T_1 and T_p are the total CPU time when using 1 and p processors. The simulation presented in this paper were run on a 32-core i7 CPU (3.7GHz) workstation. T_1 is approximately 150 min. The parallel efficiency and the speedup coefficients are plotted in **Figure 11**. As can be seen, the parallel CEST model achieves linear and even super-linear speedup when the number of processors used are small ($\leq$ 4). When the number of processors increases the speedup increases but also becomes flattened and the parallel efficiency drops linearly. Despite that 4 processors appear to be the optimal number for the current simulation in terms of parallel efficiency, as many as 10 processors can be used to reduce the total CPU time of simulation as a priority. In the current case, T_{10} is approximately 22 min.

5. DISCUSSION

This paper describes the parallelization of the IHRC–CEST model using the Message Passing Interface (MPI) library. The MPI parallelization approach allows the CEST model to be run optimally on a wide variety of computer architectures ranging from multi–core desktops to massively parallel supercomputers. Moreover, in the parallel CEST model simple Eulerian advection is replaced with high–order, monotonic semi–Lagrangian (SL) advection scheme. The high–order SL advection enables to use a larger model time–step,while maintaining numerical stability. The purpose of parallelizing the CEST model, and improving the advection efficiency, is to enable finer resolution ensemble forecasts to be undertaken at the IHRC on multi–core desktop machines. This allows for the most detailed bathymetric data available to be employed in forecast–mode surge simulations and thus facilitates the best possible representation of coastal topography. The use of finer computational grids for storm surge is known to improve predictions of the magnitudes and extent of storm surge flooding (Zhang et al., 2008). Results presented in this paper show that the wall clock time can be dramatically reduced through the use of a multicore desktop.

DATA AVAILABILITY STATEMENT

The raw data supporting the conclusions of this article will be made available by the authors, without undue reservation.

AUTHOR CONTRIBUTIONS

YL: conceptualization, methodology, validation, investigation, writing the original draft, visualization, and data curation. QC: software, validation, writing the review, editing, and data curation. DK: conceptualization, methodology, software, validation, investigation, and writing the original draft. KZ: supervision, conceptualization, and writing the review and editing. All authors contributed to the article and approved the submitted version.

FUNDING

This work was supported, in main, by Florida Public Hurricane Loss Model (FPHLM) project at International Hurricane Research Center of Florida International University.

REFERENCES

Blain, C. A., Westerink, J. J., and Luettich, R. A. (1994). The influence of domain size on the response characteristics of a hurricane storm surge model. *J. Geophys. Res. Oceans* 99, 18467–18479. doi: 10.1029/94JC01348

Blumberg, A. F., and Herring, H. J. (1987). "Circulation modeling using orthogonal curvilinear coordinates," in *Three Dimensional Models of Marine and Estuarine Dynamics. Elsevier Oceanography Series*, eds J. Nihoul and B. Jamart, vol. 45 (Elsevier Science, Amsterdam), 55–88.

Casulli, V. (1990). Semi-implicit finite difference methods for the two-dimensional shallow water equations. *J. Comput. Phys.* 86, 56–74. doi: 10.1016/0021-9991(90)90091-E

Chen, Q., Zang, J., Kelly, D. M., and Dimakopoulos, A. S. (2018). A 3D parallel Particle-In-Cell solver for wave interaction with vertical cylinders. *Ocean Eng.* 147, 165–180. doi: 10.1016/j.oceaneng.2017.10.023

Courant, R., Friedrichs, K., and Lewy, H. (1967). On the partial difference equations of mathematical physics. *IBM J. Res. Dev.* 11, 215–234. doi: 10.1147/rd.112.0215

Fedkiw, R., Stam, J., and Jensen, H. (2001). Visual simulation of smoke. *SIGGRAPH* 28, 15–22. doi: 10.1145/383259.383260

Garratt, J. R. (1977). Review of drag coefficients over oceans and continents. *Month. Weather Rev.* 105, 915–929. doi: 10.1175/1520-0493(1977)105andlt;0915:RODCOOandgt;2.0.CO;2

Holland, G. J. (1980). An analytic model of the wind and pressure profiles in hurricanes. *Month. Weather Rev.* 108, 1212–1218. doi: 10.1175/1520-0493(1980)108andlt;1212:AAMOTWandgt;2.0.CO;2

Kelly, D. M., Teng, Y.-C., Li, Y., and Zhang, K. (2015). A numerical model for storm surges that involve the inundation of complex landscapes. *Coast. Eng. J.* 57, 1–30. doi: 10.1142/S0578563415500175

Kowaleski, A. M., Morss, R. E., Ahijevych, D., and Fossell, K. R. (2020). Using a WRF-ADCIRC ensemble and track clustering to investigate storm surge hazards and inundation scenarios associated with Hurricane Irma. *Weather Forecast.* 35, 1289–1315. doi: 10.1175/WAF-D-19-0169.1

Large, W. G., and Pond, S. (1981). Open ocean momentum flux measurements in moderate to strong winds. *J. Phys. Oceanogr.* 11, 324–336. doi: 10.1175/1520-0485(1981)011andlt;0324:OOMFMIandgt;2.0.CO;2

Moretti, G. (2002). Thirty-six years of shock fitting. *Comput. Fluids* 31:719–723. doi: 10.1016/S0045-7930(01)00072-X

Myers, V., and Malkin, W. (1961). *Some Properties of Hurricane Wind Fields as Deduced From Trajectories*. Technical Report National Hurricane Research Project No. 49, Weather Bureau, US Department of Commerce, Washington, DC.

Nair, R., Côté, J., and Staniforth, A. (1999). Monotonic cascade interpolation for semi-Lagrangian advection. *Q. J. R. Meteorol. Soc.* 125, 197–212. doi: 10.1002/qj.49712555311

Pandolfi, M., and Zannetti, L. (1977). "Numerical investigations about the predictions of free surface shallow water motions," in *Proceedings 6th Australasian Hydraulics and Fluid Mechanics Conference* (Adelaide, SA), 364–368.

Powell, M. D., Houston, S. H., Amat, L. R., and Morisseau-Leroy, N. (1998). The HRD real-time hurricane wind analysis system. *J. Wind Eng. Indust. Aerodyn.* 77–78:53–64. doi: 10.1016/S0167-6105(98)00131-7

Press, W., Flannery, B., Teukolsky, S., and Vetterling, W. (1992). *Numerical Recipes: The Art of Scientific Computing, 2nd Edn*. New York, NY: Cambridge University Press.

Szpilka, C., Dresback, K., Kolar, R., Feyen, J., and Wang, J. (2016). Improvements for the Western North Atlantic, Caribbean and Gulf of Mexico ADCIRC Tidal Database (EC2015). *J. Mar. Sci. Eng.* 4, 72. doi: 10.3390/jmse4040072

Taylor, A., and Glahn, B., (2008). "Probabilistic Guidance for Hurricane Storm Surge," in *Preprints, 19th Conference on Probability and Statistics, 88th Amer. Meteor. Soc. Annual Meeting* (New Orleans, LA), 8.

Yanenko, N. N. (1971). *The Method of Fractional Steps: The Solution of Problems of Mathematical Physics in Several Variables*. New York, NY: Springer-Verlag.

Zhang, K., Li, Y., Liu, H., Rhome, J., and Forbes, C. (2013). Transition of the coastal and estuarine storm tide model to an operational storm surge forecast model: a case study of the Florida coast. *Weather Forecast.* 28, 1019–1037. doi: 10.1175/WAF-D-12-00076.1

Zhang, K., Liu, H., Li, Y., Xu, H., Shen, J., Rhome, J., et al. (2012). The role of mangroves in attenuating storm surges. *Estuarine Coast. Shelf Sci.* 102–103, 11–23. doi: 10.1016/j.ecss.2012.02.021

Zhang, K., Xiao, C., and Shen, J. (2008). Comparison of the CEST and SLOSH models for storm surge flooding. *J. Coast. Res.* 24, 489–499. doi: 10.2112/06-0709.1

Conflict of Interest: The authors declare that the research was conducted in the absence of any commercial or financial relationships that could be construed as a potential conflict of interest.

Publisher's Note: All claims expressed in this article are solely those of the authors and do not necessarily represent those of their affiliated organizations, or those of the publisher, the editors and the reviewers. Any product that may be evaluated in this article, or claim that may be made by its manufacturer, is not guaranteed or endorsed by the publisher.

frontiers in Climate

ORIGINAL RESEARCH
published: 19 August 2021
doi: 10.3389/fclim.2021.610593

Assessing Damages to Built and Natural Environments: Linking Hydrodynamic and Geospatial Enviro-Economical Models

Hanadi S. Rifai[1]*, *Amin Kiaghadi*[1,2] *and Daniel W. Burleson*[1]

[1] Civil and Environmental Engineering, University of Houston, Houston, TX, United States, [2] Computational Hydraulics Group, Oden Institute, University of Texas at Austin, Austin, TX, United States

In this study, a novel framework was developed to provide a holistic damage assessment caused by severe hydrologic events whether individually or as a compound event. The novel framework uses a developed hurricane-specific water quality model, Environmental Fluid Dynamic Code-Storm Surge model (EFDC-SS) and an ArcGIS-based framework, the Facility Economic Damage and Environmental Release Planning (FEDERAP) to assess damages to the built and natural environment. The developed framework could be used to compare different hurricanes and storms with a focus on land inundation, spill destination in both land and water and their associated risks, as well as economic loss including both physical and secondary losses. The results showed different spreading mechanisms during surge and rainfall-based hurricanes. While storm surge pushed contaminants (from spills) upstream, the rainfall-based hurricane caused a larger footprint of contamination on land. Though different in spreading patterns, spills during both hurricane types can widely spread miles away from the release location in a very short period of time. The FEDERAP economic loss model showed that facility area, average land elevation, the number of storage tanks and process units at the facility, and daily production are key drivers in the calculated total losses for a given hydrologic event.

Keywords: compound flooding, inundation, spills and leaks, ADCIRC, EFDC

OPEN ACCESS

Edited by:
Valentina Prigiobbe, Stevens Institute of Technology, United States

Reviewed by:
Roohollah Noori, University of Tehran, Iran
Juan L. Garzon, University of Algarve, Portugal

***Correspondence:**
Hanadi S. Rifai
rifai@uh.edu

Specialty section:
This article was submitted to Climate Risk Management, a section of the journal Frontiers in Climate

Received: *26 September 2020*
Accepted: *27 July 2021*
Published: *19 August 2021*

Citation:
Rifai HS, Kiaghadi A and Burleson DW (2021) Assessing Damages to Built and Natural Environments: Linking Hydrodynamic and Geospatial Enviro-Economical Models. Front. Clim. 3:610593. doi: 10.3389/fclim.2021.610593

INTRODUCTION

Storm surge, the rise in water level due to wind and pressure stresses, is known to be the most devastating aspect of a hurricane due to the retention time of inundated areas, currents, and water pressures within affected regions (Godoy, 2009; Naito et al., 2012). The literature is replete with studies that have demonstrated the catastrophic impacts of storm surge on residential areas (e.g., Robertson et al., 2007; Frazier et al., 2010) as well as on industrial regions (e.g., Cruz et al., 2001; Cauffman et al., 2006; Pine, 2006; Godoy, 2007; Harris and Wilson, 2008; Santella et al., 2010; Hallegatte et al., 2011; Burleson et al., 2015). However, in recent years, hurricanes with historical rainfall (e.g., Hurricane Harvey with >125 cm of rainfall in Houston, Texas, United States) have also caused billions of dollars in damages to the economy (e.g., Kiaghadi and Rifai, 2019; NCDC, 2020). The catastrophic impacts of severe hydrologic events whether from storm surge or inland flooding can be amplified when they occur concurrently or in sequence (compound flooding). In addition, numerous articles in the general literature have reported on environmental impacts of

hurricanes, both in built and natural environments and encompassing damages from the hurricane itself and from cascading impacts associated with hurricanes (referred as secondary losses) such as failures in environmental infrastructure and spills and leaks from industrial and hazardous waste facilities (e.g., Chang et al., 1997; Khan et al., 2001; Verter and Kara, 2001; Hoobler et al., 2003; Ashley et al., 2008; Srinivas and Nakagawa, 2008; Kim et al., 2011; Liao et al., 2011; Qi and Altinakar, 2011; Eldrandaly and AbdelAziz, 2012; Mamauag et al., 2013; Kiaghadi et al., 2018; Kiaghadi and Rifai, 2019; Kiaghadi et al., 2020). However, and to the best knowledge of the authors, there is no integrated framework that covers both economic and environmental impacts at the detailed facility level due to vulnerabilities to storm surge, inland flooding, or compound flooding.

Despite the recent progress in hydrodynamic models to simulate compound flooding events (e.g., Bilskie et al., 2016; Moftakhari et al., 2017; Kumbier et al., 2018; Zhang et al., 2019; Loveland et al., 2021), there is still no single model that could accurately represent the complex nature of such events that involve various forcing and processes (Santiago-Collazo et al., 2019). To address the lack of a seamless framework integrating all these processes, nested (most common) and dynamic (most challenging) coupling of various models (i.e., two or three) have been used by researchers across the globe (e.g., Santiago-Collazo et al., 2019; Loveland et al., 2021). Additionally, the majority of the aforementioned modeling efforts have focused on land inundation and physical damages and less attention has been paid to environmental impacts such as spills and leaks (Kiaghadi et al., 2018). While the results of hydrodynamic or geospatial models could be used to estimate the occurrence probability of spill and leaks (Burleson et al., 2015; Kiaghadi et al., 2020), simulating the fate and transport of spills and leaks during compound flooding events requires more complex hydro-environmental modeling. For this purpose and depending on the nature of the hydro-environmental modeling effort (i.e., hindcast or forecast), a hydrodynamic model with a mass transport module, individually or in combination with an infrastructure failure model, is required. A modeling system developed for hindcasting could work with observed values at its boundary conditions without the need for other models while for forecasting purposes, it is required to have other models to provide flux and water heights at the boundaries. As one of the few examples in the literature, Kiaghadi et al. (2018) coupled the U.S Environment Protection Agency's (EPA) Environmental Fluid Dynamic Code (EFDC) code (Hamrick, 1992) to the SWAN (Simulating WAves Nearshore) + ADCIRC (Advanced Circulation) hurricane simulation model from Hope et al. (2013) and a stochastic tank failure model developed by Kameshwar and Padgett (2015). The developed Environmental Fluid Dynamic Code-Storm Surge model (EFDC-SS) uniquely captures storm surge, local runoff, and compound flooding effects on the fate and transport of pollutants in the environment associated with severe hydrologic events.

In the case of a compound flooding event, when both storm surge and local runoff are present, the residential impact would be more severe in areas prone to fluvial and pluvial flooding (Huang et al., 2001). Thus, the focus of this study is on industrial parcels where both storm surge and local runoff could cause inundation. Losses during extreme events entail both primary (direct losses to product or infrastructure due to inundation) and secondary losses such as environmental cleanup and downtime that may result from the inundation in addition to catastrophic losses of units/processes that have been discussed in previous research on hurricanes (e.g., Cauffman et al., 2006; Pine, 2006; Santella et al., 2010; Burleson et al., 2015) and tsunamis (Srinivas and Nakagawa, 2008; Naito et al., 2012).

Numerous researchers have reported on damages experienced by industrial facilities during hurricanes such as significant failure of electrical centers, processing buildings, control centers (Harris and Wilson, 2008), structural failure, floating tanks, and significant production downtime due to power failure (Cruz et al., 2001; Godoy, 2007; Santella et al., 2010). Productivity loss has been discussed previously in the literature (e.g., Bailey and Levitan, 2008; Cruz and Krausmann, 2013) but never accounted for in damage estimates associated with natural disasters. Furthermore, only a few studies have discussed potential environmental impacts during hurricanes (e.g., Ashley et al., 2008; Santella et al., 2010); however, environmental cleanup has not been accounted for in any of them. Moreover, studies on tank failure have been limited to conducting surveys in the aftermath of extreme events to report losses (e.g., Cauffman et al., 2006; Pine, 2006; Godoy, 2007; Naito et al., 2012) as opposed to rigorous studies aimed at providing a framework to predict failure based on locations and elevation. While various tools have been developed and used to assess hazardous waste transport (e.g., Zografos et al., 2000; Verter and Kara, 2001; Kim et al., 2011), community businesses (Yang et al., 2009), and population impact (Qi and Altinakar, 2011), there is no framework for assessing the vulnerability of industrial facilities to compound flooding that encompass both primary and secondary losses. Additionally, and despite the presence of some Geographic Information System (GIS)-based tools such as Hazards United States-Multi Hazard (HAZUS-HM, https://www.fema.gov/hazus) that could be used to estimate the regional losses due to varios hazards, there is a gap for a framework that could capture losses based on detailed industrial facility data at the parcel resolution.

To estimate damages at industrial parcels that encompass physical damage from inundation as well as secondary losses from environmental spills and releases and downtime effects on productivity, an ArcGIS-based framework, the Facility Economic Damage and Environmental Release Planning (FEDERAP) framework was developed in this study. Unlike previous ArcGIS-based toolboxes (e.g., Chang et al., 1997; Khan et al., 2001; Verter and Kara, 2001; Hoobler et al., 2003; Kim et al., 2011; Liao et al., 2011; Qi and Altinakar, 2011; Eldrandaly and AbdelAziz, 2012; Mamauag et al., 2013), the developed model is the first effort that integrates secondary losses from environmental releases and facility downtime into the overall loss assessment. This paper presents the coupling of the ADCIRC+SWAN model with EPA's EFDC model as a framework for assessing environmental and economic damages associated with storm surge and the cascading effects of storm surge that include failures in environmental

infrastructure such as wastewater plants, hazardous waste facilities and failures in industrial infrastructure including unit processes and above ground storage tanks that store chemicals and petrochemicals. The paper demonstrates the implementation of the developed coupled models to the Houston-Galveston (HSC-GB) region, and more specifically in the HSC-GB Estuary in Texas, United States that will be collectively referred to as the GBS, for Hurricanes Ike and Harvey in 2008 and 2017, respectively.

MATERIALS AND METHODS

Study Region

The Houston Ship Channel (HSC) region (**Figure 2**), located in Harris County, Texas, United States, was selected for demonstrating the developed coupled modeling and economic damage framework. The HSC itself is a highly industrialized area with more than 900 industrial facilities and more than 4,300 above ground storage tanks (Burleson et al., 2015; Kiaghadi et al., 2018). The HSC is tidally influenced and geographically extends from the Port of Houston, near downtown Houston, Texas, to the Gulf of Mexico. The navigational channel average width and depth are 162 and 13.7 m, respectively. This region is an ideal setting for the study due to the historical record of hurricanes in the Houston-Galveston region (Needham and Keim, 2012) combined with the significant presence of chemical and petrochemical industries.

EFDC-SS: Coupling ADCIRC + SWAN and EFDC Models

In this paper, the Kiaghadi et al. (2018) EFDC-SS model is used to simulate pollutant transport from spills during a rainfall-based hydrologic event. The EFDC-SS framework developed by Kiaghadi et al. (2018) has sufficient spatial, temporal, and stratification resolution to: (1) investigate the compound effects of inundation from rainfall and storm surge that may lead to spills and leaks from environmental infrastructure and industrial facilities, (2) provide water velocity estimates that can be used to understand erosion, sediment transport, and the probability of damage to physical infrastructure such as above-ground storage tanks within industrial facilities, (3) investigate the transport and trajectory of pollutant releases as surge water moves inland and recedes back to the ocean, (4) provide pollution sourcing input functions to air quality models for hydrocarbon spills on land or in riverine systems that volatilize and create airshed plumes, and (5) assess the economic loss and recovery periods when combined with other economic models (e.g., coupled with FEDERAP) as shown in **Figure 1**. However, this study is focuced on 1, 3, and 5.

In brief, a detailed grid for the HSC was developed that includes wet (within the waterway) and dry cells (on land) with a total of 42,975 cells. The cells are 96 × 96 m with a total 396 km^2 area coverage. The bathymetry data were combined from various sources and dry and wet depth values of 0.12 and 0.15 m, respectively, were assigned to dry and wet cells, respectively. In this case, when the water depth is <0.12 m, the cell is excluded from hydrodynamic calculations. The coupling of EFDC to ADCIRC + SWAN was completed *via* a surge-based head boundary condition at the mouth of the HSC before it reaches Upper Galveston Bay (see **Figure 2**). For the headwater boundary, the Water Surface Elevations (WSEs) throughout a given severe storm duration were extracted from a gauge maintained by the National Oceanic and Atmospheric Administration (NOAA) or the SWAN + ADCIRC model when no measured data was available (e.g., Hurricane Ike). Since the SWAN + ADCIRC model developed by Hope et al. (2013) was calibrated for Hurricane Ike, using varios observed data, it is assumed that the WSEs values at at the mouth of HSC have the same accuracy as the NOAA gauge. However, using headwater boundary conditions from two different sources may result in some uncertainties in intrepting the results. The discharge flow rates were incorporated into EFDC-SS as headwater flow boundary conditions at the locations of bayou outfalls into the HSC (see flow boundary locations in **Figure 2**). No wind within the EFDC-SS domain and no direct rainfall on the model grid were considered in this study. The effect of rainfall was incorporated in the model through the flow boundaries and the wind effect was accounted in the SWAN + ADCIRC model. Furthermore, in this study, the inundation duration was defined as the duration in which a cell initially dry remains wet before the flooding recedes. However, and a limitation of numerical models, it is worth mentioning that if an originally dry cell (land with a water depth of zero) becomes wet (inundated with positive water depths) and loses its connectivity with the adjacent cells, it remains wet for the rest of the simulation period.

Release Locations 1–3 (see **Figure 2**) were selected because tanks located within these areas showed the highest probability of failure during Hurricane Ike and Harvey. The results of the calibrated EFDC-SS for Hurricane Harvey (RMSE of 0.87 m for 265 high water marks) was used to estimate the probability of failure for all ∼4,300 above ground storage tanks using the stochastic method developed by Kameshwar and Padgett (2015). The resulting probabilities and potential spill volumes were used to set-up the tracer module and simulate the fate and transport of potential spills during compound events. A passive tracer dye was used to estimate the trajectory of the dissolved phase of a spill. However, it should be noted that using a passive tracer dye limits the ability to capture weathering processes (i.e., evaporation and emulsification) and the chemical reactions among chemicals. Three release locations with the highest probability of failure (Release Locations 1–3 in **Figure 2**) were chosen for spill simulations. In the case of a spill, the waterbody is not the only contaminated matrix and due to high WSEs and inundation, chemicals released during a spill can reach and pollute surrounding land areas, and possibly volatilize to the airshed (this aspect was not considered in this study). The cells in the model domain toggle between being dry and wet throughout the storm. One of the novel aspects of the study is in including the effect of spills on land in addition to waterways.

FEDERAP Economic Damage Framework

The Facility Economic Damage and Environmental Release Planning (FEDERAP) framework combines an ArcGIS toolbox with Excel-based economic-function worksheets for estimating

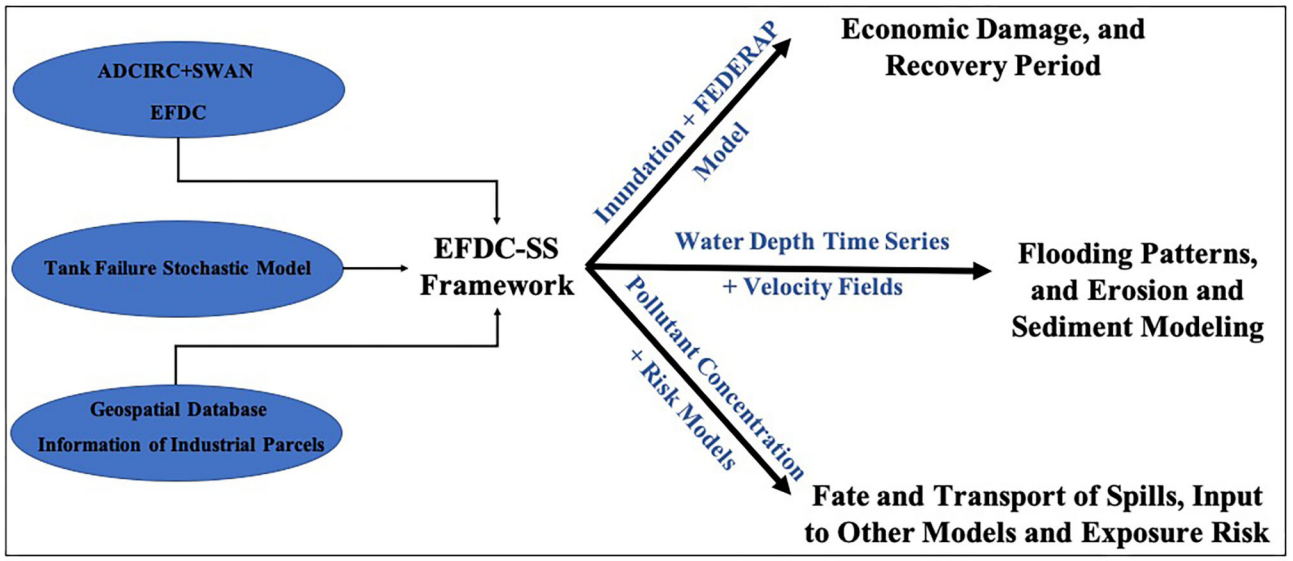

FIGURE 1 | EFDC-SS framework with the input information/models and potential applications.

costs for a single facility and to accumulate costs across an entire industrial complex. The GIS toolbox is used to develop spatial analysis data for various storm surge levels for a given facility (for example, to determine areas within an industrial facility that are inundated at a given storm surge level). Built-in tools such as Clip, Select by Location, and raster conversion tools were used in an intentional order to accurately evaluate the inundation of the facility infrastructure. The result is several geodatabases of shapefiles and statistics that represent the inundation for each aspect of the facility at multiple storm surge levels. The data from these geodatabases are exported into a tabular format for economic damage assessment within the FEDERAP Excel Analysis. The Excel worksheets allow users to compile the spatial analysis data from the GIS toolbox and use the information in conjunction with economic loss algorithms in order to predict losses for a given storm surge level for a specific facility.

The FEDERAP framework requires a spatial analysis to determine the extent of inundation of a given facility, its unit-processes, and storage tanks for a given storm surge depth. This spatial analysis is undertaken using the results from the EFDC-SS model scenarios described above. For the purposes of this research, inundation is defined to occur in any part of the geographic study extent where the elevation of land is lower than the predicted storm surge level. The inputs to the spatial analysis toolbox include:

i. *Facility boundary*. Facility boundaries are represented using a polygon shapefile with multiple objects that accurately represent the entire facility. The data were derived from parcel boundaries and ownership information from the Harris County Appraisal District (HCAD, https://hcad.org) and vcrified with 0.3 × 0.3 m (1 × 1 ft) aerial photography from the Houston-Galveston Area Council (HGAC) GIS database (https://gishub-h-gac.hub.arcgis.com/).
ii. *Water surface elevation (WSE) of interest*. The outputs of the EFDC-SS are used here. Alternatevily, the user could specify a minimum and maximum value for WSE to be used in the analysis. The model loops over the WSE range using a step of one unit. For example, for a minimum storm surge of ∼3 m (10 ft) and a maximum of ∼4.6 m (15 ft), storm surge levels of 3.04, 3.35, 3.66, 3.96, 4.27, and 4.57 m (10, 11, 12, 13, 14, and 15 ft) would be evaluated within the toolbox (6 loops).
iii. *Unit-processes*. A polygon shapefile defining each unit-process as a single object is used for this input. A unit-process is defined in this research as a region within the facility where chemical or oil refining occurs and/or is processed. The data were obtained from the HGAC aerial photography described above.
iv. *Storage Tanks*. A separate polygon shapefile is used to represent the various storage tank types within the HSC: horizontal, fixed-top vertical, and floating-top vertical tanks (illustrated in **Figure 3**). The shape of the object in the input file reflects the shape of the tank (circular for vertical tanks and oval for horizontal tanks). The data were obtained from the HGAC aerial photography described above.
v. *Elevation for Region*. The elevation for the region input is a point file with elevation locations throughout the region in which the facility is located. The FEDERAP toolbox includes commands to extract only the elevation for the facility within the boundary specified; ArcGIS point to raster conversion is utilized based on least squares to develop a high-density elevation-point surface for the entire facility. Alternatively, Digital Elevation Models (DEMs) compiled from Light Detection and Ranging (LiDAR) could be used.

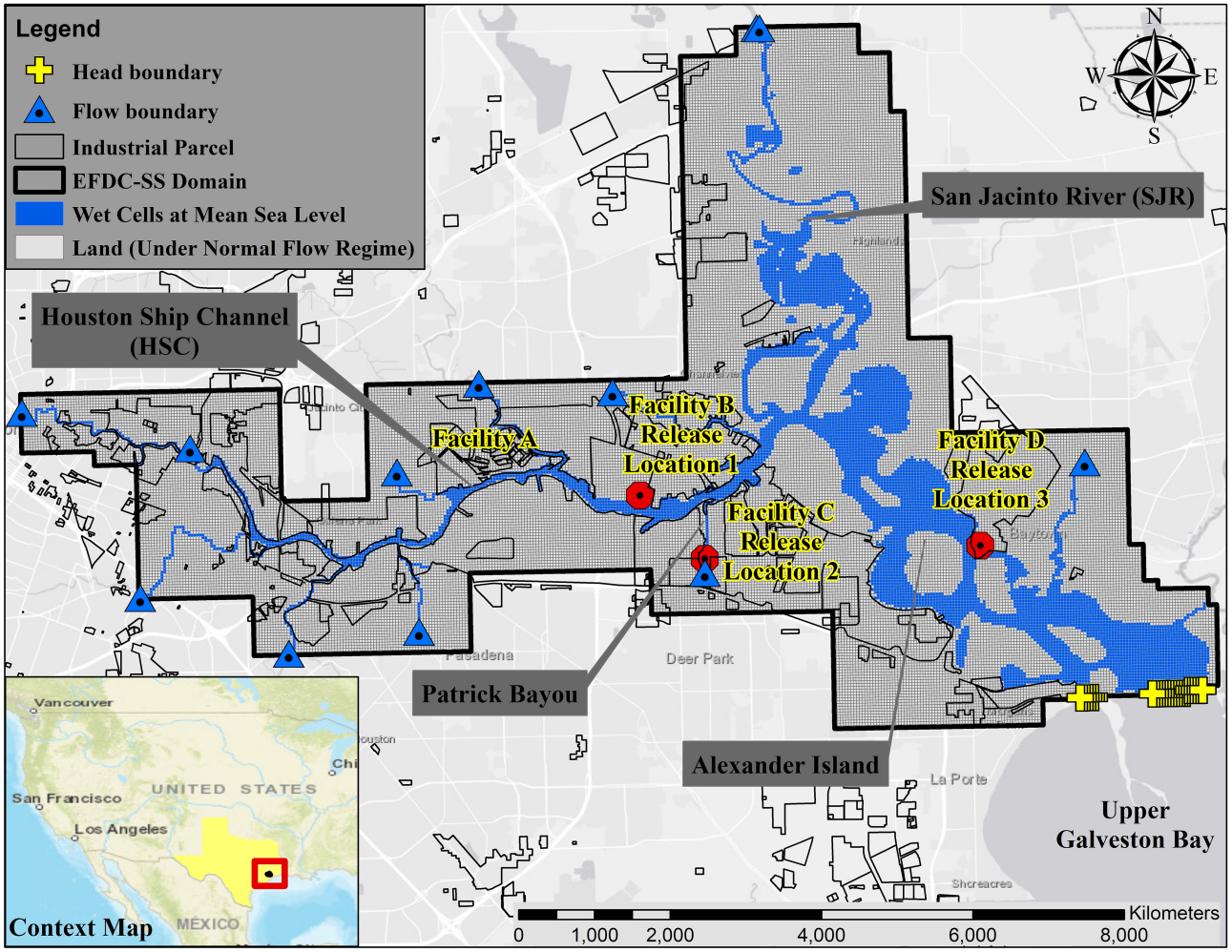

FIGURE 2 | Modeled domain with EFDC-SS.

The FEDERAP framework encompasses four categories of loss as shown in **Figure 4**: (1) facility loss, (2) unit process loss, (3) environmental release loss, and (4) productivity loss. Each of these components is a function of inundation caused by the storm surge level and is associated with models of economic losses due to inundation. The economic loss variables used in the analysis for each facility ranged between a high and a low value, therefore, 3 estimates of economic losses were developed: high, low and average. The framework incorporates aspects of downtime, production, and potential cleanup costs that have not been previously combined into a single model for evaluating vulnerability. Each of these categories is explained in more detail in the following sections.

Category 1: Facility Inundation Loss

Facility inundation, defined as the part of a facility that is covered with water for a given WSE, is a key driver in FEDERAP similar to many of the developed models and regression such as HAZUS (Vickery et al., 2006). In FEDERAP, the percent of the facility area that is inundated for a given WSE is calculated using the detailed elevation data within the facility. Land value is based on the property-appraised value of the land parcels for the facility from the Harris County Appraisal District (HCAD) as noted above. Losses in facility value are modeled based on the percent of the facility that is under water for a given hydrologic event, as shown in **Table 1**; this input economic loss function can be altered by the user.

Category 2: Unit Process Loss

Unit-processes, locations within a facility that are used to process (i.e., make and move) chemicals have a value relative to the overall production of the facility in addition to the intrinsic value of the structure itself. For each unit-process, a percent inundation is calculated and associated with a cost of refurbishment or a replacement cost using the relationship shown in **Table 1**. While recent reports have estimated costs for construction of process units at ~$340 million with refurbishment estimated at $60 million (Eggleston, 2014), convervative estimates were used in

FIGURE 3 | Types of storage tanks from left to right (floating top vertical, horizontal, and fixed top vertical).

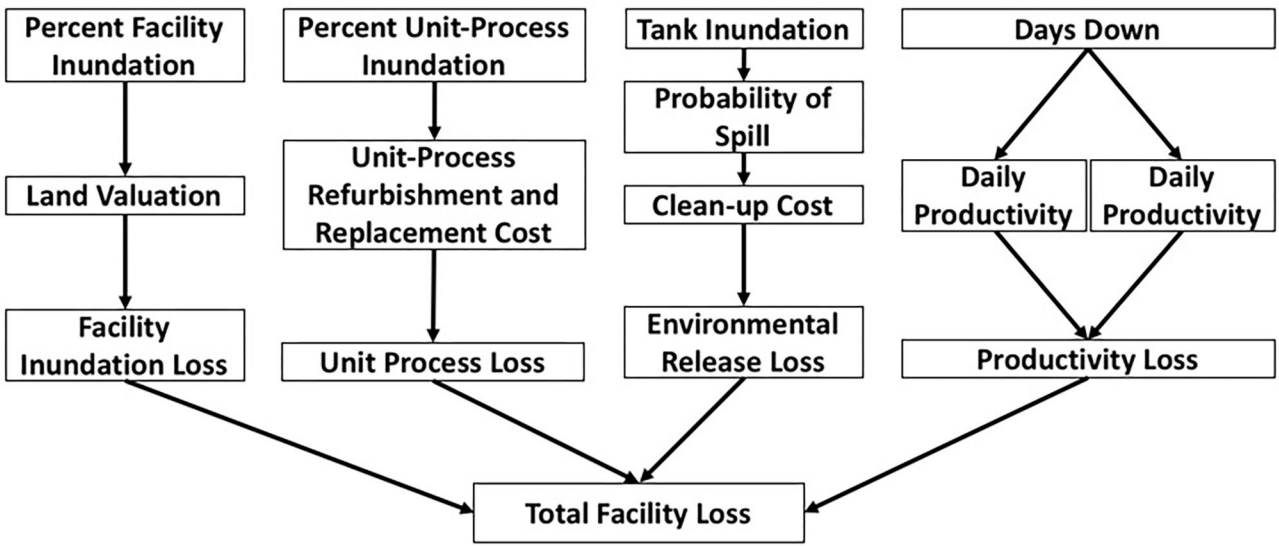

FIGURE 4 | The FEDERAP model framework.

the study as shown in **Table 1**. As with facility losses in the previous section, the algorithm in **Table 1** can be customized by the user.

Category 3: Environmental Release Loss

The environmental losses modeled in FEDERAP are based on an estimate of the tanks that would be inundated for a specific storm surge level that are calculated using the EFDC-SS model presented in the previous section. A tank is designated as inundated if the elevation of the bottom of the tank is below the WSEs caused by the extreme event. It is, however, unlikely that all inundated tanks would experience failure, thus a certain percentage of inundated tanks is modeled to fail. In this research, the percent of tanks that experience failure when inundated ranges from 20 to 50% depending on the type of tank (see **Table 1**); these modeled percentages are also a model variable that can be refined given specific data on tank structural integrity as discussed previously. The percent of total tanks inundated for each hydrologic event is applied to the total stored product for the facility to determine the projected spill quantity. Spills from previous hurricanes have had significant impact on contaminant levels in water that would require cleanup (Reible et al., 2006; Freund et al., 2014). A cost of cleanup of $31 dollars per liter of product released is applied to the projected spill amount based on work presented in Etkin (2000). The total environmental loss is the sum of the loss associated with cleanup of the spilled volume and an estimated cost for replacing the tank structure itself. For example, a facility having 10 fixed top vertical tanks that are inundated at a storm surge level of ∼6 m (20 feet) with a total volume of stored product of ∼1,893 L(500 gallons) would experience a loss of 20% of the product or ∼378.5 L (i.e., 378.5 L with an associated cleanup cost of 378.5 L × $31/liter or $11,733.5). In this case, two tanks would fail and assuming a replacement cost of $1,000 per tank, the structural cost would be $2,000 yielding a total environmental cost of ∼$13,733 for the facility at the ∼ 6 m (20 ft) surge level.

TABLE 1 | (A) Land value loss as a function of facility inundation, **(B)** Loss algorithm for unit process inundation, **(C)** Storage tank types and their modeled failure under surge and **(D)** Modeled relationship between non-operational days and percent inundation of facilities.

A. Facility inundation (Percent)	**Land value loss (Percent of land value)**
0	0
10	25
25	50
50	75
75	100
B. % Inundation of unit process	**Unit damage ($)**
20 (Refurbishment)	1,000,000
50 (Complete Loss)	10,000,000
C. Tank type	**% Failure for Inundated Tanks**
Fixed top vertical tank	20
Floating top vertical tank	50
Horizontal tank	30
D. Facility inundation	
Inundation percent	Days down
0%	7
20%	14
50%	28
75%	56
Unit-processes inundation	
Units inundation percent	Additional days down
0%	0
20%	7
50%	14
75%	21
Environmental cleanup	
Volume of Release (in liters)	Additional days down
0	0
37.85 million (10 million gallon)	7
75.71 million (20 million gallon)	14
113.56 million (30 million gallon)	21

Category 4: Productivity Loss

Productivity loss, as explained above, is the loss resulting from a disruption of normal business operations; sometimes referred to as "downtime." In FEDERAP, downtime is modeled using the number of days that the facility is not operational in addition to the loss of physical product that would have been produced during the lost days (e.g., refined gasoline). The downtime is modeled using three key variables: the percent inundation of the facility, unit-process inundation, and the volume of released product resulting from a spill scenario (this triggers cleanup activities which cause further days of downtime). The modeled relationship between the percent inundation of the facility and days down is shown in **Table 1D**; for 75% inundation, for instance, 56 days of inactivity are projected based on the overall inundation. The total downtime, however, will be adjusted upwards if process units were inundated: a 20% inundation of process units adds 7 more downtime days to the 56 (**Table 1D**). Additionally, loss of products, for example, a release of 75.7 million liters (20 million gallons) of product will add 14 more downtime days to account for emergency response and cleanup that would needed. Thus, in the above example scenario, a total of 77 downtime days (56 + 7 + 14) are projected. The relationships shown in **Table 1D** were developed based on personal communications (*via* phone and/or in person interviews) with facility and emergency management personnel in Texas and can be customized for other regions or for a specific facility.

The downtime loss is estimated based on the number of days down and the daily revenue of the facility. Thus, for a facility that has daily revenue of $300K and using the 77 days down in the example above, the total downtime loss will be ∼$23.1 million. Also included in the productivity loss is the cost associated with loss of production. Continuing with the example in this section, based on an estimated 10,000 barrels of oil-produced daily at the facility with a cost of $100 per barrel, a total production loss of $1 million is accrued per day during the 77 days of downtime ($77 million for production loss). The total productivity loss for the example is $100.1 million (the sum of the production loss of $77 million and the downtime loss of $23.1 million).

The Excel-based economic model (**Table 2**) has a total of seven worksheets that extract data from the geodatabases as discussed above. The first sheet incorporates general information about a facility including total land area, number of unit-processes, daily revenue and production. The next four sheets determine the results for each of the four categories of losses in the FEDERAP framework described above. The four loss estimation worksheets require the output statistics from the statistics geodatabase, as noted in **Table 2**. The losses are calculated for each category within the appropriate sheet in the Excel model. It is also here that users can modify the cost modeling algorithms and customize them for their specific application. The outputs from the FEDERAP Excel analysis are summarized in the final two sheets of the economic excel-based model. For each hydrologic event, the loss for each category and the total loss are both shown in tabular form as are loss curves showing the total loss and contribution from each of the four categories.

Modeling Scenarios

The fate and transport of potential spills and their footprint on land, during compound flooding events were simulated for Hurricane Ike (2008) and Hurricane Harvey (2017), with storm surge and rainfall as the dominant sources of flooding, respectively. In other words, Hurricane Harvey (2017) was used to investigate how local flows emanating from different watersheds can affect land inundation and spill fate and transport compared to a surge-based event (e.g., Hurricane Ike in 2008). The EFDC-SS scenarios were named based on the storm type and release locations. For instance, Ike-3 represent a simulation with inputs from Hurricane Ike and tank failure at Release Location 3 (see **Figure 2**) resulting in a total of 6 scenarions (3 Release Locations for Ike and Harvey). The inundation patterns during these two types of hurricanes were compared. The extent of lands affected by the spill (both upstream and downstream of release

TABLE 2 | FEDERAP Excel sheets.

Sheet name	Inputs	Outputs
Cover page—facility information	Total number of unit-processes, tanks, daily revenue, property value, production, and total area (user-defined)	None
Facility inundation	Total area inundated (from statistics geodatabase, Section FEDERAP Economic Damage Framework)	Facility Land Damage ($)
Unit-process Loss	Total number of unit processes inundated at 20 and 50% (from statistics geodatabase, Section FEDERAP Economic Damage Framework)	Unit-process Damage ($)
Environmental releases loss	Total number of tanks inundated (from statistics geodatabase, Section FEDERAP Economic Damage Framework)	Environmental Clean-up Damage ($)
Productivity loss	None	Daily Revenue Loss, Production Loss, Total Productivity Loss
Facility loss summary table	None	Summary of all the above outputs
Facility loss summary graphs	None	Loss curves for each category and the total loss for the facility

$ indicates United States dollars.

location) were compared for Hurricane Harvey and Hurricane Ike for various release locations.

In this paper, while the EFDC-SS model is applied to three release locations (1–3), the FEDERAP framework is applied to four facilities identified as A (west of Release Location 1) and B (Release Location 1), C (Release Location 2), and D (Release Location 3). The locations and characteristics of the 4 facilities are shown in **Figure 2** and **Table 3**, respectively. While Release Locations 1–3 from the EFDC-SS spill simulations were selected solely based on the probability of tank failure, the 4 identified facilities in the FEDERAP analysis were uniquely selected for their differing properties and to illustrate the rigor and range of possibilities for modeling damage associated with critical infrastructure. As mentioned earlier, the FEDERAP framework loops over the maximum WSE using a step of one unit. For Hurricane Ike, Kiaghadi et al. (2018) evaluated three scenarios included Hurricane Ike, Hurricane Ike worst-case scenario with regards to its landfall location by moving it to 150 miles southwest of its actual landfall location along the Texas coast, and Hurricane Ike worst landfall location scenario with a 30% increase in wind speed. The maximum modeled WSEs in the study area for the three scenarios ranged between 4.5 and 7.6 m (15—25 ft). Thus the FEDERAP framework was run within this range.

A sensitivity analysis with FEDERAP further illustrates the rigor of the developed framework in estimating upper and lower bounds for damages and losses on a facility basis or for a group of facilities or an entire region with different types of critical infrastructure. A sensivity analysis was conducted to illustrate the utility of FEDERAP and the developed loss estimation framework. The sensitivity analysis was performed on Facility A, with a relatively large area of 0.77 km^2 (191 acres) and an average elevation above 6 m. This facility has a number of tanks and process-units at various elevations and locations within the facility boundary (**Table 3**). The modeled losses for facility A ranged from $360 million to $3 billion and were non-linear relative to storm surge (referred to as the base case). Ten variables that affect cost estimates in FEDERAP were evaluated in the sensitivity analysis; each was varied between a lower (halved) and higher (doubled) value relative to the base run for Facility A. For example, the property value was varied between the range of half the base case value and double the base case value. Another example is the cost of cleanup of a release that was halved and doubled in the sensitivity analysis. The results sections include the results of EFDC-SS scenarios on both hydrodynamics and fate and transport of spills as well as FEDRAP model results.

RESULTS AND DISCUSSION

EFDC-SS Hydrodynamics

Total inundated areas at the peak of the event was slightly higher during Hurricane Harvey (63.35 km^2) compared to Hurricane Ike (59.72 km^2). Compared to Hurricane Ike, Hurricane Harvey flooded more areas in the northern parts of the model domain, as shown in **Figure 5**, presumably because of higher flows in the San Jacinto River (SJR, historical high flow rates as high as 10,000 m^3/s during Hurricane Harvey). In contrast, higher land inundation was observed within the southern parts of the domain and in shallow side bays during Hurricane Ike. The western parts of the model showed very similar inundation during both events. The different spatial distribution of inundated areas during different types of compound flooding events, emphasizes the need for considering all flooding sources (individually and in combination) in flood management. For instance, the results presented in Kiaghadi et al. (2018) shows that only focusing on storm surge (as is common practice for industrial corridors) could lead to underestimating the WSEs in northern parts of the system.

The bottom/land elevation as well as the water depth time-series at several originally dry locations (dry at mean sea level) of the study area during Hurricane Ike and Harvey were shown in **Figure 6**. Different flooding patterns, as shown in **Figure 6**, were observed during the two different hurricane types across the modeling domain. A rapid increase in water depth (**Figure 6**), across the domain, was observed during Hurricane Ike, which was a surge-dominated event, followed by a rapid recession of the inundation. The entire inundation duration

TABLE 3 | Facility characteristics for the modeled Case Study facilities in the HSC.

Facility Characteristic	Facility A	Facility B	Facility C	Facility D
Area (km^2)	0.77 (191 acres)	0.27 (66 acres)	7.09 (1752 acres)	4.01 (1008 acres)
Average Elevation (m)	6.1 (20 ft.)	5.5 (18 ft.)	7 (23 ft.)	6.4 (21 ft.)
Fixed top vertical tanks (#)	59	77	400	161
Floating top vertical tanks (#)	30	0	83	52
Horizontal Tanks (#)	22	18	17	7
Unit-Process (#)	15	5	25	34

 # indicates numbers.

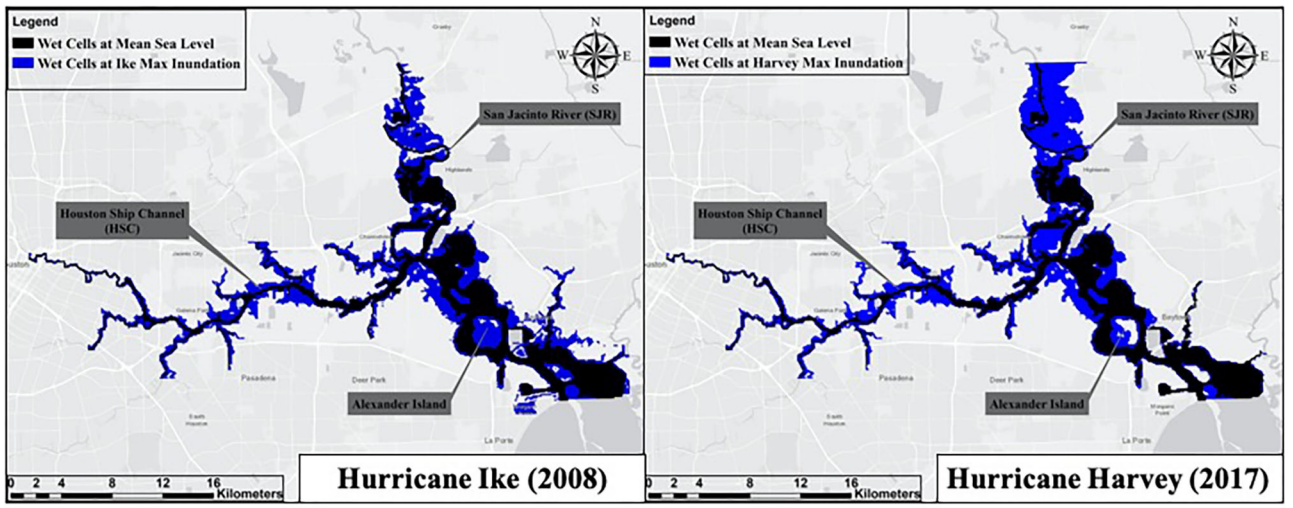

FIGURE 5 | Comparison of maximum inundated areas for Hurricane Ike (left) and Hurricane Harvey (right).

due to the storm surge (Hurricane Ike) was <24 h. However, due to the discharges emanating from the greater Houston bayous, a second peak in water depth and inundation pattern was observed during Hurricane Ike making the entire event last for 2.5 days everywhere except the SJR (4.5 days). Continuous water release from Lake Houston dam caused the elongated flood in areas adjacent to SJR (P3 in **Figure 6**). In the absence of a strong storm surge (about 0.6 m), the inundation process during Hurricane Harvey was driven by tidally forced in the downstream boundaries and local runoff in the flow boundaries (dominant). Considering that the travel time for most of the bayous in the study area is around 2–7 days (Petersen, 2006), Hurricane Harvey caused longer (between 5 and 6 days) and wider-spread land inundation compared to Hurricane Ike as shown in **Figure 6**. The peak water depth was almost the same for both hurricanes except areas closer to the downstream boundary of the model (P4 close to the mouth of Galveston Bay in **Figure 6**). Lower water depths and consequently lower inundation in the southern portion of the modeling domain during Hurricane Harvey compared to Ike is mainly due to the dictation of the downstream boundary condition. In other words, despite the high volume of water discharged to the system during Hurricane Harvey, the water surface elevation at the final water receptor was not significantly changed.

EFDC-SS Tank Failure and Pollutant Transport

The estimated probabilities of failure for the above-ground storage tanks within the study area during both modeled hurricanes are shown in **Figure 7**. Considering the aforementioned logic in the previous section and the fact that inundation was for a longer period of time during Harvey (**Figure 6**), a higher number of tanks with high probabilities of failure in the western part of the HSC during Hurricane Harvey (**Figure 7**) could be justified. In addition, tanks located adjacent to the rivers/bayous were more prone to failure during Harvey due to historic flow rates leading to overbanking (with higher depth compared to Ike) and flooding the tanks. For the southern part of the system (Release Location 3 in **Figure 7**), the probabilities were almost the same as the maximum WSEs in the two events were very close in that region. The tanks located north of Release Location 3 were in a higher elevation area (see **Figure 6**) so they did not become inundated during either of the two events.

As discussed in Kiaghadi et al. (2018), the release time relative to the peak of storm is a key parameter during an even like Hurricane Ike where the direction of the flow could change during the storm. However, the release time could not change the spread pattern (except the velocity) in a flow-dominated event

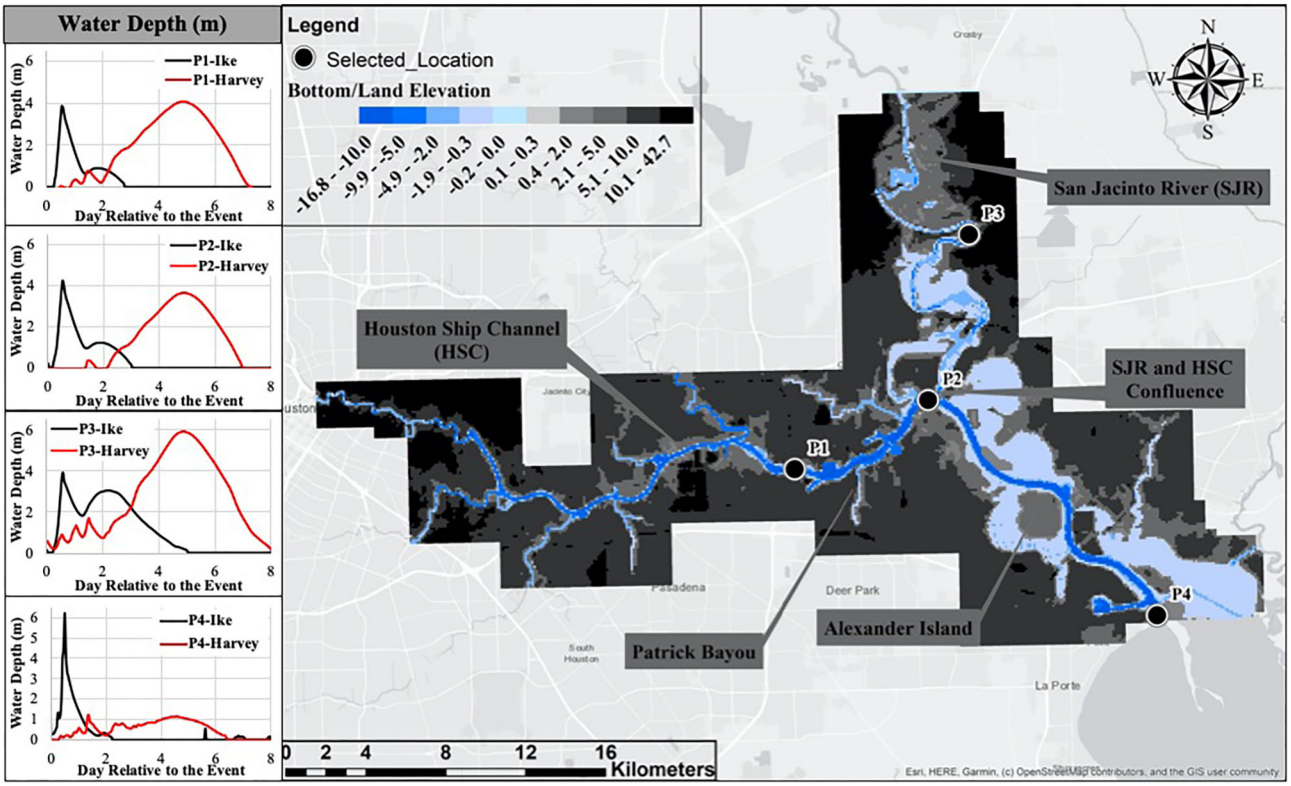

FIGURE 6 | Bottom/land elevation in the study area and water depth time-series at several originally dry (dry at mean sea level) locations of the study area during Hurricanes Ike and Harvey.

such as Hurricane Harvey that the flow has always the same direction during the event. The dye concentrations for a release at the peak of the hydrograph during Hurricane Harvey for all of three release locations, are shown in **Figure 8**. Unlike Hurricane Ike scenarios shown in Kiaghadi et al. (2018), the conservative tracer was not spread upstream of Release Location 1 during Hurricane Harvey. In contrast, detectable dye concentrations were observed in north of the HSC confluence with the SJR (see **Figure 6** for location) 1 week after the release (**Figure 8**). During Hurricane Harvey, dye concentrations 24 h after the release were lower than Ike. Also, 1 week after the release, dye concentrations were significantly lower within the system during Hurricane Harvey as compared to Ike, mainly due to continuous high flow rates. In other words, faster velocities during Harvey flooding (the results of the EFDS-SS simulations) caused the majority of the dye to pass through the boundary in a very short time and led to very low concentrations of dye remaining in the system after 1 week. For Release Location 2, Kiaghadi et al. (2018) showed that during Hurricane Ike a significant amount of dye mass remained in Patrick Bayou (Release Location 2, see **Figure 2** for location), due to trapping within the bayou, that acted as a continuous source of dye that polluted the western part of the HSC after a week. For the same location, different mass transport behavior was observed during Hurricane Harvey. Here again, faster water velocities during Harvey caused more flushing and transportation of the contaminants in the HSC. The spread of the spill at Release Location 3 was very similar during both hurricanes. Just like Release Location 1, for Release Location 3, no upstream spread was observed during Hurricane Harvey. However, after water levels were back to normal (when water surface elevations are back to the mean sea level), tidal movements transferred the remaining contaminants in the system to the upstream regions. With regards to contaminant transport to the final receptor (Galveston Bay), the two hurricanes showed different behaviors for Release Locations 1 and 2 but similar behavior for location 3.

The final percentage of the tracer dye (as a surrogate to the contaminant of interest) that reached Galveston Bay and the time for 85% of dye mass to reach Galveston Bay is shown in **Table 4**. The high percentage of mass within a low period of time reaching the final receptor indicates the risk of widespread contamination of a potential spill. In <3 days the majority of the modeled spill will reach the final receptor with larger water volume where dilution makes remediation efforts very difficult. In addition, in the first few days during the events (especially the rainfall-based events where the high flow rates last for more than a week), the priority is on saving lives; and, because of the presence of debris

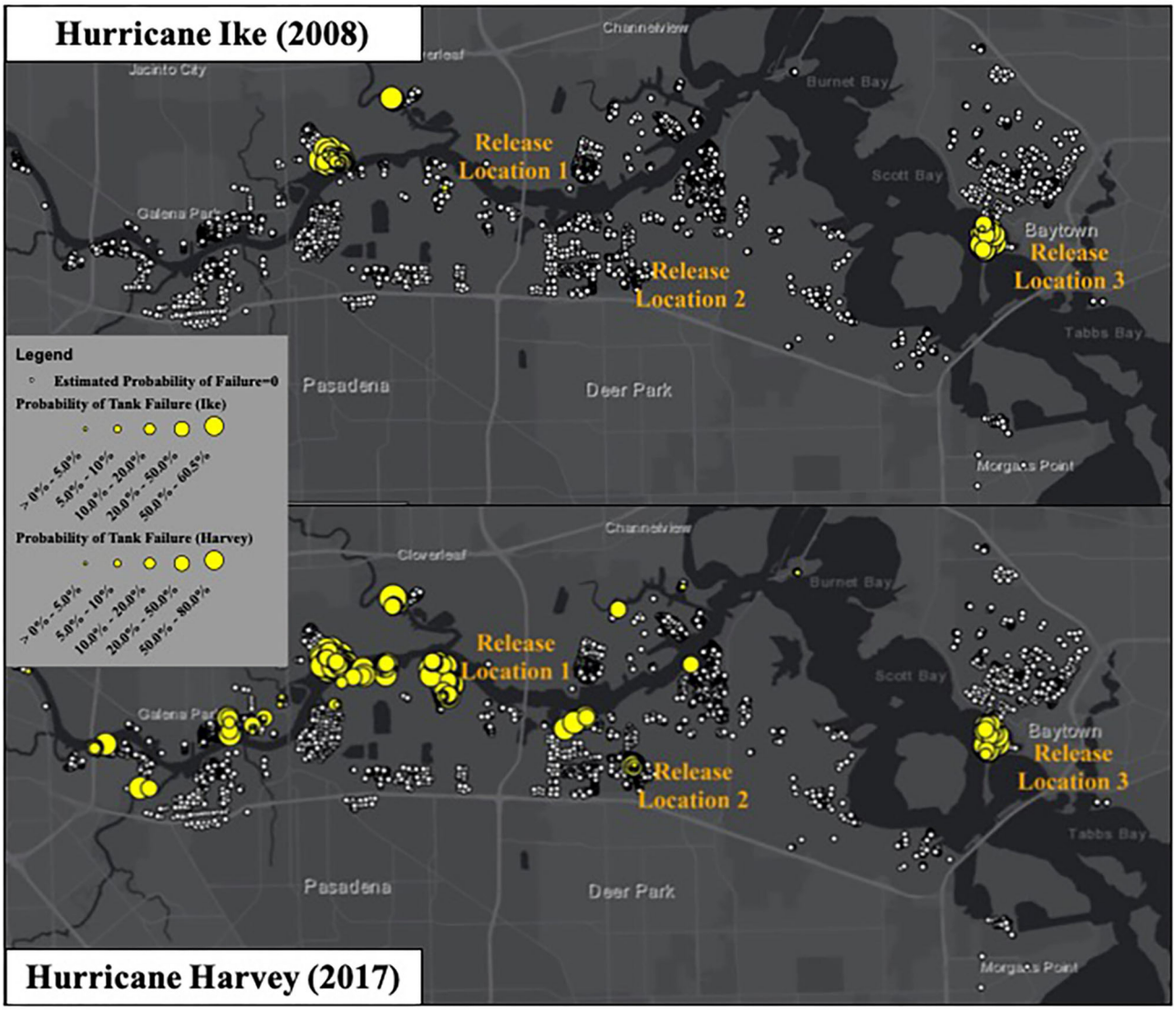

FIGURE 7 | Estimated probability of failure for the ~4300 above ground storage tanks in the study area for Hurricane Ike (top) and Hurricane Harvey (bottom). Due to the absence of industrial tanks, the northern section of the domain (San Jacinto River, SJR area) is not shown.

in the water, it is not possible to limit the spread or remove the contaminants from the water.

Lands that were affected by the spill from different locations during Hurricane Ike and Harvey are shown in **Figure 9**. The affected land is directly related to the flooding extent and whether there were any contaminants in the water that caused the inundation or passed through the wet cell during the inundation period. Compared to Harvey, surge driven spill scenarios caused by Ike created a smaller environmental footprint of the spill on land for Release Locations 1 and 2 and a larger footprint for location 3. A spill from Release Location 1 could potentially affect 8.65 and 9.52 km^2 of land, with almost 0.7 and 1% of the total spill mass retained on land during Hurricane Ike and Harvey, respectively. The contaminated lands for Release Locations 2 and 3 were 6.29 and 7.95 km^2 for Hurricane Ike and 9.36 and 2.75 km^2 for Hurricane Harvey. Downstream of the HSC-SJR confluence and upstream of Alexander Island were identified as the most polluted lands after Hurricane Harvey. Alexander Island (see **Figure 2** for the location) and upstream of the HSC mouth were the most affected areas for Hurricane Ike. It is noted again that this does not account for air plume formation and transport onto land from spills in the waterway that may represent a significant health risk to nearby populations. The retention of contaminants on land could pose a threat to both natural and built environment. Thus, the developed framework could be used to identify the locations that might need remediation and a guideline for sampling efforts after severe storms.

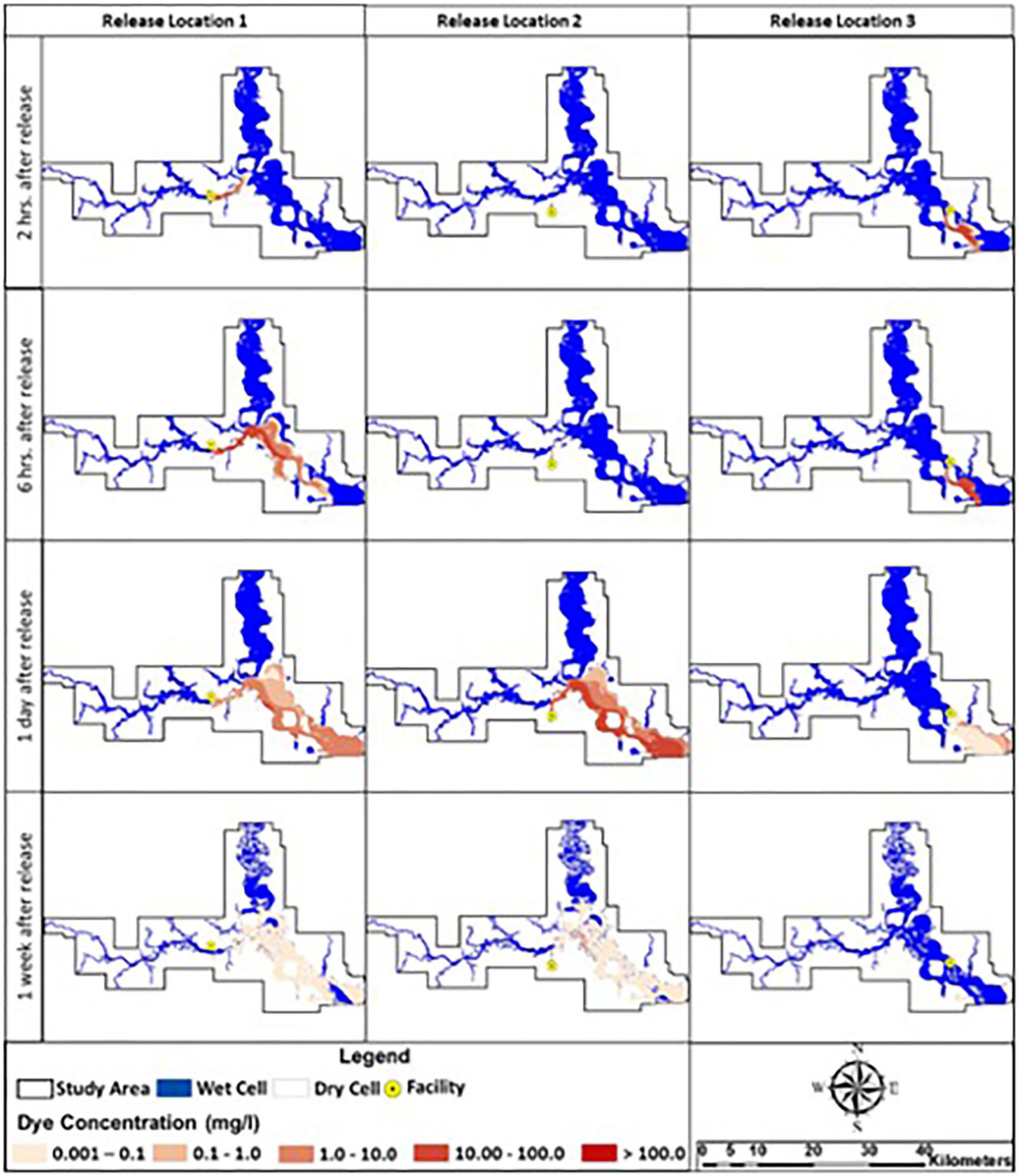

FIGURE 8 | Dye concentration for Hurricane Harvey at various times during and following the event for different release locations. Blue cells represent concentrations below 0.001 mg/l.

TABLE 4 | Results for the Ike and Harvey spill scenarios with their corresponding release times, final percentage of mass in GB, and time lapse for 85% of the dye mass leaving the model domain.

Scenario	Release time	Percent Mass in Bay ~15 days after dye release	Time (days) for 85% of dye mass to reach Galveston Bay
Ike-1	9/13/08 12:00	91.5	1.46
Ike-2	9/13/08 12:00	27.3	N/A
Ike-3	9/13/08 12:00	92.7	1.29
Harvey-1	8/23/17 00:00	>97.1*	0.95
Harvey-2	8/23/17 00:00	>96.1*	2.67
Harvey-3	8/23/17 00:00	>95.1*	1.29

*N/A, Not Applicable; the total dye passed through the open boundary was <85% of total dye released. *Dye simulation runs for Hurricane Harvey were performed for a shorter period of time after the reseals (1 week); values reported as greater than represent mass portion of mass transported to Galveston Bay 1 week after the spill.*

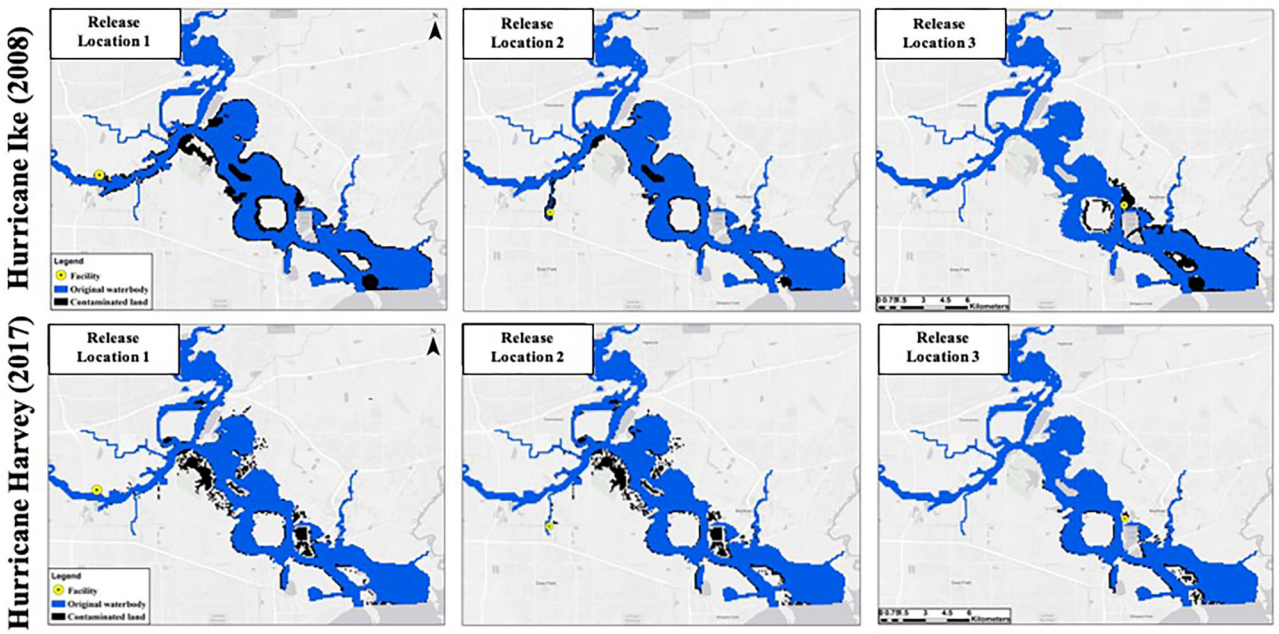

FIGURE 9 | Comparison of land affected by spills from different locations within the model domain for Hurricane Ike (top) and Hurricane Harvey (bottom).

FEDERAP Projected Losses

The total loss estimates for each of the facilities are shown in **Figure 10**. The total modeled losses ranged from $30 million to $500 million for WSEs between 4.5 and 5.2 m (15–17 ft) while the total losses ranged from $80 million to $7 billion for WSEs near 7.6 m (25 ft). As can be seen in **Figure 10**, Facilities A and B loss curves are similar and distinctly different from C and D. While loss curves for A and B increase gradually and exhibit separation between the three scenarios shown (low, medium, and high), the loss curves for facilities C and D are almost superimposed up to WSEs around 5.8 m. Beyond this WSE, facilities C and D exhibit distinctly different losses that reflect the difference in facility characteristics (area, elevation, tanks, and unit-processes). Facility C has a larger area (but more of the area is at a higher elevation) and more tanks, whereas facility D has a lower average elevation and more process units. Thus, and as can be seen in **Figure 10**, the loss curves increase steadily for facility C beyond WSEs of 5.8 (19 ft) m whereas facility D experiences an exponential rise in losses between 6.4 (21 ft) and 7 (23 ft) m that stabilize beyond 7 m. It is noted that Facility B has a relatively smaller area and a smaller number of tanks and process units which explains the difference in the relative magnitude of losses when compared to the other facilities. It is also noted that facility D is the only facility that did not exhibit any sensitivity to the high, medium and low cost scenarios for inundation levels below 6.4 m (21 ft). This is because the facility is located at a relatively higher base elevation than the other facilities, similar to facility C, but unlike facility C; facility D has a relatively lower number of tanks.

The individual components of the total losses for each facility can be studied further to determine the main driver for losses as WSE increases. As discussed above in the Methods, economic loss variables had low and high values estimates as well as a calculated average value. For modeled high losses estimates, for

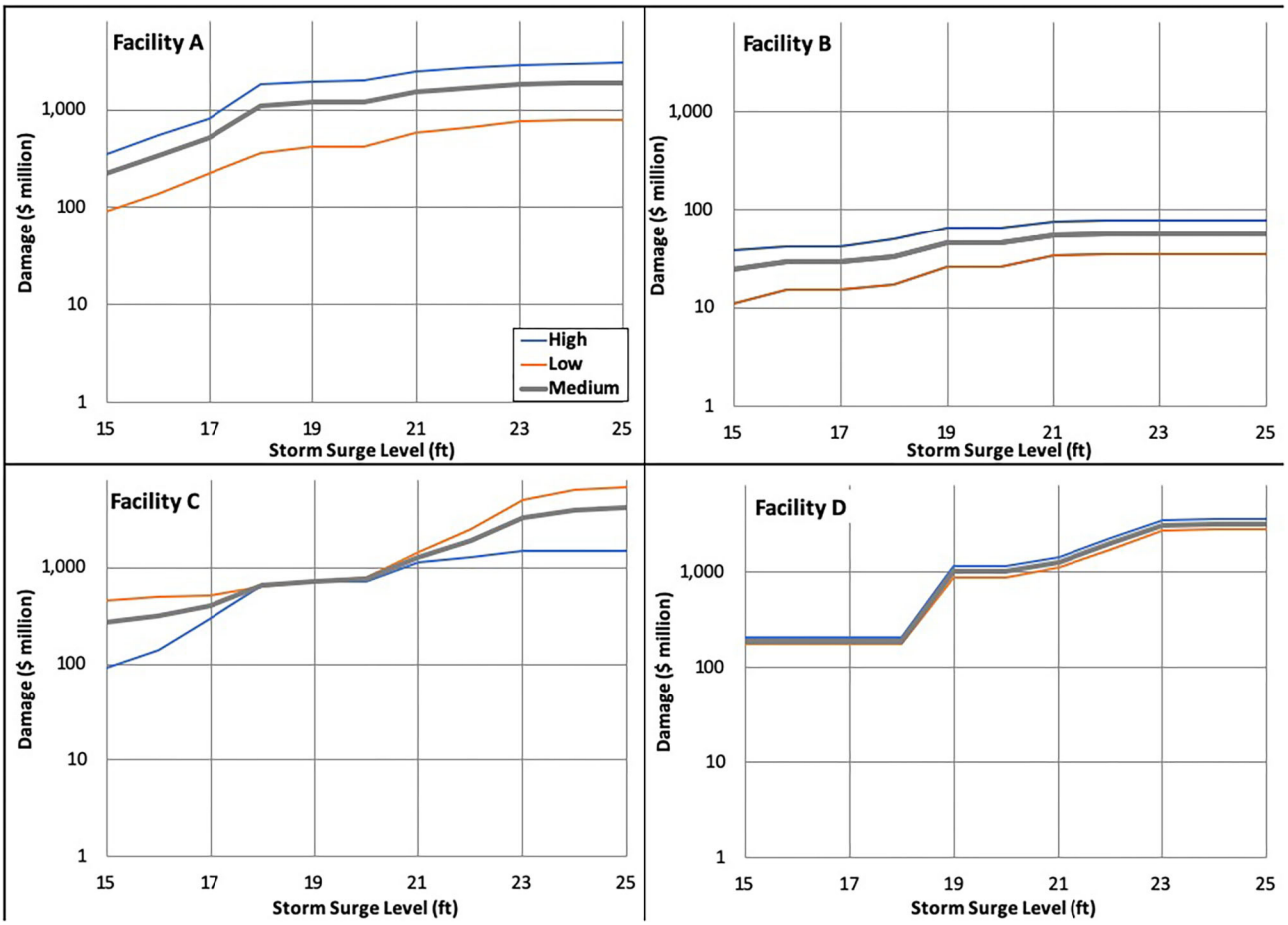

FIGURE 10 | FEDERAP projected losses for 3 scenarios of cost models (blue line: higher estimate, gray line: medium estimate, red line: lower estimate).

example, as inundation increases, the downtime causes losses to rise significantly. For three of the four facilities, production loss was the most important driver for losses in the modeled scenarios (data not shown). This finding would likely change based on the specific event, its impacts, and variables used in the model. Additionally, probabilistic modeling using the developed economic modeling will further inform analyses for individual facilities or an industrial complex such as the Houston Ship Channel. For Facilities A and C, environmental release plays a significant role due to the number of tanks on site and the locations of the tanks. For Facility C in particular, environmental release is the largest component for losses. Facility C exhibits relatively high tank density (more than one tank per acre) and the resulting losses for this facility are due to the large number of tanks at low elevations (the majority of the facility and its unit-processes are not inundated even at high storm surge levels of ∼7 m). The results from the analysis with the four facilities can be synthesized to allow general conclusions to be made for the entire HSC industrial region and beyond. For instance, when comparing across the 4 facilities, it was found that losses are at their lowest when the facility is <20% inundated and their highest once inundation exceeds 75% as would be expected. The results on a spatial basis were somewhat less intuitive, however. For facilities to the east near the mouth of the HSC, the initial response to storm surge level rise is minimal but begins a step increase at ∼6 m (Facilities C and D). The two facilities investigated on the western portion of the study area have a more gradual loss curve to storm surge with increases occurring at 5.2 and 6 m. Thus, having an understanding of the relationship between facility elevations, storm surge levels, and expected losses (in addition to impacted infrastructure) is critical and can only be gleaned with the modeling framework presented here. Such an understanding, when developed, enables decision-makers to evaluate various mitigation strategies based on vulnerability, hazard, and risk within a projected losses framework.

The data in **Figure 11** illustrate sensitivity analysis results for Facility A. The modeled losses for Facility A ranged from $360 million to $3 billion and were non-linear relative to storm surge levels (**Figure 11** base run). The results of the sensitivity analysis for a surge level of between 4.6 m (15 ft) and 7.6 m (25 ft) ranged from $280 million to $4.2 billion indicating a high degree of sensitivity in modeling results to the assumed cost relationships. Results also indicated that damage

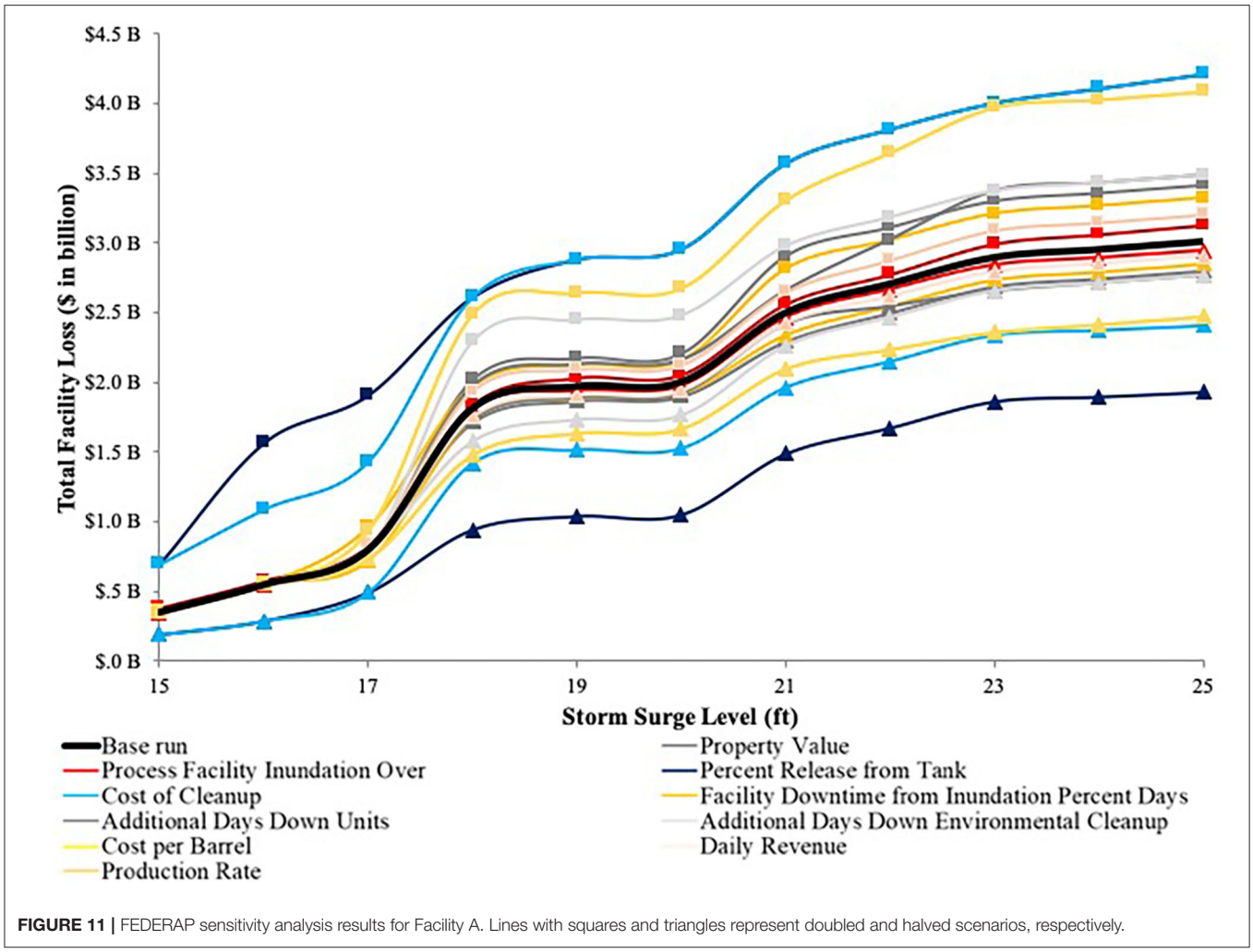

FIGURE 11 | FEDERAP sensitivity analysis results for Facility A. Lines with squares and triangles represent doubled and halved scenarios, respectively.

estimates were most sensitive to environmental losses (cleanup cost and additional days down). At the lower modeled storm surge levels, FEDERAP damage estimates did not change in response to changes in most inputs except for percent tank release and cleanup costs. For these two variables, damage estimates increased more than 40% as the storm surge level increased from 4.6 m (15 ft) to 5.5 m (18 ft). When the storm surge level exceeds 5.5 m (18 ft), more of the facility infrastructure becomes inundated causing higher dependency on values used for production losses. Overall, the loss model had limited sensitivity to daily revenue, property value, and losses related to unit-processes with the major driver being productivity and environmental (spill) losses. The interplay between facility characteristics and the modeled cost relationships and their effect on total losses highlights the need for tools such as FEDERAP and the importance of integrating this type of analysis into decision-making for addressing vulnerability of critical industrial infrastructure.

It is important to acknowledge the limitations of the FEDERAP model in its current formulation. While chemical spills are included in FEDERAP, the interaction among stored chemicals within and between facilities in the water is not presently accounted for. The storm surge level is considered but the period of time where storm surge is present within the HSC is not accounted for in terms of pollutant dispersion within the inundated zones; longer storm surge durations are expected to push pollutants farther upstream and disperse them onto a larger area. The length of time and interaction among stored chemicals may need to be investigated using water quality and contaminant transport models in order to refine the cleanup losses determined in the FEDERAP framework. In addition, a facility may be operational but in reality may be prohibited from operating normally due to damages in nearby facilities and/or debris in the Channel or continued emergency response and cleanup activities. Lastly, this analysis is not probabilistic in nature and does not include risk (the risk of incurring a specific storm surge level); however, the model can be readily adapted to incorporate risk and probability when data on hurricane risks are developed in the future.

CONCLUSIONS

The results from the water quality model driven by storm surge (EFDC-SS) model containing both land and waterbodies showed the different mechanisms of spill spread under different hurricane types. While spreading differently, spills during a severe hydrologic event can widely spread miles away from the release location in a very short period of time and pollute both land and water in addition to the airshed. The developed framework could be applied to investigate the fate and transport of spills during compound flooding events. While damage assessments to date have failed to account for the complexities of industrial facility vulnerabilities to hurricanes and severe storm surge events, the Facility Economic Damage and Environmental Release Planning (FEDERAP) provides a modeling framework that allows for investigating the complex relationships between storm surge level and the specific losses that would be experienced by a specific facility or an entire industrial region. This research demonstrates that industrial regions should be evaluated using tools that reflect their specificity. In addition, this paper demonstrates that property loss is a relatively small component when compared to other losses that could be incurred due to storage tank damage or damage to process units. This research also demonstrates that storm surge levels are directly related to incurred damages and losses at industrial facilities and that storm surge above a facility specific threshold value would cause losses to increase at a steeper slope because of environmental pollution and loss of productivity. Without detailed studies and model scenarios similar to what is presented in this study, it would be very difficult to anticipate areas (and communities), whether on land or in water, that would be most vulnerable to contamination in a given medium (air, soil, water, biota). The methodology developed in this study can be easily applied to similar severe storms prone coastal plain estuaries such as the Hudson River in New York, Delaware Bay between New Jersey and Delaware, and other estuaries along the Gulf Coast. Future work could address some of the limitations of the study and expand on its capabilities. For instance, dynamic coupling of SWAN + ADCIRC with the EFDC, FEDERAP, and the tank failure model could provide a near real-time predictive and planning tool.

DATA AVAILABILITY STATEMENT

The original contributions presented in the study are included in the article/supplementary material further inquiries can be directed to the corresponding authors.

AUTHOR CONTRIBUTIONS

HR, AK, and DB brainstormed the research ideas and contributed in writing the manuscript equally. DB and AK did the majority of analyses under HR supervision. All authors contributed to the article and approved the submitted version.

FUNDING

The National Science Foundation award #1759440 provided funding for this research. Additional funding was received from the Hurricane Resilience Research Institute, the Severe Storm Prediction, Evaluation, and Evacuation from Disaster Center, the Texas Commission on Environmental Quality, and the US EPA. DSI, LLC is acknowledged for granting a license for use of the EFDC model and its interfaces to develop EFDC-SS. Their support is gratefully acknowledged.

REFERENCES

Ashley, N. A., Valsaraj, K. T., and Thibodeaux, L. J. (2008). Elevated in-home sediment contaminant concentrations—The consequence of a particle settling–winnowing process from Hurricane Katrina floodwaters. *Chemosphere* 70, 833–840. doi: 10.1016/j.chemosphere.2007.07.010

Bailey, J. R., and Levitan, M. L. (2008). Lessons learned and mitigation options for hurricanes. *Process Safety Prog.* 27, 41–47. doi: 10.1002/prs.10218

Bilskie, M. V., Hagen, S. C., Alizad, K., Medeiros, S. C., Passeri, D. L., Needham, H. F., et al. (2016). Dynamic simulation and numerical analysis of hurricane storm surge under sea level rise with geomorphologic changes along the northern Gulf of Mexico. *Earth's Futur.* 4, 177–193. doi: 10.1002/2015EF000347

Burleson, D. W., Rifai, H. S., Proft, J. K., Dawson., C. N., and Bedient, P. B. (2015). Case study: vulnerability of an industrial corridor in texas to storm surge. *Nat. Hazard.* 77, 1183–1203. doi: 10.1007/s11069-015-1652-7

Cauffman, S. A., Phan, L. T., Sadek, F., Fritz, W. P., Duthinh, D., and Rossiter, W. J. (2006). "Performance of physical structures in hurricane katrina and hurricane rita: a reconnaissance report (NIST TN 1476)," in *National Institute of Standards and Technology*, 222. Availale online at: http://fire.nist.gov/bfrlpubs/build06/art016.html (accessed 24 November, 2014).

Chang, N.-B., Wei, Y. L., Tseng, C. C., and Kao, C. Y. J. (1997). The design of a GIS-based decision support system for chemical emergency preparedness and response in an urban environment. *Comput. Environ. Urban Syst.* 21, 67–94. doi: 10.1016/S0198-9715(97)01009-0

Cruz, A., and Krausmann, E. (2013). Vulnerability of the oil and gas sector to climate change and extreme weather events. *Clim. Change* 121, 41–53. doi: 10.1007/s10584-013-0891-4

Cruz, A. M., Steinberg, L. J., and Luna, R. (2001). Identifying hurricane-induced hazardous material release scenarios in a petroleum refinery. *Nat. Hazard Rev.* 2, 203–210. doi: 10.1061/(ASCE)1527-6988(2001)2:4(203)

Eggleston, K. (2014). "Valero refinery expansions pushed forward by eagle ford production growth—$730 Million," in *Eagle Ford Shale*. Available online at: http://eaglefordshale.com/pipeline-midstream-news/valero-refinery-expansions-pushed-forward-by-eagle-ford-production-growth/ (accessed 16 Febuary, 2015).

Eldrandaly, K. A., and AbdelAziz, N. M. (2012). Enhancing ArcGIS decision making capabilities using an intelligent multicriteria decision analysis toolbox. *J. Environ. Inform.* 20, 44–57. doi: 10.3808/jei.201200219

Etkin, D. S. (2000). "Worldwide analysis of oil spill cleanup cost factors," in *Procceding 23rd Arctic and Marine Oilspill Program Tech. Sem*, 161–174.

Frazier, T. G., Wood, N., Yarnal, B., and Bauer, D. H. (2010). Influence of potential sea level rise on societal vulnerability to hurricane storm-surge hazards, Sarasota County, Florida. *Appl. Geograph.* 30, 490–505. doi: 10.1016/j.apgeog.2010.05.005

Freund, A., Zuckerman, N., Luo, H., Hsu, H.-H., and Lucchini, R. (2014). Diesel and silica monitoring at two sites following hurricane sandy. *J. Occup. Environ. Hyg.*11, D131–D143. doi: 10.1080/15459624.2014.904518

Godoy, L. A. (2007). Performance of storage tanks in oil facilities damaged by Hurricanes Katrina and Rita. *J. Perform. Constr. Facil.* 21, 441–449. doi: 10.1061/(ASCE)0887-3828(2007)21:6(441)

Godoy, L. A. (2009). "Hurricane failures of tanks for the oil industry," in *Proceedings from International Association for Shell and Spatial Structures (IASS) Symposium, Valencia, Spain, 28 September−2 October* 2009, 114–126.

Hallegatte, S., Ranger, N., Mestre, O., Dumas, P., Corfee-Morlot, J., Herweijer, C., et al. (2011). Assessing climate change impacts, sea level rise and storm surge risk in port cities: a case study on Copenhagen. *Clim. Change* 104, 113–137. doi: 10.1007/s10584-010-9978-3

Hamrick, J. M. (1992). *A Three-Dimensional Environmental Fluid Dynamics Computer Code: Theoretical and Computational Aspects. Special Report in Applied Marine Science and Ocean Engineering; no. 317*. Virginia Institute of Marine Science, William & Mary. doi: 10.21220/V5TT6C

Harris, S. P., and Wilson D. O. (2008). Mitigating Hurricane storm surge perils at the DeLisle Plant. *Process Saf. Prog.* 27, 177–184. doi: 10.1002/prs.10226

Hoobler, B. M., Vance, G. F., Hamerlinck, J. D., Munn, L. C., and Hayward, J. A. (2003). Applications of land evaluation and site assessment (LESA) and a geographic information system (GIS) in East Park County, Wyoming. *J. Soil Water Conserv.* 58, 105–112. Available online at: https://www.jswconline.org/content/58/2/105/tab-article-info

Hope, M. E., Westerink, J. J., Kennedy, A. B., Kerr, P. C., Dietrich, J. C., Dawson, C., et al. (2013). Hindcast and validation of Hurricane Ike (2008) waves, forerunner, and storm surge. *J. Geophys. Res. Ocean.* 118, 4424–4460. doi: 10.1002/jgrc.20314

Huang, Z., Rosowsky, D. V., and Sparks, P. R. (2001). Long-term hurricane risk assessment and expected damage to residential structures. *Reliabil. Eng. Syst. Saf.* 74, 239–249. doi: 10.1016/S0951-8320(01)00086-2

Kameshwar, S., and Padgett, J. E. (2015). "Fragility assessment of above ground petroleum storage tanks under storm surge," in *2th International Conference on Applications of Statistics and Probability in Civil Engineering*. Vancouver, Canada.

Khan, F. I., Husain, T., and Abbasi, S. A. (2001). "Safety weighted hazard index (SWeHI)—a new, user-friendly tool for swift yet comprehensive hazard identification and safety evaluation in chemical process industries. *Process Saf. Environ. Protect.* 79, 65–80. doi: 10.1205/09575820151095157

Kiaghadi, A., Govindarajan, A., Sobel, R. S., and Rifai, H. S. (2020). Environmental damage associated with severe hydrologic events: a LiDAR-based geospatial modeling approach. *Nat. Hazards* 20:4099. doi: 10.1007/s11069-020-04099-1

Kiaghadi, A., and Rifai, H. S. (2019). Chemical, and microbial quality of floodwaters in Houston following Hurricane Harvey. *Environ. Sci. Technol.* 53, 4832–4840. doi: 10.1021/acs.est.9b00792

Kiaghadi, A., Rifai, H. S., and Burleson, D. W. (2018). Development of a storm surge driven water quality model to simulate spills during hurricanes. *Mar. Pollut. Bull.* 129, 714–728. doi: 10.1016/j.marpolbul.2017.10.063

Kim, M., Miller-Hooks, E., and Nair, R. (2011). A Geographic information system-based real-time decision support framework for routing vehicles carrying hazardous materials. *J. Intell. Transport. Syst.*15, 28–41. doi: 10.1080/15472450.2011.544584

Kumbier, K., Carvalho, R. C., Vafeidis, A. T., Woodroffe, C. D., and Carvalho, R. C. (2018). Investigating compound flooding in an estuary using hydrodynamic modelling: a case study from the Shoalhaven River, Australia. *Hazards Earth Syst. Sci.* 18, 463–477. doi: 10.5194/nhess-18-463-2018

Liao, Z. L., Xu, Z. X., Li, Y. X., Wang, D. B., and Borrebach, M. J. (2011). GIS development for environmental hazard management based on gridding management. *J. Environ. Inform.* 17, 83–90. doi: 10.3808/jei.201100190

Loveland, M., Kiaghadi, A., Dawson, C. N., Rifai, H. S., Misra, S., Mosser, H., et al. (2021). Developing a modeling framework to simulate compound flooding: when storm surge interacts with riverine flow. *Front. Clim.* 2:609610. doi: 10.3389/fclim.2020.609610

Mamauag, S. S., Alino, P. M., Martinez, R. J. S., Muallil, R. N., Doctor, M. V. A., Dizon, E. C., Cabral, R. B. (2013). A framework for vulnerability assessment of coastal fisheries ecosystems to climate change—Tool for understanding resilience of fisheries (VA–TURF). *Fish. Res.* 147, 381–393. doi: 10.1016/j.fishres.2013.07.007

Moftakhari, H. R., Salvadori, G., AghaKouchak, A., Sanders, B. F., and Matthew, R. A. (2017). Compounding effects of sea level rise and fluvial flooding. *Proc. Natl. Acad. Sci. U.S.A.* 114, 9785–9790. doi: 10.1073/pnas.1620325114

Naito, C., Cox, D., Yu, Q., and Brooker, H. (2012). Fuel Storage container performance during the 2011 Tohoku, Japan, Tsunami. *J. Perform. Constr. Facil.* 27, 373–380. doi: 10.1061/(ASCE)CF.1943-5509.0000339

NCDC. (2020). *Billion-Dollar Weather and Climate Disasters. NOAA's National Climatic Data Center*. Available online at: https://www.ncdc.noaa.gov/billions/events (accessed May 17, 2020).

Needham, H. F., and Keim, B. D. (2012). A storm surge database for the US Gulf Coast. *Int. J. Climatol.* 32, 2108–2123. doi: 10.1002/joc.2425

Petersen, T. M. (2006). *Spatial and Temporal Modeling of Escherichia Coli Sources and Load Allocations in an Urban, Watershed Ph. D. Dissertation Civil, and Environmental Engineering*. Houston,Texas: University of Houston.

Pine, J. (2006). Hurricane Katrina and oil spills: Impacts on coastal and ocean environment. *Oceanography.* 19, 37–39. doi: 10.5670/oceanog.2006.61

Qi, H., and Altinakar, M. S. (2011). A GIS-based decision support system for integrated flood management under uncertainty with two dimensional numerical simulations. *Environ. Modelli. Softw.* 26, 817–821. doi: 10.1016/j.envsoft.2010.11.006

Reible, D., Haas, C., Pardue, J., and Walsh, W. (2006). Toxic and contaminant concerns generated by Hurricane Katrina. *J. Environ. Eng.* 132, 565–566. doi: 10.1061/(ASCE)0733-9372(2006)132:6(565)

Robertson, I., Riggs, H., Yim, S., and Young, Y. (2007). Lessons from Hurricane Katrina Storm Surge on Bridges and Buildings. *J. Waterway Port Coast. Ocean Eng.* 133, 463–483. doi: 10.1061/(ASCE)0733-950X(2007)133:6(463)

Santella, N., Steinberg, L. J., and Sengul, H. (2010). Petroleum and hazardous material releases from industrial facilities associated with hurricane Katrina. *Risk Anal.* 30, 635–649. doi: 10.1111/j.1539-6924.2010.01390.x

Santiago-Collazo, F. L., Bilskie, M. V., and Hagen, S. C. (2019). A comprehensive review of compound inundation models in low-gradient coastal watersheds. *Environ. Model. Softw.* 119, 166–181. doi: 10.1016/j.envsoft.2019.06.002

Srinivas, H., and Nakagawa, Y. (2008). Environmental implications for disaster preparedness: lessons learnt from the Indian Ocean Tsunami. *J. Environ. Manage.* 89, 4–13. doi: 10.1016/j.jenvman.2007.01.054

Verter, V., and Kara, B. Y. (2001). A GIS-Based framework for hazardous materials transport risk assessment. *Risk Anal. Int. J.* 21, 1109–1120. doi: 10.1111/0272-4332.216179

Vickery, P. J., Lin, J., Skerlj, P. F., and Twisdale,. L. A., Huangx,' K. (2006). HAZUS-MH Hurricane Model Methodology. II: damage and loss estimation. *Nat. Hazards Rev.* 7, 94–103. doi: 10.1061/(ASCE)1527-6988(2006)7:2(94)

Yang, Z., Lindell, M. K., and Prater, C. S. (2009). Vulnerability of community businesses to environmental disasters. *Disasters* 33, 38–57. doi: 10.1111/j.1467-7717.2008.01061.x

Zhang, Y. J., Ye, F., Yu, H., Sun, W., and Moghimi, S., Myers, E., et al. (2019). Simulating compound flooding events in a hurricane. *Ocean Dyn.* 70, 621–640. doi: 10.1007/s10236-020-01351-x

Zografos, K. G., Vasilakis, G. M., and Giannouli, I. M. (2000). Methodological framework for developing decision support systems (DSS) for hazardous materials emergency response operations. *J. Hazard. Mater.* 71, 503–521. doi: 10.1016/S0304-3894(99)00096-5

Conflict of Interest: The authors declare that the research was conducted in the absence of any commercial or financial relationships that could be construed as a potential conflict of interest.

Publisher's Note: All claims expressed in this article are solely those of the authors and do not necessarily represent those of their affiliated organizations, or those of the publisher, the editors and the reviewers. Any product that may be evaluated in this article, or claim that may be made by its manufacturer, is not guaranteed or endorsed by the publisher.

frontiers in Climate

ORIGINAL RESEARCH
published: 31 August 2021
doi: 10.3389/fclim.2021.610062

Skew Surge and Storm Tides of Tropical Cyclones in the Delaware and Chesapeake Bays for 1980–2019

John A. Callahan[1]*, *Daniel J. Leathers*[2] and *Christina L. Callahan*[2]

[1] Delaware Geological Survey, Department of Geography and Spatial Sciences, University of Delaware, Newark, DE, United States, [2] Department of Geography and Spatial Sciences, Center for Environmental Monitoring and Analysis, University of Delaware, Newark, DE, United States

Coastal flooding poses the greatest threat to human life and is often the most common source of damage from coastal storms. From 1980 to 2020, the top 6, and 17 of the top 25, costliest natural disasters in the U.S. were caused by coastal storms, most of these tropical systems. The Delaware and Chesapeake Bays, two of the largest and most densely populated estuaries in the U.S. located in the Mid-Atlantic coastal region, have been significantly impacted by strong tropical cyclones in recent decades, notably Hurricanes Isabel (2003), Irene (2011), and Sandy (2012). Current scenarios of future climate project an increase in major hurricanes and the continued rise of sea levels, amplifying coastal flooding threat. We look at all North Atlantic tropical cyclones (TC) in the International Best Track Archive for Climate Stewardship (IBTrACS) database that came within 750 km of the Delmarva Peninsula from 1980 to 2019. For each TC, skew surge and storm tide are computed at 12 NOAA tide gauges throughout the two bays. Spatial variability of the detrended and normalized skew surge is investigated through cross-correlations, regional storm rankings, and comparison to storm tracks. We find Hurricanes Sandy (2012) and Isabel (2003) had the largest surge impact on the Delaware and Chesapeake Bay, respectively. Surge response to TCs in upper and lower bay regions are more similar across bays than to the opposing region in their own bay. TCs that impacted lower bay more than upper bay regions tended to stay offshore east of Delmarva, whereas TCs that impacted upper bay regions tended to stay to the west of Delmarva. Although tropical cyclones are multi-hazard weather events, there continues to be a need to improve storm surge forecasting and implement strategies to minimize the damage of coastal flooding. Results from this analysis can provide insight on the potential regional impacts of coastal flooding from tropical cyclones in the Mid-Atlantic.

Keywords: tropical cyclone, hurricane, Mid-Atlantic, storm surge, coastal flooding, tidal analysis, natural hazard, coastal risk

OPEN ACCESS

Edited by:
Valentina Prigiobbe, Stevens Institute of Technology, United States

Reviewed by:
Jase Bernhardt, Hofstra University, United States
James Booth, City College of New York (CUNY), United States

***Correspondence:**
John A. Callahan
john.callahan@udel.edu

Specialty section:
This article was submitted to Climate Risk Management, a section of the journal Frontiers in Climate

Received: *24 September 2020*
Accepted: *12 July 2021*
Published: *31 August 2021*

Citation:
Callahan JA, Leathers DJ and Callahan CL (2021) Skew Surge and Storm Tides of Tropical Cyclones in the Delaware and Chesapeake Bays for 1980–2019. Front. Clim. 3:610062. doi: 10.3389/fclim.2021.610062

INTRODUCTION

Coastal storms are a multi-threat natural hazard, often including heavy rain, strong winds, large waves, rip currents, and storm surge, all of which must be considered collectively when assessing risk and devising mitigation strategies. According to the National Oceanic and Atmospheric Administration (NOAA), for the years 1980 – 2019, 17 of the top 25 costliest natural disasters

in the US were caused by tropical cyclones (TCs) (NOAA National Centers for Environmental Information, 2020). Coastal flooding, primarily from storm surge and waves, from these storms poses the greatest threat to human life and is often the source of much of the damage (Blake and Gibney, 2011; Rappaport, 2014; Chippy and Jawahar, 2018; Weinkle et al., 2018).

Two of the largest estuaries in the United States, the Delaware and Chesapeake Bays, have been significantly impacted by strong TCs in recent decades, notably Hurricanes Sandy (2012), Irene (2011), and Isabel (2003). These two estuaries, located in the Mid-Atlantic coastal region, house ∼27 million inhabitants, a high density of metropolitan areas, transportation networks, industrial ports, and currently are under active development (Sanchez et al., 2012; Chesapeake Bay Program, 2020). Alongside large investments in public and private infrastructure, the region also hosts numerous critical natural ecosystems, saltmarshes and freshwater wetlands, agricultural fields, and forested lands threatened by degradation and erosion. Coastal flooding has been deemed an important natural hazard in this region (Boesch et al., 2018; Delaware Emergency Management Agency, 2018) and can have a tremendous economic impact on current and future waterfront areas (Li et al., 2020).

Impacts from coastal flooding are highly dependent upon both the natural and social vulnerability of a location (i.e., it is hyper-local), as well as the human response to implement adaptation measures (e.g., dune/berm systems, shoreline hardening), and therefore can vary drastically over short distances. The wide diversity of land use and vulnerable communities make it difficult to plan for this region as a whole. It is critical that we understand the severity and geographic variability of storm surge to properly assess the risk, aid in preparedness, and ultimately reduce the severe impacts from coastal flooding (Council on Climate Preparedness Resilience, 2016).

Water levels in the Delaware and Chesapeake Bays have been well-monitored by tide-gauge networks for several decades, particularly at NOAA National Water Level Observation Network (NWLON) sites operated through the Physical Oceanographic Real-Time System (PORTS) for each bay. Although this is primarily due to the importance of marine navigation and public safety, many of these gauges are particularly high quality, have very long records, and have been well-cited for monitoring sea-level rise and climate studies (Holgate et al., 2013; Sweet et al., 2017a; NOAA National Ocean Service National Water Level Observation Network, 2020; NOAA National Ocean Service Physical Oceanographic Real-Time System, 2020). Relative sea-level rise (SLR) (Sallenger et al., 2012; Kopp, 2013; Boon et al., 2018) and high-tide flooding (Sweet et al., 2014, 2020) rates in the region have increased in recent decades as compared to the early-mid twentieth century and are expected to continue increasing into the near future (Callahan et al., 2017; Sweet et al., 2017a; Boesch et al., 2018). Increases in sea levels lead directly to higher probabilities of coastal flood events (Rahmstorf, 2017; Sweet et al., 2017b).

The Mid-Atlantic region lies in a climatic transition zone, between continental and marine climate types, split in the Fourth National Climate Assessment (Jay et al., 2018) between the Northeast (Delaware Bay and upper Chesapeake Bay) and the Southeast (lower Chesapeake Bay) Regions. Mid-Atlantic weather is often dictated by the relative position of the westerly polar jet stream (often times directly above in the winter), flanked by baroclinic instability from warm ocean waters to the east and atmospheric uplift along the Appalachian front to the west (Leathers et al., 1998; Strobach et al., 2018). Coastal flooding is observed year-round from East Coast winter storms (Hirsch et al., 2001), surface high pressure systems (spring to fall) and tropical systems (summer to fall), with a higher percentage of TC-caused extreme flood events in the southern portions of the region (Booth et al., 2016). Although the Mid-Atlantic has been impacted by tropical systems less frequently than some other portions of the U.S., recent tropical cyclones and their associated storm surge and river flooding have caused damages in excess of $80 billion (Smith and Katz, 2013), hundreds of injuries, and loss of life across this heavily populated and economically sensitive region of the country.

Several climatologies of tropical weather systems and their impacts have been completed for the Atlantic and Gulf coast regions of the U.S. (i.e., Simpson and Lawrence, 1971; Landsea and Franklin, 2013; Elsner and Kara, 1999; Muller and Stone, 2001; Xie et al., 2005; Keim et al., 2007; McAdie et al., 2009). Results from these studies (Keim et al., 2007) indicate that the Mid-Atlantic experiences return periods of 4–10 years for any tropical cyclone (including tropical storms and hurricanes), 35–100 years for hurricanes of any strength, and >100 years for Category 3 and above hurricanes. These return periods are significantly longer than other areas along the Atlantic and Gulf coasts of the U.S., due mainly to the inland position of the Mid-Atlantic coastline.

In additions to sea levels, sea-surface temperatures (SSTs) in the equatorial and North Atlantic are also expected to increase under future global warming scenarios, leading to an increase in the number of severe tropical cyclones (Kossin et al., 2017; Knutson et al., 2020). Recent research has also shown trends in tropical cyclone location moving northward, increases in rapid intensification and surface wind speeds, and decrease in translational speed (Kossin, 2018; Knutson et al., 2019; Murakami et al., 2020; Yang et al., 2020). All of these suggest the extreme importance to understand current and past coastal flooding due to TCs.

Numerous studies have utilized storm surge to measure frequency or impact of coastal storms along the US Atlantic Coast (Dolan and Davis, 1992; Zhang et al., 2000; Bernhardt and DeGaetano, 2012; Colle et al., 2015) or globally (Marcos et al., 2015; Mawdsley and Haigh, 2016). However, few have focused on tropical systems occurring in the Delaware and Chesapeake Bays, or the Mid-Atlantic in general.

SURGEDAT is a database specifically designed to store storm surge data. It contains 700 tropical surge events around the world and more than 8,000 unique tropical high water marks along the U.S. Gulf and Atlantic Coasts since 1880, however, only a few records are located in the Mid-Atlantic region (Needham et al., 2015). The USACE North Atlantic Comprehensive Coastal Survey report (US Army Corps of Engineers, 2014) and FEMA Region 3 Coastal Storm Surge Study

(Federal Emergency Management Agency, 2013) included many simulated tropical systems in their storm surge modeling work due to the dearth of observational data in the region. Booth et al. (2016) looked at all extreme storm surge events and the relative influence of tropical cyclones for select gauges in the Mid-Atlantic. They found that for large coastal flood events, tropical systems were the most likely cause, whereas for less severe events, the relative importance of tropical systems decreased and extratropical cyclones increased. Wilkerson and Brubaker (2013) investigated the spatial variability of storm surge in the lower Chesapeake Bay over all extreme coastal flooding events but included only a few tropical cyclones. Rashid et al. (2019) looked at interannual and multi-decadal variability of extreme storm surge during the peak extratropical (November – April) and tropical (May – October) seasons. Although they included surges from all types of storm events, they concluded that the Mid-Atlantic region varied differently than the Northeast and Southeast portions of the U.S. Atlantic Coast at long time scales.

The overall goal of the current study is to improve understanding of the magnitude and spatial variability of tropical cyclone-caused coastal flooding in the Delaware and Chesapeake Bays. The first part of the paper focuses on the computation of skew surge at tide gauges for each TC event. Skew surge is not commonly used to assess the surge produced by a storm although it may be a more appropriate measure of risk of storm surge (refer to Section Skew Surge and Harmonic Analysis for more details). The remaining parts of the paper focus on grouping tide gauges with similar skew surge response into sub-bay geographic regions, as well as grouping TCs into clusters that exhibit similar spatial patterns of skew surge. This information will aid in local planning, emergency preparedness, and communication outreach regarding the hazards of coastal storms in the region.

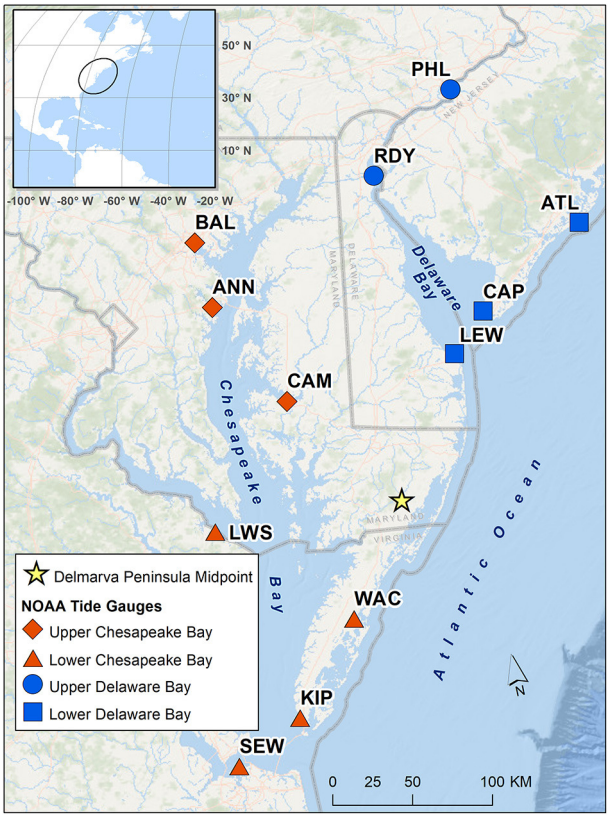

FIGURE 1 | Map of the Delaware and Chesapeake Bays highlighting NOAA tide gauges used in the current study. The inset overview map shows the 750 km circular buffer around the Delmarva Peninsula reference point (yellow star) computed from the mean latitude and longitude of the six ocean coastal gauges: Atlantic City (ATL), Cape May (CAP), Lewes (LEW), Wachapreague (WAC), Kiptopeke (KIP), and Sewells Point (SEW).

MATERIALS AND METHODS

Study Region

The Delaware and Chesapeake Bays, connected *via* the Chesapeake and Delaware (C & D) Canal, surround the Delmarva Peninsula (**Figure 1**). Both bays are heavily tidally influenced with freshwater inputs from the major river systems of the Delaware River, Susquehanna River, and Potomac River. Tidal water levels are impacted by many environmental characteristics, including the geometry of the coastline, bathymetry, bottom friction/dissipation effects, reflection of the wave near the head of the bay (Lee et al., 2017) as well as prevailing remote winds and ocean currents. Storm surge, while also impacted by these factors, is additionally influenced by characteristics of the storm itself, such as storm size and direction of travel, duration, atmospheric pressure, wind speed and wind direction relative to the coastline (Ellis and Sherman, 2015; National Hurricane Center, 2019). Coastal flood levels in this region are the net effect of numerous complex hydrodynamics at play.

The Delaware Bay has a classical funnel shape, width of about 18 km at its mouth between Cape Henlopen and Cape May, expanding to ∼45 km at its widest point (Wong and Münchow, 1995), with an average bathymetry of about 7 m, although deep scour in the middle of the lower part of the bay can extend to over 20–25 m (Eagleson and Ippen, 1966; Harleman, 1966; Salehi, 2018). The converging coastlines toward the head of the bay amplifies tides in the northern regions, where the tidal range is over 2 m compared to <1.5 m near the mouth (Lee et al., 2017; Ross et al., 2017). This contrasts with the Chesapeake Bay, a much longer bay, more dendritic in form with many tributaries, ranging in width from 5.6 to 56 km. The Chesapeake Bay is relatively shallow at median depth of about 6 m, with only 18% of its surface area at depths above 12 m, although a narrow navigation channel width depths > 9 m exists along the east side of the main channel (Patrick, 1994; Xiong and Berger, 2010). Tidal range is ∼0.7 m in the northern reaches, dipping to 0.3 m at the middle of the bay, increasing to 0.9 m at the mouth (Zhong and Li, 2006; Lee et al., 2017; Ross et al., 2017).

Tidal cycle patterns in this region are mainly semi-diurnal, albeit the tides transition in the Chesapeake Bay from semi-diurnal in the lower portion to a mixed tidal regime in the upper portions, forming a mix of progressive and standing waves throughout the bay system (Xiong and Berger, 2010; Ross et al., 2017). The average seasonal cycle of mean sea level is similar across the bays, a bimodal distribution with the maximum in fall

TABLE 1 | Tide gauges used in the current study.

Station	Abbr.	NOAA ID	Bay	Coordinates	Data gaps	Percent Hourly	Missing TCs
Philadelphia	PHL	8545240	Delaware	39.933000, −75.142667	0	99.23%	0
Reedy Point	RDY	8551910	Delaware	39.558333, −75.573333	5	95.61%	2
Lewes	LEW	8557380	Delaware	38.781667, −75.120000	0	99.73%	1
Cape May	CAP	8536110	Delaware	38.968333, −74.960000	2	98.35%	0
Atlantic City	ATL	8534720	Delaware	39.356667, −74.418333	2	98.08%	1
Baltimore	BAL	8574680	Chesapeake	39.266667, −76.580000	0	99.66%	1
Annapolis	ANN	8575512	Chesapeake	38.983333, −76.481667	1	98.70%	1
Cambridge	CAM	8571892	Chesapeake	38.571667, −76.061667	1	98.84%	1
Lewisetta	LWS	8635750	Chesapeake	37.995000, −76.465000	2	98.72%	1
Kiptopeke	KIP	8632200	Chesapeake	37.165000, −75.988333	0	99.78%	3
Sewells Point	SEW	8638610	Chesapeake	36.946667, −76.330000	0	100.00%	0
Wachapreague	WAC	8631044	Chesapeake	37.608333, −75.685000	6	89.30%	11

Number of data gaps and percent hourly data based upon time period 1980 – 2019. Data gaps represent number of continuous gaps of 745 h (∼1 month) or more. Number of missing tropical cyclones (TCs) is a subset of North Atlantic TCs that crossed into the 750 km buffer around Delmarva over the same time period.

(October) and secondary maximum in late spring (May-June), primarily caused by periodic fluctuations in atmospheric weather systems and coastal water steric effects (NOAA National Ocean Service Center for Operational Oceanographic Products Services, 2020a).

Tropical Cyclone Data

Tropical cyclone information used in this study is extracted from the International Best Track Archive for Climate Stewardship (IBTrACS) North Atlantic Basin dataset Version 4 (Knapp et al., 2018). IBTrACS is a collection of global best track data for cyclones that achieved tropical or sub-tropical status at some point in their lifetime. Data were obtained from multiple research centers around the world and are stored in a centralized location for standardized distribution (Knapp et al., 2010). IBTrACS has been endorsed by the World Meteorological Organization non-government domain Tropical Cyclone Programme as an official archiving and distribution resource for tropical cyclone best track data.

For the current study, TCs were limited to those occurring in the North Atlantic Ocean basin during the time period 1980–2019 with tracks that cross within a 750 km radius circular buffer around the Delmarva Peninsula. Distance to Delmarva was computed as the great circle distance using the GRS80 reference ellipsoid from a reference location along the Delmarva coastline to the TC center listed in each IBTrACS record. The Delmarva coastal reference location (latitude = 38.137778, longitude = −75.416944) was determined by computing the mean latitude and longitude coordinates of the six coastal tide gauges used in the study, namely Atlantic City (ATL), Cape May (CAP), Lewes (LEW), Wachapreague (WAC), Kiptopeke (KIP), and Sewells Point (SEW) (**Figure 1**; **Table 1**). The large 750 km radius, relative to the typical size of TCs, was chosen to be sure to capture TCs that could significantly impact water levels (Zhang et al., 2000; Booth et al., 2016). This resulted in a subset of 144 TCs with median annual count of 3.5 TCs. The monthly distribution closely matches, although occurring slightly earlier in the season, the distribution of all North Atlantic TCs (**Figure 2**). However, the annual percentage of all North Atlantic TCs that are near Delmarva can be quite variable, with a minimum of 5% in 2010 and a maximum of 50% occurring in 1985 and 2004.

IBTrACS notes the original source of information for each storm record. The data source for all the selected TCs from 1980 through 2018 is the U.S. National Hurricane Center (NHC) Hurricane Database 2 (HURDAT2) (Landsea and Franklin, 2013). TCs from the 2019 season were listed as NHC provisional status and likely were the operational best track estimate (i.e., have not yet been reanalyzed post-season). Specific data retained from the IBTrACS dataset include the TC name and storm ID, center latitude and longitude, date and time, and storm status (e.g., hurricane, tropical storm, and tropical disturbance). Although HURDAT2 records correspond to 00, 06, 12, and 18Z times, IBTrACS interpolates many variables to 3-hourly observations using splines for positional data or linearly for non-positional data. GIS shapefiles of storm tracks were also obtained from IBTrACS.

Water Level Data

Tide gauges selected for this study were limited to NOAA operational tide gauges in and immediately around the Delaware and Chesapeake Bays. Requirements were that the gauge maintained nearly continuous record of hourly water levels for the time period 1980–2019, evenly located throughout the region, a set of harmonic constituents identified for making tidal predictions, and a vertical tidal datum conversion factor to North American Vertical Datum of 1988 (NAVD88). In all, 12 gauges were selected; five associated with the Delaware Bay and seven with the Chesapeake (**Figure 1**; **Table 1**). All selected gauges are part of NOAA NWLON and PORTS networks.

Hourly and High/Low water level data were downloaded from NOAA Center for Operational Oceanographic Products and Services (CO-OPS) API for Data Retrieval (NOAA National Ocean Service Center for Operational Oceanographic Products Services, 2020b). High/Low data represent the exact time and

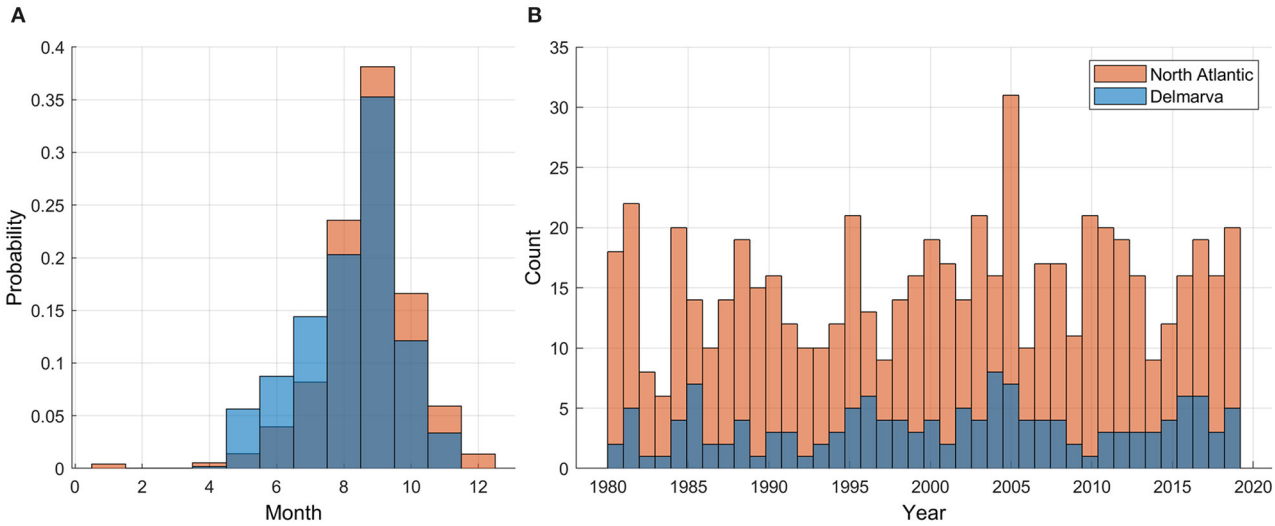

FIGURE 2 | Monthly **(A)** and annual **(B)** distribution of all 1980 – 2019 North Atlantic tropical cyclones and the subset of those whose track crosses the 750 km buffer around Delmarva Peninsula.

magnitude of each Higher-High, High, Low, and Lower-Low tidal peak. Hourly data represent the observed water level on each hour (e.g., 21:00, 22:00). The 40 years of hourly data at each gauge were manually inspected for errors and inconsistencies. Small periods of data clusters (2–16 h) were removed from the hourly time series (on seven occasions across all gauges) that existed within larger time periods of missing data to better represent the number and length of existing data gaps. No data from the High/Low time series were removed. Data gaps of 1 or 2 h (<10 across all gauges) were filled using linear interpolation. Larger data gaps were not filled. **Table 1** lists the number of data gaps that spanned 745 h (∼1 month) or greater as well as the percentage of valid hourly data points. Reedy Point and Wachapreague had the highest number of large data gaps, five and six, respectively, and lowest percentage of valid hourly data (based on a maximum of 14,610 h during 1980 – 2019), 95.61 and 89.30%, respectively. Water level records were compared against the dates of the TCs while within the 750 km buffer of Delmarva. Very few of the 144 TCs were missing from the water level records. Wachapreague had the largest amount of missing data due to a 2.5-year period (200,511–200,804) when valid Hourly and High/Low data were unavailable.

Skew Surge and Harmonic Analysis

This study uses skew surge as the measure of flooding contributed by each tropical storm. Skew surge is defined as the difference between the maximum observed total water level and the maximum predicted tidal level during a tidal cycle, even if the observed and predicted tidal peaks are offset (i.e., skewed) from each other (**Figure 3**; Pugh and Woodworth, 2014). Each tidal cycle therefore has one value of skew surge. By measuring the height of water levels above highest predicted tide, skew surge represents the increase of water levels more clearly separated from the astronomically forced-tides and tide-surge interactions (Batstone et al., 2013; Mawdsley and Haigh, 2016; Williams et al., 2016; Stephens et al., 2020). With respect to preparedness, skew surge represents a truer estimate of the amount of water a location observes above what they expected from high tides alone. Hourly non-tidal residual (NTR, the difference between coincident total water level and predicted tide) is a more common measure of storm surge. However, the statistically computed hourly NTR includes known and unknown non-linear interactions between tides and low-frequency surge produced by a storm, which are complex and dependent upon many environmental factors (Bernier and Thompson, 2007; Spicer et al., 2019). As well, often during coastal flooding storm events, the maximum NTR does not coincide exactly with predicted high tide peak e.g., Hurricane Ernesto 2006 at Sewells Point and Hurricane Sandy 2012 at Reedy Point tide gauges had their largest residuals occur near predicted low tide. Overall, skew surge is less dependent upon tide-surge interactions and independent of tidal phase, proving to be advantageous in developing joint probability estimates of extreme water levels for long-term planning, and therefore less prone to misleading conclusions drawn from NTR estimates of surge (Williams et al., 2016).

Predicted tides were computed at each gauge through harmonic analysis based on hourly total water level time series using the U-Tide Matlab software package (Codiga, 2011). Harmonic analysis incorporated the set of 37 harmonic constituents defined by NOAA for their official tide predictions in this region (NOAA National Ocean Service Center for Operational Oceanographic Products Services, 2020c). This set of 37 constituents are based on known astronomically-cyclic motions of the Earth-Sun-Moon system and local resonances due to water depth and geomorphology of the region that are tidally significant; other tidal constituents were either too small a magnitude or too long a period (i.e., multiple years) to significantly alter daily tidal predictions (NOAA, 2019).

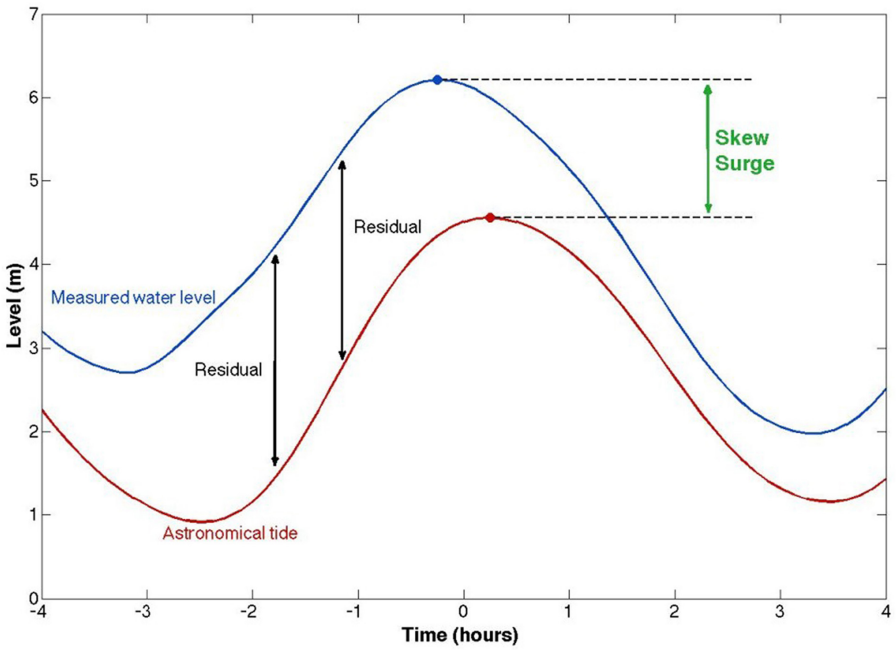

FIGURE 3 | Diagram of skew surge during a tidal cycle. In the above example, the total water level and predicted tide peaks are skewed from one another. The maximum hourly non-tidal residual occurs closer to low tide than to high tide (Source: Mawdsley and Haigh, 2016).

Additionally, the seven constituents noted by Harris (1991) relevant for US East Coast water levels were included in the harmonic analysis. The same set of 44 constituents were used for all tide gauges. A lowpass filter was not applied to the hourly NTR as this could also remove meteorological forcing on water levels at these frequencies, which occur when tropical systems move quickly through the Mid-Atlantic region on the order of a tidal cycle or less.

Harmonic analysis was performed in 1-year segments over each calendar year (Jan – Dec) instead of on the full 40-year time period simultaneously. For time periods with data gaps of 1 month or larger, the harmonic analysis was performed on a 3-year period, centered on the year with most missing data, to ensure capture of the seasonal variation. Annual computations minimizes timing errors that can lead to the leakage of tidal energy into the non-tidal residual (Merrifield et al., 2013) and minimizes the impact of sea-level rise as the increasing trend is absorbed into the model through the annual mean. Moreover, a 40-year analysis would have resulted in harmonics fit to average conditions and therefore would not account for changing constituent magnitudes that could result from deepening water level or other changing environmental conditions (Ross et al., 2017). Similarly, the Sa (solar annual) and SSa (solar semi-annual) constituents' periods of ∼12 and 6 months, respectively, are largely influenced by seasonal weather conditions and storm tracks, leading to high interannual variation; harmonic analysis tests without these two constituents resulted in large discontinuities between adjacent years.

Over each tidal cycle, the maximum of the observed TWL peaks between the High/Low and hourly time series was aligned with predicted tide peaks within +/- 3 h of each other. The time offset was extended to +/- 6 h if no High/Low or TWL peaks were found within +/- 3 h (this was required for < 100 tidal peaks across all gauges over the study time period, and occurred only for gauges within the Chesapeake Bay). Total resultant count was 28,231 tidal peaks per gauge for 1980–2019. The difference between the maximum observed TWL and maximum predicted tide level over each tidal cycle was computed as skew surge.

Daily Weather Maps provided by the NOAA Central Library Data Imaging Project (Ritterbush, 2012) were reviewed alongside observed water levels during the approach to Delmarva of each of the 144 TCs. A time window was manually identified that encapsulated each TC's likely direct influence on water levels within our study region, with a priority to capture the maximum tidal peaks. A tidal peak is defined in this study as the point of high tide within each tidal cycle, and the maximum tidal peak is the high tide with the maximum water level around each TC. Since observed high tides can occur a few hours before or after the predicted high tide, the time of the tidal peak is defined here as the time of the predicted high tide. It often occurred that winds from surface high pressure systems and/or mid-latitude cyclones and associated fronts were influencing water levels in one or both of the bays coincidentally with the approach of the TC. NHC Tropical Cyclone Reports were also consulted for TCs from 1994 to 2019, as necessary (National Hurricane Center, 2020). In cases where a suitable time window without other identifiable weather systems could not be determined, the TC was removed from further analysis. TCs that seemed to have little to no effect on water levels (e.g., they were far away from Delmarva) were left in the analysis provided that no other weather system was

noticeably impacting the study region at that time, resulting in a near-zero (slightly positive or negative) skew surge for some storms. Although there is potential for false-positive errors (i.e., removing a TC that should remain), this method provides a more conservative approach to assessing surge levels and spatial variability specifically attributed to tropical cyclones.

Median time window was 24 h before and 18 h after the TC's closest approach to Delmarva, although in rare cases the window was extended to several days. Ultimately, 38 TCs were removed from the analysis, leaving a total of 106, ∼2.6 per year on average. For the remainder of this study, this subset of storms will be referred to as Delmarva TCs. Maximum skew surge and maximum TWL ("storm tide") at all tidal peaks occurring within each Delmarva TC's time window were extracted. Storm tides and skew surges were detrended about the mean and normalized by the standard deviation over all 1980 – 2019 tidal peaks at each gauge independently. The detrending and standardization allows for a more direct spatial and temporal comparison of the relative influence of each storm. The detrended, normalized storm tide and skew surge are referred to as the storm tide index (STI) and skew surge index (SSI), respectively.

Distributions of skew surge and SSI values from TCs were computed at each tide gauge over all Delmarva TCs ($N = 106$). SSI was then compared to STI for each storm using Spearman Rank correlation. Spearman Rank correlation, a non-parametric method, was chosen over the Pearson Product-Moment method to compute correlations considering TC-caused skew surges (as well as storm tides and the normalized, detrended indexes) do not follow a Normal distribution (refer to section Delmarva Tropical Cyclone Storm Tide and Skew Surge Summary). Correlations were computed for skew surge against maximum NTR for each storm. Skew surge instead of SSI was chosen for this comparison as the NTR time series was not detrended or normalized.

SSI was also compared to the distance of each Delmarva TC's closest approach to the Delmarva Peninsula, regardless of the storm's track direction of movement. Influence of distance on storm surge is compounded by storm size, strength of winds, direction of winds, direction of storm movement, and the location of the tide gauge relative to the storm's direction (e.g., the right or left front quadrant of the TC). The only storm-specific characteristic used in the current study is the location of the TC storm track, and many of the other relevant characteristics are not available in IBTrACS for the full 40-yr time period (most only since 2004). It is not the intent of this study to determine which of these variables are most important to storm surge. However, the distance away of the storm track is often cited and frequently used in storm preparation and awareness campaigns.

Regional Skew Surge

Since each gauge location has unique tidal characteristics (e.g., mean sea level, tidal range), the STI and SSI derived for each Delmarva TC were averaged over all gauges within each bay. The gauges at Atlantic City and Wachapreague were included with Delaware Bay and Chesapeake Bay, respectively, as listed in **Table 1**. This allowed for a distinct measure of TC-based water levels per bay for each storm with equal relative weights across gauges. Missing data were ignored in the averaging as no storm had more than one gauge with missing information.

To investigate sub-bay geographic variability, cross-correlations and Principal Components Analysis (PCA) were performed on the STI and SSI to identify tide gauges with similar responses. Cross-correlations were computed using Spearman Rank coefficient. PCA with variable clustering was run on the STI and SSI to aid in grouping of gauges into like regions. Sub-bay regions are defined as groups of adjacent tide gauges with higher correlations with each other than with gauges immediate outside their group. STI and SSI for each storm were then averaged across gauges that lie within the identified sub-bay regions. Distributions and cross-correlations among regions were also computed. Each Delmarva TC was then ranked based on mean SSI for each bay and sub-bay region. Storms that were highly ranked in one region/bay as opposed to the others were noted.

Additionally, K-Means clustering was run on the Delmarva TC spatial pattern of SSI across all 12 tide gauges, from upper Delaware Bay to lower Chesapeake Bay. The spatial pattern of SSI is termed the "surge profile" of the storm. JMP Pro 15 statistical software was used to perform the clustering. K-Means is an unsupervised clustering technique that aggregates vectors of data (in our case, each storm's 12 data points of SSI at each gauge) into common sets based on each vector's (i.e., storm's) distance to a set number (K) of means in each dimension. The mean of each dimension is moved upon each pass of the algorithm to minimize the cumulative distance of each vector to its cluster mean. Although K-Means is sensitive to the sort order of the input data, several tests of different sort orders resulted in very similar clustering of storms. The cubic clustering criterion score was used to determine the optimum number of clusters. To determine if a storm's surge profile is associated with the location of its track though the Delmarva region, storm tracks were plotted for all storms within each K-Means cluster. A qualitative (rather than quantitative) assessment was performed on the storm's track position relative to the surge profile.

RESULTS

Delmarva Tropical Cyclone Storm Tide and Skew Surge Summary

Mean storm tides over all Delmarva TCs (**Table 2**) range from a minimum of 0.48 m at ANN to a maximum of 1.36 m at PHL. Higher storm tides are observed in the Delaware Bay than in the Chesapeake Bay as well as in upper bays compared to the lower bays. This geographic pattern in storm tides nearly identically ($r = 0.99$) matches the pattern of the MHHW tidal datum currently published by NOAA. After detrending and normalization, the relationship of STI to MHHW flips to a strong negative relationship ($r = -0.61$). Largest STI values are in the Chesapeake over the Delaware Bay, and in the lower bays over the upper bays. PHL and RDY have the highest mean storm tides but lowest mean STI. Relationship of

TABLE 2 | Mean and standard deviation of storm tide and skew surge of Delmarva tropical cyclones, 1980 – 2019.

Station		Storm tide		STI		Skew surge		SSI		Tidal datum	
	N	Mean	SD	Mean	SD	Mean	SD	Mean	SD	MSL	MHHW
Philadelphia	106	1.36	0.23	1.30	0.84	0.22	0.23	1.12	1.25	1.09	0.12
Reedy Point	105	1.12	0.19	1.26	0.76	0.18	0.20	1.04	1.16	0.99	−0.02
Lewes	105	0.90	0.27	1.45	1.07	0.24	0.27	1.48	1.75	0.62	−0.12
Cape May	106	1.00	0.25	1.37	0.96	0.22	0.24	1.40	1.60	0.74	−0.14
Atlantic City	106	0.86	0.27	1.32	1.05	0.22	0.27	1.31	1.74	0.61	−0.12
Baltimore	106	0.52	0.26	1.40	1.12	0.21	0.27	1.17	1.49	0.25	−0.01
Annapolis	106	0.48	0.24	1.46	1.13	0.20	0.24	1.20	1.45	0.20	−0.02
Cambridge	106	0.54	0.21	1.44	1.04	0.19	0.21	1.22	1.33	0.29	−0.03
Lewisetta	106	0.51	0.24	1.58	1.24	0.20	0.22	1.38	1.51	0.21	−0.02
Kiptopeke	104	0.62	0.27	1.75	1.40	0.24	0.26	1.71	1.93	0.32	−0.15
Sewells Point	106	0.71	0.33	1.82	1.65	0.28	0.32	1.80	2.15	0.35	−0.08
Wachapreague	97	0.86	0.30	1.54	1.30	0.26	0.27	1.54	1.77	0.57	−0.11

Storm tides and tidal datums referenced to NAVD88 meters. Mean Seal Level (MSL) and Mean Higher-High Water (MHHW) tidal datums defined by NOAA for the current National Tidal Datum Epoch (NTDE) 1983–2001. STI/SSI, storm tide/skew surge index (detrended and normalized versions of storm tide/skew surge over study time period).

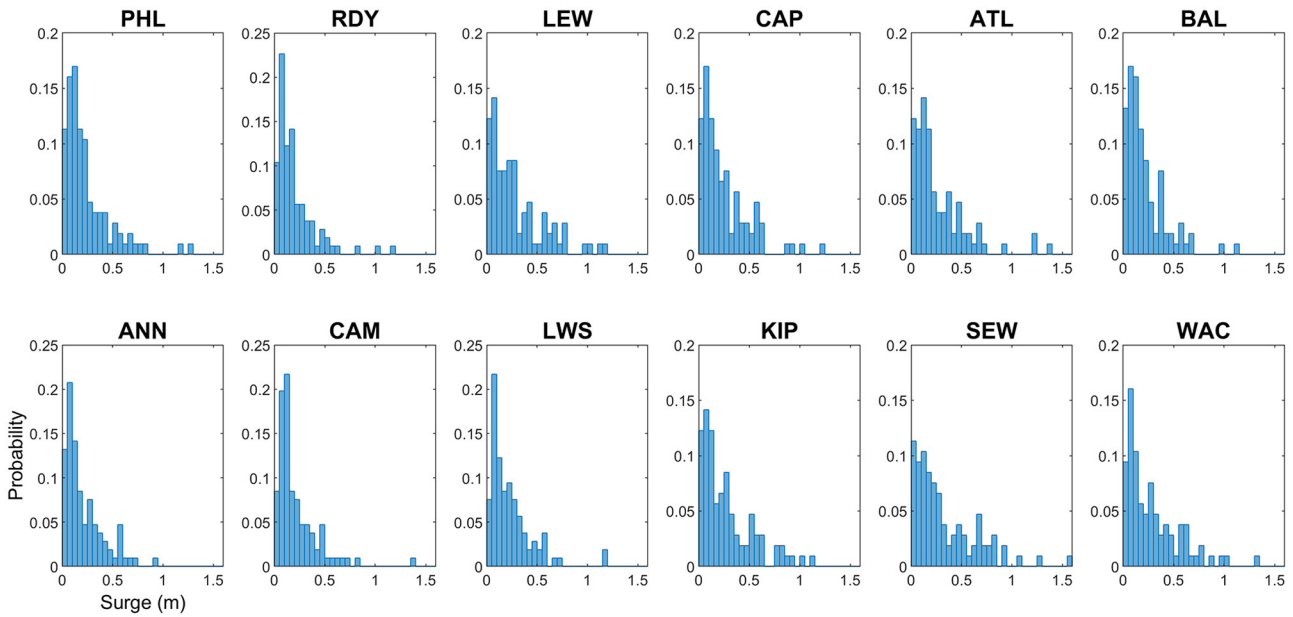

FIGURE 4 | Probability distribution of skew surge (meters) for Delmarva tropical cyclones, 1980 – 2019.

storm tides to MSL is similar as to MHHW albeit weaker ($r = -0.39$).

Mean skew surges are more consistent geographically than storm tides, showing very little change across the study region, although the standard deviations and range are similar to storm tides at only 1/2 to 1/6 of the magnitude of the mean. Higher mean skew surges are toward the extreme upper and lower ends and smaller means toward the middle of each bay, ranging from a minimum of 0.18 m at RDY to a maximum of 0.28 m at SEW. Mean skew surges show very little relationship to MHHW and a negative relationship to MSL ($r = -0.42$). After detrending and normalization, the relationship of SSI to MHHW and MSL stayed negative but strengthened ($r = -0.35$ and -0.67, respectively). Larger mean SSI values are found in the lower bays over the upper bays, and in the Chesapeake Bay over the Delaware Bay.

Distribution of skew surge for the Delmarva TCs do not follow a Normal distribution, confirmed by Anderson-Darling test statistic (**Figure 4**). Shape of the distributions show the typical characteristics of upper tail (extreme values) portion of a normally distributed population, asymmetric right-skewed with a greater number of outliers on the upper end than the lower end. Storm tide distributions (**Supplementary Figure 3**)

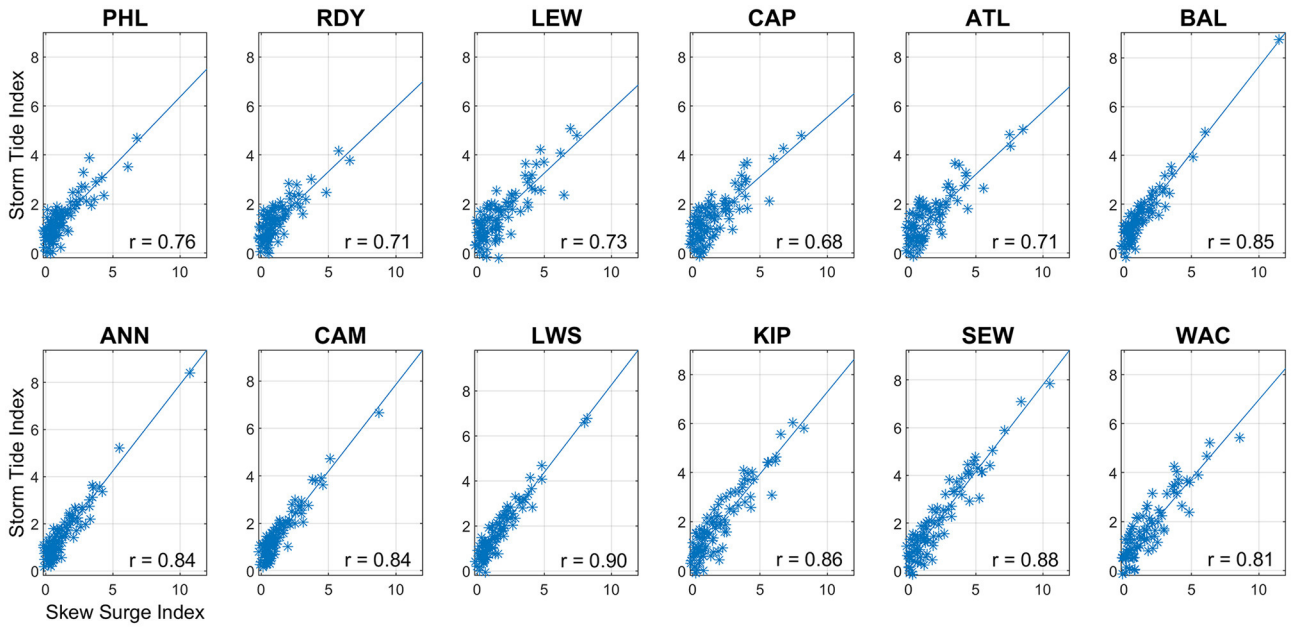

FIGURE 5 | Scatterplot, least-squares regression line, and correlation coefficient of skew surge index (SSI) against storm tide index (STI) for Delmarva tropical cyclones, 1980 – 2019.

are more evenly distributed but still show a skewed upper end tail (Box plots of these distributions are shown in **Supplementary Figure 4**). Many studies have shown extreme high coastal flood levels from tide gauges follow similar extreme value distributions (Tebaldi et al., 2012; Sweet et al., 2014; US Army Corps of Engineers, 2014; Marcos et al., 2015; Moftakhari et al., 2015; Booth et al., 2016; Rashid et al., 2019). The larger population of tidal peak maximum TWL and skew surge (1980–2019, $N = 28{,}231$) from which the Delmarva TC-based storm tides and skew surges were extracted, did indeed closely follow the Normal distribution over the long-term once detrended. The steepest curves (i.e., highest probability of smaller surges) occur in the upper bays except for the most north gauges in each bay, namely PHL and BAL, The detrended and normalized STI and SSI distributions for each gauge (not shown) hold essentially the same characteristics except with the expected shifted means and deviations.

SSI exhibits a strong, positive relationship to STI at all tide gauges (**Figure 5**). Correlations are consistent among sites within each bay, with Delaware Bay at 0.70 – 0.76 and Chesapeake Bay showing higher correlations at 0.82 – 0.89. Sites in the lower bays demonstrate slightly more scatter than in the upper bay, although correlations at all sites are statistically significant at the $p = 0.01$ level. The amount of scatter represents the number of storms with larger relative differences between storm-produced surge and total water level. Hurricane Isabel 2003 is the extreme event in the upper Chesapeake Bay as it produced significantly larger skew surge and storm tide than other storms.

Similarly, skew surge exhibits a strong, positive relationship to maximum NTR (**Figure 6**). Correlations at all sites are statistically significant at the $p = 0.01$ level. The diagonal dashed line represents one-to-one ratio. Deviations from this line denote storm events when maximum residual occurred at tidal phases other than at tidal peaks. Largest differences occur during the largest skew surge events at the upper Delaware Bay sites, which also have the lowest correlations and relatively broad scatter, even at low surge levels. Over a single tidal cycle, skew surge must be equal to or less than maximum NTR, by definition, however during a storm event that covers multiple tidal cycles, this does not necessarily need to be the case. In our analysis, across all storms and gauges, skew surge was greater than maximum NTR by more than 1 cm only about 25 times, with a maximum difference of ∼4 cm.

An inverse relationship is evident between SSI and distance to TC closest approach, with correlations ranging from $r = -0.26$ at SEW to $r = -0.37$ at both LEW and CAP (**Supplementary Figure 5**). Highest correlations are in lower Delaware Bay and lowest correlations in the lower Chesapeake Bay. Although correlations are statistically significant at the 0.01 level, there is broad scatter and several outliers. Similar SSI amounts, especially at lower surge levels, were produced by storms from nearly all distances.

Sub-bay Regionalization

Cross-correlations on SSI and STI produced from Delmarva TCs across all 12 tide gauges showed strong regional relationships (**Figure 7** and **Supplementary Tables 1**, **2**). Natural groupings of gauges of $r = 0.88$ and above (red regions in **Figure 7**) emerge within the same geographic regions. Strong distinctions can be noted between gauges in the upper bay and lower bay regions. PCA with variable clustering was run on the SSI and STI (results not shown) and supported results from the

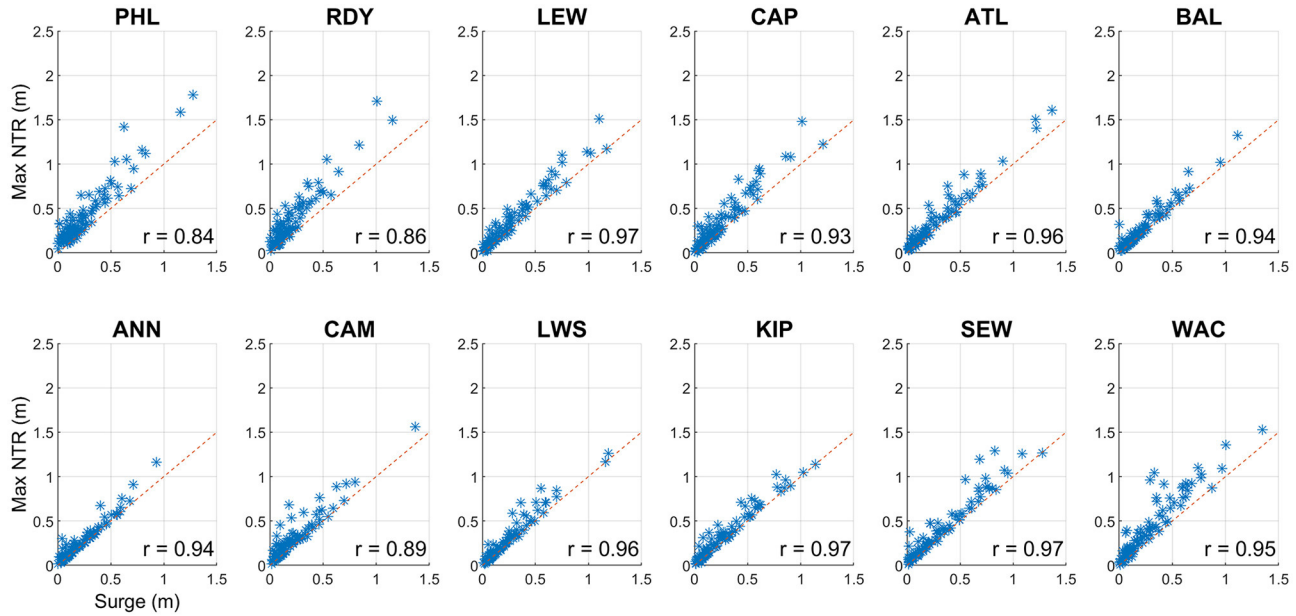

FIGURE 6 | Skew surge against maximum hourly non-tidal residual (NTR) for Delmarva tropical cyclones, 1980 – 2019. Values in meters. Dashed red line represents to 1:1 ratio.

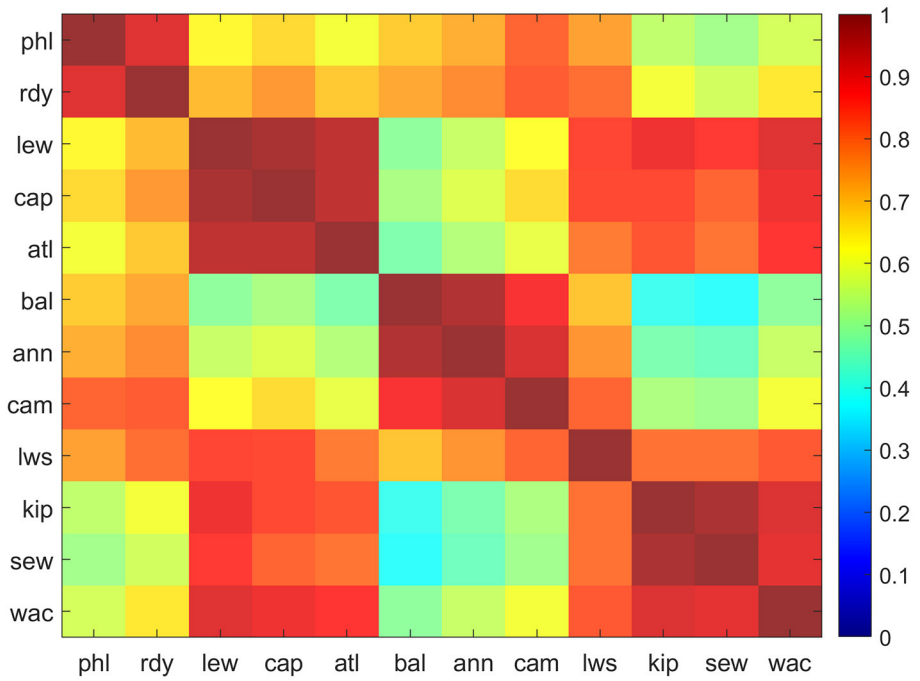

FIGURE 7 | Corrgram of cross-correlation of skew surge index (SSI) for Delmarva tropical cyclones, 1980 – 2019. Correlation values computed using Spearman Rank method. Red (blue) colors represent higher (lower) correlations. Regions of gauges with similar correlations are easily identifiable as adjacent, like colors. All correlations are statistically significant at 0.01 level.

cross-correlation analysis. Results indicate regions as: Upper Delaware Bay (PHL, RDY), Lower Delaware Bay (LEW, CAP, ATL), Upper Chesapeake Bay (BAL, ANN, CAM), and Lower Chesapeake Bay (KIP, SEW, WAC). Observations at LWS showed similar correlations with gauges in both the upper and lower Chesapeake Bay regions and had the lowest correlations with

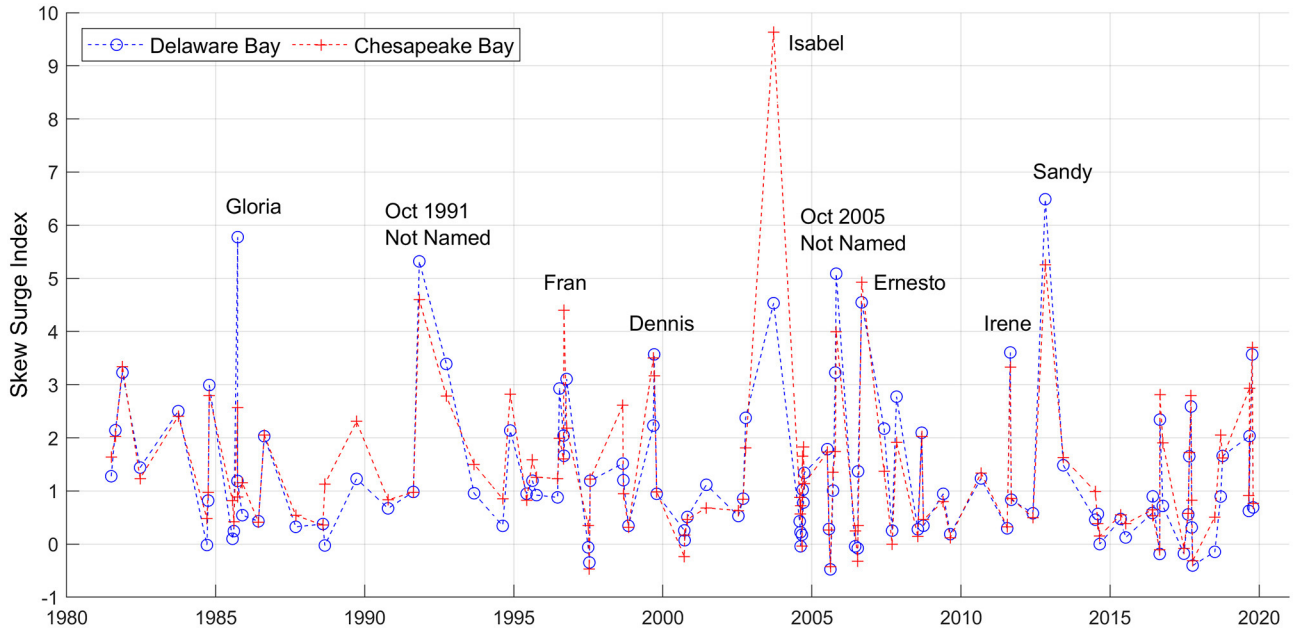

FIGURE 8 | Skew surge index (SSI) of Delmarva tropical cyclones, 1980 – 2019, spatially averaged over the Delaware (blue) and Chesapeake (red) Bays.

gauges in its immediate vicinity. Hence, LWS was not assigned to any sub-bay region. Cross-correlations run on long-term daily maximum skew surge and TWL for 1980–2019 (results not shown) support the same geographic regions. Although not in the same geographic region, LEW correlates highly with gauges in the lower Chesapeake Bay, while WAC correlates highly with gauges in the lower Delaware Bay.

SSI values were spatially averaged across each of the sub-bay regions for each Delmarva TC. The Chesapeake Bay regions have higher mean SSI values than the corresponding Delaware Bay regions, and the lower bay regions have higher mean SSI than upper bay regions. Most notably, the lower bay regions have higher correlations to each other than to their respective upper bay regions, and likewise for the upper bay regions. Relationship between the Upper and Lower Chesapeake regions show the lowest correlation of any pair of groups ($r = 0.50$).

Distributions of regional mean SSI (**Supplementary Figure 6**) do not follow a Normal distribution, confirmed by Anderson-Darling statistic, but are more closely related to extreme value distributions similar to distributions of tide gauges. Upper bays experience a steeper, more uniform decline than lower bays, although all regions include outlier storms in the far upper end. Additionally, regional SSI against STI showed similar behavior as tide gauge analysis. Most of the deviations occur at the lower SSI values and the upper bays have slightly more scatter than lower bays. Chesapeake Bay shows higher correlations of SSI to STI ($r = 0.86$ in both upper and lower Bay regions) than does Delaware Bay ($r = 0.73$ and 0.72 for the upper and lower Bay regions, respectively).

Top Surges of Delmarva Tropical Cyclones

SSI values were spatially averaged over all gauges within each bay boundary (i.e., LWS was included for the Chesapeake Bay; ATL and WAC were not included for either bay) for each Delmarva TC (**Figure 8**). As noted earlier, large variations exist although most storms have mean SSI values under 2. Larger events typically have mean SSI values between 2 and 7. Mean SSI across all storms are 1.31 and 1.42 for the Delaware and Chesapeake Bays, respectively. Although many storms have similar mean SSI for each bay, especially for the smaller surge events, some stand out for their differences. Hurricanes Isabel (2003) and Fran (1996) impacted the Chesapeake more than the Delaware Bay by the largest margin, whereas likewise, Hurricanes Gloria (1985) and Sandy (2012) impacted the Delaware more than the Chesapeake Bay. The top 10 Delmarva TCs with the largest differences in mean SSI are listed in **Supplementary Table 3**.

The top 25 Delmarva TCs were ranked by mean SSI for each bay (**Table 3**). The year and month represent the time of the storm's closest approach, the great majority occurring in September and October. Status column represents the most common value of the IBTrACS USA_STATUS attribute while the storm was present within the 750 km buffer around Delmarva, including times before and after the storm's closest approach. Both bays have many top storms in common, notably Hurricanes Sandy (2012), Isabel (2003), and Not Named (1991), claiming 3 of the top 5 spots in each bay.

Delmarva TCs also show significant sub-bay regional differences. **Supplementary Tables 4**, **5** list the top 25 Delmarva TCs ranked separately for each of the four sub-bay regions. Surprisingly, Hurricane Isabel (2003) was the top ranked storm for the Upper Delaware Bay although it is typically known as

TABLE 3 | Top 25 Delmarva tropical cyclones, ranked by skew surge index (SSI), spatially averaged over the Delaware and Chesapeake Bays, 1980 – 2019.

	Delaware bay				Chesapeake bay			
Rank	**Name**	**Year**	**Month**	**Status**	**Name**	**Year**	**Month**	**Status**
1	SANDY	2012	10	EX	ISABEL	2003	9	HU
2	GLORIA	1985	9	HU	SANDY	2012	10	EX
3	NOT_NAMED	1991	10	EX	ERNESTO	2006	9	EX
4	WILMA	2005	10	HU	NOT_NAMED	1991	10	EX
5	ISABEL	2003	9	HU	FRAN	1996	9	TD
6	ERNESTO	2006	9	EX	WILMA	2005	10	HU
7	IRENE	2011	8	HU	MELISSA	2019	10	EX
8	FLOYD	1999	9	HU	DENNIS	1999	9	TS
9	MELISSA	2019	10	EX	IRENE	2011	8	HU
10	DANIELLE	1992	9	TS	NOT_NAMED	1981	11	SS
11	NOT_NAMED	1981	11	SS	FLOYD	1999	9	HU
12	JOSEPHINE	1996	10	EX	DORIAN	2019	9	HU
13	NOT_NAMED	2005	10	EX	DANIELLE	1992	9	TS
14	JOSEPHINE	1984	10	HU	HERMINE	2016	9	EX
15	BERTHA	1996	7	TS	JOSEPHINE	1984	10	HU
16	NOEL	2007	11	EX	JOSE	2017	9	TS
17	DEAN	1983	9	TS	GORDON	1994	11	HU
18	JOSE	2017	9	TS	BONNIE	1998	8	HU
19	KYLE	2002	10	TS	GLORIA	1985	9	HU
20	HERMINE	2016	9	EX	DEAN	1983	9	TS
21	DENNIS	1999	9	TS	JOSEPHINE	1996	10	EX
22	EDOUARD	1996	9	HU	HUGO	1989	9	HU
23	DENNIS	1981	8	TS	FLORENCE	2018	9	HU
24	BARRY	2007	6	EX	HANNA	2008	9	TS
25	HANNA	2008	9	TS	CHARLEY	1986	8	TS

Year and Month note the time of TC's closest approach to Delmarva. Status represents the most common value of USA_STATUS attribute in the IBTrACS database while the TC is within the 750 km buffer. EX, Extratropical; HU, Hurricane; TS, Tropical Storm; TD, Tropical Depression; SS, Subtropical Storm; DB, Disturbance. Refer to the IBTrACS Version 4 Technical Documentation for more details.

a Chesapeake Bay flood event. Hurricanes Hugo (1989), Fran (1996), and Hanna (2008) produced higher surges in upper bays than lower bay regions (**Supplementary Figure 8**), whereas Hurricane Gloria (1985), Not Named (1991), and Hurricane Irene (2011) produced higher surges in the lower bay regions. (Note that Not Named (1991) may be better known as the Halloween Blizzard of 1991 or The Perfect Storm of 1991).

Spatial Patterns of Skew Surge

Analogous to grouping tide gauges based on their cross-correlations of SSI, the Delmarva TCs were grouped using the K-Means clustering algorithm based on their spatial pattern and magnitude of SSI (i.e., surge profile) throughout the study region. Only Delmarva TCs with valid surge data at all 12 tide gauges ($N = 93$) were used as input to the clustering algorithm. Numbers of clusters from 3 to 15 were tested with 13 clusters ultimately chosen based on the cubic clustering criterion score. Each cluster of TCs represents a unique combination of magnitude and pattern of variability of SSI. Six of the clusters contained a single TC and another contained only two TCs; these were typically the TCs with largest SSI magnitude or differences between upper and lower bays. Individual clusters with similar profiles were manually plotted together into a series of six panels. **Figures 9A–F** displays surge profiles from all Delmarva TCs used in the cluster analysis, with like colors in each panel representing individual clusters. Storm tracks associated with the TCs in each of the clusters were also mapped accordingly in six panels in **Figures 10A–F**. Although the grouping of clusters into each panel was a manual process done primarily for visualization purposes, the grouping in panel A was based on SSI magnitude whereas the grouping in panels C through F was based on SSI variability.

Clusters 1-2 (panel A) include TCs with the lowest overall SSI magnitude (generally less than 2) and minor spatial variation. Cluster 2 has larger SSI values and is out of phase from cluster 1 in regards of upper vs lower bay SSI values. Cluster 3 (panel B) has slightly larger SSI values but less variation than clusters 1 and 2. Clusters 4–5 (panel C) also have higher SSI values but also more noticeable variation, with larger values in the lower bays than upper bays. Storm tracks for the great majority of these TCs are positioned either to the east of or directly over Delmarva. Two TCs plotted in panel C were exceptions, Dennis (1999) in Cluster 4 and Florence (2018) in cluster 5. Both had close approaches to the south of Delmarva raisin water levels

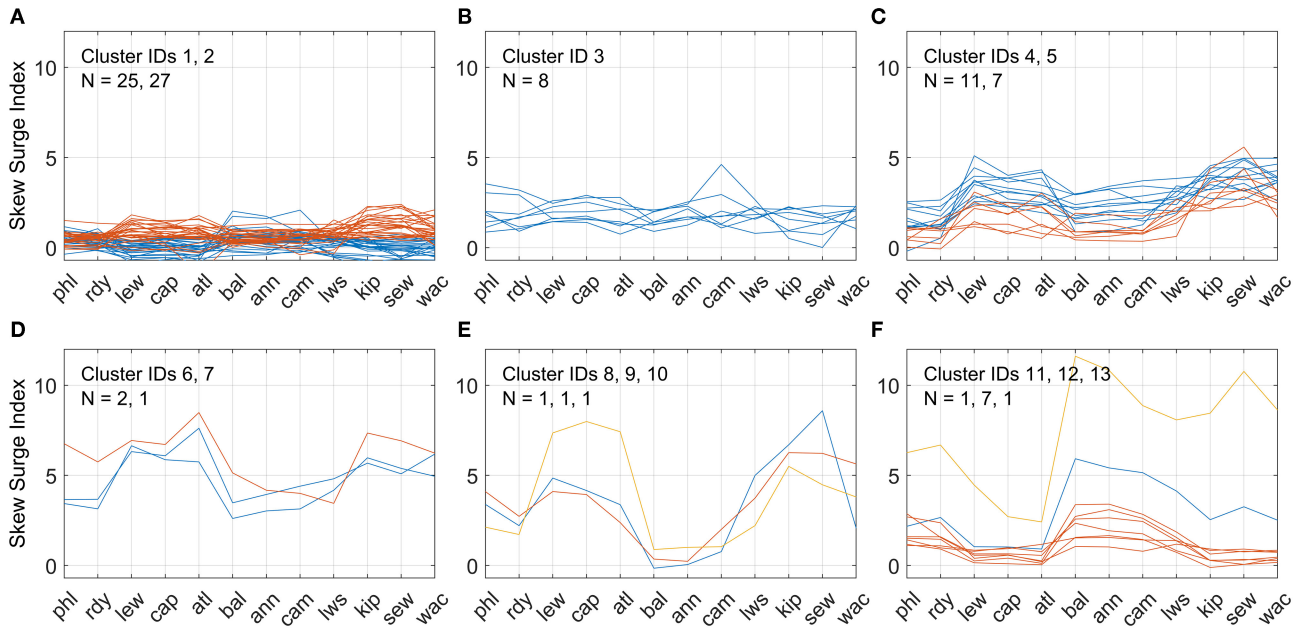

FIGURE 9 | (A–F) Clusters of skew surge index (SSI) spatial profiles of Delmarva tropical cyclones, 1980 – 2019 based on K-Means clustering algorithm. In all, 13 clusters were identified K-Means and manually combined into six panels based on magnitude and spatial variation for visualization purposes. Like colors within each panel represent TCs within a single cluster, with blue, orange, and yellow representing the first, second, and third cluster listed in each panel, respectively. *N* represents the number of TCs per cluster.

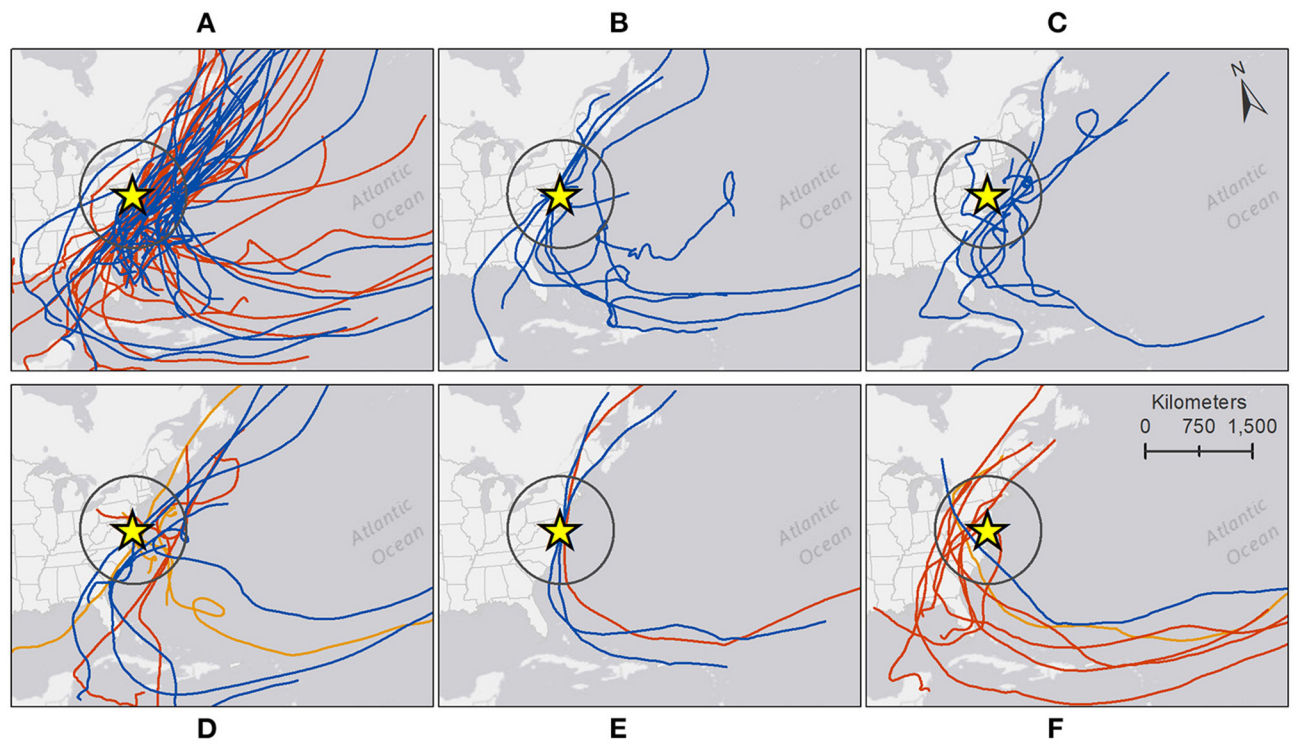

FIGURE 10 | (A–F) Individual tracks of Delmarva tropical cyclones, 1980 – 2019, for each of the clusters identified by the K-Means algorithm on the skew surge index (SSI) profiles. Each map panel corresponds to the same panel of SSI profile plots in **Figure 9**. Colors of each cluster also match those in **Figure 9**.

in the Delaware and Chesapeake Bays before changing direction traveling west/northwest, before curving north and passing the study region on the west side.

Clusters 6–7 (panel D) and 8–10 (panel E) include TCs with large SSI magnitudes in the lower bays and greater variation, with clusters 8–10 showing anomalously low SSI values in the upper Chesapeake Bay. Each of these clusters contained a single TC, except for cluster 6 which contained two TCs. The three TCs in clusters 6–7, Hurricanes Sandy (2012), Wilma (2005), and Not Named (1991), were all large, late-season TCs that transitioned to ETCs and whose tracks were east of Delmarva. Similarly, the three TCs in clusters 8–10, Hurricanes Gloria (1985), Floyd (1999), and Irene (2011), have nearly identical tracks passing directly over Delmarva in a more south-to-south direction. Lastly, clusters 11–13 (panel F) include TCs that show higher SSIs in the upper bays than in the lower bays. Cluster 12 shows the lowest overall SSIs of the three, similar to cluster 1. Tracks of most of these TCs pass to the west of Delmarva, most notably Hurricanes Isabel (2003) and Fran (1996), which produced the largest and second largest SSI, respectively, in the upper Chesapeake Bay.

DISCUSSION

The goal of the current study is to quantify the magnitude and regional differences of skew surge in the Delaware and Chesapeake Bays from tropical cyclones rather than the more common flood events due to extra-tropical cyclones (ETCs). Although future increases are projected in the number of major TCs and TC intensification (Kossin et al., 2017), the exact response of ETC cyclogenesis and frequency under global warming is still unclear. TCs make up a significant portion of the top flood events and receive much attention in research activities, emergency preparation action, and public awareness campaigns. Our focus was not to examine the storm-specific characteristics (e.g., storm size, atmospheric pressure, wind speed and direction) that contribute to storm surge but rather focus on the net effect of all of these, which is the ultimate metric to use from a risk management perspective.

Since skew surge is used in this study rather than maximum NTR, surge values for a particular storm may not match previous reports, such as in NOAA's NHC Tropical Cyclone Reports (National Hurricane Center, 2020). Maximum NTR can be a reliable indicator of storm surge in areas without significant tide-surge interaction, such as open coastal locations on the US Atlantic Coast (Zhang et al., 2000; Bernier and Thompson, 2007; Mawdsley and Haigh, 2016). This was tested on the Delaware and Chesapeake Bay gauges using Quantile-Quantile (Q-Q) plots and two-sample Anderson-Darling tests. These were run on the NTR during four different tidal phases: High Tide (+/- 1.5 h from high tidal peak), Falling Tide, Low Tide (+/- 1.5 h from low tidal peak), and Rising Tide. As examples, **Supplementary Figures 1**, **2** show plots for LEW and PHL. None of the gauges in our study appear to exhibit significant tide-surge interaction, in agreement with previous studies.

Closer inspection of the NTR time series did reveal small oscillations at tidal frequencies. Low-pass filters designed to remove these components could be applied to the NTR time series (Shirahata et al., 2016), however, filters can easily decrease amplitude of the signal and care must be taken to not remove water level oscillations (e.g., surge) caused by TCs moving quickly through the region. Additionally, for TCs with durations of multiple tidal cycles, maximum NTR often occurs over low predicted tide, and not indicative of amount of flooding over the next (or previous) high tide. Hence, maximum NTR is dependent upon numerous factors, and perhaps not as reliable (Batstone et al., 2013) or useful (Williams et al., 2016) an estimate of meteorological component of increased sea level as skew surge.

Figure 6 shows very high correlation coefficients between skew surge and max NTR for Delmarva TCs. High correlations values indicate how well-skew surge and max NTR are linearly related, not necessarily how close they are in magnitude. Across all gauges and Delmarva TCs, maximum NTR is greater than skew surge by 10 cm or more for 29% of events, and by 20 cm or more for 11.5% of events, most prominently at the upper Delaware Bay sites. This difference in timing could be indicative of tide-surge interactions or other phenomena occurring in this region but is beyond the scope of this paper. Large differences at large surge levels can lead to misinterpretation and potential overestimation of the amount of flooding from major, usually well-publicized, storms.

Due to the geomorphology and bathymetry of the region, tides are higher and exhibit wider range in the upper Delaware Bay than in other regions. Delmarva TC storm tides in the upper Delaware Bay were accordingly the highest in the study region (**Table 2**). Interaction of tides and surge, in addition to spatially variable relative sea-level rise, are complex yet play a large role in the amount coastal flooding a location observes. Detrending and normalizing storm tides and skew surges removes this influence, allowing for a better comparison of gauges over space and of storms over time. Gauges in the upper Delaware Bay resulted in the lowest STI, potentially meaning that the relative coastal flooding due to TCs is least in the upper Delaware Bay and most in the lower Chesapeake Bay. Likewise, STI shows a strong negative correlation to MHHW, decreasing relative influence of TC flooding in areas of higher tides.

The same concept holds true for storm surge. Results in **Tables 2**, **4** show that the Chesapeake Bay regions experience higher relative surges from TCs than the Delaware Bay. Likewise, the lower bays experience higher relative surges from TCs than do the upper bays. Relative influence of TC surge is expected to increase toward the south and east. TCs that stay just offshore, keeping Delmarva sites in the front left quadrant, bring strong southeast and east winds as they travel north/northeast direction, pushing water directly on the ocean coast an into the bays. As they pass, northwest winds that parallel the coast induce Ekman transport into the bays, at times competing against the local winds, increasing the surface water levels in the lower bays more than upper bays (Garvine, 1985). Differences in surge among TCs depend on duration, size, and strength of wind field.

Cross-correlations (**Figure 7**) and PCA on SSI demonstrate sub-bay geographic differences. LWS has similar correlations to gauges in both the lower and upper Chesapeake Bay regions but not as strong as among gauges within those regions. Generally, surge at LWS tended to follow the behavior of lower bay gauges during TCs that were east of Delmarva and of upper bay gauges

TABLE 4 | Means and cross-correlations of spatially averaged skew surge index (SSI) of Delmarva tropical cyclones, 1980 – 2019.

Region	Mean SSI	Cross-Correlation of SSI			
		Delaware Bay Upper	Delaware Bay Lower	Chesapeake Bay Upper	Chesapeake Bay Lower
Upper Delaware	1.08	1.00	0.68	0.79	0.59
Lower Delaware	1.39	0.68	1.00	0.56	0.88
Upper Chesapeake	1.19	0.79	0.56	1.00	0.49
Lower Chesapeake	1.70	0.59	0.88	0.49	1.00

All correlations statistically significant at the 0.01 level.

during TCs that were west of Delmarva, although the magnitude was usually somewhere between. The central location of LWS makes it valuable for assessing surge in the Chesapeake Bay albeit problematic if assigned to either an upper or lower bay region.

Table 4 shows that lower regions in each bay respond to TCs more similarly to each other than to their respective upper regions. The distance between the bay inlets is relatively small compared to the size of the TC and their tracks, and drivers such as wind direction or Ekman transport would impact these areas similarly. This may run counter to public perception since many outreach and planning activities tend to focus on The Delaware and Chesapeake Bays separately. The Bays fall into separate NWS Forecast Offices, who are responsible for sending out real-time weather and coastal flood advisories, and have separate state initiatives and SLR planning committees (Callahan et al., 2017; Boesch et al., 2018). This is understandable considering the funding sources and political directives, however, perhaps the results of this study show that regions of each bay could be addressed collectively regarding surge risk hazards.

The World Meteorological Organization states that hurricanes are named to help with "disaster risk awareness, preparedness, management, and reduction," and names are retired "due to sensitivity" from the destruction they cause (World Meteorological Organization, 2020). Ranking of storms can be looked upon in a similar vein by meteorologists and emergency managers, recalling local knowledge from pervious experiences to help in outreach. As well, it could provide scientists and planners analog storms with similar surge potential to compare against. Separate ranking by geographic region helps focus preparedness efforts.

Highly ranked storms in both bays include Hurricanes Isabel (2003), Wilma (2005), Ernesto (2006), Sandy (2012), and Not Named (1991). All of these were very large, strong storms with wide reaching wind fields that transitioned to extratropical near Delmarva. The high wind speeds and longer duration of swell directed at Delmarva contributed to the extreme surge levels from these storms. Surge from Isabel (2003) was an extreme outlier in the Chesapeake Bay compared to the other TCs primary due to its linear track, traveling southeast to northwest while keeping the Chesapeake in its right-front quadrant, continually pushing water up the bay (National Hurricane Center, 2014). Gloria (1985) would be Isabel's counterpart for the Delaware Bay, although its fast speed and track to the east of Delmarva limited its most severe impacts to the lower bay region.

Negative correlations between SSI and TC minimum distance to Delmarva were consistent across all sites, as expected (**Supplementary Figure 5**). However, the significant amount of scatter and outliers prohibit a direct quantifiable relationship. Results from the clustering analysis show similar information. For example, TC tracks in clusters 1–2 and 4–5 are indistinguishable yet those TCs produce varying magnitudes and spatial patterns of SSI. Likewise, TC tracks in clusters 3 and 8–10 are all positioned nearly directly over Delmarva, yet TCs in cluster 3 produce only minimal variation whereas TCs in clusters 8–10 produced very large variations.

Although the clustering was based solely on surge profiles, some similarities in tracks do exist. A large majority of the TC tracks were positioned directly over or just offshore to the east of Delmarva. The most common surge profile exhibits larger SSI values in the lower bays than upper bays ($N = 51$, from clusters 2, 4, 5, 6, 7, 8, 9, and 10), followed by larger SSI values in upper bays than lower bays ($N = 34$, from clusters 1, 11, 12, and 13) and minimal difference between the upper and lower bays ($N = 8$, from cluster 3). TCs that produce the largest SSI in the upper Chesapeake Bay pass by Delmarva to the west, whereas TCs that produce very low SSI values in the upper Chesapeake Bay yet large SSI values in the lower Chesapeake Bay pass directly over Delmarva. Generally, these results may imply that although distance and location of storm track may play a role, other storm-related factors are also involved in producing the observed surge amount a particular site may receive. Results of the current work could be extended with additional TC data (e.g., size, wind speed, duration, direction of travel) and a more rigorous statistical treatment.

In order to generalize some of the conclusions in this paper, a similar methodology could be applied to extratropical flood events at the same tide gauge locations. As well, a more thorough statistical analysis of surge magnitudes and spatial variation compared to specific TC meteorological characteristics and TC track location would quantify the relative contributions of the major drivers of TC-caused surge in the Delaware and Chesapeake Bays. Tropical cyclones, like all coastal storms, are multi-hazard weather events, with storm surge the most destructive and lethal hazard. In a changing environment, there continues to be a need to improve storm surge forecasting and implement strategies to minimize the damage of coastal flooding (Council on Climate Preparedness Resilience, 2016; Rahmstorf, 2017; Chippy and Jawahar, 2018). Results from this analysis

can provide insight on the potential regional impacts of coastal flooding from tropical cyclones in the Mid-Atlantic region.

BENEFIT OF RESEARCH TO SCIENTIFIC COMMUNITY

This research will develop skew surge values for tropical storms over the past 40 years in the Mid-Atlantic. It will also summarize skew surge over regions of multiple tide gauges and investigate geographic difference among surge level and storm tracks. Skew surge is not a commonly used estimate of surge although it has been gaining acceptance and is well-positioned for separating the meteorological and tidal contributions to flood events. Impacts of coastal flooding from tropical storms are not commonly studied in the Mid-Atlantic, although it is highly developed and critical coastal region experiencing high rates of sea level rise. With the prospect of increased severe tropical cyclones in the future, a better understanding of the surge produced by these systems, both in spatial variability and magnitude, is important for developing mitigation and adaptation strategies to protect against these hazards.

DATA AVAILABILITY STATEMENT

The dataset of Delmarva Tropical Cyclone skew surges and storm tides generated for this study can be found at the figshare repository: https://figshare.com/account/home#/projects/89696.

AUTHOR CONTRIBUTIONS

JC, DL, and CC conceived the idea of investigating storm surge from tropical cyclones in the U.S. Mid-Atlantic. JC and DL designed the analysis framework. JC obtained all of the necessary data, performed the statistical analysis, and wrote the manuscript. DL and CC helped with results interpretation and manuscript revisions. CC contributed to the design of graphics and generated all maps. All authors contributed to the article and approved the submitted version.

ACKNOWLEDGMENTS

The authors would like to thank the National Oceanic and Atmospheric Administration for providing a large database of water level data for public use. The authors would also like to thank Dr. Daniel L. Codiga, Graduate School of Oceanography, University of Rhode Island, and Dr. Richard Pawlowicz, Department of Earth, Ocean and Atmospheric Sciences, University of British Columbia, for their help in understanding the operation of U-Tide and performing harmonic analysis.

SUPPLEMENTARY MATERIAL

The Supplementary Material for this article can be found online at: https://www.frontiersin.org/articles/10.3389/fclim.2021.610062/full#supplementary-material

REFERENCES

Batstone, C., Lawless, M., Tawn, J., Horsburgh, K., Blackman, D., McMillan, A., et al. (2013). A UK best-practice approach for extreme sea-level analysis along complex topographic coastlines. *Ocean Eng.* 71, 28–39. doi: 10.1016/j.oceaneng.2013.02.003

Bernhardt, J. E., and DeGaetano, A. T. (2012). Meteorological factors affecting the speed of movement and related impacts of extratropical cyclones along the U.S. east coast. *Nat. Hazard.* 61, 1463–1472. doi: 10.1007/s11069-011-0078-0

Bernier, N. B., and Thompson, K. R. (2007). Tide-surge interaction off the east coast of Canada and northeastern United States. *J. Geophys. Res.* 112:C06008. doi: 10.1029/2006JC003793

Blake, E. S., and Gibney, E. J. (2011). *The Deadliest, Costliest, and Most Intense United States Tropical Cyclones From 1851to 2010 (and Other Frequently Requested Hurricane Facts). NOAA Technical Memorandum NWS NHC-6*, (Miami FL: NOAA National Hurricane Center). 49.

Boesch, D. F., Boicourt, W. C., Cullather, R. I., Ezer, T., Galloway, G. E. Jr., Johnson, Z. P., et al. (2018). *Sea-Level Rise: Projections for Maryland 2018.* (Cambridge, MD: University of Maryland Center for Environmental Science) 27.

Boon, J. D., Mitchell, M., Loftis, J. D., and Malmquist, D. L. (2018). *Anthropogenic Sea Level Change: A History of Recent Trends Observed in the U.S. East, Gulf and West Coast Regions*, Special Report No. 467 in Applied Marine Science and Ocean Engineering, prepared by Virginia Institute of Marine Science, VA, 76.

Booth, J. F., Rider, H. E., and Kushnir, Y. (2016). Comparing hurricane and extratropical storm surge for the Mid-Atlantic and Northeast Coast of the United States for 1979–2013. *Environ. Res. Lett.* 11:94004. doi: 10.1088/1748-9326/11/9/094004

Callahan, J. A., Horton, B. P., Nikitina, D. L., Sommerfield, C. K., McKenna, T. E., and Swallow, D. (2017). *Recommendation of Sea-Level Rise Planning Scenarios for Delaware: Technical Report, prepared for Delaware Department of Natural Resources and Environmental Control (DNREC) Delaware Coastal Programs* (Delaware Dept of Natural Resources and Environmental Control), 116.

Chesapeake Bay Program (2020). *State of the Chesapeake*. Available online at: https://www.chesapeakebay.net/state (accessed August 18, 2020).

Chippy, M. R., and Jawahar, S. S. (2018). Storm surge and its effect-a review on disaster management in coastal areas. *Civil Eng. Res. J.* 4:555649. doi: 10.19080/CERJ.2018.04.555649

Codiga, D. L. (2011). *Unified Tidal Analysis and Prediction Using the UTide Matlab Functions. GSO Technical Report 2011-01*. South Kingstown, RI: Graduate School of Oceanography, University of Rhode Island, 60.

Colle, B. A., Booth, J. F., and Chang, E. K. M. (2015). A review of historical and future changes of extratropical cyclones and associated impacts along the US East Coast. *Curr. Climate Change Rep.* 1, 125–143. doi: 10.1007/s40641-015-0013-7

Council on Climate Preparedness and Resilience (2016). *Opportunities to Enhance the Nation's Resilience to Climate Change* (Washington, DC), 46.

Delaware Emergency Management Agency (2018). *State of Delaware All-Hazard Mitigation Plan* (Dover, DE), 308.

Dolan, R., and Davis, W. E. (1992). An intensity scale for Atlantic coast Northeast storms. *J. Coastal Res.* 8, 840–853.

Eagleson, P. S., and Ippen, A. T. (1966). *Estuary and Coastline Hydrodynamics*. New York, NY: McGraw-Hill Book Co.

Ellis, J. T., and Sherman, D. J. (2015). "Perspectives on coastal and marine hazards and disasters," in *Coastal Marine Hazards, Risks, and Disasters,* eds J. F. Shroder, J. T. Ellis, and D. J. Sherman (Elsevier). doi: 10.1016/B978-0-12-396483-0.00001-7

Elsner, J. B., and Kara, A. B. (1999). *Hurricanes of the North Atlantic: Climate and Society*. New York, NY: Oxford University Press.

Federal Emergency Management Agency (2013). *Region III: Coastal Analysis and Mapping. Region 3 Storm Surge Study*. Available online at: https://sites.google.com/site/r3coastal/home/storm-surge-study (accessed April 9, 2020).

Garvine, R. W. (1985). A simple model of estuarine subtidal fluctuations forced by local and remote wind stress. *J. Geogr. Oceans* 90, 11945–11948. doi: 10.1029/JC090iC06p11945

Harleman, D. R. F. (1966). "Real estuaries, in estuary and coastline hydrodynamics," in *Tidal Dynamics in Estuaries: Real Estuaries. Estuary and Coastline Hydrodynamics*, ed A. T. Ippen (New York, NY: McGraw-Hill), 522–545.

Harris, D. L. (1991). "Reproducibility of the harmonic constants. Tidal Hydrodynamics," in ed B. P. Parker (Hoboken, NJ: John Wiley and Sons), 753–771.

Hirsch, M. E., A. T., and Degaetano, and, S. J., Colucci (2001). An east coast winter storm climatology. *J. Climate* 14, 882–899. doi: 10.1175/1520-0442(2001)014<0882:AECWSC>2.0.CO;2

Holgate, S. J., Matthews, A., Woodworth, P. L., Rickards, L. J., Tamisiea, M. E., Bradshaw, E., et al. (2013). New data systems and products at the permanent service for mean sea level. *J. Coastal Res.* 29, 493–504. doi: 10.2112/JCOASTRES-D-12-00175.1

Jay, A., D. R., Reidmiller, C. W., Avery, D., Barrie, B. J., DeAngelo, A., Dave, M., et al. (2018). "Overview," in *Impacts, Risks, and Adaptation in the United States: Fourth National Climate Assessment, Volume II,* eds D. R. Reidmiller, C. W. Avery, D. R. Easterling, K. E. Kunkel, K. L. M. Lewis, T. K. Maycock, et al. (Washington, DC: U.S. Global Change Research Program), 33–71.

Keim, B., Muller, R., and Stone, G. (2007). Spatiotemporal patterns and return periods of tropical storm and hurricane strikes from Texas to Maine. *J. Climate* 20, 3498–3509. doi: 10.1175/JCLI4187.1

Knapp, K. R., Diamond, H. J., Kossin, J. P., Kruk, M. C., and Schreck, C. J. (2018). International Best Track Archive for Climate Stewardship (IBTrACS) Project, Version 4. [North Atlantic Basin since 1980]. NOAA National Centers for Environmental Information. Non-government domain (accessed May 18, 2020).

Knapp, K. R., Kruk, M. C., Levinson, D. H., Diamond, H. J., and Neumann, C. J. (2010). The International Best Track Archive for Climate Stewardship (IBTrACS): unifying tropical cyclone best track data. *Bullet. Am. Meteorol. Soc.* 91, 363–376. doi: 10.1175/2009BAMS2755.1

Knutson, T., Camargo, S. J., Chan, J. C. L., Emanuel, K., Ho, C.-H., Kossin, J., et al. (2020). Tropical cyclones and climate change assessment: part II: projected response to anthropogenic warming. *Bullet. Am. Meteorol. Soc.* 1, E303–E322. doi: 10.1175/BAMS-D-18-0194.1

Knutson, T., Camargo, S. J., Chan, J. C. L., Emanuel, K., Ho, C.-H., Kossin, J.ames, Mohapatra, M., et al. (2019). Tropical cyclones and climate change assessment: part I: detection and attribution. *Bullet. Am. Meteorol. Soc.* 1, 1987–2007. doi: 10.1175/BAMS-D-18-0189.1

Kopp, R. E. (2013). Does the mid-Atlantic United States sea level acceleration hot spot reflect ocean dynamic variability? *Geophys. Res. Lett.* 40, 3981–3985. doi: 10.1002/grl.50781

Kossin, J. P. (2018). A global slowdown of tropical-cyclone translation speed. *Nature* 558:104–107. doi: 10.1038/s41586-018-0158-3

Kossin, J. P., Hall, T., Knutson, T., Kunkel, K. E., Trapp, R. J., Waliser, D. E., et al. (2017). "Extreme storms," in *Climate Science Special Report: Fourth National Climate Assessment, Volume I*, eds D. J. Wuebbles, D. W. Fahey, K. A. Hibbard, D. J. Dokken, B. C. Stewart, and T. K. Maycock (Washington, DC: U.S. Global Change Research Program), 257–276. doi: 10.7930/J07S7KXX

Landsea, C. W., and Franklin, J. L. (2013). Atlantic hurricane database uncertainty and presentation of a new database format. *Monthly Weather Rev.* 141, 3576–3592. doi: 10.1175/MWR-D-12-00254.1

Leathers, D. J., Kluck, D. R., and Kroczynski, S. (1998). The severe flooding event of January 1996 across North-Central Pennsylvania. *Bullet. Am. Meteorol. Soc.* 79, 785–797. doi: 10.1175/1520-0477(1998)079<0785:TSFEOJ>2.0.CO;2

Lee, S. B., Li, M., and Zhang, F. (2017). Impact of sea level rise on tidal range in Chesapeake and Delaware Bays. *J. Geophys. Res. Oceans* 122, 3917–3938. doi: 10.1002/2016JC012597

Li, M., Zhang, F., Barnes, S., and Wang, X. (2020). Assessing storm surge impacts on coastal inundation due to climate change: case studies of Baltimore and Dorchester County in Maryland. *Nat. Hazard.* 103, 2561–2588. doi: 10.1007/s11069-020-04096-4

Marcos, M., Calafat, F. M., Berihuete, A., and Dangendorf, S. (2015). Long-term variations in global sea level extremes. *J. Geophys. Res. Oceans* 120, 8115–8134. doi: 10.1002/2015JC011173

Mawdsley, R. J., and Haigh, I. D. (2016). Spatial and temporal variability and long-term trends in skew surges globally. *Front. Marine Sci.* 3, 1–29. doi: 10.3389/fmars.2016.00029

McAdie, C. J., Landsea, C. W., Neumann, C. J., David, J. E., Blake, E. S., and Hammer, G. R. (2009). "Tropical cyclones of the North Atlantic Ocean, 1851–2006: with 2007 and 2008 Track Maps Included," in *National Oceanic and Atmospheric Administration Historical Climatology Series 6-2*, 243.

Merrifield, M. A., Genz, A. S., Kontoes, C. P., and Marra, J. J. (2013). Annual maximum water levels from tide gauges: contributing factors and geographic patterns. *J. Geophys. Res. Oceans* 118, 2535–2546. doi: 10.1002/jgrc.20173

Moftakhari, H. R., AghaKouchak, A., Sanders, B. F., Feldman, D. L., Sweet, W., Matthew, R. A., et al. (2015). Increased nuisance flooding along the coasts of the United States due to sea level rise: past and future, *Geophys. Res. Lett.* 42, 9846–9852. doi: 10.1002/2015GL066072

Muller, R. A., and Stone, G. W. (2001). A climatology of tropical storm and hurricane strikes to enhance vulnerability prediction for the Southeast U.S. coast. *J. Coastal Res.* 17, 9949–9956. Available online at: https://journals.flvc.org/jcr/article/view/81519

Murakami, H., Delworth, T. L., Cooke, W. F., Zhao, M., Xiang, B., and Hsu, P. C. (2020). Detected climatic change in global distribution of tropical cyclones. *Proc. Natl. Acad. Sci. U. S. A.* 117, 10706–10714. doi: 10.1073/pnas.1922500117

National Hurricane Center (2014). *NOAA, Tropical Cyclone Report for Hurricane Isabel* (Miami, FL: NOAA National Hurricane Center), 30.

National Hurricane Center (2019). *NOAA, Storm Surge Overview*. Available online at: https://www.nhc.noaa.gov/surge/ (accessed January 10, 2019).

National Hurricane Center (2020). *NOAA, Tropical Cyclone Reports*. Available online at: https://www.nhc.noaa.gov/data/tcr/ (accessed May 20, 2020).

Needham, H. F., Keim, B. D., and Sathiaraj, D. (2015). A review of tropical cyclone-generated storm surges: global data sources, observations, and impacts. *Rev. Geophys.* 53, 545–591. doi: 10.1002/2014RG000477

NOAA (2019). *NOAA's Center for Operational Oceanographic Products and Services, User Services Team*.

NOAA National Centers for Environmental Information (2020). *U. S. Billion-Dollar Weather and Climate Disasters*.

NOAA National Ocean Service Center for Operational Oceanographic Products and Services (2020a). *Sea Level Trends*. Available online at: https://tidesandcurrents.noaa.gov/sltrends/ (accessed August 18, 2020).

NOAA National Ocean Service Center for Operational Oceanographic Products and Services (2020b). *API for Data Retrieval*. Available online at: https://api.tidesandcurrents.noaa.gov/api/prod/ (accessed April 9, 2020).

NOAA National Ocean Service Center for Operational Oceanographic Products and Services (2020c). *NOAA Tide Predictions*. Available online at: https://tidesandcurrents.noaa.gov/tide_predictions.html (accessed April 9, 2020).

NOAA National Ocean Service National Water Level Observation Network. (2020). *NOAA National Ocean Service National Water Level Observation Network*. Available online at: https://www.tidesandcurrents.noaa.gov/nwlon.html (accessed August 18, 2020).

NOAA National Ocean Service Physical Oceanographic Real-Time System. (2020). *NOAA National Ocean Service Physical Oceanographic Real-Time System*. Available online at: https://tidesandcurrents.noaa.gov/ports.html (accessed August 18, 2020).

Patrick, R. (1994). *Rivers of the United States, Volume 1: Estuaries*. Hoboken, NJ: John Wiley and Sons, 1994. ISBN: 978-0-471-30345-9

Pugh, D., and Woodworth, P. (2014). *Sea-Level Science: Understanding Tides, Surges, Tsunamis and Mean Sea-Level Changes*. Cambridge: Cambridge University Press. doi: 10.1017/CBO9781139235778

Rahmstorf, S. (2017). Rising hazard of storm-surge flooding. *Proc. Natl. Acad. Sci. Commentary*. 114, 11806–11808. doi: 10.1073/pnas.1715895114

Rappaport, E. (2014). Fatalities in the United States from Atlantic tropical cyclones new data and interpretation. *Bullet. Am. Meteorol. Soc. Insights Innov.* 2014, 341–346. doi: 10.1175/BAMS-D-12-00074.1

Rashid, M., Wahl, T., Chambers, D., Calafat, F., and Sweet, W. (2019). An extreme sea level indicator for the contiguous United States coastline. *Sci. Data* 6:326. doi: 10.1038/s41597-019-0333-x

Ritterbush, J. (2012). US daily weather maps project. *Ref. Rev*. 26, 39–39. doi: 10.1108/09504121211195333

Ross, A. C., Najjar, R. G., Li, M., Lee, S. B., Zhang, F., and Liu, W. (2017). Fingerprints of sea level rise on changing tides in the Chesapeake and Delaware Bays. *J. Geophys. Res. Oceans* 122, 8102–8125. doi: 10.1002/2017JC012887

Salehi, M. (2018). Storm surge and wave impact of low-probability hurricanes on the lower delaware bay—calibration and application. *J. Mar. Sci. Eng*. 6:54. doi: 10.3390/jmse6020054

Sallenger, A. H., Doran, K. S., and Howd, P. A. (2012). Hotspot of accelerated sea-level rise on the Atlantic coast of North America. *Nat. Climate Change* 2, 884–888, doi: 10.1038/nclimate1597

Sanchez, J. R., G., Kauffman, K., and Reavy, A., Homsey (2012). *"Chapter 1.7 - Natural Capital Value" in the Technical Report for the Delaware Estuary and Basin. Partnership for the Delaware Estuary. PDE Report No*, (Partnership for the Delaware Estuary). *17-07*, 70–75. Available online at: https://s3.amazonaws.com/delawareestuary/TREB+douments/TREB+2017+complete.pdf

Shirahata, K., Yoshimoto, S., Tsuchihara, T., and Ishida, S. (2016). Digital filters to eliminate or separate tidal components in groundwater observation time-series data. *Jap. Agri. Res. Quart.* 50, 241–252. doi: 10.6090/jarq.50.241

Simpson, R. H., and Lawrence, M. (1971). *Atlantic Hurricane Frequencies Along the United States Coastline. NOAA Tech. Memo. NWS-SR-58* (Fort Worth, TX: NOAA Southern Region Headquarters), 14.

Smith, A. B., and Katz, R. W. (2013). US billion-dollar weather and climate disasters: data sources, trends, accuracy and biases. *Nat. Hazard*. 67, 387–410. doi: 10.1007/s11069-013-0566-5

Spicer, P., Huguenard, K., Ross, L., and Rickard, L. N. (2019). High-frequency tide-surge-river interaction in estuaries: causes and implications for coastal flooding. *J. Geophys. Res. Oceans* 124:15466. doi: 10.1029/2019JC015466

Stephens, S. A., Bell, R. G., and Haigh, I. D. (2020). Spatial and temporal analysis of extreme storm-tide and skew-surge events around the coastline of New Zealand. *Nat. Hazard. Earth Syst. Sci.* 20, 783–796. doi: 10.5194/nhess-20-783-2020

Strobach, E., Sparling, L. C., Rabenhorst, S. D., and Demoz, B. (2018). Impact of inland terrain on mid-atlantic offshore wind and implications for wind resource assessment: a case study. *J. Appl. Meteorol. Climatol*. 57, 777–796. doi: 10.1175/JAMC-D-17-0143.1

Sweet, W., Dusek, G., Carbin, G., Marra, J., Marcy, D., and Simon, S. (2020). *2019 State of U.S. High Tide Flooding with a 2020 Outlook. NOAA Technical Report NOS CO-OPS 092* (Silver Spring, MD: National Ocean Service Center for Operational Oceanographic Products and Services), 24.

Sweet, W. V., Horton, R. M., Kopp, R. E., LeGrande, A. N., and Romanou, A. (2017a). "Sea level rise," in *Climate Science Special Report: Fourth National Climate Assessment, Volume I*, eds D. J. Wuebbles, D. W. Fahey, K. A. Hibbard, D. J. Dokken, B. C. Stewart, and T. K. Maycock (Washington, DC: U.S. Global Change Research Program), 333–363. doi: 10.7930/J0VM49F2

Sweet, W. V., Kopp, R. E., Weaver, C. P., Obeysekera, J., Horton, R. M., Thieler, E. R., et al. (2017b). *Global and Regional Sea Level Rise Scenarios for the United States. NOAA Technical Report NOS CO-OPS* (Silver Spring, MD: National Ocean Service Center for Operational Oceanographic Products and Services) 083, 75.

Sweet, W. V., Park, J., Marra, J. J., Zervas, C. E., and Gill, S. (2014). *Sea Level Rise and Nuisance Flood Frequency Changes around the United States. NOAA Technical Report NOS CO-OPS* (Silver Spring, MD: National Ocean Service Center for Operational Oceanographic Products and Services) 073, 66.

Tebaldi, C., Strauss, B. H., and Zervas, C. E. (2012). Modeling sea level rise impacts on storm surges along US coasts, *Environ. Res. Lett*. 7:014032. doi: 10.1088/1748-9326/7/1/014032

US Army Corps of Engineers (2014). *North Atlantic Coast Comprehensive Study (NACCS), State Chapter D-7: State of Delaware,* 142. Available online at: https://www.nad.usace.army.mil/CompStudy/

Weinkle, J., Landsea, C., Collins, D., Musulin, R., Crompton, R. P., Klotzbach, P. K., and Pielke, R. Jr (2018). Normalized hurricane damage in the continental United States 1900–2017. *Nat. Sustainabil*. 165:2. doi: 10.1038/s41893-018-0165-2

Wilkerson, C. N., and Brubaker, J. (2013). "Analysis of extreme water levels in the lower chesapeake bay," in *Proceedings of the 2012 OCEANS Conference*. Hampton Roads, VA. doi: 10.1109/OCEANS.2012.6405098

Williams, J., Horsburgh, K. J., Williams, J. A., and Proctor, R. N. F. (2016). Tide and skew surge independence: new insights for flood risk. *Geophys. Res. Lett*. 43, 6410–6417. doi: 10.1002/2016GL069522

Wong, K.–C., and Münchow, A. (1995). Buoyancy forced interaction between estuary and inner shelf: observation. *Continental Shelf Res.* 15, 59–88. doi: 10.1016/0278-4343(94)P1813-Q

World Meteorological Organization (2020). *Tropical Cyclone Naming.* Available online at: https://public.wmo.int/en/our-mandate/focus-areas/natural-hazards-and-disaster-risk-reduction/tropical-cyclones/Naming (accessed August 15, 2020).

Xie, L., Yan, T., Pietrafesa, L. J., Morrison, J. M., and Karl, T. (2005). Climatology and interannual variability of North Atlantic hurricane tracks. *J. Climate* 18, 5370–5381. doi: 10.1175/JCLI3560.1

Xiong, Y., and Berger, C. R. (2010). Chesapeake bay tidal characteristics. *J. Water Resourc. Protect*. 2, 619–628. doi: 10.4236/jwarp.2010.27071

Yang, H., Lohmann, G., Lu, J., Gowan, E. J., Shi, X., Liu, J., et al. (2020). Tropical expansion driven by poleward advancing mid-latitude meridional temperature gradients. *JGR Atmos*. 2020:5042. doi: 10.5194/egusphere-egu2020-5042

Zhang, K., Douglas, B. C., and Leatherman, S. P. (2000). Twentieth-century storm activity along the U.S. East Coast. *J. Climate* 13, 1748–1761. doi: 10.1175/1520-0442(2000)013<1748:TCSAAT>2.0.CO;2

Zhong, L., and Li, M. (2006). Tidal energy fluxes and dissipation in the chesapeake bay. *Continental Shelf Res*. 26, 752–770. doi: 10.1016/j.csr.2006.02.006

Conflict of Interest: The authors declare that the research was conducted in the absence of any commercial or financial relationships that could be construed as a potential conflict of interest.

Publisher's Note: All claims expressed in this article are solely those of the authors and do not necessarily represent those of their affiliated organizations, or those of the publisher, the editors and the reviewers. Any product that may be evaluated in this article, or claim that may be made by its manufacturer, is not guaranteed or endorsed by the publisher.

GLOSSARY

NOAA Tide Gauge Locations, Philadelphia (PHL), Reedy Point (RDY), Lewes (LEW), Cape May (CAP), Atlantic City (ATL), Baltimore (BAL), Annapolis (ANN), Cambridge (CAM), Lewisetta (LWS), Kiptopeke (KIP), Sewells Point (SEW), Wachapreague (WAC); **CO-OPS**, NOAA Center for Operational Oceanographic Products and Services; **DEMA**, Delaware Emergency Management Agency; **ETC**, Extratropical Cyclone (sometimes called mid-latitude cyclones); **FEMA**, Federal Emergency Management Agency; **HURDAT2**, Atlantic Hurricane Database (HURDAT2); **IBTrACS**, International Best Track Archive for Climate Stewardship; **MHHW**, Mean Higher-High Water tidal datum; **MSL**, Mean Sea Level tidal datum; **NAVD88**, North American Vertical Datum 1988; **NCEI**, NOAA National Centers for Environmental Information; **NHC**, NOAA National Hurricane Center (division of the National Weather Service); **NOAA**, National Oceanic and Atmospheric Administration; **NOS**, NOAA National Ocean Service; **NTDE**, National Tidal Datum Epoch; **NTR**, Non-tidal residual; **NWLON**, NOAA NOS National Water Level Observation Network; PORTS, NOAA National Ocean Service Physical Oceanographic Real-Time System; **SSI**, Storm Surge Index; **SST**, Sea Surface Temperature; **STI**, Storm Tide Index; SURGEDAT, A database specifically designed to store storm surge data with 700 tropical surge events around the world and more than 8,000 unique tropical high water marks along the U.S. Gulf and Atlantic Coasts since 1880; **TC**, Tropical Cyclone; **TWL**, Total water level; **USACE**, US Army Corps of Engineers; **WMO**, World Meteorological Organization.

frontiers in Climate

ORIGINAL RESEARCH
published: 05 November 2021
doi: 10.3389/fclim.2021.684834

Estimation of Return Levels for Extreme Skew Surge Coastal Flooding Events in the Delaware and Chesapeake Bays for 1980–2019

John A. Callahan[1]* *and Daniel J. Leathers*[2]

[1] *Delaware Geological Survey, Department of Geography and Spatial Sciences, University of Delaware, Newark, DE, United States,* [2] *Center for Environmental Monitoring and Analysis, Department of Geography and Spatial Sciences, University of Delaware, Newark, DE, United States*

Extreme storm surges can overwhelm many coastal flooding protection measures in place and cause severe damages to private communities, public infrastructure, and natural ecosystems. In the US Mid-Atlantic, a highly developed and commercially active region, coastal flooding is one of the most significant natural hazards and a year-round threat from both tropical and extra-tropical cyclones. Mean sea levels and high-tide flood frequency has increased significantly in recent years, and major storms are projected to increase into the foreseeable future. We estimate extreme surges using hourly water level data and harmonic analysis for 1980–2019 at 12 NOAA tide gauges in and around the Delaware and Chesapeake Bays. Return levels (RLs) are computed for 1.1, 3, 5, 10, 25, 50, and 100-year return periods using stationary extreme value analysis on detrended skew surges. Two traditional approaches are investigated, Block Maxima fit to General Extreme Value distribution and Points-Over-Threshold fit to Generalized Pareto distribution, although with two important enhancements. First, the GEV *r*-largest order statistics distribution is used; a modified version of the GEV distribution that allows for multiple maximum values per year. Second, a systematic procedure is used to select the optimum value for *r* (for the BM/GEVr approach) and the threshold (for the POT/GP approach) at each tide gauge separately. RLs have similar magnitudes and spatial patterns from both methods, with BM/GEVr resulting in generally larger 100-year and smaller 1.1-year RLs. Maximum values are found at the Lewes (Delaware Bay) and Sewells Point (Chesapeake Bay) tide gauges, both located in the southwest region of their respective bays. Minimum values are found toward the central bay regions. In the Delaware Bay, the POT/GP approach is consistent and results in narrower uncertainty bands whereas the results are mixed for the Chesapeake. Results from this study aim to increase reliability of projections of extreme water levels due to extreme storms and ultimately help in long-term planning of mitigation and implementation of adaptation measures.

Keywords: extreme value analysis, storm surge, coastal flooding, flood risk, Mid-Atlantic, tidal analysis

OPEN ACCESS

Edited by:
Valentina Prigiobbe, Stevens Institute of Technology, United States

Reviewed by:
Brilliant Mareme Petja, Water Research Commission, South Africa
Ming Luo, Sun Yat-sen University, China

***Correspondence:**
John A. Callahan
john.callahan@udel.edu

Specialty section:
This article was submitted to Climate Risk Management, a section of the journal Frontiers in Climate

Received: *24 March 2021*
Accepted: *13 October 2021*
Published: *05 November 2021*

Citation:
Callahan JA and Leathers DJ (2021) Estimation of Return Levels for Extreme Skew Surge Coastal Flooding Events in the Delaware and Chesapeake Bays for 1980–2019. Front. Clim. 3:684834. doi: 10.3389/fclim.2021.684834

INTRODUCTION

Coastal flooding poses the greatest threat to human life and is often the source of much of the damage resulting from the storm surge and waves of coastal weather systems (Blake and Gibney, 2011; Rappaport, 2014; Chippy and Jawahar, 2018; Weinkle et al., 2018). Relative sea-level rise (SLR) rates and high-tide flooding frequency and magnitude along the US East Coast have increased in recent decades and are expected to continue increasing into the near future (Sweet et al., 2017a, 2018; Oppenheimer et al., 2019) with recent studies estimating mean sea levels are rising faster than predicted (Grinsted and Christensen, 2021). The US Mid-Atlantic coast is noted for especially high SLR rates (Sallenger et al., 2012; Kopp, 2013; Boon et al., 2018; Piecuch et al., 2018) and states and counties in this region view coastal flooding as one of their most severe and pervasive natural hazards to prepare for (Callahan et al., 2017; Boesch et al., 2018; Dupigny-Giroux et al., 2018). Increases in sea levels lead directly to higher frequencies of coastal flooding from high tides as well as minor and major coastal storms (Lin et al., 2016; Dahl et al., 2017; Garner et al., 2017; Rahmstorf, 2017; Sweet et al., 2017b; Muis et al., 2020; Taherkhani et al., 2020).

Many of the largest coastal flooding events along the US Mid-Atlantic coast are caused by tropical cyclones (TCs), most notably Hurricanes Isabel in 2003 and Sandy in 2012. For both the US Atlantic and Gulf Coasts, tropical cyclones are the costliest and most damaging weather and climate events (Smith, 2021). Under current global warming scenarios, atmospheric water vapor content and sea-surface temperatures (SSTs) in the North Atlantic Ocean are projected to increase, leading to an increase in the number of severe tropical cyclones, decreases in the forward translational speed, increases in wind speed, and increases in the rate of intensification, especially near the coasts (Kossin et al., 2017; Kossin, 2018; Knutson et al., 2019, 2020; Murakami et al., 2020; Yang et al., 2020; Wang and Toumi, 2021).

Although TCs may gather much of the attention, the threat of major coastal flooding in the region is year-round (Dupigny-Giroux et al., 2018). TCs can account for 40–60% of the top 10 flood events with higher relative percentages in the southern part of the region (Booth et al., 2016; Callahan et al., 2021b), however, the great majority of all coastal flood events, ∼85–90%, in the Mid-Atlantic come from non-tropical weather systems (Callahan et al., 2021b). East Coast winter storms, surface high pressure systems, extratropical cyclones (ETCs), and frontal systems regularly impact the region throughout the year (Hirsch et al., 2001; Thompson et al., 2013). ETCs in the Mid-Atlantic in the winter and spring are often dictated by the relative position of troughs in the westerly polar jet stream, directing low-pressure systems to travel northeastward up the coast over warmer waters, often intensifying into strong nor-Easter storms. The intensity and winds of ETCs, as well as associated beach erosion and other damages due to coastal flooding, are also projected to increase due to climate change, however projections of ETC storm tracks and landfalling TCs due to changing synoptic atmospheric patterns (i.e., "storminess") in the Mid-Atlantic is inconclusive (Hall et al., 2016; Mawdsley and Haigh, 2016; Dupigny-Giroux et al., 2018). Studies have found that US East Coast sea levels vary with synoptic oscillations (Colle et al., 2015; Wahl and Chambers, 2015; Sweet et al., 2020), leading, Rashid Md et al. (2019) to conclude that interannual and multi-decadal variability of extreme storm surge in the Mid-Atlantic was in a transition zone between more clear relationships found in the Northeast and Southeast portions of the US Atlantic Coast.

Water levels in the Delaware and Chesapeake Bays, two of the largest estuaries in the US located in the Mid-Atlantic, have been well monitored for several decades by high-quality tide-gauge networks, well-suited for climate studies (Holgate et al., 2013; Sweet et al., 2017a; NOAA NWLON, 2020; NOAA PORTS, 2020). This highly developed, economically critical region includes many commercial industries, vast amounts of public and private infrastructure, and provides important ecosystem services (Sanchez et al., 2012; Partnership for the Delaware Estuary (PDE), 2017; Chesapeake Bay Program, 2020). Impacts and costs associated with coastal flooding are highly dependent upon both the natural and social vulnerability, the amount of exposure, and adaptation measures in place (Hallegatte et al., 2013; Hinkel et al., 2014). Extreme coastal flooding can overwhelm protections in place and can have profound negative effects in this region, such as saltwater intrusion, loss of wetland forests and low-lying agricultural fields, beach erosion, damage to infrastructure from surge and waves, and flooding of roads and personal property putting human life at risk. Extreme events often include multiple hazards that compound the damage, leading to their net impact to be greater than the sum of its parts (Kopp et al., 2017; Moftakhari et al., 2017).

Estimating frequency and severity of extreme coastal flooding is difficult as, by definition, these events do not occur often. This lack of observational data makes it difficult to develop robust statistical or physical predictive models at the usual level of confidence although planning and design for extremes are essential to avoid the most severe consequences (Walton, 2000; Calafat and Marcos, 2020). Numerous hazard/risk assessments and flood insurance premiums rely on the FEMA 100-year (i.e., 1% annual chance) base flood elevations. However, many local decisions on infrastructure development, major capital investments, and adaptation planning require estimates of extreme flood levels at shorter-term return periods. Construction and maintenance of paved surfaces (10–20 years) and major roadways and bridges (50–70 years or more) for transportation as well as for wastewater treatment plants, residential development,

NOAA Tide Gauge Locations: PHL, Philadelphia; RDY, Reedy Point; LEW, Lewes; CAP, Cape May; ATL, Atlantic City; BAL, Baltimore; ANN, Annapolis; CAM, Cambridge; LWS, Lewisetta; KIP, Kiptopeke; SEW, Sewells Point; WAC, Wachapreague.

Abbreviations: BM, Block Maxima; ETC/TC, extratropical cyclone/tropical cyclone; EVA/EVD, extreme value analysis/extreme value distribution; GEV, generalized extreme value distribution; GEVr, generalized extreme value *r*-largest order distribution; GoF, goodness-of-fit test; GP, Generalized Pareto distribution; HA, harmonic analysis; MLE, maximum likelihood estimation; MHHW, Mean Higher-High Water tidal datum; MSL, Mean Sea Level tidal datum; NAVD88, North American Vertical Datum of 1988; NTDE, National Tidal Datum Epoch; NTR, non-tidal residual; NWLON, NOAA NOS National Water Level Observation Network; PORTS, NOAA National Ocean Service Physical Oceanographic Real-Time System; POT, points over threshold; RL, return level; SLR, sea-level rise; SST, sea surface temperature; SE, standard error; TWL, total water level.

dams/levees, beach replenishment, and wetland restoration are examples of projects in the region that require estimates of return level probabilities at time periods <100 years (DNREC, 2012; Johnson, 2013; Callahan et al., 2017; Delaware Emergency Management Agency (DEMA), 2018).

A common method to estimate the frequency of extremes (i.e., extreme value analysis, or EVA) is by assuming the largest values from an observational record can be modeled by a statistical distribution distinct from the parent distribution. Two families of extreme value distributions have been shown to model extreme values well: the generalized extreme value (GEV) distribution and the Generalized Pareto (GP) distribution (Coles, 2001). The GEV distribution can be fit to the set of maximum values of discrete, non-overlapping blocks within a time series, such as annual maximum values; this is termed the Block Maxima (BM) approach. Data points using this approach are evenly distributed over time, however, non-extreme data points from years with abnormally low values may be forced into the model fit, biasing the results. In contrast, the GP distribution can be fit to the upper tail of the parent distribution, i.e., the set of values that are greater than a pre-selected threshold; this is termed the Points-Over-Threshold (POT) approach. POT is a more natural interpretation of modeling extreme results although the data points may come in temporal clusters and selection of a threshold is subjective. Which approach is considered "better" is non-trivial and dependent upon the parent distribution of the data, time period, sample size, as well as the metric used to measure each model performance (Walton, 2000; Wong et al., 2020).

Numerous studies have performed EVA of total water levels (TWL) using a variety of methods along the US coastlines; a few recent examples can be found in Wahl et al. (2017), Kopp et al. (2019), Oppenheimer et al. (2019), Sweet et al. (2020), and Wong et al. (2020). TWL is an important measure of flooding, however, it is inherently influenced by location-specific tidal ranges and timing of the storm event relative to the phase of the tide whereas storm surge is generally more closely associated with the characteristics of the storm. EVA of storm surge has been performed along the US Atlantic coasts using both the BM/GEV (Grinsted et al., 2012; Sweet et al., 2014) and POT/GP (Bernier and Thompson, 2006; Tebaldi et al., 2012; U. S. Army Corps of Engineers, 2014; Booth et al., 2016; Hall et al., 2016) approaches, or comparing the two methods (Walton, 2000; Wong et al., 2020). EVA methods such as bootstrap simulations (U. S. Army Corps of Engineers, 2014; Garner et al., 2017) and global modeling (Muis et al., 2020) on storm surge have also been investigated.

The aforementioned studies defined storm surge as the maximum difference between TWL and predicted tide, often called the maximum non-tidal residual (NTR). Skew surge, however, is arguably a more accurate measure of storm surge and most appropriate for long-term planning and estimating extreme flood levels. It is defined as the difference between the maximum observed TWL and the maximum predicted tide during a tidal cycle, even if the observed and predicted tidal peaks are offset (i.e., skewed) from each other (Pugh and Woodworth, 2014). It represents the meteorologically-forced increase of water levels due to the net effect of winds, atmospheric pressure (i.e., inverse barometer effect), nearby river discharge, and wave setup, and is more clearly separated from the astronomically forced-tides and potential complex hydrodynamics of tide-surge interactions (Batstone et al., 2013; Mawdsley and Haigh, 2016; Williams et al., 2016; Stephens et al., 2020). Skew surge levels are consistently less than the measures of maximum NTR up to 30% (Hall et al., 2016; Callahan et al., 2021a). There have been few studies of skew surge in the Mid-Atlantic. Mawdsley and Haigh (2016) analyzed long term trends of skew surge and Williams et al. (2016) investigated tide-skew surge independence, but only a few Mid-Atlantic tide gages were included in those analyses and neither performed traditional EVA on skew surges. Callahan et al. (2021a) computed skew surge at the same tide gauges as the current study but only analyzed TCs.

Specific goals of this study are two-fold. First goal is to estimate extreme skew surges within the Delaware and Chesapeake Bays and investigate sub-bay geographic differences. Many tide gauges in these bays started collecting data in the late 1970s and only recently has there been sufficient geographic coverages of gauges with records of at least 40 years of continuous hourly data. Second goal is to compare the two common traditional EVA approaches by implementing objective criteria for model parameter selection. The BM approach is enhanced to incorporate the GEVr distribution, a slightly modified form of the GEV distribution that allows for the inclusion of multiple values (the r-largest orders) per year instead of only the annual maximum (see Skew Surge Return Levels section for details), addressing the primary issue with the traditional BM approach of the low number of data incorporated in the model. It is not the intent of this paper to determine the "best" EVA approach to use in all cases, but rather to better understand the differences between them and to increase reliability of projections of extreme water levels due to storms, ultimately helping in long-term planning of mitigation and implementation of adaptation measures.

MATERIALS AND METHODS

Study Region

The Delmarva Peninsula, located in the US Mid-Atlantic, is flanked on both sides by the Delaware and Chesapeake Bays (**Figure 1**). Tidal water levels and storm surges are influenced by the geomorphological environment, geometry of the coastline, bathymetry, bottom friction/dissipation effects, and reflection of the wave near the head of the bay (Lee et al., 2017). Storm surge is additionally influenced by storm size and direction of travel, duration, atmospheric pressure, wind speed and wind direction relative to the coastline (Ellis and Sherman, 2015). The Delaware Bay has a classical funnel shape, with pockets of deep scour in the wider lower bay, amplifying tidal range and storm surge in the northern regions (Wong and Münchow, 1995; Lee et al., 2017; Ross et al., 2017). The Chesapeake Bay, by contrast is longer, shallower, exhibits a more dendritic tributary landscape, and its lowest tidal ranges are toward the center (Zhong and Li, 2006; Lee et al., 2017; Ross et al., 2017). Although coastal

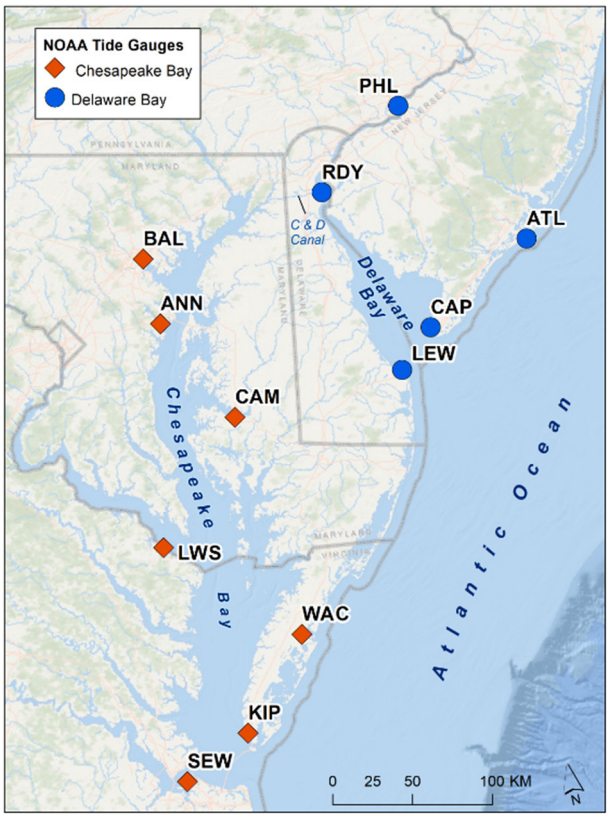

FIGURE 1 | Map of the Delaware and Chesapeake Bays with the 12 NOAA tide gauges used in the current study: PHL, Philadelphia; RDY, Reedy Point; CAP, Cape May; ATL, Atlantic City; BAL, Baltimore; ANN, Annapolis; CAM, Cambridge; LWS, Lewisetta; KIP, Kiptopeke; SEW, Sewells Point; WAC, Wachapreague.

storms threaten the region year-round, mean water levels follow a bimodal seasonal distribution with the maximum in fall (Oct) and secondary maximum in late spring (May–Jun), primarily caused by periodic fluctuations in atmospheric weather systems and coastal water steric effects (NOAA CO-OPS, 2020a). The largest coastal flood events typically occur either during peak hurricane season (Sept–Nov) or during the winter/early spring from nor'easters (Dec–Mar).

Water Level Data and Computation of Skew Surge

Tide gauges selected for this study were limited to NOAA operational tide gauges in and immediately around the Delaware and Chesapeake Bays. Requirements were that each gauge maintained nearly continuous record of hourly water levels for the time period 1980–2019, evenly located throughout the region, a set of harmonic constituents identified for making tidal predictions, and a vertical tidal datum conversion factor to North American Vertical Datum of 1988 (NAVD88). In all, 12 gauges were selected; 5 associated with the Delaware Bay and 7 with the Chesapeake (**Figure 1**; **Table 1**). All selected gauges are part of NOAA NWLON and PORTS networks.

TABLE 1 | Tide gauges used in the current study.

Station	Code	NOAA ID	Bay	Large data gaps	Percent hourly
Philadelphia	PHL	8545240	Delaware	0	99.23%
Reedy Point	RDY	8551910	Delaware	5	95.61%
Lewes	LEW	8557380	Delaware	0	99.73%
Cape May	CAP	8536110	Delaware	2	98.35%
Atlantic City	ATL	8534720	Delaware	2	98.08%
Baltimore	BAL	8574680	Chesapeake	0	99.66%
Annapolis	ANN	8575512	Chesapeake	1	98.70%
Cambridge	CAM	8571892	Chesapeake	1	98.84%
Lewisetta	LWS	8635750	Chesapeake	2	98.72%
Kiptopeke	KIP	8632200	Chesapeake	0	99.78%
Sewells Point	SEW	8638610	Chesapeake	0	100.00%
Wachapreague	WAC	8631044	Chesapeake	6	89.30%

Percent hourly data based upon total number of hours in 1980–2019. Number of large data gaps represent continuous gaps of 745 h (~1 month) or more.

Hourly and High/Low water level data were obtained from the NOAA Center for Operational Oceanographic Products and Services (NOAA CO-OPS, 2020b). High/Low data represent the exact time and magnitude of each Higher-High, High, Low, and Lower-Low tidal peak. Hourly data represent the observed water level on each hour (e.g., 21:00, 22:00). The 40 years of hourly data at each gauge were manually inspected for errors and inconsistencies. A few small data clusters (of 2–16 h) within larger gaps of missing data were removed (on seven occasions across all gauges) and small data gaps of 1–2 h (<10 across all gauges) were filled using linear interpolation. **Table 1** lists the number of data gaps that spanned 745 h (~1 month) or greater as well as the percentage of valid hourly data points used in the analysis. Wachapreague had the largest amount of missing data due to a 2.5-year period (200511–200804) when valid Hourly and High/Low data were unavailable.

Skew surge was computed at each tidal peak over 1980–2019 using modeled predicted time series as reference. Total count was a maximum of 28,231 tidal peaks over the study time period, less any missing data. The observed maximum TWL at each peak was extracted from the High/Low dataset; the maximum hourly value was used if High/Low data were not available. The observed and predicted peaks were aligned within ±3 h of each other, which was extended to ±6 h if no High/Low or TWL peak alignment was found, such as due to prolonged surge; this occurred for <100 peaks over the entire study time period and only for gauges in the Chesapeake Bay.

Predicted tides were generated through Harmonic Analysis (HA) based on hourly water levels. The HA incorporated 37 tidal constituents defined by NOAA for their official tide predictions in this region (NOAA CO-OPS, 2020c) and seven tidal constituents noted by Harris (1991) relevant for the US East Coast. Computations were performed in 1-year increments (3-year increments if greater than 1 month of data were missing within a year). Annual computations minimize timing errors that can lead to the leakage of tidal energy into the

non-tidal residual (Merrifield et al., 2013). It also essentially removes the SLR trend and minimizes inherent constituent biases when computed over long time periods, which could result from changing physiographical environmental conditions (Ross et al., 2017) or from changing seasonal weather patterns that strongly influence the Sa (solar annual) and SSa (solar semi-annual) constituents (NOAA CO-OPS, 2007). More details on the computation of skew surge can be found in Callahan et al. (2021a).

Mean and standard deviation of skew surge, as well as maximum TWL for comparison, were computed to get a sense of the overall parent distribution. To help achieve stationarity and independence of data samples required by EVA, two further processes were performed on each gauge's time series. First, the data were linearly detrended about the 1980–2019 mean (**Table 2**). Second, maximum peaks of skew surge were separated temporally by 30 h to ensure at least two high tides between each extreme event. Specifically, multiple surges above each selected threshold (defined following approaches in Block Maxima/GEVr Approach and Points-Over-Threshold/GP Approach sections) within 30 h of each other were treated as from a single event and only the maximum value was chosen.

Block Maxima/GEVr Approach

The BM approach of modeling extreme values is to select the maximum value within equal, independent blocks of time over the study period, which are usually fit to the GEV distribution. One-year blocks are commonly chosen (as in the current study) since a common ultimate goal is to estimate water levels of multiyear-based return periods for long-term planning purposes. Using the BM approach in this traditional way results in 40 data points over the years 1980–2019. The GEV distribution actually represents the combined generalized form of the Fréchet, Weibull, and Gumbel distributions, which have cumulative distribution functions (CDF) defined by Equation 2.1.

$$F(x|\mu,\sigma,\xi) = Pr(X > x) = \begin{cases} \exp\left[-\left(1+\xi\left(\frac{x-\mu}{\sigma}\right)\right)^{-1/\xi}\right], & \xi \neq 0, \\ \exp\left[-\exp\left(-\left(\frac{x-\mu}{\sigma_\mu}\right)\right)\right], & \xi = 0, \end{cases} \quad (2.1)$$

where the quantity $1 + \xi(x-\mu)/\sigma = \max(1+\xi(x-\mu)/\sigma, 0)$, with location parameter μ, scale parameter $\sigma > 0$, and shape parameter ξ. The shape parameter controls the shape of the tail. The second line of Equation 1 ($\xi = 0$) represents the Gumbel distribution and is found by taking the limit as $\xi \to 0$. When $\xi > 0$ (Frechet), the tail is thicker than the Gumbel (i.e., "heavy-tailed") with no upper bound, whereas for $\xi < 0$ (Weibull), the distribution has a hard upper limit at $\mu - \sigma/\xi$. Coles (2001) provides a detailed description of the BM/GEV approach.

A drawback of this approach is the limited number of data points (i.e., one per year) used to fit the model. Therefore, this method was generalized to include more than one value for each independent block of time by Weissman (1978) and later justified for use in hydrological studies, including modeling sea level extremes, by Tawn (1988). This extension of the BM approach allows for the use of the *r*-largest order statistics per year, permitted that $r << $ total number of events per year. The key distinction of fitting data to the GEVr distribution, as opposed to the GEV distribution, is the choice of *r*. At $r = 1$, the GEV and GEVr are identical distributions. Since *r* is not a specific parameter in the GEVr probability density function, it cannot be estimated in the same way as μ, ξ, or σ.

Several orders of *r* were tested from 1 to 20 events per year. For each *r*, model parameters were estimated, and a series of hypothesis tests run. The upper limit choice of 20 was subjective but reasonable, as it would increase the number of data points significantly (20×40 years $= 880$, ~3% of all tidal peaks over 1980–2019) while keeping $r << 730$, the maximum number of twice-daily skew surge events per year. Ideally, *r* should be large enough to include enough points to improve the robustness of the model but not large enough to introduce bias from the parent distribution and contaminating the EVD model fit.

A set of rules were developed by G'Sell et al. (2016) and furthered by Bader et al. (2017) to automate the selection of an optimum value of *r*. These rules are based on the sequential hypothesis tests for each *r* using the ForwardStop score and unadjusted *p* value generated from parametric bootstrap and entropy difference tests. The ForwardStop score is an adjusted *p*-value to control for the incremental false discovery rate, similar to a weighted mean of *p*-values of all tests on previous *r* values (Bader et al., 2017). The over-riding principal here is to start with a minimum number of data points and slowly increase the sample size until the data points do not satisfactorily fit the GEVr distribution. Following guidance provided in Bader et al. (2017), the following procedure was adopted to identify the optimum *r*.

1. Start with $r = 1$ and note the ForwardStop score from the parametric bootstrap test. Incrementally increase *r* by 1 until

TABLE 2 | Mean and standard deviation of maximum total water level (TWL) and skew surge for all tidal peaks observed during 1980–2019.

Station	Max TWL		Skew surge		Tidal datum		
	Mean	SD	Mean	SD	MHHW	MSL	GT
PHL	1.01	0.27	0.02	0.19	1.09	0.12	2.04
RDY	0.81	0.25	−0.01	0.17	0.99	−0.02	1.78
LEW	0.52	0.26	0.01	0.16	0.62	−0.12	1.42
CAP	0.65	0.26	0.01	0.15	0.74	−0.14	1.66
ATL	0.51	0.26	0.02	0.16	0.61	−0.12	1.40
BAL	0.19	0.24	0.00	0.18	0.25	−0.01	0.51
ANN	0.16	0.22	0.00	0.17	0.20	−0.02	0.44
CAM	0.25	0.20	0.00	0.16	0.29	−0.03	0.62
LWS	0.21	0.20	0.00	0.14	0.21	−0.02	0.46
KIP	0.27	0.20	0.01	0.14	0.32	−0.15	0.90
SEW	0.33	0.21	0.01	0.15	0.35	−0.08	0.84
WAC	0.50	0.24	0.02	0.15	0.57	−0.11	1.36

Mean Seal Level (MSL), Mean Higher-High Water (MHHW), and Great Diurnal Range (GT) tidal datums defined by NOAA for the current National Tidal Datum Epoch (NTDE) 1983–2001. Water levels and datums referenced to NAVD88 meters.

the ForwardStop score fails hypothesis test at the $\alpha = 0.05$ level. If a failure occurs, that *r* is rejected and select the *r* just prior to the failed test.
2. If no *r* values are rejected after traversing all 20, use the ForwardStop score from the entropy difference test and repeat Step 1.
3. If no *r* values were rejected following Step 2, then repeat Steps 1–2 using the unadjusted p-values computed for each *r* instead of the ForwardStop score.
4. If no *r* values were rejected following Step 3, increase α to 0.10 and repeat Steps 1-3.

Using these guidelines, an optimum *r* was selected for each gauge. The Goodness-of-Fit (GoF) was then tested between the Gumbel distribution ($\xi = 0$) fit and the Fréchet/Weibull distribution ($\xi \neq 0$) fit using the negative log-likelihood ratio test (ratio must be greater than 0.95) and Akaike Information Criterion (AIC) test (the difference in AIC score between sequential tests must be > 2, described in Burnham and Anderson, 2004). Maximum likelihood estimation (MLE) was used for all GEVr model fits. Temporal declustering of skew surge peaks was performed on an annual basis in order for each of the *r*-largest orders per year to be an independent event.

Points-Over-Threshold/GP Approach

In contrast to the BM approach, the POT approach is a more natural way of statistically modeling the upper tail of a parent distribution. The entire study period is treated as a single block and the EVD includes only observations over a certain threshold value (i.e., exceedances) regardless of time the event occurred. The threshold is derived from a suitably high quantile level (e.g., 97% quantile is commonly used). Exceedances are then fit to the Generalized Pareto (GP) distribution. Like the GEV, the GP distribution represents a family of three distributions, differentiated by the model shape parameter, the CDFs of which are in Equation 2.2.

$$F\left(x|\mu,\,\sigma_\mu,\,\zeta\right) = Pr\left(X < x \mid X > \mu\right) = \begin{cases} 1 - \left[1 + \xi\left(\frac{x-\mu}{\sigma_\mu}\right)\right]^{-1/\xi}, & \xi \neq 0, \\ 1 - exp\left[-\left(\frac{x-\mu}{\sigma_\mu}\right)\right], & \xi = 0, \end{cases} \quad (2.2)$$

where the quantity inside the brackets $\left[y\right] = \max\left(\left[y\right], 0\right)$, suitably high threshold μ, threshold-dependent scale parameter $\sigma_\mu > 0$, and shape parameter ξ. The condition is that all values of x must be larger or equal to the threshold μ. Behavior of the parameters is similar to that in the GEV. The shape parameter controls the shape of the tail. The second line of Equation 2.2 is found by taking the limit as $\xi \to 0$, resulting in the Exponential distribution. A heavy tail occurs when $\xi > 0$ (Pareto distribution) with no upper bound, whereas a thinner tail and a fixed upper bound occurs when $\xi < 0$ (Beta distribution). Coles (2001) provides a detailed description of the POT/GP approach.

Threshold quantiles were tested from 90–99.5% exceedance probabilities in increments of 0.5% (from 1 to 20 thresholds), resulting in the maximum number of possible skew surge peaks used to model GP to be ∼2,920 (90%) to 146 (99.5%). A threshold should be chosen to include enough upper tail exceedances that will improve the robustness of the model but not too many exceedances such that the lower values introduce bias from the parent distribution. Scarrott and MacDonald (2012) reviewed various methods on selecting the optimum threshold, including numerical tests and graphical diagnostics, such as Quantile-Quantile and Mean Residual Life plots. Many of these selection methods are subjective, time-consuming when investigating many sites, and often result in multiple acceptable answers. Diagnostic plots were used in the current study (**Supplementary Figures 1–24**), however, to better compare results with BM/GEVr approach, a similar standardized methodology was employed for selecting an optimum threshold.

The rules developed by G'Sell et al. (2016) and Bader et al. (2017) were applied to automate the selection of the optimum threshold of the POT/GP approach in Bader et al. (2018). Unadjusted *p*-values from Anderson-Darling test were chosen in Bader et al. (2018) for threshold sequential hypothesis testing after a comparison among several other GoF tests. Although, Bader et al. (2018) recommends using ForwardStop score, based on skew surge data in the current study, ForwardStop rejects very few thresholds and the unadjusted *p*-values performed well in Bader et al. (2018) tests. Using the same over-riding principal here as with the BM/GEVr approach, start with the least number of data points and slowly increase the sample size until the data points do not satisfactorily fit the GP model. This is essentially working backwards, from the highest to lowest threshold, noted as the RawDown approach in Bader et al. (2018). A RawUp approach, working upwards from the minimum threshold (i.e., most data points) until a hypothesis test was accepted, was also described in Bader et al. (2018) but carries a higher chance for contaminating the EVD than the RawDown approach. Ultimately, the following rules were adopted to identify the optimum threshold.

1. Start with highest threshold percentage (99.5%) and note the unadjusted *p*-value from the Anderson-Darling test. Incrementally decrease the threshold percentage by 0.5% until the GP model fit fails hypothesis test at $\alpha = 0.05$ level. If a failure occurs, that threshold is rejected and select the threshold just prior to the failed test.
2. If the highest threshold (99.5%) is rejected on the first test but the second (99.0%) is not rejected, then skip the highest threshold and continue working downward until next rejection occurs. This allows for the opportunity to include more *exceedances* in the model and assumes the rejection occurred by chance.
3. If no thresholds were rejected following Step 2, increase α to 0.10 and repeat Steps 1–2.

Using these guidelines, an optimum threshold was selected for each gauge. Temporal declustering was performed separately for each threshold on all exceedances over the entire study period at once. Declustering therefore significantly reduced the actual number of skew surge events used in fitting the GP model by ∼30–70%.

As with the GEVr model, MLE was used for all GP model fits.

Skew Surge Return Levels

Lastly, return level (RL) skew surges were estimated for 1.1, 3, 5, 10, 25, 50, and 100-year return periods for each EVA modeling approach. A RL represents a threshold that the probability of exceedance in any 1 year is the inverse of the return period. For example, 100-year RL has a 1.0% (0.01) probability of being exceeded in any 1 year. Since the 1-year RL is undefined within the BM/GEVr approach, 1.1-year was used instead for comparison.

Although probability quantiles can be easily extracted from the GP theoretical distribution using the fitted parameters, they cannot be viewed as annual probabilities of return levels, such as can be done using the BM/GEVr approach. Therefore, an estimate of the probability of a skew surge exceeding a selected threshold in a year on average must be included in RL calculations using the POT/GP approach. This is found by dividing the total number of declustered skew surge events above the selected threshold by the total number of years (40).

A qualitative review was performed on the estimated model parameters and return levels, with their 95% standard errors (SE) modeled using the selected optimum *r* (BM/GEVr) and threshold (POT/GP). Differences between the EVA modeling approaches and spatial variations were noted.

The harmonic analysis and tidal data processing work was done using the U-Tide package (Codiga, 2011) and standard modules in the Matlab programming environment. Temporal declustering was performed using the *POT* package (Ribatet and Dutang, 2019) and the EVA model fitting and RL extraction were performed using the *eva* package (Bader and Yan, 2020), both of the R statistical computing software environment.

RESULTS

Skew Surge

Mean skew surges are consistent and very close to zero across all tide gauges whereas TWL shows much larger geographic variation (**Table 2**). Although differences are minor, largest skew surges (0.2 m) are at PHL and the open ocean gauges at ATL and WAC. TWL is consistently higher in the Delaware Bay than the Chesapeake Bay. Within each bay, the Delaware Bay upper regions have higher max TWL than the lower regions, whereas this pattern is reversed in the Chesapeake Bay. Spatial pattern of max TWL aligns with the Mean Higher-High Water (MHHW) and Great Diurnal Range (GT) tidal datums (**Figure 3**), which do not align with the spatial pattern of skew surge. Standard deviations of skew surge show slightly more geographic variation (ranging 0.14–0.19 m) with a similar spatial pattern to the max TWL and Mean Sea Level (MSL) tidal datum. Largest deviations are in the upper bays and lowest in the central Chesapeake Bay.

None of the gauges showed statistically significant trends in skew surge except for PHL, which showed a slight negative trend of ~ -0.3 mm/year, nevertheless, all gauge time series were detrended. Note that for comparison, all gauges showed statistically significant increasing trends in max TWL consistent with local SLR rates (further analysis was not performed on max TWL within this study.)

As an example of the parent vs. upper tail distributions, **Figure 2** (left panel) shows the histogram of all detrended skew surges for the LEW tide gauge over the entire study time period with a zoomed-in view of the upper tail (right panel). The

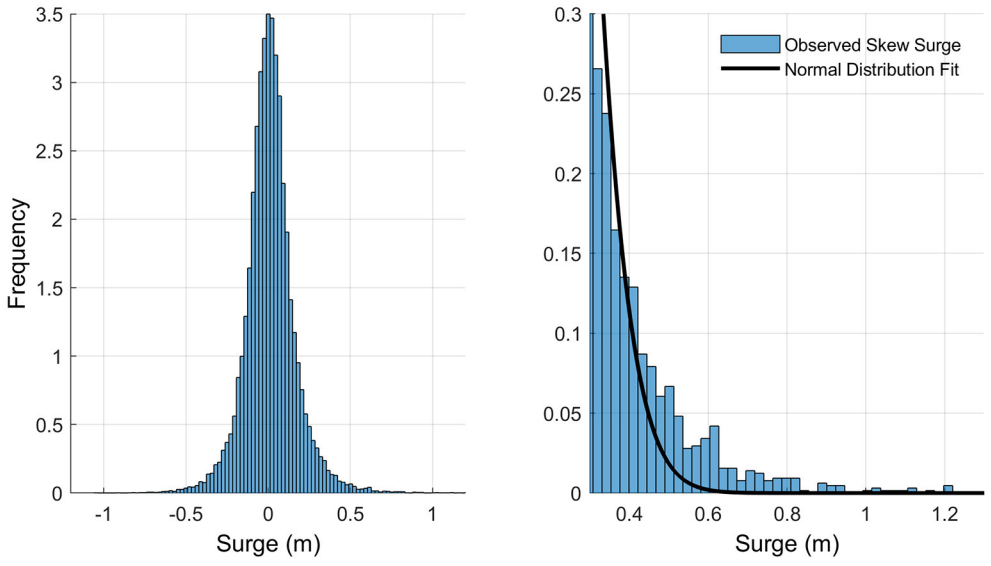

FIGURE 2 | Example demonstrating the "fat tail" nature of skew surge distribution for the NOAA tide gauge at Lewes, DE. Histogram includes all detrended skew surges over 1980–2019 (left panel). Upper tail of the same data with Normal distribution model fitted to all data points (right panel). Note the upper tail of the theoretical parent distribution under-represents empirical skew surge.

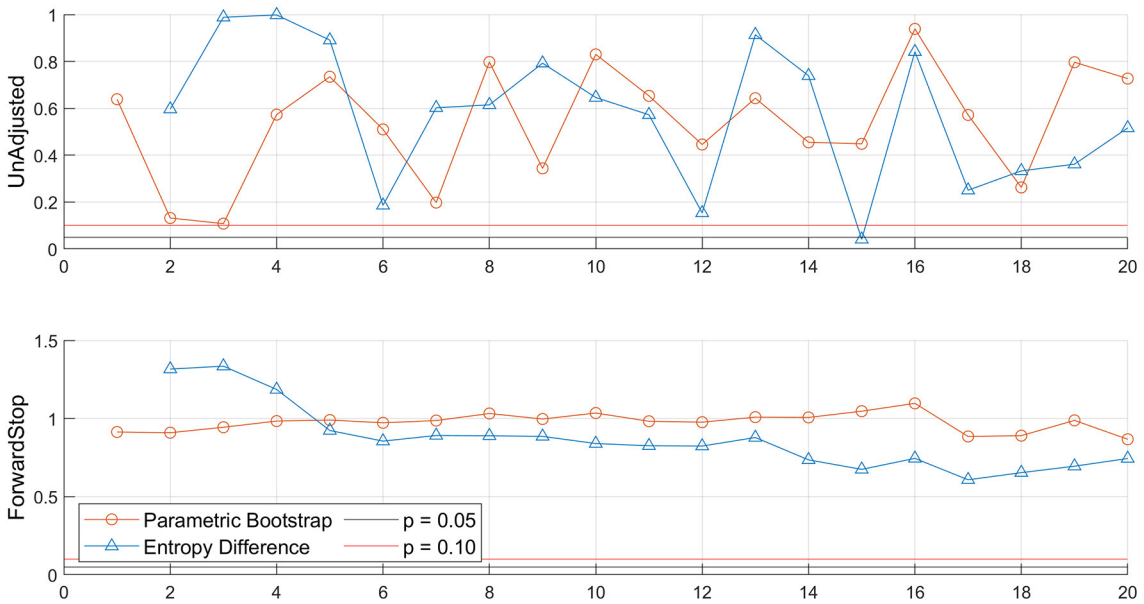

FIGURE 3 | Example demonstrating GEVr Unadjusted *p*-values (top panel) and ForwardStop (bottom panel) results based on the Parametric Bootstrap and Entropy Difference tests for $r = 1$–20, as defined in Bader et al. (2017). Following the guidelines outlined for the current study, optimum $r = 14$. Skew surge data for the NOAA Lewes tide gauge over 1980–2019.

Normal distribution fit the parent distribution at $p < 0.01$, yet significantly underestimates the empirical data in much of the upper tail, emphasizing the importance of modeling extremes of skew surge separately from the parent distribution.

Model Parameter Selection

Figure 3 shows an example of the GEVr sequential hypothesis testing for the LEW gauge. No rejections occurred (below $\alpha = 0.05$) using ForwardStop score from either the parametric bootstrap or entropy difference procedures. Starting from $r = 1$ and sequentially comparing the unadjusted *p*-values, the first rejection occurs at $r = 15$, resulting in the optimum $r = 14$. Testing for the optimum threshold in the POT/GP approach worked in the same way, albeit starting on the right side of the unadjusted *p*-values plot and working downward until a rejection occurs following guidance in Points-Over-Threshold/GP Approach Section.

Table 3 and **Figure 4** show resultant model parameters estimated after selecting the optimum *r* in the BM/GEVr approach at each gauge. The number of skew surge events per year that were fit to the GEVr distribution, ranges from $N = 120$ ($r = 3$ at CAP, ANN, SEW) to $N = 560$ ($r = 14$ at LEW). Both the location and scale parameters have small, consistent SE relative to their magnitude across all sites. The shape parameter is the most uncertain of all the parameters, although SE is relatively consistent across all sites. Uncertainty is inversely related to the total number of skew surge events ultimately used in the EVA after declustering; the lower the number of events, the smaller the SE. Shape parameter is positive at all sites except at WAC where it is slightly negative. Based on the negative log-likelihood ratio and AIC difference tests, none of sites favor the use of the GEVr Gumbel ($\xi = 0$) distribution over the GEVr Fréchet/Weibull ($\xi \neq 0$) distribution.

TABLE 3 | Results from GEVr distribution model fit of extreme skew surges for tide gauges in the Mid-Atlantic region.

Station	*r*	Npks	Location	Scale	Shape
PHL	7	280	0.636 (0.017)	0.134 (0.012)	0.082 (0.058)
RDY	11	440	0.547 (0.015)	0.117 (0.010)	0.039 (0.046)
LEW	14	560	0.699 (0.023)	0.180 (0.017)	0.102 (0.044)
CAP	3	120	0.602 (0.018)	0.128 (0.013)	0.121 (0.083)
ATL	6	240	0.700 (0.022)	0.166 (0.014)	0.034 (0.059)
BAL	12	480	0.611 (0.016)	0.128 (0.012)	0.113 (0.047)
ANN	3	120	0.566 (0.016)	0.112 (0.012)	0.165 (0.085)
CAM	11	440	0.561 (0.014)	0.111 (0.010)	0.062 (0.047)
LWS	10	400	0.507 (0.013)	0.106 (0.009)	0.064 (0.049)
KIP	4	160	0.566 (0.019)	0.140 (0.013)	0.075 (0.071)
SEW	3	120	0.671 (0.025)	0.178 (0.017)	0.093 (0.081)
WAC	11	418	0.691 (0.020)	0.156 (0.012)	−0.057 (0.043)

R is the number of largest maxima per year included in the analysis. Npks is the number of skew surge events after 30-h temporal declustering and is equal to r multiplied by the number of years of data. Location, scale, and shape are model parameters fit using maximum likelihood estimation with 95% standard error in parentheses.

Similarly, **Table 4** and **Figure 3** summarize the results after selecting the optimum threshold using the POT/GP approach at each gauge. Threshold percentages range from 94.5% (ATL, $N = 732$) to 99.0% (LEW, ANN, KIP, and SEW, $N = 160$, 194, 139, and 142, respectively.) Gauges that have the same optimum threshold still result in different total number of skew surge events due to temporal declustering. Scale parameter SE is low

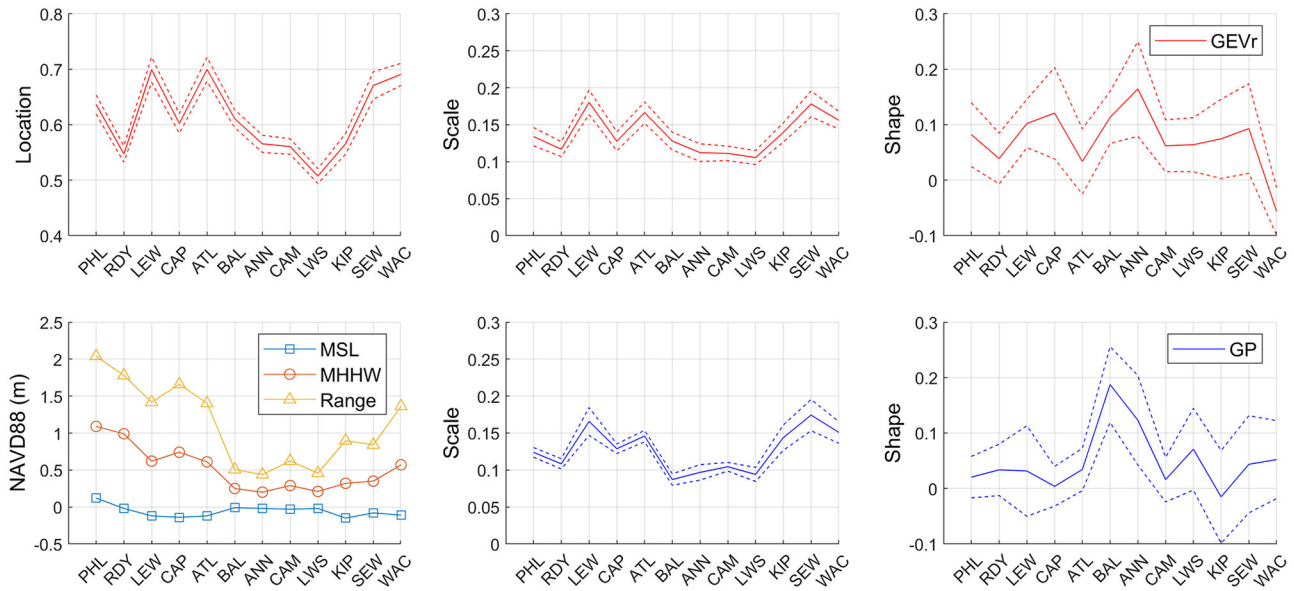

FIGURE 4 | Model fit parameters of extreme skew surges to the GEVr (red, top row) and GP (blue, bottom row) distributions. Location is a model parameter only for GEVr distribution. Dotted lines represent the 90% confidence interval. Mean Sea Level (MSL), Mean Higher-High Water (MHHW), and Great Diurnal Range (GT) tidal datums defined by NOAA for the current National Tidal Datum Epoch 1983–2001 referenced to NAVD88 meters.

TABLE 4 | Results from GP distribution model fit of extreme skew surges for tide gauges in the Mid-Atlantic region.

Station	Threshold	Npks	Scale	Shape
PHL	94.50	744	0.124 (0.006)	0.020 (0.037)
RDY	96.50	497	0.108 (0.007)	0.034 (0.046)
LEW	99.00	160	0.166 (0.019)	0.032 (0.082)
CAP	93.50	784	0.129 (0.007)	0.004 (0.036)
ATL	94.00	732	0.146 (0.008)	0.034 (0.038)
BAL	98.50	301	0.087 (0.008)	0.187 (0.068)
ANN	99.00	194	0.097 (0.010)	0.123 (0.081)
CAM	96.00	641	0.104 (0.006)	0.016 (0.040)
LWS	98.50	211	0.094 (0.009)	0.071 (0.074)
KIP	99.00	139	0.144 (0.017)	−0.015 (0.084)
SEW	99.00	142	0.174 (0.021)	0.044 (0.088)
WAC	98.00	224	0.151 (0.015)	0.052 (0.070)

Npks is the number of skew surge events above threshold percent quantile after 30-h temporal declustering. Scale and shape are model parameters fit using maximum likelihood estimation (MLE) with 95% standard error in parentheses.

while the shape parameter SE is relatively high across all sites. Shape parameter is positive at all sites except at KIP where it is slightly negative. Spatial patterns and relative uncertainties of both the scale and shape parameter estimates are generally similar between the two approaches.

Supplementary Figures 1–12 (BM/GEVr) and **13–24** (POT/GP) show diagnostic plots of the model fit using the optimally selected *r* and threshold values at each tide gauge. Included are probability-probability (PP) and quantile-quantile (QQ) plots of the modeled vs. empirical data, and histograms overlaid with model fit PDF curve. The PP plots and histograms show good agreement between the model and observations. For most gauges, the QQ plots show a few outliers with the observed skew surge levels higher than modeled quantile estimates. The LEW gauge did not show this behavior but rather at the largest values, the modeled quantiles were larger than the observed data.

Skew Surge Return Levels

Skew surge return levels for 1.1, 3, 5, 10, 25, 50, and 100-year return periods with 90% confidence intervals (i.e., uncertainty) are shown in **Table 5** for BM/GEVr and **Table 6** for POT/GP. For the sake of brevity and ease of comparison, only the mean values are plotted in **Figure 5**. Note the more traditional continuous RL curves with confidence intervals are included in **Supplementary Figures 25–26**, and additionally plotted with empirical data in panel 4 of **Supplementary Figures 1–24**. RLs increase in a consistent manner with longer return periods at all sites under both modeling approaches. For BM/GEVr, 100-year RLs range from 1.07 m (LWS) to 1.79 m (LEW) with generally largest values starting in the lower bay regions, decreasing to a minimum in the central regions, then increasing toward the upper regions. This pattern is similar across all RLs. LEW and SEW have the largest RLs for most return periods, except for the 1.1-year return period, where the maximum RL is at ATL (although several other sites are very close). Longer return periods demonstrate more spatial variation in RLs. Using POT/GP, 100-year RLs range from 1.08 m (LWS) to 1.56 m (LEW), with approximately the same spatial pattern as with BM/GEVr.

There are few differences in RLs between approaches (**Table 7**; **Figure 6**). The most noticeable is that the 1.1-year RLs using

TABLE 5 | Estimated skew surge return levels for 1.1, 3, 5, 10, 25, 50, and 100-year return periods modeled using the BM/GEVr approach for tide gauges in the Mid-Atlantic region.

Station	1.1-year	3-year	5-year	10-year	25-year	50-year	100-year
PHL	0.52 (0.04)	0.76 (0.12)	0.85 (0.16)	0.97 (0.25)	1.13 (0.40)	1.25 (0.55)	1.38 (0.74)
RDY	0.45 (0.04)	0.65 (0.09)	0.73 (0.12)	0.82 (0.18)	0.95 (0.27)	1.04 (0.35)	1.14 (0.45)
LEW	0.55 (0.06)	0.87 (0.16)	0.99 (0.23)	1.16 (0.35)	1.38 (0.55)	1.56 (0.75)	1.76 (0.99)
CAP	0.50 (0.05)	0.72 (0.12)	0.81 (0.18)	0.93 (0.30)	1.10 (0.54)	1.24 (0.81)	1.39 (0.99)
ATL	0.56 (0.06)	0.85 (0.14)	0.96 (0.20)	1.09 (0.30)	1.26 (0.48)	1.39 (0.66)	1.53 (0.88)
BAL	0.50 (0.04)	0.73 (0.11)	0.82 (0.15)	0.94 (0.23)	1.10 (0.36)	1.24 (0.49)	1.38 (0.65)
ANN	0.47 (0.04)	0.67 (0.11)	0.76 (0.16)	0.87 (0.26)	1.04 (0.47)	1.18 (0.64)	1.34 (0.72)
CAM	0.47 (0.04)	0.66 (0.09)	0.74 (0.13)	0.83 (0.20)	0.95 (0.31)	1.05 (0.41)	1.15 (0.54)
LWS	0.42 (0.03)	0.61 (0.09)	0.67 (0.12)	0.76 (0.18)	0.88 (0.27)	0.98 (0.37)	1.07 (0.48)
KIP	0.45 (0.05)	0.70 (0.13)	0.79 (0.19)	0.91 (0.31)	1.07 (0.55)	1.20 (0.79)	1.33 (1.11)
SEW	0.52 (0.07)	0.84 (0.16)	0.96 (0.24)	1.12 (0.39)	1.33 (0.70)	1.51 (1.02)	1.69 (1.43)
WAC	0.55 (0.06)	0.83 (0.11)	0.92 (0.14)	1.02 (0.19)	1.15 (0.26)	1.24 (0.32)	1.32 (0.39)

90% confidence intervals in parentheses.

TABLE 6 | Estimated skew surge return levels for 1.1, 3, 5, 10, 25, 50, and 100-year return periods modeled using the POT/GP approach for tide gauges in the Mid-Atlantic region.

Station	1.1-year	3-year	5-year	10-year	25-year	50-year	100-year
PHL	0.66 (0.06)	0.79 (0.11)	0.86 (0.14)	0.95 (0.19)	1.08 (0.27)	1.18 (0.35)	1.28 (0.44)
RDY	0.56 (0.06)	0.68 (0.10)	0.74 (0.27)	0.83 (0.18)	0.95 (0.26)	1.04 (0.34)	1.14 (0.43)
LEW	0.72 (0.08)	0.90 (0.16)	0.99 (0.22)	1.12 (0.35)	1.29 (0.61)	1.43 (0.88)	1.56 (1.23)
CAP	0.62 (0.06)	0.75 (0.11)	0.82 (0.14)	0.91 (0.19)	1.03 (0.27)	1.12 (0.34)	1.21 (0.42)
ATL	0.71 (0.08)	0.88 (0.14)	0.97 (0.18)	1.08 (0.25)	1.25 (0.36)	1.37 (0.46)	1.50 (0.58)
BAL	0.61 (0.06)	0.76 (0.13)	0.84 (0.19)	0.97 (0.30)	1.16 (0.52)	1.33 (0.77)	1.53 (1.09)
ANN	0.58 (0.06)	0.71 (0.11)	0.78 (0.16)	0.88 (0.25)	1.03 (0.42)	1.16 (0.60)	1.30 (0.84)
CAM	0.58 (0.05)	0.69 (0.09)	0.74 (0.11)	0.82 (0.15)	0.93 (0.21)	1.01 (0.27)	1.09 (0.34)
LWS	0.52 (0.05)	0.63 (0.10)	0.69 (0.13)	0.77 (0.20)	0.89 (0.32)	0.98 (0.44)	1.08 (0.60)
KIP	0.59 (0.07)	0.73 (0.12)	0.80 (0.16)	0.89 (0.25)	1.02 (0.41)	1.11 (0.58)	1.20 (0.80)
SEW	0.69 (0.09)	0.88 (0.16)	0.98 (0.23)	1.12 (0.35)	1.31 (0.60)	1.46 (0.85)	1.61 (1.17)
WAC	0.68 (0.08)	0.85 (0.22)	0.94 (0.36)	1.07 (0.32)	1.25 (0.51)	1.38 (0.77)	1.53 (1.25)

90% confidence intervals in parentheses.

BM/GEVr (0.45–0.56 m) are significantly lower than using POT/GP (0.52–0.72 m) at all sites. At the other extreme, BM/GEVr 100-year RLs are generally higher, mostly in the upper bay regions, with LEW (0.19 m) and CAP (0.17 m) showing the largest positive differences between methods. BAL (−0.15 m) and WAC (−0.20 m) are exceptions, with higher 100-year RLs using POT/GP. Most return periods between 3-year and 50-year show small differences in RLs across most gauges.

Uncertainty also increases with longer return periods under both approaches, as expected. At 1.1-year return period the uncertainties are <0.10 m, and range 0.18–0.39 m at 10-year, and 0.30–1.43 m at 100-year. Sites in the Chesapeake Bay, under both approaches, exhibit spatial variation in uncertainty similar to that of the mean RL estimates, with the largest uncertainties in the lower bay regions, smallest in the central regions, and increasing in the upper regions. WAC is an exception to this with small uncertainty under BM/GEVr. Sites in the Delaware Bay also show this same pattern in uncertainty with BM/GEVr but not POT/GP, under which CAP and ATL (sites in the lower bay region) show small uncertainties.

Generally, uncertainties under both approaches are very similar to each other at shorter return periods. At longer return periods in the Delaware Bay, uncertainties are smaller using POT/GP for most sites. At longer return periods in the Chesapeake Bay, generalization is more difficult; BAL (−0.44 m at 100-year) and WAC (−0.87 m at 100-year) have significantly smaller uncertainties using BM/GEVr while many other sites have smaller uncertainties using POT/GP.

DISCUSSION

The focus areas of the current study is to investigate the magnitude and geographic variation within the Delaware and Chesapeake Bays of estimated return levels of skew surge for ∼1-year to 100-year return periods and to compare the two

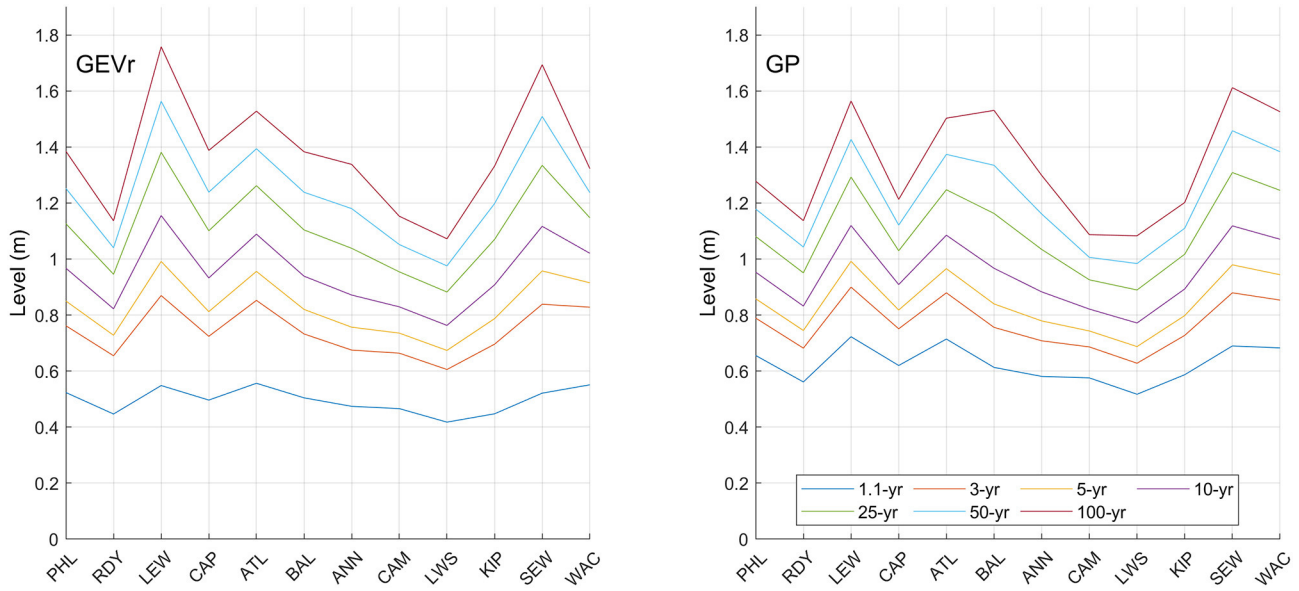

FIGURE 5 | Estimated skew surge return levels for periods of 1.1, 3, 5, 10, 25, 50, and 100 years using the BM/GEVr (left panel) and POT/GP (right panel) approaches for tide gauges in the Mid-Atlantic region, 1980–2019.

TABLE 7 | Difference in estimated skew surges and 90% confidence intervals (in parentheses) for 1.1, 3, 5, 10, 25, 50, and 100-year return periods modeled from GEVr and GP distribution for tide gauges in the Mid-Atlantic region.

Station	1.1-year	3-year	5-year	10-year	25-year	50-year	100-year
PHL	−0.13 (−0.02)	−0.03 (0.01)	−0.01 (0.02)	0.01 (0.06)	0.05 (0.13)	0.07 (0.20)	0.11 (0.30)
RDY	−0.11 (−0.02)	−0.03 (−0.01)	−0.02 (−0.15)	−0.01 (0.00)	−0.01 (0.00)	0 (0.01)	0 (0.02)
LEW	−0.17 (−0.03)	−0.03 (0.01)	0 (0.01)	0.04 (0.00)	0.09 (−0.06)	0.14 (−0.13)	0.19 (−0.23)
CAP	−0.12 (−0.02)	−0.03 (0.01)	−0.01 (0.04)	0.02 (0.11)	0.07 (0.27)	0.12 (0.47)	0.17 (0.57)
ATL	−0.16 (−0.02)	−0.03 (0.00)	−0.01 (0.02)	0 (0.05)	0.01 (0.12)	0.02 (0.20)	0.03 (0.30)
BAL	−0.11 (−0.02)	−0.02 (−0.03)	−0.02 (−0.04)	−0.03 (−0.08)	−0.06 (−0.17)	−0.10 (−0.28)	−0.15 (−0.44)
ANN	−0.11 (−0.02)	−0.03 (−0.01)	−0.02 (0.00)	−0.01 (0.02)	0 (0.05)	0.02 (0.05)	0.04 (−0.12)
CAM	−0.11 (−0.02)	−0.02 (0.01)	−0.01 (0.02)	0.01 (0.05)	0.03 (0.09)	0.05 (0.14)	0.07 (0.21)
LWS	−0.10 (−0.02)	−0.02 (−0.01)	−0.01 (−0.01)	−0.01 (−0.02)	−0.01 (−0.04)	−0.01 (−0.07)	−0.01 (−0.12)
KIP	−0.14 (−0.02)	−0.03 (0.01)	−0.01 (0.03)	0.01 (0.06)	0.05 (0.13)	0.09 (0.21)	0.13 (0.31)
SEW	−0.17 (−0.02)	−0.04 (0.00)	−0.02 (0.01)	0 (0.04)	0.03 (0.10)	0.05 (0.18)	0.08 (0.26)
WAC	−0.13 (−0.02)	−0.03 (−0.11)	−0.03 (−0.22)	−0.05 (−0.13)	−0.10 (−0.26)	−0.15 (−0.45)	−0.20 (−0.87)

Negative values mean GP estimates are greater than GEVr estimates.

most common traditional EVA approaches. Although skew surge is arguably one of the best and simplest measures of the meteorological drivers of coastal flooding, as it is the portion of flood depth above the high tide level, its wider use in literature has only recently gained attention. This work was done strictly through empirical data (rather than using simulated events or scenario-based projections) over the past 40 years and statistically analyzed through stationary EVA on detrended skew surges. Observational data showed minimal trends over this time period, hence results from this study should not be appreciably different than non-stationary EVA that allows for temporally varying or multivariable dependent location and scale parameters. To test the robustness of the methods, the POT/GP approach presented here was applied to max TWL and resulting return levels compared against those found in U. S. Army Corps of Engineers (2014), who performed a similar EVA using longer time periods. Seven tide gauges were analyzed in both studies: LEW, CAP, ATL, BAL, ANN, CAM, and SEW. Although they used different thresholds, detrending methods, and reference periods, the general spatial and temporal trends were consistent between the two studies, including the intervals between the 50-year and 100-year RLs. Largest differences were found for longer return periods at BAL and ANN, sites that have experienced extreme coastal flooding outliers (Callahan et al., 2021b).

Due to the approximate independence of skew surge to SLR and tidal phase (i.e., likely minor influences of tide-surge

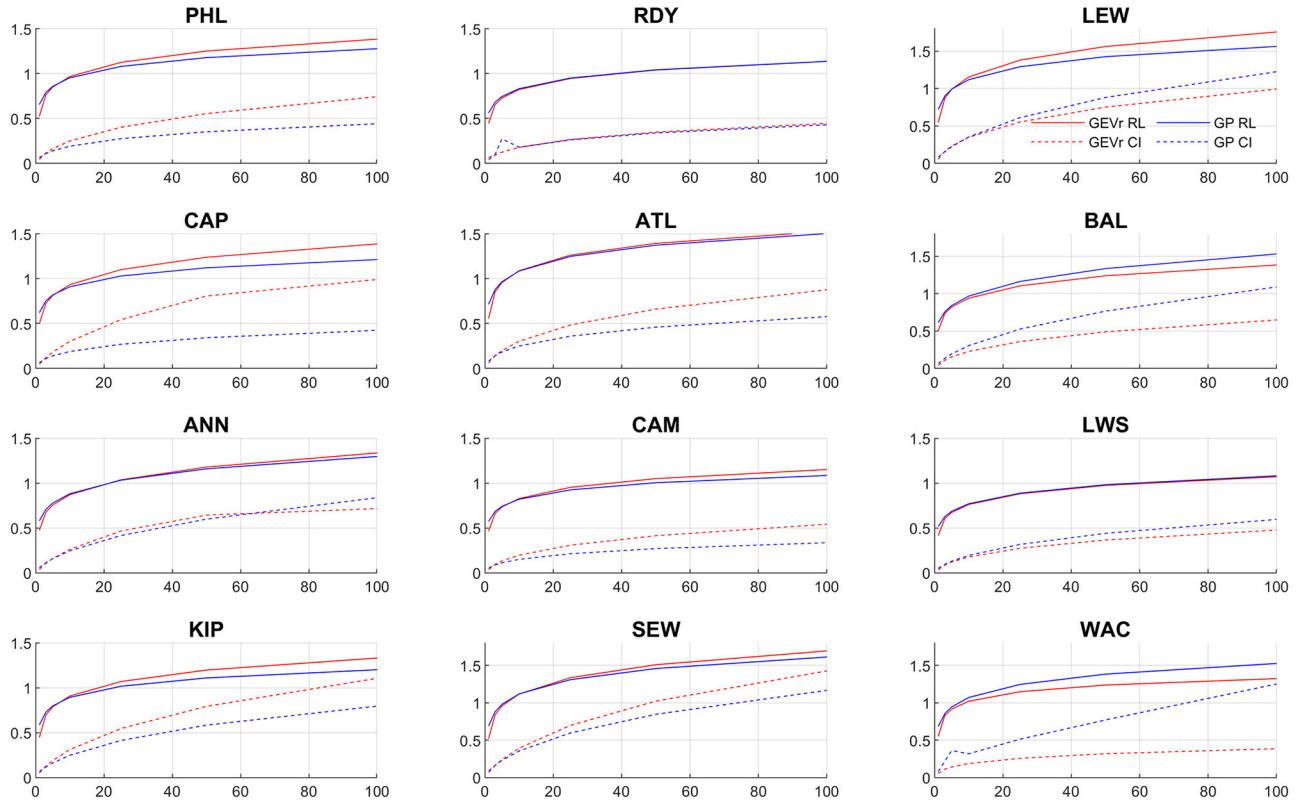

FIGURE 6 | Estimated return levels (solid line) and 90% confidence intervals (dotted line) using the BM/GEVr (red line) and POT/GP (blue line) approaches.

interactions at our sites), extreme return levels can reasonably be linearly added to future SLR scenarios as a first approximation for planning (Delaware Flood Avoidance Workgroup (DE FAW), 2016; Federal Emergency Management Agency (FEMA), 2016). For example, if a structure is designed to withstand the 50-year flood event, the 50-year return levels can be added to the expected high tide (either the MHWW or Highest Astronomical Tide datum) under an appropriate SLR planning scenario. It should be noted that skew surge computed in this study includes contributions from other aspects associated with extreme flooding events, such as nearby river discharge and wave setup, which ultimately likely benefits many long-term planning activities. As well, trends in skew surge were minor and mean values were within a few centimeters of zero over 1980–2019 (**Table 2**), however, an adjustment to skew surge RLs due to detrending could be performed. Care is warranted when making linear adjustments too far into the future due to the expected exponential increase in SLR and uncertainty in future extreme storm conditions along the Mid-Atlantic (Callahan et al., 2017, 2021b).

Largest return levels across most return periods occur within the bay boundaries in the lower regions, and not in the upper regions of the bays and ocean coast sites that typically show higher surges and TWLs. Specially, LEW and SEW gauges, both located on the southwest side of the mouth of each bay, consistently show the largest RLs throughout the region. One explanation is that many large coastal flood events are associated with ETCs, often as traditional nor'easters. For these storms, the low-pressure center off the coast brings strong northeast winds, which drives enhanced surges into the bays through Ekman transport as well as direct winds piling up water on the southwest sides of the lower bays. This would be most effective in the lower Delaware Bay, where the width of the Bay reaches 45 km. The upper Delaware Bay, although it experiences large tidal ranges and increased surges (due to conical shape of coastline and from the increased volume of water entering the bay from southeasterly to easterly winds), may not experience the worst impacts from the most extreme storm events and may actually see decreases in surges from northerly winds that also occur during nor'easters. The upper Chesapeake Bay does not exhibit the same high TWL, MHHW, or surges as in the upper Delaware Bay (primarily due to the overall size, shape, and depth of the Chesapeake Bay), however, extreme skew surge RLs in both upper regions are comparable to each other. This supports results in Callahan et al. (2021a), which found the upper bays were highly correlated with each other from TC-caused skew surges, more so than with their respective lower bay regions. TCs can account for close to 40–60% of the largest (top 10) coastal flooding events in the Mid-Atlantic, with smaller relative percentages over larger number of events (Booth et al., 2016; Callahan et al.,

2021b). In particular for the upper Chesapeake Bay, Hurricane Isabel in 2003 caused extreme coastal flooding compared to other events, directly influencing higher return period RLs and their uncertainties.

RLs tend to be at a minimum within each bay closer to the central regions, CAM and LWS in the Chesapeake and RDY in the Delaware Bays. These areas have the lowest mean skew surges throughout the region and typically do not experience the worst wind-driven impacts from coastal storms. Likewise, these areas also exhibit the smallest uncertainties throughout the region across many return periods.

A secondary focus of this study is to provide insight into the two most common approaches of stationary EVA applied to Mid-Atlantic skew surge. To that end, the GEVr distribution was combined with the BM approach to address the small sample size of the traditional annual max BM/GEV approach, and a standardized method for selecting optimum *r* and threshold was incorporated. The use of GEVr increases the robustness of the model fit and puts the number of data points more comparable to the POT/GP approach, however, there are some disadvantages of using a BM approach. Large surge events could be missed, for example, if an individual year has more major coastal flood events than the selected optimum *r* (i.e., false positives). At the other end, non-extreme surge events could be included, for example, if an individual year has less major coastal flood events than the selected optimum *r*, introducing bias from the parent distribution (i.e., false negatives). Use of the POT/GP approach circumvents these issues as it is irrespective of time, solely focused on the upper tail of the parent distribution. A potential trade-off is if the majority of extreme events occur toward either end of the study time period, direct interpretation of annual return levels from the mean number of events per year is more difficult. From review of the data used in the current study, clustering of major skew surge events occurring on either end of the time period was not present.

The choice of optimum *r* or threshold is a tricky problem to address. It is usually a subjective process, including graphical and numerical diagnostic information, and choosing among multiple appropriate candidates. The current study incorporates a standardized methodology of sequential hypothesis texting that can be applied to all sites simultaneously while allowing for variable *r*/threshold selection per site. Although stopping rules and goodness of for tests are still subjective within this methodology, they are data-driven, based on statistical results from Bader et al. (2017, 2018). Choice of stopping rules influences the number of data points (*r*-largest orders or threshold exceedances), and hence, directly influence the uncertainty in model parameters. Uncertainty in RLs do not consistently show strong dependence on the number of peaks included in the model fit. This potential relationship of RL uncertainty and optimum *r*/threshold should be explored further in future work.

Changes in storm frequency and intensity ("storminess"), either observed or projected due to climate change, were not addressed in this study. As stated above, skew surge is closely related to the meteorological characteristics driving the flooding and relatively independent of SLR or tides. Trends in skew surge are therefore influenced by oscillations and trends in oceanic-atmospheric circulation patterns that support enhanced cyclogenesis or steer storms along the coast. Common teleconnections associated with the frequency or magnitude of surges in the Mid-Atlantic region include the North Atlantic Oscillation, Pacific-North American oscillation, El Nino/Southern Oscillation, and Atlantic Meridional Overturning Circulation, several of which have been included as covariates in non-stationary EVA or joint-probability models of surges in recent years (Ezer et al., 2013; Sweet et al., 2014; Hamlington et al., 2015; Wahl and Chambers, 2015; Kopp et al., 2019; Little et al., 2019; Rashid Md et al., 2019). The 40-year time period of the current study is long enough to capture several oscillations of many of these teleconnections, essentially averaging out their influence. Extreme RLs then can be viewed as based on relative average synoptic conditions, however, the probability of occurrence of an extreme surge event in any single year is dependent upon the presence and strength of teleconnection patterns, and assessment should be performed as near to the year in question as possible.

Other aspects of this study could have influenced extreme surge estimates. Most notably is the length of the data record, as is usually the case in EVA. Although there exists general agreement with results in U. S. Army Corps of Engineers (2014), 40 years of data to estimate 100-year RL is not ideal. Comparing EVA results on skew surge using the methods presented in the current study on a subset of gauges with much longer records, perhaps one gauge per sub-bay region, could offer insight into the robustness of the current study statistical results. Additionally, the set of 44 constituents used in the HA computation of the predicted tide may not capture all the tidal oscillations present at every site, thereby impacting the magnitude of skew surge (albeit these changes likely would be minimal). The choice of 30 hours was subjective and may not be optimum at all sites to separate individual skew surge events, although it is rare for a single storm event to reach extreme surge levels multiple times separated by two or more high tides.

CONCLUSION

Understanding extreme events is important because of their potential for disproportionate damage and threat to public health, which will aid in mid- to long-term planning of many coastal communities and critical ecosystems along their shores. Across most of the return periods, the largest return levels occur at LEW and SEW, which are within the bay boundaries in the southwest side of the lower regions of their respective bay. Likewise, minimum return levels occur near the central regions of each bay, at RDY and LWS. This may seem counterintuitive for the Delaware Bay where the upper bay (PHL) experiences high water levels and tidal ranges but is consistent with wind and ocean current patterns for offshore storms in this region.

Determination of which approach is "best" for modeling extreme skew surge events in the Mid-Atlantic is not a goal of the current study. Nevertheless, differences between the approaches are highlighted and some general recommendations can be made.

Overall, both approaches provide similar results. Confidence in model parameters is good and consistent across all sites between both approaches, with narrow confidence intervals for the location and scale parameters. Confidence is less for shape parameter but is generally the same for both approaches. Not many differences in magnitude of RLs exist, especially for 3-year to 100-year return periods, which helps justify comparisons of extreme levels of surge among previous EVA studies in this region (at least for skew surge).

For the 1.1-year return period, the POT/GP approach provides more consistent values in respect to other return periods across both bays. This is likely due to the effects of estimating RLs from the GEVr distribution close to 1-year. For the Delaware Bay at longer return periods, the POT/GP also seems to perform well (lower uncertainty) at most sites and therefore could be used at all return periods up to 100 years. This finding is supported by U. S. Army Corps of Engineers (2014) statements that traditional BM/GEV approach tends to overestimate and have larger uncertainties when compared to POT/GP. Recommendations are more mixed for the Chesapeake Bay for return periods at 3-year and above. Results at ANN and LWS are nearly identical for both approaches. For KIP and SEW, sites in the lower Chesapeake Bay, lower uncertainties and slightly lower RLs tend toward the POT/GP approach. Conversely, BAL (upper region) and WAC (ocean coast) tend toward the use of the BM/GEVr approach.

DATA AVAILABILITY STATEMENT

The datasets presented in this study can be found in online repositories. The names of the repository/repositories and accession number(s) can be found below: the dataset of extreme skew surge return levels, estimated using both BM/GEVr and POT/GP approaches, at each tide gauge analyzed for this study can be found at the figshare repository, https://figshare.com/account/home#/projects/101024.

AUTHOR CONTRIBUTIONS

JC and DL conceived the idea of investigating extreme coastal flood levels in the U.S. Mid-Atlantic Delaware and Chesapeake Bays. JC designed the analysis framework, obtained all the necessary data, performed the statistical analysis, and wrote the manuscript. DL helped with results interpretation and manuscript revisions. All authors contributed to the article and approved the submitted version.

ACKNOWLEDGMENTS

The authors would like to thank the National Oceanic and Atmospheric Administration for providing a large database of water level data for public use. The authors would also like to thank Dr. Daniel L. Codiga, Graduate School of Oceanography, University of Rhode Island, and Dr. Richard Pawlowicz, Department of Earth, Ocean and Atmospheric Sciences, University of British Columbia, for their help in understanding the operation of U-Tide and performing harmonic analysis.

BENEFIT OF RESEARCH TO SCIENTIFIC COMMUNITY

Extreme storm surges can overwhelm many coastal flooding protection measures in place and cause severe damages to private communities, public infrastructure, and natural ecosystems, particularly in the Mid-Atlantic region. However, by definition, extreme events are rare and difficult to model due to small sample sizes. Results from this study provide estimates of extreme skew surge, a less often studied but robust measure of the meteorological component of coastal flood levels, for return periods of 1.1 to 100 years. This study also aims to increase understanding and reliability of projections of extreme water levels using methods commonly found in the literature and ultimately help in long-term planning of mitigation and implementation of adaptation measures.

SUPPLEMENTARY MATERIAL

The Supplementary Material for this article can be found online at: https://www.frontiersin.org/articles/10.3389/fclim.2021.684834/full#supplementary-material

REFERENCES

Bader, B., and Yan, J. (2020). *eva: Extreme Value Analysis with Goodness-of-Fit Testing*. R package version 0.1.2

Bader, B., Yan, J., and Zhang, X. (2017). Automated selection of *r* for the *r* largest order statistics approach with adjustment for sequential testing. *Stat. Comput.* 27, 1435–1451. doi: 10.1007/s11222-016-9697-3

Bader, B., Yan, J., and Zhang, X. (2018). Automated threshold selection for extreme value analysis via ordered goodness-of-fit tests with adjustments for false discovery rate. *Ann. Appl. Stat.* 12, 310–329. doi: 10.1214/17-AOAS1092

Batstone, C., Lawless, M., Tawn, J., Horsburgh, K., Blackman, D., McMillan, A. D., et al. (2013). A UK best-practice approach for extreme sea-level analysis along complex topographic coastlines. *Ocean Eng.* 71, 28–39. doi: 10.1016/j.oceaneng.2013.02.003

Bernier, N. B., and Thompson, K. R. (2006). Predicting the frequency of storm surges and extreme sea levels in the northwest Atlantic. *J. Geophys. Res. Oceans* 111:10. doi: 10.1029/2005JC003168

Blake, E. S., and Gibney, E. J. (2011). *The Deadliest, Costliest, and Most Intense United States Tropical Cyclones From 1851 to 2010 (and Other Frequently Requested Hurricane Facts)*. NOAA Technical Memorandum NWS NHC-6

Boesch, D. F., Boicourt, W. C., Cullather, R. I., Ezer, T., Galloway, G. E. Jr., et al. (2018). *Sea-level Rise: Projections for Maryland 2018*. Cambridge, MD: University of Maryland Center for Environmental Science

Boon, J. D., Mitchell, M., Loftis, J. D., and Malmquist, D. L. (2018). Anthropogenic *Sea Level Change: A History of Recent Trends Observed in the U.S. East, Gulf and West Coast Regions*. Special Report No. 467 in Applied Marine Science and Ocean Engineering. Gloucester Point, VA: Virginia Institute of Marine Science.

Booth, J. F., Rider, H. E., and Kushnir, Y. (2016). Comparing hurricane and extratropical storm surge for the Mid-Atlantic and Northeast

Coast of the United States for 1979–2013. *Environ. Res. Lett*. 11:094004. doi: 10.1088/1748-9326/11/9/094004

Burnham, K. P., and Anderson, D. R. (2004). Multimodel inference: understanding AIC and BIC in model selection. *Sociol. Methods Res.* 33, 261–304. doi: 10.1177/0049124104268644

Calafat, F. M., and Marcos, M. (2020). Probabilistic reanalysis of storm surge extremes in Europe. *Proc. Natl. Acad. Sci. USA*. 117, 1877–1883. doi: 10.1073/pnas.1913049117

Callahan, J. A., Horton, B. P., Nikitina, D. L., Sommerfield, C. K., McKenna, T. E., and Swallow, D. (2017). *Recommendation of Sea-Level Rise Planning Scenarios for Delaware: Technical Report*. Delaware Department of Natural Resources and Environmental Control (DNREC) Delaware Coastal Programs.

Callahan, J. A., Leathers, D. J., and Callahan, C. L. (2021a). Skew surge and storm tides of tropical storms in the Delaware and Chesapeake Bays for 1980–2019. *Front. Clim.* 86. doi: 10.1002/essoar.10506586.1

Callahan, J. A., Leathers, D. J., and Callahan, C. L. (2021b). *Comparison of Extreme Coastal Flooding Events Between Tropical and Mid-Latitude Weather Systems in the Delaware and Chesapeake Bays for 1980–2019*. EarthArXiv [Preprint]. Available online at: https://www.essoar.org/doi/abs/10.1002/essoar.10506864.1 (accessed April 26, 2021).

Chesapeake Bay Program (2020). *State of the Chesapeake*. Available online at: https://www.chesapeakebay.net/state (accessed August 18, 2020).

Chippy, M. R., and Jawahar, S. S. (2018). Storm surge and its effect—a review on disaster management in coastal areas. *Civil Eng. Res. J.* 4:555649. doi: 10.19080/CERJ.2018.04.555649

Codiga, D. L. (2011). *Unified Tidal Analysis and Prediction Using the UTide Matlab Functions*. GSO Technical Report 2011-01. Graduate School of Oceanography, University of Rhode Island

Coles, S. (2001). *An Introduction to Statistical Modeling of Extreme Values*. London: Springer.

Colle, B. A., Booth, J. F., and Chang, E. K. M. (2015). A review of historical and future changes of extratropical cyclones and associated impacts along the US East Coast. *Curr. Clim. Change Rep*. 1, 125–143. doi: 10.1007/s40641-015-0013-7

Dahl, K. A., Fitzpatrick, M. F., and Spanger-Siegfried, E. (2017). Sea level rise drives increased tidal flooding frequency at tide gauges along the U.S. East and Gulf Coasts: projections for 2030 and 2045. *PLoS ONE* 12:2. doi: 10.1371/journal.pone.0170949

Delaware Emergency Management Agency (DEMA) (2018). *State of Delaware All-Hazard Mitigation Plan*. DEMA.

Delaware Flood Avoidance Workgroup (DE FAW) (2016). *Avoiding and Minimizing Risk of Flood Damage to State Assets: A Guide for Delaware State Agencies*. Delaware Flood Avoidance Workgroup

DNREC, (2012). *Preparing for Tomorrow's High Tide: Sea Level Rise Vulnerability Assessment for the State of Delaware*, pp. 210. Available online at: https://documents.dnrec.delaware.gov/coastal/Documents/SeaLevelRise/AssesmentForWeb.pdf

Dupigny-Giroux, L. A., Mecray, E. L., Lemcke-Stampone, M. D., Hodgkins, G. A., Lentz, E. E., Mills, K. E., et al. (2018). "Northeast," in Impacts, Risks, and Adaptation in the United States: *Fourth* National Climate Assessment, Volume II, eds D. R. Reidmiller, C. W. Avery, D. R. Easterling, K. E. Kunkel, K. L. M. Lewis, T. K. Maycock et al. (Washington, DC: U.S. Global Change Research Program), 69–742. doi: 10.7930/NCA4.2018.CH18

Ellis, J. T., and Sherman, D. J. (2015). "Perspectives on coastal and marine hazards and disasters," in *Coastal Marine Hazards, Risks, and Disasters*, eds J. F. Shroder, J. T. Ellis, and D. J. Sherman (Amsterdam: Elseiver).

Ezer, T., Atkinson, L. P., Corlett, W. B., and Blanco, J. L. (2013). Gulf Stream's induced sea level rise and variability along the U.S. mid-Atlantic coast. *J. Geophys. Res. Oceans* 118, 685–697. doi: 10.1002/jgrc.20091

Federal Emergency Management Agency (FEMA) (2016). *Guidance for Flood Risk Analysis and Mapping Coastal Flood Frequency and Extreme Value* Analysis. FEMA.

Garner, J., Mann, M. E., Emanuel, K. A., Kopp, R. E., Lin, N., Alley, R. B., et al. (2017). Impact of climate change on New York City's coastal flood hazard: Increasing flood heights from the preindustrial to 2300 CE. *Proc. Natl. Acad. Sci. USA*. 114, 11861–11866. doi: 10.1073/pnas.1703568114

Grinsted, A., and Christensen, J. H. (2021). The transient sensitivity of sea level rise. *Ocean Sci.* 17, 181–186. doi: 10.5194/os-17-181-2021

Grinsted, A., Moore, J. C., and Jevrejeva, S. (2012). Homogeneous record of Atlantic hurricane surge threat since 1923. *PNAS* 109, 19601–19605. doi: 10.1073/pnas.1209542109

G'Sell, M. G., Wager, S., Chouldechova, A., and Tibshirani, R. (2016). Sequential selection procedures and false discovery rate control. *J. R. Stat. Soc. Ser. B* 2016, 423–444. doi: 10.1111/rssb.12122

Hall, J. A., Gill, S., Obeysekera, J., Sweet, W., Knuuti, K., and Marburger, J. (2016). *Regional Sea Level Scenarios for Coastal Risk Management: Managing the Uncertainty of Future Sea Level Change and Extreme Water Levels for Department of Defense Coastal Sites Worldwide*. U.S. Department of Defense, Strategic Environmental Research and Development Program.

Hallegatte, S., Green, C., Nicholls, R. J., and Corfee-Morlot, J. (2013). Future flood losses in major coastal cities. *Nat. Clim. Change* 3:802. doi: 10.1038/nclimate1979

Hamlington, B. D., Leben, R. R., Kim, K.-Y., Nerem, R. S., Atkinson, L. P., and Thompson, P. R. (2015). The effect of the El Niño-Southern Oscillation on U.S. regional and coastal sea level. *J. Geophys. Res. Oceans* 120, 3970–3986. doi: 10.1002/2014JC010602

Harris, D. L. (1991). "Reproducibility of the harmonic constants," in *Tidal Hydrodynamics*, ed B. P. Parker (New York, NY: Wiley), 753–771.

Hinkel, J., Lincke, D., Vafeidis, A. T., Perrette, M., Nicholls, R. J., Tol, R. S., et al. (2014). Coastal flood damage and adaptation costs under 21st century sea-level rise. *Proc. Natl. Acad. Sci. USA* 111, 3292–3297. doi: 10.1073/pnas.1222469111

Hirsch, M. E., Degaetano, A. T., and Colucci, S. J. (2001). An east coast winter storm climatology. *J. Clim*. 14, 882–899. doi: 10.1175/1520-0442(2001)014andlt;0882:AECWSCandgt;2.0.CO;2

Holgate, S. J., Matthews, A., Woodworth, P. L., Rickards, L. J., Tamisiea, M. E., Bradshaw, E., et al. (2013). New data systems and products at the permanent service for mean sea level. *J. Coast. Res*. 29, 493–504. doi: 10.2112/JCOASTRES-D-12-00175.1

Johnson, Z. P. (2013). *Climate Change and Coast Smart Construction: Infrastructure Siting and Design Guidelines*. Annapolis, MD: Maryland Department of Natural Resources.

Knutson, T., Camargo, S. J., Chan, J. C. L., Emanuel, K., Ho, C.-H., Kossin, J., et al. (2019). Tropical cyclones and climate change assessment: Part I: detection and attribution. *Bull. Am. Meteorol. Soc*. 100, 1987–2007. doi: 10.1175/BAMS-D-18-0189.1

Knutson, T., Camargo, S. J., Chan, J. C. L., Emanuel, K., Ho, C.-H., Kossin, J., et al. (2020). Tropical cyclones and climate change assessment: Part II: projected response to anthropogenic warming. *Bull. Am. Meteorol. Soc.* 10, E303–E322. doi: 10.1175/BAMS-D-18-0194.1

Kopp, R. E. (2013). Does the mid-Atlantic United States sea level acceleration hot spot reflect ocean dynamic variability? *Geophys. Res. Lett*. 40, 3981–3985. doi: 10.1002/grl.50781

Kopp, R. E., Gilmore, E. A., Little, C. M., Lorenzo-Trueba, J., Ramenzoni, V. C., and Sweet, W. V. (2019). Usable science for managing the risks of sea-level rise. *Earth's Fut.* 7, 1235–1269. doi: 10.1029/2018EF001145

Kopp, R. E., Hayhoe, K., Easterling, D. R., Hall, T., Horton, R., Kunkel, K. E., et al. (2017). "Potential surprises—compound extremes and tipping elements," in *Climate Science Special Report: Fourth National Climate Assessment, Volume I*, eds. D. J. Wuebbles, D. W. Fahey, K. A. Hibbard, D. J. Dokken, B. C. Stewart, and T. K. Maycock (Washington, DC: U.S. Global Change Research Program), 411–429. doi: 10.7930/J0GB227J

Kossin, J. P. (2018). A global slowdown of tropical-cyclone translation speed. *Nature* 558, 104–107. doi: 10.1038/s41586-018-0158-3

Kossin, J. P., Hall, T., Knutson, T., Kunkel, K. E., Trapp, R. J., Waliser, D. E., et al. (2017). "Extreme storms," in *Climate Science Special Report: Fourth National Climate Assessment, Volume I*, eds D. J. Wuebbles, D. W. Fahey, K. A. Hibbard, D. J. Dokken, B. C. Stewart, and T. K. Maycock (Washington, DC: U.S. Global Change Research Program), 257–276.

Lee, S. B., Li, M., and Zhang, F. (2017). Impact of sea level rise on tidal range in Chesapeake and Delaware Bays. *J. Geophys. Res. Oceans* 122, 3917–3938. doi: 10.1002/2016JC012597

Lin, N., Kopp, R. E., Horton, B. P., and Donnelly, J. P. (2016). Hurricane Sandy's flood frequency increasing from 1800 to 2100. *Proc. Natl. Acad. Sci. USA* 14, 12071–12075. doi: 10.1073/pnas.1604386113

Little, C. M., Hu, A., Hughes, C. W., McCarthy, G. D., Piecuch, C. G., Ponte, R. M., et al. (2019). The relationship between U.S. East Coast Sea Level and the Atlantic meridional overturning circulation: a review. *J. Geophys. Res. Oceans* 124:9. doi: 10.1029/2019JC015152

Mawdsley, R. J., and Haigh, I. D. (2016). Spatial and temporal variability and long-term trends in skew surges globally. *Front. Mar. Sci.* 3, 1–29. doi: 10.3389/fmars.2016.00029

Merrifield, M. A., Genz, A. S., Kontoes, C. P., and Marra, J. J. (2013). Annual maximum water levels from tide gauges: Contributing factors and geographic patterns. *J Geophy Res: Oceans*, 118:2535–2546. doi: 10.1002/jgrc.20173

Moftakhari, H. R., AghaKouchak, A., Sanders, B. F., and Matthew, R. A. (2017). Cumulative hazard: the case of nuisance flooding. *Earth's Fut.* 5, 214–223. doi: 10.1002/2016EF000494

Muis, S., Irazoqui, A. M., Dullaart, J., de Lima, R. J., Madsen, K. S., Su, J., et al. (2020). A high-resolution global dataset of extreme sea levels, tides, and storm surges, including future projections. *Front. Mar. Sci.* 7:263. doi: 10.3389/fmars.2020.00263

Murakami, H., Delworth, T. L., Cooke, W. F., Zhao, M., Xiang, B., and Hsu, P. C. (2020). Detected climatic change in global distribution of tropical cyclones. *PNAS* 117, 10706–10714. doi: 10.1073/pnas.1922500117

NOAA CO-OPS. (2007). *Tidal Analysis and Prediction.* NOAA Special Publication National Ocean Service (NOS) Center for Operational Oceanographic Products and Services (CO-OPS).

NOAA CO-OPS. (2020a). *Sea Level Trends*. NOAA National Ocean Service Center for Operational Oceanographic Products and Services (CO-OPS). Available online at: https://tidesandcurrents.noaa.gov/sltrends/ (accessed August 18, 2020).

NOAA CO-OPS. (2020b). *API for Data Retrieval*. NOAA National Ocean Service Center for Operational Oceanographic Products and Services (CP-OPS). Available online at: https://api.tidesandcurrents.noaa.gov/api/prod/ (accessed April, 9, 2020).

NOAA CO-OPS. (2020c). *NOAA Tide Predictions.* NOAA National Ocean Service Center for Operational Oceanographic Products and Services (CO-OPS). Available online at: https://tidesandcurrents.noaa.gov/tide_predictions.html (accessed April 9, 2020).

NOAA NWLON (2020). *NOAA National Ocean Service National Water Level Observation Network (NWLON).* Available online at: https://www.tidesandcurrents.noaa.gov/nwlon.html (accessed August 18, 2020).

NOAA PORTS (2020). *National Ocean Service Physical Oceanographic Real-Time System (PORTS).* Available online at: https://tidesandcurrents.noaa.gov/ports.html (accessed August 18, 2020).

Oppenheimer, M., Glavovic, B. C., Hinkel, J., van de Wal, R., Magnan, A. K., Abd-Elgawad, A., et al. (2019). "Sea level rise and implications for low-lying islands, coasts and communities," *in IPCC Special Report on the Ocean and Cryosphere in a Changing Climate*, eds H.-O. Pörtner, D. C. Roberts, V. Masson-Delmotte, P. Zhai, M. Tignor, E. Poloczanska, et al. (Geneva:IPCC).

Partnership for the Delaware Estuary (PDE) (2017). "Technical Report for the Delaware Estuary and Basin 2017," in *PDE Report No. 17-07*, eds L. Haaf, S. Demberger, D. Kreeger, and E. Baumbach (Wilmington, DE: PDE).

Piecuch, C. G. P., Huybers, C. C., Hay, A. C., Kemp, C. M., Little, J. X., Mitrovica, R. M., Ponte, and, M. P., Tingley (2018). Origin of spatial variation in US East Coast sea-level trends during 1900–2017. *Nature* 564, 400–404. doi: 10.1038/s41586-018-0787-6

Pugh, D., and Woodworth, P. (2014). *Sea-Level Science: Understanding Tides, Surges, Tsunamis and Mean Sea-Level Changes*. Cambridge: Cambridge University Press.

Rahmstorf, S. (2017). Rising hazard of storm-surge flooding. *PNAS Comment*. 114, 11806–11808. doi: 10.1073/pnas.1715895114

Rappaport, E. (2014). Fatalities in the United States from Atlantic Tropical cyclones new data and interpretation. *Bull. Am. Meteor. Soc. Insights Innov*. 95, 341–346. doi: 10.1175/BAMS-D-12-00074.1

Rashid Md, M., Wahl, T., Chambers, D. P., Calafat, F. M., and Sweet, W. V. (2019). An extreme sea level indicator for the contiguous United States coastline. *Sci. Data* 6:326. doi: 10.1038/s41597-019-0333-x

Ribatet, M., and Dutang, C. (2019). *POT: Generalized Pareto Distribution and Peaks Over Threshold.* R package version 1.1–7.

Ross, A. C., Najjar, R. G., Li, M., Lee, S. B., Zhang, F., and Liu, W. (2017). Fingerprints of sea level rise on changing tides in the Chesapeake and Delaware Bays. *J. Geophys. Res. Oceans* 122, 8102–8125. doi: 10.1002/2017JC012887

Sallenger, A. H., Doran, K. S., and Howd, P. A. (2012). Hotspot of accelerated sea-level rise on the Atlantic coast of North America. *Nat. Clim. Change* 2, 884–888. doi: 10.1038/nclimate1597

Sanchez, J. R., Kauffman, G., Reavy, K., Homsey, A. (2012). *"Chapter 1.7—Natural Capital Value" in Technical Report for the Delaware Estuary and Basin*. Partnership for the Delaware Estuary. PDE Report No. 17-07, 70–75.

Scarrott, C., and MacDonald, A. (2012). A review of extreme value threshold estimation and uncertainty quantification. *Stat. J.* 10, 33–60. Available online at: https://www.ine.pt/revstat/pdf/rs120102.pdf

Smith, A. B. (2021). *2020 U.S. Billion-Dollar Weather and Climate Disasters in Historical Context. Beyond the Data.* Available online at: https://www.climate.gov/news-features/blogs/beyond-data/2020-us-billion-dollar-weather-and-climate-disasters-historical (accessed March 1, 2021).

Stephens, S. A., Bell, R. G., and Haigh, I. D. (2020). Spatial and temporal analysis of extreme storm-tide and skew-surge events around the coastline of New Zealand. *Nat. Hazards Earth Syst. Sci.* 20, 783–796. doi: 10.5194/nhess-20-783-2020

Sweet, W., Dusek, G., Carbin, G., Marra, J., Marcy, D., and Simon, S. (2020). *2019 State of U.S. High Tide Flooding with a 2020 Outlook*. NOAA Technical Report NOS CO-OPS 092.

Sweet, W. V., Dusek, G., Obeysekera, J., and Marra, J. J. (2018). *Patterns and Projections of High Tide Flooding Along the U.S.* Coastline Using a Common Impact Threshold. NOAA Technical Report NOS CO-OPS 086.

Sweet, W. V., Horton, R. M., Kopp, R. E., LeGrande, A. N., and Romanou, A. (2017a). "Sea level rise," in Climate Science Special Report: *Fourth* National Climate Assessment, Volume I, eds D. J. Wuebbles, D. W. Fahey, K. A. Hibbard, D. J. Dokken, B. C. Stewart, and T. K. Maycock (Washington, DC: U.S. Global Change Research Program), 333–363.

Sweet, W. V., Kopp, R. E., Weaver, C. P., Obeysekera, J., Horton, R. M., Thieler, E. R., and Zervas, C. (2017b). *Global and Regional Sea Level Rise Scenarios for the United States*. NOAA Technical Report NOS CO-OPS 083.

Sweet, W. V., Park, J., Marra, J. J., Zervas, C. E., and Gill, S. (2014). *Sea Level Rise and Nuisance Flood Frequency Changes around the United States.* NOAA Technical Report NOS CO-OPS 073.

Taherkhani, M., Vitousek, S., Barnard, P., Frazer, N., Anderson, T., and Fletcher, C. (2020). Sea-level rise exponentially increases coastal flood frequency. *Sci. Rep.* 10, 1–17. doi: 10.1038/s41598-020-62188-4

Tawn, J. A. (1988). An extreme-value theory modle for dependent observations. *J. Hydrol.* 101, 227–250. doi: 10.1016/0022-1694(88)90037-6

Tebaldi, C., Strauss, B. H., and Zervas, C. E. (2012). Modeling sea level rise impacts on storm surges along US coasts. *Environ. Res. Lett.* 7:014032. doi: 10.1088/1748-9326/7/1/014032

Thompson, P. R. G. T., Mitchum, C., Vonesch, and, J., Li (2013). Variability of winter storminess in the eastern United States during the twentieth century from tide gauges. *J. Climatol.* 26, 9713–9726. doi: 10.1175/J.C.L.I.-D.-12-00561.1

U. S. Army Corps of Engineers (2014). *North Atlantic Coast Comprehensive Study (NACCS), State Chapter D-7: State of Delaware*. US ACE.

Wahl, T., and Chambers, D. P. (2015). Evidence for multidecadal variability in US extreme sea level records. *J. Geophys. Res. Oceans* 120, 1527–1544. doi: 10.1002/2014JC010443

Wahl, T., Haigh, I. D., Nicholls, R. J., Arns, A., Dangendorf, S., Hinkel, J., and Slangen, A. B. A. (2017). Understanding extreme sea levels for broad-scale coastal impact and adaptation analysis. *Nat. Commun.* 8:16075. doi: 10.1038/ncomms16075

Walton, T. L. Jr. (2000). Distributions for storm surge extremes. *Ocean Eng.* 27, 1279–1293. doi: 10.1016/S0029-8018(99)00052-9

Wang, S., and Toumi, R. (2021). Recent migration of tropical cyclones toward coasts. *Science* 371, 514–517. doi: 10.1126/science.abb9038

Weinkle, J., Landsea, C., Collins, D., Musulin, R., Crompton, R. P., Klotzbach, P. K., et al. (2018). Normalized hurricane damage in the continental United States 1900–2017. *Nat. Sustain.* 1, 808–813. doi: 10.1038/s41893-018-0165-2

Weissman, I. (1978). Estimation of parameters and larger quantiles based on the k-largest observations. *J. Am. Stat. Assoc*. 73, 812–815. doi: 10.2307/2286285

Williams, J., Horsburgh, K. J., Williams, J. A., and Proctor, R. N. F. (2016). Tide and skew surge independence: new insights for flood risk. *Geophys. Res. Lett*. 43, 6410–6417. doi: 10.1002/2016GL069522

Wong, K.–C., and Münchow, A. (1995). Buoyancy forced interaction between estuary and inner shelf: observation. *Continent. Shelf Res*. 15, 59–88. doi: 10.1016/0278-4343(94)P1813-Q

Wong, T. E., Torline, T., and Zhang, M. (2020). *Evidence for Increasing Frequency of Extreme Coastal Sea Levels*. arXiv [Preprint]. Available online at: https://arxiv.org/abs/2006.06804 (accessed January 29, 2021).

Yang, H., Lohmann, G., Lu, J., Gowan, E. J., Shi, X., Liu, J., and Wang, Q. (2020). Tropical expansion driven by poleward advancing mid-latitude meridional temperature gradients. *J. Geophys. Res. Atmos*. 125:e2020JD033158. doi: 10.1029/2020JD033158

Zhong, L., and Li, M. (2006). Tidal energy fluxes and dissipation in the Chesapeake Bay. *Continent. Shelf Res*. 26, 752–770. doi: 10.1016/j.csr.2006.02.006

Conflict of Interest: The authors declare that the research was conducted in the absence of any commercial or financial relationships that could be construed as a potential conflict of interest.

Publisher's Note: All claims expressed in this article are solely those of the authors and do not necessarily represent those of their affiliated organizations, or those of the publisher, the editors and the reviewers. Any product that may be evaluated in this article, or claim that may be made by its manufacturer, is not guaranteed or endorsed by the publisher.

Advantages of publishing in Frontiers

OPEN ACCESS
Articles are free to read for greatest visibility and readership

FAST PUBLICATION
Around 90 days from submission to decision

HIGH QUALITY PEER-REVIEW
Rigorous, collaborative, and constructive peer-review

TRANSPARENT PEER-REVIEW
Editors and reviewers acknowledged by name on published articles

Frontiers
Avenue du Tribunal-Fédéral 34
1005 Lausanne | Switzerland

Visit us: www.frontiersin.org
Contact us: frontiersin.org/about/contact

REPRODUCIBILITY OF RESEARCH
Support open data and methods to enhance research reproducibility

DIGITAL PUBLISHING
Articles designed for optimal readership across devices

FOLLOW US
@frontiersin

IMPACT METRICS
Advanced article metrics track visibility across digital media

EXTENSIVE PROMOTION
Marketing and promotion of impactful research

LOOP RESEARCH NETWORK
Our network increases your article's readership